UNIVERSITAT DE BARCELONA

The origin and tectono-sedimentary structure of the Alboran Basin

Laura Gómez de la Peña

ADVERTIMENT. La consulta d’aquesta tesi queda condicionada a l’acceptació de les següents condicions d'ús: La difusió d’aquesta tesi per mitjà del servei TDX (**www.tdx.cat**) i a través del Dipòsit Digital de la UB (**diposit.ub.edu**) ha estat autoritzada pels titulars dels drets de propietat intel·lectual únicament per a usos privats emmarcats en activitats d’investigació i docència. No s’autoritza la seva reproducció amb finalitats de lucre ni la seva difusió i posada a disposició des d’un lloc aliè al servei TDX ni al Dipòsit Digital de la UB. No s’autoritza la presentació del seu contingut en una finestra o marc aliè a TDX o al Dipòsit Digital de la UB (framing). Aquesta reserva de drets afecta tant al resum de presentació de la tesi com als seus continguts. En la utilització o cita de parts de la tesi és obligat indicar el nom de la persona autora.

ADVERTENCIA. La consulta de esta tesis queda condicionada a la aceptación de las siguientes condiciones de uso: La difusión de esta tesis por medio del servicio TDR (**www.tdx.cat**) y a través del Repositorio Digital de la UB (**diposit.ub.edu**) ha sido autorizada por los titulares de los derechos de propiedad intelectual únicamente para usos privados enmarcados en actividades de investigación y docencia. No se autoriza su reproducción con finalidades de lucro ni su difusión y puesta a disposición desde un sitio ajeno al servicio TDR o al Repositorio Digital de la UB. No se autoriza la presentación de su contenido en una ventana o marco ajeno a TDR o al Repositorio Digital de la UB (framing). Esta reserva de derechos afecta tanto al resumen de presentación de la tesis como a sus contenidos. En la utilización o cita de partes de la tesis es obligado indicar el nombre de la persona autora.

WARNING. On having consulted this thesis you’re accepting the following use conditions: Spreading this thesis by the TDX (**www.tdx.cat**) service and by the UB Digital Repository (**diposit.ub.edu**) has been authorized by the titular of the intellectual property rights only for private uses placed in investigation and teaching activities. Reproduction with lucrative aims is not authorized nor its spreading and availability from a site foreign to the TDX service or to the UB Digital Repository. Introducing its content in a window or frame foreign to the TDX service or to the UB Digital Repository is not authorized (framing). Those rights affect to the presentation summary of the thesis as well as to its contents. In the using or citation of parts of the thesis it’s obliged to indicate the name of the author.

The origin and tectono-sedimentary structure of the Alboran Basin

Memoria de tesis doctoral presentada por

Laura Gómez de la Peña

Para optar al Grado de Doctor por la Universitat de Barcelona

Esta memoria se ha llevado a cabo dentro del programa de doctorado de Ciències de la Terra de la Universitat de Barcelona, bajo la dirección del Dr. César Rodríguez Ranero y la Dra. Eulàlia Gràcia Mont, y ha sido tutelada por la Dra. Eulàlia Masana Closa.

Barcelona, Mayo de 2017

Mai enrera

Agradecimientos / Acknowledgments

En primer lugar, quiero dar las gracias a mis dos directores de tesis, César y Eulàlia, por todo su tiempo, su dedicación y la confianza puesta en mí desde el primer momento. Gracias por haberme dado esta oportunidad (y tantas otras) y ayudarme y apoyarme durante todo el camino.

A Ben de Mol y Alcinoe Calahorrano, por todas las horas que han pasado enseñándome los misterios del procesado. Gracias por hacer vuestros mis problemas con el Claritas y por estar siempre dispuestos a echarme una mano. A mi tutora en la UB, Eulàlia Masana, por ser tan resolutiva y por su paciencia con los trámites administrativos.

A mis supervisores y compañeros de estancia. Por un lado, a Michella Giustiniani y Umberta Tinivella, porque además de enseñarme ciencia convirtieron Trieste en mi segunda casa. *Grazie mille!* A Héctor, por descubrirme Trieste, por sus consejos y por convertirse en un amigo en tan poco tiempo. Por otro lado, a Dirk Klaeschen, por toda su paciencia y su física, y a Ingo Grevemeyer, por estar siempre dispuesto a discutir los datos y por enseñarnos que Kiel no es el fin del mundo. A Gerd, por poner un poco de luz en el invierno del norte.

Volviendo al principio, a José Luis Granja y a Pilar Llanes, y en general al departamento de Geodinámica de la Complutense, por animarme a venir aquí y porque siempre me reciben con una sonrisa. Gracias por descubrirme este mundo y seguir acompañándome en el camino.

A mi compañera inseparable de aventuras, Marina, porque juntas hemos llegado hasta aquí, y juntas seguiremos el viaje. *Gràcies per estar sempre al meu costat, literal i figuradament, i per tot lo que m'has ensenyat (inclòs que és possible guanyar al Kracken!!).* A Clàudia, por todo su apoyo, su energía y su optimismo. *Merci per els vespres de teràpia, per tots els somriures i els ànims quan mes em feien falta.* A Sergio, por ser geólogo-informático y dedicar su tiempo a facilitarnos la vida. A Estela, Miquel, Albert, Slaven y Dani, por todos los momentos compartidos, que espero sigan siendo muchos más. A todos ellos, porque han pasado de ser compañeros de trabajo a ser amigos, y han convertido Barcelona en mi hogar. Y a todo el BCSI en general, porque de todos he aprendido algo y han sido muchos los cafés, las tardes de cervezas, las ilusiones y las risas compartidas hasta llegar aquí.

No me puedo olvidar de mis grandes apoyos, Carlos y Leticia, porque mientras brindemos por Skype no habrá distancia que nos separe. Gracias por estar ahí en los malos momentos, y sobre todo, gracias por seguir compartiendo conmigo los buenos. Os quiero.

A mis princesas de barrio, Elena y Lydia, porque aunque vayamos por caminos diferentes, seguimos buscando puntos de encuentro. Y a Saray, porque su fuerza y su positivismo son contagiosos.

A mi familia, con un cariño muy especial a mis abuelos, pero sobre todo a mis padres, que aunque nunca me han entendido del todo me han apoyado incondicionalmente, y han hecho de padres, de sucursal de banco, de psicólogos, de chico de los recados y de todo lo que ha hecho falta con tal de verme feliz.

A todos los que de alguna u otra forma habéis formado parte de esta travesía, GRACIAS.

Funding

The author of this thesis has benefited from a four-year "Formación de Profesorado Universitario" (FPU) fellowship (reference AP2012-1579) from "Ministerio de Educación, Cultura y Deporte" (MECD) between 2013 and 2017. The author was also granted, with two stays: two months at the Istituto nazionale di oceanografia e di geofisica sperimentale (OGS) (Trieste, Italy), financed by a Short-Term Scientific Missions inside the COST Action Flows (COST-STSM-ECOST-STSM-ES1301-180814-045667), and a short stay within the framework of the FPU of three months at the Department of Marine Geodynamics of the GEOMAR Helmholtz-Centre for Ocean Research Kiel (Kiel, Germany) (EST14/00512).

The unpublished data used in this study and different parts of the work have been supported within the framework of the ESF TopoEurope TOPOMED project (CGL2008–03474-E/BTE), and National Projects EVENT-DEEP (CGL2006–12861-C02- 02) and SHAKE (CGL2011–30005-C02-02).

This work was carried out within the Grup de Recerca Consolidat de la Generalitat de Catalunya Barcelona Centre for Subsurface Imaging (B-CSI) (2014SGR940). The group computer and software facilities have been largely funded with the projects Kaleidoscope, CO-DOS, Geomargen-1, and CODOS-Phase2 funded by Repsol.

Contents

PART I: INTRODUCTION

PART II: DATA AND METHODS

PART III: RESULTS

PART IV: DISCUSSION

PART V: CONCLUSIONS & FORWARD LOOK

ANNEXES

Summary

In this PhD thesis I present a geological and geophysical study of the westernmost Mediterranean basin: the Alboran Basin. This basin is located between the Iberian Peninsula and North Africa, and it is surrounded by the Betics and Rif orogenic ranges. Along the Alboran basin, runs the boundary between the Iberian and African tectonic plates. Although several studies have been carried out in this area, the processes that led to the formation of the basin in the present-day compressive setting, and the prior processes that controlled the deep structure of the basin and its later evolution still remained unclear. This study aims to: 1) unveil the nature of the basement of the basin, 2) define a coherent seismostratigraphy for the entire basin and analyse the evolution of the basin on the basis of the sedimentary record, 3) explore the northeaster transition between the Alboran Basin and the Algero-Balearic Basin through the study of the Palomares Margin, and 4) characterize two of the most prominent tectonic structures in the area that have been poorly studied, the Yusuf Fault and the Alboran Ridge front fault. The results of this thesis will be integrated in a geodynamic model of the area, and will help to improve the regional seismic and tsunami hazard assessment model.

In order to perform a whole-basin scale study of the Alboran Basin, we have used a comprehensive grid of Multichannel Seismic reflection (MCS) profiles. This seismic dataset has been acquired in the frame of different projects, most of them acquired by our group (TOPOMED, EVENT-DEEP, and IMPULS) and completed with vintage data (CAB, ESCI, CONRAD). The main dataset presented in this thesis comes from the TOPOMED-GASSIS cruise (October 2011, P.I: E. Gràcia and C. Ranero). During this cruise, new deep-penetration seismic data was acquired using leading edge technology that allows the imaging of the basin at a crustal scale. For the first time, the new deep multichannel seismic equipment of the RV "Sarmiento de Gamboa" was used for acquisition of the seismic survey. Two high volume G-gun arrays (162/140 bar, 2000/2500 psi) and up to 6 km long Sercel multichannel digital streamer (408/480 active channels) were towed behind the vessel. The result is a comprehensive dataset of multichannel seismic profiles with unprecedented quality. This dataset allowed us to use state of the art processing and imaging techniques to obtain a deep image of the tectonic structures, and also a relatively good resolution of the sedimentary infill of the basin. The main steps of the processing flow in time domain include: 1) minimum-phase conversion, 2) real geometry definition accounting for streamer feathering, 3) spherical divergence correction, 4) predictive deconvolution in Tau-P domain (to eliminate the bubble and short periods multiple reverberations), 5) surface consistent deconvolution, 6) Surface Related multiple elimination (SRME) demultiple, 7) Radon filter demultiple, normal-move-out correction based on velocity semblance analysis, 8) Dip Move Out (DMO) correction, 9) stretching mute, 10) amplitude recovery, 11) time migration and 12) time and spatial variant band-pass filter.

To complete this study, we have also processed the EVENT-DEEP and ESCI profiles, re-processed the CONRAD profiles, and analyzed and interpreted the whole dataset. We have performed Pre-Stack Depth Migrations to selected profiles to obtain the real geometry of the structures, and we have also integrated wide angle seismic (WAS), bathymetric, well and dredge data in this work.

The results reveal that three different crusts coexists in the Alboran Basin: a) a thin continental crust underneath the West Alboran and Malaga basins, b) a magmatic arc crust in the central part of the Alboran Sea and the East Alboran Basin, and c) the North African continental crust, below the Pytheas and Habibas basins. The basin is configured in a fore-arc basin (West Alboran and Malaga basins), a magmatic arc

(central and east Alboran), being the back-arc of the system the easternmost part of the East Alboran Basin and mainly, the Algero-Balearic Basin.

The seismostratigraphic study supported an early Miocene initiation of the extension in the West Alboran and Malaga basins, followed by a Langhian-Serravallian extension in the North African margin. These depocenters were separated by a lithospheric strike-slip fault that allows the independent evolution of each of them, and the westward migration of the West Alboran and Malaga basins. In the Tortonian, magmatic activity linked to the subduction system led to the formation of the volcanic arc. In the Messinian, extensional processes ended and the contractive reorganization of the basin occurred. The present-day active tectonic structures were mainly formed during the Pliocene, following weak lithospheric zones that coincide with the edges of the crustal domains.

The geomorphologic and tectonic study of the Palomares margin supports that this contractive reorganization is not a widespread process, as only few minor faults are reactivated and most of the deformation is gathered at crustal faults. This hypothesis is confirmed by the characterizations of the Yusuf Fault and the Alboran Ridge Front Fault. The results on both fault systems are coherent, and point out a minimum total slip of ~20 km in a SE-NW direction since the top of the Messinian (5.3 Ma). Taking into account the convergence rates between the Iberian and African plates, the total shortening between these two plates since the Messinian is ~24 km, supporting that most of the strain is accommodated by these two faults. These results highlight the importance of a further seismogenic potential characterization of the area to improve the earthquake and tsunami hazard models in the region.

The integration of all the results presented in this thesis together with the most recent tomographic studies (i.e., TOPOIBERIA project), offers the opportunity to review the existing geodynamic models of the area. The main aspects that should be explored further are: i) the Iberian plate subduction below the African plate, ii) the observed distribution of the slab, iii) the different crustal domains coexisting offshore and the Moho depth distribution on-land, and iv) the basin evolution.

We conclude that the formation of the Alboran basin took place during the Miocene. The extensional processes were controlled by the geodynamics and evolution of the subduction system, including the westward slab roll-back and lithosphere tearing. At the end of the Messinian, extension in the basin finished as a consequence of the ceased of the subduction. The Plio-Quaternary represents the deformational stage of the basin, led by the Iberian – African plate convergence. The distribution of the active tectonic structures in this compressive setting has been controlled by the inherited lithospheric structure, which defines the areas of weaknesses where these faults developed.

Presentation of this thesis

i. Motivation

The main motivation of this study is to advance in the understanding of the tectonic and sedimentary processes that led to the formation of the Alboran Basin, and the deformation process that occurred later due to the convergence between the African and Eurasian plates.

The Alboran basin has a complex geological evolution. It was mainly formed during the Miocene by extensive processes in a plate convergent setting (e.g. Comas et al., 1999; Gelabert et al., 2002; Rosenbaum et al., 2002; Faccena et al., 2004; Booth Rea et al., 2007). However, the evolution and processes that led to basin formation and current deformation are still under discussion.

The Alboran Basin (Western Mediterranean) is located between the Iberian Peninsula and North Africa. This area is characterized by a diffuse deformation between Iberia and Africa. This region is not a "typical" plate boundary where most of the deformation is accommodated by a series of well-defined structures, but it corresponds to a wide deformation zone, related to the NW-SE trending convergence (4.5 – 5.6 mm/yr) between the African and Eurasian plates (McClusky et al., 2003; Nocquet, 2012). Deformation here is distributed over a large number of faults that in cases strand offshore and onshore regions (e.g. Sanz de Galdeano et al., 1990; Andeweg and Cloetingh, 2001; Gràcia et al., 2006). Active structures in the south Iberian Margin (Gulf of Cadiz and Alboran Sea) are of great interest because they imply a seismic and tsunami hazard for the adjacent regions. Seismicity in the region is mainly characterized by shallow earthquakes of low to moderate magnitude (Mw < 6.4), however, historical records indicate that large magnitude earthquakes (Mw ≥ 8.0 and MSK Intensity X-XI) have also ocurred in this region (e.g. Gràcia et al., 2003a, 2006, 2012; Zitellini et al., 2009; Bartolome et al., 2012; Martínez-Loriente et al., 2013, 2016). These events with long recurrence periods possibly of >1000 years), involve a seismic and tsunamigenic hazard for a region that cannot be characterized only with the instrumental records (< 100 years). Thus, to analyse the seismic hazard of this area is necessary to study the active faults, although they may not be currently associated to significant seismic activity.

With the aim to improve the knowledge of the sedimentary and tectonic processes going on in the Alboran basin, the TOPOMED-GASSIS cruise took place in October 2011. The main goal of the TOPOMED-GASSIS cruise was to characterize the crustal and upper mantle structure of the Gibraltar Arc and Alboran Basin and to link recent (post-Tortonian) tectonics and vertical movements with the deep lithospheric structure. To accomplish this goal, the modern multichannel seismic equipment of the RV "Sarmiento de Gamboa" was used to acquire the seismic data. The result was a regional deep-penetration high-quality dataset, which allowed us to use state of the art processing and imaging techniques to obtain the deep tectonic structure of this region. The combination with other modern shallower-penetration datasets (e.g. EVENT-DEEP survey) and available (RV Conrad survey) and reprocessed datasets (ESCI-Alboran survey) has allowed us to study novel aspects of the Alboran Basin formation and evolution.

The analysis of this brand new data provide an opportunity to characterize the tectonic, sedimentary and magmatic structures using seismic images of good resolution and deep penetration, that vintage seismic datasets fail to provide. Results of this work also shed a new light into the regional geodynamic processes and their relation with the lithosphere dynamics.

ii. Objectives

The aim of this work is to characterize the crust, the sedimentary infill and the tectonic structure of the Alboran Sea region, throughout the processing, analysis and interpretation of multichannel seismic profiles. The new dataset has been integrated in the geological and geophysical database available in the area. We have performed a multiscale and multidisciplinary approach of the different observations, focusing on the formation, sedimentary infill and deformation processes that have occurred in the Alboran Basin and neighbouring areas.

The **main goal** of this thesis is to characterize the opening of the Alboran Basin and its later deformation. This goal has been achieved through the study of the crust and upper mantle structure, of the sediment record and its depocenters evolution, and of the tectonic structures. The final objective is to integrate all observations in an updated geodynamic evolution model of the area.

In order to achieve this objective, the following **specific objectives** are proposed:

1) To characterize the crustal structure along the basin

The crust found below the Gibraltar Arc System is believed to be highly heterogeneous. Although Travel Time Tomography studies identify this zone as a complex region, the resolution of these studies fails to determine the different crustal domains below the Alboran Basin and the relation between them. Based on the Multichannel Seismic profiles, we are going to define the different crustal domains below the basin and their transitions. This will allow us to better understand the basin configuration.

2) To define a seismostratigraphic framework for the entire basin, stablishing the correlation between sub-basins

Recent seismostratigraphic studies at the Alboran Basin are usually focus on a particular area (Soto et al., 2010; Martínez-García et al., 2011; Medaouri et al., 2012; Soto et al., 2012; Martínez-García et al., 2013; Medaouri et al., 2014; Do Couto et al., 2016; Moreno et al., 2016). Studies focusing on the entire Miocene evolution of a particular region basin are scarce (Soto et al., 2010; Medaouri et al., 2012; Medaouri et al., 2014, Do Couto et al. 2016), and the ones covering the entire basin present vintage or poorly processed data (Watts et al., 1993; Comas et al., 1999), which resolution is too low for detailed stratigraphy analysis. We propose to unify the seismic stratigraphy for the entire basin, integrating previous studies and well information. This allows the unit correlation between the different depocenters, and to stablish the particular evolution history of each depocenter to finally study the evolution of the entire basin.

3) To characterize the northeastern limit of the Alboran Basin, represented by the Palomares margin

The Palomares margin represents the northeast transition between the Alboran Basin and the Algero-Balearic Basin. The depth crustal structure of this margin has been recently studied by our group (Giaconia et al., 2015), and we focus on the shallower structure of the margin, characterizing the geomorphologic features thanks to a new high-resolution bathymetry, and tectonically active structures linked to geomorphologic features, studying new seismic images. Results shed light on the tectonic and sedimentary recent evolution of the margin and its geodynamics evolution.

4) To characterize the Yusuf Fault

The Yusuf Fault is a first order tectonic structure of the Alboran Basin. However, the evolution history of this fault remains unclear, as previous studies focus on shallow structure during the most recent stages (Martinez Garcia et al., 2011; 2013) or the density of the seismic data used was not enough for detailed fault characterization (Medaouri et al., 2014). In this work, we study the Yusuf Fault deep and shallow structure along basically its entire length to its connection with the Alboran Ridge. This characterization is used to estimate fault displacement along the fault, to understand its role in the current stress regime and to refine the geodynamic model of the area.

5) To characterize the Alboran Ridge

Similarly to the Yusuf Fault, the Alboran Ridge is one of the most prominent structures in the area, although the knowledge of its deepen structure and evolution is limited. We have tried to better characterize this structure through the analysis of the sedimentary record and a quantification of the deformation along the ridge. These results are included in a modified geodynamic model of the area.

All these observations will contribute to a better understanding of the origin and deformation of the Alboran Basin. The results shown in this thesis, together with the most recent results about the mantle configuration and previous studies of kinematic reconstructions and magmatic affinity of crustal domains are integrated in the discussion section (Part IV, this volume) with the aim of integrate all results in a novel geodynamic model of the region.

iii. Organization of this volume

In order to achieve the above objectives and to present the results in a clear structure, we organized this volume in five parts. Each of these parts is subdivided in chapters, and each of the chapters focused on a different topic. This volume is organized on the basis of the following parts and chapters structure:

Part I: Introduction	*Chapter 1:* Basic concepts *Chapter 2:* Geological setting
Part II: Data and methods	*Chapter 3:* Multichannel reflection data *Chapter 4:* Refraction data
Part III: Results	*Chapter 5:* Crustal domains *Chapter 6:* Basin evolution *Chapter 7:* The Palomares margin *Chapter 8:* The Yusuf Fault *Chapter 9:* The Alboran Ridge
Part IV: Discussion	*Chapter 10:* Implications for geodynamic models
Part V: Conclusions and Forward look	*Chapter 11:* Conclusions *Chapter 12:* Forward look
References	
Annexes	*List of acronyms* *Scientific output related with this thesis*

Part I is the introductory section, composed by two chapters. Chapter 1 is about the basic concepts of plate tectonics and brief summary of the main structural elements of a subduction zone. Chapter 2 focuses on the geological setting of the Alboran Basin, with an overview on the Western Mediterranean opening, the unique geodynamic setting of the Alboran Basin, and its tectonic and sedimentary structure.

Part II describes the data and methodology used. It includes two chapters, one for each different type of data used in this thesis and their specific methodology. Chapter 3 presents the multichannel seismic reflection data as well as the processing sequence in time and depth. Chapter 4 includes wide-angle seismic data and processing aimed at imaging.

Results are exposed in **Part III**. This is the main part of this volume, in which processed data are presented, analysed and interpreted. Chapter 5 studies the deep structure of the basin, focusing on the full-crust characteristics. Chapter 6 studies the stratigraphy of the entire basin and the basin evolution. Chapter 7 presents the Palomares margin (north-eastern Alboran Basin in transition to Algerian-South Balearic Basin). This chapter is especially focused on the shallow tectonic and sedimentary structure as the deep configuration of this margin was recently studied by our group (Giaconia et al., 2015). Chapter 8 and 9 focus on two important tectonic structures of the area that were not studied in detail previously: the Yusuf Fault (Chapter 8) and the Alboran Ridge (Chapter 9). Overall, we describe the sedimentary infill of the entire Alboran Basin as a sum of different sub-basins or depocenters, as well as the origin and deformation of the whole basin on the basis of the study of crustal domains and main tectonic structures.

Part IV includes the discussion (Chapter 10). We used this part to discuss the dataset as a whole. In Chapter 10 we discuss the geodynamic models proposed for the Gibraltar Arc system and evaluate them in the light of recent studies and new data, including the new results shown in this thesis. We discuss a geodynamic model for the entire Alboran Basin and discuss how geodynamic processes may relate to lithosphere structure.

Part V comprises conclusions (Chapter 11) and forward look (Chapter 12).

Finally, we have included the bibliographic references quoted in this thesis; and in the **Annexes**, the list of acronyms and the scientific output related with this thesis.

Part I

INTRODUCTION

"Wherever he saw a hole he always
wanted to know the depth of it. To him,
this was important"

Jules Verne
(Journey to the Centre of the Earth)

Chapter 1

Basic concepts

In this Chapter, we introduce basic concepts necessary to understand the geological context of this work. We will present general concepts of plate tectonics, and specifically, we focus on the structure of subduction zones.

1.1. Fundamentals of plate tectonics

The fundamentals of the theory of Plate Tectonics was developed during the 60's (e.g. Heezen, 1960; Dietz, 1961; Vine and Matthews, 1963; Wilson, 1963; Wilson, 1965; Isacks et al., 1968; Le Pichon, 1968; Morgan, 1968), although its fundaments are based on the Continental Drift theory (Wegener, 1915) later supported by paleomagnetic data. Advances in the surveys of the bathymetry of the seafloor confirmed seafloor spreading (e.g. Hess, 1962; Vine and Matthews, 1963), and global seismicity distribution. All these knowledge together with the proposal of convection currents in the mantle as driver mechanism and its capacity to explain paleogeography and paleobiologic data, allowed the general acceptance of the Plate Tectonics Theory in the earlies 70's (Smith, 1973; Cox and Hart, 1986; Hamblin, 1992; Kearey et al., 2009).

In the plate tectonics framework, the external part of the Earth is composed by the lithosphere (Fig. 1.1). This is a rigid layer, under brittle deformation. The lithosphere is made up of a numbers of plates (lithospheric or tectonic plates), moving relative to each other. Most of the plates are large although small ones or "microplates" are also recognized. The lithosphere includes the crust and the uppermost part of the mantle (e.g. Cox and Hart, 1986; Hamblin, 1992). The crust can be divided into two main types in function of its composition: continental crust and oceanic crust. Each of these crustal types presents different characteristics. The continental crust is characterized by an average thickness of 35 km and a mean density of 2.7 g/cm3 (e.g. Christensen et al., 1995; Allaby, 2008). It presents a great variability due to the different composition (sedimentary, metamorphic and igneous rocks) and the variability on the formation processes (melting, crystallization, accretion, metamorphism, magmatism). The continental crust is broadly divided into two layers: the continental upper crust, associated with an average granodiorite composition, and the continental lower crust, closer to an average granulite composition. In contrast, the oceanic crust has a mean thickness of 6-7 km (White et al., 1992). It is generated at the Mid-Oceans Ridges, and it is characterized by layer structure (see Figure 1.2 for details). Oceanic lithosphere is usually the main type of lithosphere recycled in the mantle in the subduction zones.

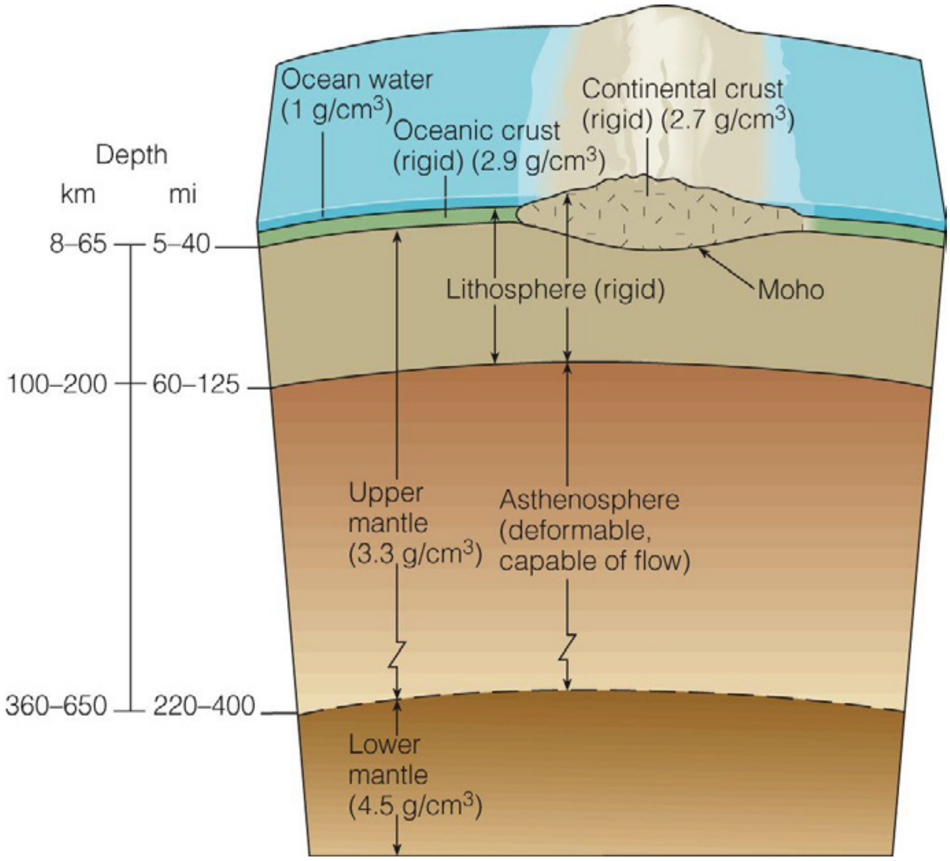

Figure 1.1: *Scheme of the internal structure of the Earth. Extracted from <u>http://www.geogrify.net/GEO1/Lectures/IntroPlanetEarth/FourSpheres.html</u>. Mean thickness (in km and miles) is depicted at the left, and mean density values are shown on the drawing.*

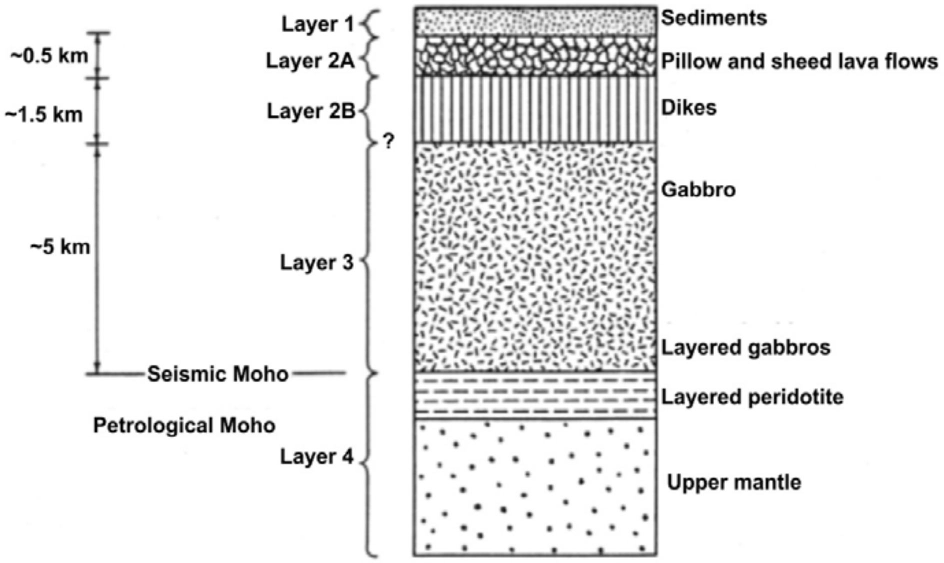

Figure 1.2: *Standard layered structure of oceanic crust (Kennett, 1982). Mean thickness values and oceanic crust composition are detailed for each layer.*

Lithospheric plates are moving above a highly viscous, mechanically weak, low-velocity layer, known as the asthenosphere, which is part of the upper mantle and has a plastic behaviour (e.g. Cox and Hart, 1986; Hamblin, 1992). Tectonic interactions between plates occur at plate boundaries where most seismic and volcanic activity takes place (Fig. 1.3).

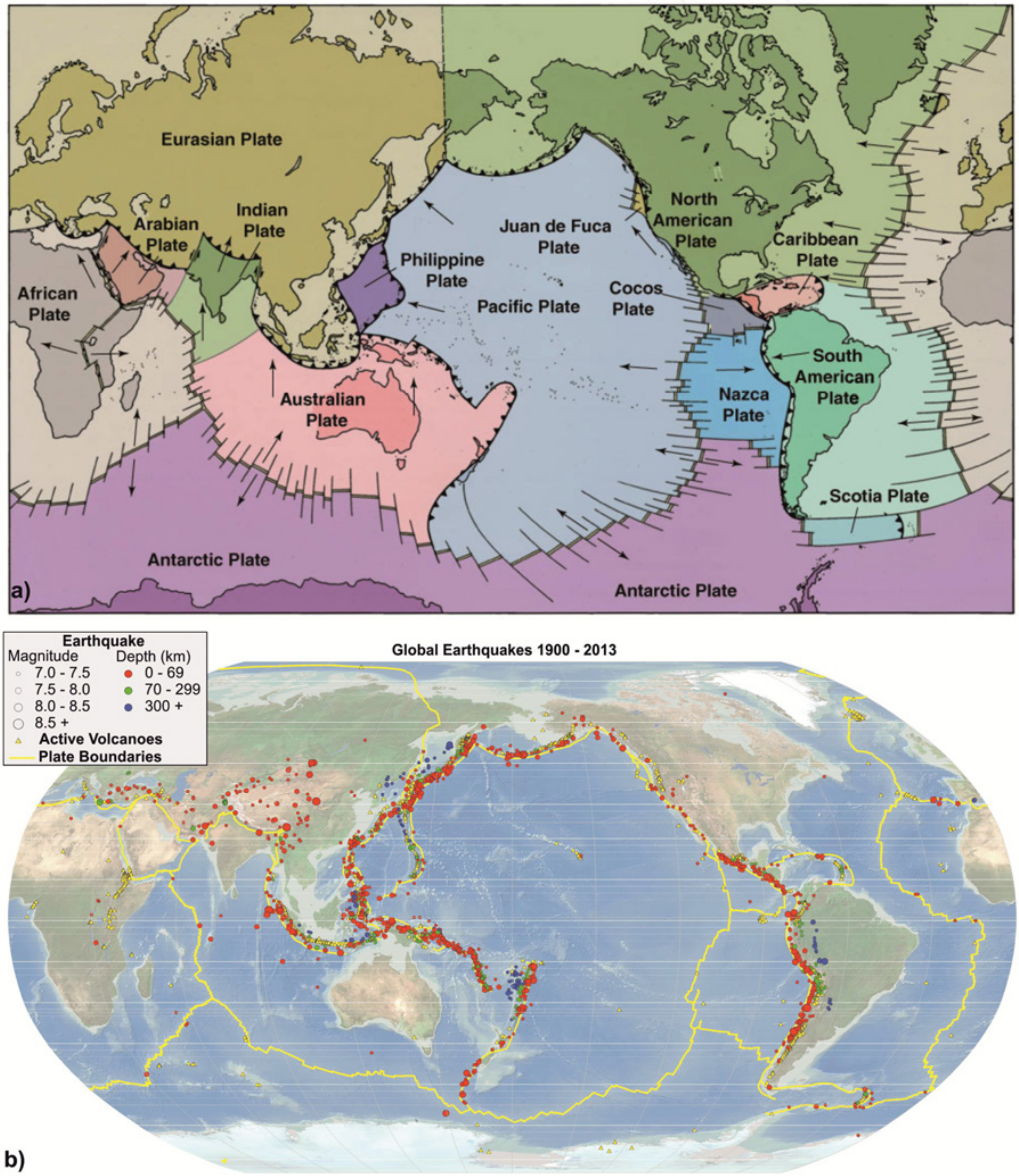

Figure 1.3: ***a)*** *Main tectonic plates.* ***b)*** *Worldwide seismicity map (published by USGS) between years 1900 and 2013. Coloured circles correspond to earthquakes; yellow triangles are active volcanoes and the yellow line point out the plates boundaries. Comparing both figures, it is noted that plate boundaries are the main zones where seismic and volcanic activity occurs.*

There are three types of plate boundaries on the basis of the relative plate motion (Fig. 1.4) (e.g. Hamblin, 1992; Whitsmarsh et al., 1996; Kearey et al., 2009):

i. **Transform or conservative:** In this case, lithospheric plates are not created nor destroyed. They move relative to each other in a lateral way, generating transform faults. Examples of this type of boundary are the oceanic St. Paul and Romanche Fracture Zones in the Atlantic Ocean, and the continental San Andreas Fault (California, USA) and Alpine Fault (New Zealand).

ii. **Divergent or constructive:** Lithospheric plates move away from each other, producing the thinning of the lithosphere and generating new oceanic lithosphere (i.e. oceanic accretion). These boundaries are represented by rifted margins and Mid-Oceans Ridges in oceanic areas. Examples of this type of boundaries in an oceanic setting are the Mid-Atlantic Ridge and the East Pacific Rise, while an example in a continental area is the East African Rift.

iii. **Convergent or destructive:** Plates converge to each other. When two lithospheres present the same density, the collision results in a mountain range, as the Himalayas (Indian-European plates). On the other hand, when there is a density variation, the densest lithosphere plunges beneath the less dense one. This generates a subduction process that causes volcanism and seismic activity. This process is taking place on either borders of the Pacific Ocean, as well as in the SE Indian Ocean.

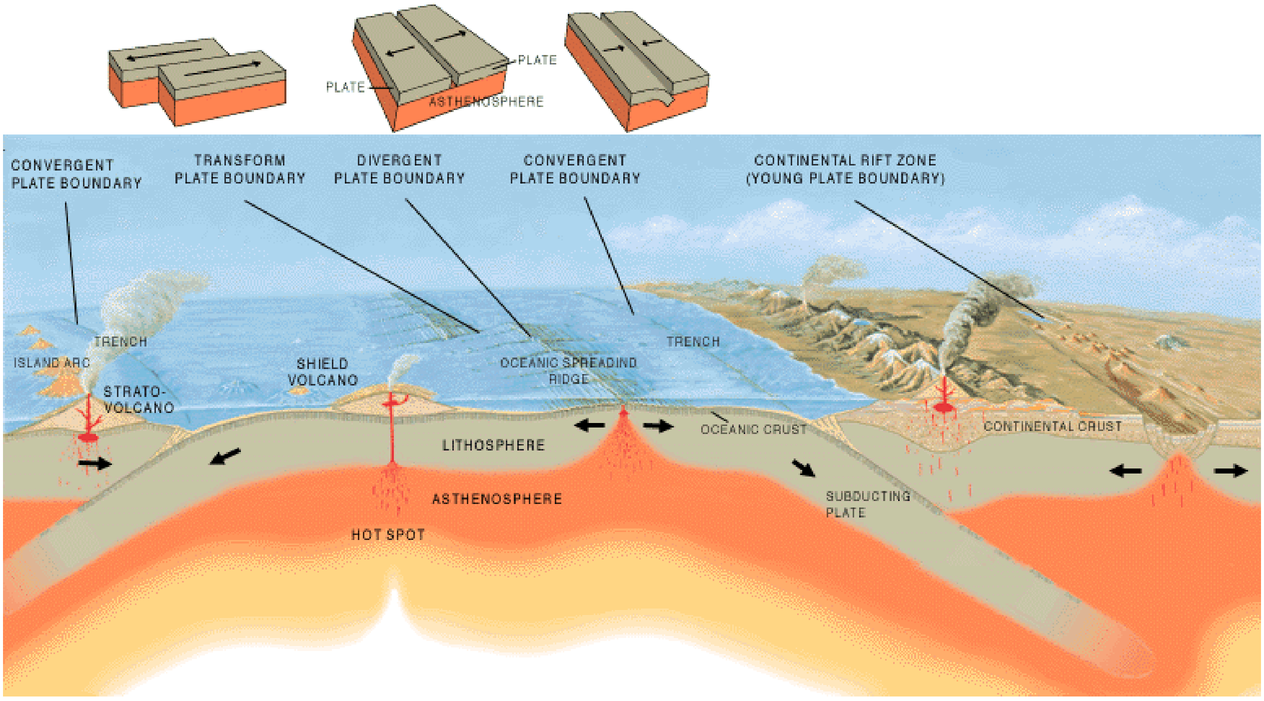

Figure 1.4: *Cartoon of the different interactions between plates. At transform boundaries (right upper sketch), plates are moving in a lateral way in relation to each other. At divergent boundaries (middle upper sketch), they are moving away from each other. At convergence boundaries (left upper sketch), they are approaching (extracted from http://www.crystalinks.com/tectonicplate.png).*

The main driving mechanism of the plate motion is convection in the mantle (e.g. Hamblin, 1992, Keary et al., 2009). There are several forces controlling the plate motion, including: i) slab pull, derived of the sinking slab, ii) ridge-push, as along the ridge the two plates are going away each other, iii) basal drag, caused by the movement of the asthenosphere with respect to the lithosphere, iv) friction along transform faults and v) friction between the converging slabs in a subduction zone (Fig. 1.5) (Hamblin, 1992; Heuret and Lallemand, 2005).

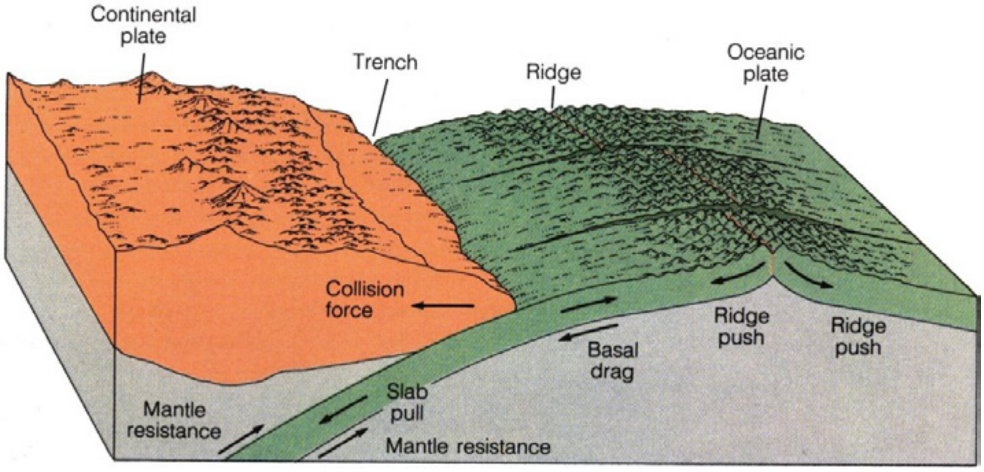

Figure 1.5: *Sketch of the main forces (black arrows) active on the plates.*

1.2. Basics about Subduction Zones

The long-time result of a plate convergent setting involving an oceanic plate is a subduction zone (e.g. von Huene and Scholl, 1991; Hamblin, 1992; Fowler, 2005; Kearey et al., 2009). When a lithospheric plate has an oceanic nature and the density between the two plates differs, the oceanic plate, denser than a continental plate and denser than a young oceanic plate, subducts below the other (von Huene and Scholl, 1991; Hamblin, 1992; Fowler, 2005). As a result of the subduction process, new fluid-rich material is introduced in the upper mantle. As the temperature increases with depth, these rocks begin to loss their water content, hydrating the mantle above them. This process decreases the melting temperature of the mantle, generating magmatism and leading to extensional processes in a plate convergence setting (e.g. Taylor, 1995; Stern, 2002; Kearey et al., 2009). Although the particular characteristics of each subduction system are determined by individual factors, such as the nature of the plates, convergence rate, age of the subducting plate, slab angle or plate boundary geometry, all these systems present common morphostructural elements (Stern, 2002; Fowler, 2005; Kearey et al., 2009; McCaffrey, 2009), such as seismic activity distribution and lithologies generated by the magmatic and metamorphic processes occurring there (Hamilton, 1979; Stern, 2002; Allen and Allen, 2005; Fowler, 2005; Kearey et al., 2009) (Fig. 1.6).

A mature and stable subduction zone forms an arc-trench complex, often called volcanic arc or island-arc (Fig. 1.6) (Stern, 2002). The main elements of an arc-trench complex (Fig. 1.6) are the fore-arc, the magmatic arc, and the back-arc basin, which are described below.

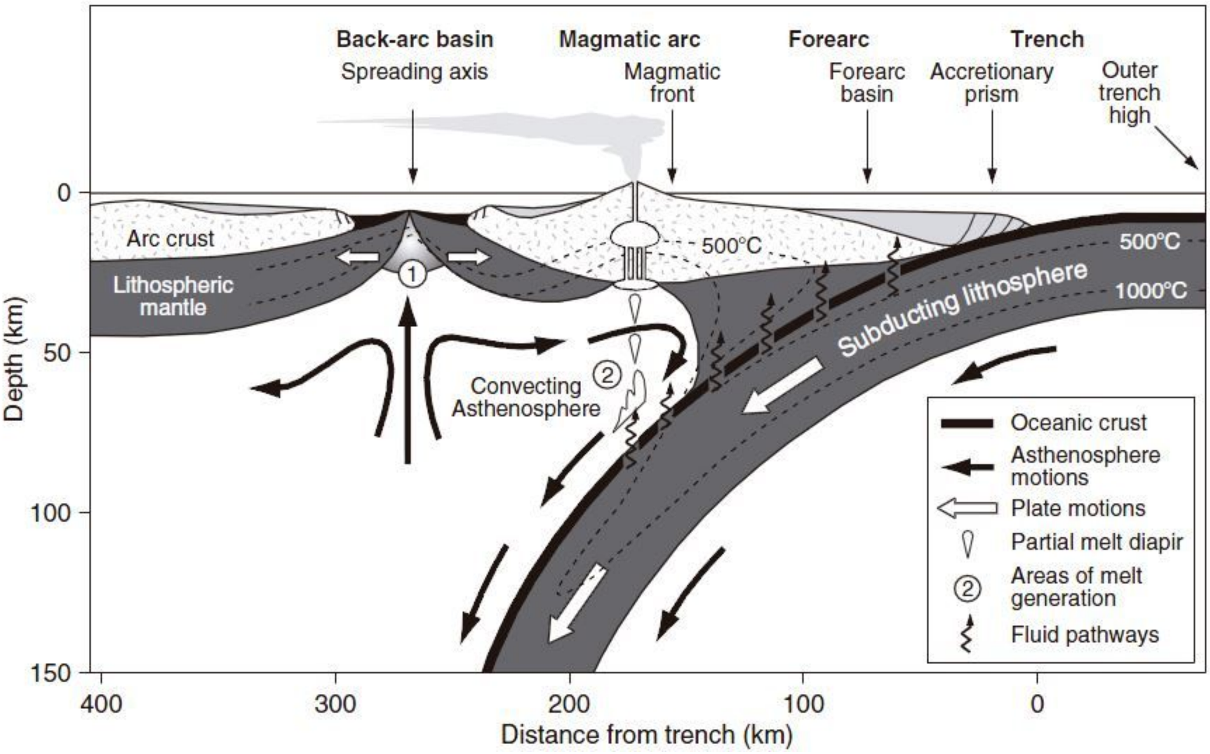

Figure 1.6: *Schematic section of a subduction system. Convergent plate boundaries are characterized by a sequence of geological features as shown above (Stern, 2002).*

1.2.1. Fore-arc basin

The fore-arc regions are located in front of the magmatic arc, above the subducting plate (Fig. 1.6). The fore-arc corresponds to a flexural basin and the subsidence in this area is controlled by the subduction geometry and the slab pull (Underwood et al., 2003). Formational mechanism are still under debate (e.g. Fuller et al., 2006; Noda, 2016), and are usually attribute to subsidence (e.g. Dickinson, 1995). A recent classification proposed by Noda (2016) gathers them in function of the sedimentary flux (accretionary or non-accretionary) and in function of the long-term strain field (extensional or compressional). When there is sedimentation, the sediments can be accreted by the compression and form an accretionary prism, which are highly deformed sedimentary bodies located above the trench (Fig. 1.6) (Stern, 2002).

1.2.2. Magmatic arc

Above the subducting lithosphere, the melting of the mantle wedge derives in magmatic activity due to the presence of fluids released from the subducted materials. This fusion processes always takes place at the same depth, between ~40 and ~120 km (Tatsumi et al., 1983; Pearce and Peate, 1995; Kushiro, 2007), so the distance between the arc and the trench is conditioned by the subduction angle (Fig. 1.7). This magmatic activity usually develops aligned arrays of volcanic islands. Regarding its composition these magmas are generally fractionated, porphyritic and wet (Gill, 1981; Stern, 2002). They are enriched in non-conservative elements, and belong to the calk-alkaline or the tholeiitic series, depending on the composition of the subduction crust and the melting depth (Fig. 1.8) (e.g. Tatsumi et al., 1983; Pearce and Peate, 1995; Kushiro, 2007). Both lava series could form the complete spectrum of rock types, from basalt through rhyolite, being the most abundant the andesite type (e.g. Pearce and Peate, 1995).

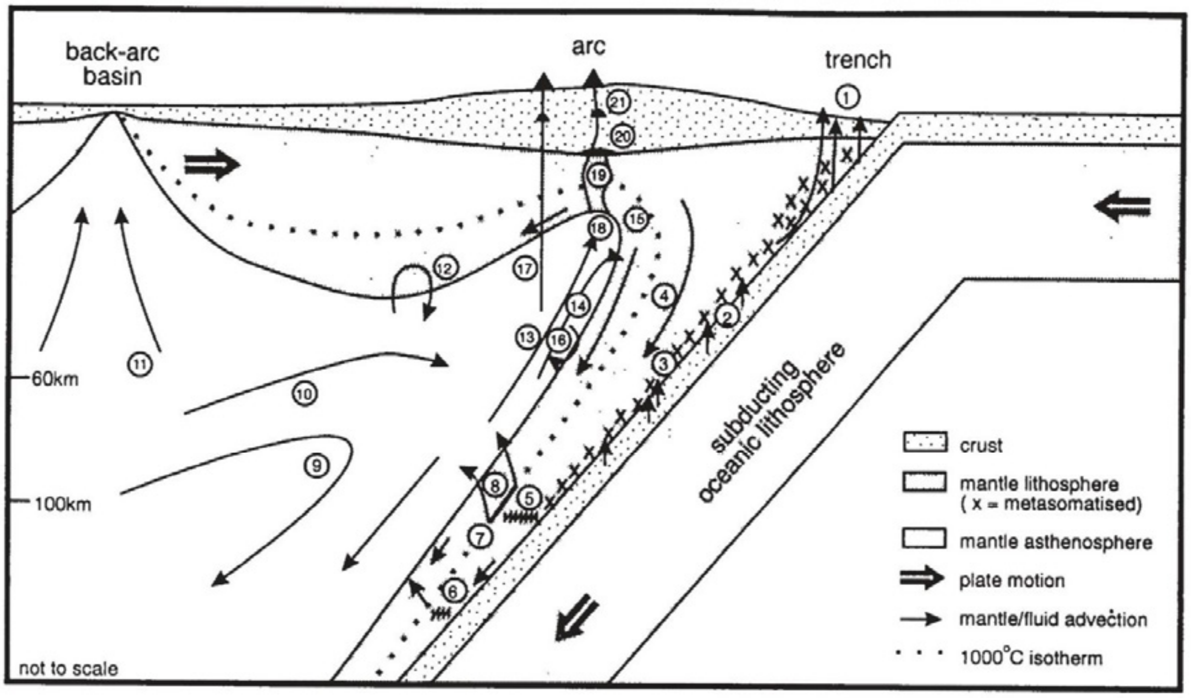

Schematic summary of the processes affecting arc magma composition.

Slab dehydration and melting 1. fluid loss via accretionary prisms and serpentinite seamounts, 2. dehydration ± partial melting of subducting oceanic crust and sediment.

Transport of subduction component 3. hybridization of subduction component and down-dragged mantle lithosphere, 4. slab-induced downward drag of hybridized mantle, 5. rerelease and lateral migration of aqueous fluids by amphibole breakdown at about 100 km depth, 6. rerelease of aqueous fluids by breakdown of other hydrous phases at greater depth, 7. initiation of hydrous melting of mantle at about 1000°C, 8. migration of small-volume hydrous melts through cross-fed mantle to the base of the melting column.

Mantle source processes 9. slab-driven "corner flow" of mantle into the mantle wedge, 10. replenishment of the melting column by mantle advection, 11. mantle source depletion by small-volume melt loss in back-arc region, 12. mantle source enrichment by delamination of sub-continental lithosphere.

Melting column processes 13. buoyancy-driven mantle counterflow, 14. decompression-melting of the mantle from about 60 km depth, 15. separation of residual mantle from the melting column aided by slab-induced downward drag, 16. column depletion by imperfect separation or reincorporation of residual mantle, 17. selective tapping of the melting column.

Lithosphere-melt interactions 18. melt segregation at the base of the lithosphere; 19. interaction with, and crystallization within, mantle lithosphere; 20. magma-assimilation-storage-homogenization at the base of the crust; 21. assimilation–fractional crystallization at shallower crustal levels.

Figure 1.7: *Cartoon of a subduction zone, with the processes related with magmatic activity depicted (Pearce and Peate, 1995).*

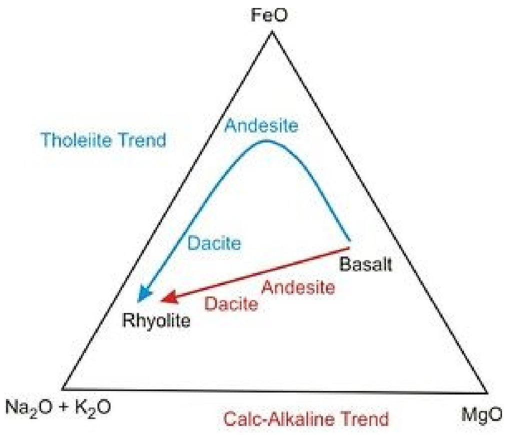

Figure 1.8: *AFM (alkaline, iron, magnesium) diagram for the tholeiitic and calk-alkaline volcanic series.*

1.2.3. Back-arc basin

Back-arc basins are located behind the magmatic arc and above the upper plate (Fig. 1.6). By definition, back-arc basins can be oceanic basins behind intra-oceanic magmatic arcs or continental basins behind continental margin magmatic arcs without foreland fold-thrust belts (Kearey et al., 2009). When the lithosphere is continental, as in the Andean-type margins, the back-arc is often a flexural subsidence basin controlled by the arc boundary main faults. When the lithosphere is oceanic, the back-arc region is usually under extension. These types of basins are of relatively young age (< 10 Ma) and are some of the most rapidly extending regions on the Earth, such as the Aegean Sea or the SW Pacific back-arc basins (Allen and Allen, 2005). This extensional process is similar to that occurring in mid-ocean ridges, although the basaltic crust (MORB: mid-ocean ridge basalts) formed in these two environments has some differences such as the N-MORB vs. E-MORB (enriched in rare-earth elements) (e.g. Taylor, 1995; Kearey et al., 2009). For instance, magnetic anomalies are poorly developed or even not recognized in back-arc crust, and the geochemical affinity of these rocks is greatly influenced by the subduction process (Kearey et al., 2009).

Now, we are going to focus on the oceanic back-arc basins, specifically on the case of the Western Mediterranean basins. Martínez et al. (2007) proposed that this type of basins might occur in two different settings. On the first one, the subducting plate sinks faster that the convergence rate, producing a slab roll-back (Heuret and Lallemand, 2005; Martinez et al., 2007) (Fig. 1.9). On the second model, the process occurs on the other way around. The slab acts as an anchor in the mantle, and the subducting plate remains fixed. The overriding plate moves away the trench, giving as a result the extension within the back-arc region (Scholz and Campos, 1995; Martinez et al., 2007) (Fig. 1.9).

In general, the evolution of back-arc basins is usually characterized by an episodic behaviour through time (e.g. Faccenna et al., 2004; Martinez et al., 2007). The kinematics of these basins is greatly influenced by the shape of the subduction zone, and, therefore, by the geometry of the two convergent plates. Changes in the plan geometry of the converging plates conditioned the existence of extensional processes in the back-arc, as they are related with the stress distribution (Martinez et al., 2007).

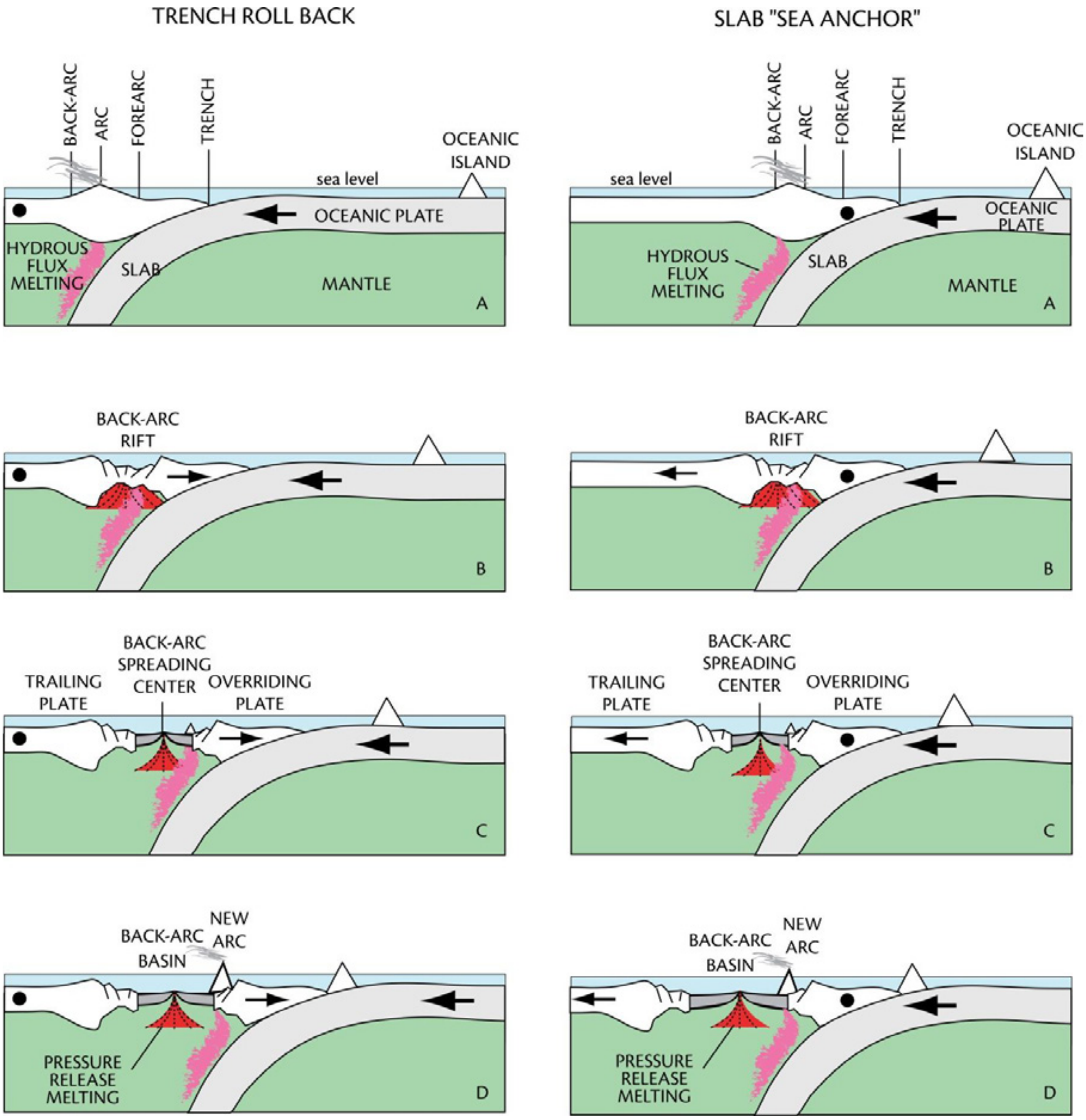

Figure 1.9: *Models of back-arc opening from Martinez et al., 2007. Left panels show the evolution of the slab roll-back model, while right panels show a slab "sea anchor" system (see text for details). The black dot marks the fixed plate.*

The generation of these basins is highly dominated by the magmatic activity (Stern, 2002; Martinez et al., 2007). The subducted lithologies lose their fluids during the subduction process, allowing the hydration of the mantle and facilitating the generation of melts. In this context, two melt-generations occurred: the one that support the magmatic-arc and the one that feeds the seafloor spreading axis (Fig. 1.6, 1.9) (Martinez et al., 2007). Associated to this magmatic activity, hydrothermal and vent system are often found in spreading ridges located in active back-arc basins (e.g. Bendel et al., 1993; Gràcia et al., 1994; Ishibashi and Urabe, 1995; Martinez et al., 2007). Some of the western Mediterranean basins are back-arc basins, as the Tyrrhenian or the Liguro-Provençal basins, and exhibits some of these characteristics. It is specially noticed the change in their behaviour through time, related to changes in the subduction system configuration (e.g. Rosenbaum et al., 2002; Faccenna et al., 2004; Schettino and Turco, 2011).

Chapter 2

Geological setting

The Alboran Sea basin is located in the Western Mediterranean (Fig. 2.1), between the Iberian Peninsula and North Africa, running from 5°30’W to 0°30’W and from 35°0’N to 37°30’N. Along this basin and surrounding land runs the diffuse deformation zone between the Iberian and African plates. This boundary is poorly defined because it corresponds to a wide deformation zone, associated to the NW-SE convergence (4.5 – 5.6 mm/yr) between the African and Eurasian plates (Serpelloni et al., 2007; Nocquet, 2012). Deformation here is distributed over a large number of faults offshore and onshore with some structures that extend from emerged to submarine segments (Fig. 2.1) (Sanz De Galdeano, 1990; Andeweg and Cloetingh, 2001; Gràcia et al., 2006). The basin is surrounded by the Betic and the Rif-Tell mountain ranges at the north and the south, respectively, forming the Gibraltar Arc System (Fig. 2.1).

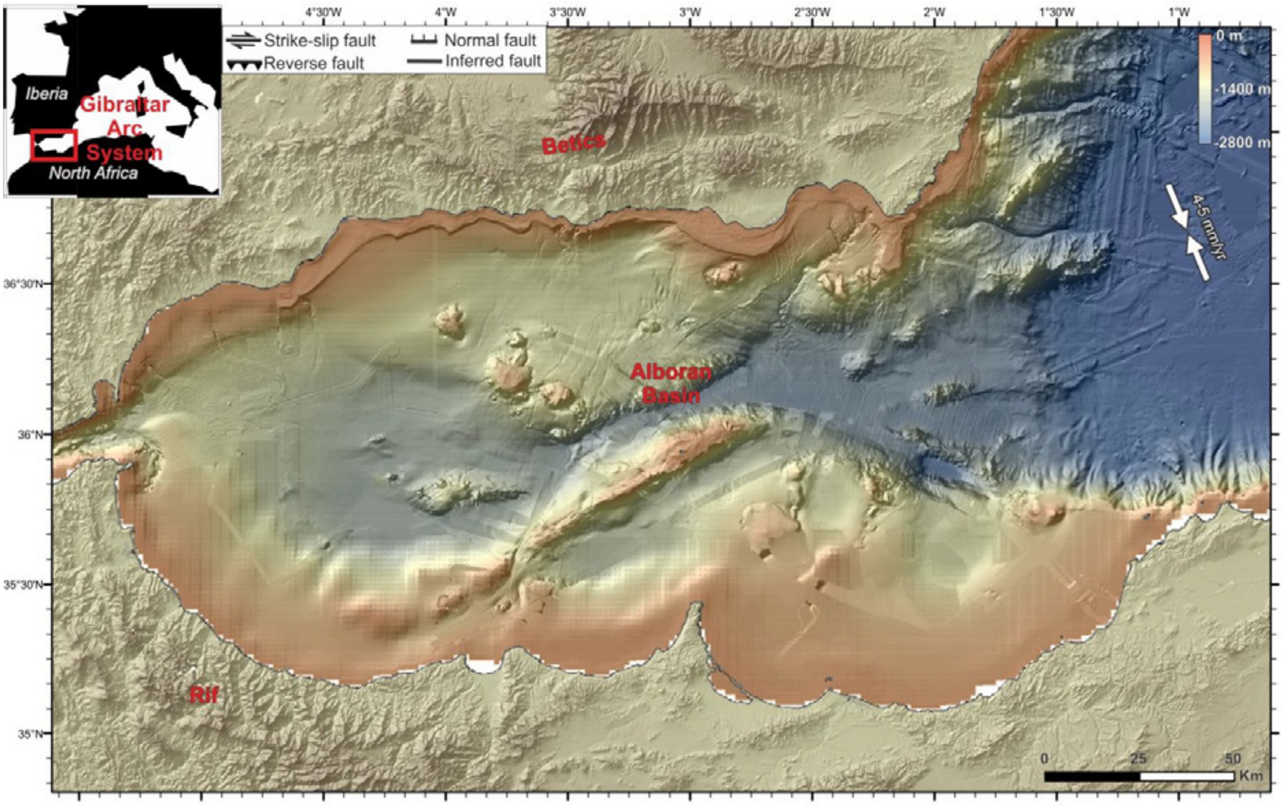

Figure 2.1: *Regional bathymetric map of the Alboran Sea constructed from swath-bathymetric data acquired during the IMPULS-06, EVENT-10, TOPOMED-11, SHAKE-15 and IDRISSI-16 marine cruises (e.g. Gràcia et al., 2006, 2012) and a compilation of existing datasets from IEO (Ballesteros et al., 2008) and GEBCO. Land topography is from the SRTM-3 grid. Main tectonic structures are displayed (Gràcia et al., 2006; 2012). The opposite white arrows depict the 4-5mm/yr convergence rate between the Eurasian and African plates (Stich et al., 2006; Koulali et al., 2011; Palano et al., 2013). Inset: Location of the depicted area (Gibraltar Arc System) with a red rectangle.*

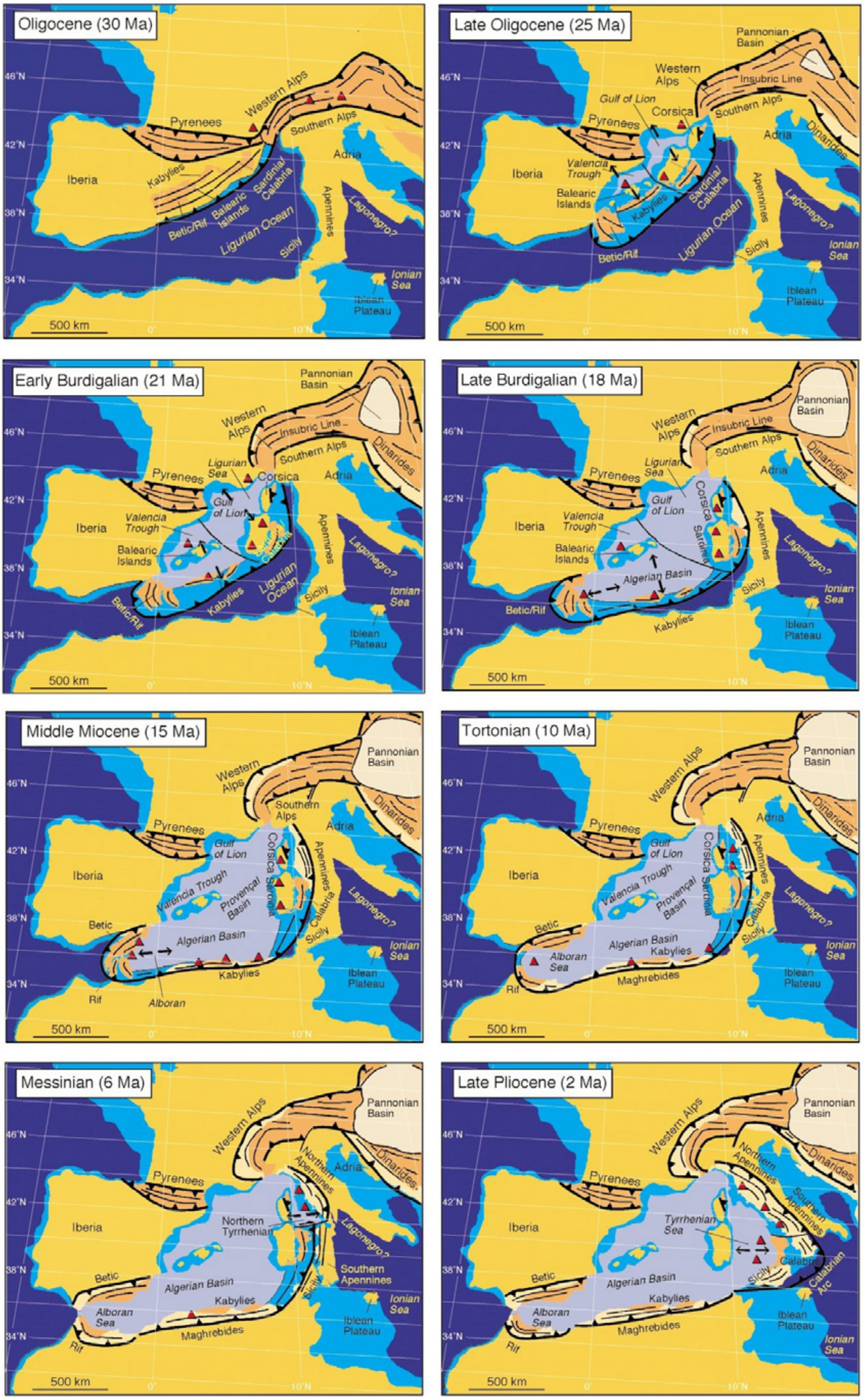
Oligocene (30 Ma)
46°N
42°N
38°N
34°N
Western Alps
Pyrenees
Southern Alps
Iberia
Kabylies
Sardinia/Calabria
Balearic Islands
Betic/Rif
Adria
Apennines
Lagonegro?
Ligurian Ocean
Sicily
Ionian Sea
Iblean Plateau
500 km
0°
10°N
Late Oligocene (25 Ma)
Pannonian Basin
Western Alps
Insubric Line
Gulf of Lion
Corsica
Southern Alps
Pyrenees
Dinarides
Adria
Iberia
Valencia Trough
Balearic Islands
Kabylies
Sardinia/Calabria
Apennines
Lagonegro?
Ionian Sea
Ligurian Ocean
Betic/Rif
Sicily
Iblean Plateau
500 km
Early Burdigalian (21 Ma)
Pannonian Basin
Western Alps
Insubric Line
Southern Alps
Dinarides
Ligurian Sea
Pyrenees
Corsica
Adria
Gulf of Lion
Iberia
Valencia Trough
Sardinia/Calabria
Balearic Islands
Apennines
Lagonegro?
Kabylies
Ligurian Ocean
Sicily
Ionian Sea
Betic/Rif
Iblean Plateau
500 km
Late Burdigalian (18 Ma)
Pannonian Basin
Western Alps
Insubric Line
Southern Alps
Dinarides
Ligurian Sea
Pyrenees
Adria
Gulf of Lion
Corsica
Sardinia
Iberia
Valencia Trough
Apennines
Balearic Islands
Lagonegro?
Algerian Basin
Sicily
Ionian Sea
Betic/Rif
Kabylies
Iblean Plateau
500 km
Middle Miocene (15 Ma)
Pannonian Basin
Western Alps
Southern Alps
Dinarides
Pyrenees
Adria
Gulf of Lion
Corsica
Sardinia
Apennines
Iberia
Valencia Trough
Provençal Basin
Lagonegro?
Betic
Calabria
Algerian Basin
Sicily
Ionian Sea
Kabylies
Iblean Plateau
Rif
Alboran
500 km
Tortonian (10 Ma)
Pannonian Basin
Western Alps
Adria
Dinarides
Pyrenees
Gulf of Lion
Corsica
Sardinia
Apennines
Iberia
Valencia Trough
Provençal Basin
Lagonegro?
Betic
Calabria
Algerian Basin
Kabylies
Sicily
Ionian Sea
Alboran Sea
Maghrebides
Iblean Plateau
Rif
500 km
Messinian (6 Ma)
Pannonian Basin
Western Alps
Northern Apennines
Adria
Dinarides
Pyrenees
Iberia
Northern Tyrrhenian
Lagonegro?
Southern Apennines
Betic
Algerian Basin
Kabylies
Sicily
Ionian Sea
Alboran Sea
Maghrebides
Iblean Plateau
Rif
500 km
Late Pliocene (2 Ma)
Pannonian Basin
Western Alps
Northern Apennines
Dinarides
Pyrenees
Southern Apennines
Iberia
Tyrrhenian Sea
Calabria
Sicily
Betic
Algerian Basin
Calabrian Arc
Kabylies
Iblean Plateau
Alboran Sea
Maghrebides
Ionian Sea
Rif
500 km

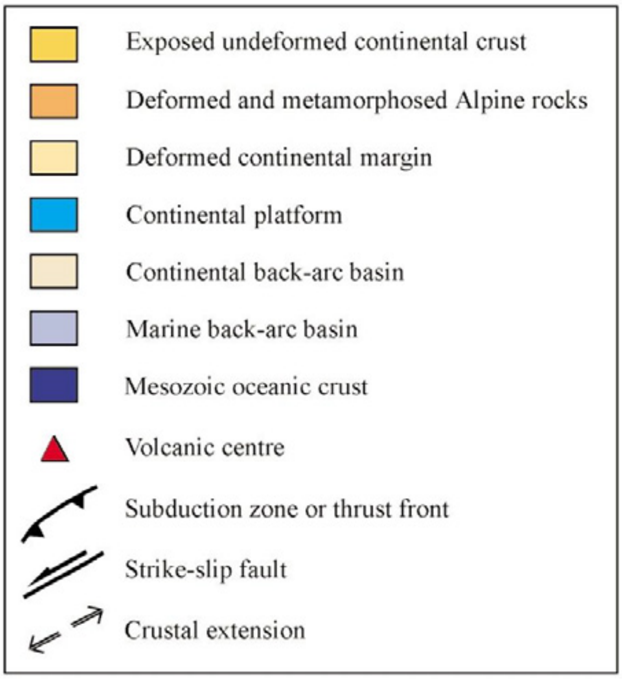

Figure 2.2: *Reconstruction of the tectonic evolution of the western Mediterranean since the Oligocene (Rosenbaum et al., 2002).*

2.1. The Western Mediterranean

The Alboran basin, which belongs to the Western Mediterranean basins, has a complex geological evolution. The origin and evolution of the Western Mediterranean has been a focus of debate since the 1980's, since the first kinematic reconstruction, further models were carried out on the basis of field geological work, magnetic surveys, palaeomagnetism, volcanic rock geochemistry and seismic data (Rehault et al., 1984; Dewey et al., 1989; Lonergan and White, 1997; Gelabert et al., 2002; Rosenbaum et al., 2002; Frizon de Lamotte et al., 2011; Faccenna et al., 2014). All these researches proposed hypotheses for the opening of the Western Mediterranean Basins formed as a consequence of extensional processes in a compressional setting (e.g. Dewey et al., 1989; Lonergan and White, 1997; Van Hinsbergen et al., 2014), which led to interpret them as back-arc basins (Fig 2.2). The Cenozoic evolution of the Western Mediterranean basins has been commonly interpreted to share three general stages (e.g. Faccena et al., 2014 and references therein):

1. Before ~30-35 Ma: The subduction of the African plate below the European plate results in a compressive regime along the margin of the upper plate. This convergence led to the formation of the Alpine type belts, as the Apennines, the Dinarides or the Betic – Rif orogens.

2. After 30-35 Ma: There is a change in the back-arc regions, where extension occurred after compression. Some of the orogenic wedges collapsed and the exhumation of high-temperature metamorphic rocks took place at the back-arc setting, while a high-pressure low-temperature metamorphism was still occurring in the subduction zones.

3. After Miocene (~23 Ma): The arcs became narrow as a consequence of the arching and bending produced by the slab retreat. In some regions, as the Tyrrhenian or the Alboran basins, the slab is largely detached from the upper plate. Subduction associated volcanism has occurred at all back-arc regions.

The first tomographic studies represented a qualitative leap, adding the mantle structure to previous models. First results (e.g. Blanco and Spakman, 1993; Calvert et al., 2000) show positive velocity anomalies reaching down to 660 km depth below the main basins, as the Liguro-Provençal, Tyrrhenian and Alboran seas, which have been interpreted as subducted slabs. New tomographic results (Wortel and Spakman, 2000; Spakman and Wortel, 2004) provided higher resolution images of the velocity anomalies that allowed the definition of these slabs (Fig. 2.3). These new results pointed out two fundamental aspects of the Western Mediterranean subduction: (i) a fragmented subduction zone instead of a continuous slab as the first models proposed (Fig. 2.4), and (ii) a detached slab in some points (Fig. 2.5) providing the first firm conceptual models for basin evolution. Further refinements of the models followed with the integration of GPS data, receiver functions analysis and seismicity records (e.g. Bezada et al., 2013; Levander et al., 2014; Palomeras et al., 2014; Thurner et al., 2014; Mancilla et al., 2015; Villaseñor et al., 2015). Higher-resolution mantle images obtained through Full Wave Form Inversion (FWI) (Fichtner and Villaseñor, 2015) are in agreement with these characteristics (Fig. 2.5).

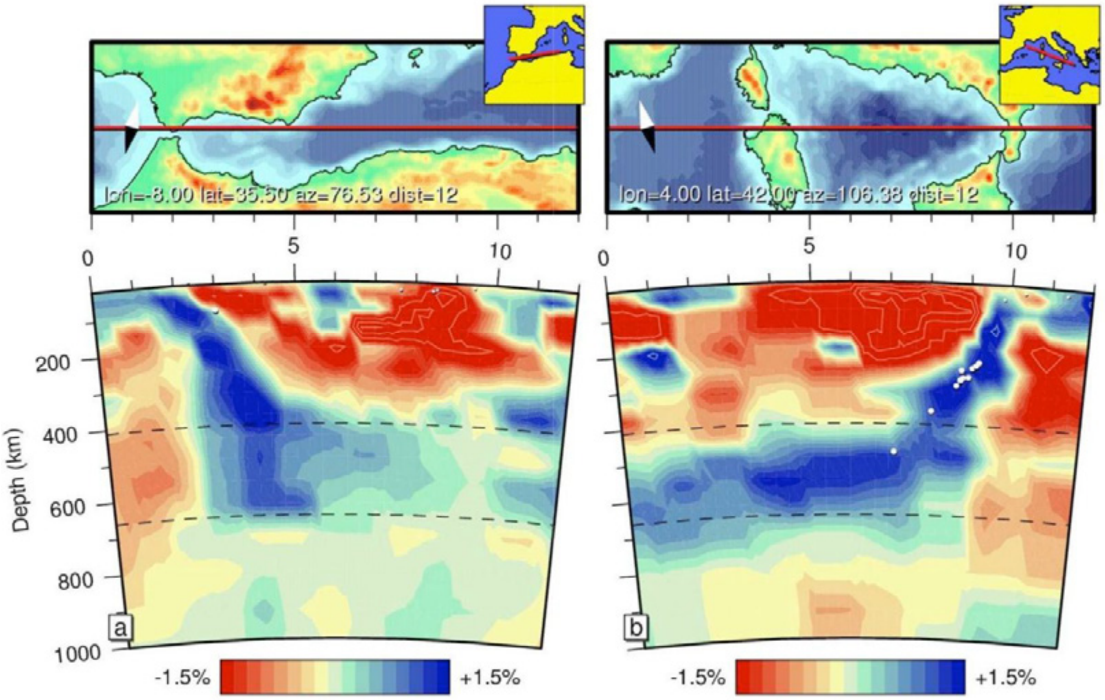

Figure 2.3: *Tomographic sections across the Alboran Basin and North Africa (left side) and across the Tyrrhenian Basin (right side). The white side of the diamond symbol points to the north, and the dot circles represent earthquakes with magnitude over 4.8 that occur within 25 km to the vertical section. Dashed lines indicate the 410 km and 660 km mantle discontinuities. Two high velocity zones are well defined under the Gibraltar Arc and under the Calabrian Arc, constraining the geometry of these slabs (Spakman and Wortel, 2004).*

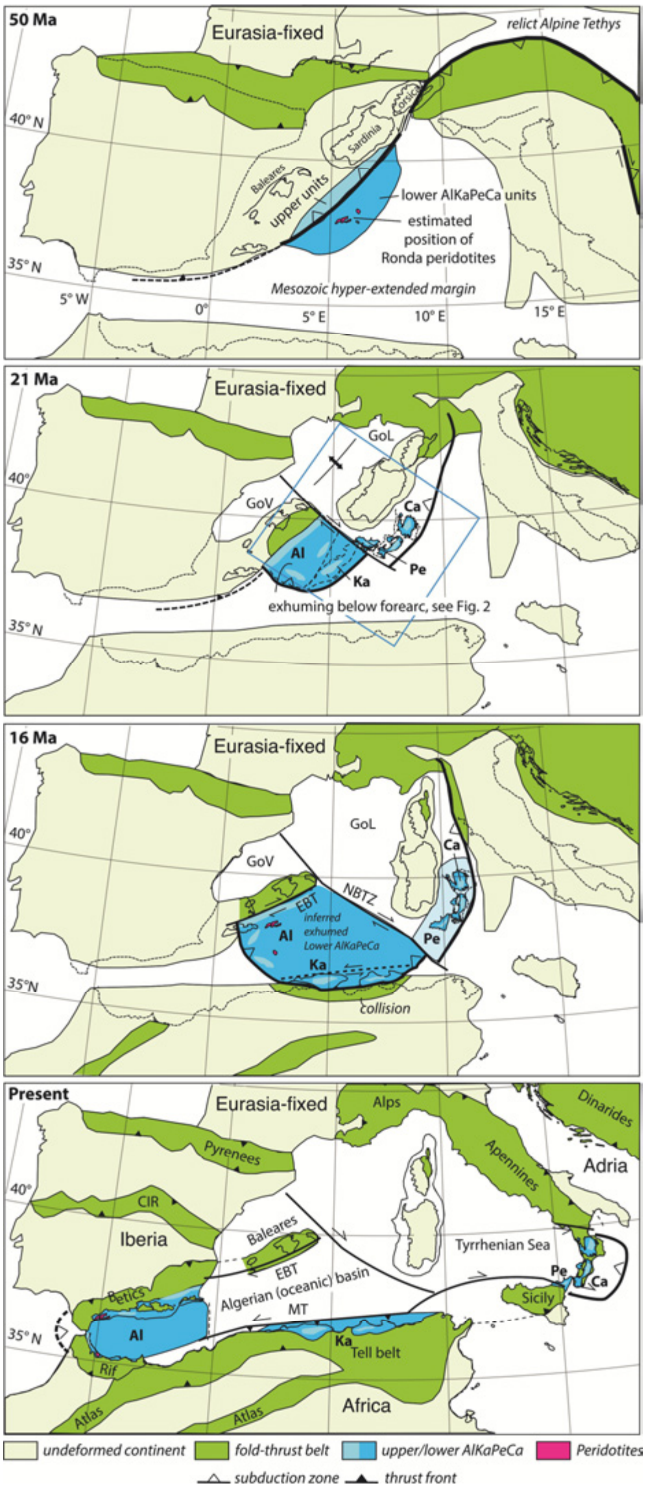

Figure 2.4: *Tectonic reconstruction of the evolution of the western Mediterranean proposed by van Hinsbergen et al., (2014). The main difference with the previous models (Figure 2.2) is based on the discontinuity of the subduction zone. Al: Alboran, Ca: Calabria, CIR: Central Iberain Ranges, EBD: Emile Baudot Transform, GoL: Gulf of Lions, GoV: Gulf of Valencia, Ka: Kabylides, NAT: North African Transform, NBTZ: North Balearic Transform Zone, Pe: Peloritani Mountains.*

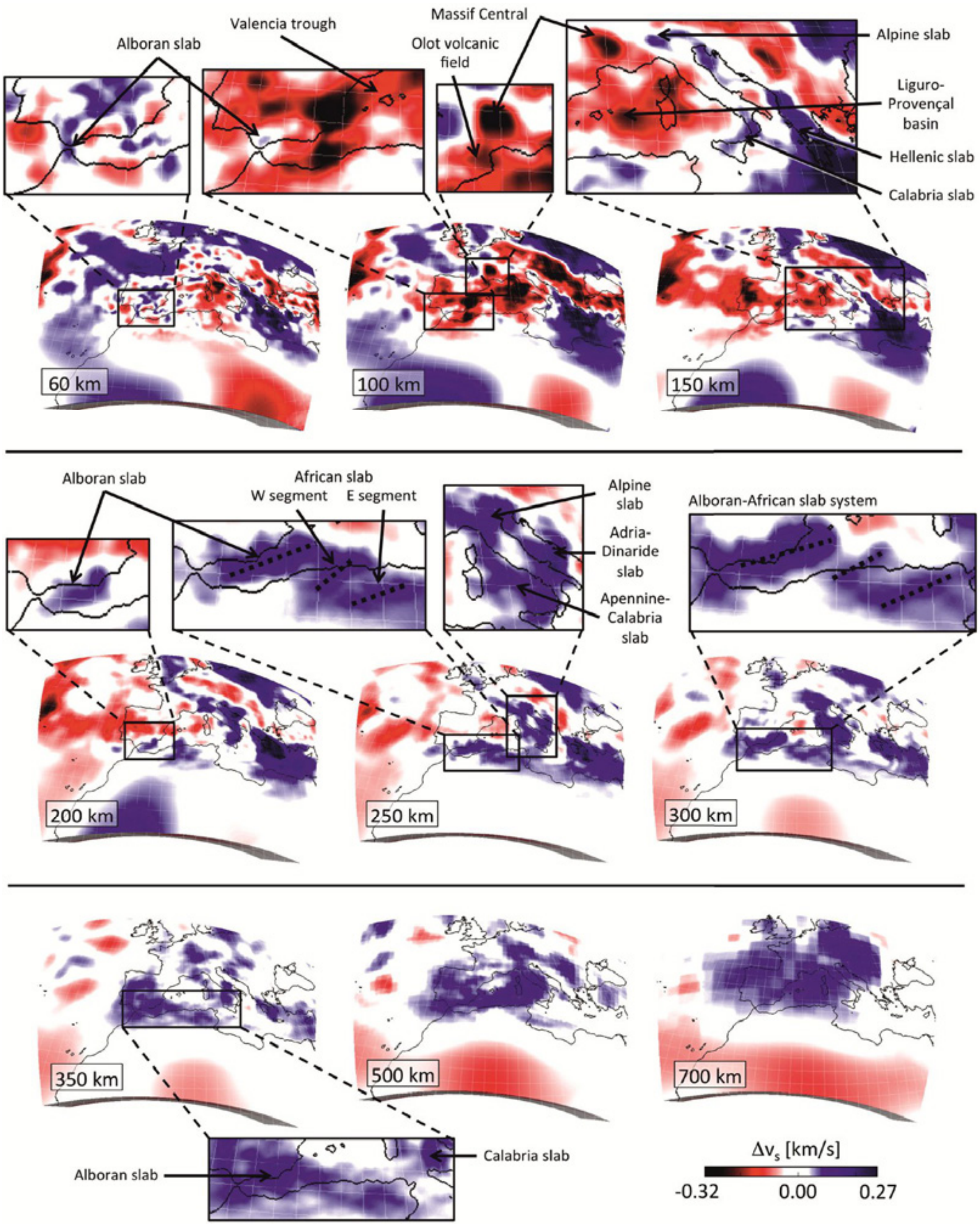

Figure 2.5: *Full-waveform tomographic model of the western Mediterranean (Fichtner and Villaseñor, 2015). Resolution of the model allows the imaging of the slab from 60 km depth till around 500 km depth. Detail of the upper images shows how the Alboran slab remains under the Straits of Gibraltar, but it is detached under the Betics at it shallower part (till ~200 km). Looking at the deeper sections, up to three slabs can be identified along the North African margin (between 250 km – 300 km, and marked with dashed lines) (from Fichtner and Villaseñor, 2015).*

In this geological framework, the particular evolution of the Alboran Basin remains however debated. It is an extensional area surrounded by the Betic and Rif – Tell Orogenic Belts. It was mainly formed during the Miocene by extensive processes in a plate convergent setting (e.g. Rodríguez-Fernández et al., 1999; Rosenbaum et al., 2002; Gelabert et al., 2002; Faccenna et al., 2004; Booth-Rea et al., 2007). Different hypotheses have been proposed in order to explain the origin of the extension (e.g. Dewey, 1988; Platt and

Vissers, 1989; García-Dueñas et al., 1992; Blanco and Spakman, 1993; Royden, 1993; Seber et al., 1996; Lonergan and White, 1997; Zeck, 1999; Calvert et al., 2000; Platt et al., 2006), taking into account the different geological and geophysical observations in this region. The hypotheses argue for three main processes (see "Chapter 11: Implications for geodynamic models" for further information):

(i) post-orogenic extensional collapse related to the convective removal of continental lithospheric mantle (Dewey, 1989; Platt and Vissers, 1989),

(ii) delamination of lithospheric mantle beneath the orogen (García-Dueñas et al., 1992; Seber et al., 1996; Calvert et al., 2000), and

(iii) subduction of oceanic lithosphere and associated slab roll-back (Royden, 1993; Lonergan and White, 1997) or/and slab break-off (Blanco and Spakman, 1993; Zeck, 1999).

Due to the limited resolution of the first tomographic models, there was not enough accuracy to discriminate between models. Most recent studies point to a subduction model combining slab roll-back and slab break-off as the most plausible model. The integration of the recent tomographic data results in new models combining both, slab roll-back and slab break-off as the trigger extensional mechanism in the Alboran Basin (e.g. Spakman and Wortel, 2004; Bezada et al., 2013; Chertova et al., 2014; Van Hinsbergen et al., 2014; Fichtner and Villaseñor, 2015). In that way, the Alboran Basin is the result of the extensional processes occurring in the upper plate due to the slab roll-back and slab detachment (e.g. Spakman and Wortel, 2004; Gutscher et al., 2012; Bezada et al., 2013; Chertova et al., 2014; Faccenna et al., 2014; Fichtner and Villaseñor, 2015; Van Hinsbergen et al., 2014). The different geometries and evolutions proposed for the subduction geodynamic models are discussed in "Chapter 10: Implications for geodynamic models".

Although traditionally the Alboran Basin has been explained as a back-arc basin (e.g. Jolivet et al., 1999; Rosenbaum et al., 2002; Faccenna et al., 2004), the integration of the depth structure and nature of the basement data support that the magmatic activity divides the basin into three main regions: a) the fore-arc basin, represented by the West Alboran Basin, b) the magmatic arc on the central part and East Alboran basin, and c) the easternmost part of the back-arc basin itself, which would be represented by the Algero-Balearic Basin (e.g. Booth-Rea et al., 2007; Duggen et al., 2008).

2.2. The Gibraltar Arc System

The Gibraltar Arc system is the westernmost termination of the Alpine orogen in the Mediterranean. It has its origin in the subduction of the Tethys lithosphere beneath the NW segment of the African and Iberian plates. This subduction process led to the later collision of the Alboran domain with the passive margins of European (Iberian) and African plates, generating the Betic (South Iberia) and the Rif (North-western Africa) orogenic belts and the Alboran Sea basin between them (e.g. Jolivet et al., 1999; Gelabert et al., 2002; Rosenbaum et al., 2002; Faccenna et al., 2004; Schettino and Turco, 2006; Schettino and Turco, 2011).

2.2.1. The Gibraltar Arc System evolution

The complex geological history of the Gibraltar Arc system starts in the Upper Triassic (~230 Ma), when, as a consequence of the forces driving the opening of the Atlantic, the Tethyan rift started following a preexisting plate boundary between Iberia and north Africa (now Morocco). At the Lower Jurassic (~185 Ma), Tethyan oceanic lithosphere was formed (e.g. Schettino and Turco, 2011; Martínez-Loriente et al., 2014). For the evolution of the Gibraltar Arc system, the opening of the Ligurian Tethys ocean (located between Iberia and Africa), is especially important. This oceanic lithosphere is the one that during the Alpine orogeny will be subducted and will generate the Mediterranean alpine orogenic belts, such as the Betics and the Rif in the Gibraltar Arc system, and most of the Mediterranean basins, such the Alboran Sea (e.g. Schettino and Turco, 2006, 2011).

The Alpine subduction begun at the Lower Cretaceous (~120 Ma), although it is interpreted to the Ligurian oceanic lithosphere in the Eocene-Oligocene, when a N-dipping subduction zone formed on the Southern European margin and NE Iberia (Fig. 2.2). This stage is interpreted as a E-W subduction trench, with a north dipping slab (Gelabert et al., 2002; Schettino and Turco, 2006; Schettino and Turco, 2011). Following a slab roll-back model for the Gibraltar Arc region, this subduction has as a direct consequence in the formation of the Betic Cordillera in South Spain, the Rif orogen in North Africa, and the Alboran basin that is located in between during the Late Oligocene – Early Miocene (e.g. Rosenbaum et al., 2002; Faccena et al., 2004). The basin is generated by the passive subduction process, driven by the negative buoyancy of the Ligurian lithosphere, and the westward retreat of the trench zone (e.g. Schettino and Turco, 2011).

From the Oligocene onwards, the characteristics of the subduction are the key factors that controlled and determined the evolution of the Gibraltar Arc system (Wortel and Spakman, 2000; Gelabert et al., 2002; Rosenbaum et al., 2002; Faccenna et al., 2004). The Betic – Rif orogenic belt results from the collision of the Alboran domain with the passive margins of Iberia and Africa, as a consequence of the Tethyan realm subduction. On the other hand, the Alboran basin was formed in this compressive setting due to extensional processes related to the subduction velocity and the slab retreat (Wortel and Spakman, 2000; Rosenbaum et al., 2002) (Fig. 2.6).

During the Oligocene (~33 – 23 Ma), the subducted slab migrated progressively to the south (Fig. 2.2). The direct consequences are (i) the N-S back-arc extension in the Gulf of Lions and Ligurian basins, (ii) the first compressive episode in the North of Africa, and (iii) the first volcanic activity represented by tholeiitic dyke intrusions (Rosenbaum et al., 2002; Duggen et al., 2004; Duggen et al., 2008).

The Neogene is a period of major changes, characterized by the westward retreat of the slab (Fig. 2.2, 2.6). All these changes in the subduction zone and stress field are reflected in the tectonic evolution history of the Alboran Basin and surrounding areas (Fig. 2.7). Extension took place in a convergent setting (e.g. Dewey et al., 1989; Van Hinsbergen et al., 2014) due to tectonic mechanisms such as slab roll-back and slab tearing under the Maghrebian and Betic margins. These processes have driven two processes: a) shortening in a direction perpendicular to plate convergence, and b) extension that favored exhumation of high-pressure rocks at the core of orogens (e.g. Lonergan and White, 1997; Martínez-Martínez et al., 2002; Faccenna et al., 2004; Booth-Rea et al., 2015; Mancilla et al., 2015). As consequence of slab roll-back and slab tearing under the southeastern Iberia and north African margins, shortening occurred parallel to plate convergence trend and extension in perpendicular sense (e.g. Lonergan and White, 1997; Faccenna et al., 2004; Stich et al., 2006; Koulali et al., 2011; Booth-Rea et al., 2015; Palano et al., 2015). Through the analysis of the metamorphic basement, an Oligocene age for the first extensional episode in the Alboran Basin has been established (Platt et al., 1996; Soto and Platt, 1999). The extensional process that led to the basin formation took place mainly during the Early and the Middle Miocene in the Western Alboran Basin (Fig. 2.6), and from the Late Miocene until the latemost Tortonian in the Eastern Alboran and the Algero-

Balearic basins (e.g. Krautworst and Brachert, 2003; Booth-Rea et al., 2004; Giaconia et al., 2014). Onshore, in the eastern region, different mechanisms of extension have been proposed. Extension was mainly driven by magmatic accretion south of the Carboneras Fault (Rutter et al., 2012), and by normal faulting north of it (e.g. Krautworst and Brachert, 2003; Booth-Rea et al., 2004; Giaconia et al., 2014).

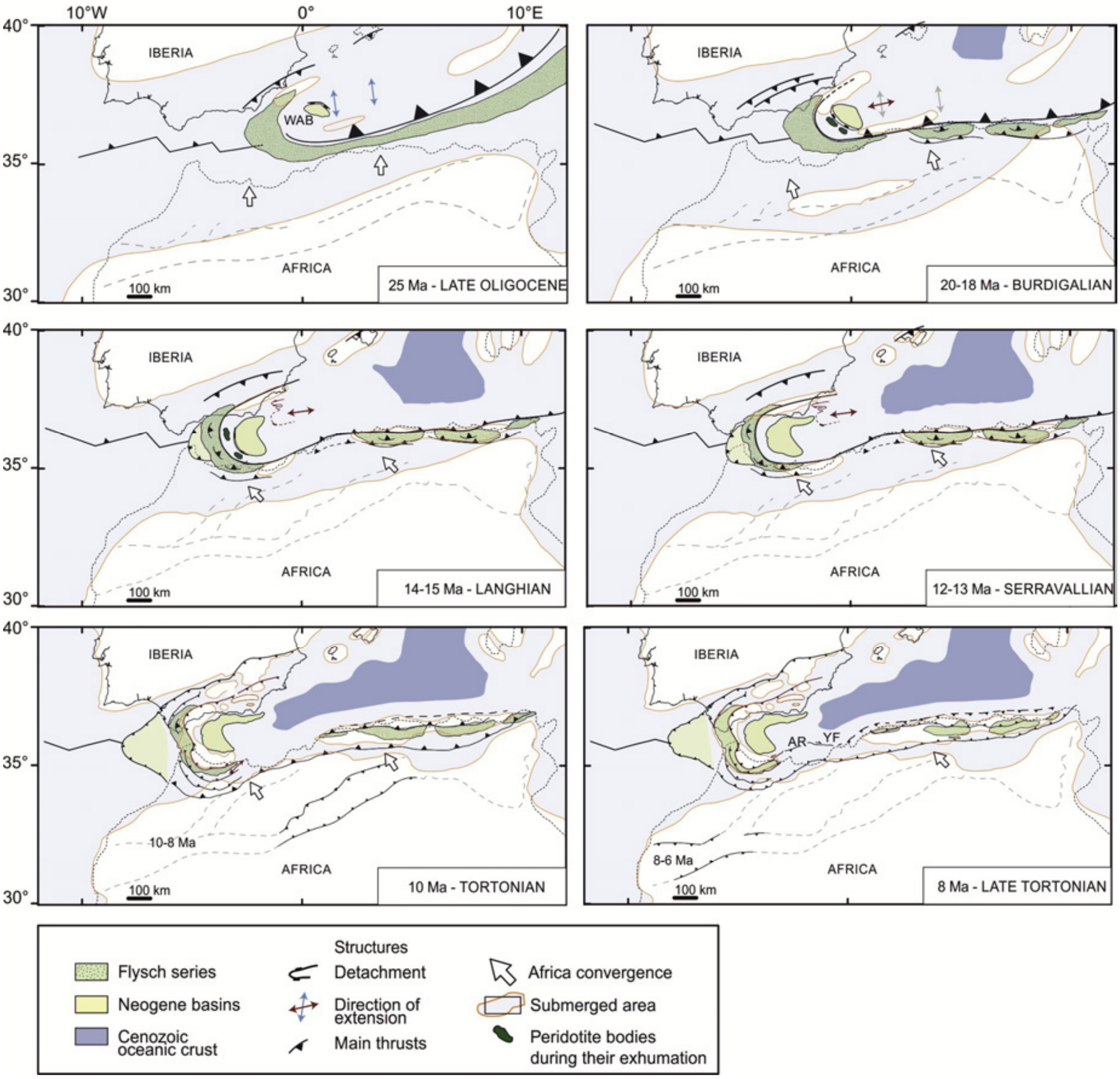

Figure 2.6: *Paleogeographic reconstructions of the Alboran Basin area displaying the main tectono-sedimentary events during the evolutionary sequence since Late Oligocene until Late Tortonian (Do Couto et al., 2016).*

The Messinian (7.2 – 5.3 Ma) is characterized by the Mediterranean Salinity Crisis (MSC, ~5.6 – 5.5 Ma). This event is interpreted to result from the closure of the Straits of Gibraltar and African and Iberian passways, which produced a rapid sea-level drop, implying subaerial erosion and deep-basin salt deposits. The Messinian ended with the Zanclean flooding (e.g. Hsü et al., 1973, 1977; Krijgsman et al., 1999; Duggen et al., 2003; Rouchy and Caruso, 2006; Rohling et al., 2008; Garcia-Castellanos et al., 2009; Garcia-Castellanos and Villaseñor, 2011; Roveri et al., 2014). The limit between the Messinian and the Pliocene is a key seismic marker, the "M" reflector, which can be recognized all over the Mediterranean

Sea with different seismic characters (e.g. Hsü et al., 1973; Sage et al., 2005; Lofi et al., 2011). There are numerous evidences of this widespread event, such as erosional channels, canyons and terraces, along most of the Alboran Basin (Estrada et al., 2011; Juan et al., 2016).

Afterwards, from Late Tortonian to present, the dominant mechanism affecting the Alboran Basin has been the NW–SE trending plate convergence that defined the basin's present-day physiography and tectonic structures (e.g. Watts et al., 1993; Comas et al., 1999; Wortel and Spakman, 2000; Rosenbaum et al., 2002; Gràcia et al., 2006; Lo Iocano et al., 2008; Gràcia et al., 2012; Moreno et al., 2016; Gràcia et al., submitted 2017; Perea et al., submitted 2017). While the West Alboran Basin has evolved as a flexural basin since the uppermost Tortonian (Do Couto et al., 2016), slab pull mechanisms still influence local tectonics in parts of the Betics and Rif, driving westward and southwestward movement respect to fixed Eurasia (Koulali et al., 2011; Galindo-Zaldivar et al., 2015; Pérez-Peña et al., 2015).

In relation to extensional processes and link with the subduction, significant magmatic activity occurred (e.g. Hoernle et al., 1999; Gill et al., 2004; Maury et al., 2000; Duggen et al., 2008) (Fig. 2.7). The first volcanic activity occurred during the Oligocene to the Early Miocene, and is mainly represented by tholeiitic dykes. They are related with extension in the basin and are found onshore in the Malaguide complex and in the Ronda peridotites (e.g. Torres-Roldan et al., 1986; Duggen et al., 2004; Marchesi et al., 2012). From the Middle Miocene to Tortonian (Late Miocene), calk-alkaline, tholeiitic and shoshonitic volcanism related to the subduction process took place (Duggen et al., 2008). During the Messinian to Quaternary, volcanism changed to alkaline, reflecting a dominance of hot asthenosphere material, rather than subduction related fluids (Duggen et al., 2004; Duggen et al., 2008).

The Alboran Basin is a seismically active zone (Fig. 2.8). Instrumentally recorded shallow to intermediate earthquakes from low to moderate magnitude ($Mw \leq 6.4$) occurred and historical records evidence that large earthquakes may have also been generated (MSK Intensity X-XI) (Stich, 2003; Gràcia et al., 2006; Stich et al., 2006; Gràcia et al., 2012; Gràcia et al., submitted 2017; Perea et al., submitted 2017). Together with the active structures of the Gulf of Cadiz, these events have a large recurrence period (> 1000 years) (Gràcia et al., 2010) and involve significant seismic and tsunamigenic hazard for the south Iberian-North African margins (e.g. Gràcia et al., 2003a; Gràcia et al., 2010; Bartolome et al., 2012; Martínez-Loriente et al., 2013; Martinez-Loriente et al., 2016) (Fig. 2.8).

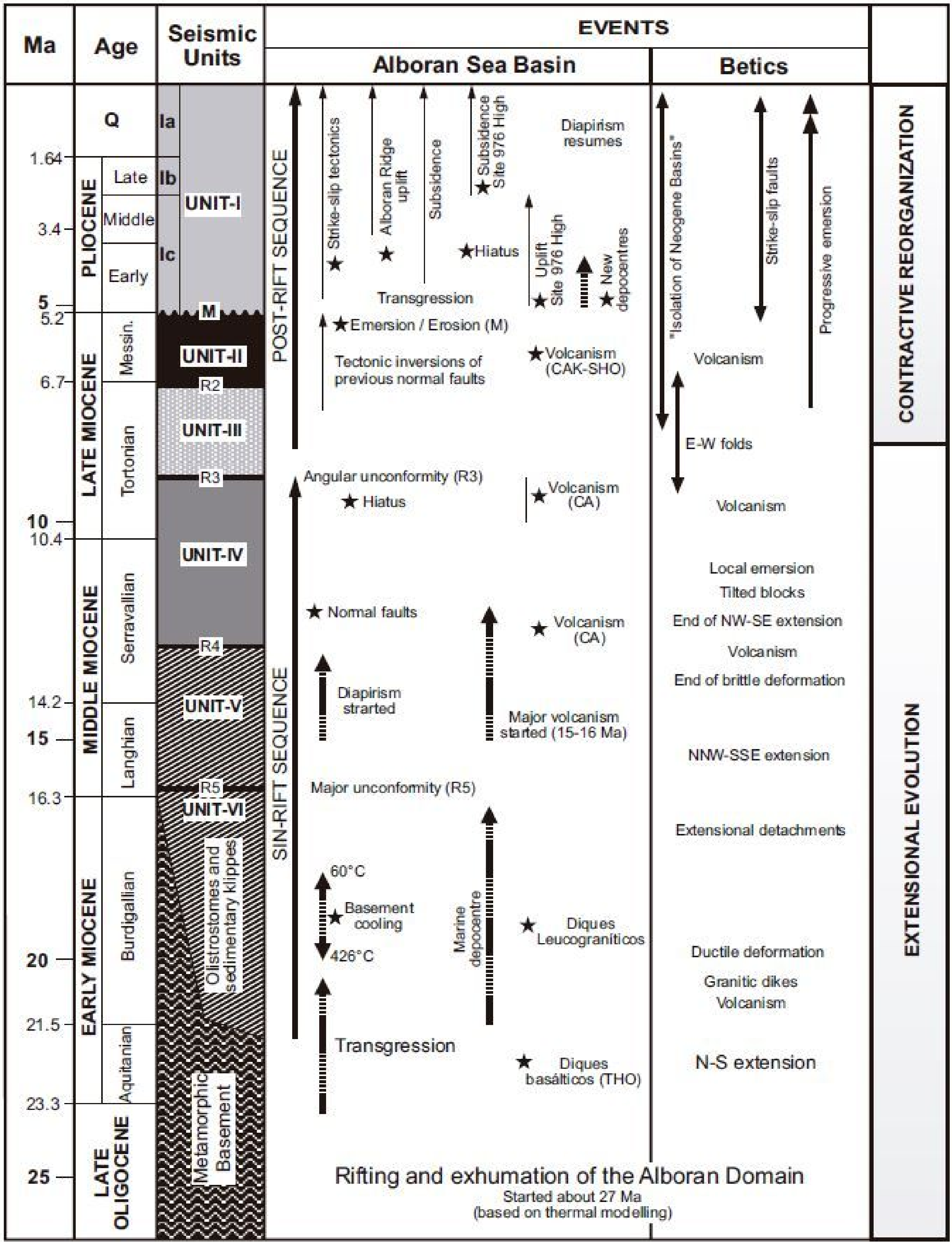

Figure 2.7: *Main tectonic events at the Alboran Sea and Betics (Martínez-García, 2012 modified from Comas et al., 1999).*

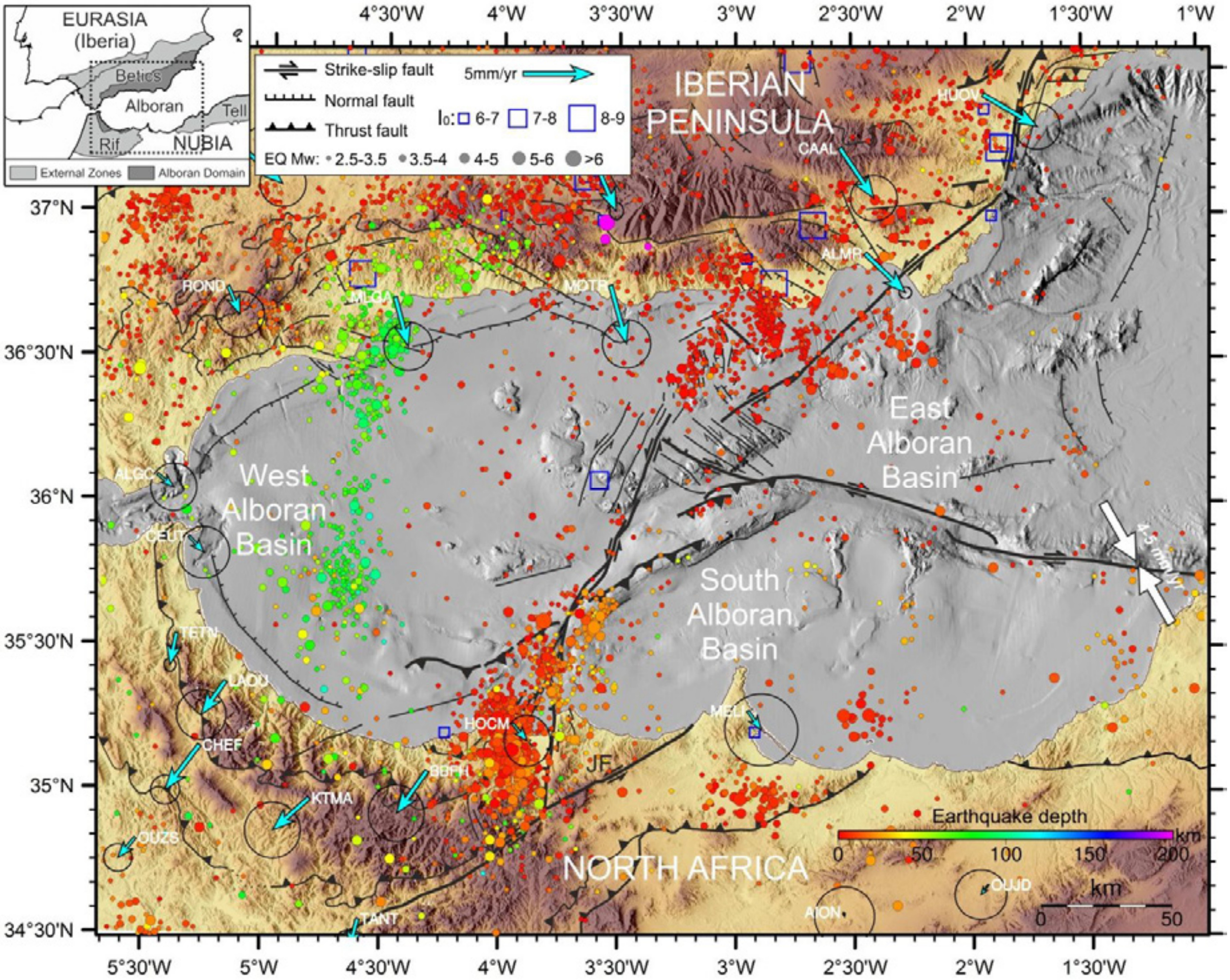

Figure 2.8: *Topography and bathymetry of the Alboran region. Main active faults are displayed (Gràcia et al., 2012, submitted 2017), together with historical (1400 – 1960, blue boxes) and instrumental seismicity (1980 – 2015, colour circles, see map legend for details) (IGN) (from http://www.ign.es/resources/noticias/Terremoto_Alboran.pdf). Light blue arrows symbolize the GPS velocity field with respect to Africa (Koulali et al., 2011), and white arrows the Eurasia-Nubia relative motion (De Mets et al., 2015). Inset: Location of the shown area. From Gràcia et al., submitted (2017).*

2.2.2. The Betic - Rif System

The western Mediterranean can be understood as the result of the interaction of European and African plates with a set of smaller tectonics plates, such as the Iberian plate and the Alboran microplate (made of a group of terrains). The actual framework is the result of a combination of compressional and extensional tectonics processes, sometimes coeval in time (e.g. Gelabert et al., 2002; Rosenbaum et al., 2002).

The Betic – Rif system results from the collision of the Alboran domain and the Iberian and African margins during the Oligocene – Miocene (~28 – ~7 Ma). The Alboran domain is an allochtonous terrain that separated from the AlKaPeCa (Alboran-Kabylides-Peloritani-Calabria) microplate (e.g. Lonergan, 1993; Vissers et al., 1995; Michard et al., 2008; Chalouan et al., 2009; Van Hinsbergen et al., 2014). This plate is the result of the stacking of different geological units due to the convergence between the European and African plates. The aperture of the different Mediterranean basins caused the fracture of the AlKaPeCa plate in different domains, as the Alboran Basin (blue areas in Figure 2.4). The continuous convergence and the subduction of the Tethyan oceanic lithosphere drove to the collision of these domains with the surrounding margins (e.g. Sanz De Galdeano, 1990; Alonso-Chaves et al., 2004).

The Betic thrust belt is located in the southeaster Iberian Peninsula (Spain), while the Rif is located in northwester Morocco (Fig. 2.1). These systems form and arcuate orogenic belt, surrounding Alboran basin, and consist of a superposition of different tectonics domains (Fig. 2.9). The Betic – Rif system is genetically associated with other alpine Mediterranean orogens, as the Apenines in Italy (Rosenbaum et al., 2002; Platt et al., 2003; Faccenna et al., 2004; Spakman and Wortel, 2004; Faccenna et al., 2014).

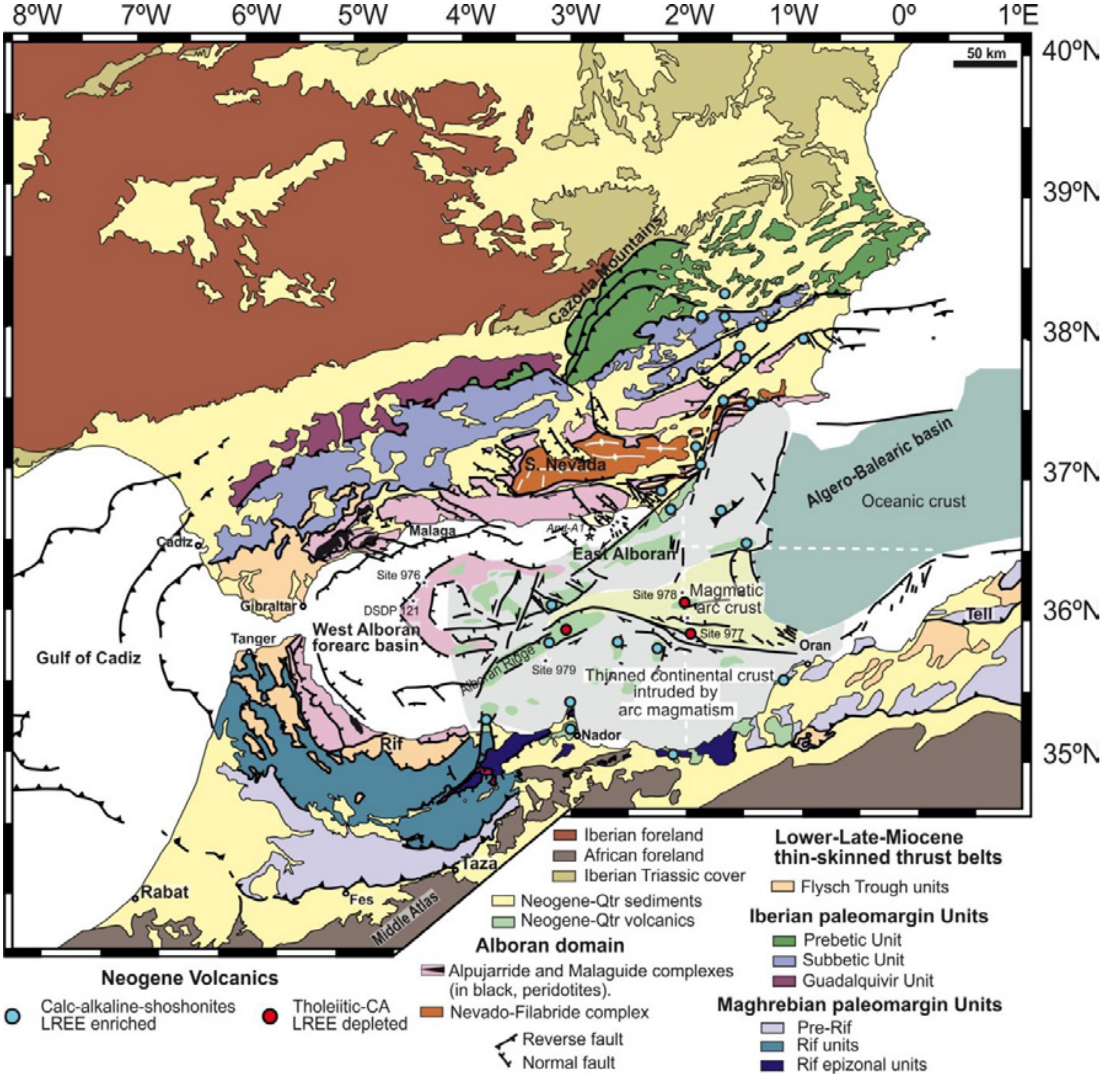

Figure 2.9: *Domains map of the Gibraltar Arc system. The Alboran Domain comprises the Betics, Rif and the West Alboran basin (Mancilla et al., 2015).*

The Betics and Rif are broadly symmetric in their tectonic structure, and present equivalent tectonic units (Fig. 2.9). These different tectonic domains that form the orogen can be separated in (i) the foreland basins, (ii) the external zones, (iii) the flysch units and (iv) the internal zones (Fig. 2.10) (e.g. Alonso-Chaves et al., 2004; Balanyá et al., 2007; Chalouan and Michard, 2004; Sanz De Galdeano, 1990; Gràcia et al., 2003a; Vergés and Fernàndez, 2012).

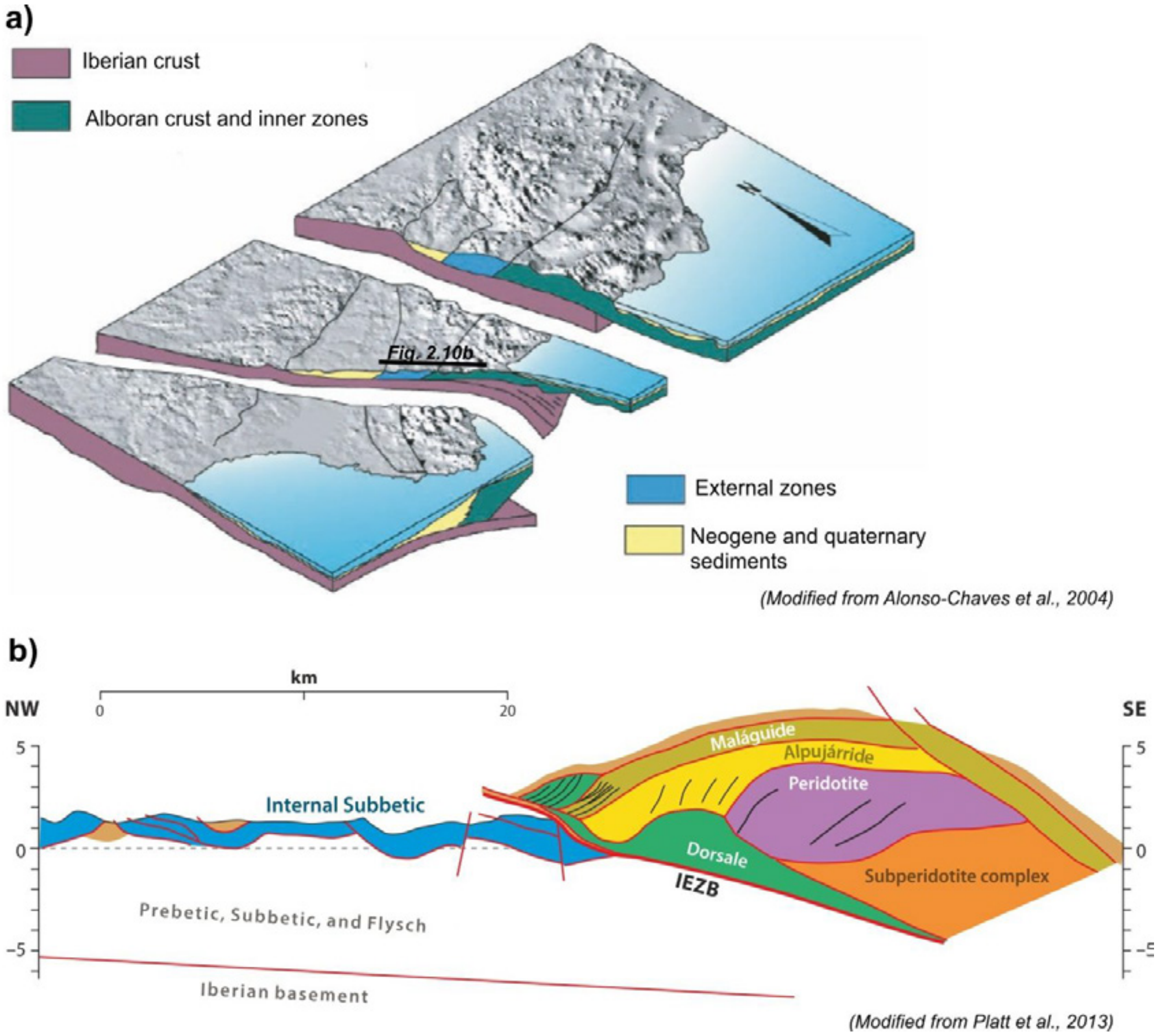

(Modified from Alonso-Chaves et al., 2004)

(Modified from Platt et al., 2013)

Figure 2.10: ***(a)*** *Cartoon showing the relationships between the main crustal units found below the Betics (modified from Alonso-Chaves et al., 2004).* ***(b)*** *Synthetic cross section along the Western Betics, including the Ronda peridotites outcrop. See Figure 2.10a for transect location (modifies from Platt et al., 2013). Domains map of the Gibraltar Arc system. The Alboran Domain comprises the Betics, Rif and the Alboran basin (Platt, 2007).*

The foreland basins correspond to the Guadalquivir Basin in south Spain and the Rharb basin in north-Morocco (Fig. 2.9). They correspond to a sedimentary sequence from the Middle Miocene until the Pliocene (Alonso-Chaves et al., 2004; Chalouan et al., 2009). To the west, a tongue-shaped tectonic body is located in the Gulf of Cadiz. It corresponds to the Guadalquivir Allochtonous Unit (Gràcia et al., 2003a), later referred to as the Gulf of Cadiz Imbricated Wedge, result of the westward migration of the system (e.g. Gràcia et al., 2003a; Iribarren et al., 2007; Vergés and Fernàndez, 2012).

The External Zones (Fig. 2.9) correspond to a fold-and-thrust belt composed by Mesozoic and Cenozoic sediments, which overlays the Iberian and Moroccan continental basements (Gràcia et al., 2003a; Alonso-Chaves et al., 2004; Crespo-Blanc et al., 2016; Sanz De Galdeano, 1990). The deformation of this unit is different between the south of Spain and the north of Africa. The Betics External Zones presents a thin-skin tectonic evolution, with upper Triassic evaporites commonly acting as detachment level, while the Rif

External Zones are characterized by a thick-skin tectonics (Mauffret et al., 2004; Crespo-Blanc and Frizon de Lamotte, 2006; Frizon de Lamotte et al., 2011).

The Flysch units are composed by deformed siliciclastic rocks ranging from Upper Jurassic to Burdigalian. The deformation is Early Miocene in age (prior to the Langhian) (Gràcia et al., 2003a; Vergés and Fernàndez, 2012). They represent the deep-sea sedimentation developed in front of the African passive margin. Nowadays, they are structurally sandwiched between the External and the Internal Zones (Alonso-Chaves et al., 2004; Vergés and Fernàndez, 2012).

The Internal Zones (Fig. 2.9) represent the inner part of the orogen and are the result of the structural superposition of three polymetamorphic terrains. From bottom to top, these terrains are the Nevado-Filabride, the Alpujarride and the Malaguide in the Betics (Fig. 2.9). Similar units in the African margin are the Sebtide for the Alpujarride complex, and the Ghomaride for the Malaguide unit (e.g. Alonso-Chaves et al., 2004; Chalouan and Michard, 2004; Sanz De Galdeano, 1990; Vergés and Fernàndez, 2012). The Nevado-Filabride and the Alpujárride/Sebtide complexes exhibit a high-pressure low temperature metamorphism, which age is not well dated. The present-day contacts between these terrains are extensional shear-zones, due to the exhumation and the denudation of the orogen (e.g. Alonso-Chaves et al., 2004; Chalouan and Michard, 2004; Sanz De Galdeano, 1990; Vergés and Fernández, 2012). Recent studies reveal that the Malaguide and Alpujarride original protolith suffered a high pressure metamorphism during Eocene times (e.g. Azañón et al., 1997; Platt et al., 2005) although this age is currently under revision. These units were originally interpreted to represent a collapsed orogeny and correspond to the Alboran domain *sensu stricto* (Dewey, 1989). The Nevado-Filabride complex had a different evolutionary history, being formed by subducted parts of the South Iberian margin (Platt et al., 2006; Booth-Rea et al., 2015). The high-pressure metamorphism affecting this unit took place later, between the Lower and the Middle Miocene (Platt et al., 2006; Booth-Rea et al., 2015).

2.2.3. The Alboran Basin

- *Structure and kinematics*

The basin has a complex geomorphology, where the main sub-basins are separately by tectonic structures and volcanic highs (Fig. 2.11). The maximum depth is around 2000 m. Four main depocenters are identified: the Western Alboran Basin (WAB), the South Alboran Basin (SAB) and the Eastern Alboran Basin (EAB) (e.g. Comas et al., 1999; Martínez-García, 2012) and the eastern Morocco and Argelian margin basins (Pytheas and Habibas basins, e.g. Medaouri et al., 2012; 2014).

The deformation associated to the NW-SE convergence (4.5 – 5.6 mm/yr) between the African and Eurasian plates (DeMets et al., 2010; Nocquet, 2012) is accommodated along a large number of faults (Fig. 2.8). The deformation is heterogeneous but mainly occurs along strike-slip and inverse faults (e.g. Gràcia et al., 2006). GPS-derived kinematic vectors indicate that there are crustal-scale tectonic structures that form boundaries of independent crustal tectonic blocks (Fig. 2.12) (Palano et al., 2015). These faults accommodate most of the plate convergence rate (Palano et al., 2015).

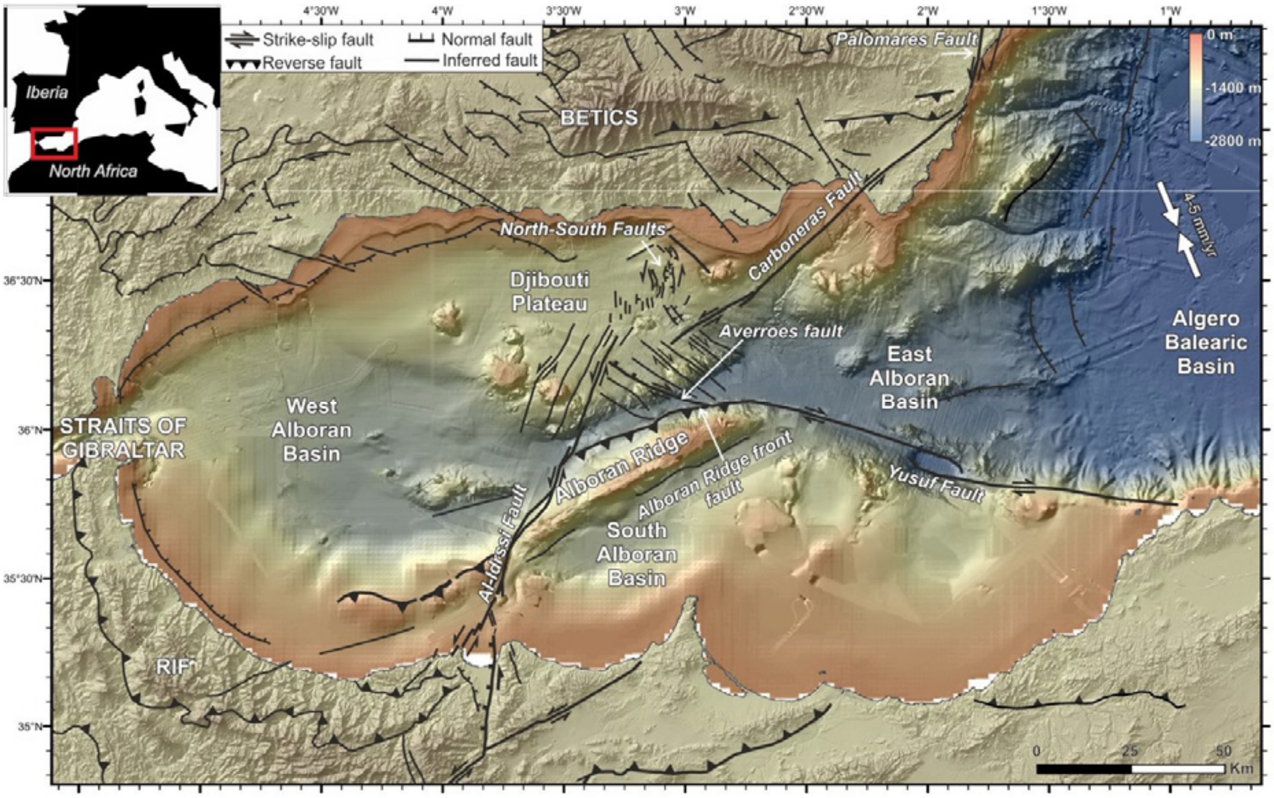

Figure 2.11 **▲:** *Same bathymetric and topographic map as Figure 2.1, with the main tectonic structures displayed (Gràcia et al., 2006, submitted 2017), as well as the main depocenters of the Alboran Basin. Inset: Location of the shown area (Gibraltar Arc System, red rectangle).*

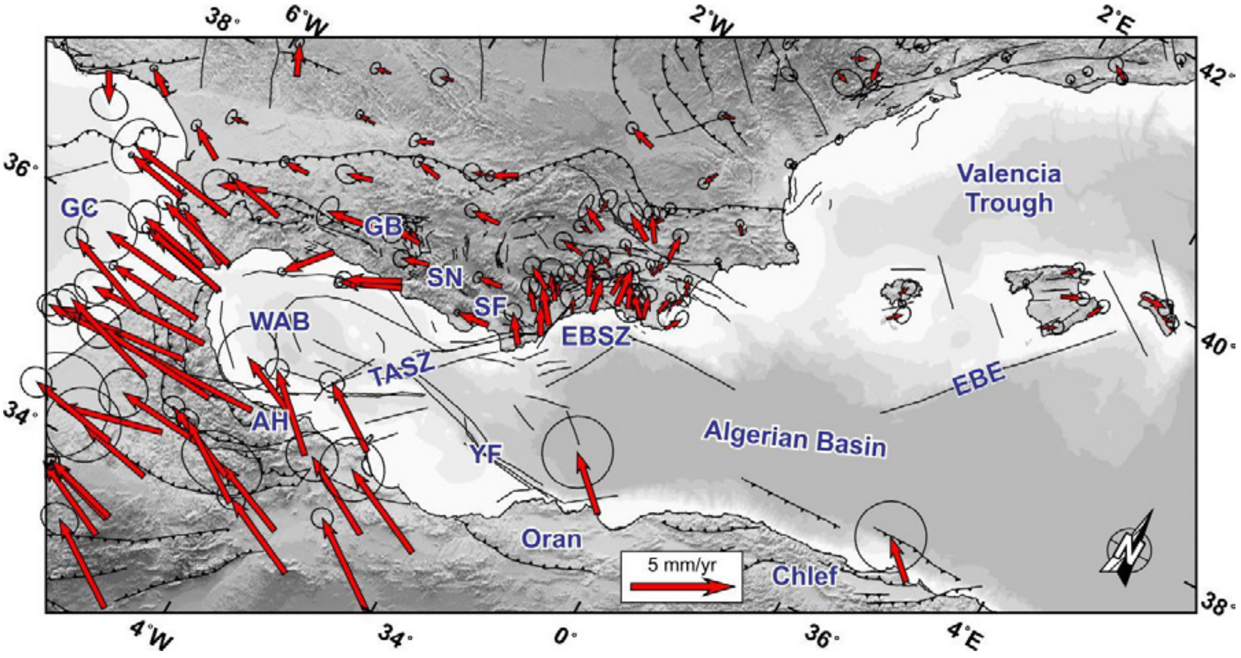

Figure 2.12 **▲:** *Detailed GNSS velocities for the Alboran and Algero Balearic Basins, taking a fixed Eurasian Plate as reference. GC, Gulf of Càdiz; WAB, Western Alboran Basin; AH, Al-Hoceima; GB, Granada Basin; SN, Sierra Nevada; SF, Sierra de Filabres; TASZ, Trans-Alboran Shear Zone; EBSZ, Eastern Betics Shear Zone; YF, Yusuf Fault; EBE, Emile Baudot Escarpment. (Palano et al., 2015).*

- *Stratigraphy*

Different stratigraphic units have been described in the sedimentary infill of the basin, on the basis of seismic reflection profiles and commercial and scientific wells. Traditionally, six different units have been identified (e.g. Alonso and Maldonado, 1992; Campos et al., 1992; Comas et al., 1992; Jurado and Comas, 1992; Comas et al., 1995; Álvarez-Marrón, 1997; Booth-Rea et al., 2007; Comas et al., 1999; Moreno, 2011; Moreno et al., 2016). However, most works are concentrated only in a particular region of the basin and the units are not consistently used across the entire basin. These units are labelled from I (top) to VI (bottom), and were deposited above the basement of the basin (the Alboran domain). A description of the units is presented below (Fig. 2.13):

- Unit I: Pliocene – Quaternary (5.3 Ma to Present-day). This unit is mainly composed by pelagic marls, muddy turbidites and hemipelagic clays. In the seismic profiles it appears as parallel reflectors of variable lateral continuity on its upper part (subunit Ia, Upper Pliocene – Quaternary), and with an overall transparent character on its lower part (subunit Ib, Lower Pliocene).

- Unit II: Messinian (7.2 Ma to 5.3 Ma). Sediments of this unit are marine sandy turbidities interbedded with carbonates and volcanoclastic layers. The upper section is made of evaporites deposits (mainly gypsum and anhydrite) related to the Messinian Salinity Crisis. The seismic expression of this unit is of rough topography, chaotic facies with strong, high amplitude and poorly continuous reflectors alternating with transparent bodies.

- Unit III: Late Tortonian. It is represented by sandstone intervals with claystones and silty-clays beds, corresponding to turbidite facies with channel like features. It is characterized by high-amplitude reflectors with parallel to divergent geometries, and strong lateral variations in thickness.

- Unit IV: Serravallian – Early Tortonian. It is formed by graded sand-silt-clays layers alternated with some volcanogenic layers. On seismic profiles, it appears with strong reflectors with low continuity that are intercalated with chaotic and transparent zones.

- Unit V: It is subdivided in two units. Sub-unit Va: Langhian – Lower Serravallian. Consists of well-graded sand-silt-clay turbidites and turbidite muds with volcanogenic layers. It is characterized by high-amplitude, discontinuous and divergent reflectors. Sub unit Vb: Langhian. It is made of undercompacted shales with interbedded sandy and sandy-pebbly intervals.

- Unit VI: Aquitanian – Burdigalian. It is only present on the West Alboran basin, and it consists of olistrostromes containing polymictic rocks embedded in an undercompacted shale matrix. These undercompacted materials are the origin of the shale diapiric processes that take place in the western part of the Alboran basin. On the seismic image, it is characterized by chaotic or transparent reflections without stratification.

These main stratigraphic units are separated in different areas by unconformities (Fig. 2.13), which seismic expression is also well identified. However, in the center of the basins different depocenters some units show a paraconformity. The unconformities are referred as R1 to R5, and also include the M (Messinian unconformity) reflector.

- R1: Messinian – Pliocene boundary (5.3 Ma). It is the Messinian unconformity, an erosive surface with high reflectivity.

- R2: Tortonian – Messinian boundary (7.2 Ma). Angular unconformity with high amplitude.
- R3: Intra-Tortonian. It is an erosive surface which fossilizes the extensional phases in the Alboran basin.
- R4: Intra-Serravallian. It is a reflector with high-amplitude and in some cases, reverse polarity.
- R5: Burdigalian – Langhian. A high amplitude reflector.

Additionally, other minor discontinuities are also identified (Fig. 2.13).

These are general sedimentary units defined for the entire Alboran Basin. Due to the different characteristics of each sub-basin, the stratigraphy presents different aspects on each. Our interpretation is based on this general units correlated with recent detailed studies on a particular area. The specific stratigraphy units defined and their characteristics have been carefully reviewed and are described in the "Chapter 6: Basin Evolution".

The basement of the basin has been dredged and drilled at few locations. Only two commercial wells reached basement: Andalucia G-1 (Jurado and Comas, 1992; Comas et al., 1999; Soto et al., 2010; Soto et al., 2012; Do Couto et al., 2016) and Habibas-1 (Medaouri et al., 2012; Medaouri et al., 2014). At these locations, metamorphic rocks have been recovered. Additionally, some basement highs have been dredged (e.g. Hoernle et al., 1999; Duggen et al., 2004; Duggen et al., 2008). At these highs, volcanic rocks were sampled. The basement assimilated to the Alboran domain is represented by metamorphic rocks similar to those found on the Betics and Rif internal zones, however much of the basin is floored by volcanic and plutonic rocks related to the subduction process (Comas et al., 1999; Hoernle et al., 1999; Duggen et al., 2004; Duggen et al., 2005; Booth-Rea et al., 2007; Duggen et al., 2008).

Figure 2.13* ►: *Summary table of the main seismo-stratigraphic units and discontinuities identified in the Alboran Basin.

	Epoch	Stage	Seismic unit			Seismic characteristics		Example
			Comas et al.	Booth-Rea et al.	Moreno			
Quaternary	Holocene		I	Ia	Ia + Ib	Ia1	Parallel, medium amplitude. Wavy discontinuous reflectors.	
	Pleistocene	Upper					High reflectivity and lateral continuity.	
		Middle						
						S1: *Strong and continuous. Locally, angular unconformity.*		
		Calabrian				Ia2	Continuous and parallel reflectors.	
						S2: *Strong unconformity.*		
		Gelasian				Ia3	High amplitude and parallel reflectors alternating with chaotic zones (mass transport deposits).	
						S3: *High intensity, continuous, reverse polarity.*		
Neogene	Pliocene	Piacenzian				Ia4	Parallel high amplitude reflectors.	
				S4: *High amplitude, discontinuous laterally.*				
		Zanclean		Ib	Ic	Ib1	Low amplitude, decreasing toward the base.	General low reflectivity.
						S5: *high amplitude, low continuity, polarity +/-/+*		
						Ib2	Low amplitude subparallel reflectors.	
	S6 = R1 = M: *erosional surface of high reflectivity.*							
	Miocene	Messinian	II		IIa	Onlap above M unconformity.	Parallel, hummocky, transparent o chaotic zones. Internal structuration due to evaporitic and volcanic levels intercalated.	
				M				
					IIb	Evaporites. Discontinuos, only local.		
				Inverse polarity reflector (evaporties base).				
					IIc	Discontinuous, chaotic. Low amplitude.		
		S7 = R2: *angular unconformity, high amplitude.*						
		Tortonian	III			High and low amplitude reflectors alternating with chaotic zones. Discontinuous.		
			R3: strong character, erosional surface. Post-date extension in the Alboran Basin.					
		Serravallian	IV			Strong low continuous reflectors combine with transparent and chaotic zones.		
			R4: *Intra-Serravallian. High amplitude and strong character.*					
		Langhian	V	Va		High amplitude, discontinuous and divergent reflectors.	Depocentres infill.	
				Strong reflector link to acoustic impedance changes.				
				Vb		Only in the West Alboran. Undercompactation.		
		R5: *Strong amplitude.*						
		Burdigalian	VI (Early Miocene)			In the West Alboran till 3ºW. Chaotic reflectors without internal stratiphication. Irregular thickness.		
		Aquitanian						
R6: *Basement top*								
¿?			BASEMENT: metamorphic or volcanic					

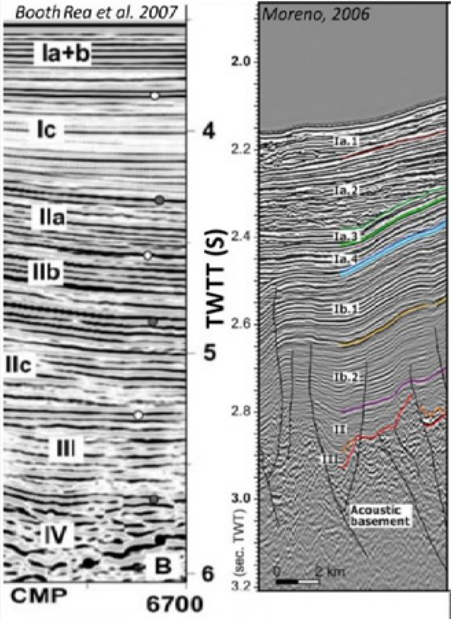

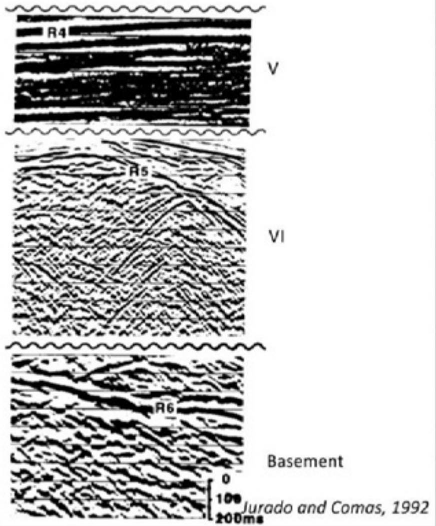

Part II

DATA AND METHODS

"L'essentiel est invisible pour les yeux"

Antoine de Saint-Exupéry
(Le Petit Prince)

Chapter 3

Multichannel seismic reflection data

3.1. Data acquisition

A signal is generated through an explosion (acoustic energy); in a point which spatial coordinates and time are known. The generated waves travel across the subsurface, being partially reflected in surfaces with a contrast of acoustic impedance, as well as other non-desiderate effects (Lowrie, 2007). Acoustic impedance is a physical property that results from the contrast in two juxtaposed layers of the product of the material density and travel velocity of the seismic waves across them. The variability of this physical property across layers is the one that allow us to image changes in lithology or different structures at depth. The objective of this method is to record these partial reflections, for a later analysis. The repetition of this process in every shot results in a seismic image of the subsurface (Yilmaz, 1987).

The energy originated by a shot and recorded as a time series by a receiver forms a seismic trace. Seismic traces are function of the amplitude and the time of the reflection (Fig. 3.1) (Yilmaz, 1987). Multichannel seismic reflection (MCS) is based in the recording of the same information in several receivers. It is a question of efficiency: In that way, the reflector surface points (i.e. points in which the acoustic impedance changes) are recorded in more than one seismic trace for each shot. Consequently, we are able to decrease the noise, which is assumed as random in each seismic trace, and amplify the real signal, which will be continually recorded in several seismic traces (Yilmaz, 1987).

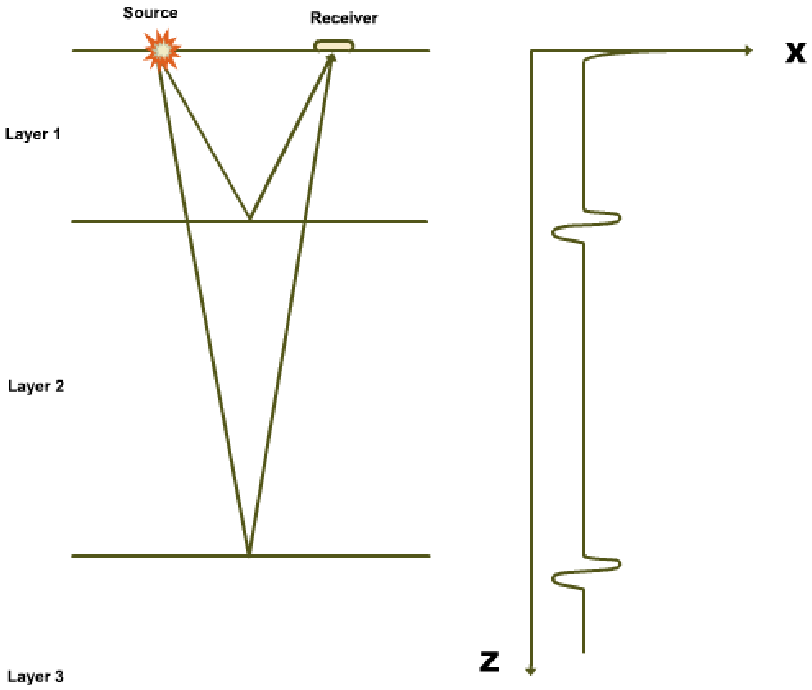

Figure 3.1: *The changes of acoustic impedance between layers produce the reflection of energy, which is then recorded a receiver (Mjelde, 2012).*

In particular, in marine MCS experiments data are acquired with instruments that are towed by a vessel. The most common source is the airgun (Fig. 3.2a, b), which produces bursts of compressed air. Usually, a combination of airguns is used, in order to attenuate the bubble effect produced by the repeated collapsed of the air bubble released from the source and obtain a signal as much similar to a spike as possible. Recording systems are located in a cable, which we refer to as the streamer (Fig. 3.2c). Inside the streamer, there are hydrophones that are the receivers that record the pressure perturbations mainly produced by the generated signal. Groups of hydrophones of the streamer are typically added before recording corresponding to a so-called channel. To help control and monitor the course and depth of the streamer, compasses (e.g. to know the deviations of the streamer along all its length, Fig. 3.2d), and "birds" (e.g. to control the streamer's depth (Fig. 3.2e), are attached all along the streamer. The last element is the tail-buoy, equipped with a differential GPS, allowing to record the precise position of the end of the streamer (Fig. 3.2f).

Figure 3.2: ***(a)*** *Air-guns array.* ***(b)*** *Detail of a G-GUN II of the array.* ***(c)*** *Streamer.* ***(d)*** *Compass.* ***(e)*** *Bird.* ***(f)*** *Tail buoy.*

3.1.1. Acquisition parameters

My Ph.D. thesis is essentially based on marine deep seismic data acquired during the TOPOMED-GASSIS cruise in October 2011. During this survey, high-quality data were obtained along and across the Alboran Sea Basin, cornerstone of my thesis. Moreover, additional data of different resolutions and acquired during previous surveys in the same area have also been available to me, allowing to perform a multi-scale approach of key marine structures.

Thus, I have also included complementary datasets, some collected also by the Barcelona-CSI research group (e.g. EVENT and EVENT-DEEP) and other national older projects (e.g. ESCI cruises) or because they are publicly available datasets (e.g. Conrad, CAB). Acquisition parameters of each survey as well as my contribution to produce the final seismic image used for this work are detailed below, ordered from the newest to the oldest one:

- ***TOPOMED-GASSIS cruise (2011)***

The main dataset used in the frame of this Ph.D. thesis were acquired during the TOPOMED-GASSIS cruise (PIs: E. Gràcia and C.R. Ranero) on board the Spanish RV "Sarmiento de Gamboa" (Fig. 3.3). During this cruise, deep-penetration seismic data were acquired that allow the imaging of the basin at a crustal scale. Two large-volume G-II gun sub-arrays (162/140 bar, 2000/2500 psi) and up to 6 km long Sercel solid state multichannel digital streamer (408 or 480 active channels respectively in two legs of the survey) were towed behind the vessel. The result is a comprehensive dataset of multichannel seismic profiles with unprecedented quality. This dataset allowed us to use modern processing and imaging techniques to obtain a deep imaging of the main tectonic structures, and a complementary good resolution of the sedimentary infill of the basin.

The acquisition parameters of the MCS profiles are described in the following table (Table 3.1)

	TOPOMED-GASSIS Leg 1	**TOPOMED-GASSIS Leg 2**
Number of active channels	408	480
Distance between channels	12.5 m	12.5 m
Total streamer length	5397 m	6332 m
Streamer depth	10 m	10 m
Distance source – first channel	150.8 m	203.7 m
CMP distance	6.25 m	6.25 m
Sample rate	2 ms	2 ms
Trace length	12 s / 14 s	19 s
Shot distance	37.5 m / 50 m	50 m
Air-guns depth	7.5 m	9 m

Table 3.1: *Acquisition parameters of the MCS profiles collected during the two legs of the TOPOMED-GASSIS cruise.*

The result of this survey is a total of 32 profiles, 29 profiles acquired in the Alboran Basin (Fig. 3.3) and 3 in the Gulf of Cadiz. For this thesis, I entirely processed all profiles acquired during the Leg 1 in the Alboran Sea, which are TM01 to TM25, but I have also used three profiles acquired during the Leg 2 across the Alboran Sea (TM27-TM29).

- ***EVENT-DEEP cruise (2010)***

The Event-Deep cruise (PI. E. Gràcia) also consisted in two legs (Fig. 3.3). To carry out two different types of resolution and penetration seismic profiles, during the cruise two seismic configurations were used: high-resolution (Leg 1) and deep penetration (Leg 2). Leg 1 focused on the shallow part, in order to study the recent-most sedimentation and active faults. Leg 2 was designed to increase the penetration, and image the deeper part of structures without losing much resolution in the sedimentary infill.

Data were acquired on board RV "Sarmiento de Gamboa". During Leg 1, a 600 m Sercel SEAL multichannel seismic streamer of 600 m (96 channels, separated 6.25 m) was rented to Exploration-Electronics Company, and a G-gun II air-gun array fired at 800 c.i. were used. For Leg 2, to ensure deeper penetration, the receiver was a 3.4 km Sercel SEAL multichannel digital streamer (276 channels, 12.5 m between channels) from UTM-CSIC and the G-gun II air-gun array configuration was increased down to 1880 c.i.

	EVENT-DEEP Leg 1	**EVENT-DEEP Leg 2**
Number of active channels	96	276
Distance between channels	6.25 m	12.5 m
Total streamer length	600 m	3450 m
Streamer depth	2.5 m	6 m
Distance source – first channel	45.6 m	114.0 m
CMP distance	3.125 m	6.25 m
Sample rate	2 ms	2 ms
Trace length	5.5 s / 8 s	12 s
Shot distance	12.5m / 18.75 m	37.5 m
Air-guns depth	2.5 m	6 m

Table 3.2: *Acquisition parameters of the MCS profiles acquired during the EVENT-DEEP cruise.*

I collaborated in processing part of the EVENT-DEEP Leg 1 profiles (EVD-100 to EVD-212B), and I entirely processed EVENT-DEEP Leg 2 profiles (EVD-1 to EVD-4). Leg 1 stack profiles were initially processed using ProMax, and I finished processing performing time migration and time and spatial variant filters with Globe Claritas. Leg 2 profiles were processed following the flow presented at section "3.2: Data processing".

- **CAB cruise (2000-2001)**

During years 2000 and 2001, Conoco Philips Company collected data in the West Alboran Basin. The result are two datasets, CAB-00 and CAB-01 surveys (Fig. 3.3), that we obtained from the "Archivo Técnico de hidrocarburos"[1] (Ministerio de Industria, Energía y Turismo, Spain). They are available as migrated TWT and depth sections.

The data were acquired by DMNG (Dalmornettegeophysica Joint Stock Company) with a Syntrak RDA streamer of 6000 m (480 channels, 12.5 m each) and an airgun array fired at 2800 c.i.

	CAB-00	**CAB-01**
Number of active channels	480	480
Distance between channels	12.5 m	12.5 m
Total streamer length	6000 m	6000 m
Streamer depth	7 m	7 m
CMP distance	6.25 m	6.25 m
Sample rate	2 ms	2 ms
Trace length	12 s	12 s
Shot distance	37.5 m	37.5 m
Air-guns depth	2.5 m	6 m

Table 3.5: *Acquisition parameters of the MCS profiles during the CAB cruises.*

No further processing has been applied to this dataset, but it has been useful for interpretation tasks.

- ***ESCI Alboran cruise (1992)***

Two seismic lines were obtained during this survey carried out on board Seismic Vessel "Bin Hai" from WesternGeco (Geco at the time) in February 1992 (Fig. 3.3). Although this is a vintage dataset, the quality of the instruments used in the acquisition and the clever planning of the lines makes of this survey a useful dataset. Raw data has been re-processed using the most advanced methods (see section "3.2: Data processing"), which allows obtaining new and accurate information.

Air-gun array was fired at 7118 c.i. (2000 psi) every 75 m, and a 4500 m (180 channels each 25m) HSSQ streamer was used.

	ESCI-Alb
Number of active channels	180
Distance between channels	25 m

---

[1] https://geoportal.minetur.gob.es/ATHv2/welcome.do

Total streamer length	4500 m
Streamer depth	15 m
Distance source – first channel	120 m
CMP distance	12 m
Sample rate	4 ms
Trace length	22 s / 18 s
Shot distance	50 m / 75 m
Air-guns depth	7.5 m

Table 3.3: *Acquisition parameters of the MCS profiles during the ESCI-Alb cruise.*

I completely reprocessed ESCI-Alb1 with the processing flow presented at section “3.2: Data processing” and I had available for my thesis ESCI-Alb2 (Fig. 3.3).

- **Conrad cruise (1988)**

The Conrad survey took place in October of 1988 on board RV “Robert D. Conrad” (Fig. 3.3). The vessel was equipped with a BOLT air-gun array fired at 5346 c.i. and a DIGICON 2.4 km long streamer with 48 active groups spaced 50 m.

	Conrad
Number of active channels	48
Distance between channels	50 m
Total streamer length	2400 m
CMP distance	25 m
Sample rate	4 ms
Trace length	20 s
Shot distance	50 m

Table 3.4: *Acquisition parameters of the MCS profiles during the Conrad cruise.*

Conrad dataset was obtained from the Academic Seismic Portal (ASP) of the University of Texas (UTIG)[2]. In this database, stack sections are available. In order to improve seismic imaging, I performed a post-stack processing flow, including deconvolution, time and space variant filter, amplitude balance and time migration (see section “3.2: Data processing” for further information).

---

[2] http://www-udc.ig.utexas.edu/sdc/

➢ Other data

Complementary seismic datasets have also been available in the frame of the Barcelona-CSI research group. I have taken advantage of previous processed and interpreted data in the Carboneras Fault area, including the high-resolution EVENT-SHELF (2008) and IMPULS (2006) cruises (PI. E. Gràcia) (Fig. 3.3).

3.2. Data processing

We should take into account that a seismic image is not an exactly image of the sub-surface. It is a representation of the wave field produced by energy travelling across the sub-surface (Stein and Wyssesion, 2003). A seismic study focuses on the record and analysis of the reflections generated by a contrast in acoustic impedance (Z). Z is defined by the equation $Z=v\rho$, were v is the seismic wave velocity and ρ is the density of the rock (Yilmaz, 1987). Changes of Z value (thus, a reflection) are associated with changes in lithology or fluid context, either related to stratigraphical changes or tectonic structure. Unfortunately, data contains noise that deteriorates the signal expression and obscures primary reflections, which are the seismic processing target.

In a seismic trace, we will find these primary reflections, but also coherent an incoherent noise. Examples of coherent noises in marine reflection experiments are the water-layer multiples, source bubbles, and refracted waves. Furthermore, it is necessary to take into account that our signal is not a perfect spike, and also that signal particularly at high frequencies is losing energy with depth. All these problems affect the quality of the seismic image, although it can be largely corrected with an adequate processing of the data.

The three mainly steps in a processing flow are the following: (i) Deconvolution, which increases the vertical resolution by compressing the generated signal (wavelet) close to a spike while suppressing reverberations, (ii) Common Mid-Point (CMP) stack, fundamental to increase the signal-to-noise ratio, and (iii) Migration, which removes the diffractions and puts the reflections closer to their real position in the sub-surface, increasing horizontal resolution (Yilmaz, 1987). With the objective of increasing signal-to-noise ratio, a processing flow in time-domain has been designed with special emphasis in frequency preservation, effective multiple attenuation, amplitude preservation and velocity determination. Dedicated processing has been applied to a total of ~3300 km of data, including TOPOMED (lines TM01-25; 1903 km in total), EVENT-DEEP Leg 2 (lines EVD-1, EVD-2a, EVD-2b, EVDT-1-3a; 300 km) and ESCI-Alb (ESCI-Alb1; 91 km) profiles (Fig. 3.3).

The success of a processing step depends not only on the correct choice of parameters to that particular process, but also on the effectiveness of previous processing steps. Although behind all these processes there are some theoretical assumptions that unfortunately not always are fulfilled, the above three main processes are robust enough and their performance is reasonably insensitive to the underlying theoretical assumptions. All other processing techniques can be considered secondary, in the sense that they help to the effectiveness of these three primary steps (Yilmaz, 1987).

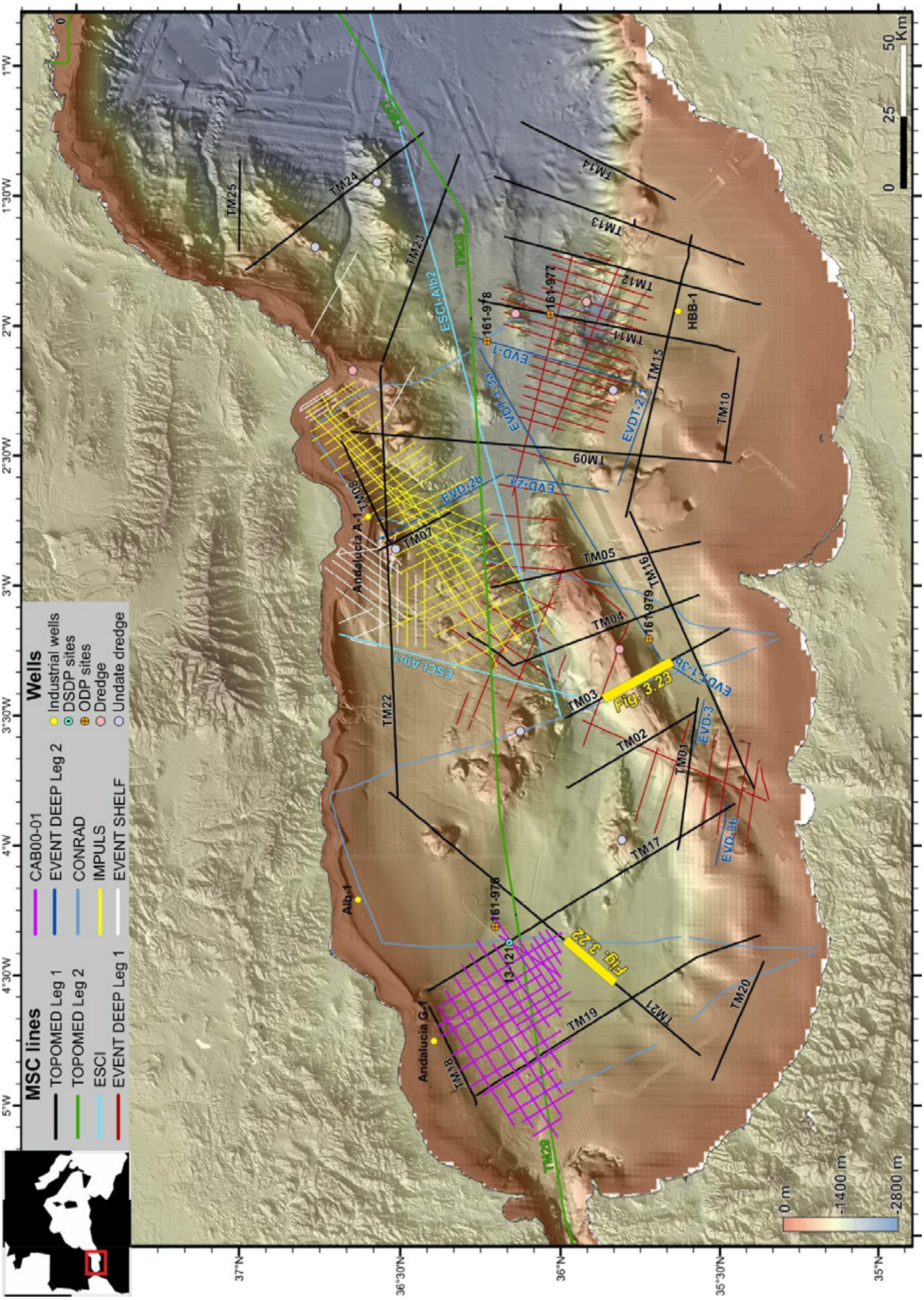
MSC lines
TOPOMED Leg 1
TOPOMED Leg 2
ESCI
EVENT DEEP Leg 1
CAB00-01
EVENT DEEP Leg 2
CONRAD
IMPULS
EVENT SHELF
Wells
Industrial wells
DSDP sites
ODP sites
Dredge
Undate dredge
0 m
-1400 m
-2800 m
0
25
50
Km
1°W
1°30'W
2°W
2°30'W
3°W
3°30'W
4°W
4°30'W
5°W
37°N
36°30'N
36°N
35°30'N
35°N
TM01
TM02
TM03
TM04
TM05
TM07
TM08
TM09
TM10
TM11
TM12
TM13
TM14
TM15
TM16
TM17
TM18
TM19
TM20
TM21
TM22
TM23
TM24
TM25
TM28
TM29
ESCI-Alb1
ESCI-Alb2
EVD-1
EVD-1-3a
EVD-1-3b
EVD-2a
EVD-2b
EVD-3
EVD-3b
EVDT-2-1
161-976
161-977
161-978
161-979
13-121
HBB-1
Andalucia A-1
Andalucia G-1
Alb-1
Fig. 3.22
Fig. 3.23

◄ ***Figure 3.3:*** *Bathymetric map of the Alboran Sea. Seismic datasets used in this thesis are depicted, including cruises Event-shelf and Impuls that have been previously processed and interpreted by B-CSI members. Profiles acquired during the TOPOMED-GASSIS (TM), EVENT-DEEP leg 2 (EVD) and ESCI are labelled. Wells and dredged sites are located, as well as Figures 3.22 and 3.23.*

The performed data processing can be divided in two parts: The first part has been carried out in time domain. It is the main part of the processing carried out with the software "*Globe Claritas*". It has been applied to all TOPOMED, EVENT-DEEP Leg2 and ESCI-Alb profiles. In order to illustrate how this flow enhanced the signal to noise ratio and improved seismic images, examples of the steps are given with line TM21 as example (Fig. 3.22, see Figure 3.23 for location). Additionally, to define the real geometry of important structures in depth, we also performed Pre-Stack Depth Migration (PSDM) of selected profiles (TM03 and TM11) (Fig., 3.23, see Figure 3.23 for location). This second part of the processing, in depth domain, has been carried out using with the processing software "*Echos Geodepth*".

3.2.1. MCS processing flow in time domain

The processing flow in the time domain (Table 3.6) has been designed to increase the signal-to-noise ratio. It can be divided in six main steps: I) Pre-processing, II) Deconvolution, III) Multiple attenuation and velocity analysis, IV) Dip Move Out correction, V) Final stack, and VI) Post-stack time migration.

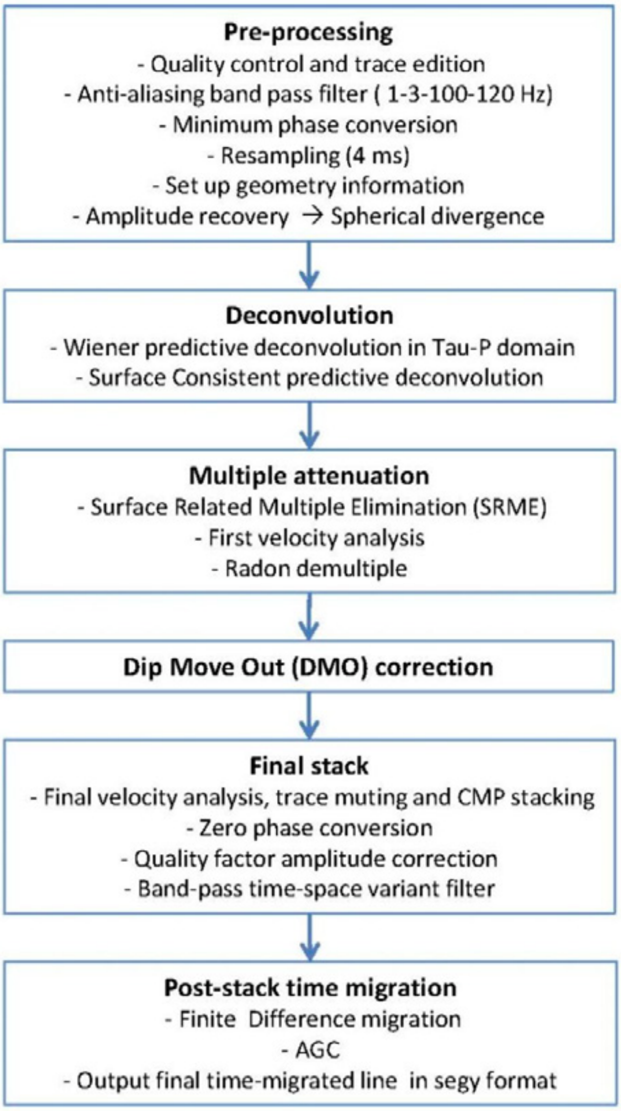

Table 3.6: *Processing flow used for processing the dataset in time domain.*

I. Pre-processing

In this step, we describe analysis of data to design the proper time processing sequence. They consisted on a first data quality control, a broad band-pass filter, minimum phase conversion, a time resample of data, addition of the geometry information, and an amplitude recovery to balance amplitude which is convenient for several processing steps like deconvolution.

During quality control, checks are carried out for missing traces determined, and bad or noisy shots. Tests are done to filter, amplitude balance or even eliminate noisy input data early on in the process flow. A delay between trigger and the air-guns shot time, applying a positive time shift correction of 50 ms was applied.

The band-pass filter consists on a Butterworth filter, designed to remove lower frequencies related to sea swell and human noises, and a high cut to prevent time aliasing of the signal. The values applied are 1-3-100-120 Hz. In the design of this filter, the Gibbs Phenomenon has been taken into account to avoid the generation of ringing.

To perform the minimum phase conversion, we have to determine the source wavelet. We carried out an autocorrelation of 100 seismic traces, starting at the seafloor time, with a window length of approximately 5 times the length of the generated signal (~500 ms). This parameter led to a 2500 ms window. The autocorrelation allowed us to find the wavelet because this generated wavelet is the same for all traces. Once we have determined the wavelet, we are able to convert it to minimum phase, and design the filter that allows converting all seismic traces to minimum phase. This step is important because most of the processes work better when the input data are in minimum phase, and it is also useful attenuating the bubble effect. Through the convolution of our minimum phase filter with the mixed phased raw data, we are able to convert this raw data to minimum phase. After the data are minimum phase, they are resampled to 4 ms to reduce data volume without losing information.

Finally, we set up the geometry information in the seg-y file headers. This is one of the most important points in a processing sequence, essential step to obtain a good stack. The correct geometry information will place the traces, and therefore, the recorded reflections on its correct position, increasing the horizontal resolution. This is fundamental to a later re-organization of the data in *Common Mid Points* (CMP). Knowing the position of the shots (source), and the channels (receivers) position, from the known position of the streamer allows to insert X, Y coordinates for each trace, and to make CMP distribution based on that positioning (Fig. 3.4).

On the basis of the field geometry information, each trace is assigned to the middle point between the shot and the receiver associated to that trace. Traces with the same middle point are grouped together, forming a *Common Mid Point* (CMP) gather. This term is usually used indistinctly with *Common Depth Point* (CDP)*,* but it must be noted that they are the same only when the reflector is horizontal (Fig. 3.5) and velocities do not vary horizontally, due to the ray path propagation geometry. The CMP groups all the traces with the same middle point shot-receiver, while the CDP refers to the traces that have been reflected in the same point at depth (Fig. 3.5) (Yilmaz, 1987).

Before starting the deconvolution process, a spherical divergent amplitude correction based on a geological velocity layers model has been applied. The goal is to recover amplitude decay at depth, especially visible on the high frequencies, due to the geometrical spreading of the wave front through the different velocity layers in depth and to the energy dissipation. The resulting brute stack of this pre-processing is shown in Figure 3.22a.

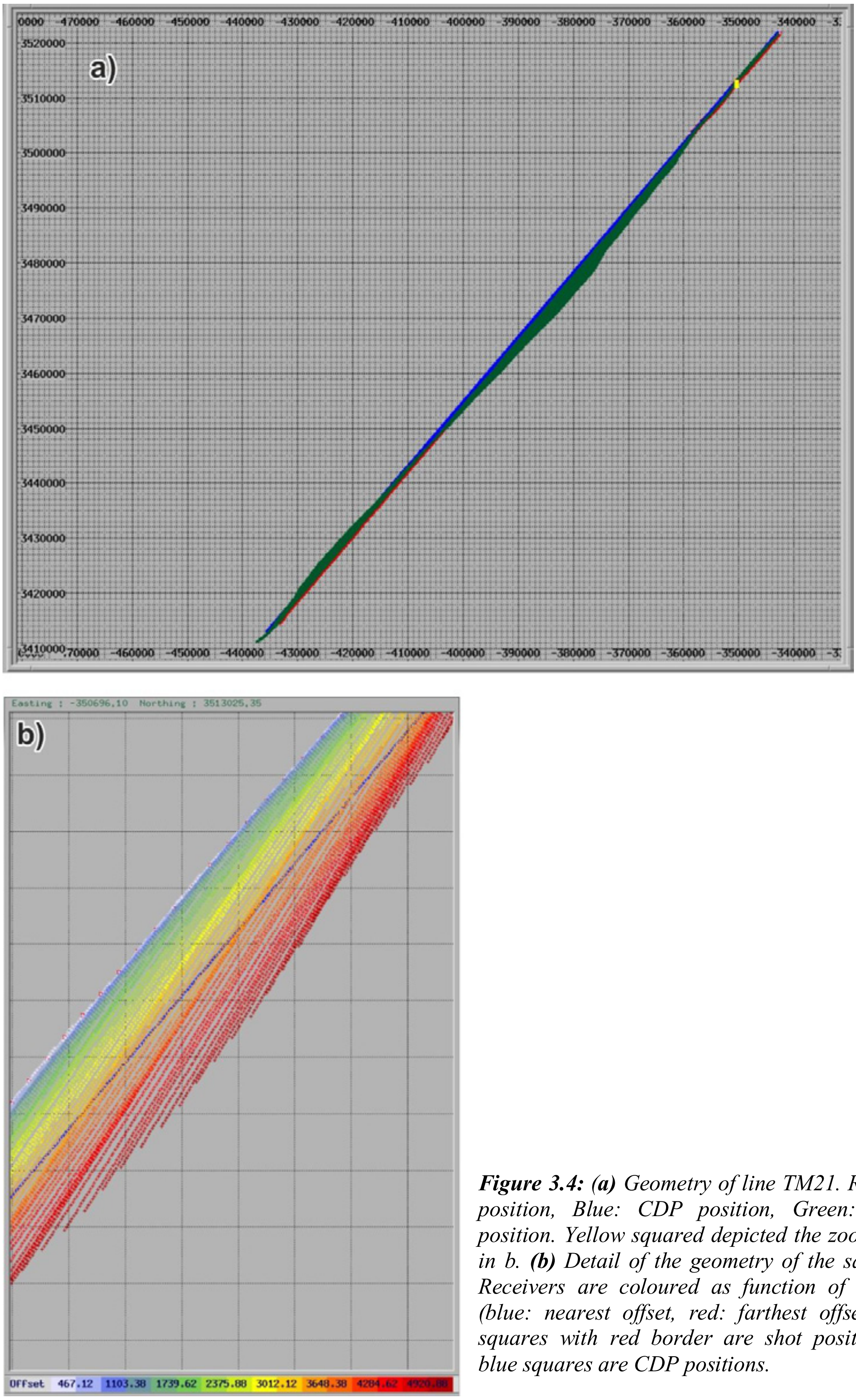

Figure 3.4: ***(a)*** *Geometry of line TM21. Red: Shots position, Blue: CDP position, Green: receiver position. Yellow squared depicted the zoomed area in b.* ***(b)*** *Detail of the geometry of the same line. Receivers are coloured as function of the offset (blue: nearest offset, red: farthest offset). White squares with red border are shot positions, and blue squares are CDP positions.*

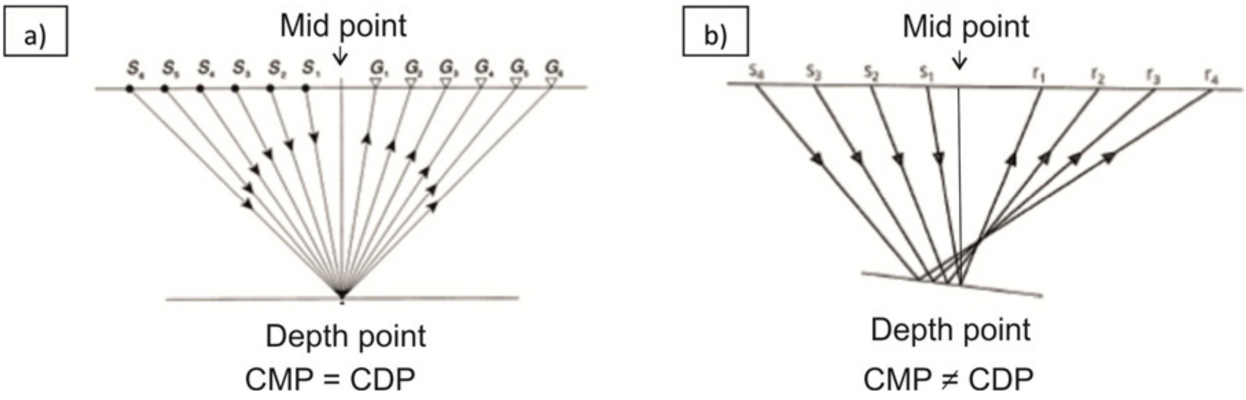

Figure 3.5: ***a)*** *CMP gather. When the reflector is an horizontal surface, the depth point for all the traces in the same, thus CMP is coincident. (Yilmaz, 1987).* ***b)*** *CMP is used when the reflector is dipping. Although the traces are in the same CMP because the mid-point between source and receiver is the same, they do not come from the same point at depth (Stein and Wyssession, 2003). S: shot; G, r: receiver.*

II. Deconvolution

Deconvolution tries to recover the reflectivity series, or in other words, the earth impulse response, removing the record of the source wavelet from the seismic trace. The main aim of this process is to bring closer the wavelet to a spike, increasing the vertical resolution (if the source wavelet sharper, two closer interfaces can show as distinct reflected arrivals), and also attenuating short-peg multiples (Fig. 3.6) (Yilmaz, 1987; *Stein and Wysession*, 2003).

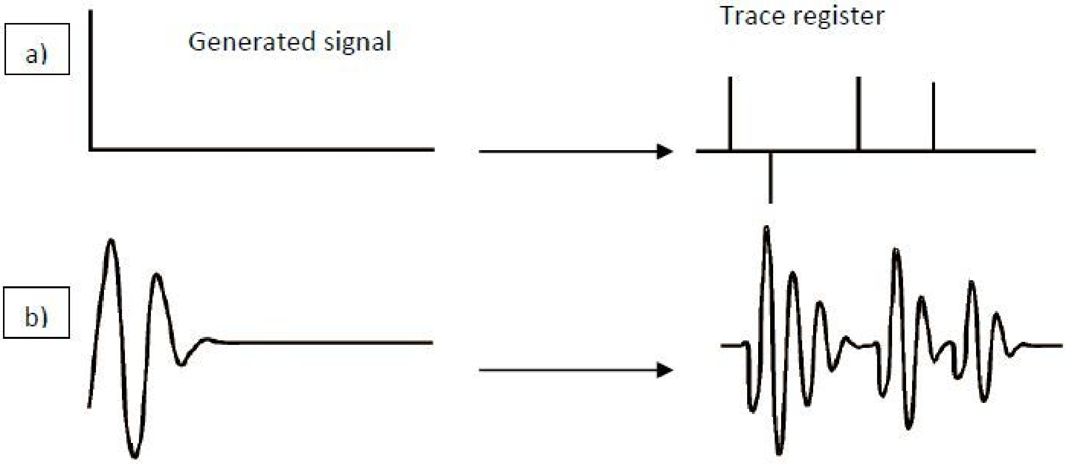

Figure 3.6: ***a)*** *The signal generated is a unique pulse (spike), so the seismic trace recorded is the earth impulse response.* ***b)*** *Usually we cannot generate a spike, so the recorded signal is the convolution between our signal and the earth impulse response (Yilmaz, 1987).*

To understand how acts the deconvolution, is necessary to understand how is done the record of a seismic trace. Earth is composed by layers of different lithologies and physical properties. From a seismic point of view, these materials are defined by its density and seismic velocity of the waves traveling across them. The seismic trace is the convolution between the earth impulse response and our wavelet (Fig. 3.7). In an ideal case, the generated wavelet would be a unique spike, and we will record just the impulse response.

As the generated signal is not a perfect spike, we carried out a deconvolution processes. The deconvolution tries to approximate as much as possible the generated wavelet to a spike, leaving in our record section just the earth impulse response (Fig. 3.7) (Yilmaz, 1987).

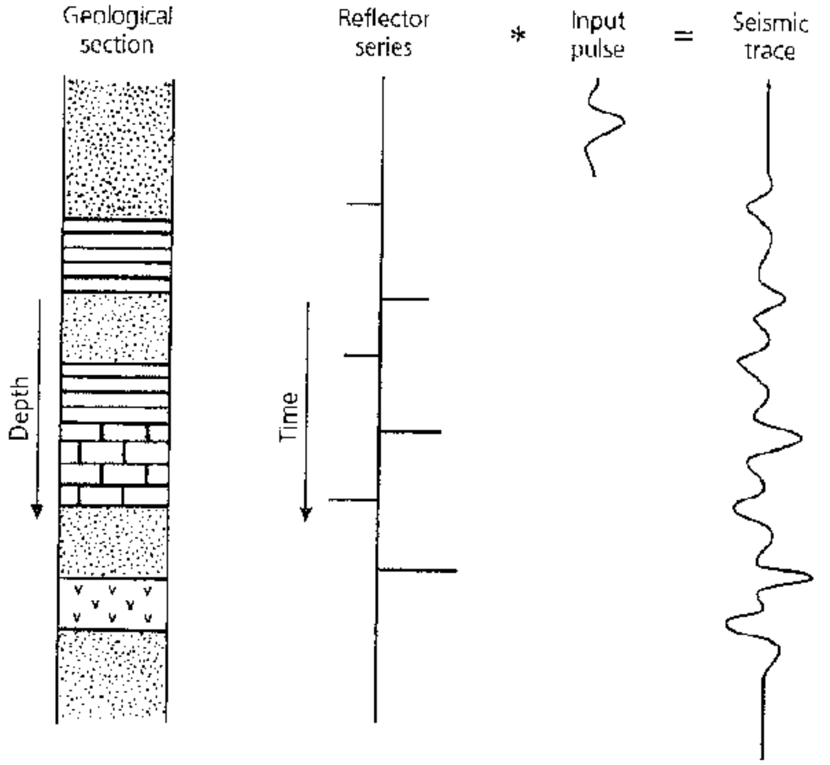

Figure 3.7: *A seismic trace in seismic reflection is the result of the convolution between the generated signal and the earth impulse response, defined by its geology. This earth impulse response has pulses at the times of acoustic impedance changes. These pulses correspond to the reflectors, which amplitude is related to the reflection coefficient. Performing the deconvolution, we approximate the generated signal to a unique spike, getting closer to the earth impulse response, which is what is we are looking for (Stein and Wysession, 2003).*

There are two types of deconvolution: deterministic and statistical. The deterministic deconvolution is carried out when the source waveform is known. When the source waveform is insufficiently known, then the solution to the deconvolution is statistical (Yilmaz, 1987). We applied two statistical deconvolutions, as the source waveform is insufficiently known.

To perform deconvolution, we need to design a filter, which will modify the wavelet of our data. The fundament of this filter is that the geology is random, so the impulse response is also random. This implies that if there is a pattern replicated along the seismic trace, it must be induced by the source wavelet. The filter can be obtained by autocorrelation of the signal, and the main objective is to convert the source wavelet in a spike (Yilmaz, 1987).

In our case, we applied two pre-stack deconvolutions to the data, (II.1) a Wiener Predictive deconvolution in Tau-P domain, and (II.2) a Surface Consistent deconvolution.

II.1) Wiener predictive deconvolution in Tau-P domain

The reason to apply the deconvolution in Tau-P domain is that the Tau-P domain solves the problem of non-stationarity due to the reflection move out. The Tau-P transform performs a plane wave decomposition of the record, representing the data in terms of zero offset intercept (Tau), versus ray parameter (p, the apparent slowness of the wave front in the horizontal direction) (Haskey and Ashdown, 1991; Stein and Wyssession, 2003; Maraj, 2011). The main advantage of performing a Wiener deconvolution in Tau-P domain is that preserves relative amplitudes and primary reflection energy. It is used to attenuate short period multiple reverberations, such as peg leg multiples and source bubble signature.

Wiener filters can be used to solve a wide range of problems. In the case of predictive deconvolution, they are used to compress the seismic wavelet, increasing in that way temporal resolution. In the limit, it can be used to spike the seismic wavelet and obtain an estimate for the earth reflectivity series (Yilmaz*,* 1987). Predictive deconvolution has two uses: (i) spiking deconvolution, and (ii) predicting the input seismogram at a future time, defined by the prediction lag. Note that the first is useful in order to sharpen the signal, and the second one to predict and attenuate multiples (Yilmaz*,* 1987).

We have applied a Wiener predictive deconvolution in Tau-P domain to sharpen the source wavelet and attenuate short period multiples (Fig. 3.22b). This deconvolution process has been performed with a spatial variant filter, designed in the shots. The filter length was variable and corresponds to the water point at each point of the seismic section, as tests reveal that it is the most effective length. The gap length was the same as the time of the bubble (in our case, between 140 and 160 ms, depending on the profile and tested for each) (Fig. 3.8a). The chosen designed window was from 100 ms below the seafloor till 7000 ms, because this window contains a representative section of the data and do not introduce noise in the deconvolution process. White noise percentage was 0.1%. The deconvolution has been applied in a single window over the whole trace, in the shot sorted data.

These parameters helped attenuate the source bubble and other short peg reverberations (Fig. 3.8b, Fig. 3.9b, Fig. 3.22a-b). It is more effective in depth water, although it also improves the seismic profiles in the shallower parts.

II.2) Surface Consistent deconvolution

Surface Consistent deconvolution looks for variations in wavelet shape caused by near-source and near-receiver conditions, and source-receiver separations. It is assumed that the source wavelet only depends on the source and receiver locations, and not of the ray path details. This process removes wavelet variations between the traces, in a surface consistent manner; removing random noise and variation of amplitudes due to near surface irregularities (Yilmaz*,* 1987).

We have performed two surface consistent deconvolution processes, the first one in shot-sorted data, and the second one in channel-sorted data (offset gathers). The chosen design and application windows are the same as for the Wiener predictive deconvolution in Tau-P domain (design window, from 100 ms below seafloor till 7000 ms, applied to the whole trace). For this deconvolution, the filter and gap lengths are fixed. The filter length was chosen to be half the length of the generated wavelet. In our case, it means values between 180 ms and 240 ms (parameters were tested for each profile specifically). The gap was defined as half the width of the source wavelet (24 ms) (Fig. 3.8c).

Surface Consistent deconvolution makes data more coherent, reduces the bubble noise and attenuates residual swell and random noise that was not removed with the first band pass filter. It produces a good vertical signal compaction and improves lateral continuity of the reflections (Fig. 3.8c, Fig. 3.9c, Fig. 3.22b-c).

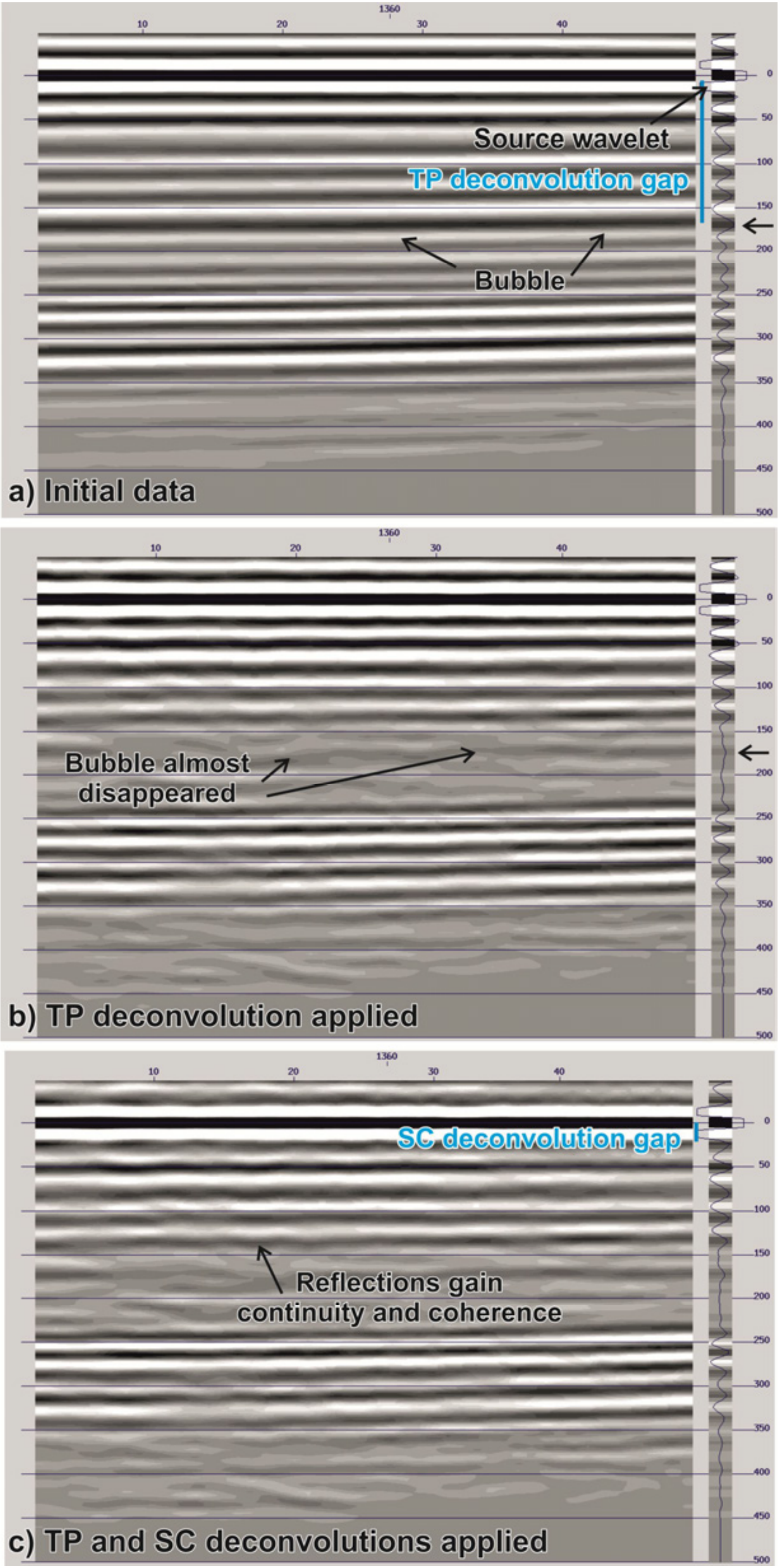

Figure 3.8: *Auto-correlation window of the first 50 channels and first 500 ms for shot 1360 after pre-processing sequence (**a**), after TP deconvolution (**b**) and after TP and SC deconvolution have been applied (**c**). It can be noticed how the TP deconvolution is very helpful in removing the bubble (identified by black arrows) and short peg multiples, and how the reflections gain overall continuity applying the SC deconvolution. The measured gaps for both deconvolutions are depicted (blue).*

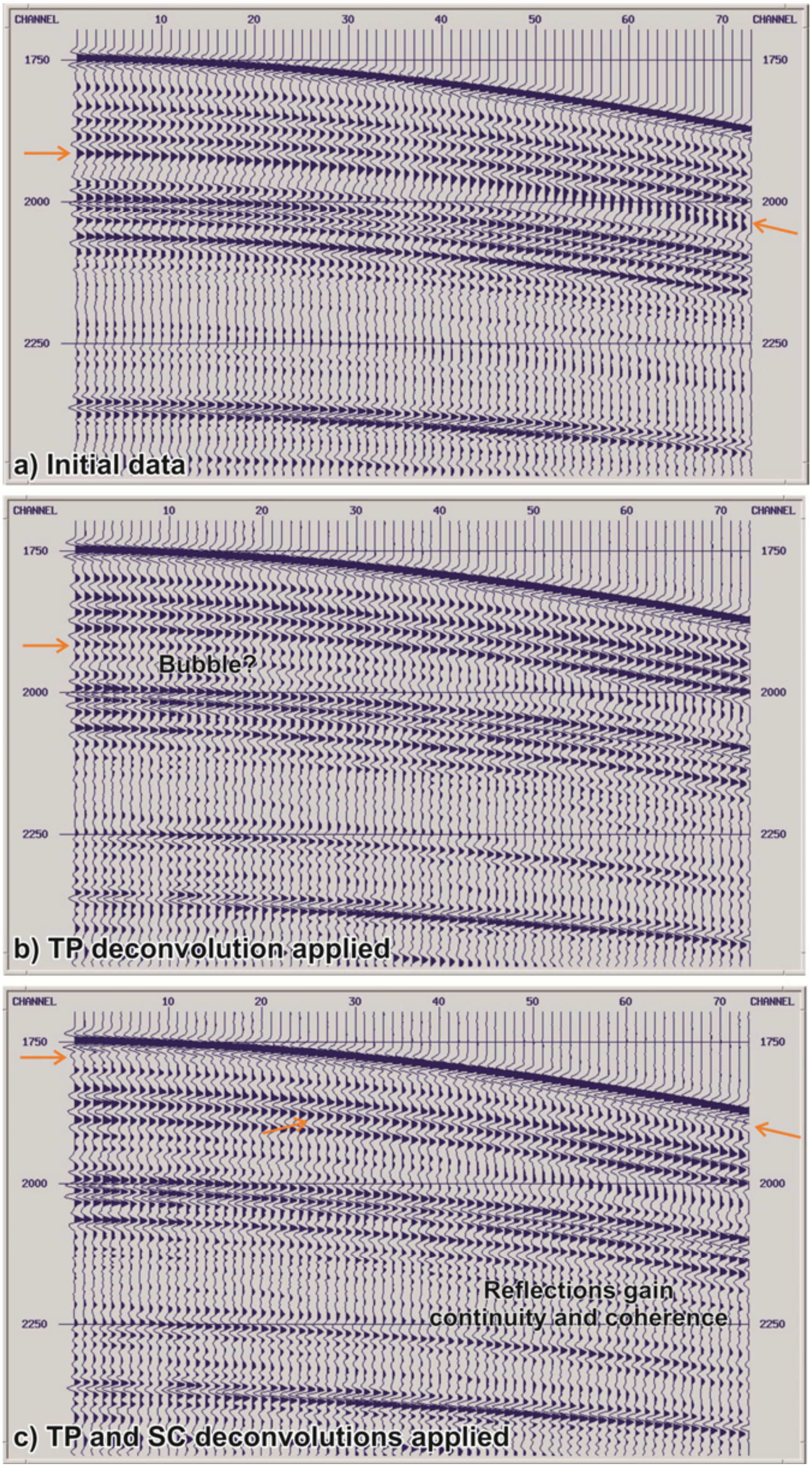

Figure 3.9: *Detailed of shot 1360 after the pre-processing (**a**), after TP deconvolution (**b**) and after TP and SC deconvolution have been applied (**c**) (vertical axis TWTT in ms). It is remarkable the effectiveness of the TP deconvolution removing the bubble noise (red arrows, b). Applying SC deconvolution, reflections gain continuity and coherence, which is especially evident in the low-amplitude recorded reflections (c). Examples of these reflections are pointed out with orange arrows in figure c.*

III. Multiple attenuation and velocity analysis

To image deep reflections the seafloor and other surface-related multiples need to be attenuated. Also, a good velocity model is fundamental to increase the signal to noise ratio to image the deep part of the seismic section. These two main problems are addressed through three processes: (*III.1*) Surface Related Multiple Elimination (SRME), (*III.2*) velocity analysis, and (*III.3*) Radon demultiple.

These three processes are complementary. Performing a first demultiple process allow us to have clearer semblance panels to obtain a better velocity models. The better our velocities are, the better will be the second demultiple process that is based in the different velocities between primary reflections and multiple ones. The SRME process is more efficient removing the multiple in near offsets, while the Radon demultiple process works better in far offsets, where the velocity divergence between primary and multiple is larger.

III.1) Surface Related Multiple Elimination (SRME)

Surface Related Multiple Elimination (SRME) technique focuses on attenuating all multiple energy relative to the surface. This process is data driven, so, no additional information to the seismic record is needed. The main advantage is that it can attenuate multiples even with very little differential move-out with respect to primary reflections, as happens in shallow waters, with peg-leg multiples or in the near offset traces (Brooymans et al. 2003)

Although SRME attenuates the multiple energy at all offsets, it works better at near offsets. Also, the best results are obtained for horizontal sediment strata, where a greater part of multiple's energy is located at near offsets traces. Although it is less efficient in rougher or steep seafloor areas (Lester and McIntosh, 2012) it work better than velocity discrimination methods. Nevertheless, it has been applied to the whole dataset with high quality results in the multiple attenuation (Fig. 3.22d).

SRME works on a multiple prediction model. This model has been constructed trace by trace, and it is subtracted from the original dataset in order to attenuate the multiple. As it works better with a zero offset configuration, we changed the geometry of our data in order to improve the results. After the SRME process, the original geometry is restored.

The subtraction of the model is done in receiver-sorted data. It is done in three steps, with two different methods applied. First, we performed a subtraction based on the publication of Y. Wang (2003). This part of the processing is comparatively very effective attenuating the multiple´s energy in complex seafloor geometries, where steep dips and diffractions are present. Second, we applied two more subtraction based in D. J. Monk adaptive subtractions (Monk, 1993). This is a trace-by-trace process, very useful in shallow waters and horizontal sedimentary layers, where dipping structures or diffraction are not present. We performed two Monk's subtractions, in order to improve the accuracy of the final result.

The SRME is highly efficient, specially looking at near offsets (Fig. 3.10, Fig. 3.22c-d). The multiple´s energy remaining at far offsets will be dealt with later, using Radon demultiple techniques (see section III.3 for details).

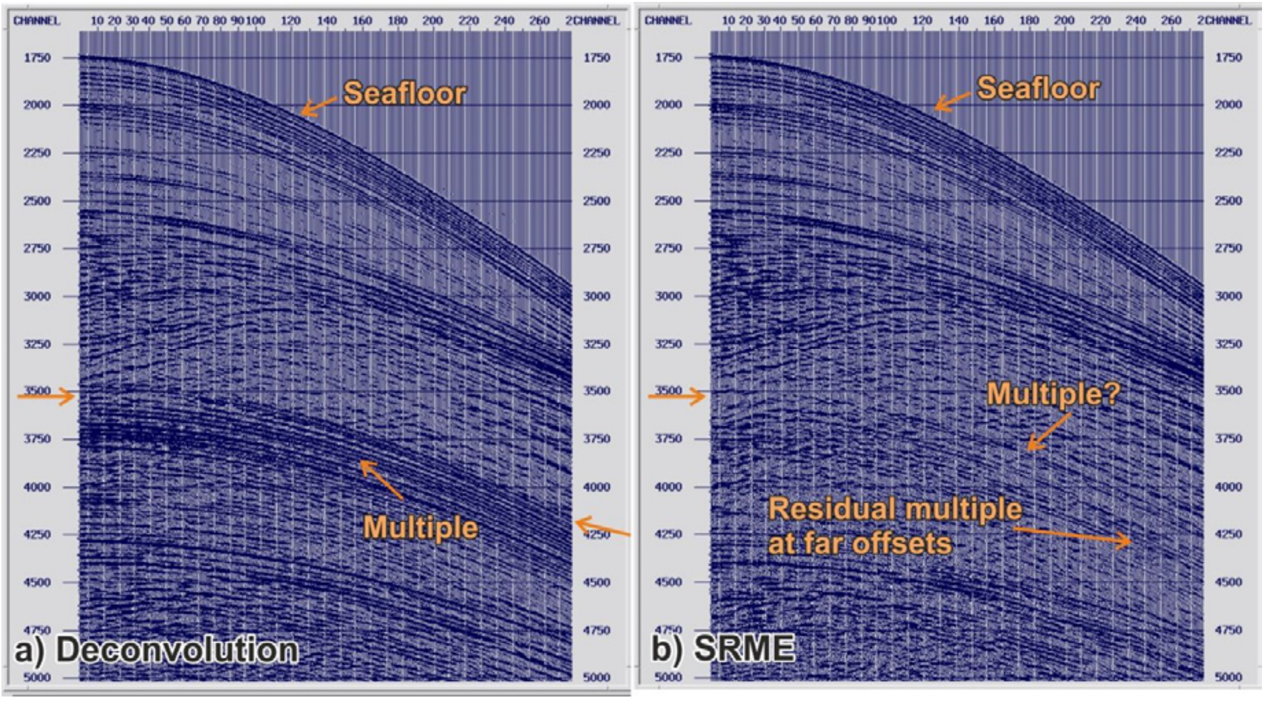

Figure 3.10: *Shot 1360 (channels from 1 till 270, TWTT from 1.7 s to 5 s) before (**a**) and after (**b**) SRME is applied. Notice the effectiveness of the SRME process removing the surface related multiples. Orange arrow indicates the estimated time of arrival of the first seafloor multiple (2 times the TWTT at the seafloor, 3500 ms). Residual multiple energy will be removed with the Radon filter (see point 3.3) (vertical axis TWTT in ms).*

III.2) Velocity analysis

As the following processes in our flow are velocity dependent (Radon and DMO), a first velocity model is required in order to continue with the processing sequence. Moreover, the velocity model is fundamental to obtain a good stack section. This velocity field is used to perform the Normal Move Out (NMO) correction. In a CMP, a reflection will appear as a hyperbola, due to the wave propagation geometry. The NMO correction removes the move out effect of the travel times, or, in other words, the offset effect. With this correction applied, we will be able to sum all the reflections coming from the same point in the same stack trace (Yilmaz*,* 1987).

To perform the first velocity analysis, we made a first approach on the basis of an interval velocity model, taking into account the geology of the area. We digitized a set of layers following geological criteria, and the velocities used coincide with average velocities of the region.

Once having a first gross regional velocity model (the one used for the brute-stack sections of Figure 19), we started with the velocity analysis to achieve an accurate velocity model. The NMO is the difference between the travel-time at some offset and at zero offset (Fig. 3.11a). The velocity needed to correct the NMO effect is the NMO velocity, which is equivalent to the velocity of the medium above the target reflection (RMS velocity). This is the velocity which best flatten the hyperbolas (Fig. 3.11b, c) (Yilmaz, 1987; Stein and Wyssession, 2003).

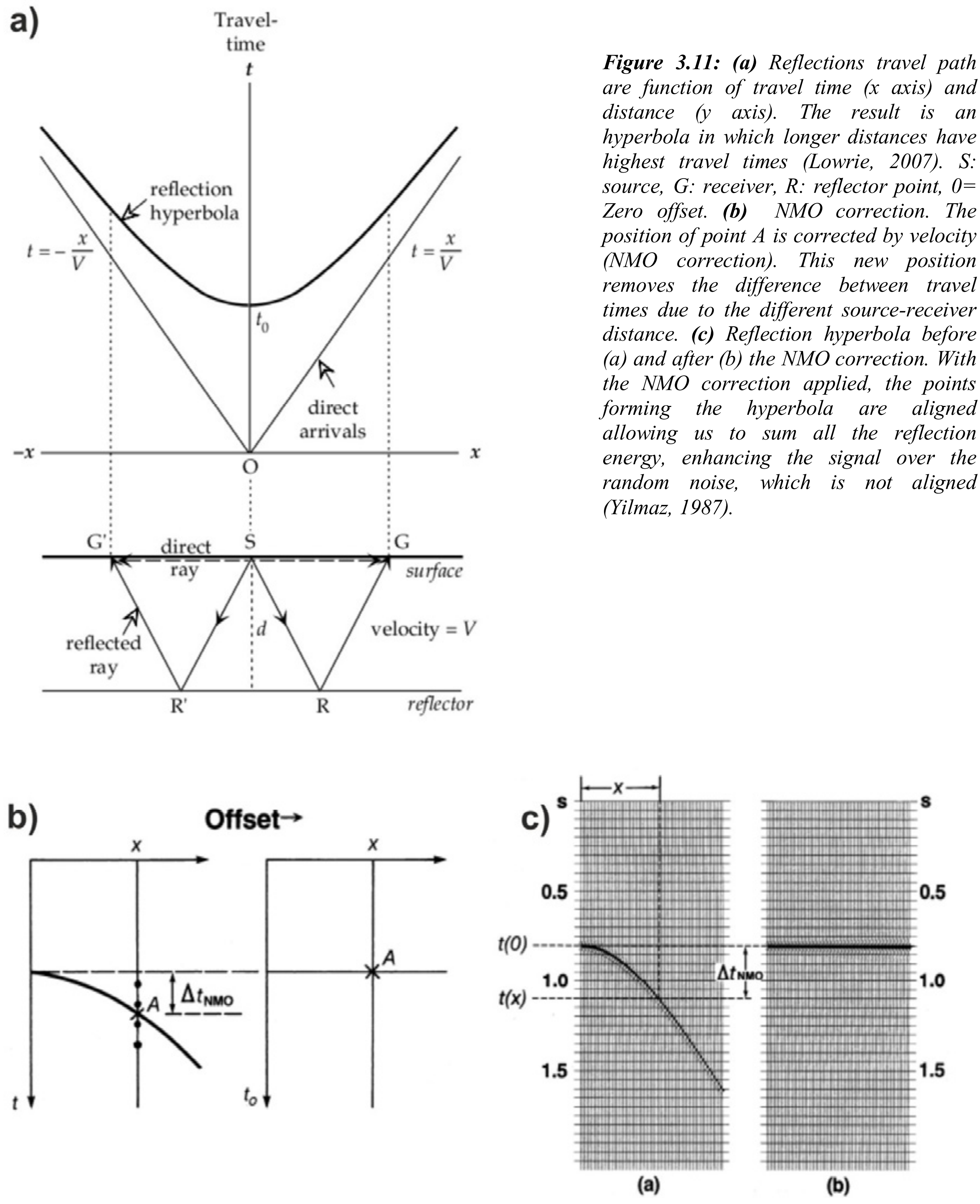

Figure 3.11: ***(a)*** *Reflections travel path are function of travel time (x axis) and distance (y axis). The result is an hyperbola in which longer distances have highest travel times (Lowrie, 2007). S: source, G: receiver, R: reflector point, 0= Zero offset.* ***(b)*** *NMO correction. The position of point A is corrected by velocity (NMO correction). This new position removes the difference between travel times due to the different source-receiver distance.* ***(c)*** *Reflection hyperbola before (a) and after (b) the NMO correction. With the NMO correction applied, the points forming the hyperbola are aligned allowing us to sum all the reflection energy, enhancing the signal over the random noise, which is not aligned (Yilmaz, 1987).*

In order to determine this NMO velocity, we performed the velocity spectrum analysis through the analysis of semblance panels. In this method, different NMO velocities are applied to the same CMP for all the travel times, and the result stacked for each velocity. The resulting panels are function of the velocity used for the NMO correction (X axis) and the travel time (TWTT, Y axis). In the points where the chosen velocity is the correct, reflection hyperboles are horizontal, given a maximum of amplitude in the semblance panel (Fig. 3.12).

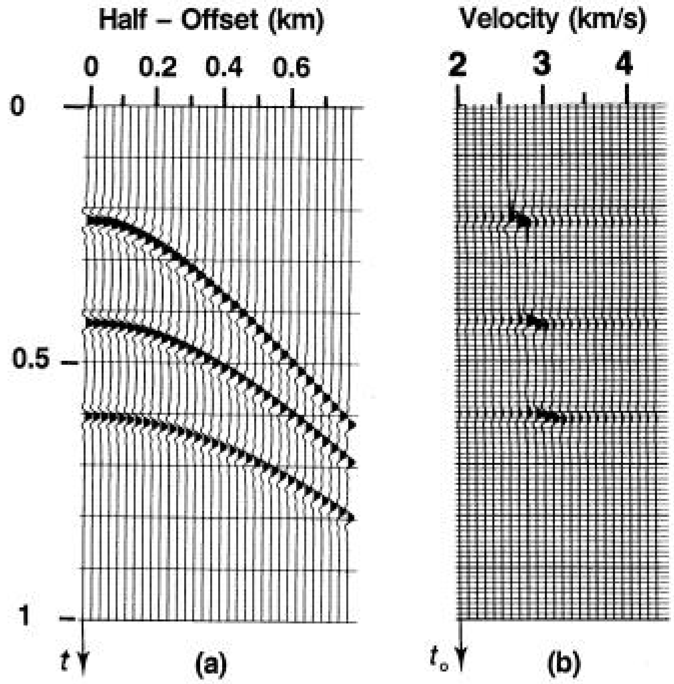

Figure 3.12: *Example of a semblance panel (**b**) from a synthetic CMP (**a**). Each trace on the semblance panel is a stack of CMP gather-traces, using a constant RMS velocity for the NMO correction. Amplitudes maximum in the semblance panel are linked with the points where the velocity is adequate. Therefore, the NMO correction is well performed, the hyperbola is horizontalized and as a result, all the trace energy is added, giving a maximum. These maximums define the RMS velocity function for each CMP (Yilmaz, 1987).*

The maximum in the semblance panels sometimes is not an exact point, making difficult the task of accuracy picking (Yilmaz, 1987). This is a robust process extremely important in order to increase the signal-to-noise ratio. Using the correct NMO velocity, the primary reflection will be aligned in phase on all traces, summing in a constructive way and giving strongly arrivals. On the other hand, other arrivals as incoherent noise or multiples will be shifted and out of phase, summing in a destructive way and so, losing amplitude (Fig. 3.13) (e.g. Stein and Wyssession, 2003).

Although not the main objective of the first velocity analysis, the better the NMO velocity model is, the better the stack will be. An accurate velocity model largely increases the resolution of the image (Fig. 3.22d-e).

III.3) Radon demultiple

Radon filtering is based on the difference in velocity between primary and multiple reflections. For that reason, to attenuate multiples requires an accurate velocity model. We applied a Parabolic Radon transform; this means that the energy have been mapped along specified parabolic trajectories defined by it NMO velocity. In the radon domain, the offset axis is replaced by stacking velocity. Ideally, the reflections with an hyperbolic shape (i.e. the multiple reflection as far as the primaries should be horizontal after the NMO correction) should be represented as a unique point in the radon space, making easier its identification and removal (Yilmaz, 1987; Lester and McIntosh, 2012).

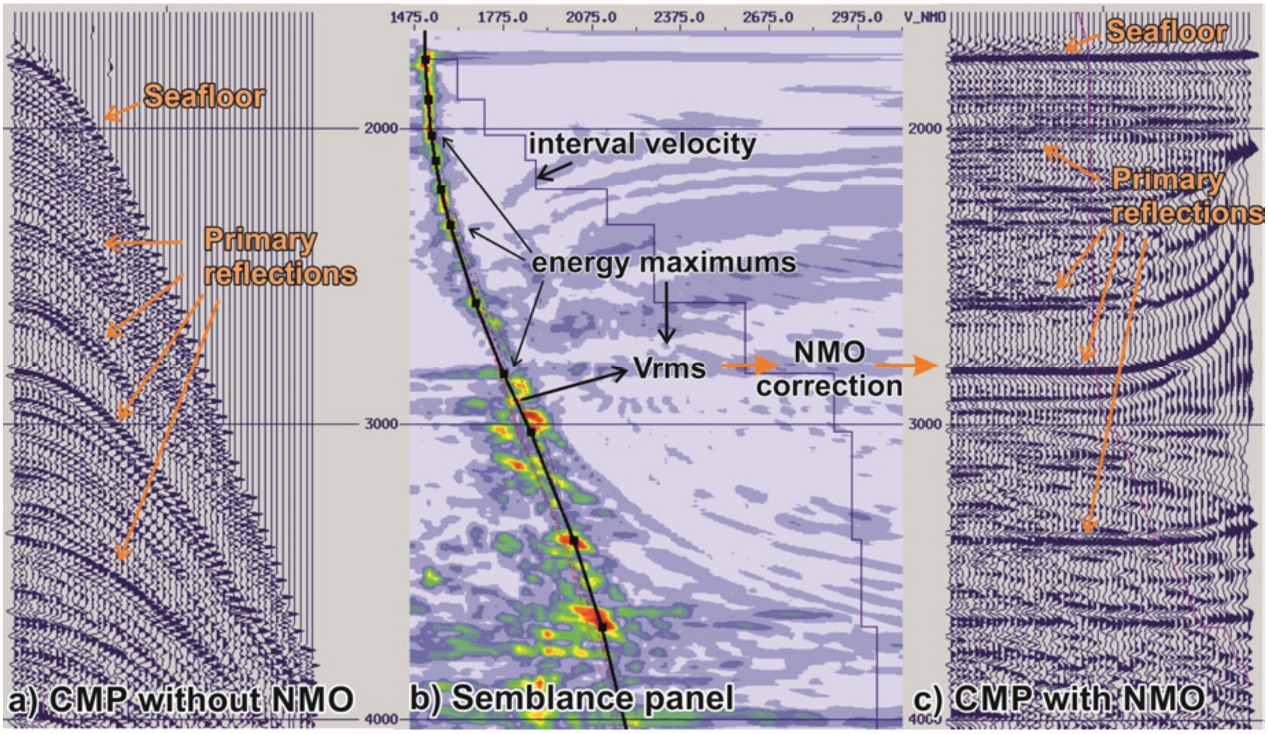

Figure 3.13: ***a)*** *CMP 7300 without NMO correction. Seafloor and other primary reflections are identified and present a hyperbolic shape due to the different travel times in function of the offset (X axis: offset increasing toward the right, Y axis: TWTT in ms).* ***b)*** *Semblance spectrum calculated for CMP 7300. Velocities (X axis) varies from 1475 m/s to 3000 m/s. Red colours correspond to energy maximums, which are associated with the properly RMS velocity (Vrms). This Vrms can be converted to interval velocity. With the Vrms, the NMO correction is applied.* ***c)*** *Same CMP with the NMO correction applied. Vrms has been found through the semblance analysis. It is noticed how this velocity removes the difference in travel time due to the offset, and the primary reflections are now horizontal, making possible the stacking of the signal energy.*

To obtain a good result, velocities must be picked with enough accuracy to distinguish between primary reflections and slower multiples. The inputs of this process are NMO-corrected CMP gathers, in which primary reflections should be horizontal while multiple arrivals should remain with hyperbolic trajectory. The flattened events would be mapped along the 0 slowness contour in the radon space, while the multiples, which are not fully NMO corrected, will be mapped into the positive slowness domain making easier its removal from the dataset (Brooymans et al. 2003; Lester and McIntosh, 2012).

This method is more efficient in areas with different high-velocity between primary reflections and multiples. It works better in far offsets, and in long-period multiples found in deep waters. On the other hand, the method has problems dealing with the multiple´s energy in the near offset or with short period reverberations. In shallow waters (< 500 ms), this process may introduce some low frequency noise, but it is removed with a band pass filter.

We performed the Parabolic Radon demultiple process above the CMP sorted dataset, with the NMO correction applied. We reorganized CMP gathers (100 m inter-trace distance) in super-gathers (inter-trace distance 12.5 m) to have better spatial mapping per input gather, to avoid spatial aliasing and obtain better results. For each profile, a designed window of the Radon filter has been tested and chosen, taking into account the dips of the hyperbolic events (multiples). This filter is based on the residual move out values at the farther offset.

The results show an attenuation of the multiple in far offsets that complements the improvement of the image obtained with the SRME (Fig. 3.14), being complementary to the SRME process that removes the multiple´s energy in the near offsets (Fig. 3.22f).

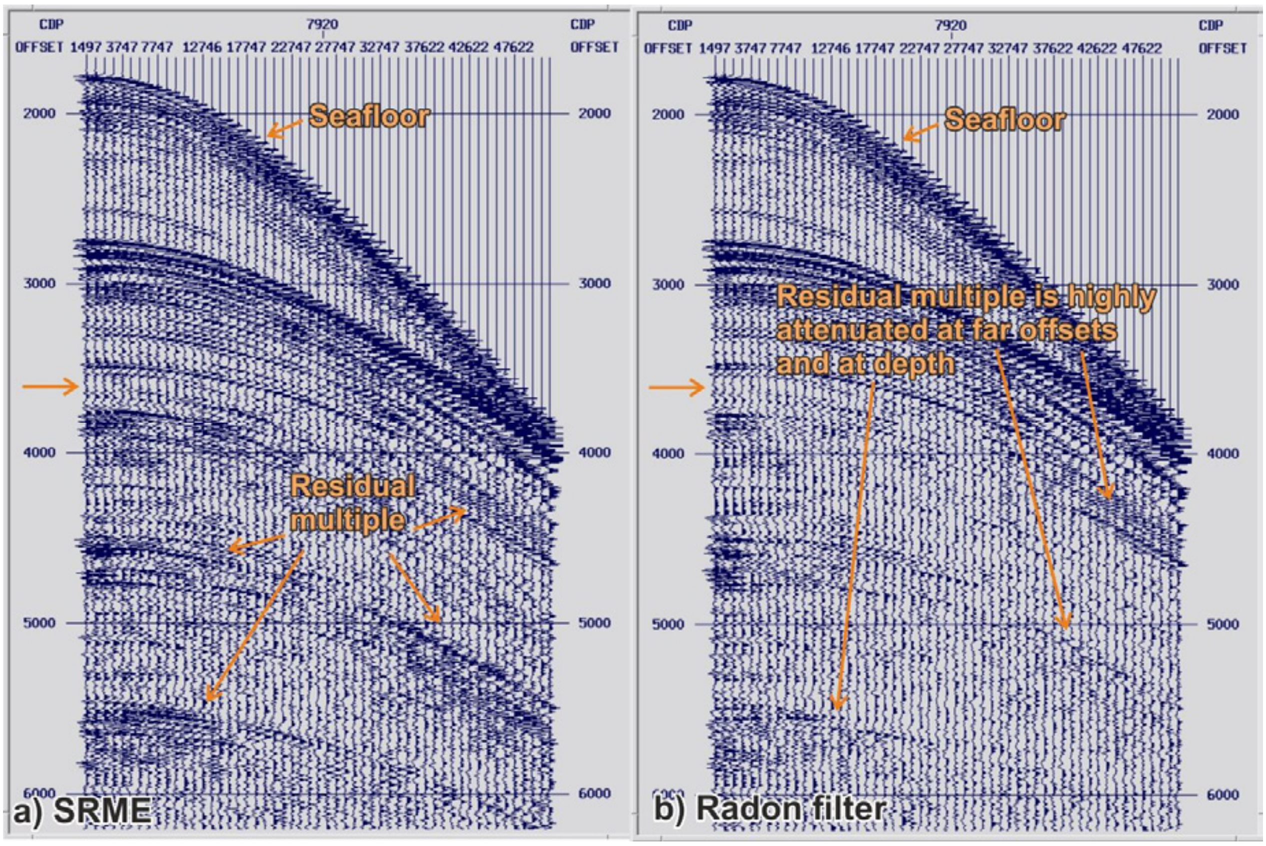

Figure 3.14: *CMP 7920 processed till SRME step (**a**) and till Radon (**b**). X axis is offset in decimetres, Y axis, TWTT in miliseconds. Is worth noticed how the Radon filter efficiently removes the residual multiple energy remaining after the SRME modelling, especially at far offsets and at the deepest parts.*

IV. Dip Move Out correction

All traces from the same CMP gather are processed and added together. When there is no dip in the reflective layers, the midpoint is directly above the reflector point, an all the traces in the CMP comes from the same point at depth. In that case, the travel time will increase according with the offset (source – receiver distance), due to the NMO effect (see section 3.2) (Fig. 3.15) (Liner, 1999).

The NMO correction has a constant dip assumption. At the points that have different NMO velocities, applying the NMO correction will allow to image one or the other dip, but not both in one image. In cases where the dip is not constant or different conflicting dips coexist, it is necessary to perform one more processing step. Dip Move Out (DMO) correction is applied to NMO corrected pre-stack data, in order to preserve conflicting dips (Yilmaz, 1987; Liner, 1999).

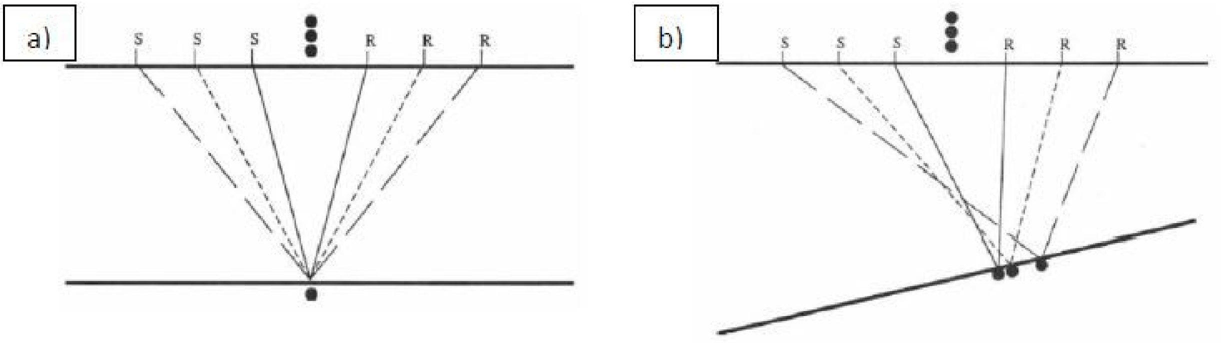

Figure 3.15: ***a****) When the reflector is horizontal, all the recorded reflections came from the same point at depth and differences in travel time can be removed with a simple NMO correction.* ***b****) This situation changes when there is a dipping reflector. Recorded reflections came from different points along the reflector, and differences in the arrivals recorded time are not only dependent on the RMS velocity. This dipping factor is corrected by performing the DMO correction (Liner, 1999).*

By performing the DMO correction, we are not only removing the offset effect of the travel time, but we are also taking into account that the reflection could be located at any point in the subsurface with the corresponding source-receiver distance. This reduces all of the possibilities to an ellipse with one focus in the source and one in the receiver (Fig. 3.16) (Liner, 1999).

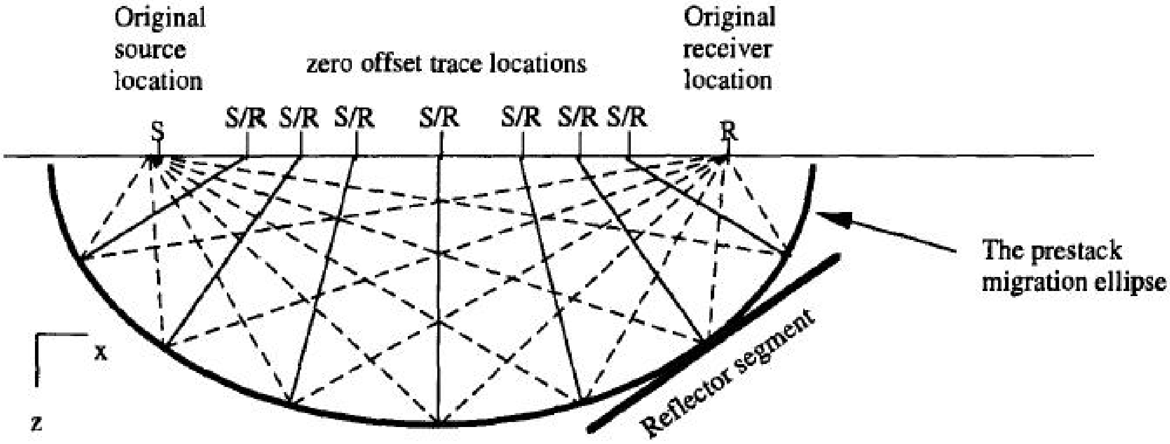

Figure 3.16: *S: Source, R: Receiver, S/R: possible paths. For one trace with one reflection event, all possible travel paths (S/R) have the same length, which resulting shape is and ellipse, known as the pre-stack migration ellipse. NMO reduces travel time effect only for horizontal events, whereas DMO does it for all the other cases (Liner, 1999), being a better approximation to the real position of the reflection and increasing the horizontal resolution of the resulting section.*

DMO is an efficient alternative to pre-stack migration as it corrects the dip effect in the NMO velocities. Combining NMO and DMO, we remove the offset and the dip effect for the pre-stack data, preserving the different dips and obtaining a dataset ready for post-stack migration (Yilmaz, 1987; Liner, 1999).

In this thesis, have performed a Kirchhoff DMO correction in time domain, in pre-stack data, sorted by offset and with the NMO correction applied. As a result, the level of random noise decreased, and side diffractions were partially removed (Fig. 3.22f-g).

V. Final stack

At this point, the pre-stack processing sequence is almost finished. To obtain the final stack section, we performed the following steps: (*V.1*) final velocity analysis, trace muting and CMP stacking, (*V.2*) Zero phase conversion, (*V.3*) quality factor amplitude correction, and (*V.4*) band-pass filter.

V.1) Final velocity analysis, trace muting and CMP stacking

To obtain the final stack section, we performed a second velocity analysis; with the same basic principles that the first one (see section 3.2). This task has been achieved by systematically analysing the semblance panels each 300 CMP (1875 m), and closer in areas where local geology requires it. The aim of this analysis is to estimate an accurate NMO velocity.

NMO correction has associated a stretching deformation, specially noted in far offset shallow reflections (Fig. 3.17) (Yilmaz, 1987; Liner, 1999). It is necessary to remove this deformation, as it can hide the primary reflections. In our case, we have designed an external mute, picked in our NMO corrected CMP (Fig. 3.18).

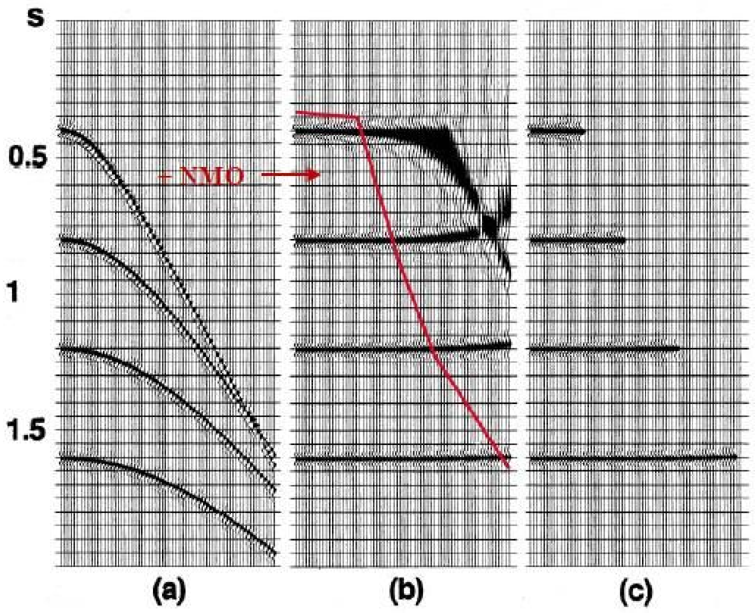

***Figure 3.17:** X axis offset, Y axis time (TWTT). **a)** Synthetic CMP. **b)** Synthetic CMP with NMO correction applied. Far offsets suffer deformation due to signal stretching. **c)** To maintain the data resolution and not introduce noise, this stretching is removed with an external mute (red line in figure b), leaving just the flat part of the reflection for stacking.*

With the aim of removing the remaining multiple energy, we picked an inner mute that helps to remove remnants multiple energy in very near offset, were despite NMO correction, multiple energy remains horizontal in the CMP corrected gathers (Fig. 3.18).

With this final NMO velocity model and the mutes, the final stack is achieved. During stacking, all reflections coming for the same point are added, enhancing the signal to noise ratio. The result is a final section, with improved crustal-scale basin structure. Stratigraphic relations between the different sedimentary layers are well imaged in the basin, but also with deep reflections, coming for intra-basement discontinuities and even from the Mohorovicic (crust – mantle boundary) discontinuity (Fig. 3.22h).

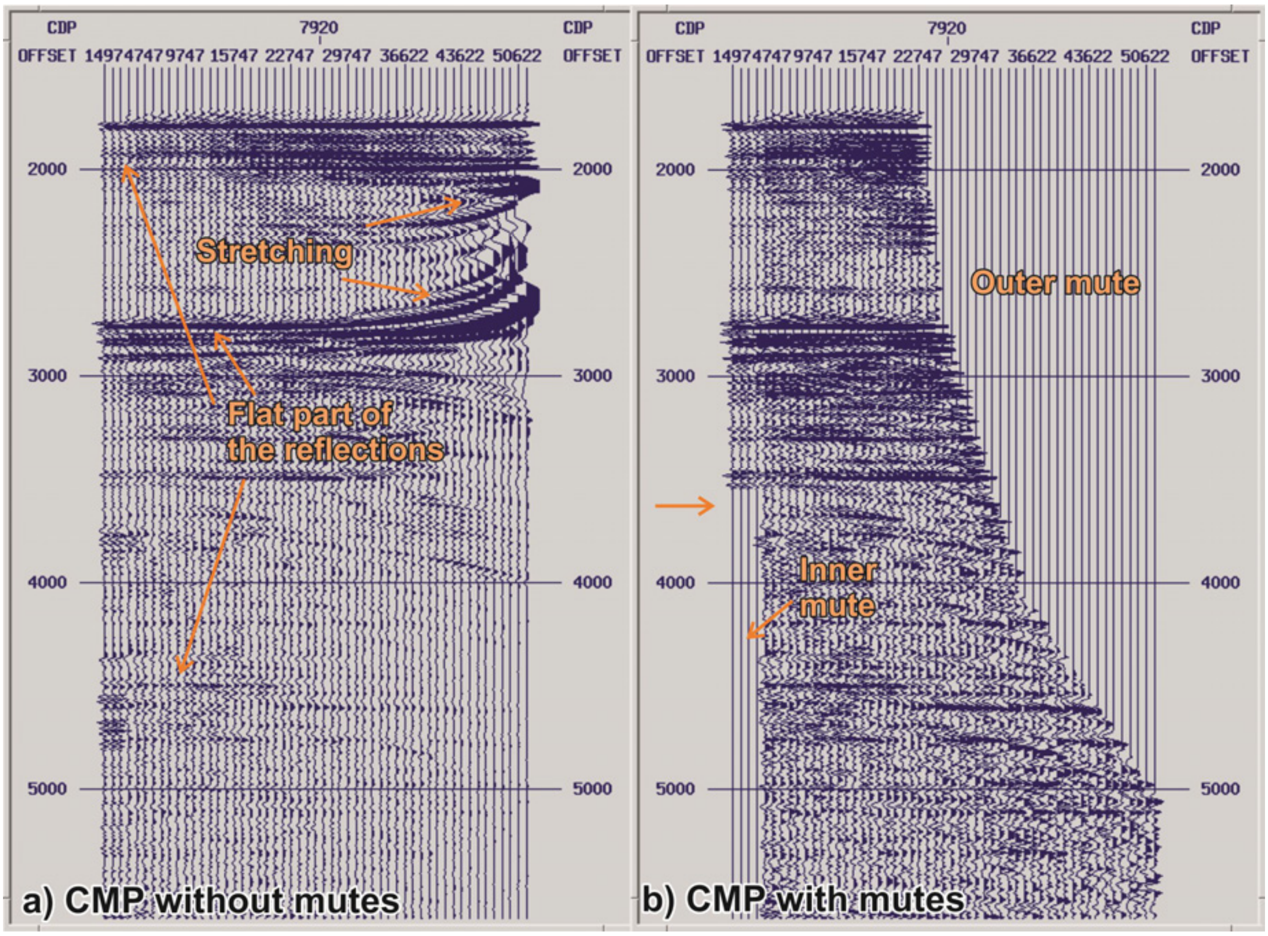

Figure 3.18: a) *CMP 7920 with the final NMO correction applied (X axis offset in dm, Y axis TWTT in ms). Deformation due to stretching is observed in the far offsets (X axis), and there is still some remaining noise of the energy of the multiple.* ***b)*** *Same CMP with the outer and inner mute applied. The outer mute removes the stretching of the reflections in the far offsets, and the inner mute allows the elimination of the residual energy of the multiple (e.g. the estimated time of arrival of the first seafloor multiple is depicted with an orange arrow in the margin). The result is a CMP prepared for the stack processes, in which only the horizontal part of the reflections is present.*

V.2) Zero phase conversion

To move the maximum wave energy coinciding with a reflection position in the seismic image, and to prepare the dataset for post-stack migration, we performed a Zero phase conversion. This conversion has been done in similar way than the Minimum phase conversion. We designed a filter, on the basis of the auto-correlation of 1000 stacked traces. In that way, we found the source wavelet, and designed the Zero phase filter applied to the whole profile through a convolution module.

V.3) Quality factor amplitude correction

We also performed a correction for the effect of energy loss through absorption and dispersion while the energy travels. This effect is quantified by the Quality Factor (or the Seismic Q). Quality factor has been estimated in a practical way performing tests with different Q values, and choosing the best result for correcting the amplitude decay.

V.4) Band-pass filtering

To remove unwanted frequency components and remaining noise, we designed a time and space variant band-pass filter. This filter has been designed for each line, following geological criteria. It has been applied following a layer model, with five manually picked horizons, which define the main geological units in the area. Time variant filtering allows us to preserve the higher frequencies in the shallower parts of the section, while they are filtered out in the deeper part where they only contain noise. The space variability takes into account lateral geological changes.

The final image is a clearer image, in which the signal to noise ratio has been notably increased from the first brute stack (Fig. 3.22h).

VI. Post-Stack Time Migration

Migration moves dipping reflections to their true position at the subsurface and collapse diffractions. Results of this process are an increment in the horizontal resolution and the obtaining a seismic image of the subsurface (Yilmaz*,* 1987).

The migration process assumes that the recorded section is zero offset, or in other words, that source and receivers are coincident. This is not true, but it can be solved by the exploding reflectors propagation model, in which every point at the reflector surface acts as a new source, generating a new wave field (Fig. 3.19) (Yilmaz*,* 1987; Stein and Wysession, 2003). The aim of the migration is to remove the effects of the propagation and distortions in the reflection positions caused by the ray-path trajectory, and also to undo the effects of diffraction, obtaining a realistic image of the subsurface (Stein and Wyssession, 2003). Different aspects solved by migration are presented in Figure 3.20.

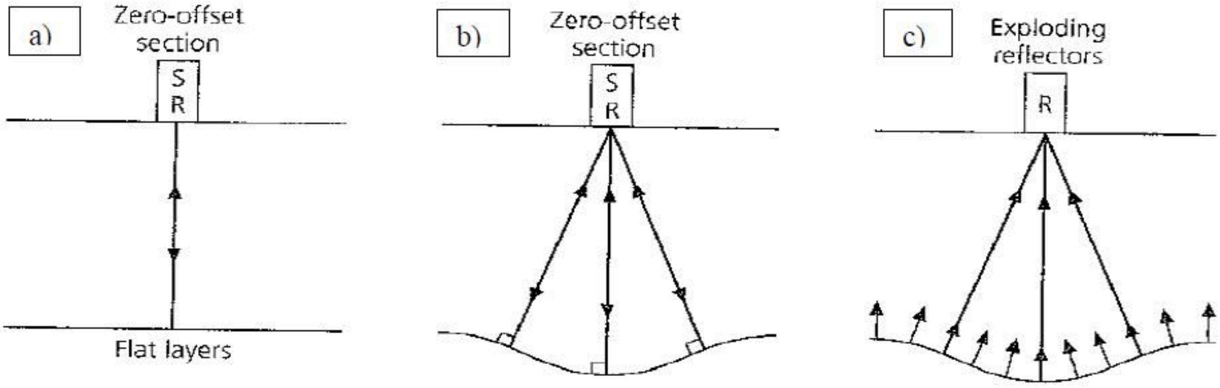

Figure 3.19: *SR: Source-Receiver pair.* ***a)*** *Zero offset seismic section from a horizontal reflector. Reflectors points are located directly below the SR.* ***b)*** *When the reflector is not horizontal, reflections paths can travel along different paths with the same longitude.* ***c)*** *When the energy arrives to the reflector, explode giving a wave field with the geometry of the reflector (exploding reflector model). Migration tries to reverse this process and find the initial wave field and the correct reflector geometry (Stein and Wyssession, 2003).*

There are multiple migration algorithms. Nowadays, none of them is able to fully solve the lateral velocity variations together with the dips variation being cost-effective (Yilmaz*,* 1987). There are different migration strategies, and the choice of one or another will depend on the geological characteristics of the section (Fig. 3.21).

a)

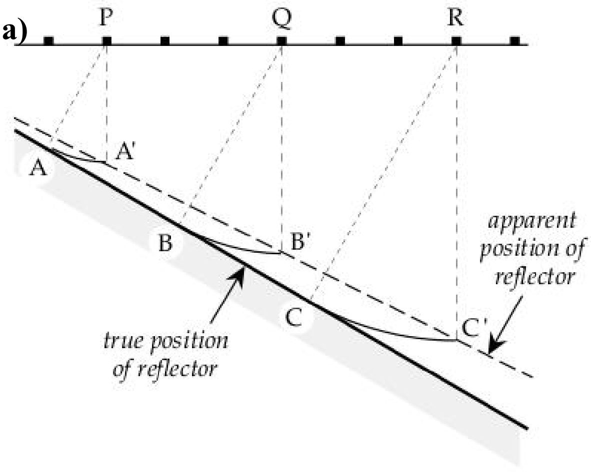

Figure 3.20a*: Dipping reflector. When a reflector is dipping (true position of reflector) and a vertical assumption of the travel paths is done, the result is a false reflector position (apparent position of reflector, dash line) (Lowrie, 2007).*

b)

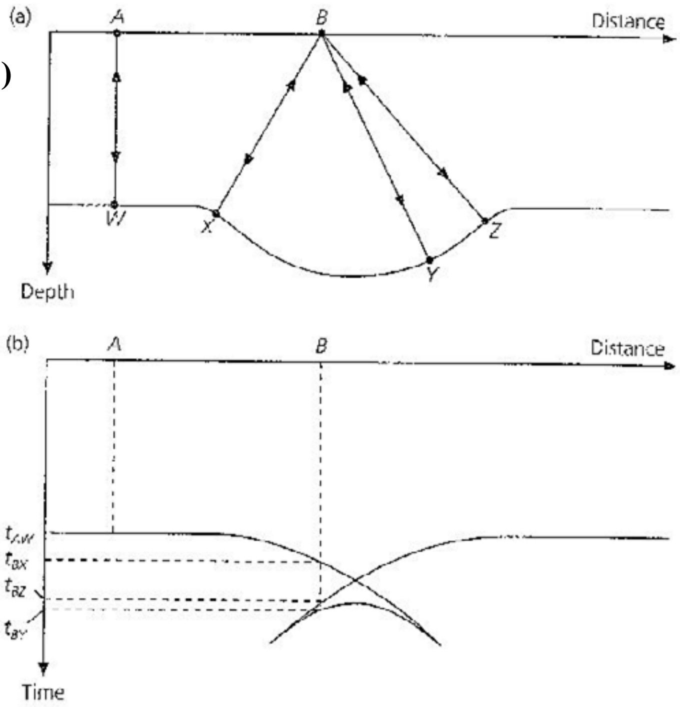

Figure 3.20b*: Bow tie structure, linked to the resulting travel times of the reflections coming from a syncline structure located just below the receivers (Stein and Wyssession, 2003).*

c)

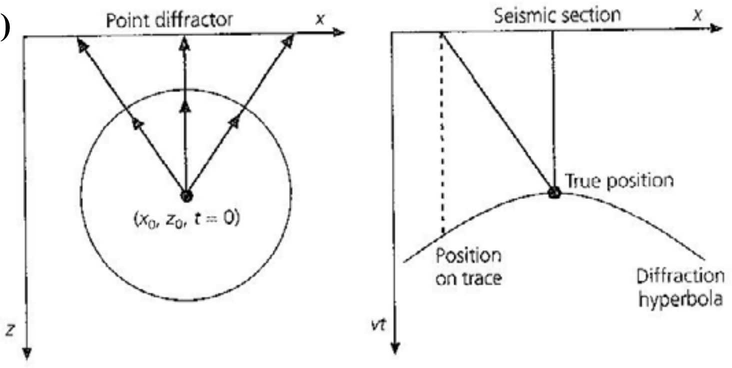

Figure 3.20c*: Diffraction hyperbole due to the generated wave field in a diffracting point (Stein and Wyssession, 2003).*

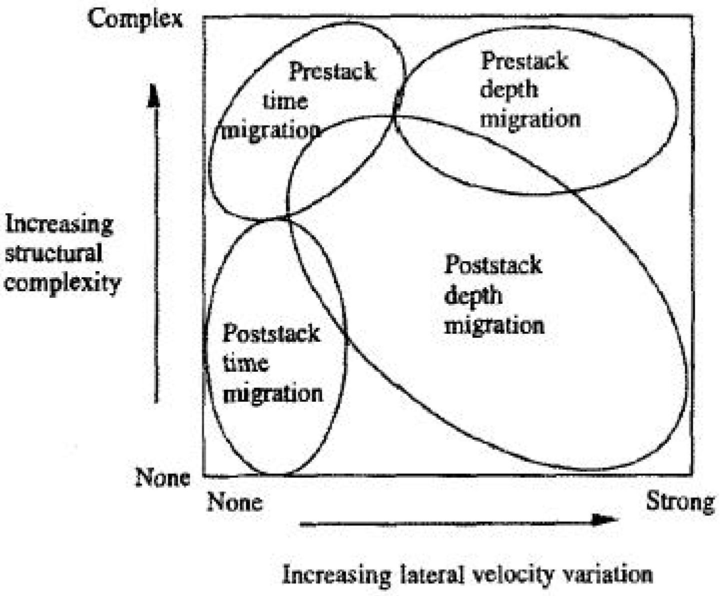

Figure 3.21: *Type of migration as function of the structural complexity (Y axis) and changes in lateral velocity (X axis). For low structural complexity and few velocity variations, post-stack time migration is enough, but increasing these values are needed to perform other types of migration to achieve a realistic image of the subsurface (Liner, 1999)*

We performed a post-stack Finite Difference migration in time domain. Finite Difference migration deal well with lateral velocity variations, but problems may appear when dealing with different dips (Yilmaz, 1987). In our case, the main input parameters are a smooth interval velocity model, a window for the time slices of 20 ms and a dip filter factor equal to the cosine of 0.65 degrees. The algorithm is supposed to be based on a X-T domain implicit 45-degree migration, but it offers reasonable results up to 60 degrees of dipping.

The resulting migrated section has increased the horizontal resolution, making clear the relation between sedimentary layers putting the reflections on their real position, and is very helpful in defining dipping structures, such as faults (Fig. 3.22h-i).

Finally, we applied a seafloor mute and a final amplitude balance. This balance is a time-variant scaling in which the scaling function follows the desired criterion (Yilmaz, 1987). In our case, we choose an Automatic Gain Control (AGC), which goal is bringing up weak signals. In order to preserve some amplitudes variation, we have applied this AGC in two windows, one for the sedimentary basin and one for the basement.

The final result is a crustal scale section, in which we are able to obtain the tectonic structure of the whole crust and also a reasonably good resolution in the sedimentary infill of the basin (Fig. 3.22j). This final output has been exported in seg-y format.

We considered that this processing flow in Time domain is optimal for the data. Tau-P deconvolution removed short-period multiples and the bubble noise, while long-period multiples were removed using the complementary SRME (especially effective in near offsets, horizontal layers, and irregular seafloor) and Radon demultiple processes (which works better in far offsets and is effective with dipping layers). The Surface Consistent deconvolution helps to increase the vertical resolution, as it compresses the signal wavelet in a unique spike, to make reflections more coherent. DMO is an approximation to a Pre-Stack Time Migration, which preserves velocity and dipping variations, collapsing part of the diffraction and filtering some incoherence noise. Finally, a more real image of the subsurface was obtained performing a Post-Stack Time Migration, which collapses diffractions and put the reflections in their true position.

Remaining incoherent noises have been further attenuated with band-pass filtering variable in space and time. Final amplitude balance was applied to recover the energy lost by geometrical spreading.

Figure 3.22 (next pages): *In order to illustrate the different steps of the processing flow and how they increased the quality and the resolution of the seismic image, the evolution of a section of profile TM21 is shown as example. Brute-stack sections were performed with a preliminary initial velocity model, based on first velocity analysis, while stack sections were performed with the final velocity model. See following figures a, b, c, d, e, f, g, h, i and j.* ***a)*** *Initial brutestack. This section is the result of the data preparation for the processing in time domain, including quality control, a gentle band-pass Butterworth filter, minimum phase conversion, geometry insertion and spherical divergence correction to recover amplitudes in depth. Resolution of the image is very poor due to low signal to noise ratio, affected by the present of coherent noises (bubble, reverberations, multiple), incoherent noises and the inaccuracy of the velocity model.* ***b)*** *Brutestack with the Tau-P deconvolution applied. This deconvolution process is highly efficient removing the bubble noise and other short peg reverberations, which is important to obtain a clearly image of the sedimentary layer.* ***c)*** *Brutestack with Tau-p and Surface Consistent deconvolution. After the SC deconvolution, reflections gain in continuity and amplitudes of low energy reflections are enhanced over the surrounding noise.* ***d)*** *Brutestack after the SRME demultiple process. It points out the great potency of this technique removing the multiple´s energy without damaging the signal below it.* ***e)*** *Same section as d, but stacked with the final velocity model that results from the semblance analysis. Here is clearly the importance of the velocity model to achieve a good seismic image. Reflections gain in resolution in the shallow and the deep parts of the profile, where registered signal is recovered, and incoherent noise level is decreased.* ***f)*** *In order to remove the remaining multiple energy we have applied a Radon filter. With this filter, we remove the dip events from the NMO corrected CMP gathers, where the primaries reflections are supposed to be horizontal. This technique reduces the multiple especially in the far offsets. It is important to check that there is no dip information loses in the stacked section.* ***g)*** *To reduce the remaining dipping coherent noise and reduce the diffraction hyperboles, we have performed a Dip Move Out correction before the final stack. Result is a section with a better definition of the reflections, which is especially notice at irregular surfaces (where diffractions are generated) or in dipping reflections.* ***h)*** *Final stack section. This section includes muting, zero phase conversion, amplitudes recovery through the Q factor and a time and spatial variant band-pass filter. Result is a section with a high signal to noise ratio, with a low level of noise and no spike amplitudes that will be a properly input for the migration.* ***i)*** *Time migration. In the migrated section, dipping events are well defined and diffractions collapsed, allowing a good interpretation of sedimentary and tectonic structures.* ***j)*** *Time migration with and Automatic Gain Control (AGC) applied. The AGC allows recovering the amplitudes in depth. The result of the time domain processing flow is a high quality, clear and high-resolution image, in which sedimentary layers and tectonic structures can be satisfactorily identified and interpreted.*

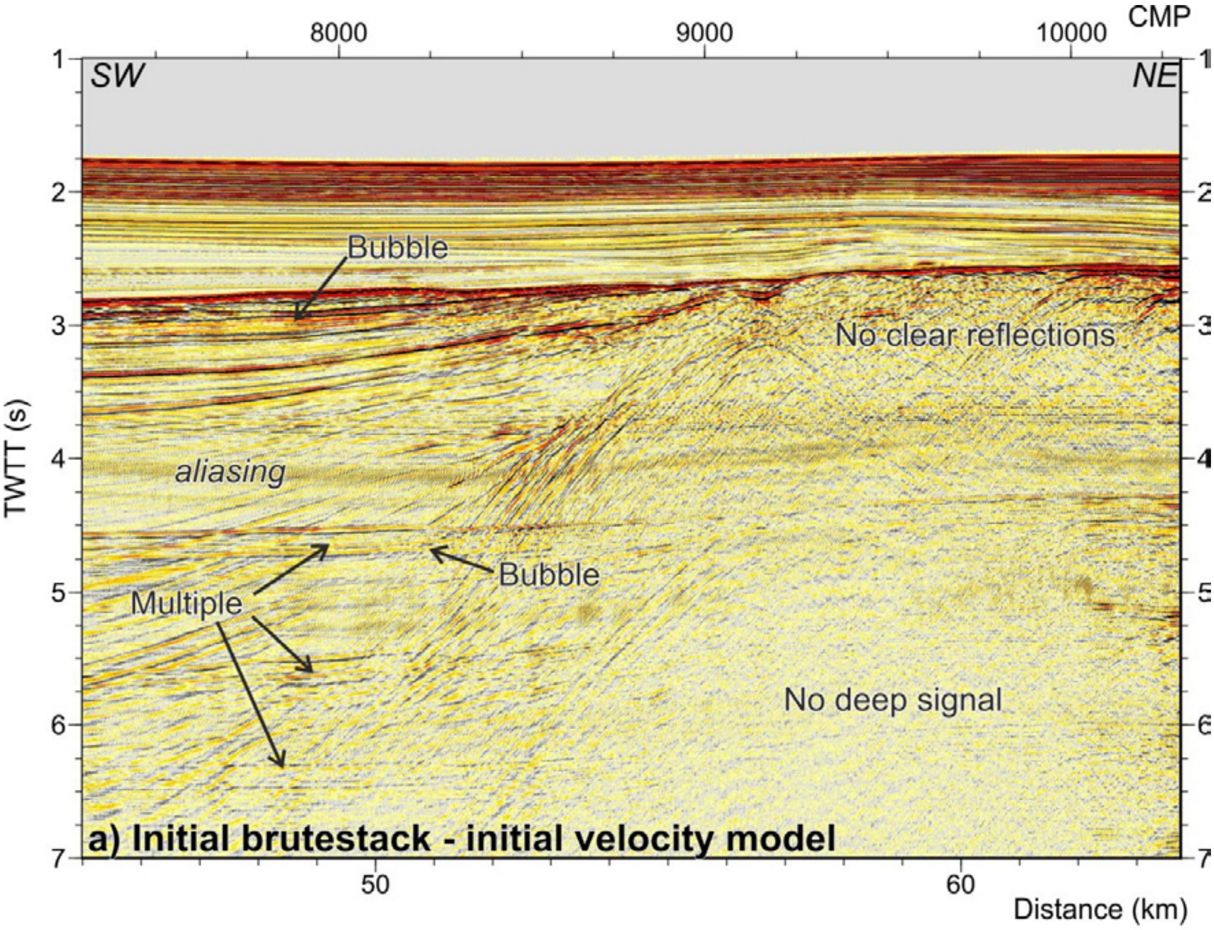
CMP
8000
9000
10000
SW
NE
TWTT (s)
1
2
3
4
5
6
7
Bubble
No clear reflections
aliasing
Bubble
Multiple
No deep signal
a) Initial brutestack - initial velocity model
50
60
Distance (km)

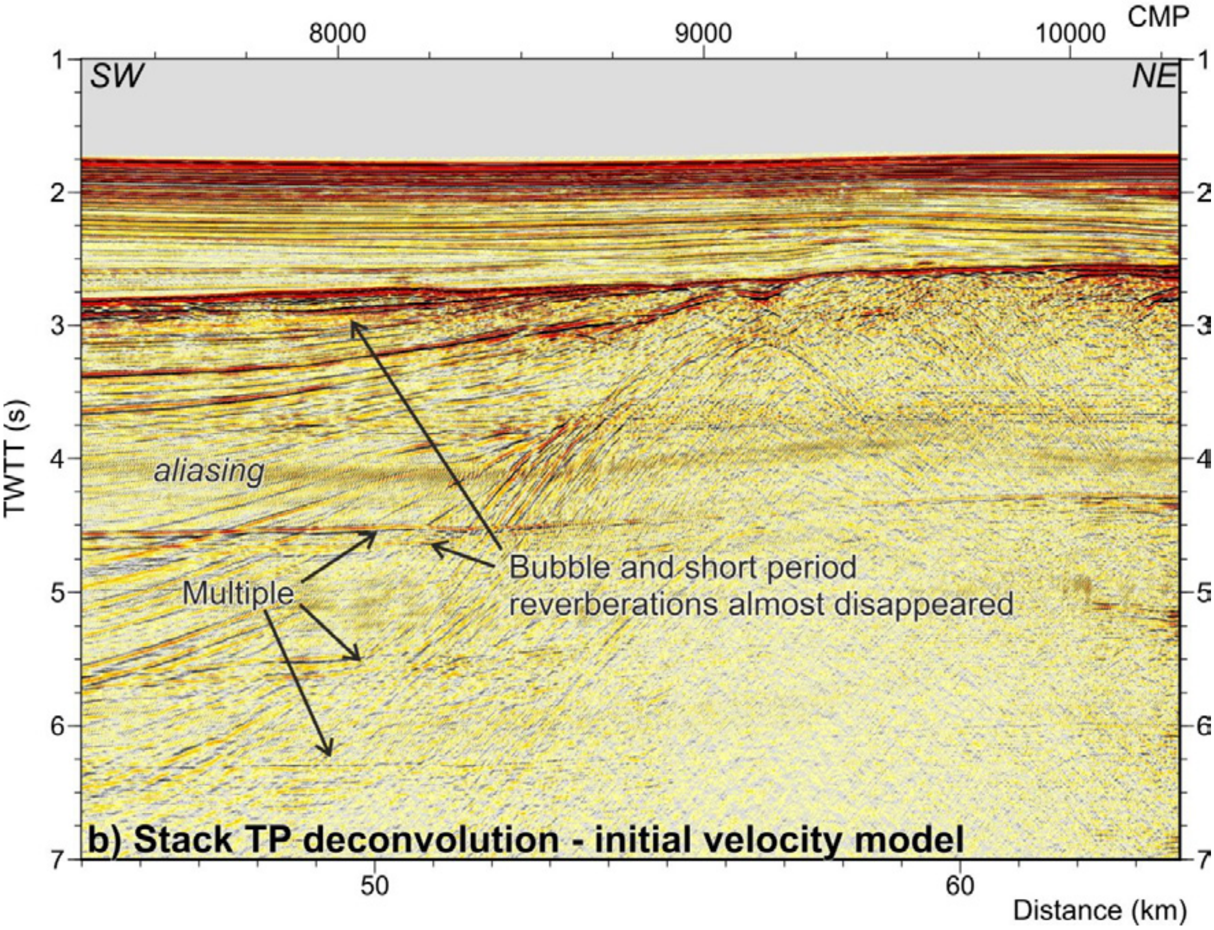
CMP
8000
9000
10000
SW
NE
TWTT (s)
1
2
3
4
5
6
7
aliasing
Multiple
Bubble and short period
reverberations almost disappeared
b) Stack TP deconvolution - initial velocity model
50
60
Distance (km)

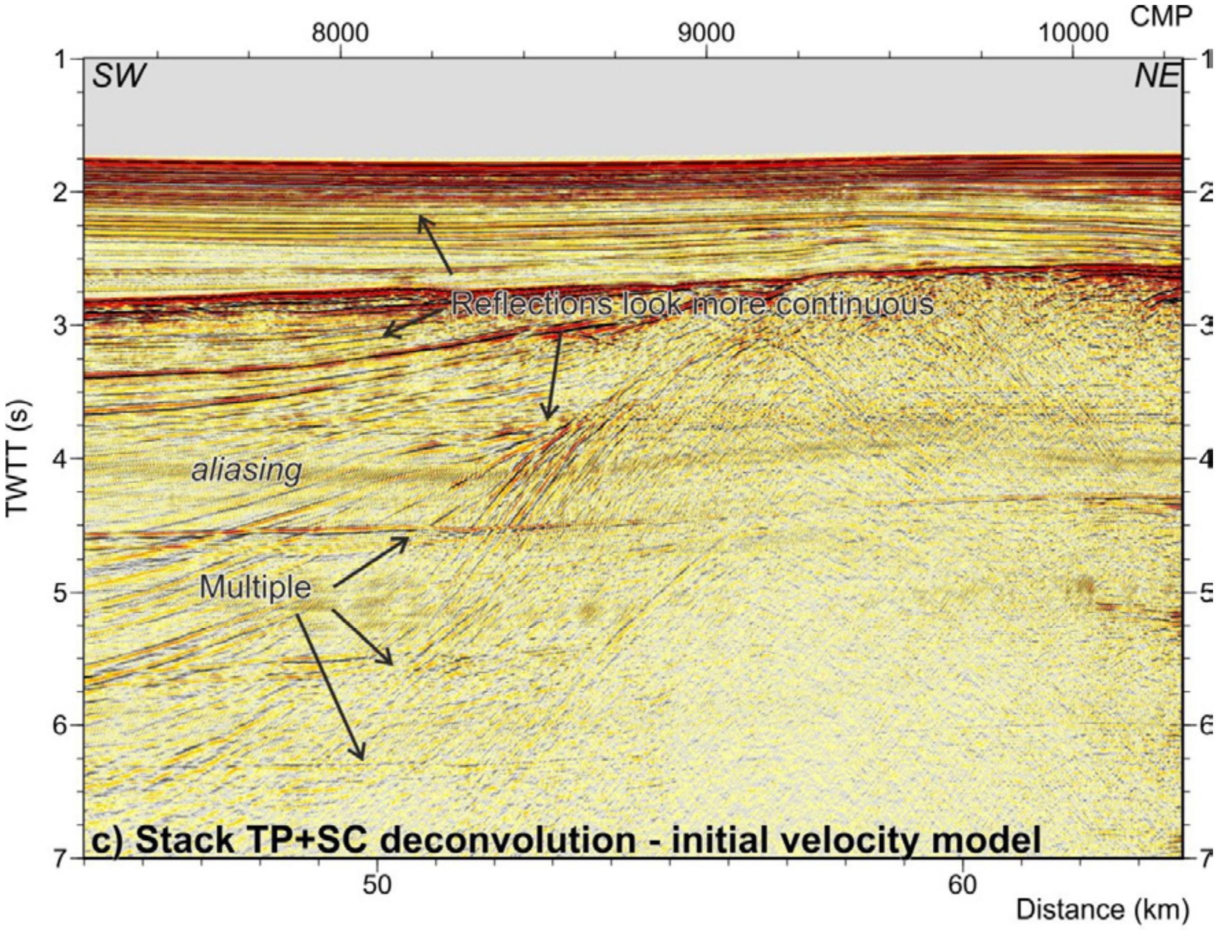
CMP
8000
9000
10000
SW
NE
TWTT (s)
1
2
3
4
5
6
7
Reflections look more continuous
aliasing
Multiple
c) Stack TP+SC deconvolution - initial velocity model
50
60
Distance (km)

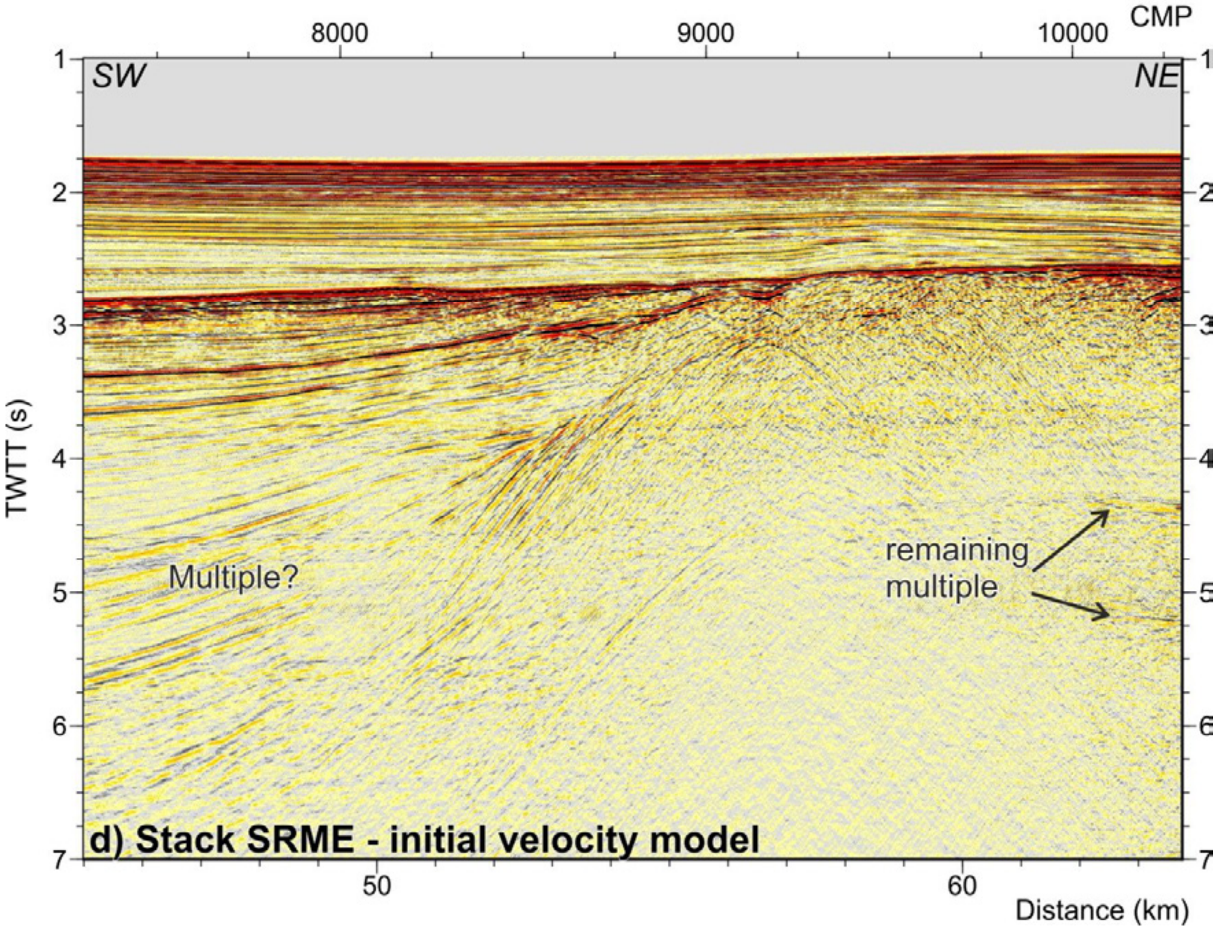
CMP
8000
9000
10000
SW
NE
TWTT (s)
1
2
3
4
5
6
7
Multiple?
remaining
multiple
d) Stack SRME - initial velocity model
50
60
Distance (km)

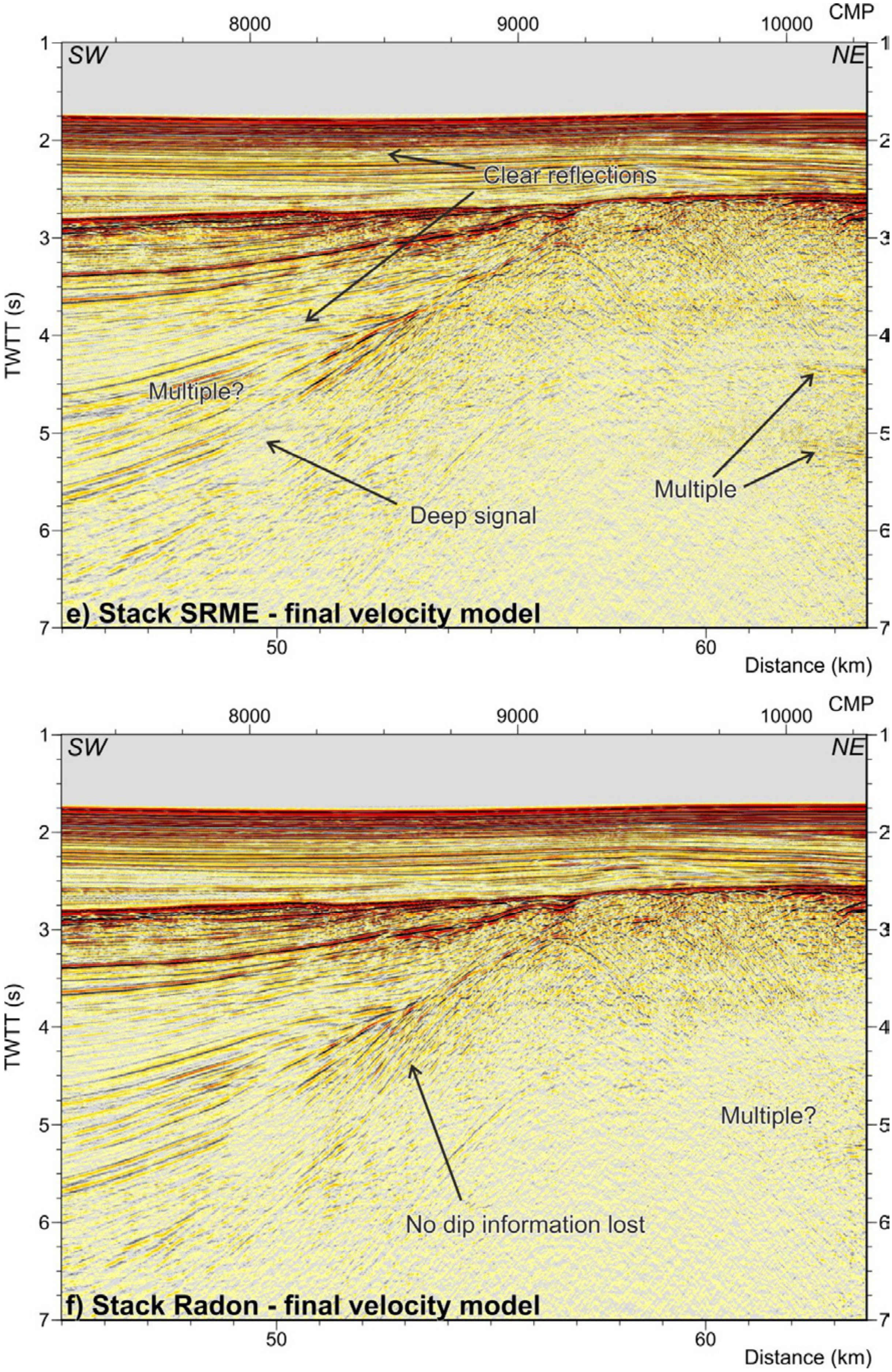
CMP
8000
9000
10000
SW
NE
TWTT (s)
1
2
3
4
5
6
7
Clear reflections
Multiple?
Deep signal
Multiple
e) Stack SRME - final velocity model
50
60
Distance (km)
CMP
8000
9000
10000
SW
NE
TWTT (s)
1
2
3
4
5
6
7
No dip information lost
Multiple?
f) Stack Radon - final velocity model
50
60
Distance (km)

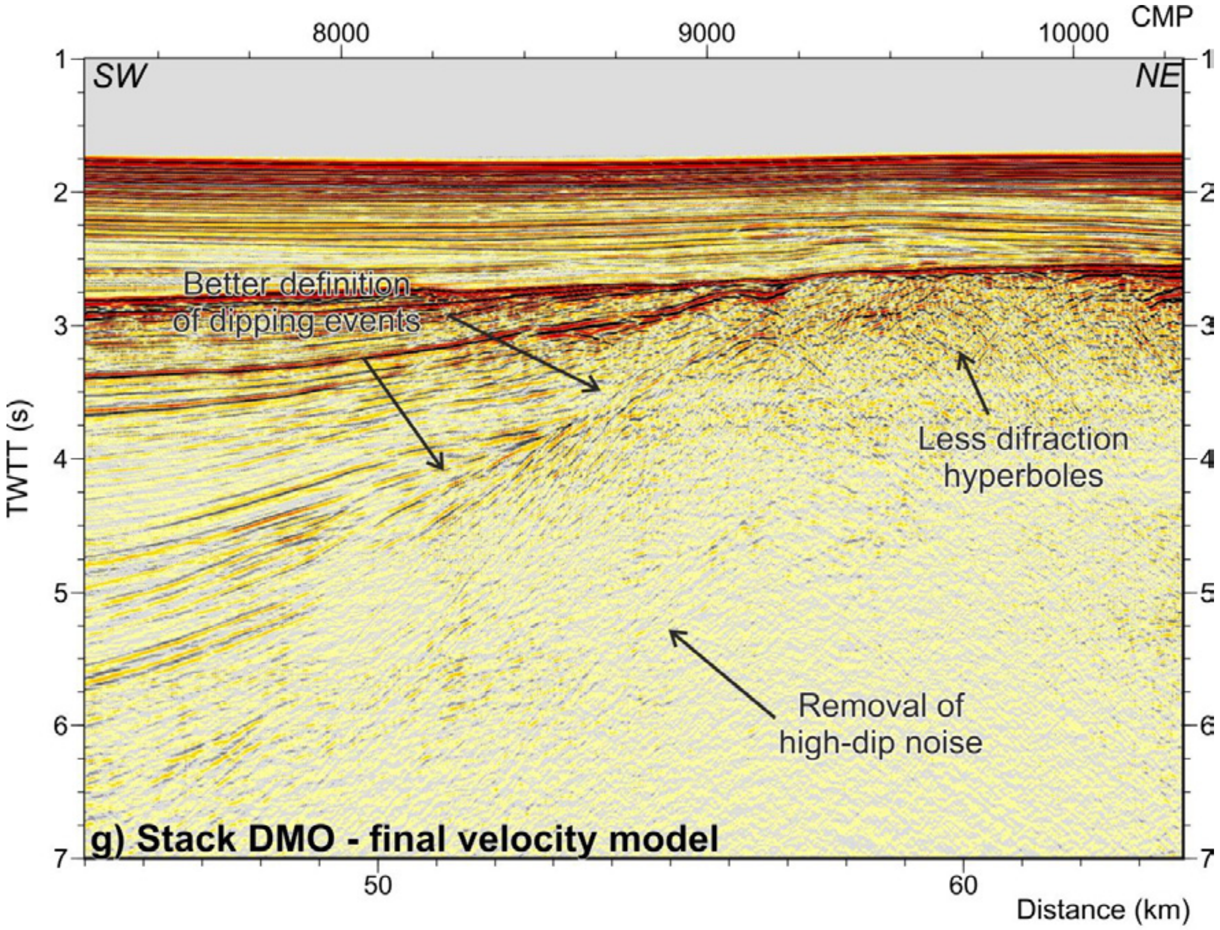
CMP
8000
9000
10000
SW
NE
Better definition of dipping events
Less difraction hyperboles
Removal of high-dip noise
g) Stack DMO - final velocity model
TWTT (s)
1
2
3
4
5
6
7
50
60
Distance (km)

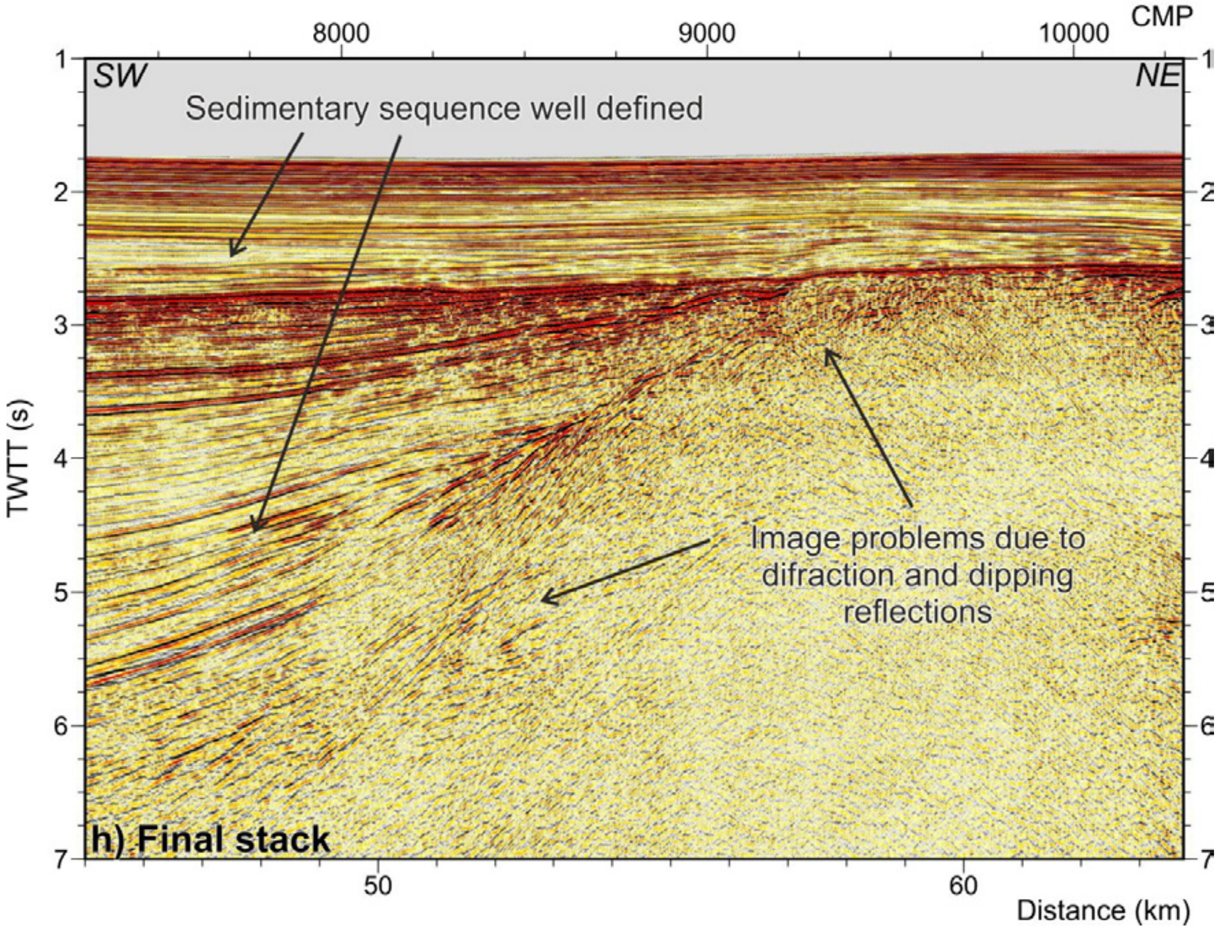
CMP
8000
9000
10000
SW
NE
Sedimentary sequence well defined
Image problems due to difraction and dipping reflections
h) Final stack
TWTT (s)
1
2
3
4
5
6
7
50
60
Distance (km)

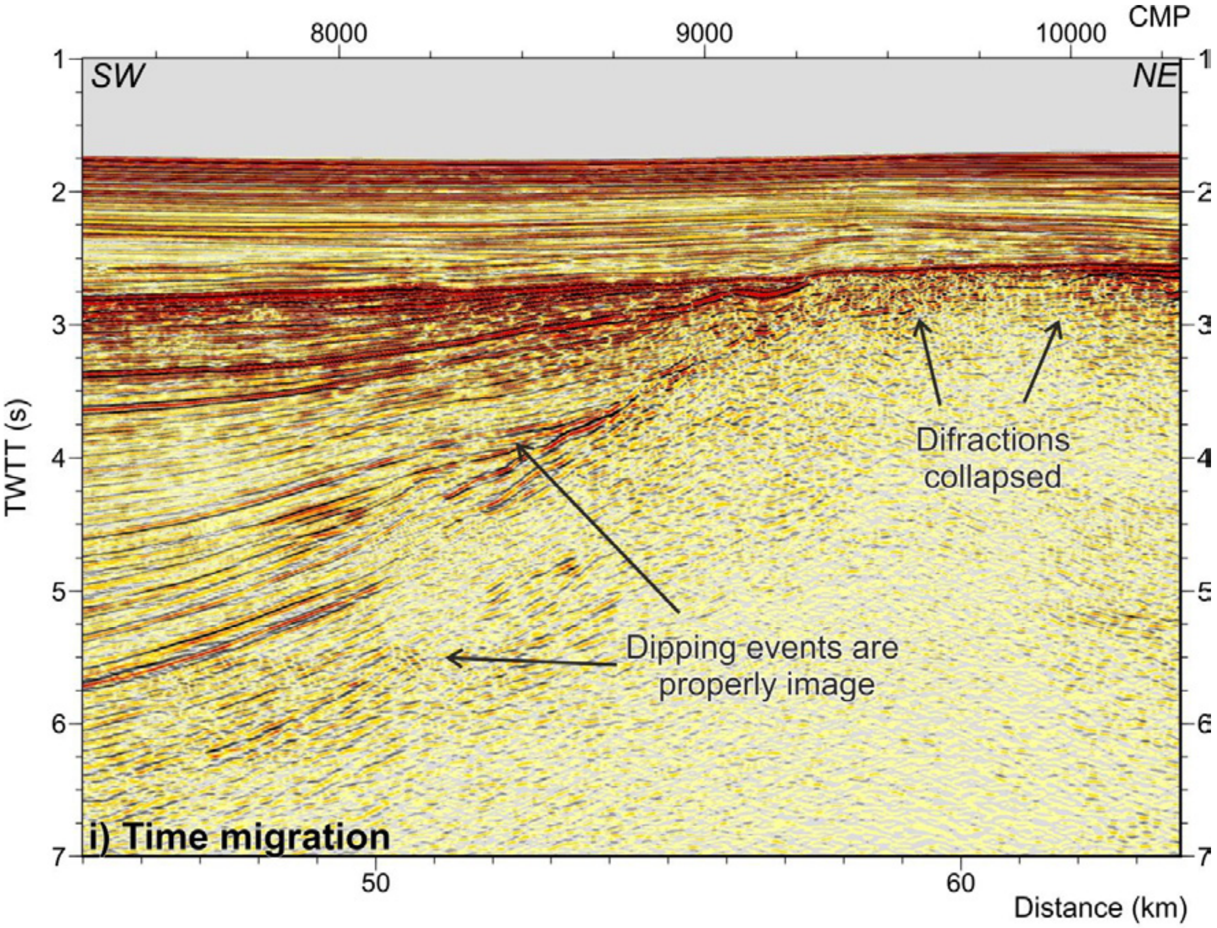
CMP
8000
9000
10000
SW
NE
TWTT (s)
1
2
3
4
5
6
7
Difractions collapsed
Dipping events are properly image
i) Time migration
50
60
Distance (km)

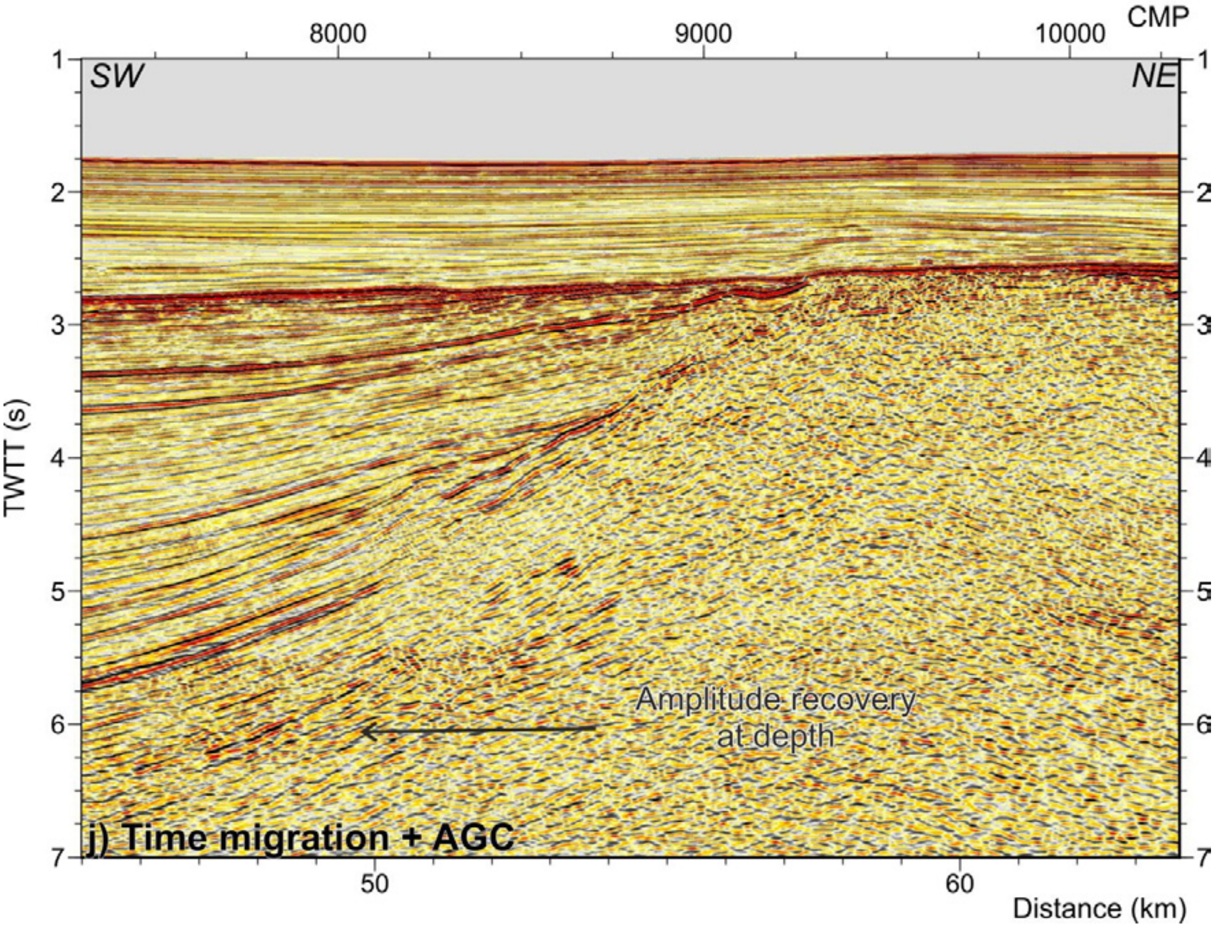
CMP
8000
9000
10000
SW
NE
TWTT (s)
1
2
3
4
5
6
7
Amplitude recovery at depth
j) Time migration + AGC
50
60
Distance (km)

3.2.2. MCS processing flow in Depth Domain

The result of our processing flow in Time Domain is good enough to allow an accurate interpretation of the seismic profiles. However, processing in time is not always the best available result, especially when with complex structures and lateral velocity variations. In these cases, Pre-Stack Depth Migration (PSDM), provides a real geometry of the tectonic and sedimentary structures in depth.

The objectives of this part of the processing flow were to obtain an image in depth of just two selected profiles from TOPOMED cruise (TM03 and TM11, Fig. 3.3), which run across two of the most important structures of the Alboran basin: the Alboran Ridge and the Yusuf Fault. Only two lines were migrated in depth due to the time required for this time of imaging.

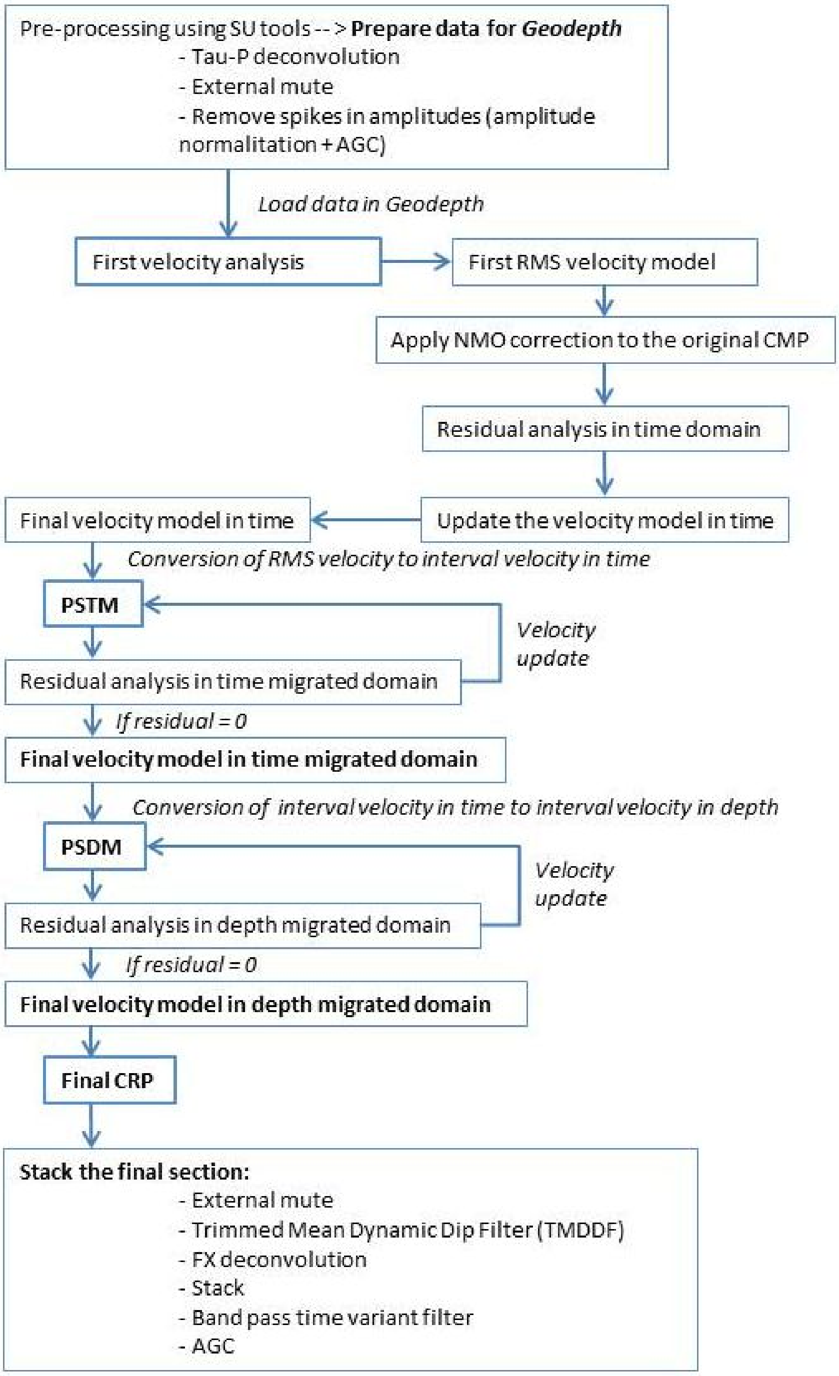

Table 3.7: *Processing flow in depth domain. PSTM: Pre-Stack Time migration. PSDM: Post-Stack Depth Migration. CRP: Common Reflection Point gathers.*

The goal of this processing flow in Depth Domain was to perform a PSDM of these profiles. Additional processing has been carried out, in order to improve the results of the PSDM. All the processing flow is shown in Table 3.7. The flow can be divided in three steps: (I) pre-processing, (II) PSDM and (III) stack the final section.

I. Pre-processing sequence

In order to prepare the data for the velocity analysis and the PSDM, we performed the processing using Seismic Unix tools. This processing sequence has been developed in shot-sorted data. The input dataset has been applied in the processing flow in Time Domain till the last demultiple process (Radon, step 3 in the previous section 3.2.1. Processing flow in Time Domain).

This pre-processing includes a second Tau-P deconvolution in shot-sorted data, to remove dipping arrivals that are not real and some spikes in amplitudes, which are problematic at the time of performing the PSDM. Also, we have applied a gentle external mute in the shallower CMP, in order to reduce the noise introduced by the far offsets in these shallower sections. Finally, we removed the remaining amplitudes spikes performing amplitude normalization plus an AGC.

II. Pre-Stack Depth Migration

When there complex structures are present and we have lateral velocities variation, a Post-Stack Time Migration is not enough to obtain a good image of the sub-surface (see Fig. 3.21). The behaviour of the waves travelling across the sub-surface will be defined when a PSDM is applied. If more than a ray is associated with a reflector point, or the rays are deviated laterally between CMP, performing a PSDM is mandatory to obtain an accurate and realistic image of the sub-surface (Yilmaz*,* 1987).

The base of a good PSDM is a good velocity model in depth (Yilmaz*,* 1987). Velocity analysis had been carried out in three steps, in order to obtain the best possible results:

a) Velocity analysis in time domain.

b) Velocity analysis in time migrated domain.

c) Velocity analysis in depth migrated domain.

This velocity analysis has been done with the module “Geodepth velocity modelling”, through semblance analysis (see section 3.2 for further explanation of this technique in the time domain processing). This analysis consists on finding out the right velocity looking for the maximum energy. After the first velocity model in time, the model is updated using the residual analysis. This is a precise analysis in which searching the difference between the current velocity model and the real one, doing a second semblance analysis. On this way, it is possible to adjust small variations of the velocity, improving the velocity model to obtain the best possible result. The residual analysis is done in time domain, time migrated domain, and, finally, in depth domain. With this strategy, it is easier to start picking the velocity model in time domain, as it is less sensitive to errors than the depth domain, and updated it in the time migrated and later depth domains.

Carrying out all this work with the velocities is mandatory, because having a good velocity model is essential to have a good and realistic final image in depth. The output of the PSDM are *Common Reflection Point* gathers (CRP). CRP gathers consist of traces with the same migrated position in depth. If the velocity model used for the PSDM is correct, then all reflections show a flat character without any NMO correction applied (Yilmaz*,* 1987).

The last step to obtain a PSDM migration section has been processing and stacking this CRP, in order to reduce the noise and obtain a seismic section (Table 3.7).

III. Stacking the final section

To obtain the stacked PSDM final section, further processing was applied to the dataset to remove remaining noise. This processing includes an external mute, which allows to delete the wavelet stretching in far offsets, a Trimmed Mean Dynamic Dip Filter to remove high-amplitude noise and locally weak coherent events, and a FX deconvolution to laterally enhance the signal. The stack section is the result of stacking CRP gathers with this processing flow applied. Finally, we have applied a depth and spatial variant band-pass filter, to filter undesired remaining frequencies, following the criteria as in the Time Domain.

The sections presented are two profiles, which show an image in depth of two of the main structures in the Alboran Sea: the Yusuf Fault and the Alboran Ridge. Depth migration is done with an interval depth velocity model, which allows lateral changes in the velocity field. These changes are not well defined in time, so in presence of strong lateral velocity variations (like in our study area) the PSDM is more accurate than a migration in time. These PSDM sections not only image the real geometry of the structures in depth, also allow to improve the characterization of the sedimentary infill of the basin. In the depth image, the contacts between the different sedimentary units and its internal structure are clearer than in the time section (Fig. 3.23).

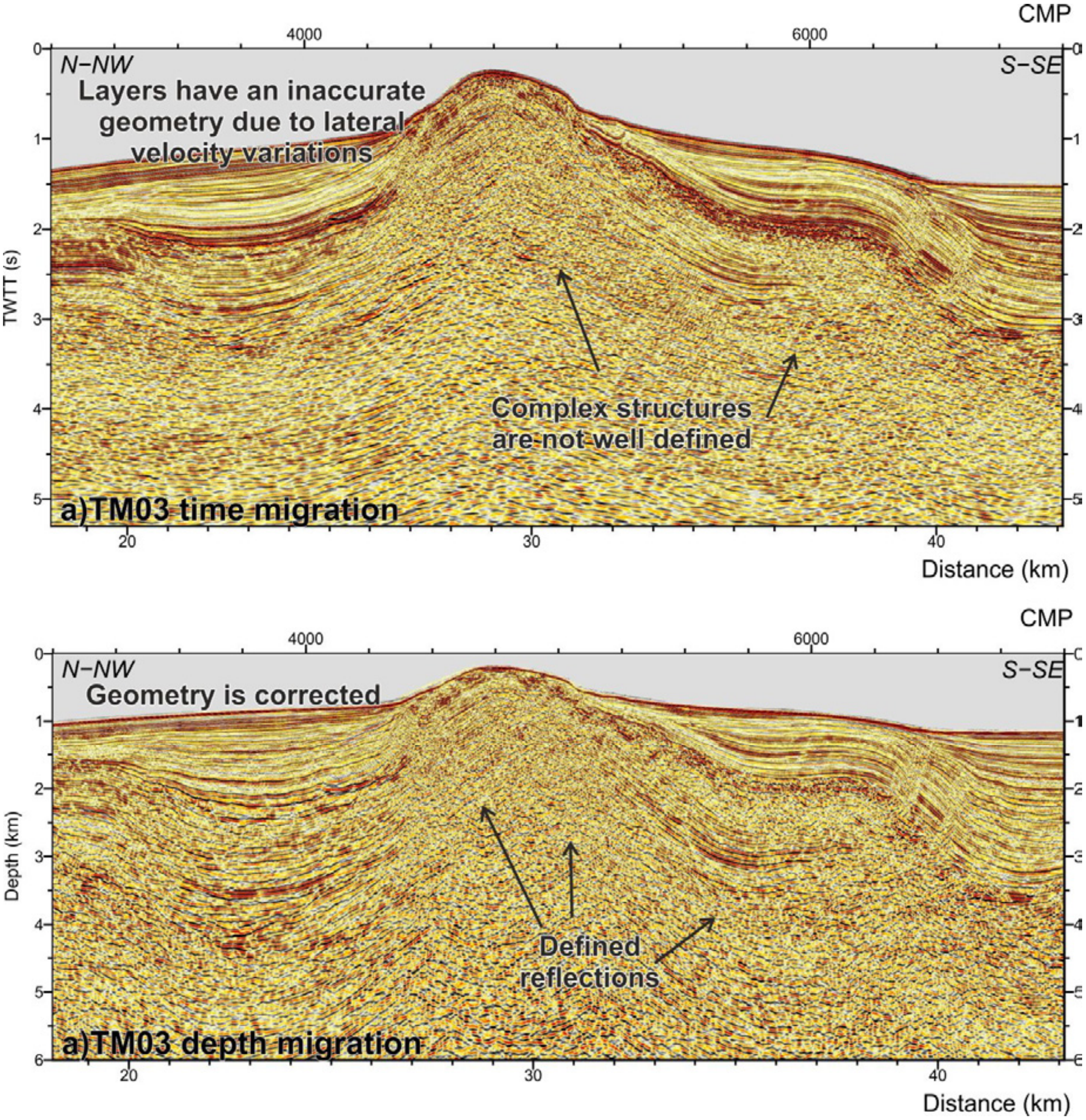

Figure 3.23: a) *Time migrated and* ***b)*** *depth migrated section of profile TM03. Vertical exaggeration is similar for both images (VE~1.5). The PSDM section solves the main problems of time migration. First of all, the resulting geometry is the real geometry at depth, while in the time migration layers are deformed following the changes in the travel velocity across them. Furthermore, complex structures are better defined in the depth section, where dipping reflections and points with different dips are imaged.*

Chapter 4

Wide angle seismic data

4.1. Data acquisition

Wide Angle Seismic (WAS) profiling is an active seismic method using both reflected and refracted waves with typically long offsets of tens of km (although shorter offsets are used for shallow targets). These waves result from the propagation of acoustic signal through the media, arriving at high depths due to the long offsets between sources and receivers and travelling at lower angles than near vertical reflections, so that they map for longer times the medium velocity. Modelling these data provides information of the velocity field through the medium and the geometry of the geological discontinuities.

The acquisition system is composed by a seismic source and a set of receivers, in marine surveys typically deployed on the seafloor. Receivers are Ocean Bottom Seismometers (OBS) and Ocean Bottom Hydrophones (OBH) (Fig. 4.1). The difference resides in that OBS measure the three components of motion with a seismometer, while OBH measure just pressure variations in one direction. After the survey, OBH/S are liberated from their anchors and float up to the sea surface, where they are recovered. The seismic source usually consists on an array of airguns (as in MCS data) towed by the vessel. As this method is used to image at a crustal scale, the source is set deeper than in MCS experiments. In that way, it has lower frequencies in the source wavelet that attenuate less than higher ones as they propagate. Firing distance is also longer than in MCS experiments, to avoid the background noise produced by the noise from the previous shots in the water layer (the wrap around noise).

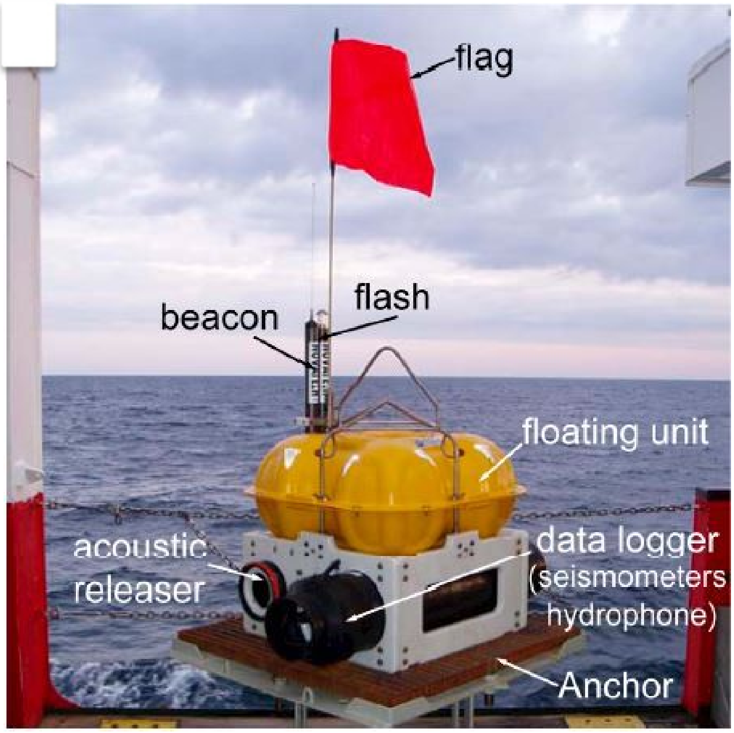

Figure 4.1: *OBH ready for deployment (from Prada, 2014).*

The generated rays suffer reflections or refractions following the Snells's law (Fig. 4.2). This behaviour is function of the source – receiver distance. When the source – receiver distance reaches the critical distance, the ray is critically refracted, and travels parallel to the boundary between the two layers through the one with faster velocity (Fig. 4.2) (e.g. Lowrie, 2007).

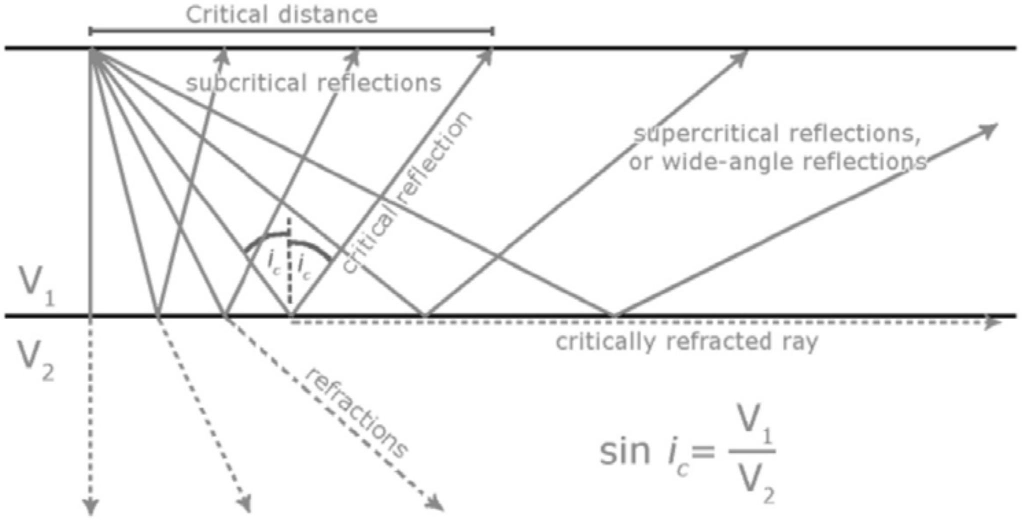

Figure 4.2: Schematic representation of the evolution of reflections and refractions as the source – receiver distance increases, following the Snell's law. i_c*= critical angle,* v_1*=velocity of layer 1,* v_2*=velocity of layer 2,* $v_1 < v_2$.

The data recorded consist of a continuous temporal trace than includes, at different offsets, the seismic events produced by the different seismic phases (Fig. 4.3). This traces are sorting by source - receiver offset, providing the so-called "common receiver gather" or "record section", where each trace corresponds to a shot (Fig. 4.3).

4.1.1. Acquisition parameters

During my Ph.D. thesis, I used WAS data to perform Mirror Imaging. To apply this modern technique, WAS data acquired in the WESTMED project (cruise M69/2, August-September 2006, Fig. 4.4) on board RV "Meteor" were used. A 32-litres BOLT air-guns array at 140 bar, fired every 60 s were used. To carry out the survey, 20 OBH and 5 OBS from GEOMAR (Kiel, Germany) were available, and land stations were also placed (but they are not used in Mirror Imaging since they have no multiple energy). The distance between receivers depends on the total length of the profile. Below we give details for the profiles processed (P2 and P5).

Acquisition parameters are described in the following table (Table 4.1).

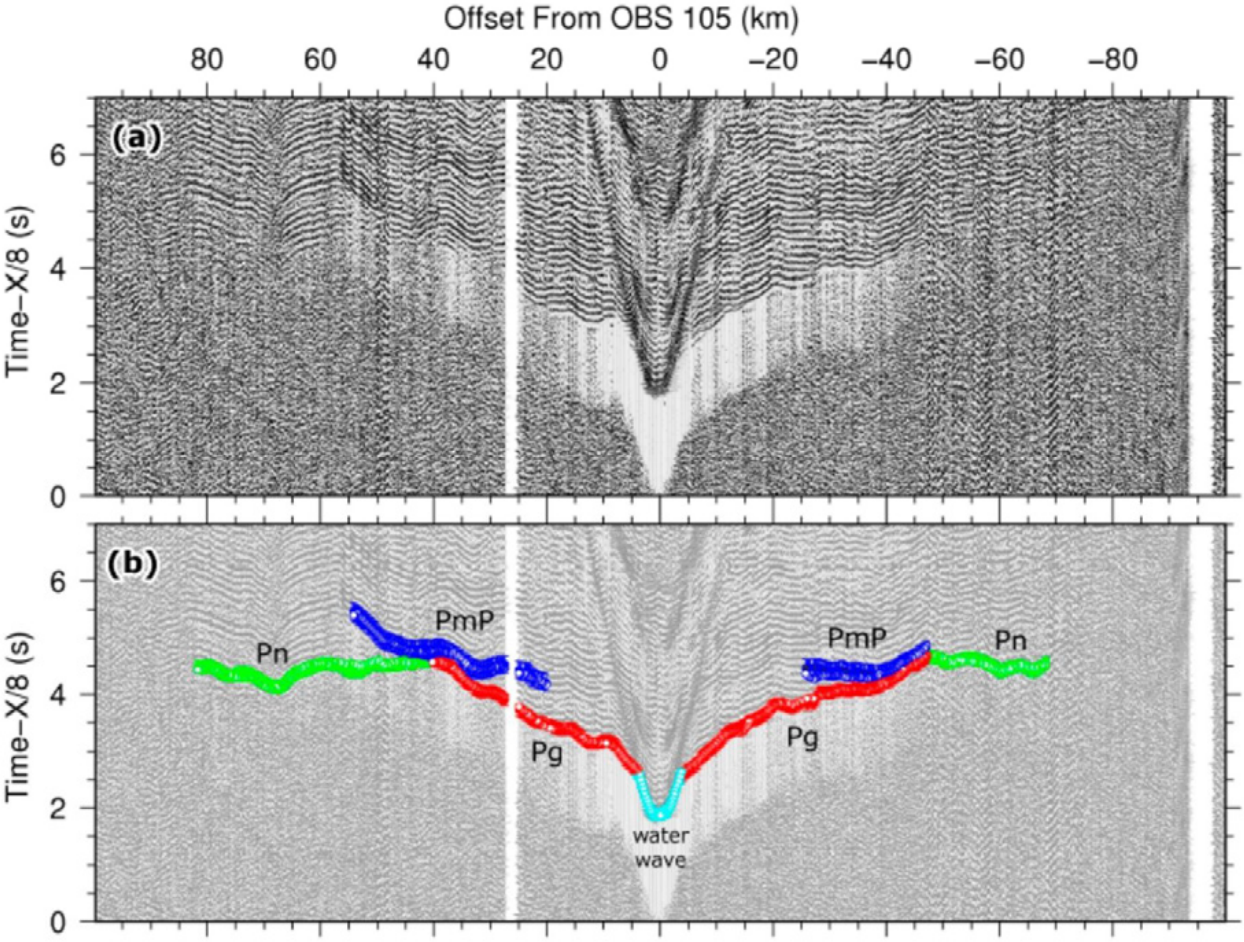

Figure 4.3: *Record section, obtained during the MEDOC WAS experiment (Tyrrhenian Sea, 2010).* ***(a)*** *Uninterpreted section.* ***(b)*** *Interpreted section, with the crust refracted waves depicted in red (Pg), the mantle refracted waves in green (Pn) and the reflected waves at the Moho in blue (PmP). The water wave is depicted with light blue (from Guzman Vendrell, 2015).*

	M69/2 – P2	**M69/2 – P5**
Number of receivers	25	23
Distance between receivers	10 km	7.5 km
Total profile length	250 km	200 km
Shot distance	~210 m	~210 m
CMP distance	25 m	25 m
Sample rate	4/5 ms	4/5 ms
Trace length	22s	22 s

Table 4.1: *Acquisition parameters of the WAS data during the WESTMED project.*

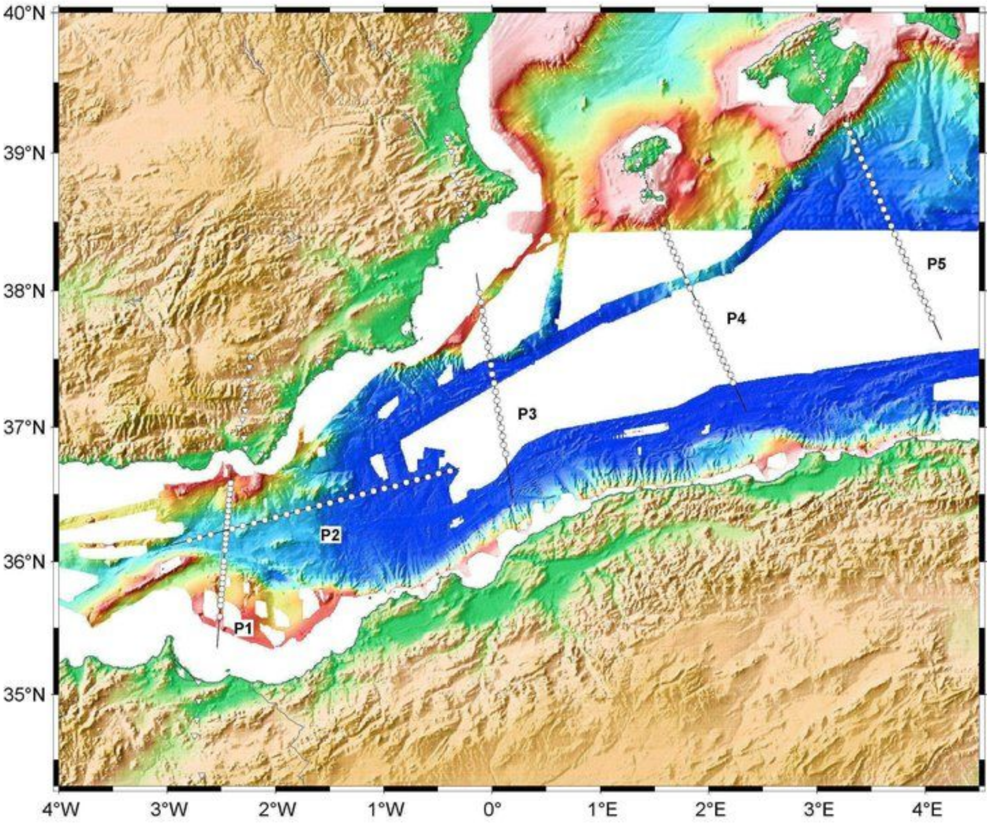

Figure 4.4: *Profiles acquired during the M69/2 cruise, in the frame of the WESTMED project. Profiles P2 (Alboran Basin) and P5 (South-East of Mallorca) have been used for this study.*

4.2. Data processing: Mirror Imaging

The Mirror Imaging method consists in obtaining an image of the sub-surface, similar to the ones obtained with multichannel seismic reflection streamer methods, using the multiple reflections of wide-angle seismic data recorded with Ocean Bottom Seismometers and Ocean Bottom Hydrophones (OBS/OBH).

Some of the advantages of using wide-angle data instead of multichannel seismic reflection data are than (i) the OBS/OBH are less sensitive to the obstacles and allow a more complete coverage, facilitating wide-azimuth geometries, (ii) the record is generally less noisy, and (iii) are better for doing 4D studies, as you can deploy the receptors and leave them for a long period of time (Grion et al., 2007; Dash et al., 2009).

In most cases, multiples are considered as noise, but to perform this method the water-layer multiples are treated as signal. This is because multiple reflections are formed by the same acoustic signal as the primaries, but differ in the travel path across the medium (Fig. 4.5) (Dash et al., 2009). This is the reason why they can provide additional information under correct conditions. Illumination of the multiple reflections is wider because of a different travel path under the sub-surface as the distance between the source and the receivers is longer, so they can provide information of the sub-surface in areas where primary waves collected on OBS cannot (Fig. 4.6) (Grion et al., 2007; Dash et al., 2009).

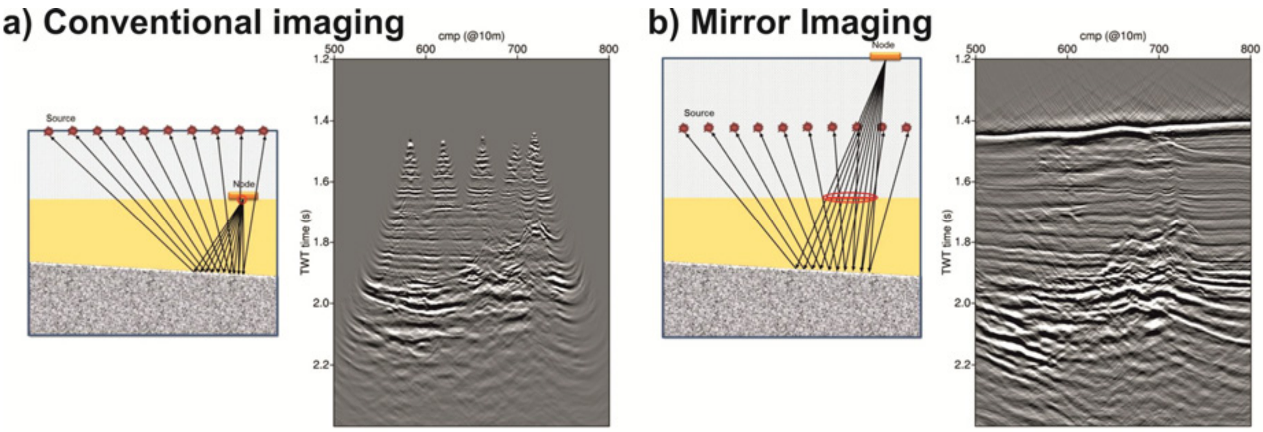

Figure 4.5* ▲*: *(**a**) Conventional imaging ray-paths and coverage vs. (**b**) mirror imaging ray-paths and coverage. Illuminated zone by conventional imaging (**a**) is narrower than the illuminated zone using the mirror imaging (**b**) (red ellipse on the figures). For instance, the seafloor can be imaged with multiple waves and not only primary waves (Liu et al., 2011)*

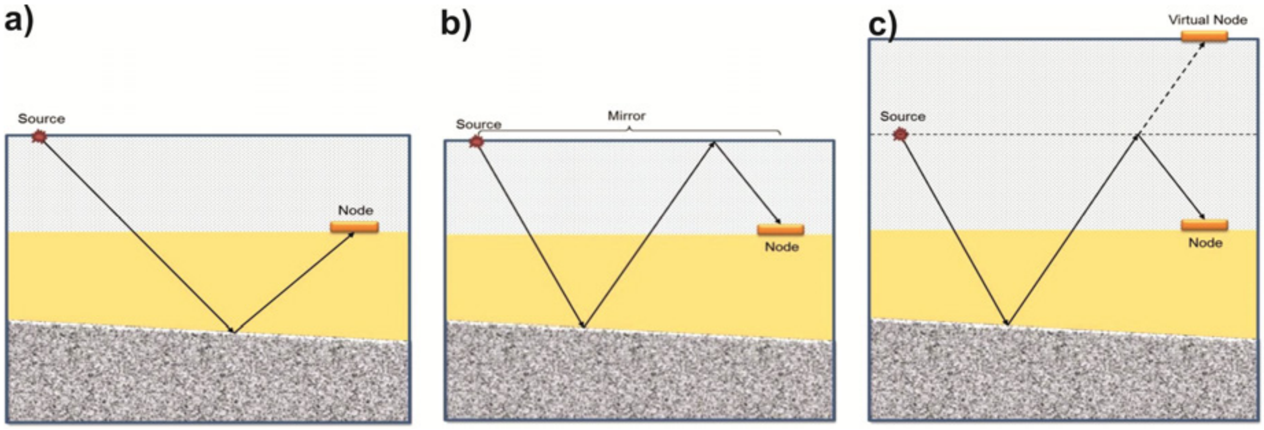

Figure 4.6* ▲*: *Ray paths of primaries (**a**) and multiples (**b**). For migration, multiple can be treated as a primary assuming that the data is not recorded on the seafloor but above, in a layer at twice thickness of water depth (**c**) (Ronen et al., 2005)*

The method is called Mirror Imaging because the sea surface acts as a mirror of the seafloor (Fig. 4.6) (Grion et al., 2007; Dash et al., 2009). Using multiple reflections we gain in the illumination width, but given that it is OBS records there is a limited illumination fold (Fig. 4.5). This technique works better in deep-water areas, where the primaries and the water-layer multiples are clearly separated in records (Dash et al., 2009).

Two dataset are needed to obtain an image: the record of the water-layer multiple in the OBS/OBH and the velocity model. The steps of the processing flow are detailed in Table 4.2.

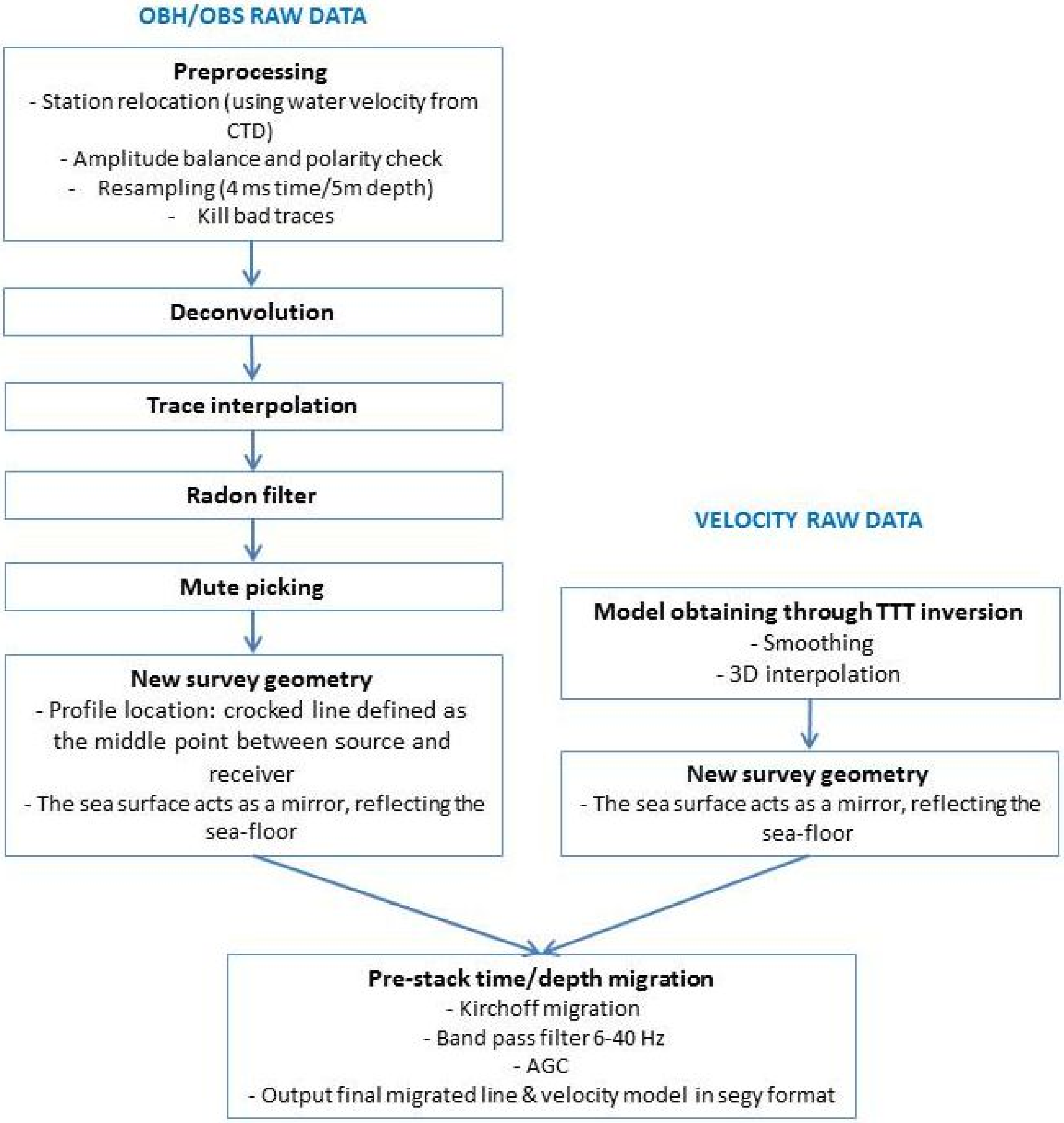

Table 4.2: *Processing flow to perform Mirror Imaging.*

In order to obtain a good result, seismic OBS/OBH data has been cleaned and processed before the migration. We relocated the stations in their real position based on water wave arrivals, applied a balance of the amplitudes, performed a deconvolution to reduce swell noise and low-period reverberations, interpolated traces to increase spatial coverage and avoid aliasing during migration, attenuated incoherent noise, and applied a Radon filter to reduce coherent noise. In addition, it is needed to create the new survey geometry, in which the sea surface acts as a mirror of the seafloor (Fig. 4.7).

We used the velocity models obtained through Travel Time Tomographic inversion (TTT) of the same dataset using wide-angle long-offset first arrivals and reflections (I. Grevemeyer, pers. commun. 2016). The velocity model was smoothed and mirror-imaging geometry introduced.

To obtain the image, we carried out a pre-stack Kirchoff migration, both in time and in depth. The inputs of this process are the processed OBS/OBH seismic data and the velocity model that we have, in time and in depth. To visualize the data, we have applied a band-pass filter 6-40 Hz and an AGC.

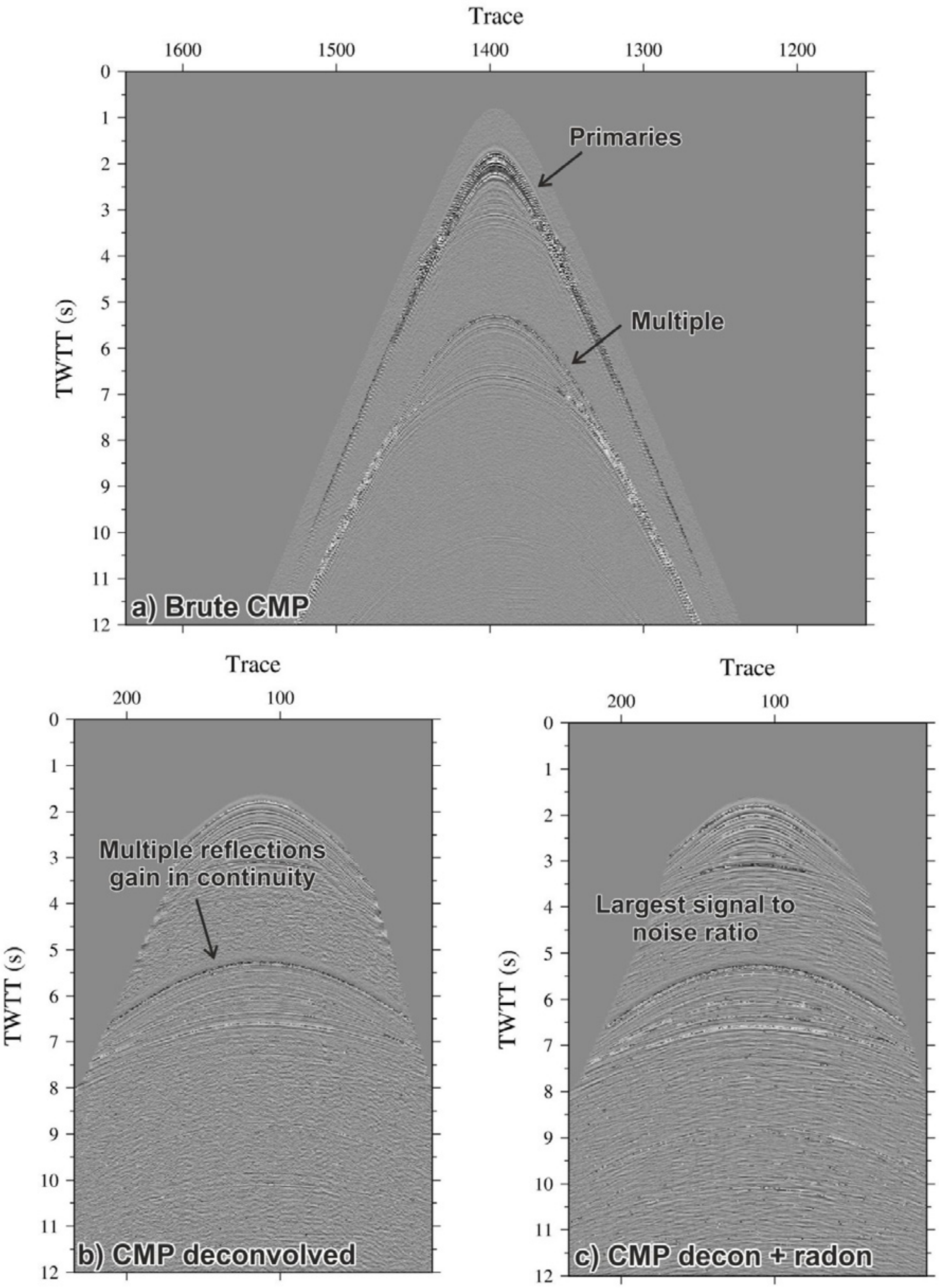

Figure 4.7: a) *Raw CMP (OBH28, profile P2), before processing. The seafloor multiple (our target) is easily identified.* ***b)*** *Same CMP after trace interpolation and deconvolution applied. We reduced the level of incoherent noise, and achieved a good continuity of the multiple reflections.* ***c)*** *Same as b, with Radon filter applied. We can observe how the resolution inside the multiple reflections increased. This is due to the higher signal-to-noise ratio, as Radon filter reduce the level of coherent noise.*

Finally, we obtained an image in which the horizontal trace spacing coming from the migration is of 25m. Although the OBS distance on this survey (not planned for Mirror Imaging) it ~10 km which is too wide for the detailed imaging of the subsurface structure, the image shows that the main sedimentary and tectonics structures are identified and that the method is useful for data sets with no coincident streamer records (Fig. 4.8).

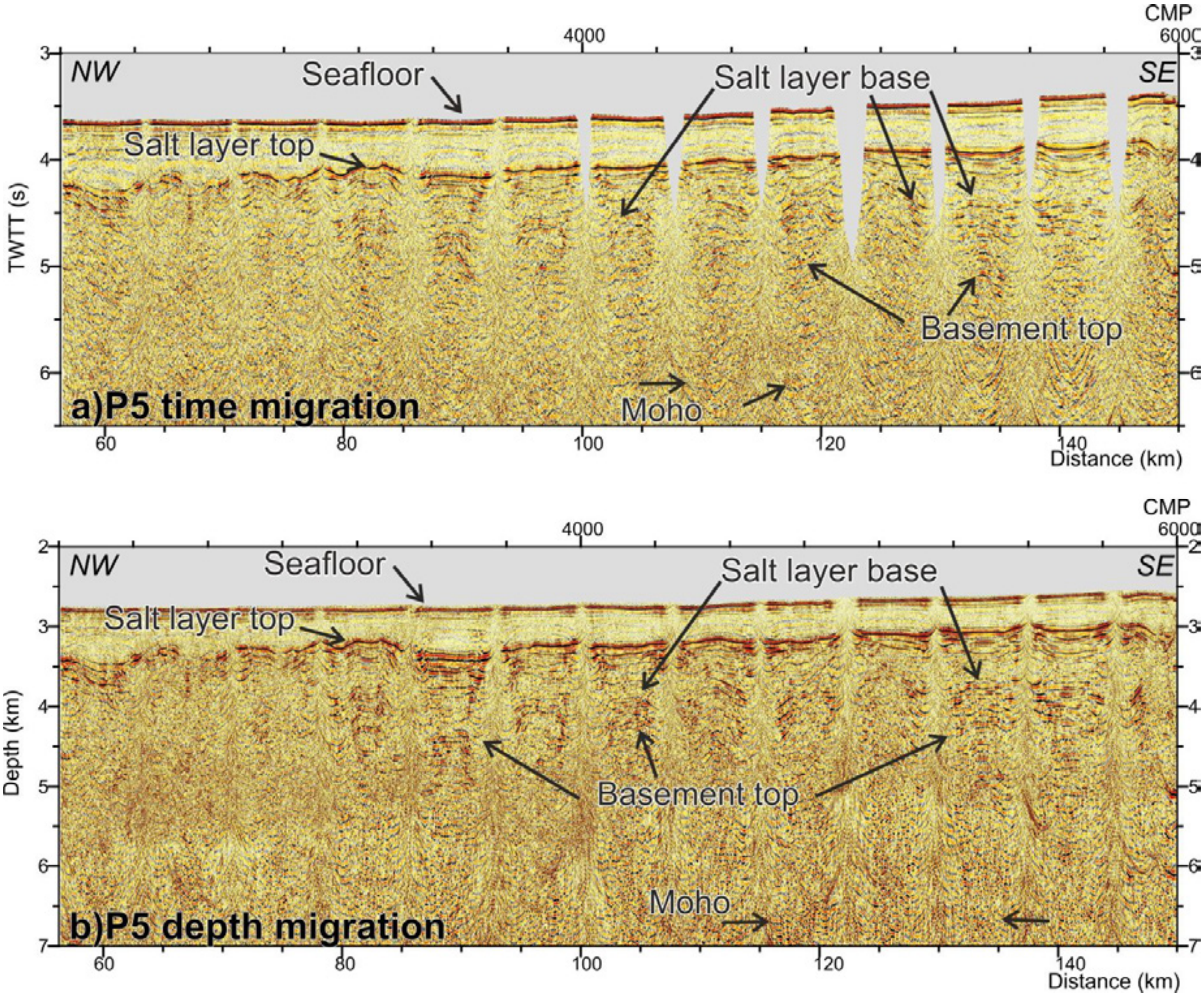

Figure 4.8: *Mirror imaging results. A section of profile P5 is shown in time migration (**a**) and in depth (**b**). Although data acquisition were not planned to perform mirror imaging, resulting section has enough resolution to characterize the main sedimentary layers (as the salt layer), the basement top, and depth reflections, such as the Moho. Sedimentary and tectonic structures are better identified in depth section, due to the nature of the methodology.*

Part III

RESULTS

“Πάντα ῥεῖ καὶ οὐδὲν μένει”

(*Everything flows, nothing stands still*)

Heraclitus of Ephesus

Chapter 5

Crustal domains

The Gibraltar Arc system results from the interaction among two large tectonics plates, the Iberian and African plates, and several exotic terrains that collectively are known as Alboran Domain (e.g. Sanz De Galdeano, 1990; Gelabert et al., 2002; Rosenbaum et al., 2002; Alonso-Chaves et al., 2004). The evolution of the Alboran Basin, located at the inner part of this system (Fig. 5.1), has been proposed to be linked to the evolution of the subduction system. A combination of slab roll-back and slab tearing (Wortel and Spakman 2000; Spakman and Wortel, 2004; Bezada et al., 2013; Chertova et al., 2014; Faccenna et al., 2014; Van Hinsbergen et al., 2014; Fichtner and Villaseñor, 2015) has probably affected the entire system, and conditioned subsidence patterns of the basin, and the magmatic activity that led to the generation of new basements during the Tortonian (Hoernle et al., 1999; Duggen et al., 2004; Duggen et al., 2005; Booth-Rea et al., 2007), and the processes taking place at the shallower parts of the basins and the seafloor.

Although the deep structure of the the region around the Alboran Basin has been recently extensively studied (e.g. Mancilla et al., 2015) the crustal and upper mantle structure under the Alboran Basin remains inadequately mapped. A first approximation to the crustal structure was performed by Soto et al. (2008), on the basis of thermal modelling. The outcome was a general model of the entire Gibraltar Arc system, although with not enough resolution to determine the crustal structure under the basin. Results from global tomography (typically travel time methods) usually focuses on mantle structure due to limitations in resolution (e.g. Wortel and Spakman, 2000; Spakman and Wortel, 2004; Chertova et al., 2014). Recent velocity models obtained with full-waveform inversion method (Fichtner and Villaseñor, 2015) imaged the crust and mantle, although the resolution of the model in the crust is limited by data availability and not precise enough to characterize the crust under the basin. However, results are similar to those obtained from receiver function analysis (Mancilla et al., 2015). Few previous multichannel seismic reflection studies focused on the deep structure of the basin and they are composed by few profiles with local character (e.g. ESCI-Alb project). They provided limited local information on the structure at depth (Booth-Rea et al., 2007). Basement dredges, scientific and commercial (oil-industry) well data of the basement are scarce, and the lack of an extensive wide-angle seismic study across the basin hinders an accurate understanding of the regional structure.

In this chapter, we propose a comprehensive study of the Alboran Basin crustal characteristics on the basis of the TOPOMED-GASSIS (2011) multichannel seismic reflection profiles, acquired with the objective of imaging the full crustal structure. The main objectives of this chapter are: (i) To characterize the different types of crust within the Alboran Basin; (ii) To link these different basements with their respective crustal domains, on the basis of seismic images, and available dredged samples and scientific and commercial well information, and the integration of previous studies; and (iii) To explain the basin configuration taking into account the different crustal structures identified.

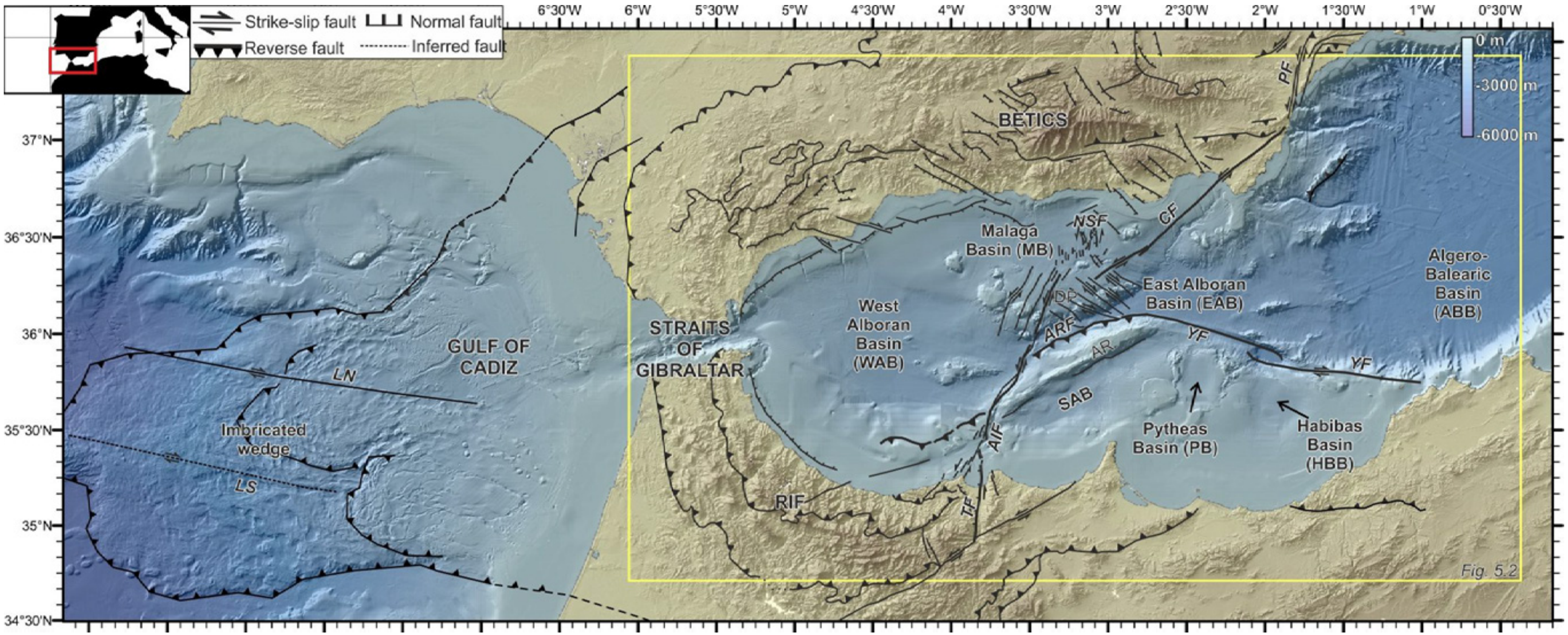

Figure 5.1: *Regional bathymetric map of the Alboran Sea constructed from multibeam data acquired during our cruises in the Alboran Sea (Gràcia et al., 2006, 2012, submitted 2017), the SARAS cruise (PI: d'Acremont & Gorini; d'Acremont et al., 2014; Lafosse et al. 2016; Rodriguez et al. 2017), and of the Gulf of Cadiz (Gràcia et al., 2003a,b, 2010; Zitellini et al., 2009; Bartolomé et al., 2012; Martínez-Loriente et al., 2013, 2016) completed with IEO bathymetry (Ballesteros et al., 2008) and released SRTM-3 and GEBCO digital data. Main depocenters and tectonic structures are displayed (Gràcia et al., 2006, 2012, submitted 2017). The yellow rectangle depicts the area presented in Figure 5.2. Inset: Location of the shown area (red rectangle). ABB: Algero Balearic Basin, AIF: Al-Idrissi Fault, AR: Alboran Ridge, ARF: Alboran Ridge Front Fault, CF: Carboneras Fault, DP: Djibouti Plateau, EAB: East Alboran Basin, NSF: North-South Faults; PF: Palomares Fault; SAB: South Alboran Basin, TF: Trougout Fault, WAB: West Alboran Basin, YF: Yusuf Fault.*

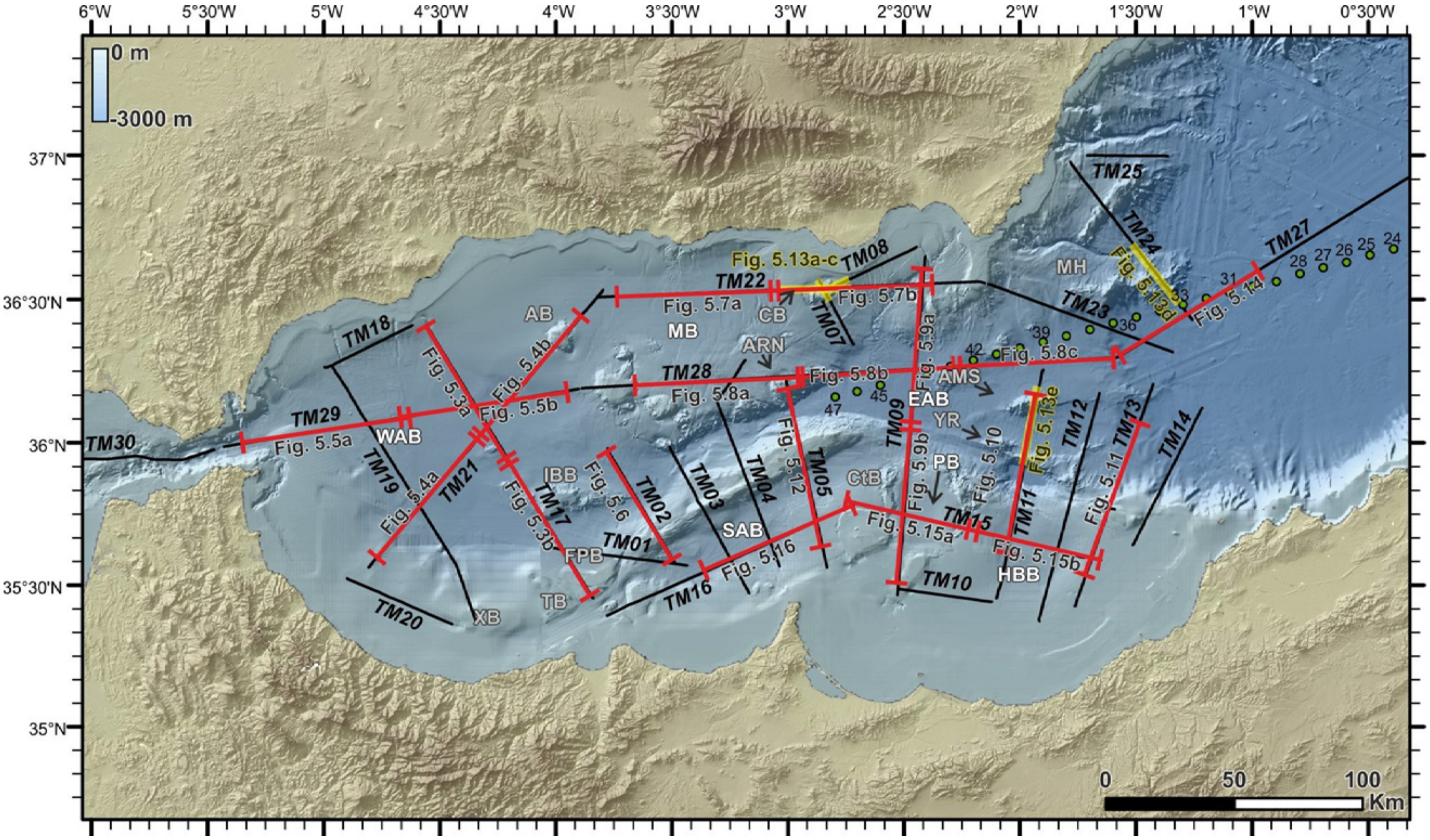

Figure 5.2: *Colour shaded-relief bathymetric map of the Alboran Basin (see Figure 5.1 for location). The TOPOMED-GASSIS MCS profiles acquired in 2011 onboard the RV Sarmiento de Gamboa are depicted. Red and yellow lines display the seismic profiles presented in this chapter. TM: Topomed-Gassis cruise MCS profiles. Green dots depicted the OBH/OBS position during the acquisition of P02 profile (WESTMED Project). Volcanic basement outcrops shown in the seismic profiles are labelled: AB: Algarrobo Bank, AMS: Al-Mansour Seamount, ARN: Adra Ridge North, CB: Chella Bank, CtB: Catifa Bank, EAB: East Alboran Basin, FPB: Francesc Pagès Bank; HBB: Habibas Basin, IBB: Ibn-Batouta Bank, MB: Malaga Basin, MH: Maimonides High, SAB: South Alboran Basin, TB: Tofiño Bank, WAB: West Alboran Basin, XB: Xauen Bank, YR: Yusuf Ridge.*

5.1. Data used in this chapter

The 29 profiles acquired during the TOPOMED-GASSIS cruise are the basis of this chapter, as they allow us to image the crust and the upper mantle of the Alboran Basin. The processing of this dataset has been focused to image the deeper part of the basins while keeping a relatively good resolution in the sedimentary units (see "Chapter 3: Multichannel seismic reflection data").

The tracks of the seismic profiles displayed in this chapter are presented in Figure 5.2.

5.2. Crustal domains

On the basis of the TOPOMED-GASSIS profiles and the correlation with scientific and commercial wells available in the Alboran Basin, we have identified three different types of crust: (i) a thin continental crust (metamorphic terrain where drilled) under the West Alboran Basin (WAB) and Malaga Basin (MB), (ii) a magmatic crust under the Djibouti Plateau, the NE Alboran Basin and the East Alboran Basin (EAB), and (iii) a continental crust (metamorphic where drilled) at the NW African margin. These different crustal-types and the transition between them are established through the structures imaged on the MCS profiles, as will be described along this section. This chapter focuses on the deep structure of the basin. The term basement will be referred to the assemblage of rock underlying the oldest stratified rocks identified in the region (continental, volcanic arc, or oceanic type), and the term crust is used to describe both, sedimentary record and basement.

5.2.1. West Alboran and Malaga basins continental crust

The WAB and the MB are located respectively in the West and Northwest Alboran Basin (Fig. 5.1). These two sub-basins are deep sedimentary depocenters, accumulating more than 6 s TWTT of sediments, which deposit began at the Late Aquitanian – Burdigalian (~21 Ma). The basement of these basins has been sampled at 2 drill sites where they cored metamorphic rocks of Late Oligocene – Early Miocene age (e.g. Comas et al., 1992; Comas et al., 1999).

In the WAB (profiles TM17, TM21 and TM29, Figs. 5.3, 5.4 and 5.5), the top of the metamorphic basement is located between 5 and 7 s TWTT under the basin depocenter (Fig. 5.3a CMP 20000-16000, Fig. 5.4a CMP 2000-8000) and rises towards two highs with tops at ~2 s TWTT (Figs. 5.3a CMP 16000 - 10000, 5.4a CMP 8000-10000). Towards the Straits of Gibraltar, the basin thins as the basement top reaches shallower to ~1.5 s TWTT (Fig. 5.5a CMP 22000-18000). The bottom of the basement is commonly defined by events that we interpret as Moho reflections (Figs. 5.3, 5.4, 5.5). The Moho boundary is defined by discontinuous reflections (e.g. Fig. 5.3a CMP 20000-16000) of somewhat higher amplitude than the more transparent crust. The Moho occurs between 7-8 s TWTT in the northern sector (Fig. 5.3a CMP 20000-16000) and between 8-10 s on its southwestern sector (Fig. 5.4a CMP 2000-10000). Below the basement highs Moho is difficult to clearly defined, although some indistinct events are identified (Fig. 5.3a CMP ~14000, ~12000). Under the basin, basement thickness is only ~1.5-2.5 s TWTT. At basement highs, basement thickness is ~ 5 s TWTT (Figs. 5.3a-b CMP 16000-8000, 5.4a CMP 7000-11000). Towards the Straits of Gibraltar, the Moho is identified at ~8 s TWTT, and the basement thickens, reaching ~7 s TWTT thickness (Fig. 5.5a CMP 22000-18000).

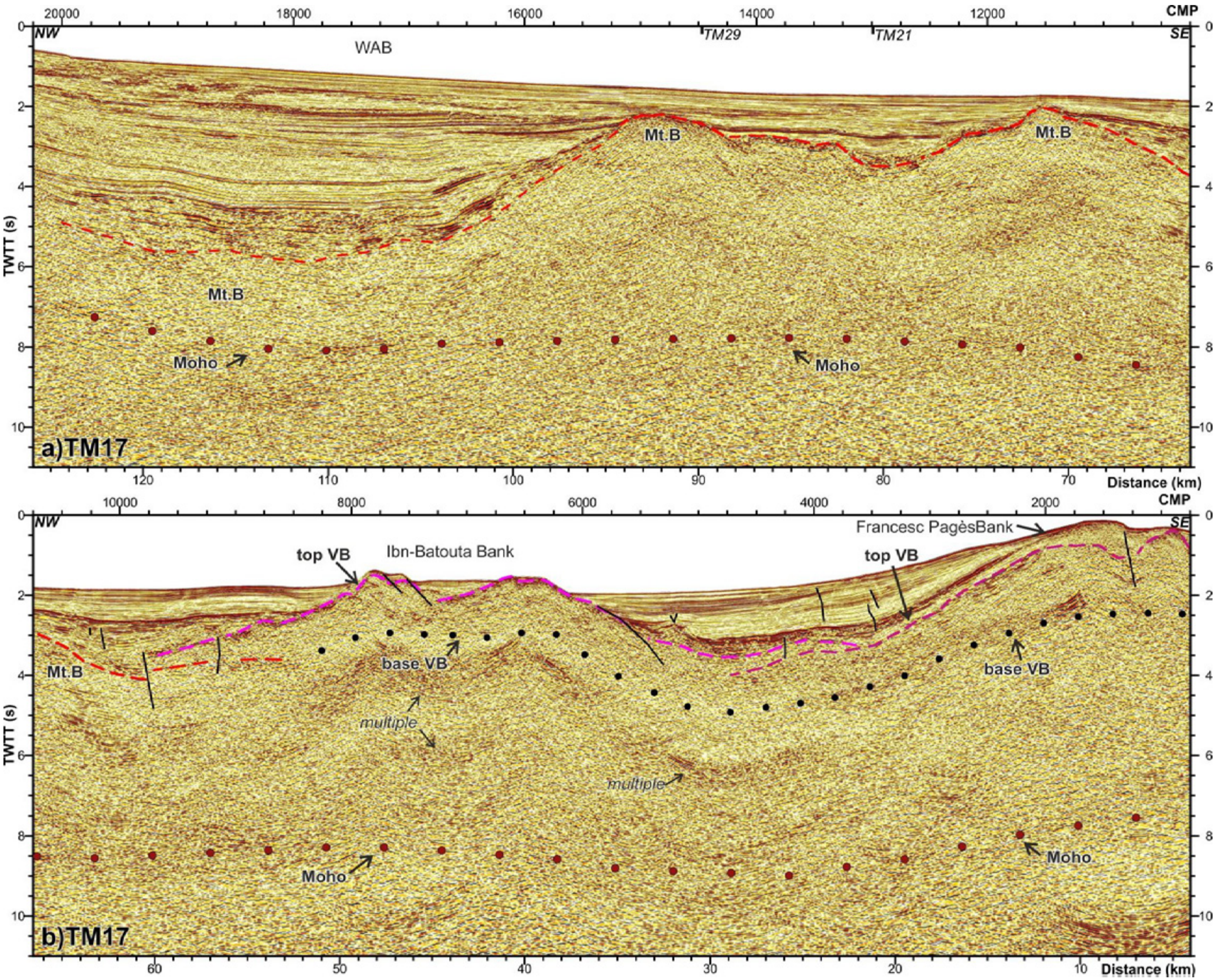

Figure 5.3: *Time migration of profile TM17 (see location in Figure 5.2). This profile is divided in a) Northern section and b) Southern section. Crustal structure is displayed. The top of the metamorphic basement is displayed with a red dashed line, and the top of the volcanic basement is shown with pink dashed lines. The base of the volcanic basement is displayed with black filled dots, and the Moho of the thin continental crust is displayed with light brown dots. Mt.B: metamorphic basement, VB: volcanic basement. Main structures are identified. Vertical exaggeration is of ~x:1 taking into account basement velocities (>3500 m/s).*

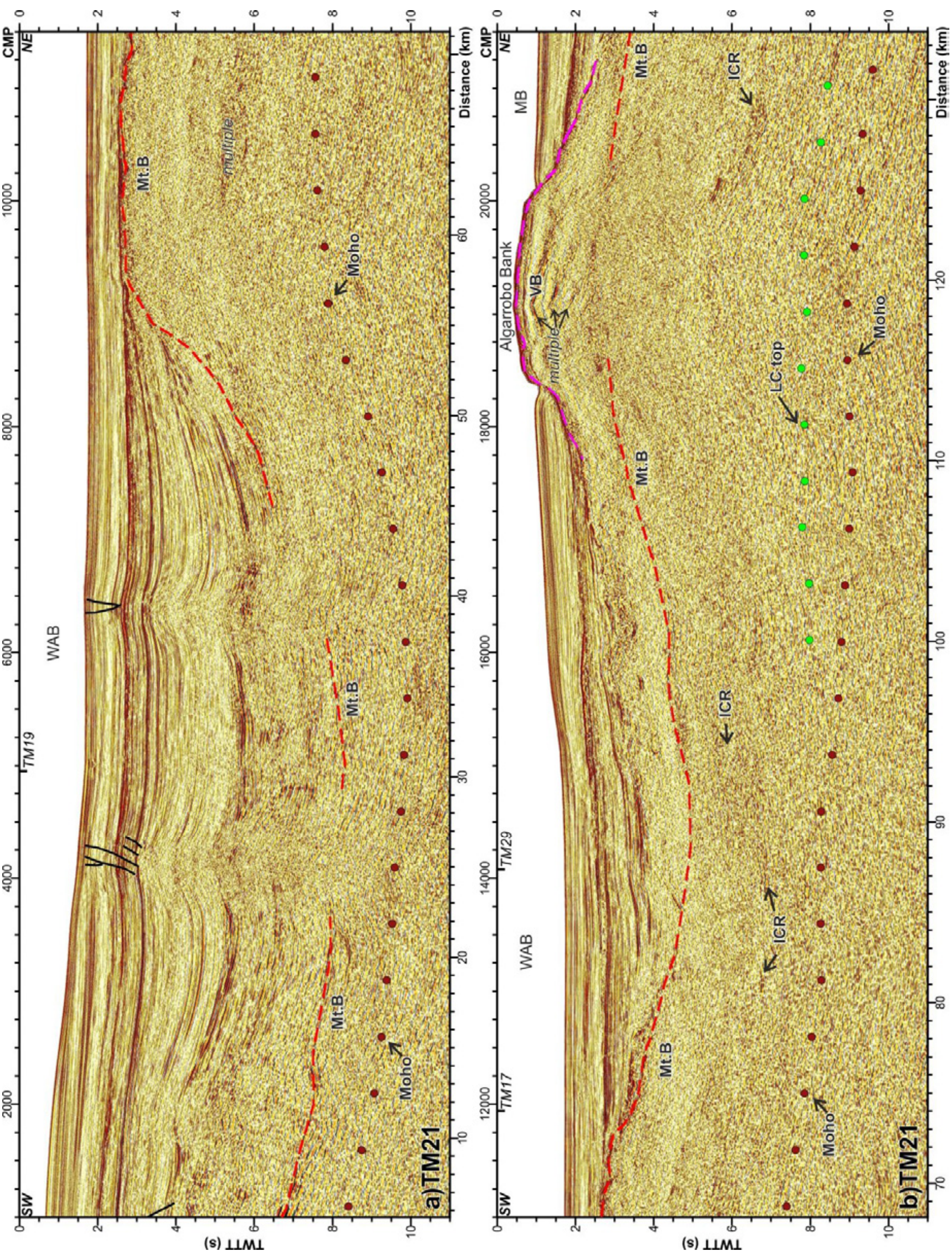
a)TM21
b)TM21
SW
NE
CMP
TWTT (s)
Distance (km)
WAB
MB
Mt.B
multiple
Moho
TM19
TM17
TM29
Algarrobo Bank
VB
LC-top
ICR
0
2
4
6
8
10
2000
4000
6000
8000
10000
12000
14000
16000
18000
20000
20
30
40
50
60
70
80
90
100
110
120

◄ ***Figure 5.4:*** *Time migration of profile TM21 (see location in Figure 5.2). This profile is divided in a) Southwestern section and b) Northeastern section Crustal structure is displayed. The top of the metamorphic basement is displayed by a red dashed line and the top of the volcanic basement by pink dashed lines. The top of the lower crust top is displayed with green dots, and the Moho of the thin continental crust is displayed with light brown dots. Mt.B: metamorphic basement, VB: volcanic basement. ICR: Intra-Crustal Reflection. LC: Lower Crust. Main structures are identified. Vertical exaggeration is of ~x:1 taking into account basement velocities (>3500 m/s).*

Under the WAB, the crust shows a homogenous aspect, with poor continuity reflections (Fig. 5.3a CMP 20000-16000, Fig. 5.4a CMP 1000-10000). At the southern part of the WAB, below the basement highs, a few intra-crustal reflections (ICR) are identified (Fig. 5.4b). The southern and eastern parts of the WAB are characterized by basement highs cropping out at the seafloor that indicate that metamorphic continental basement is affected by younger magmatic activity (Fig. 5.3b, 5.5b, 5.6), resulting in a gradual change in the basement type, from the metamorphic basement flooring the most of the WAB to the volcanic basement found in the southeast WAB and the SAB.

Profile TM21 (Fig. 5.4) images the transition between the WAB and the MB (Fig. 5.4b). These two basins present continuity in the characteristics regarding sedimentary infill and basement nature, however, crustal thickness are different. The basement top at the MB occurs at ~4-5 s TWTT (Fig. 5.7a), shallower than in the WAB (Figs. 5.3a, 5.4a). A deepening of the Moho occurs from ~8 s TWTT depth at the WAB to ~10 s TWTT depth at the MB (Figs. 5.4b, 5.7). Thus, the basement under the MB is ~5.5 s TWTT thickness (Fig. 5.7).

The seismic image displays a change in the reflectivity of the crust, which we can divide into two: a) the upper crust, with a low reflectivity character and <~4 s TWTT thick, and b) the lower crust, characterized by a higher reflectivity and <~2.5 s TWTT thick. The boundary between the upper and lower crust is abrupt, defined by relatively continuous, high-amplitude set of reflections at ~7-8 s TWTT (green-filled circles in Figure 5.7), getting progressively indistinct towards the west, and disappearing at the WAB (Fig. 5.4b). The crust under the MB presents a banded aspect, and the Moho reflection presents an aspect similar to the WAB, with sparse reflections than gain continuity towards the east, characterized by high amplitude and low frequency (Fig. 5.7a CMP 6000-10000, Fig. 5.7b CMP 12000-18000).

The eastern end of the MB is abruptly defined by the Carboneras Fault (Fig. 5.7b CMP ~18000) than marks the basement boundary with magmatic arc crust, located to the east. Volcanic constructions occur near the boundary (e.g. Algarrobo Bank, Fig. 5.4b CMP 18000-20000; Chella Bank, Fig. 5.7b CMP 12000-160000), but they have a local character and are not affecting the crustal configuration.

However, at eastern the Carboneras Fault we observe a different basement, without the banded pattern on its upper part (Fig. 5.8, 5.7), and a shallower Moho (Fig. 5.7b).

***Figure 5.5* ►:** *Time migration of profile TM29 (see location in Figure 5.2). This profile is divided in a) Western section and b) Eastern section. Crustal structure is displayed. The top of the metamorphic basement is displayed with a red dashed line, and the top of the volcanic basement is shown with pink dashed lines. The base of the volcanic basement is displayed with black filled dots. The top of the lower crust top is displayed with green dots and the Moho of the thin continental crust is displayed with light brown dots. Mt.B: metamorphic basement, VB: volcanic basement. Main structures are identified. Vertical exaggeration is of ~x:1 taking into account basement velocities (>3500 m/s).*

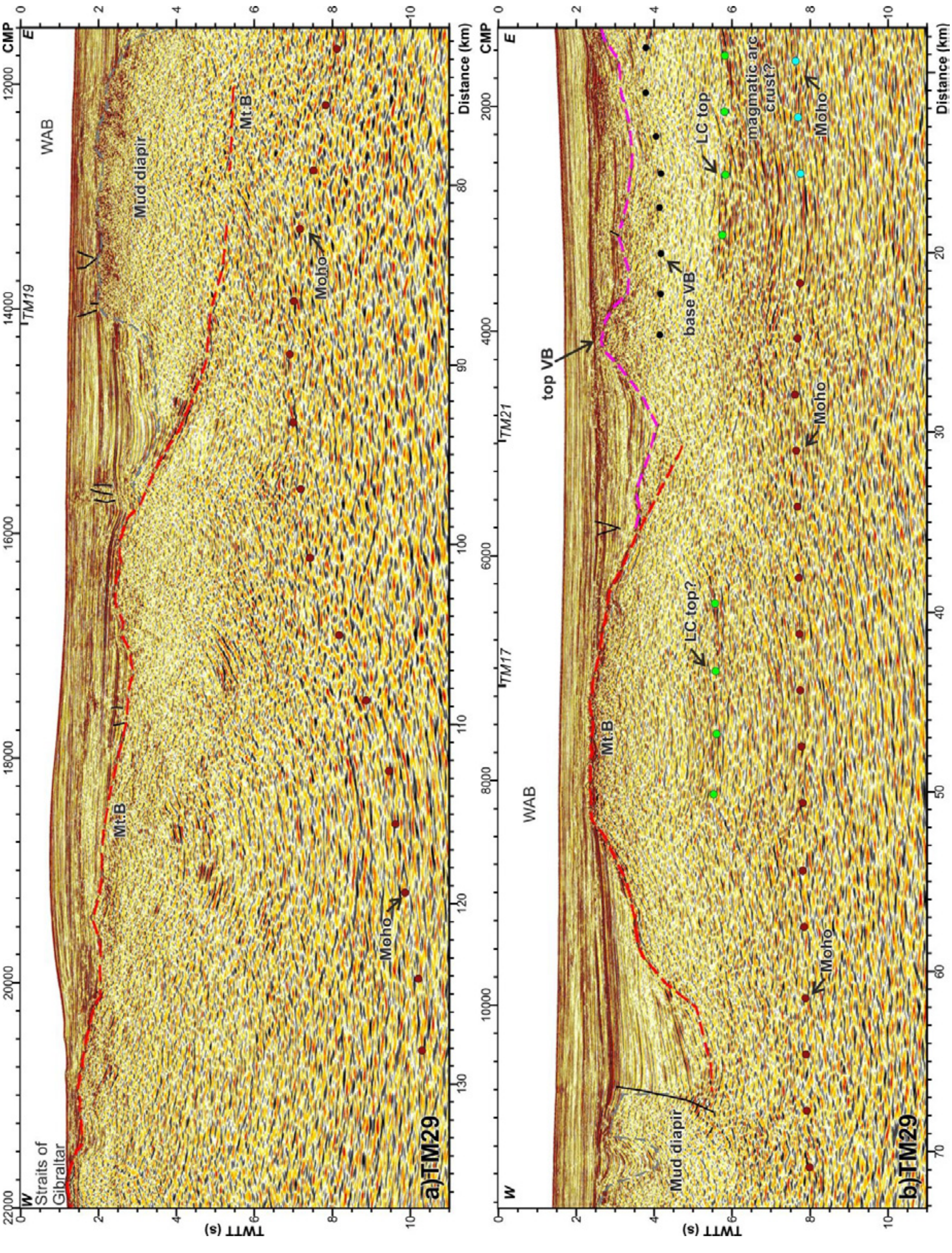
CMP
Distance (km)
TWTT (s)
E
W
Straits of Gibraltar
WAB
Mud diapir
Mt.B
Moho
TM19
a)TM29
top VB
base VB
LC top
magmatic arc crust?
TM21
TM17
LC top?
b)TM29

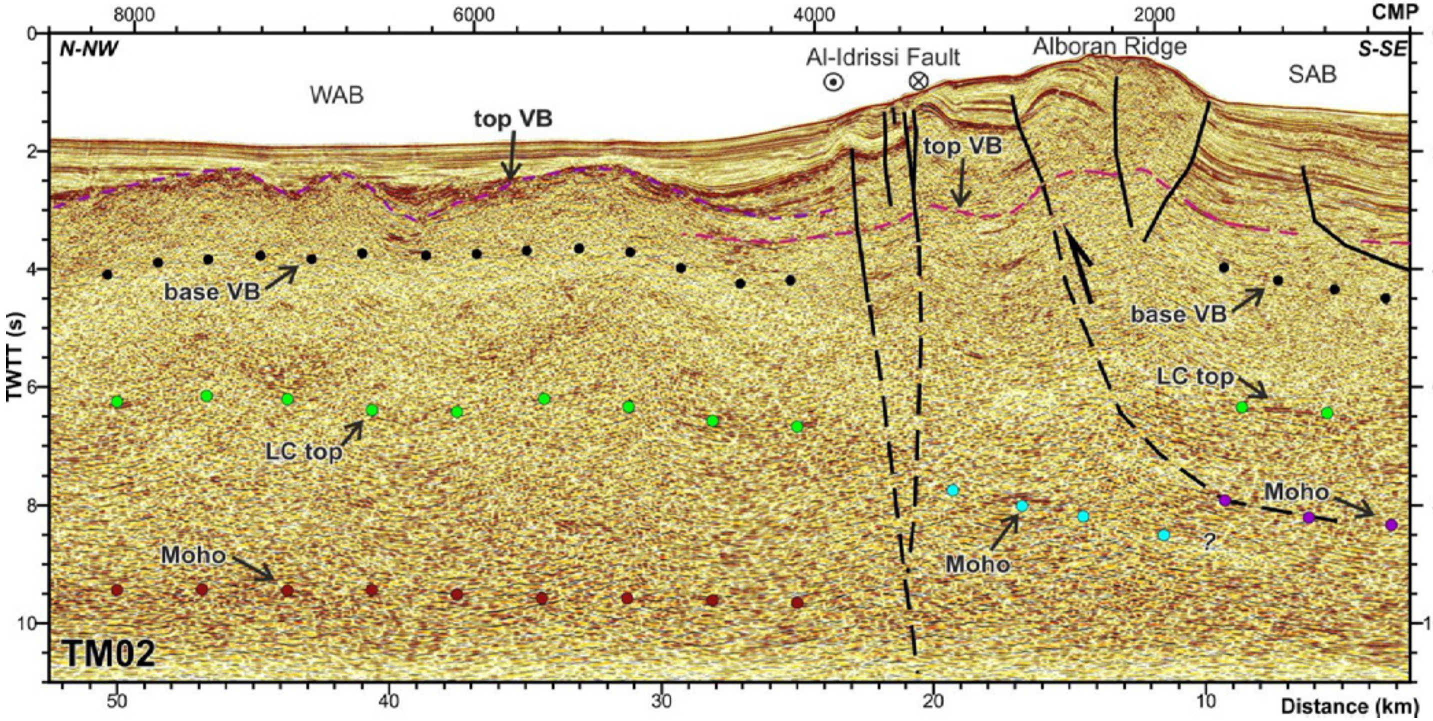

Figure 5.6: *Time migration of profile TM02 (see location in Figure 5.2). Crustal structure is displayed. The top of the metamorphic basement is displayed with a red dashed line, and the top of the volcanic basement is shown with pink dashed lines. The base of the volcanic basement is displayed with black filled dots, the Moho of the thin continental crust is displayed with light brown dots, the Moho of the magmatic arc crust is displayed with blue dots and the Moho of the thick continental crust is displayed with purple dots. Mt.B: metamorphic basement, VB: volcanic basement. Main structures are identified. Vertical exaggeration is of ~x:1 taking into account basement velocities (>3500 m/s).*

5.2.2. Magmatic crust

At the Eastern Alboran Basin (EAB), a Late Serravallian – Tortonian volcanic basement has been described from rock samples and seismic images (e.g. Duggen et al., 2004; Booth-Rea at al., 2007). The top of this basement is found ranging between ~0.5-4 s TWTT depth (e.g. Fig. 5.7a), and shows an irregular reflectivity characterised by short segments forming a complex sub-horizontal pattern (Figs. 5.8, 5.9) possibly formed by a succession of different volcanic units (Fig. 5.8c CMP 8000-4000) (e.g. Duggen et al., 2004; Duggen et al., 2008; see "Chapter 6: Basin evolution" for further details). This basement internal structure exhibits in its upper part discontinuous reflections with a wavy aspect (Fig. 5.8). The base of the volcanic units is not a sharp well defined boundary in the seismic images, but it can be mapped by a change in reflectivity, as the volcanic units present a higher reflectivity than the middle crust over which they were deposited/emplaced (black dots at Figures 5.7a, 5.8, 5.9).

The Moho occurs at ~8 s TWTT, the top of the lower crust (LC) is <~6 s TWTT, and the basement thickness, measured from the top of volcanics to the Moho, is ~5 s TWTT thick. A boundary between upper (~2 s TWTT thick) and lower (~3 s TWTT thick) crusts is delineated by an abrupt reflectivity contrast with the lower crust, with higher reflectivity and relatively continuous reflections (top mark by green dots in Figures 5.8, 5.9). On this area, there are few Moho reflections and with low continuity, and the Moho boundary has been delineated at the base of the high reflectivity lower crust (Fig. 5.8c). Towards the south, the magmatic crust is separated from the rather different North African continental crust through the Yusuf Fault (Fig. 5.9b CMP 11000-12000, Fig. 5.10 CMP 7000-9000, Fig. 5.11 CMP 7000-8000) and through the Alboran Ridge front fault (Fig. 5.12 CMP 2000-8000).

Main evidence of magmatic arc activity in the Alboran Basin are located between 4º15´W and 1ºW (Fig. 5.2) (e.g. Duggen et al., 2004; Duggen et al., 2005; Duggen et al., 2008). This magmatism can be generalized, as in the case of the Djibouti Plateau (Figs. 5.1, 5.8a) or Adra Ridge (Figs. 5.2, 5.8b) or in the Alboran Ridge area (Fig. 5.1, 5.12). But it is also affecting the metamorphic basement, where isolated volcanic edifices are found (Comas et al., 1999; Duggen et al., 2008; Martínez-García et al., 2011). In our images, such volcanic edifices are characterized by high amplitude wavy reflections that usually form aprons on the flanks of the volcanic construction (Fig. 5.3b CMP 10000-4000, Ibn-Batouta Bank; Fig. 5.4b CMP 17000-21000, Algarrobo Bank; Fig. 5.7a CMP 2500-60000, El Sabinar Bank; Fig. 5.135a-c, Fig. 5.13 CMP15000-13000, Al-Mansour Seamount). On bathymetric maps, they usually present a circular shape, (Fig. 5.2), especially evident in the Chella Bank (Fig. 5.13a-c), with a mean diameter of ~30 km (Fig. 5.4b CMP 17000-21000, Algarrobo Bank; Fig. 5.7a CMP 2500-60000, El Sabinar; Fig. 5.135a-c, Fig. 5.13 CMP15000-13000, Al-Mansour Seamount). In areas floored by volcanic rocks, volcanic edifices are also found (Fig. 5.13d-e). In these areas, elongated ridges are more common than conical edifices (Fig. 5.2), with a mean width of 20 km and different lengths, being the Maimonides High the longest one, with more than 50 km length (Fig. 5.13d, Maimonides High, Fig. 5.13e, Yusuf Ridge and Al-Mansour Seamount). They display clear constructional stratigraphy of mainly volcanoclastic strata, perhaps interlayered with some lava flows, although the latter are not clearly distinguishable in the seismic images.

***Figure 5.7* ►:** *Time migration of profile TM22 (see location in Figure 5.2). This profile is divided in a) Western section and b) Eastern section. Crustal structure is displayed. The top of the metamorphic basement is displayed with a red dashed line. The top of the volcanic basement with pink dashed lines. The base of the volcanic basement is displayed with black dots, the lower crust top is displayed with green dots, the continental Moho is displayed with brown dots and the magmatic arc Moho is displayed with blue dots. Mt.B: metamorphic basement, VB: volcanic basement. ICR: Intra-Crustal Reflection. LC: Lower Crust. Main structures are identified. Vertical exaggeration is of ~x:1 taking into account basement velocities (>3500 m/s).*

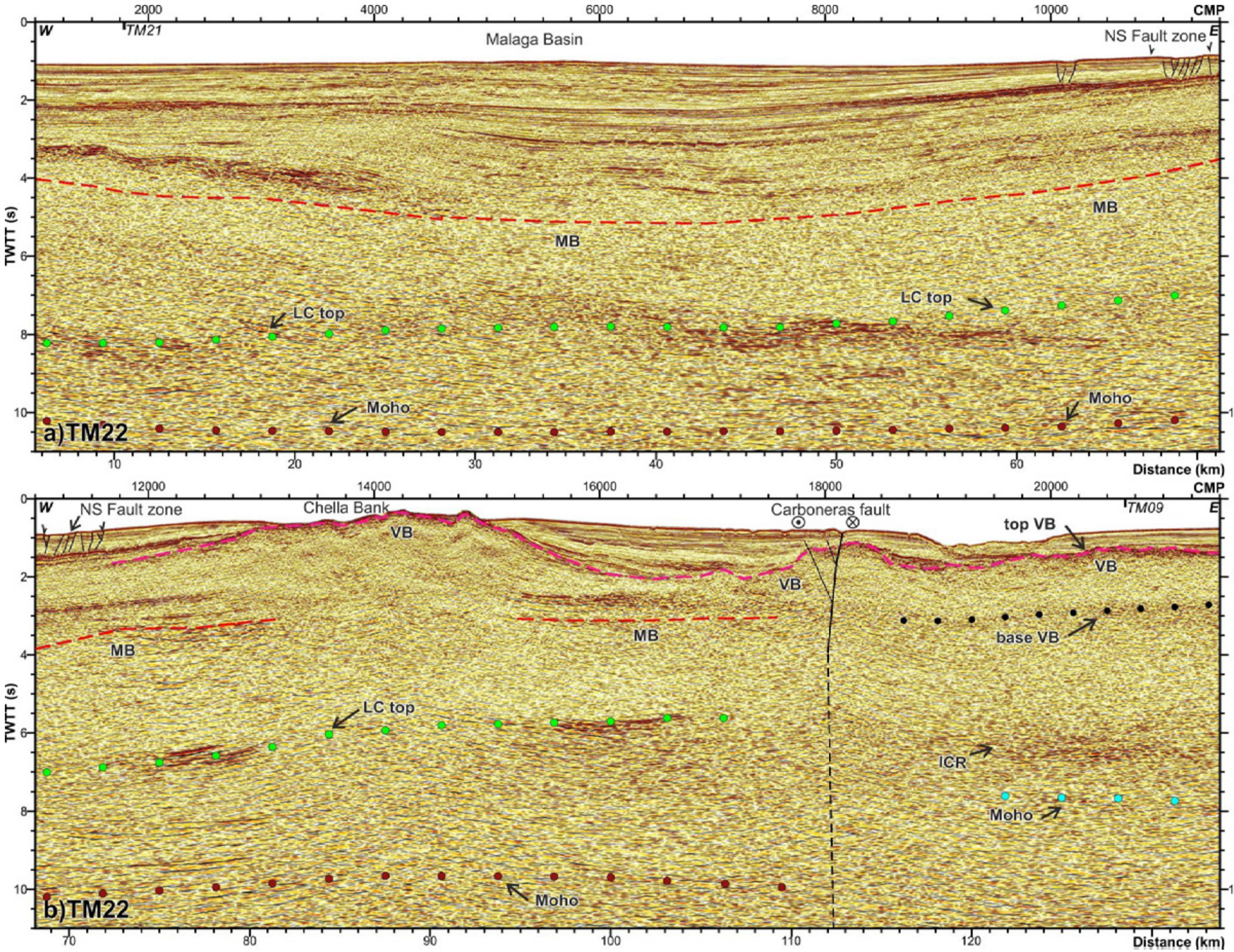
a)TM22
CMP
2000
4000
6000
8000
10000
W
E
TM21
Malaga Basin
NS Fault zone
MB
MB
LC top
LC top
Moho
Moho
TWTT (s)
0
2
4
6
8
10
Distance (km)
10
20
30
40
50
60
b)TM22
12000
14000
16000
18000
20000
NS Fault zone
Chella Bank
Carboneras fault
TM09
top VB
VB
VB
VB
MB
MB
base VB
LC top
ICR
Moho
Moho
70
80
90
100
110
120

Magmatic crust transitions towards the east, to thinner oceanic crust located in the Algero-Balearic Basin (Fig. 5.14) (Booth-Rea et al., 2007; Mauffret, 2007; Billi et al., 2011; Grevemeyer et al., 2011; Leprêtre et al., 2013; Bouyahiaoui et al., 2015). In the seismic profiles, this oceanic crust is characterized by a high-reflectivity layered lower crust ~1 s TWTT thick, with continuous high-amplitude reflections, and a low-reflectivity thin upper crust <1 s TWTT thick (Fig. 5.14a CMP 24000-18000), with a basement thickness of ~3 s TWTT.

On the mirror imaging depth migrated section, the top of a high amplitude layer can be identified ~5-6 km depth. On the basis of previous interpretations, which defined the magmatic arc thickness between ~9-15 km thick and the oceanic crust thickness between 6-10 km (Booth-Rea et al., 2007), we related this reflections to the lower crust top (Fig. 5.14b).

5.2.3. North African continental crust

Five profiles are shown that characterize the North African crust: profiles TM15 (Fig. 5.15) and TM16 (Fig. 5.16), running parallel to the margin, and the southern parts of profiles TM09 (Fig. 5.9b), TM11 (5.10) and TM13 (5.11), perpendicular to it. Additionally, profiles TM09, TM11 and TM13 runs across the Yusuf Fault (Fig. 5.9b CMP 11000-12000, Fig. 5.10 CMP 7000-9000, Fig. 5.11 CMP 7000-8000), the crustal-scale boundary between the fully magmatic arc crust and the North African continental crust.

The basement flooring the Habibas (HBB) and Pytheas (PB) basins (Fig. 5.1) has been drilled and described as metamorphic rocks dated from Late Triassic – Early Jurassic (HBB-1 well, Medaouri et al., 2014). This basement top is defined by two units, as the lower unit shows a discontinuous character (Fig. 5.9b CMP 11000-15000, Fig. 5.10 CMP 2000-8000, Fig. 5.11 CMP 2000-6000, Fig. 5.15). These units define syncline geometry between ~1 and ~4s TWTT depth, and are of Early Tortonian – Pre Tortonian age (>~7.2 Ma) (see "Chapter 6: Basin evolution" for details).

In the upper part of the crust there is a low-reflectivity zone, followed by a deeper high-reflectivity area (e.g. Fig. 5.15). The top of this high-reflectivity layer (HR) has been depicted with pink dots in Figures 5.9b and 5.15. Below it, the ICRs are frequent, and although they present a scattered aspect in profiles perpendicular to the margin (i.e. profile TM09, Fig. 5.9b), there are highly continuous reflections in the profiles parallel to the margin (profiles TM15 and TM16, Fig. 5.15b and Fig 5.16 CMP 5000-2000). A well-defined boundary between upper and lower crust is not observed. The Moho is interpreted as delineated by the lower reflections of a high reflectivity zone (e.g. Fig. 5.15b). Under the HBB and PB the Moho is located at ~10 s TWTT depth (Fig. 5.9b, 5.15), resulting in a basement thickness of <7 s TWTT.

Moving towards the west, towards the South Alboran Basin (SAB) (Fig. 5.1), the North African basement is affected by magmatic activity. Here, the basement of the sedimentary basin is covered by a volcanic layer visible in the seismic images. This volcanic rocks has been sampled in the northern uplifted flank of the Alboran ridge, and are date as Late Serravallian - Tortonian (Hoernle et al., 1999; Duggen et al., 2004; Duggen et al., 2005; Duggen et al., 2008; Lustrino et al., 2011). Under the SAB, both, the basement top and the Moho gradually shoal (Fig. 5.16). The top of the volcanic basement is found at ~1-3.5 s TWTT depth, and the Moho ranges from ~10 s TWTT to ~8 s TWTT, depicting a basement thickness < 5 s TWTT under the SAB (Fig. 5.16).

Figure 5.8a, b►: *Time migration of profile TM28 (see location in Figure 5.2). This profile is divided in a) Western section, b) central section and c) Eastern section. Crustal structure is displayed. Top of the volcanic basement is displayed with pink dash lines, base of the volcanic basement is displayed with black dots, lower crust top is displayed with green dots, and the magmatic arc Moho is displayed with blue dots. VB: volcanic basement. LC: Lower Crust. Main structures are identified. Vertical exaggeration is of ~x:1 taking into account basement velocities (>3500 m/s).*

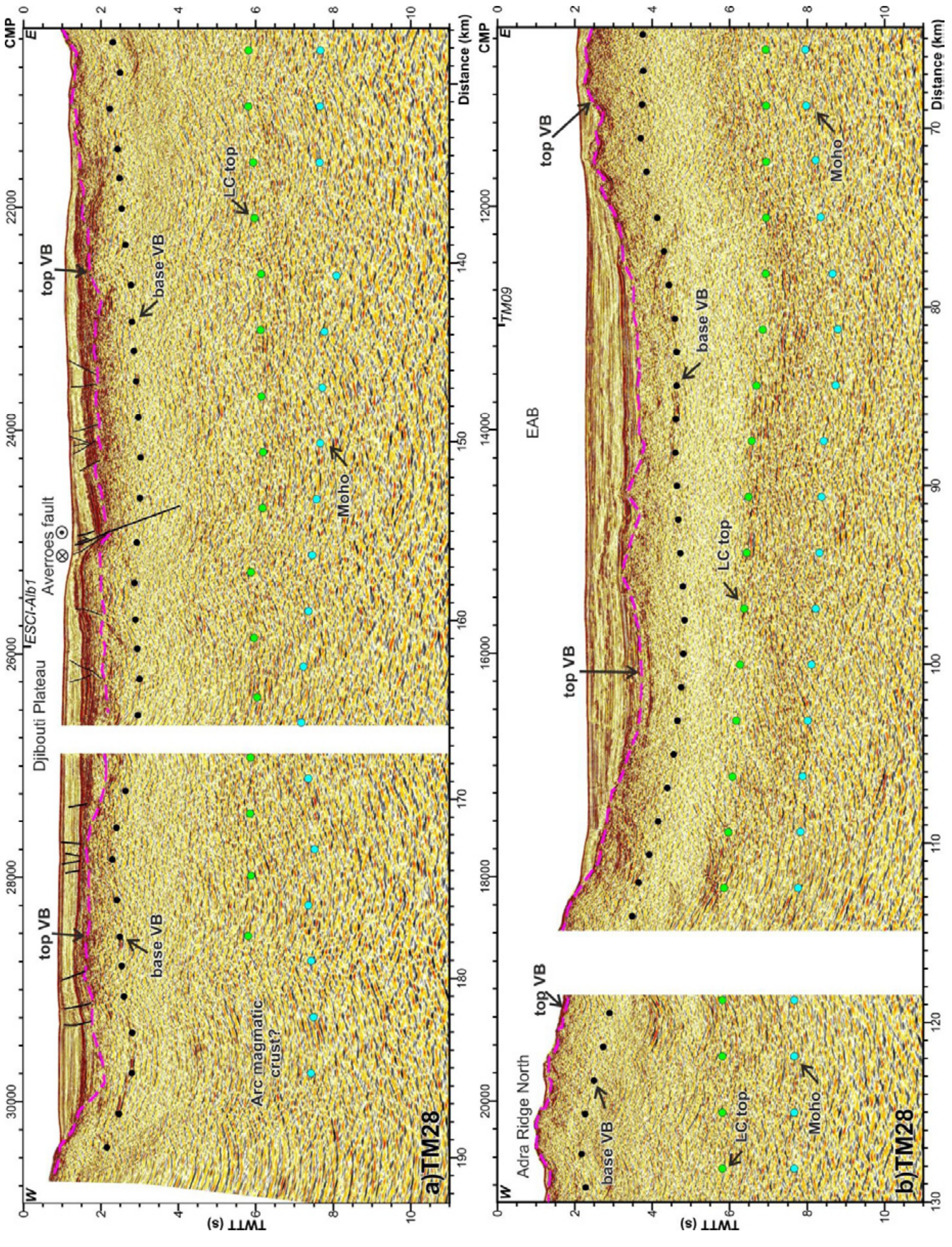
a)TM28
W
E
CMP
TWTT (s)
Distance (km)
0
2
4
6
8
10
22000
24000
26000
28000
30000
140
150
160
170
180
190
top VB
base VB
LC top
Moho
Averroes fault
Djibouti Plateau
ESCI-Alb1
Arc magmatic crust?
b)TM28
12000
14000
16000
18000
20000
70
80
90
100
110
120
130
EAB
TM09
Adra Ridge North

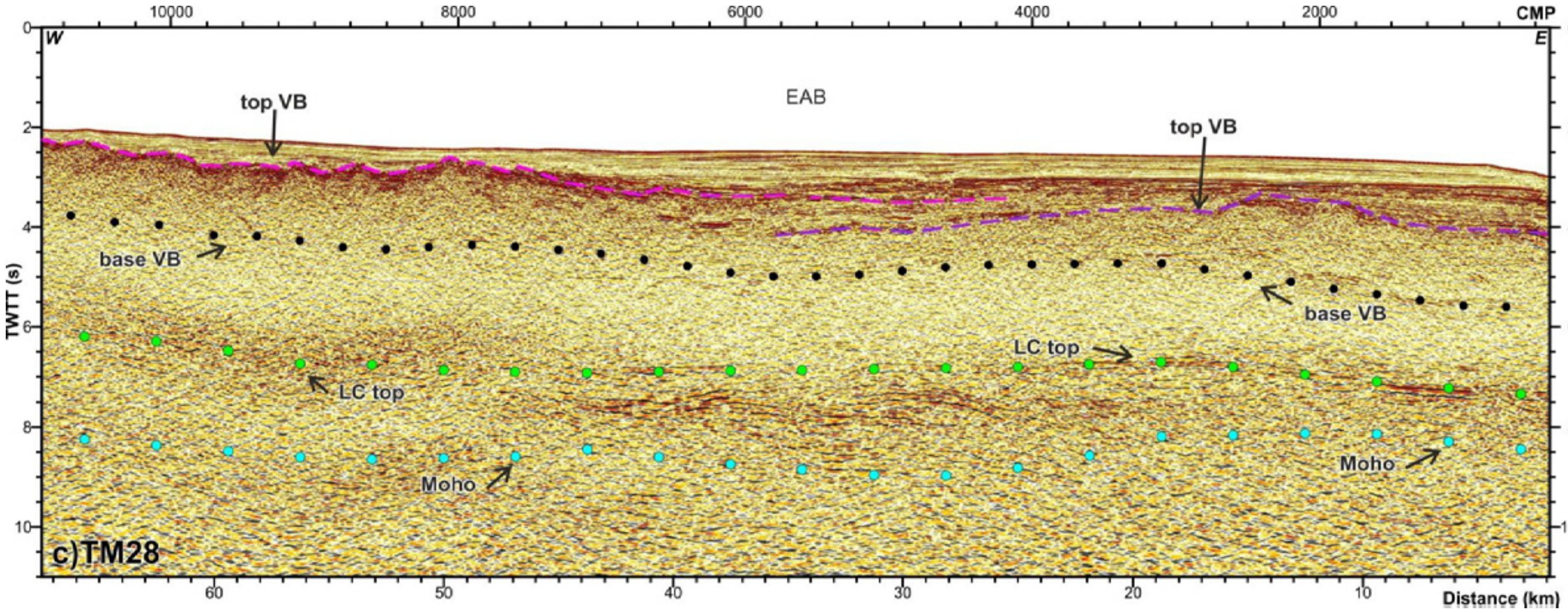

Figure 5.8c▲: *Time migration of profile TM28 (see location in Figure 5.2). This profile is divided in a) Western section, b) central section and c) Eastern section. Crustal structure is displayed. Top of the volcanic basement is displayed with pink dash lines, base of the volcanic basement is displayed with black dots, lower crust top is displayed with green dots, and the magmatic arc Moho is displayed with blue dots. VB: volcanic basement. LC: Lower Crust. Main structures are identified. Vertical exaggeration is of ~x:1 taking into account basement velocities (>3500 m/s).*

Figure 5.9 ▼: *Time migration of profile TM09 (see location in Figure 5.2). This profile is divided in a) Northern section and b) Southern section. Crustal structure is displayed. Top of the volcanic basement is displayed with pink dash lines, base of the volcanic basement is displayed with black dots, lower crust top is displayed with green dots, and the magmatic arc Moho is displayed with blue dots. At the southern section, top of the metamorphic basement is displayed with green and grey dash lines, the top of a high reflectivity body at the upper crust is displayed with magenta dots and the North African continental Moho is displayed with purple dots. Mt.B: metamorphic basement, VB: volcanic basement. ICR: Intra Crustal Reflection. LC: Lower Crust, HR: High reflectivity. Main structures are identified. Vertical exaggeration is of ~x:1 taking into account basement velocities (>3500 m/s).*

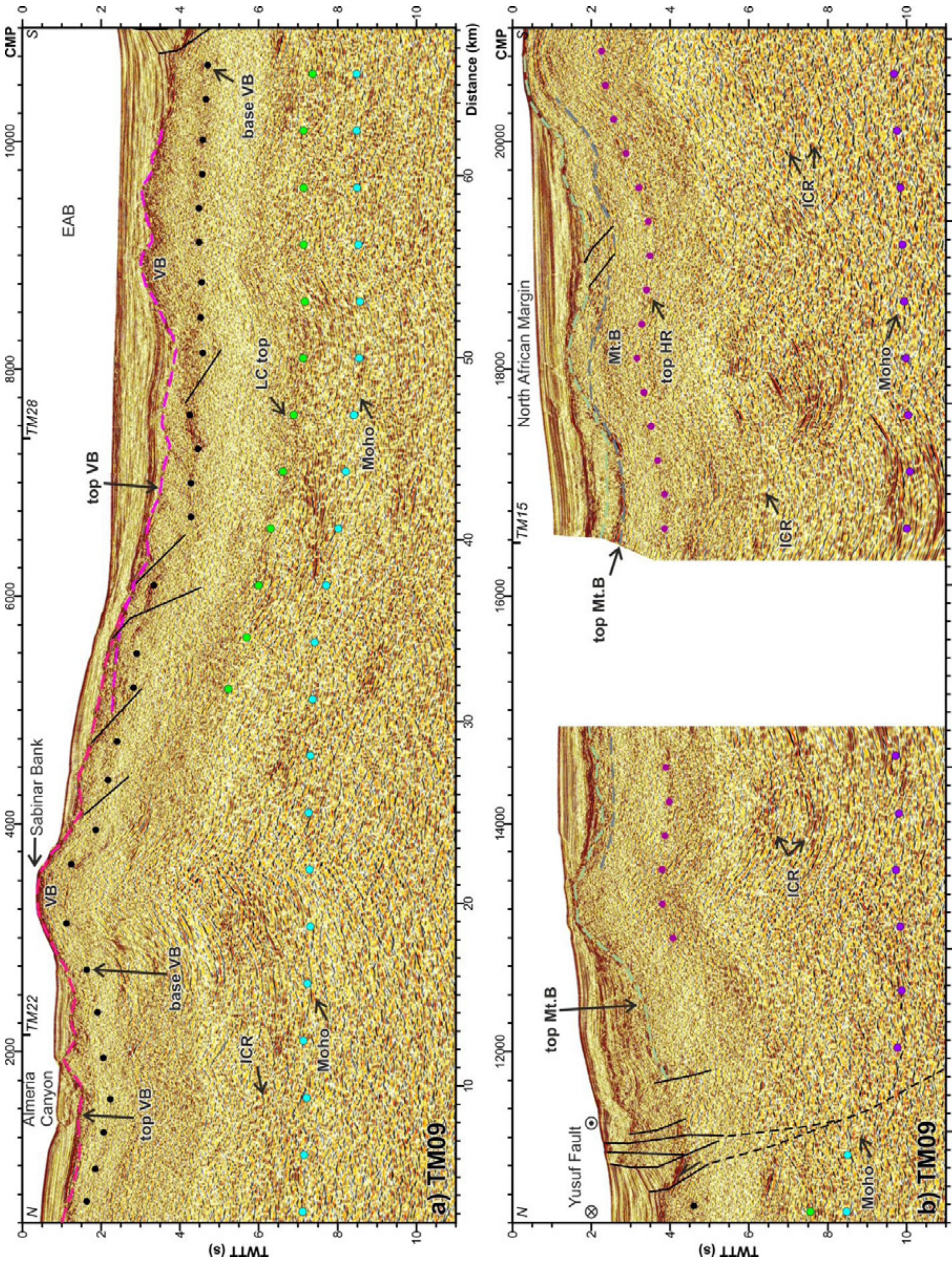
a) TM09
N
S
CMP
2000
4000
6000
8000
10000
Distance (km)
10
20
30
40
50
60
TWTT (s)
0
2
4
6
8
10
Almeria Canyon
Sabinar Bank
EAB
TM22
TM28
VB
top VB
base VB
ICR
Moho
LC top
b) TM09
N
S
CMP
12000
14000
16000
18000
20000
Distance (km)
70
80
90
100
110
120
TWTT (s)
Yusuf Fault
top Mt.B
Mt.B
top HR
ICR
Moho
TM15
North African Margin

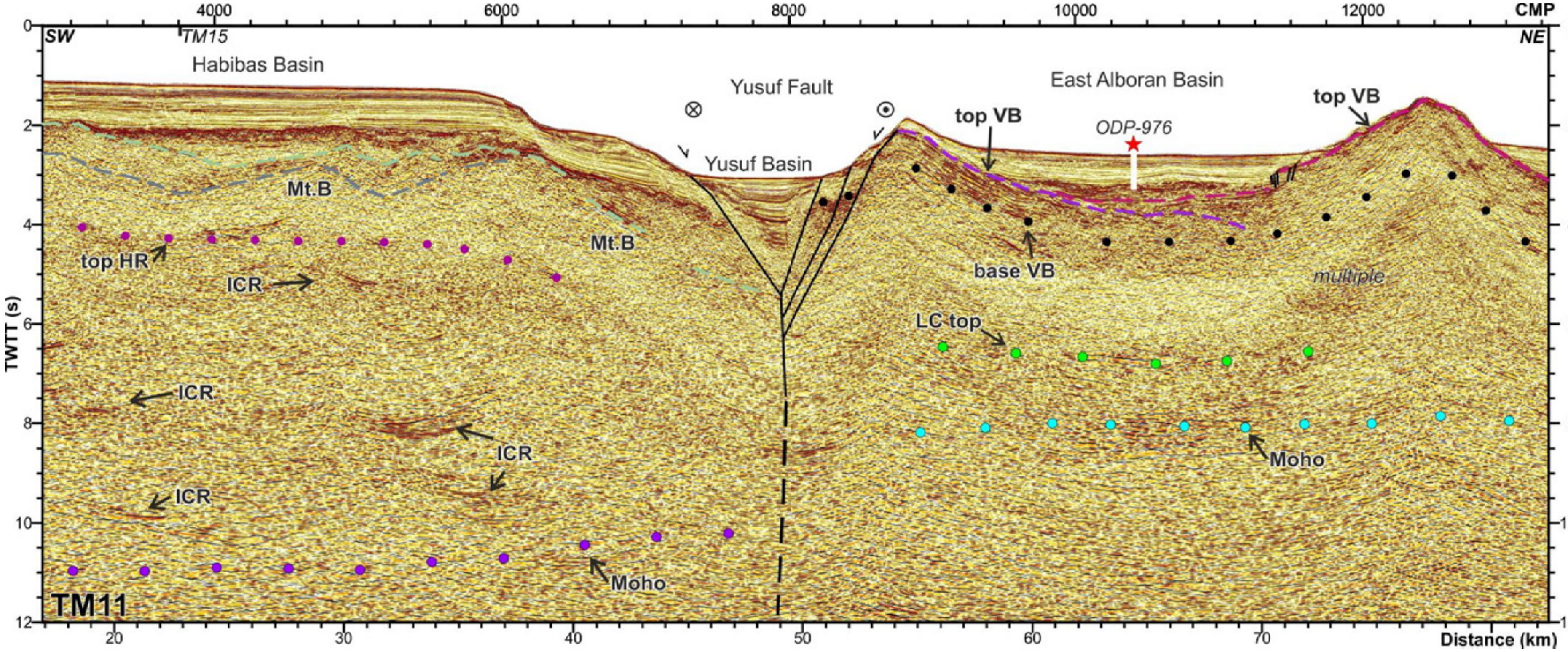

Figure 5.10: *Time migration of profile TM11 (see location in Figure 5.2). Crustal structure is displayed. Top of the volcanic basement is displayed with pink dash lines, base of the volcanic basement is displayed with black dots, lower crust top is displayed with green dots, and the magmatic arc Moho is displayed with blue dots. At the southern section, top of the metamorphic basement is displayed with green and grey dash lines, the top of a high reflectivity body at the upper crust is displayed with magenta dots and the North African continental Moho is displayed with purple dots. Mt.B: metamorphic basement, VB: volcanic basement. ICR: Intra Crustal Reflection. LC: Lower Crust, HR: High reflectivity. Main structures are identified. Vertical exaggeration is of ~x:1 taking into account basement velocities (>3500 m/s).*

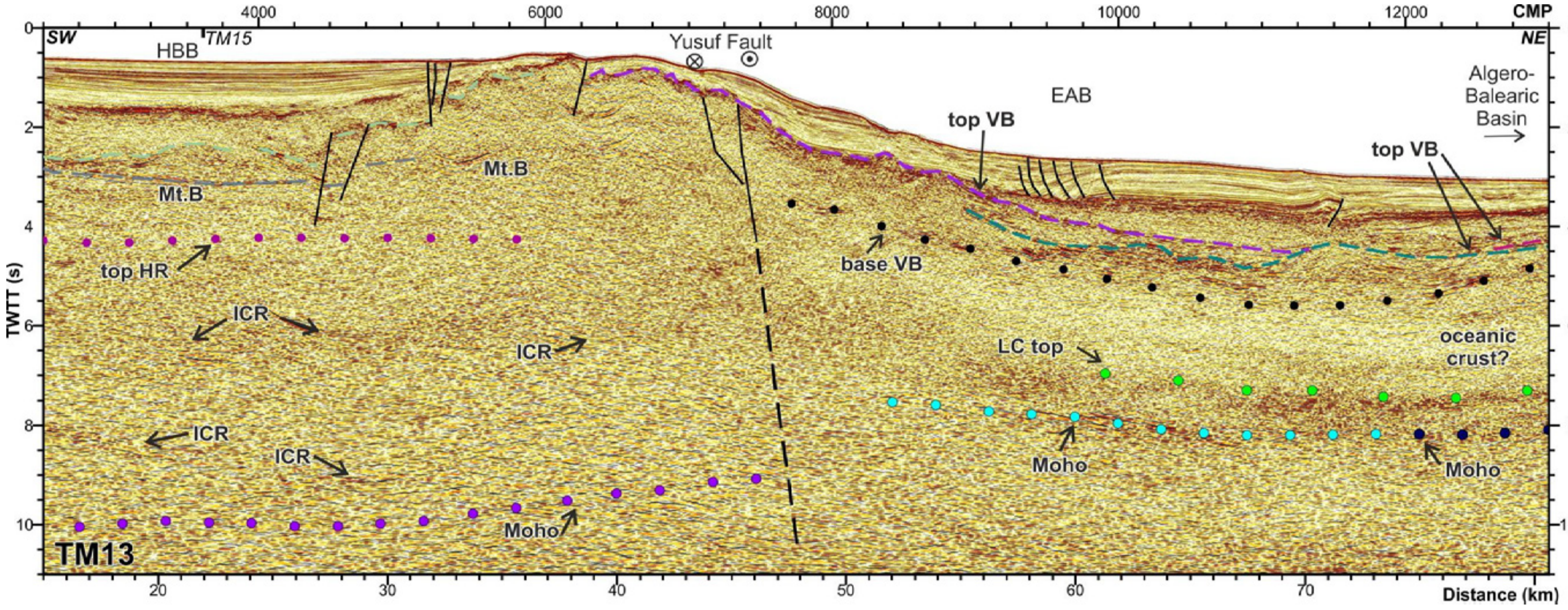

Figure 5.11: *Time migration of profile TM13 (see location in Figure 5.2). Crustal structure is displayed. Top of the volcanic basement is displayed with pink dash lines, base of the volcanic basement is displayed with black dots, lower crust top is displayed with green dots, and the magmatic arc Moho is displayed with blue dots. At the southern section, top of the metamorphic basement is displayed with green and grey dash lines, the top of a high reflectivity body at the upper crust is displayed with magenta dots and the North African continental Moho is displayed with purple dots. Mt.B: metamorphic basement, VB: volcanic basement. ICR: Intra Crustal Reflection. LC: Lower Crust, HR: High reflectivity. Main structures are identified. Vertical exaggeration is of ~x:1 taking into account basement velocities (>3500 m/s).*

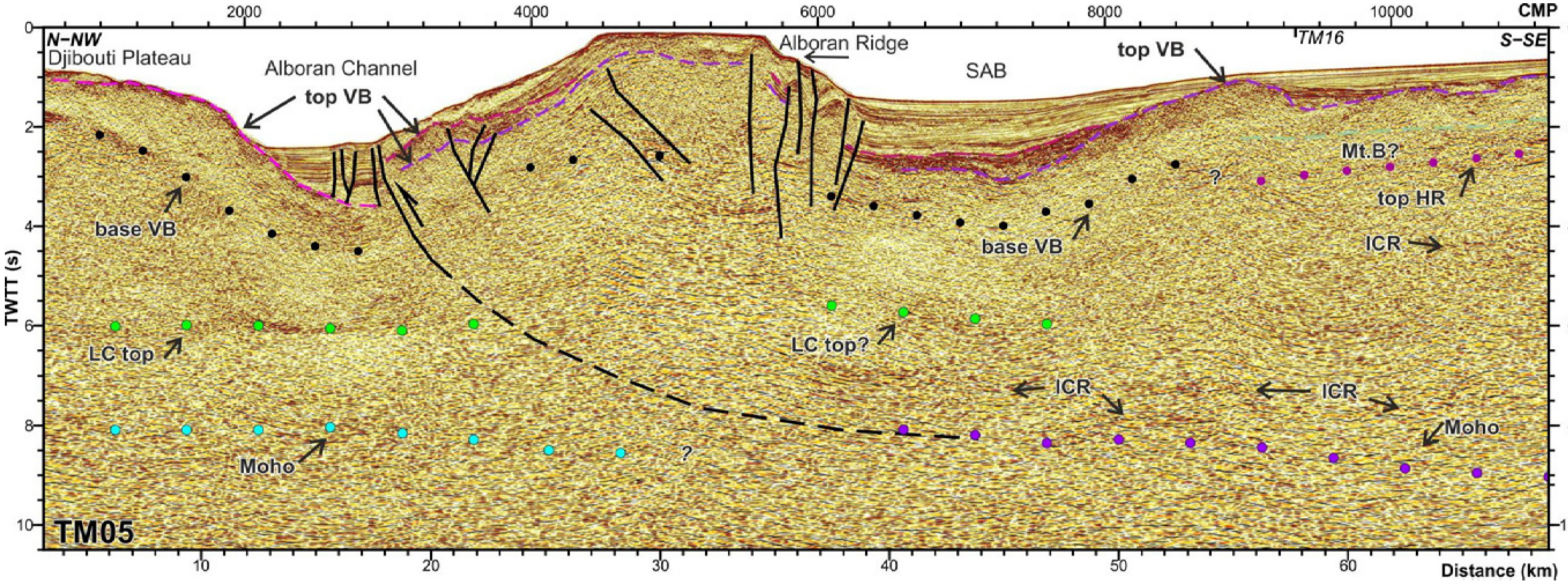

Figure 5.12: *Time migration of profile TM05 (see location in Figure 5.2). Crustal structure is displayed. Top of the volcanic basement is displayed with pink dash lines, base of the volcanic basement is displayed with black dots, lower crust top is displayed with green dots, and the magmatic arc Moho is displayed with blue dots. At the southern section, top of the metamorphic basement is displayed with a green dash line, the top of a high reflectivity body at the upper crust is displayed with magenta dots and the North African continental Moho is displayed with purple dots. Mt.B: metamorphic basement, VB: volcanic basement. ICR: Intra Crustal Reflection. LC: Lower Crust, HR: High reflectivity. Main structures are identified. Vertical exaggeration is of ~x:1 taking into account basement velocities (>3500 m/s).*

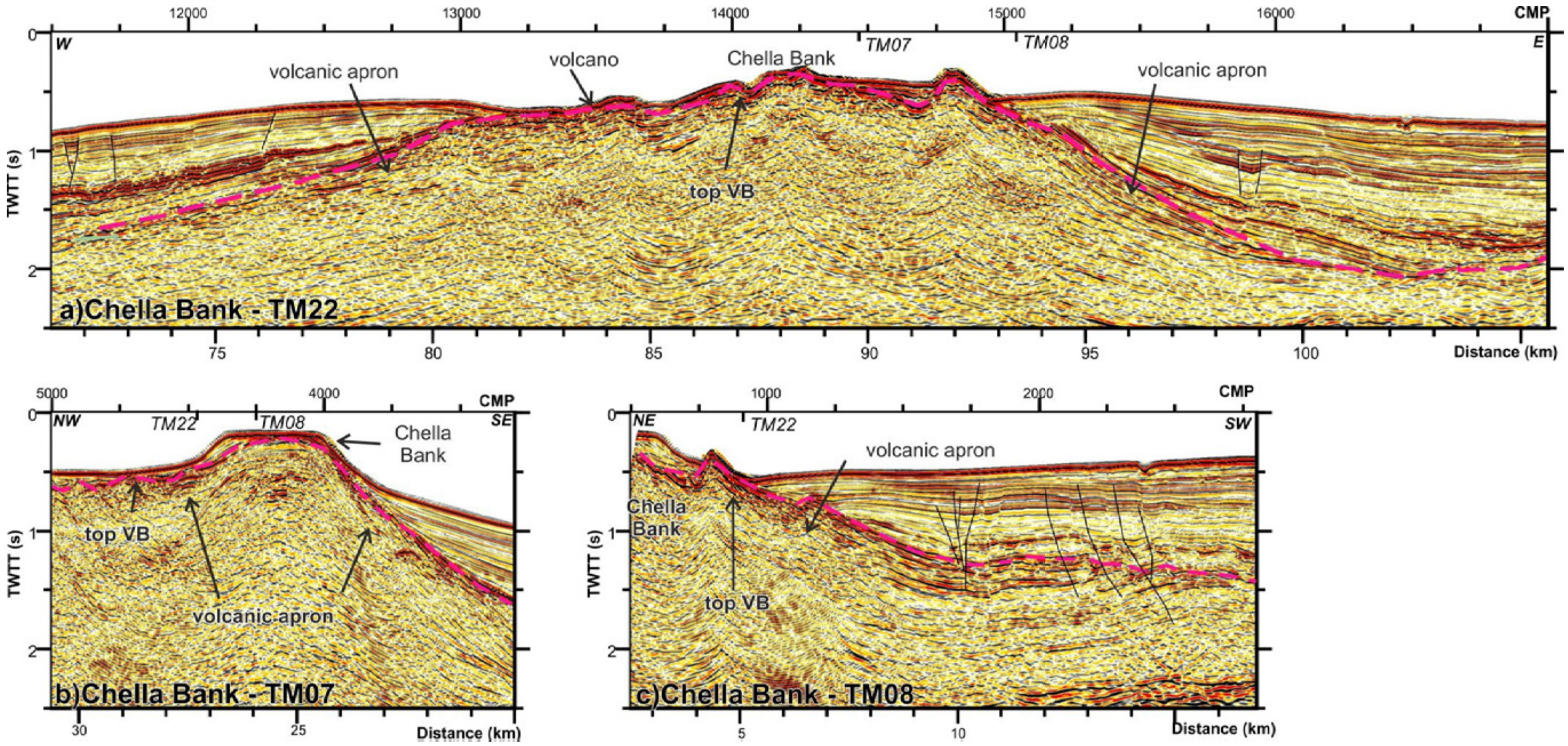

Figure 5.13: *Detail of the volcanic edifices.* ***(a, b and c)*** *Cross-sections of the Chella Bank. Three radial transects are performed, and the three of them shows the same characteristics: and irregular basement top and aprons towards the high flanks. VB: volcanic basement. Vertical exaggeration is of ~x:1.8 taking into account a 3000 m/s velocity.*

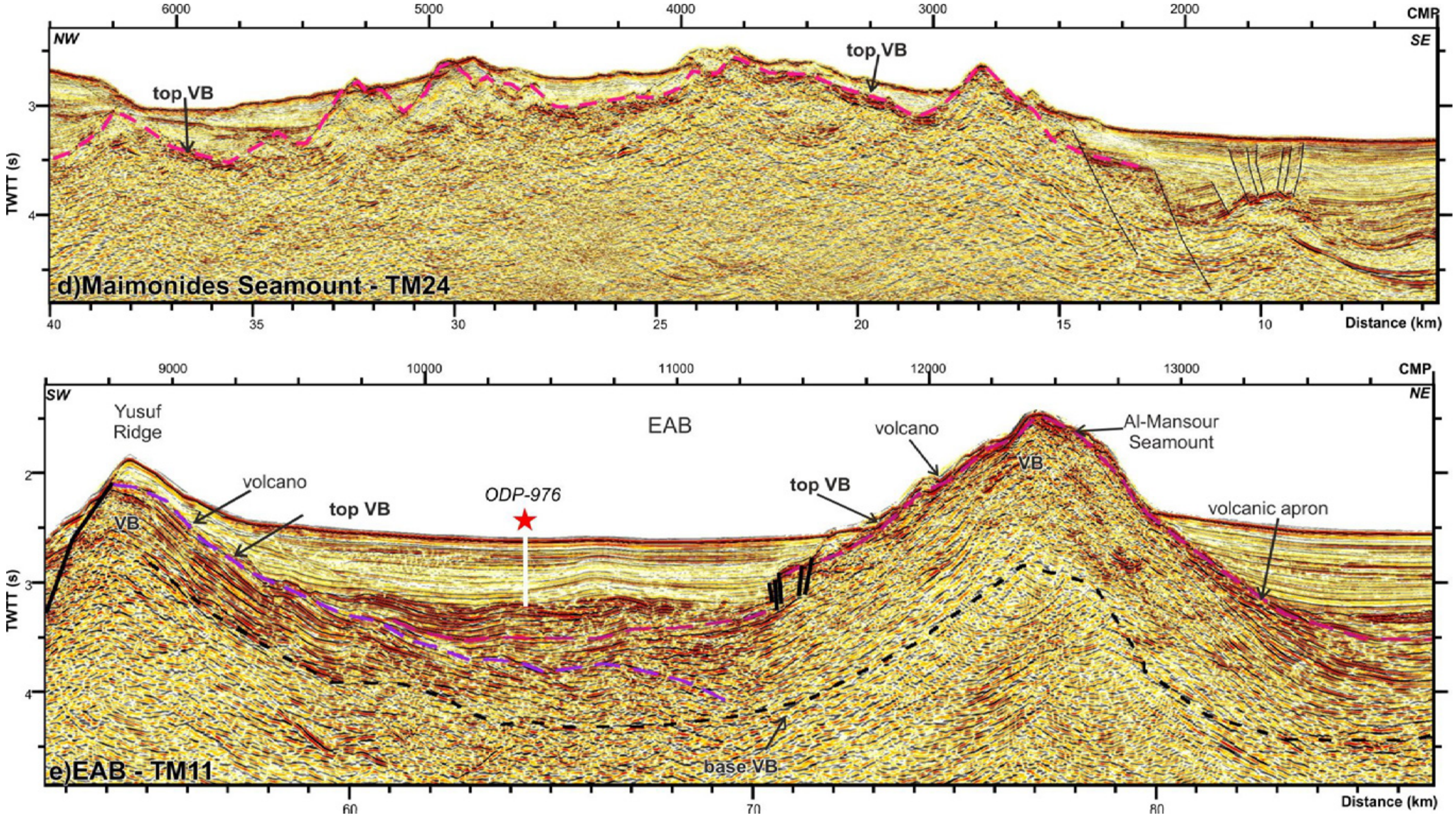

Figure 5.13 (continuation): *Detail of the volcanic edifices.* ***(d)*** *Detailed image of the Maimonides High. An irregular basement top forming conical highs is imaged. VB: volcanic basement.* ***(e)*** *Detail images of the Yusuf Ridge and Al-Mansour volcanic outcrops. Internal wavy reflections developing apron shapes towards the highs flanks are imaged. VB: volcanic basement. Vertical exaggeration is of ~x:1.8 taking into account a 3000 m/s velocity.*

Figure 5.14a: *Time migration of profile TM27 (see location in Figure 5.2). Crustal structure is displayed. Top of the volcanic basement is displayed with a pink dash line, base of the volcanic basement is displayed with black dots, lower crust top is displayed with green dots, the magmatic arc Moho is displayed with light blue dots and the oceanic Moho is displayed with dark blue dots. Mt.B: metamorphic basement, VB: volcanic basement. ICR: Intra Crustal Reflection. LC: Lower Crust, HR: High reflectivity. Main structures are identified. Vertical exaggeration is of ~x:1 taking into account basement velocities (>3500 m/s).*

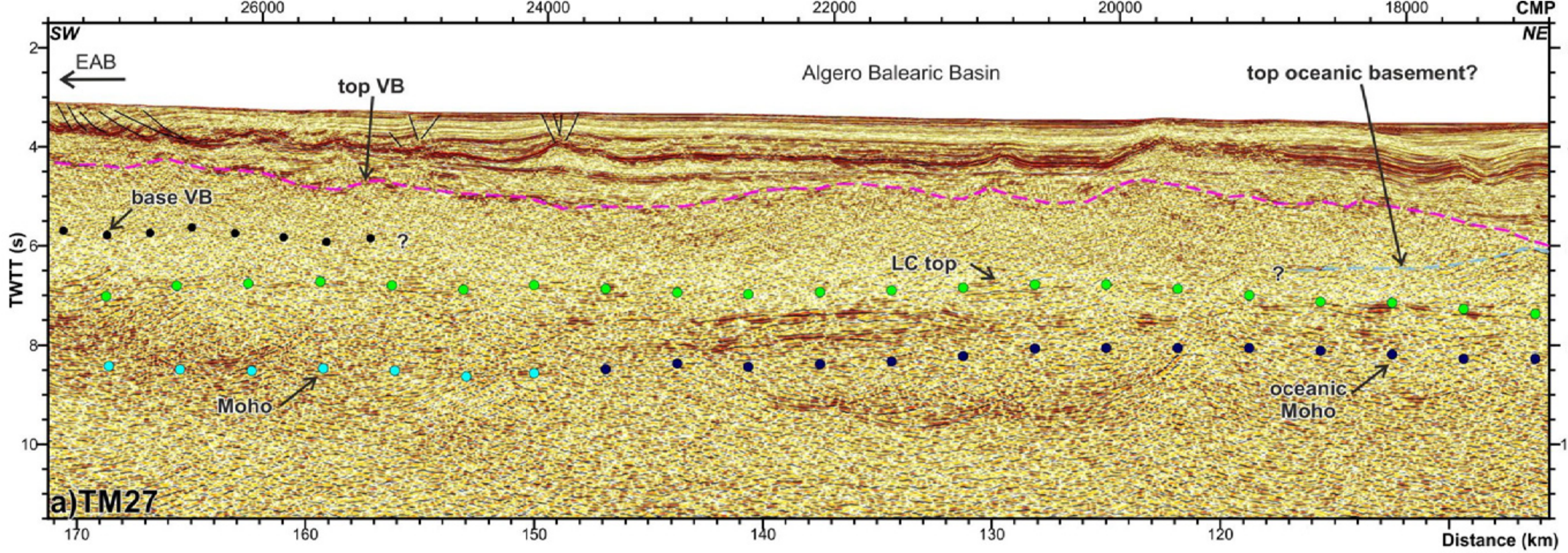

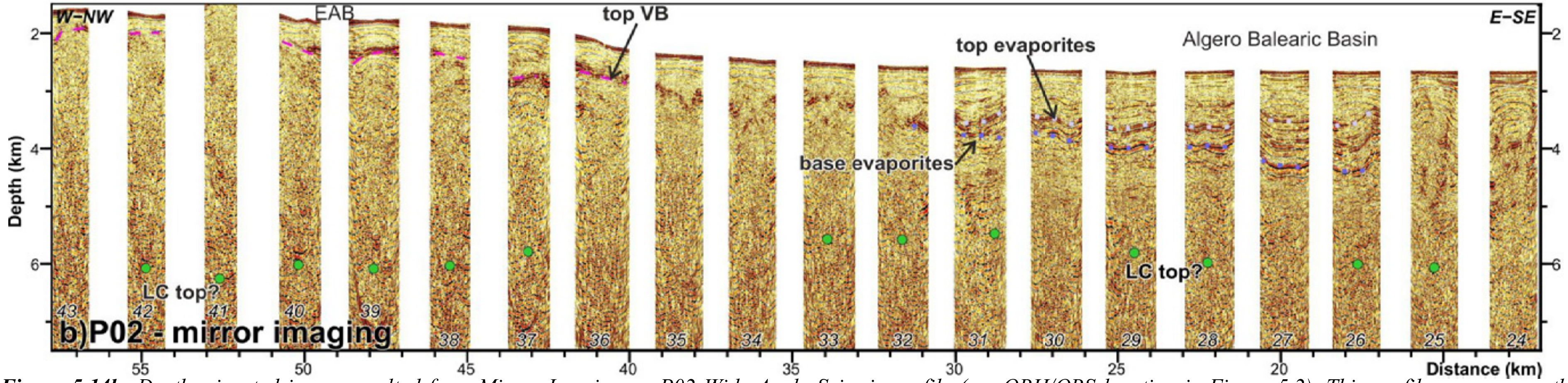

Figure 5.14b: *Depth migrated image resulted from Mirror Imaging on P02 Wide Angle Seismic profile (see OBH/OBS location in Figure 5.2). This profile runs across the transition between the oceanic crust (eastern section) and the magmatic crust (western section). Top of the volcanic basement, top of the evaporites deposit, base of the evaporites deposit, and the possible Lower Crust top (LC top) are depicted. Numbers correspond to the OBH/OBS station number.*

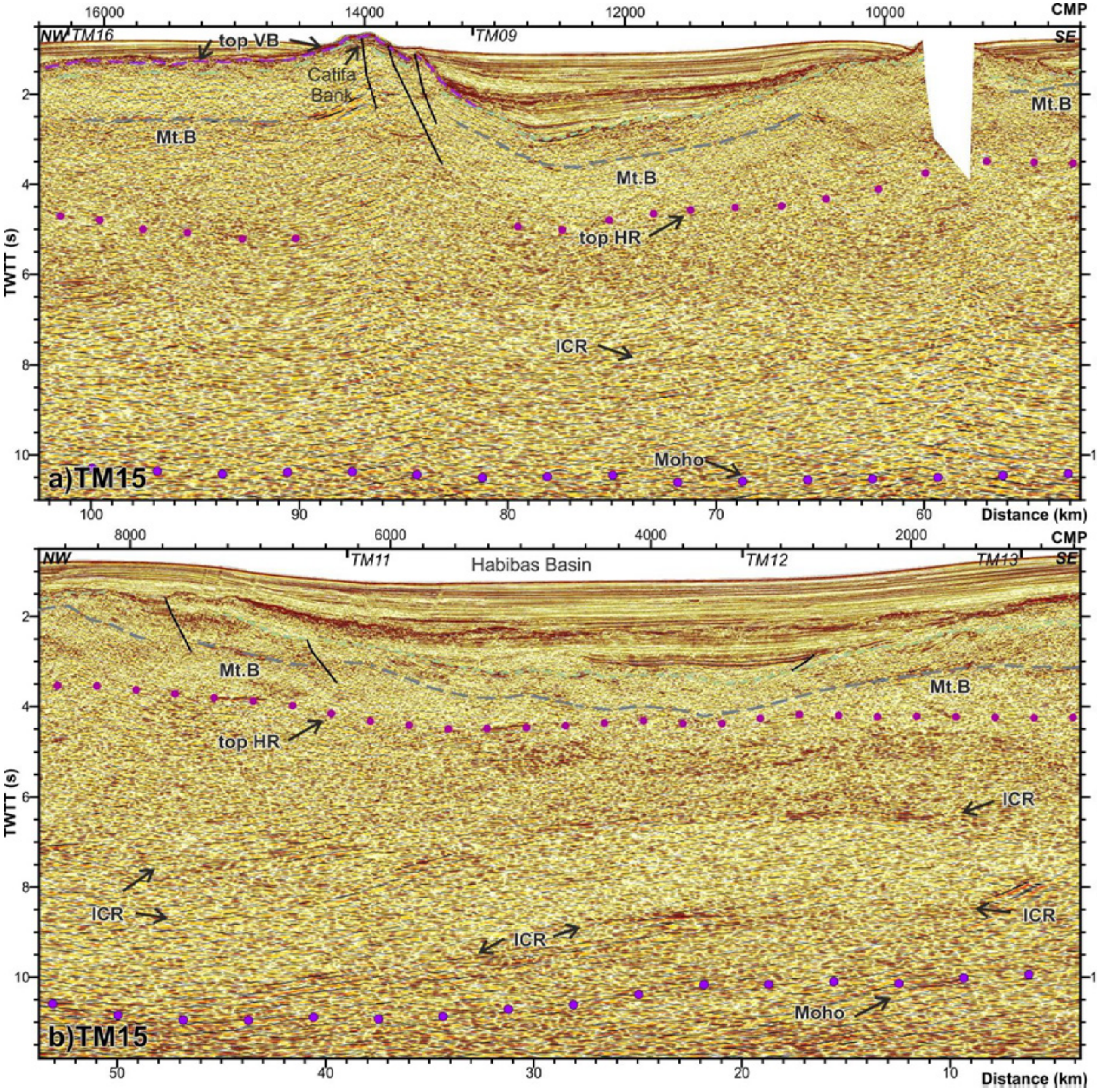

Figure 5.15: *Time migration of profile TM15 (see location in Figure 5.2). This profile is divided in a) Western section, b) central section and c) Eastern section. Crustal structure is displayed. Top of the metamorphic basement is displayed with green and grey dash lines, and top of the volcanic basement with purple dash lines, the top of a high reflectivity body at the upper crust is displayed with magenta dots and the North African continental Moho is displayed with purple dots. Mt.B: metamorphic basement, VB: volcanic basement. ICR: Intra Crustal Reflection, HR: High reflectivity. Main structures are identified. Vertical exaggeration is of ~x:1 taking into account basement velocities (>3500 m/s).*

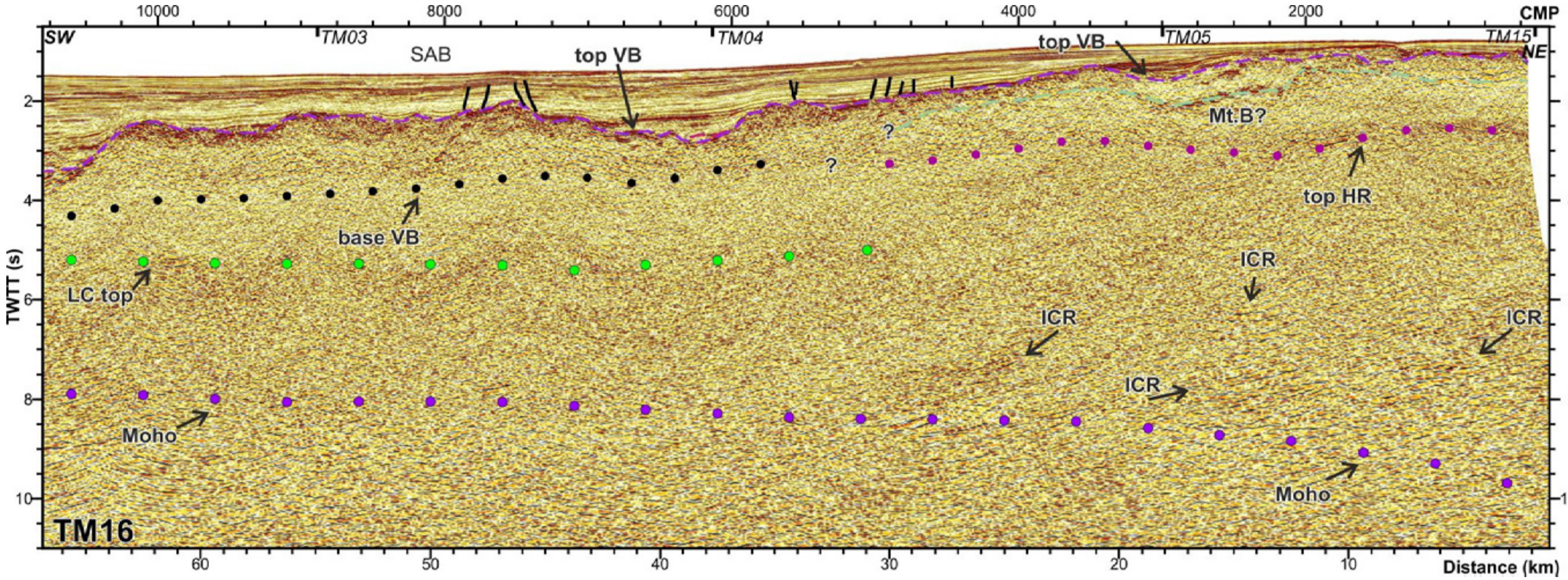

Figure 5.16: *Time migration of profile TM16 (see location in Figure 5.2). Crustal structure is displayed. Top of the volcanic basement is displayed with pink dash lines, base of the volcanic basement is displayed with black dots and lower crust top is displayed with green dots. At the NE section, top of the metamorphic basement is displayed with a green dash line and the top of a high reflectivity body at the upper crust is displayed with magenta dots. The North African continental Moho is displayed with purple dots. Mt.B: metamorphic basement, VB: volcanic basement. ICR: Intra Crustal Reflection, LC: Lower Crust, HR: High reflectivity. Main structures are identified. Vertical exaggeration is of ~x:1 taking into account basement velocities (>3500 m/s).*

5.3. Discussion

5.3.1. Crustal domains

Our data reveal the existence of three types of crustal domains, based on their thickness, seismic expression and nature of the basement. These domains are: (i) Thin continental crust under the West Alboran Basin (WAB) and Malaga Basin (MB), (ii) Magmatic arc crust under Djibouti Plateau, NE Alboran Basin and East Alboran Basin (EAB), and (iii) Continental crust under the North African margin (Fig. 5.17, 5.18). The two domains of continental crust show clear indications of intrusions and modifications by magmatism in the areas next to the magmatic-arc type basement.

- *Thin continental crust under West Alboran and Malaga basins*

At the West Alboran Basin, the basement is only ~2 s TWTT thick, or some ~6 km thick assuming an average 6 km/s velocity, which is realistic to continental crust (Fig. 5.17a). This area is characterized by a deep sedimentary basin, with up to ~6-7 s TWTT of infill (~7-8 km thick), in which the sediment sequence appears almost without tectonic deformation (see “Chapter 6: Basin evolution” for details). The basement of the WAB is of metamorphic nature where drilled by DSDP and ODP legs and the samples are interpreted to be similar to the outcrops of the Alboran Domain onland (Comas et al., 1992; Tandon et al., 1998; Kelley and Platt, 1999). A recent study based on local earthquake tomography found an arcuate high-velocity anomaly following the orogenic front shape, in the westernmost WAB and along its northern part (El Moudnib et al., 2015). This anomaly clearly coincides with the Ronda peridotites onland, and can be correlated to the Beni Bousera peridotites in the Rif (Berndt et al., 2014; Amar et al., 2015; Barcos et al., 2015; El Moudnib et al., 2015) (Fig. 5.18).

On the basis of El Moudnib et al. (2015) observations, we hypothesized that the extension occurred in this area greatly thinned the continental basement and may be related to the process of mantle exhumation of the Peridotite Massifs at ~22 Ma (Frasca et al., 2016). This age is coherent with a thinning of the basement prior of the basin formation, as the sediment record, starting at Burdigalian, does not show evidence of extension.

Towards the NE, this continental crust thickens (Fig. 5.4) towards under the MB. The sedimentary basin and the nature of the basement are similar to the WAB, although the MB basement configuration slightly differs. In the South Iberian margin under the MB, the basement is 5-6 s TWTT thick (about 15-18 km), and covered by up to ~4 s TWTT of sediment (about 4-5 km thick) (Fig. 5.17b). Few volcanic constructions are found at this area (Fig. 5.4b CMP 18000-21000, Fig. 5.7b CMP 11000-17000), so that the basement of the MB is mainly metamorphic. In sum, we interpreted this basement as the same continental crust as in the WAB, although less modified by extensional processes, and partially affected by volcanic activity.

Figure 5.17 **►*:*** *Cartoons of the crustal domains identified in the Alboran Basin.* ***(a)*** *Thin continental crust in the WAB (same location as Figure 5.4a, see Figure 5.2),* ***(b)*** *Thin continental crust in the MB (same location as Figure 5.7a, see Figure 5.2),* ***(c)*** *Magmatic arc crust (same location as Figure 5.8c, see Figure 5.2) and* ***(d)*** *North African margin continental crust (same location as Figure 5.15b, see Figure 5.2). Colour code is the same that for the interpreted seismic sections: red dash line for the top of the metamorphic basement, pink and purple dash lines for the top of the volcanic units, black dots for the volcanic base, magenta dots for the high reflectivity body top, green dots for the lower crust top, brown dots for the Moho in the thin continental crust, blue dots for the Moho in the magmatic arc crust and purple dots for the Moho in the continental North African crust. Mt.B: metamorphic basement, VB: volcanic basement. ICR: Intra Crustal Reflection, LC: Lower Crust, HR: High reflectivity.*

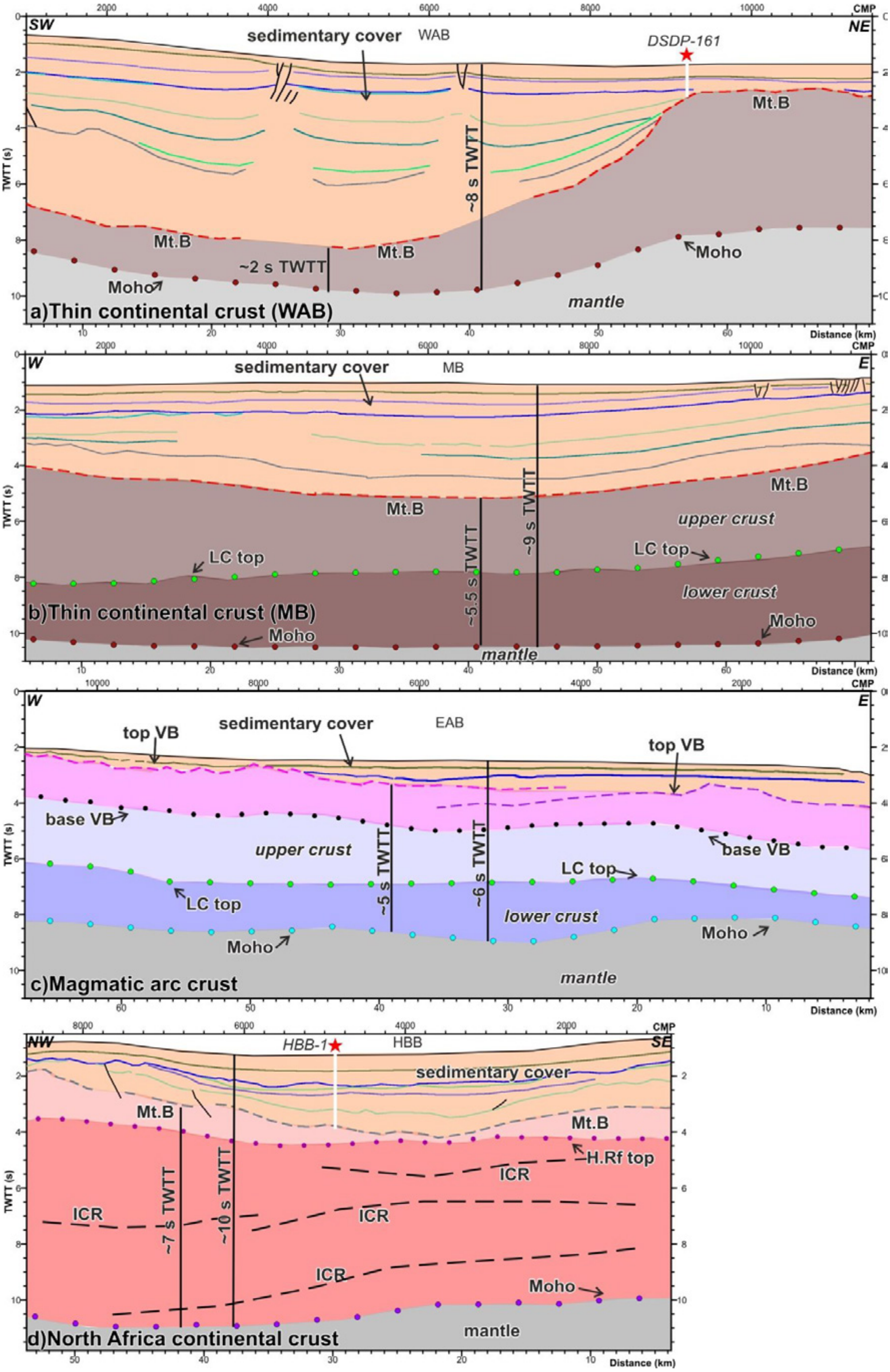
SW
NE
sedimentary cover
WAB
DSDP-161
Mt.B
~8 s TWTT
~2 s TWTT
Moho
mantle
a)Thin continental crust (WAB)
W
E
sedimentary cover
MB
Mt.B
upper crust
LC top
lower crust
~9 s TWTT
~5.5 s TWTT
Moho
mantle
b)Thin continental crust (MB)
W
E
top VB
sedimentary cover
EAB
base VB
upper crust
~5 s TWTT
~6 s TWTT
LC top
lower crust
Moho
mantle
c)Magmatic arc crust
NW
SE
HBB-1
HBB
sedimentary cover
Mt.B
H.Rf top
ICR
~7 s TWTT
~10 s TWTT
Moho
mantle
d)North Africa continental crust
TWTT (s)
CMP
Distance (km)

- *Magmatic arc type crust in the East Alboran Basin*

The central and NE parts of the Eastern Alboran Basin are floored by a magmatic basement (Booth-Rea et al., 2007) sampled at several outcropping basement highs (Duggen et al., 2004; Duggen et al., 2005; Duggen et al., 2008). Basement thickness is variable, but may reach ~5 s TWTT or ~15km (Fig. 5.17c). These parts of the basin are floored by enriched Light Rare Earth Elements (LREE) volcanic units from Late Serravallian? – Tortonian times (Duggen et al., 2004; Duggen et al., 2005; Duggen et al., 2008). Its geochemical composition is indicative of subduction-related fluids. The high reflectivity layered reflections found in the lower crust (Fig. 5.8) have been associated to magmatic layering (Booth-Rea et al., 2007; Medaouri et al., 2014).

The mean ratio between intrusive and extrusive rocks is 5:1, being aware of the variability of this values depending of the composition and the particular setting (White et al., 2006). Subsequently, the presence of important volumes of extrusive rocks (i.e. Fig. 5.2, Fig. 5.3b CMP 10000-4000, Ibn-Batouta Bank; Fig. 5.4b CMP 17000-21000, Algarrobo Bank; Fig. 5.9a CMP 2500-60000, El Sabinar Bank; Fig. 5.13a-c, Chella Bank; Fig. 5.13d, Maimonides Seamount, Fig. 5.13e, Yusuf Ridge and Al-Mansour Seamount, Fig. 5.15 CMP15000-13000 Catifa Bank) implies the existence of abundant intrusive rocks feeding the system. In the magmatic arc crust located in oceanic plates, the lower crust has been proposed to be the result of subduction-related magmatism that forms cumulates on their lower parts, altering the original oceanic nature of the crust (Kay and Kay, 1985). This supports the hypothesis relating layered lower crust with magmatic layering (Booth-Rea et al., 2007; Medaouri et al., 2014) probably produced in situ on large magma chambers.

Magmatic activity affected the Alboran Basin in different degrees, being the central part of the basin the most affected area (Fig. 5.18). Due to the volcanic nature of this area, together with crustal thickness characteristics and the inferred magmatic character of the basement, it support that this zone is part of a magmatic arc system, coherent with previous hypotheses based on seismic (Booth-Rea et al., 2007; Giaconia et al., 2015) and geochemical data (e.g. Dugget et al., 2004). Magmatic arc crust presents a large thickness variability in different locations related to the amount of extension, ranging from 10 to 35 km (Calvert, 2011), and also variability in the velocity structure, which is depending on the type of volcanic lithology (Calvert, 2011). However, magmatic arc crust often presents a similar structure: a) a shallower heterogeneous part, with sediments overlying the igneous basement and volcanic extrusives or volcanoclastics, b) an upper igneous crust usually bounded by two intracrustal reflections, and c) a deeper lower crust usually recognized by a banded aspect (Calvert, 2011). The central Alboran crust fits well with these observations, supporting a magmatic arc crust type interpretation.

***Figure 5.18* ►:** *Crustal domains of the Alboran Sea Basin (same area as Figure 5.1). The identified crustal domains are depicted (see figure legend), together with the previous domains identified at the Gulf of Cadiz (Martínez-Loriente et al., 2014) and on-land the Iberian and African margins (from Mancilla et al., 2015). Interpretation of peridotite outcrops is based on Berndt et al., 2014.*

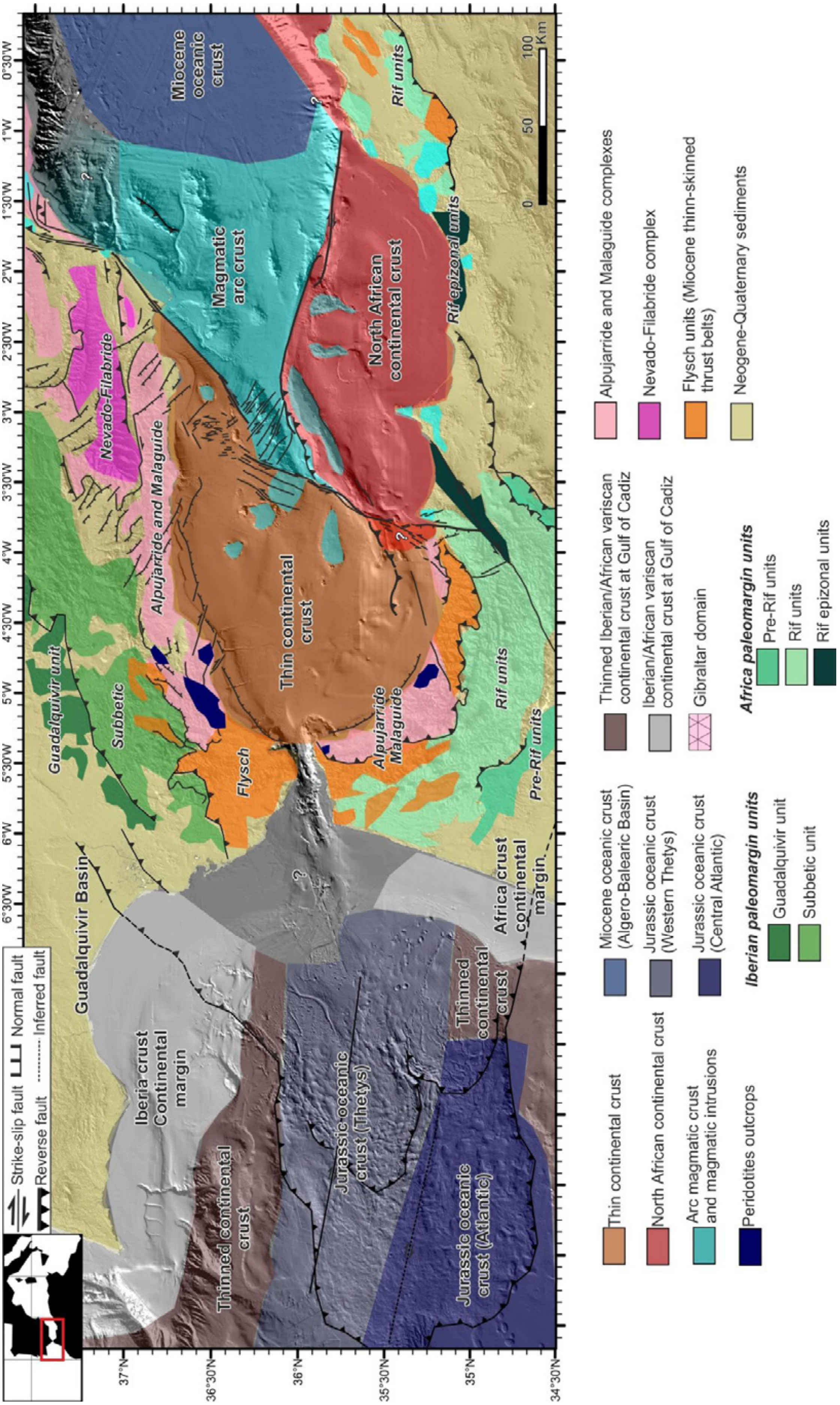
Strike-slip fault
Normal fault
Reverse fault
Inferred fault
0°30'W
1°W
1°30'W
2°W
2°30'W
3°W
3°30'W
4°W
4°30'W
5°W
5°30'W
6°W
6°30'W
37°N
36°30'N
36°N
35°30'N
35°N
34°30'N
0
50
100
Km
Miocene oceanic crust
Magmatic arc crust
North African continental crust
Thin continental crust
Nevado-Filabride
Alpujarride and Malaguide
Alpujarride Malaguide
Flysch
Subbetic
Guadalquivir unit
Guadalquivir Basin
Rif units
Rif epizonal units
Pre-Rif units
Africa crust continental margin
Iberia crust Continental margin
Thinned continental crust
Jurassic oceanic crust (Thetys)
Jurassic oceanic crust (Atlantic)
?
Thin continental crust
North African continental crust
Arc magmatic crust and magmatic intrusions
Peridotites outcrops
Miocene oceanic crust (Algero-Balearic Basin)
Jurassic oceanic crust (Western Thetys)
Jurassic oceanic crust (Central Atlantic)
Iberian paleomargin units
Guadalquivir unit
Subbetic unit
Thinned Iberian/African variscan continental crust at Gulf of Cadiz
Iberian/African variscan continental crust at Gulf of Cadiz
Gibraltar domain
Africa paleomargin units
Pre-Rif units
Rif units
Rif epizonal units
Alpujarride and Malaguide complexes
Nevado-Filabride complex
Flysch units (Miocene thinn-skinned thrust belts)
Neogene-Quaternary sediments

- *Continental crust in the North African margin*

At the southern part of the Alboran Basin occurs deepest Moho of the area, at ~10 s TWTT thick, with a basement thickness of ~7 s TWTT or ~20 km (Fig. 5.17d). The basement was reached in the HBB-1 well (Medaouri et al., 2014) revealing its metamorphic nature. Due to the nature of the basement and crustal thickness, we associated this domain with the continental crust of the North African margin, which may be quite different than the metamorphic basement under the WAB and MB.

Towards the SW, this basement is progressively affected by magmatic activity as indicated by the edifices visible in seismic images and bathymetry maps (Fig. 5.16). This magmatic arc volcanism is the responsible of the formation of the Alboran Ridge basement or of a very strong modification of the pre-existing basement there (Duggen et al., 2004; Duggen et al., 2008). Although it has a volcanic nature, the basement is ~6 s TWTT thick (Fig. 5.16), thicker than in the magmatic arc zones, and possibly of African continental nature even though wide angle data is still lacking.

- *Crustal domains integration*

In order to complete the crustal characterization of the Gibraltar Arc System, we integrated the interpreted crustal domains in the existent crustal maps of the area (Fig. 5.18). Previous to this study, the on-land domain distribution have been extensively discussed (e.g. Sanz De Galdeano, 1990; Alonso-Chaves et al., 2004; Chalouan and Michard, 2004; Balanyá et al., 2007; Platt, 2007). Recent studies constraint the crustal distribution on the Gulf of Cadiz area, in the basis of the wide-angle and multichannel seismic results (Sallares et al., 2011; Martínez-Loriente et al., 2013). However, no extensive previous study has tried to determine the crustal domains of the Alboran Basin.

5.3.2. Transition between domains

We identified two types of boundaries between the petrological domains: (i) structural boundaries and (ii) transitional boundaries (Fig. 5.18).

The thin continental crust of the WAB exhibits a progressively basement thickening towards the MB. We proposed that originally they were part of the same crust, although different degrees of extension in the area resulted in two different basement thicknesses. The stronger extensional processes affecting the WAB basement derived in a thinner continental crust, while it remained thicker below the MB. Sediment depocenters appear related to the amount of thinning.

This thin continental crust is in contact with the magmatic arc crust towards the South and East. Looking at the southern transition between thin continental domain and magmatic arc, we need to differentiate between basement transition zone and crustal boundary. The transition between the WAB metamorphic basement and the areas where volcanic basement is found (e.g. Djibouti Plateau, Alboran Ridge area) is gradual and is not controlled by tectonic features. The metamorphic basement was strongly affected by volcanic activity near this transition, and the magmatic crust was formed by extension and accretion in an arc context (Fig. 5.3, Fig. 5.6). The eastern transition between the WAB thin crust and the Djibouti Plateau magmatic arc crust is also transitional, and it is not defined by a sharp tectonic structure (Fig. 5.5b). However, the southeastern crustal boundary between thin continental crust and the magmatic arc crust appears to occur at the tectonic structure currently active as the Al-Idrissi fault (Fig. 5.6).

At the easternmost part, the thin continental crust of the MB is also in contact towards the east and the southeast with the magmatic arc crust (Fig. 5.18). Although some magmatic constructions occur on the metamorphic basement of the South Iberian continental domain, the boundary between types of crust is clearly marked by the Carboneras Fault (Fig. 5.7b CMP ~18000). This is a major tectonic structure currently active as left-lateral strike-slip fault, which activity began in the Late Miocene (Gràcia et al., 2006; Moreno et al., 2016 and references therein).

The magmatic arc crust is surrounded by the thin continental crust of the WAB and MB to the west and north, by the oceanic crust of the Algero-Balearic Basin to the east, and by the continental crust of the North African margin to the south (Fig. 5.18). The transition to the Algero-Balearic Basin is gradual, with the crust progressively thinning towards the Algero-Balearic margin while magmatic intrusions increased towards the Alboran Basin (Fig. 5.13). In the North African margin continental crust, two types of boundaries can be established: (i) a structural transition in the eastern part through the Yusuf Fault (Figs. 5.9, 5.10, 5.11, 5.18), and (ii) a smooth basement transition and a structural transition between the crusts towards the west, into the Alboran Ridge and SAB area (Figs. 5.6, 5.12, 5.18). The Yusuf Fault is a right-lateral strike-slip fault, which present-day activity begun in post-Messinian times (< 5.3 Ma) (see "Chapter 8: The Yusuf Fault" for details). We propose that this dextral strike-slip fault was created following a pre-existing weak crustal zone. We hypothesize that the Yusuf Fault could be a reactivated Continental-Ocean Transition (COT), in this case, a continent-magmatic arc transition zone. West of the North-African margin (SAB), the situation is similar to the transitions of thin continental crust towards a magmatic arc. While the Alboran Ridge front fault defines a clear tectonic crustal boundary (Fig. 5.6, Fig. 5.12), the volcanic activity interpreted from seismic images affecting the basement is not limited by this tectonic boundary, and it extends across the area affecting large portions or even the entire of the basement shown by thick accumulation of possibly extrusive in the upper part of the basement. Thus, in the S-N transition between the North African continental crust and the magmatic arc crust, the boundary of the thrust front of the Alboran Ridge (Fig. 5.6, 5.12, 5.18) seems to have reactivated some pre-existing limit that had not fully bounded arc activity. This crustal scale fault began its activity possibly right after Messinian times (< 5.33 Ma), when the continental North African margin started to overthrusts above the magmatic arc crust (see "Chapter 9: The Alboran Ridge" for details).

Finally, the contact between the western North African continental crust and the thin continental crust of the WAB (south of the WAB), is not well imaged in the seismic profiles. In the basis of the distribution of the on-land Alpujarride and Malaguide complexes (Fig. 5.18), correlating with the metamorphic rocks flooring the WAB and MB (e.g. Comas et al., 1992), we proposed that the boundary between these two crustal domains has been reactivated as the present-day Al-Idrissi Fault.

5.3.3. Basin configuration

All the above crustal observations fit with a subduction system setting. On the basis of these crustal characteristics, the Alboran Basin is structured on the following elements:

(i) a fore-arc basin, represented by the WAB and the MB;

(ii) a magmatic arc, represented by the EAB, covering from about the central region to the NE Alboran;

(iii) a back-arc basin, represented by the Algero-Balearic Basin (Fig. 5.19).

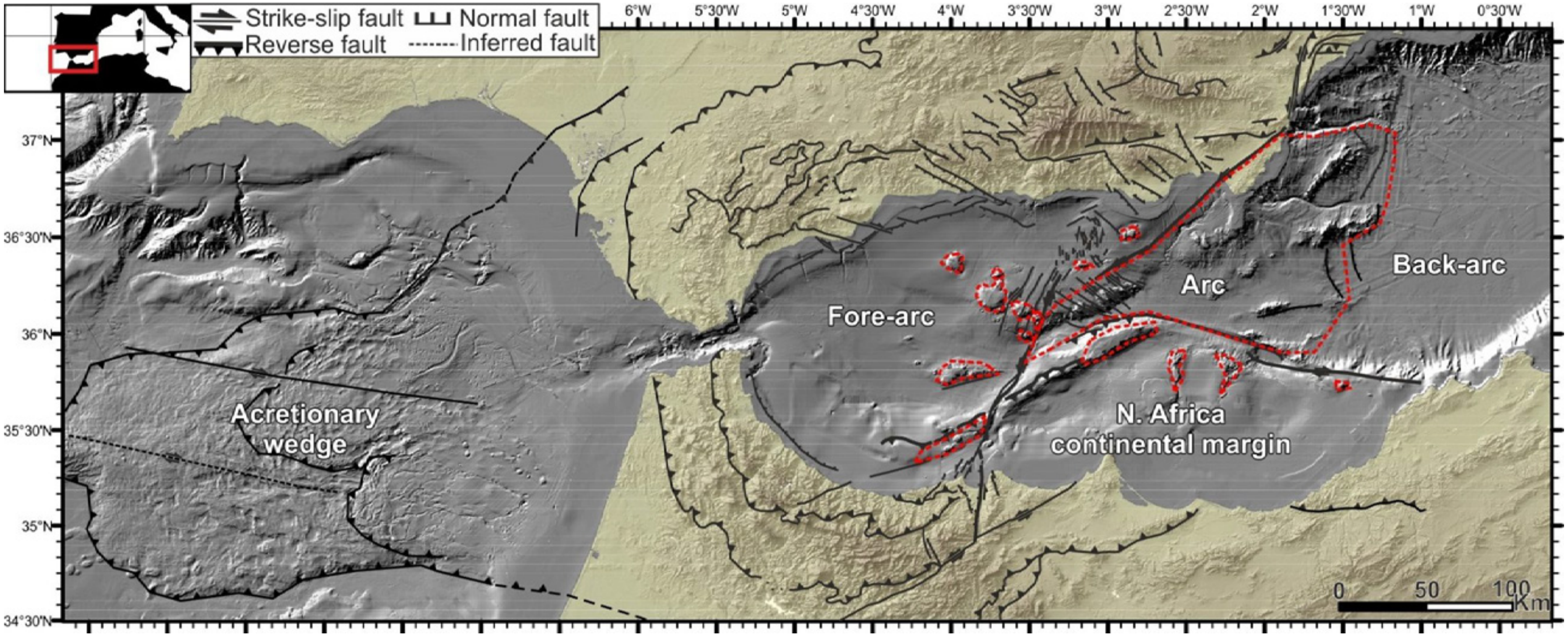

Figure 5.19: *Interpretation of the volcanic arc system, divided into fore-arc basin, magmatic arc and back-arc basin. Magmatic intrusions and basement of the magmatic arc crust domain are enclosed inside red dashed lines.*

The deformed sedimentary area located in inner Gulf of Cadiz has been further studied, although is origin is still under debate (e.g. Tortella et al., 1997; Maldonado et al., 1999; Gutscher et al., 2002; Gràcia et al., 2003a,b; Iribarren et al., 2007; Martínez-Loriente et al., 2013). Here we interpreted it as the accretionary wedge, following previous interpretations (e.g. Zitellini et al. 2009).

The continental crust flooring the Alboran Basin has progressively been modified by the evolution of the subduction system. Near the slab edge (WAB), extensional processes resulted in a thinning of the continental crust, which in some areas was so extreme that led to mantle exhumation. For instance, the existence of a high velocity body imaged under the western boundary of the WAB can be correlated with the Ronda and Beni Bousera peridotites cropping out on land (El Moudnib et al., 2015) (see Figure 5.18 for location). The lack of extensional structures observed in the area suggests a vertical tectonics subsidence model. Other fore-arc basins in similar tectonic setting (e.g. Weber Deep Basin, Pownall et al., 2016; Sandino Basin, Ranero et al., 2000), and has also been described for the WAB (Do Couto et al., 2016), subsidence in the fore-arc has been explained as the result of the slab pull, as this basins are usually located near the slab hinge.

There are other examples of these basins in the western Mediterranean, such as the Campania Plain in the Tyrrhenian arc (Milia and Torrente, 2015). These basins, characterized by an important and rapid subsidence and by their location above the slab hinge, remain fairly stable through time (Milia and Torrente, 2015; Do Couto et al., 2016; Noda, 2016; Pownall et al., 2016). This implies a migration of the basin linked to the slab migration during the slab roll-back. As the Alboran slab rolls-back towards the west (e.g. Spakman and Wortel, 2004; Bezada et al., 2013; Chertova et al., 2014a; Van Hinsbergen et al., 2014; Fichtner and Villaseñor, 2015), an eastern position for this domain is inferred, as previous studies pointed out (Booth-Rea et al., 2007; Do Couto et al., 2016).

The subduction-related fluids led to the formation of the magmatic arc (Duggen et al., 2004; Duggen et al., 2005; Duggen et al., 2008). Magmatic activity resulted in the creation of new crust below the Djibouti Plateau and EAB areas, floored by a volcanic basement (Duggen et al., 2004; Booth-Rea et al., 2007; Duggen et al., 2008), and in the presence of volcanic intrusions on the adjacent zones (Hoernle et al., 1999; Duggen et al., 2004; Duggen et al., 2005; Duggen et al., 2008).

The Algero-Balearic Basin is the back-arc basin of the system. In this area, extensional processes become enough to create new oceanic crust within the Algero-Balearic Basin (Booth-Rea et al., 2007; Mauffret, 2007; Billi et al., 2011; Grevemeyer et al., 2011; Leprêtre et al., 2013; Bouyahiaoui et al., 2015).

A detailed discussion of the basin evolution and associated kinematics is developed in “Chapter 6: Basin evolution” (this volume), and a review of the geodynamic models and the extensional mechanism that led to the basin formation is developed in Part V: Discussion (this volume).

5.4. In summary

The TOPOMED-GASSIS deep seismic survey shows for the first time across the entire Alboran basin the different configuration of the depocenters and basement, as well as and the relations between the domains. This structural configuration gives clues on the geodynamic evolution of each sub-basin, as we will present in next chapters.

On the basis of these results, we are able to define three different domains coexisting at the Alboran Basin:

(i) thin continental domain, (ii) magmatic arc domain and (iii) North-African continental domain. The boundaries between these domains can be either a smooth transition or a well-defined tectonic structure.

The thin continental domain is located below the WAB and the MB. It presents thickness variations, being characterized by a basement thickness of ~2 s TWTT under the WAB and by a basement thickness of ~5.5 s TWTT under the MB. We proposed that both domains are part of the same type of continental crust of a nature similar to metamorphic terrains onshore, affected by different degrees of extension. This part of the basin is located in a **fore-arc** setting.

The magmatic arc crust is characterized by a basement of ~5 s TWTT thick, with layered reflections on its lower part associated to magmatic intrusions. The basement of this domain is dated as Late Serravallian? – Tortonian. This domain represents the **volcanic arc** related with the subduction system.

The North-African **continental crust** is found offshore Africa. The basement has a thickness of ~7 s TWTT. Intra-crustal reflections are common in this basement. It is possibly not a part of the Alboran Domain.

The Alboran Basin crustal domains are the result of extensional processes in a plate subduction context, which modified their crustal characteristics until the current configuration. The Alboran Basin is not a back-arc basin *sensu-stricto*. It is structured in a fore-arc basin, a magmatic arc and the westernmost part of a back-arc basin. The back-arc basin of this system is mainly represented by the Algero Balearic Basin, and the easternmost Alboran Basin.

Chapter 6

Basin evolution

The Alboran Basin contains numerous highs and sub-basins, which reflect its complex geodynamic evolution. The main depocenters of these sub-basins have previously typically being studied individually. There are 6 main sub-basin described in literature: the West Alboran Basin (WAB), the Malaga Basin (MB), the South Alboran Basin (SAB), the Pytheas Basin (PB), the Habibas Basin (HBB) and the East Alboran Basin (EAB) (Fig. 6.1).

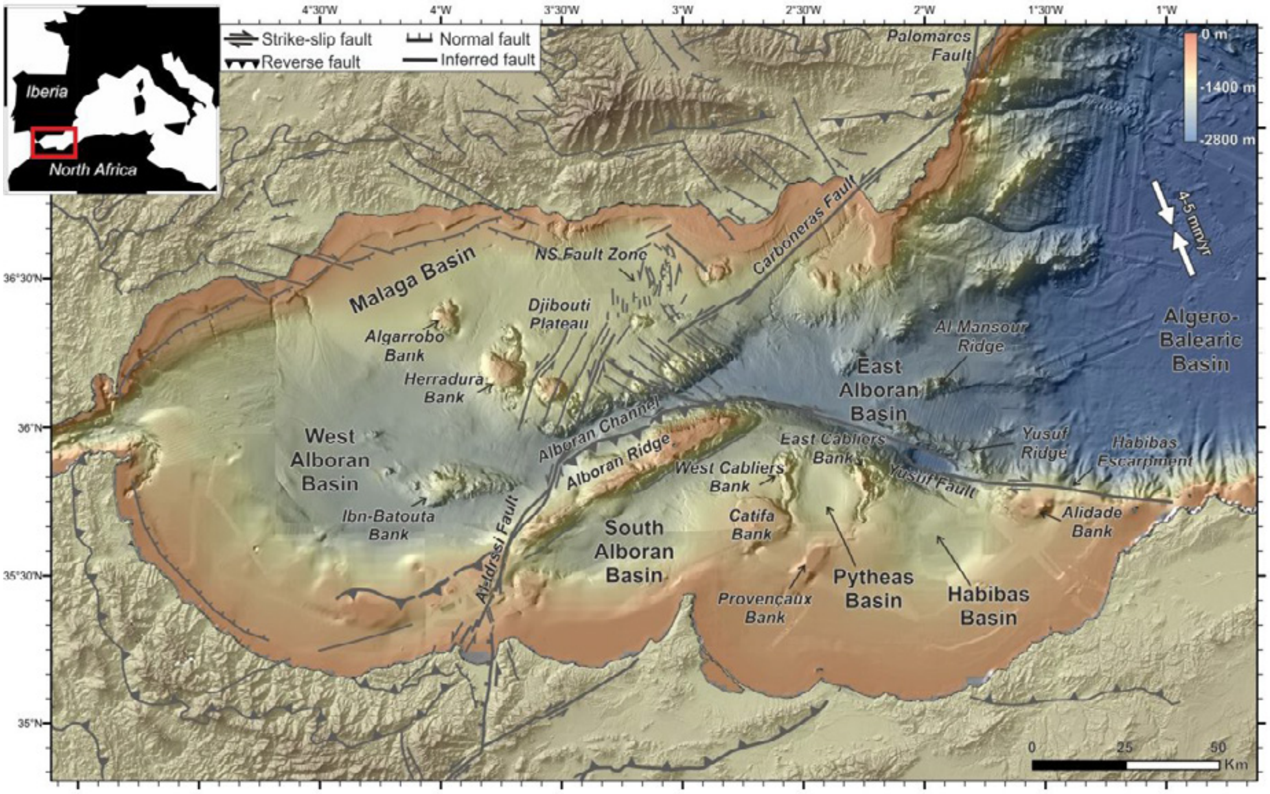

Figure 6.1: *Regional bathymetric map of the Alboran Sea constructed from swath-bathymetric data acquired during the IMPULS-06, EVENT-10, TOPOMED-11, SHAKE-15 and IDRISSI-16 marine cruises (e.g. Gràcia et al., 2006, 2012) the SARAS cruise (PI: d'Acremont & Gorini; d'Acremont et al., 2014; Lafosse et al. 2016; Rodriguez et al. 2017) and a compilation of existing datasets from IEO (Ballesteros et al., 2008) and GEBCO. Land topography is from the SRTM-3 grid. Main tectonic structures are displayed (Gràcia et al., 2012, submitted 2017). Inset: Location of the depicted area (red rectangle).*

To understand the tectono-sedimentary evolution of each sub-basin is fundamental to establish a general geodynamic model for the entire Alboran Basin. The Alboran Basin has a complex geological evolution resulting from several tectonic and depositional phases summarised in "Chapter 2: Geological setting". The phases can be divided in two: a) processes that led to basin formation, and b) processes that post-date this formation. As a consequence, there is a part of the geodynamic evolution that is different for each depocenter, while the post-Messinian evolution presents common characteristics along the entire Alboran

Basin. The sedimentary infill of each depocenter has recorded information that may help of unravel the geodynamic evolution, and it is the key to understand the formation and deformation processes of the entire basin.

The sedimentary record of each depocenter indicates that the age and tectonic evolution of the sub-basins differs. These differences are related also to the diversity of basement types found flooring the depocenters (see "Chapter 5: Crustal domains"). Regional studies of the entire Alboran Basin are mainly from the 90's (e.g. Watts et al., 1993; Comas et al., 1999). These studies proposed a general stratigraphy for the area based on the well data and its correlation with seismic profiles. However, the restricted seismic coverage and generally low quality (old acquisition and processing methods), penetration and resolution of the seismic profiles were not enough to perform a detailed analysis of the entire sediment infill. More recent works characterize in detail a particular area (e.g. Gràcia et al., 2006; Soto et al., 2010; Martínez-García et al., 2011; Gràcia et al., 2012; Medaouri et al., 2012; Soto et al., 2012; Martínez-García et al., 2013; Medaouri et al., 2014; Do Couto et al., 2016; Moreno et al., 2016), but the correlation between the different sub-basins remained beyond the scope of those works. Furthermore, most recent works are usually focused only on the Messinian and younger stratigraphy (e.g. Martínez-García et al., 2013).

In this chapter, we analyse the seismic stratigraphy of the entire Alboran Basin, focusing on the entire Neogene and Quaternary sedimentary units. The main objectives are: (i) To define a seismostratigraphy framework for the entire Alboran basin, integrating previous interpretations and available well information; (ii) To establish a correlation between units of different sub-basins, integrating previous detailed studies of each depocenter; (iii) To characterize comparatively the sedimentary record of the main depocenters of the Alboran Sea (WAB, MB, SAB, HBB and EAB); (iv) To propose an evolutionary model for each sub-basin; and (v) To integrate all sub-basins results in an updated general geodynamic model for the Alboran Basin.

6.1. Data used in this chapter

To characterize the different depocenters that compose the Alboran Basin, we analysed a new grid of seismic reflections profiles from Barcelona-CSI data (Fig. 6.2), with different resolutions and penetrations and integrate some available industry and academic data sets. This seismic grid has been described at the Methodology and Data section ("Chapter 3: Multichannel seismic reflection data"). The regional distribution of these profiles and its multiscale resolution permitted to re-evaluate the seismostratigraphy of the entire Alboran Basin.

Figure 6.2 ►: *Colour shaded-relief bathymetric map of the Alboran Ridge area. MCS profiles, commercial and scientific wells and dredges are located (see map legend for details). Location of the figures (red and yellow lines) is depicted*

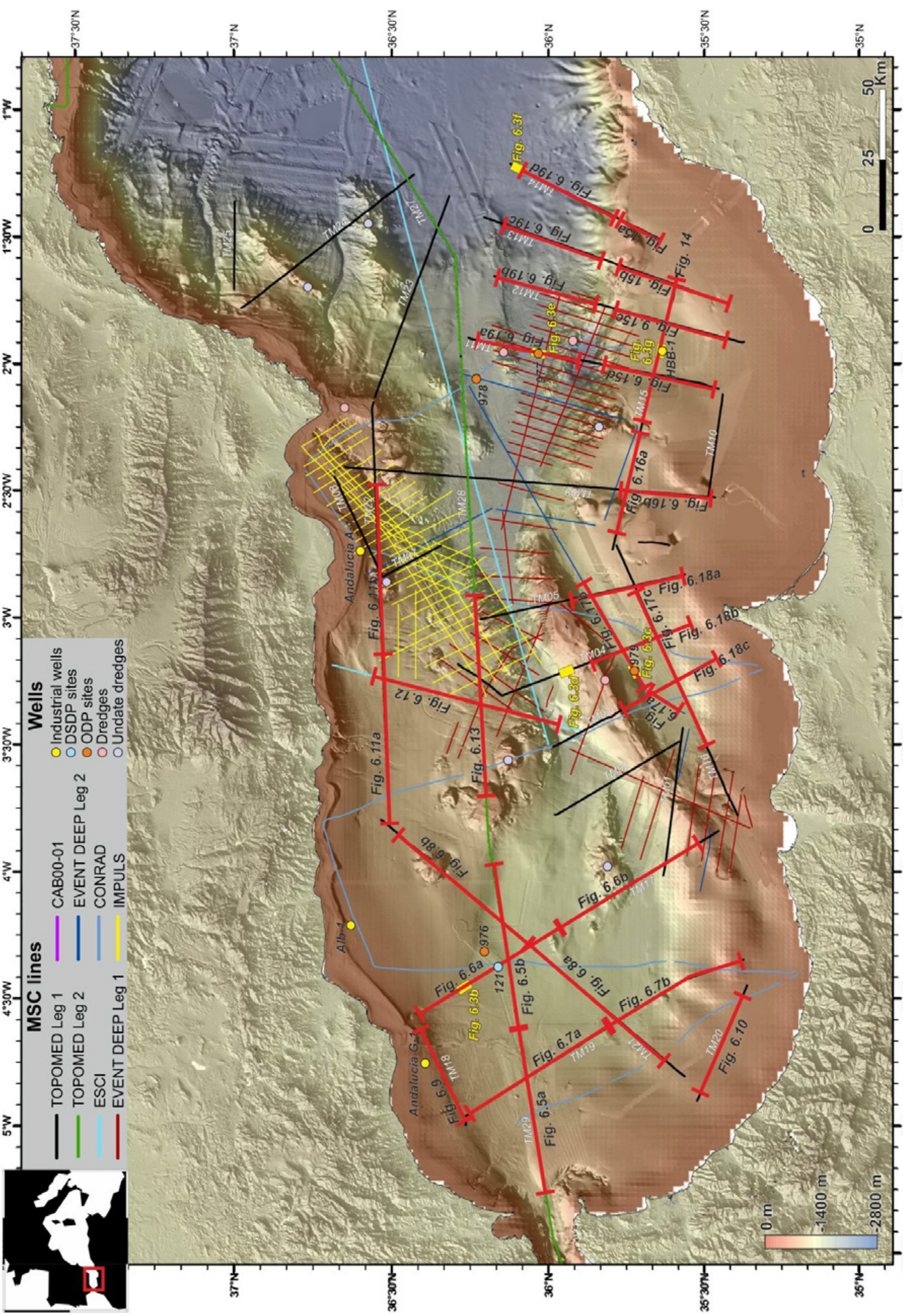
MSC lines
TOPOMED Leg 1
TOPOMED Leg 2
ESCI
EVENT DEEP Leg 1
CAB00-01
EVENT DEEP Leg 2
CONRAD
IMPULS
Wells
Industrial wells
DSDP sites
ODP sites
Dredges
Undate dredges
0 m
-1400 m
-2800 m
0
25
50
Km
5°30'W
5°W
4°30'W
4°W
3°30'W
3°W
2°30'W
2°W
1°30'W
1°W
35°N
35°30'N
36°N
36°30'N
37°N
37°30'N
Andalucia G-1
Alb-1
Andalucia A-1
HBB-1
976
121
978
977
979
Fig. 6.5a
Fig. 6.5b
Fig. 6.6a
Fig. 6.6b
Fig. 6.7a
Fig. 6.7b
Fig. 6.8a
Fig. 6.8b
Fig. 6.9
Fig. 6.10
Fig. 6.11a
Fig. 6.11b
Fig. 6.12
Fig. 6.13
Fig. 6.14
Fig. 6.15a
Fig. 6.15b
Fig. 6.15c
Fig. 6.15d
Fig. 6.16a
Fig. 6.16b
Fig. 6.17a
Fig. 6.17b
Fig. 6.17c
Fig. 6.18a
Fig. 6.18b
Fig. 6.18c
Fig. 6.19a
Fig. 6.19b
Fig. 6.19c
Fig. 6.19d
Fig. 6.3b
Fig. 6.3c
Fig. 6.3d
Fig. 6.3e
Fig. 6.3f
Fig. 6.3g
TM29
TM18
TM19
TM20
TM21
TM17
TM28
TM04
TM05
TM08
TM09
TM10
TM11
TM12
TM13
TM14
TM15
TM23
TM24
TM25

6.2. Results

6.2.1. Definition of the seismic units

The post-Messinian history of the Alboran Basin has been the focus of numerous recent works and it is reasonably well established (Moreno, 2011; Martínez-García, 2012; Martínez-García et al., 2013; Juan et al., 2016; Moreno et al., 2016). On the basis of previous studies (Jurado and Comas, 1992; Alvarez-Marrón, 1999; Comas et al., 1999; Booth-Rea et al., 2007; Soto et al., 2010; Medaouri et al., 2012; Soto et al., 2012; Medaouri et al., 2014; Giaconia et al., 2015; Do Couto et al., 2016; Juan et al., 2016) and correlation with well data (Comas et al., 1999; Soto et al., 2012; Medaouri et al., 2014), we propose a revised general basin stratigraphy for the entire Alboran Basin (Fig. 6.3). Due to the basin compartmentalization and local character of recent studies, the names and boundaries of units are not always equivalent among the different basins (Fig. 6.4). We have defined a common nomenclature for the entire Alboran Basin, integrating all previous studies and at the same time, trying to unify by correlation of the different units from one basin to another (Figs. 6.3, 6.4). The correlation between units defined in this volume and units defined in previous studies is shown in Figure 6.4, which is organized by basins. We correlate the different seismostratigraphic units by their calibrated age, but one must be aware that drill information (and thus calibration) is very limited particularly in the deep basin and even worse for older units. However, some of the main unit boundaries are regional unconformities that provide reliable -even though limited- chronostratigraphy. Also, it must be kept in mind that ages are not indicative of the same lithology in different regions, as will be discussed along this chapter. Following the literature and in order to facilitate comparison with previous works, the sediment units have been labelled in three different ways (Fig. 6.3). Most of the sedimentary units have been depicted with Roman numbers from I to VII. However, the pre-Messinian stratigraphy of the Habibas Basin is not equivalent to units I to VII, neither in their age or in their described lithologies. For this reason, the Habibas Basin units have been labelled as T (Tortonian unit), S (Tortonian - Serravallian unit) and L (Serravallian? - Langhian unit), following recent industry-well-data-calibrated interpretations (Medaouri et al., 2012; Medaouri et al., 2014). Finally, due to their local distribution, interpreted volcanic units have been labelled starting with a v, referring to its volcanic nature, and with the first letter of the area where it is found (i.e. A: Alboran Ridge area, Y: Yusuf Fault area, D: Djibouti Plateau area and C: Carboneras Fault area) (Fig. 6.3c, d, e and f). When more than a volcanic unit is identified in a given area, a number indicative of its relative age is added (e.g. vA1 corresponds to the first volcanic unit identified in the Alboran Ridge area).

The post-Messinian stratigraphy presents common characteristics along the entire Alboran Basin, while the pre-top-Messinian sequence is conditioned by the particular evolution of each depocenter. We will describe the main seismostratigraphic units of the Alboran Basin, following our nomenclature and denoting common aspects and differences among units from different sub-basins.

- *Post-Messinian units*

Unit I is Quaternary in age (Fig. 6.3). Its base has been correlated to the Gelasian-Calabrian boundary (1.8 Ma). It shows parallel continuous reflections and its thickness ranges between 0.3 and 0.5 s TWTT. In some places, it can be subdivided into two sub-units (Ia and Ib). Sub-unit Ia is Middle to Upper Pleistocene in age, and is characterized by parallel continuous reflections intercalated with chaotic bodies. Its maximal thickness reaches to 0.4 s TWTT. Sub-unit Ib is of Calabrian age (0.78 – 1.80 Ma), and is characterized by high-amplitude, parallel and continuous reflections. It presents variation in thickness, ranging between 0.1 and 0.3 s TWTT. Unit I is equivalent to unit Q (Martínez-García et al., 2013; Medaouri et al., 2014) and to

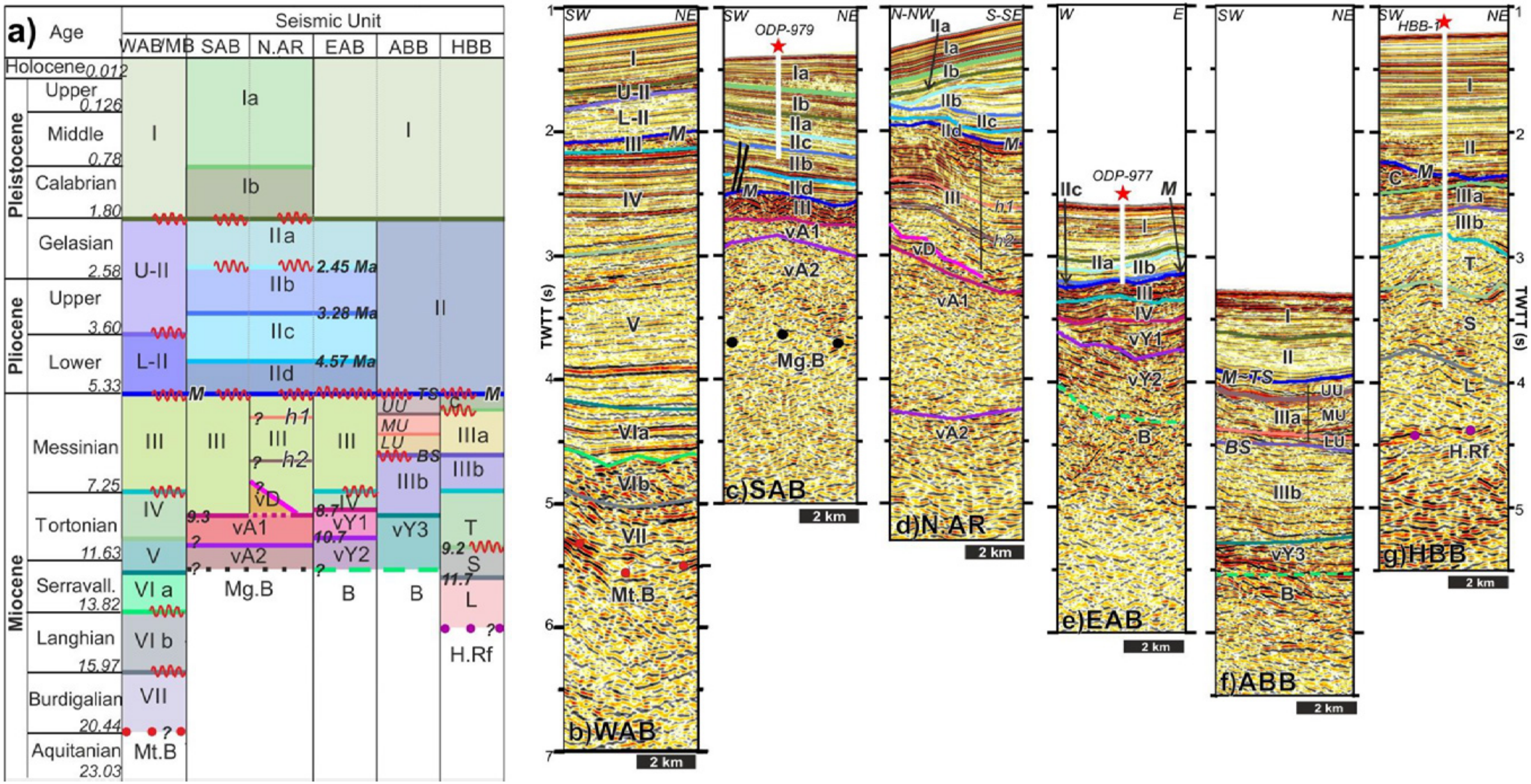

Figure 6.3: ***(a)*** *Ages and seismostratigraphic units identified in the Alboran Basin. Each column in the table represents a geographical area: WAB: West Alboran Basin, MB: Malaga Basin, SAB: South Alboran Basin, N. AR: North Alboran Ridge (Alboran Channel). EAB: East Alboran Basin, ABB: Algero-Balearic Basin and HBB: Habibas Basin. Limits between units are displayed in the same colour as the respective horizon at the seismic profiles. Red wavy lines are indicative of unconformities.* ***(b-g)*** *Examples of the seismic facies found at (a) the WAB, (b) the SAB, (c) northern AR, (d) EAB, (e) ABB and (f) HBB (see Figure 6.2 for location). UU: Upper Unit, MU: Mobile Unit, LU: Lower Unit. vA: volcanic unit in Alboran Ridge area, vY: volcanic unit in Yusuf Fault area, vD: volcaniclastic unit in Djibouti plateau area. Mt.b: Metamorphic basement, Mg. B: Magmatic basement, B: Basement, H. Rf: High Reflectivity body. Correlation with ODP Leg 161 sites is displayed.*

the upper part of unit S8 (Fig. 6.4) (Do Couto et al., 2016). This unit is described as a shale unit with interbedded sandy levels in the Habibas drill site (HBB-1, Medaouri et al., 2014) and in the commercial wells of the Iberian margin (e.g. Comas et al., 1992).

Unit II corresponds to Gelasian (Pleistocene) and Pliocene deposits. In general, it is well stratified, with parallel continuous reflections. This deposits have a geographical variability, with a thickness of <0.5 s TWTT in the EAB and 0.5-1 s TWTT in the WAB. In the WAB, unit II can be divided in two sub-units: U-II that corresponds to the Upper Pliocene-Lower Pleistocene deposits, and unit L-II, which is of Lower Pliocene age. These two units are differentiated by a marked reflectivity contrast; with L-II showing an overall low-reflectivity character. In the Alboran Ridge neighbouring areas, four internal sub-units can be differentiated, following the seismostratigraphy proposed by Martínez-García (2012). These sub-units boundaries are related to the successive compressional pulses affecting the Alboran Ridge area (see "Chapter 9: The Alboran Ridge"). The discontinuities defining these sub-units are recognized in the south part of the WAB and in the EAB, but not south of the Yusuf Fault, in the Habibas Basin, or in central and north WAB, and MB (Figs. 6.1, 6.3). Sub-unit IIa (1.80 – 2.45 Ma) is characterized by a continuous low-amplitude reflections. This sub-unit is discordant over IIb, and appears infilling a previous relief. It presents large variations in thickness, from 0.05 to 0.2 s TWTT, and it is not continuous throughout the profiles. The boundary between sub-units IIa and IIb has been interpreted as a hiatus from 2.52 to 2.45 Ma, on the basis of the correlation with ODP-161 Site 976 (Martínez-García et al., 2013). Sub-unit IIb (2.45 – 3.28 Ma) exhibits an overall low-reflectivity character, with some parallel reflections and a thickness between 0.2 and 0.5 s TWTT in the westernmost profiles. Sub-unit IIc (3.28 – 4.57 Ma) is characterized by an intercalation of high-reflectivity and low-continuity reflections with abundant low-reflectivity zones. The maximum thickness is 0.28 s TWTT, gently wedging towards the south. Finally, the Lower Pliocene unit Sub-unit IId (4.57 - 5.33 Ma), is only present in the westernmost area, near the Alboran Ridge. It appears filling the deeper part of the depocenters and it shows high-amplitude continuous reflections. Maximum thickness is 0.3 s TWTT. This unit is equivalent to unit P of Martínez-García (2012) and Medaouri et al. (2014), to the lower part of sub-units Ia and Ib of Jurado and Comas (1992) and Soto et al. (2012), and to the lower part of unit S8 of Do Couto et al. (2016) (Fig. 6.4). Unit II has been described as sands in the HBB (Medaouri et al., 2014) and as clays intercalated with sands on the other basins (Comas et al., 1999).

- *Messinian units*

Unit III corresponds to the Messinian unit. It is often -but not always- limited on its top by the Messinian Unconformity (M reflection, 5.6-5.32 Ma interval) (Clauzon et al., 1996). This is an erosive surface observed across many areas of the Mediterranean basins (e.g. Hsü et al., 1973; Rouchy and Caruso, 2006; CIESM, 2008; Roveri et al., 2014). In the Alboran Basin it possibly represents a complex surface formed by successive events: (1) erosion during the Messinian Salinity Crisis, (2) erosion during the re-flooding (Zanclean flooding, Garcia-Castellanos et al., 2009), and (3) local erosion of the basin margins and intra-basin highs (Martínez-García et al., 2013). Due to this erosive top, unit III presents high variations in thickness along the profiles. In the areas where unit III is well developed, it can be subdivided into two sub-units. Sub-unit IIIa corresponds to the Upper Messinian unit (5.33 – 5.96 Ma). It is highly heterogeneous, depending on the geographic area of deposition. In the Habibas Basin and in the western section of the Yusuf Fault, its seismic expression is characterized by low-amplitude continuous reflections, and laterally alternating with chaotic zones. At the top of sub-unit IIIa irregular sedimentary bodies are found, which are related to chaotic deposits (depicted as "c" in Figure 6.3). In the easternmost sector of the EAB and the Algero-Balearic Basins, no erosion but evaporite deposits are found inside sub-unit IIIa.

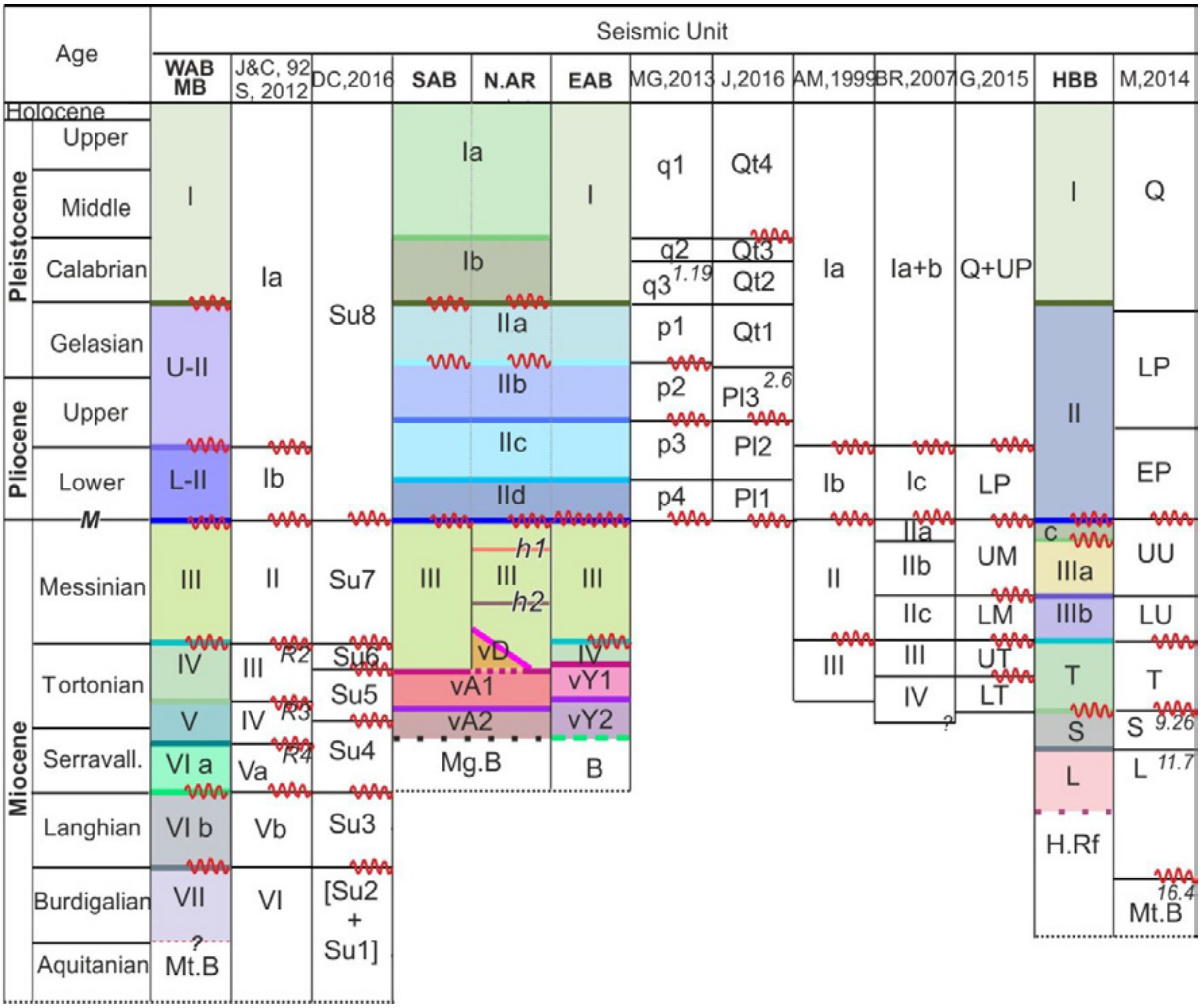

Figure 6.4: *Correlation between the seismostratigraphic units defined in this thesis and the previous units defined in the Alboran Basin depocenters. The correlation is organized by basins, starting from the WAB – MB (West Alboran and Malaga basins) (left panels), compared to Jurado and Comas 1992 (J&C, 92), Soto et al., 2012 (S, 2012) and Do Couto et al., 2016 (DC, 2016) units. In the central panels are the SAB (South Alboran Basin), N.AR (North Alboran Ridge) and EAB (East Alboran Basin) areas, compared to the Martínez-García et al., 2013 (MG, 2013), Juan et al., 2016 (J, 2016), Alvarez-Marrón, 1999 (AM, 1999), Booth-Rea et al., 2007 (BR, 2007) and Giaconia et al., 2015 (G, 2015) units. Finally, in the right section are the units of the HBB, compared with the units proposed by Medaouri et al., 2014 (M, 2014). The wavy red lines depict the inferred erosive unconformities from the mentioned studies.*

In these areas, we have been able to correlate the identified units with the Messinian Salinity Crisis units defined throughout the whole Mediterranean region (e.g. Lofi et al., 2011; Giaconia et al., 2014). They have been named to as Upper Unit, Mobile Unit and Lower Unit, respectively. The *Upper Unit (UU)* corresponds to the upper evaporites, characterized by continuous reflections formed by salt and gypsum deposits with marls and limestone alternations. It is bounded at the top by the Top Surface or Top Erosion Surface (TS/TES) depending on its erosive character that correlates with the M unconformity (Lofi et al., 2011). Below, it is found the *Mobile Unit (MU)* that is the evaporitic deposit itself mainly formed by halite (Lofi et al., 2011). The MU is characterized by an overall transparent character. The base of this unit is usually identified thanks to an inverse polarity reflection. The *Lower Unit (LU)* is the lower evaporitic deposit, associated with gypsum (Lofi et al., 2011) and characterized by low-continuous and low-amplitude seismic reflections (e.g. Booth-Rea et al., 2007). The Bottom Surface or Bottom Erosion Surface (BS/BES), depending on its erosive character, is located on its base and marks the base of the Upper

Messinian deposits. Sub-unit IIIb is correlated with the Lower Messinian deposits (5.96 – 6.25 Ma) that are characterized by parallel continuous reflections with increasing amplitude and reflection thickness from bottom to top. In the Alboran Channel and the South Alboran Basin it includes the Messinian sediments, but may also have Upper Tortonian strata since it is not calibrated by drilling. This unit shows chaotic reflections on its top followed by a well-defined package of sediments exhibiting high-amplitude continuous and parallel reflections. In order to characterize the Alboran Ridge formation, two internal reflections with unconstrained age (h1 and h2) have been mapped following two unconformities along the Alboran Ridge (Fig. 6.1, 6.3). At the WAB, sub-unit IIIb it is usually <0.2 s TWTT thick, and it is not continuous due to Messinian erosion. It is characterized by high-amplitude reflections, alternating with chaotic zones.

Our unit III is equivalent to a) the unit II proposed by Jurado and Comas (1992), Soto et al. (2012) and Booth-Rea et al. (2007), b) the unit Su7 proposed by Do Couto et al. (2016), and c) the U unit of Medaouri et al. (2014) (Fig. 6.4). In the areas where evaporites are not present, it is described as a clay unit intercalated with marls and volcaniclastic levels, with conglomerate beds on its base (Comas et al., 1999).

- *Pre-Messinian units*

The pre-Messinian stratigraphy is less studies and clearly different for each depocenter (Fig. 6.3). While a deep sedimentary basin was developed at the WAB and MB, in the SAB and the EAB the record is characterized by magmatic-volcanic rocks. At the HBB, a sedimentary depocenter was also formed, although the sedimentary units differ from the ones in the WAB & MB (Fig. 6.3).

In the WAB and MB, **unit IV** is of Tortonian age (> 6.25 Ma). It is characterized by high reflectivity parallel continuous reflections. This unit thickness is almost 1 s TWTT. At the EAB it is also present, and exhibits large thickness variation, ranging from 0.1-0.7 s TWTT. The seismic expression of this unit is also variable. It mainly exhibits a well-layered high-reflectivity character alternating with low amplitude reflections zones. It is the equivalent to unit III (Jurado and Comas, 1992; Booth-Rea et al., 2007; Soto et al., 2012) and units Su6 and upper part of Su5 (Do Couto et al., 2016) (Fig. 6.4). It has been described as clays and silty clays interbedded with sandstone (Jurado and Comas, 1992) but it has not been sampled in depocenters.

Unit V (Early Tortonian – Late Serravallian) is >1.5 s TWTT thick in some profiles. The unit shows parallel continuous reflections at the top with decreasing reflectivity towards its base. It is the equivalent to unit IV (Jurado and Comas, 1992; Booth-Rea et al., 2007; Soto et al., 2012) and the lowest part of Su5 and upper part of Su4 (Do Couto et al., 2016) (Fig. 6.4). This unit is mainly composed by silty clays, which are interbedded with volcanic layers (Jurado and Comas, 1992).

Unit VI (Serravallian and Langhian) exhibits low amplitude parallel continuous reflections, with a wide spacing between them. In some parts, this unit can be subdivided in two: sub-units VIa and VIb. Both of them present a low-reflectivity character, although unit VIb can be recognized due to the flickering aspect of its reflections, alternating with chaotic layers. Clays and marls with sandy intervals are the main components of sub-unit VIa, while sub-unit VI is mainly composed by shales associated to overpressure conditions (e.g. Jurado and Comas, 1992; Soto et al., 2012). Sub-units VIa and VIb are equivalent to units Va and Vb (Jurado and Comas, 1992; Soto et al., 2012) and units Su4 and Su3 (Do Couto et al., 2016), respectively (Fig. 6.4).

The deepest unit of the WAB and MB is **unit VII** (Burdigalian) characterized by high-reflectivity discontinuous reflections. A low-continuity set of reflection depicts the basement top. It is the equivalent to unit VI (Jurado and Comas, 1992; Soto et al., 2012) (Fig. 6.4), composed by clays and silty clays with sands, carbonate layers and a conglomerate layer on its base (Jurado and Comas 1992).

In the African continental margin (i.e. Habibas Basin), below unit III we found units T, S and L. These units have been correlated with the units proposed by Medaouri et al. (2012, 2014). Based on the ages obtained in the HBB-1 well, unit T is of Tortonian in age, unit S is Serravallian – Early Tortonian, and unit L is Langhian? – Early Serravallian (Figs. 6.3, 6.4). **Unit T** presents a low-reflectivity character alternating with well-stratified zones. It is not continuous and reaches a thickness of 0.7 s TWTT. In cores, it is a shale and marls unit with sandy intervals and pyroclastic layers (Medaouri et al., 2014). **Unit S** presents signs of deformation, with a folded base and top. Internally, it is composed by low continuous reflections with different dips evidencing folding. Its top and base are not parallel and as a consequence displays thickness variations. At the HBB-1 well cores contain clays with sandy and marl intervals (Medaouri et al., 2014). **Unit L** is characterized by low-amplitude non-parallel reflections. The base of this unit cannot be clearly identified. It is emplaced over a high reflectivity basement (Fig. 6.3f). It has been described as under compacted shale, interbedded sand and sandy-pebble intervals (Medaouri et al., 2014).

- *Volcanic units*

The correlation between volcanic units is difficult due to their local geographical distribution and the lack of enough sampling. When possible, an age coming from dredged samples was assigned to the unit, and a relative age based on the relationship with other units has been proposed. We have divided the volcanic unit in four distinct areas: the Alboran Ridge (vA units), the Yusuf Fault (vY units), the Djibouti Plateau (vD units) and the Carboneras Fault (vC units). We interpreted them as volcaniclastic units due to their seismic character and their volcanic nature as confirmed by the dredges obtained but the units may contain some lavas flows as well (Fig. 6.2) (Aparicio et al., 1991; El Bakkali et al., 1998; Hoernle et al., 1999; Maury et al., 2000; Duggen et al., 2004; Gill et al., 2004; Duggen et al., 2005; Duggen et al., 2008).

In the Alboran Ridge area, we identify two units. **Unit vA1** is mainly chaotic, with some high-amplitude reflections with low continuity, especially on the unit top. Unit vA1 outcrops at the western part of the AR, and taking into account the dredged rocks recovered from this high (9. 26 - 9.37 Ma, e.g. Duggen et al., 2004; Duggen et al., 2008) (Fig. 6.2), it is Tortonian in age. A high amplitude irregular reflection marks the limit with **unit vA2**, below it. This unit exhibits also a volcanic character, with chaotic reflections intercalated with low amplitude and low continuity reflections. These volcanic units are emplaced over a high reflectivity basement (Fig. 6.3c, 6.3d), characterized by strong reflections with low lateral continuity. Through the correlation with the East Alboran Basin and the HBB-1 well (Medaouri et al., 2014), we assumed an age prior to 11.63 Ma (Early Serravallian – Pre-Serravallian) for this high reflectivity basement.

In the Yusuf Fault area, three different volcanic units separated by unconformities are identified. The youngest of these units, **unit vY1**, crops out at the Al-Mansour Ridge (Fig. 6.1). Dredged basaltic andesites give 8.7 Ma (Duggen et al., 2004; Duggen et al., 2008) for the youngest layer of this unit. Seismically, it shows high-amplitude reflections and alternating poor- and well-stratified zones. Laterally, it is inter fingered with an older volcanic unit, **vY2**. This unit has been dredged at the Yusuf Ridge (Fig. 6.1), were andesites dated in 10.7 Ma were recovered (Duggen et al., 2004; Duggen et al., 2008). It is characterized by high-amplitude parallel reflections, exhibiting a wavy attitude. On the eastern side, a deeper unit is found, **vY3**. This unit has not been dredged, but due to its seismic character and restricted lateral extension, we inferred that is also volcanic. Internally show little structure with semi-transparent zones. The base of these units is defined by a change in the reflectivity and not by a well-defined reflection. The basement found below them is characterized by an overall low-reflectivity character that contrasts with the Habibas Basin basement (Fig. 6.3).

Under the Alboran Channel and Djibouti Plateau sedimentary units, the **vD** volcanic unit, with characteristic similar to the units at the SE**,** is recognized (Fig. 6.1).

In the Carboneras Fault area, volcanic unit **vC,** characterized by an irregular top, high amplitude and scattered reflections, is identified (see Figure 6.11). This unit extends along the northeast Alboran Basin margin into the Palomares margin. Due to its inter fingering with calibrated sediment units in the area, we propose a late Tortonian – Messinian age for this unit.

6.2.2. Basement characteristics

As discussed in "Chapter 5: Crustal domains", the basement differs among depocenters of the Alboran Basin. Here we will briefly review the knowledge about the basement of each sub-basin and the seismic characteristics that present at the seismic profiles, as the nature of the basement and its characteristics are key to understand the evolution of the sedimentary basin.

- *West Alboran and Malaga basins*

These two basins form an arcuate continuous depocenter that mimics the shape of the orogenic front in Iberia and Morocco, but they have often been studied as separated basins. They are the deepest depocenter of the entire Alboran Basin, with sediment thickness reaching ~6 s in TWTT, representing ~10 - 12 km of sediment accumulation (Soto et al., 2010; Soto et al., 2012; Do Couto et al., 2016). Their basement, drilled at Andalucia G-1 and ODP-161 Site 976, is metamorphic continental rocks (e.g. Comas et al., 1999), affected by Miocene magmatism in the eastern part. The Algarrobo, Herradura and Ibn-Batouta banks (Fig. 6.2) are volcanic (Duggen et al., 2008), but evidence of magmatism ends at the east of the WAB. The sediment infill and basement are imaged in profiles TM29 (Fig. 6.5), TM17 (Fig. 6.6), TM19 (Fig. 6.7), TM21 (Fig. 6.8), TM18 (Fig. 6.9), TM20 (Fig. 6.10), TM22 (Fig. 6.11), ESCI-Alb1 (Fig. 6.12) and TM28 (Fig. 6.13) (see Figure 6.2 for location).

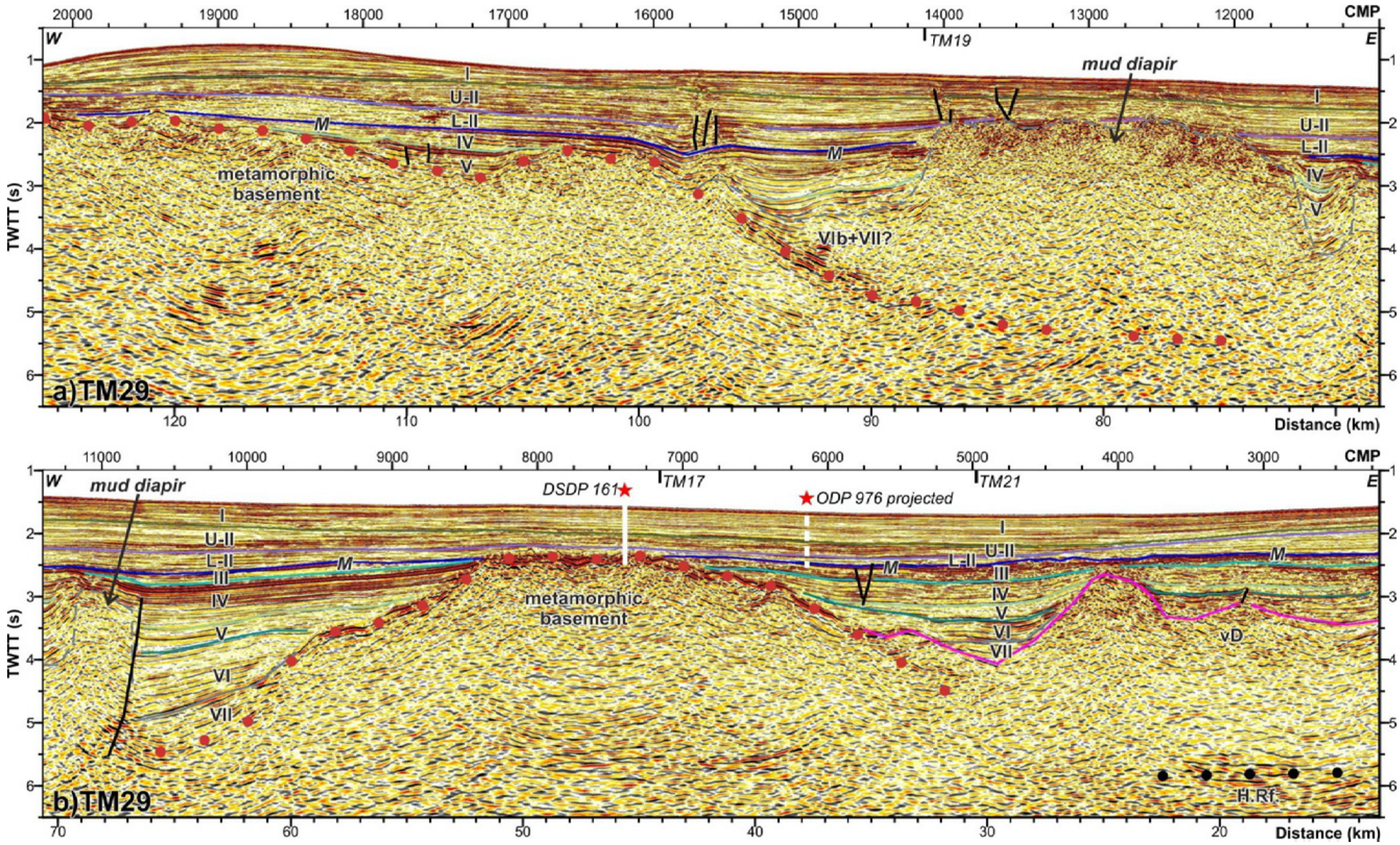

Figure 6.5: *Time migration of profile TM29 (see location in Figure 6.2). This profile is divided in a) Western section and b) Eastern section. This profile runs from the Straits of Gibraltar to the Djibouti Plateau, in a W-E direction. Above the metamorphic basement, Miocene sedimentary units are onlapping. The M reflection is a concordant limit between the L-II and the IV unit (CMP 17000-14000). At the Djibouti Plateau, it exhibits signs of erosion (CMP 6000-4000). A mud diapir is imaged between the CMP 14000-11000. This diapir seems to be fed by unit VI. Main structures and seismostratigraphic units are identified. Age of the units is defined in Figure 6.3. ODP 976: ODP Leg 161 site 976. Vertical exaggeration is of ~x:2.5 taking into account a suitable velocity for the sediments.*

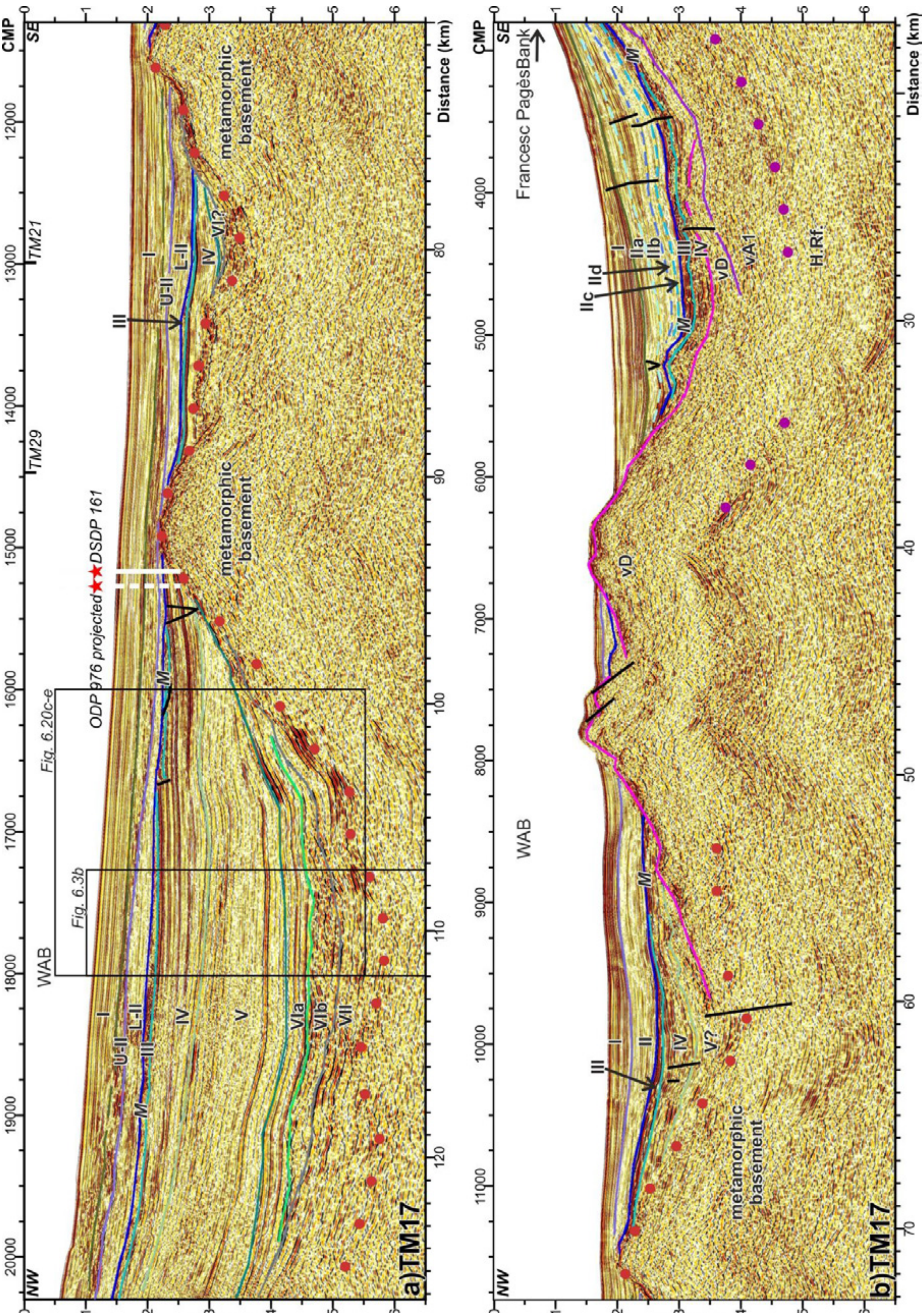
a)TM17
b)TM17
CMP
SE
NW
Distance (km)
TWTT (s)
TM21
TM29
ODP 976 projected
DSDP 161
Fig. 6.20c-e
Fig. 6.3b
WAB
metamorphic basement
Francesc PagèsBank
I
U-II
L-II
II
IIa
IIb
IIc
IId
III
IV
V
V?
VI?
VIa
VIb
VII
M
vD
vA1
H.Rf.

◄ ***Figure 6.6:*** *Time migration of profile TM17 (see location in Figure 6.2). This profile is divided in a) Northwestern section and b) Southeastern section. Profile TM17 images the WAB in a NW-SE direction. At the NW side, a deep sedimentary basin of 4.5 s TWTT is observed. In the deepest part of this depocenter, unit VII and VIb can be recognized. Unit VIb is characterized by chaotic internal reflections. Units VII, VIb and VIa have a constant thickness, and are onlapping above the basement top. Above them, it is found unit V. These units reach to a thickness of 1.5 s TWTT and got thinner towards the basement high (CMP 19000-15000), where it thickness is about 0.5 s TWTT. In some points of the profile a thin unit III is identified. It is characterized by chaotic reflections. The M reflection does not present evidences of erosive character. Unit II and I are found along the entire profile, and are not limited by the basement lows as the Miocene sequence. At the SE, the Plio-Quaternary is affected by the Alboran Ridge uplift. Main structures and seismostratigraphic units are identified. Age of the units is defined in Figure 6.3. ODP 976: ODP Leg 161 site 976. Vertical exaggeration is of ~x:2.5 taking into account a suitable velocity for the sediments.*

The top of the basement is well defined along all seismic profiles. Profile TM29 (Fig. 6.5) clearly images the geometry of the entire WAB above the metamorphic basement. The west part of the profile shows a basement top at around 2 s TWTT deepening toward the basin centre (Fig. 75a, CMP 15000-9000) where it is at ~5.5 s TWTT. On the eastern WAB flank, the basement is shallower (Fig. 6.5b, CMP 9000-6000), ~2.5 s TWTT, and it can be seen the volcanic unit of the Djibouti Plateau overlaying it. This WAB geometry is also shown in a NW-SE direction along profile TM17 (Fig. 6.6), where a shallowing of the basement is observed at the NW side, deepening to 5 s TWTT below the basin depocenter (Fig. 6.6a, CMP 19000-17000) to shoal towards the SE (Fig. 6.6a, CMP 15000-11000), where it transitions to the Djibouti Plateau and Alboran Ridge volcanic units (Figs. 6.5b, 6.6b). Profile TM21 (Fig. 6.8) is a SW-NE transect across the WAB that images the basement top at 6.5 s TWTT in the depocenter shoaling to 2.5s TWTT across the basin flank (Fig. 6.8a, CMP 9000-12000). This profile also images the strata continuation towards the MB. The transition between the two basins is marked by the Algarrobo Bank (Fig. 6.8b, CMP 18000-20000), which is part of the Djibouti Plateau volcanic unit. The top of the basement across the MB is imaged at 4-5 s TWTT on profile TM22 (Fig. 6.11). Towards the east, volcanism of the Carboneras volcanic unit is identified (Chella Bank, Fig. 6.11b CMP 13000-15000) and the transition to a volcanic arc basement is imaged. Profiles TM18 (Fig. 6.9) and TM20 (Fig. 6.10) on the edges of the WAB image the top of the basement located between 4.5 and 6 s TWTT.

- *Habibas and Pytheas basins*

Offshore the Moroccan and Algerian coasts occur the Pytheas and Habibas sub-basins (Fig. 6.1). The sedimentary infill of these basins presents similar characteristics, so they will be described together. They are bounded by basement highs, the Catifa and Provençaux banks, and two volcanic ridges (Duggen et al., 2005), West and East Cabliers (Fig. 6.1). On the bathymetry, these basins show a semi-circular shape (Fig. 6.1). The HBB is limited to the north by the Yusuf Fault, to the east by the Alidade Bank, to the west by the East Cabliers ridge and Provençaux Bank, and gradually shoals towards the south under the North African continental platform (Fig. 6.1). The PB is bounded by the East Cabliers ridge to the east, the Provençaux Bank to the south and the West Cabliers ridge Bank to the west (Fig. 6.1). The basement of the HBB sampled at HBB-1 well (Fig. 6.2), is made of continental metamorphic rocks (Medaouri et al., 2014). We present interpretations of MCS profiles TM15 (divided in the eastern and western sections, Figs. 6.14 and 6.16a), TM14 (Fig. 6.15a), TM13 (Fig. 6.15b), TM12 (Fig. 6.15c), TM11 (Fig. 6.15d) and TM09 (Fig. 6.15b).

On the seismic profiles, the basement top (base of unit L) is not identified with one continuous reflection, but appears marked by a reflective band of short events (Figs. 6.14, 6.15).

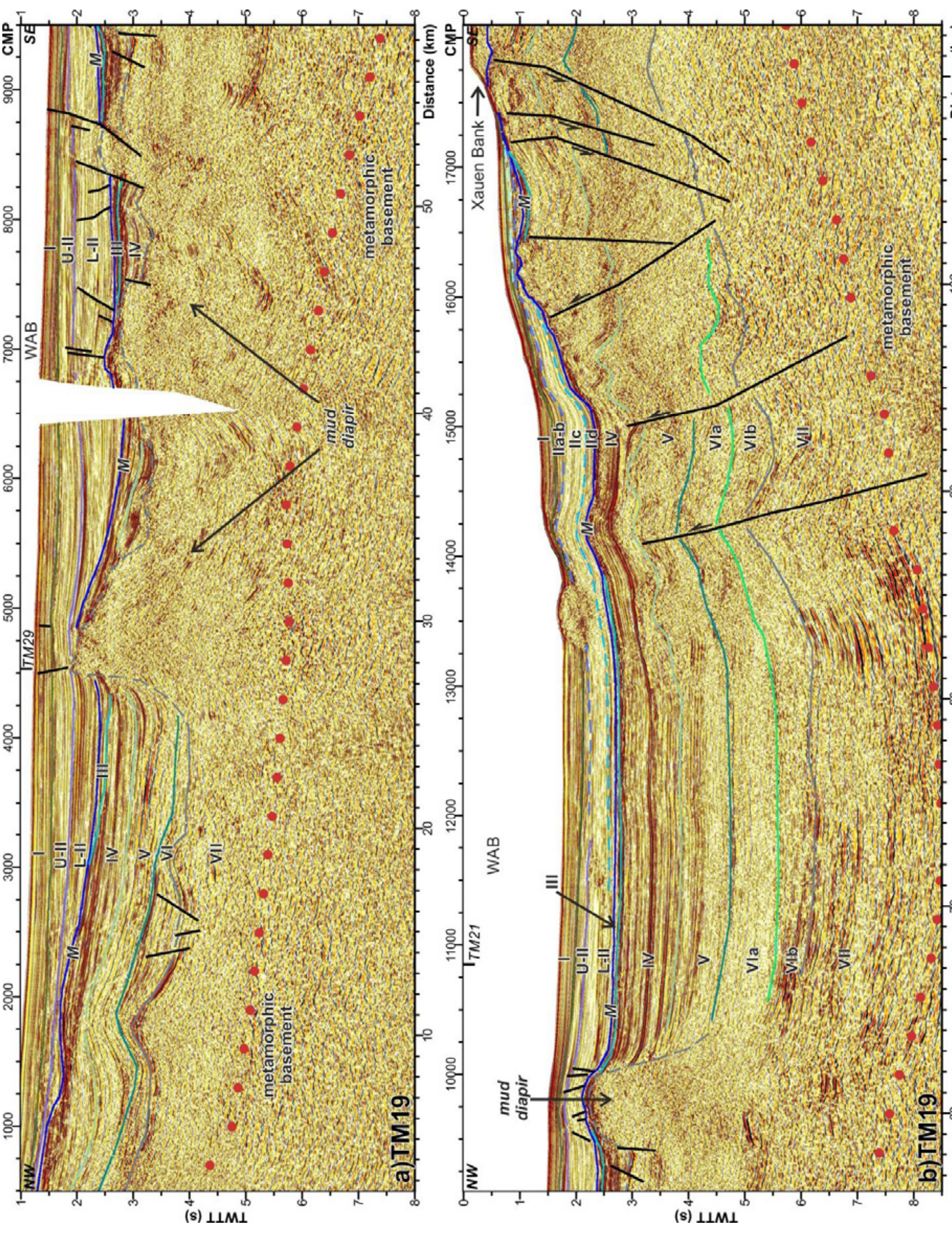
a)TM19
NW
SE
CMP
TWTT (s)
Distance (km)
WAB
TM29
I
U-II
L-II
III
IV
V
VI
VII
M
mud diapir
metamorphic basement
b)TM19
NW
SE
CMP
TWTT (s)
Distance (km)
Xauen Bank
WAB
TM21
mud diapir
I
U-II
L-II
III
IIa-b
IIc
IId
IV
V
VIa
VIb
VII
M
metamorphic basement

◄ ***Figure 6.7:*** *Time migration of profile TM19 (see location in Figure 6.2). This profile is divided in a) Northwestern section and b) Southeastern section. This profile runs parallel to profile TM17 (Fig. 6.2, 6.6), showing a westward transect of the WAB. Along this profile, stand out the mud diapirism activity. A thick unit VII, ranging between 1.5 s TWTT and 2 s TWTT, is feeding these diapirs. At the southeastern section, unit VIb is also recognized (CMP 10000-17000), and this unit is also possibly implied in the mud diapirism phenomena. Units V, IV and III are deformed by the diapirism (CMP 4000-5000), suffering folding in the diapirs margin, while unit II and I seem to be adapted to the diapir geometry, getting thinner above them (CMP 9000-10250). The southernmost section reflects the effect of the Alboran Ridge uplift (see "Chapter 9: The Alboran Ridge") and the complex structure of the Xauen Bank. Main structures and seismostratigraphic units are identified. Age of the units is defined in Figure 6.3. Vertical exaggeration is of ~x:2.5 taking into account a suitable velocity for the sediments.*

- *South Alboran Basin*

Between the African continental platform and the Alboran Ridge is located the SAB. In bathymetric maps this sub-basin is a SW-NE elongated depression (Fig. 6.1). The maximum sediment thickness is ~1.3 s TWTT. The depocenter runs parallel to the main trend of the Alboran Ridge, and the basement top gradually shallows towards the African margin. ODP Leg 161 Site 979 (Fig. 6.2) provides accurate calibration of the shallow sedimentary sequence, reaching down to the Upper Pliocene. Dredged samples reveal a volcanic nature for the basement of the Alboran Ridge that possibly extends under this basin (Aparicio et al., 1991; Duggen et al., 2004; Gill et al., 2004; Duggen et al., 2005; Duggen et al., 2008). The volcanic units overlaying the basement are further described in the next section. Profiles EVDT1-3A, EVDT1-3B, TM16 (Fig. 6.17), TM05, TM04 and TM03 (Fig. 6.18) image this basin (Fig. 6.2).

The volcanic units flooring the basin present high amplitude in the seismic profiles (Fig. 6.17, 6.18). It base is not well defined, and we mapped it along a decrease in the amplitude (black dots in Figures 6.15, 6.18). The tectonic structure of this basin is discussed in the Alboran Ridge chapter (Chapter 9, this volume).

- *East Alboran Basin and its connection with the Algero-Balearic Basin*

The EAB is a triangular shaped basin (Fig. 6.1) limited to the south by the Yusuf Fault system, to the north by the southeast Iberian continental platform and to the east by the Algero-Balearic Basin. The two largest ridges inside the basin, the Al-Mansour and the Yusuf Ridges (Fig. 6.1) have been dredged. Additionally, ODP Leg 161, sites 977 and 978 were drilled (Fig. 6.2), providing calibration of the sedimentary sequence. The transition to the Algero-Balearic Basin deep plain is gradual and occurs at water depth >2500 m (Acosta et al., 2013), when the plain shows its smoothed surface only disrupted by halokinetic structures (Camerlenghi et al., 2009; Gómez de la Peña et al., 2016).

Dredged sites indicate the volcanic nature of the basement of the EAB that in seismic images transitions to the east to oceanic crust flooring the Algero-Balearic Basin (e.g. Booth-Rea et al., 2007).

In the seismic profiles, the EAB volcanic units show high-reflectivity and alternate chaotic zones with well-layered areas. The base of these units is interpreted at a decrease with TWTT in the reflectivity, shown in the interpretation with a green dashed line (Fig. 6.19). The tectonic structure of this basin is further discussed at the Yusuf Fault chapter (Chapter 8, this volume).

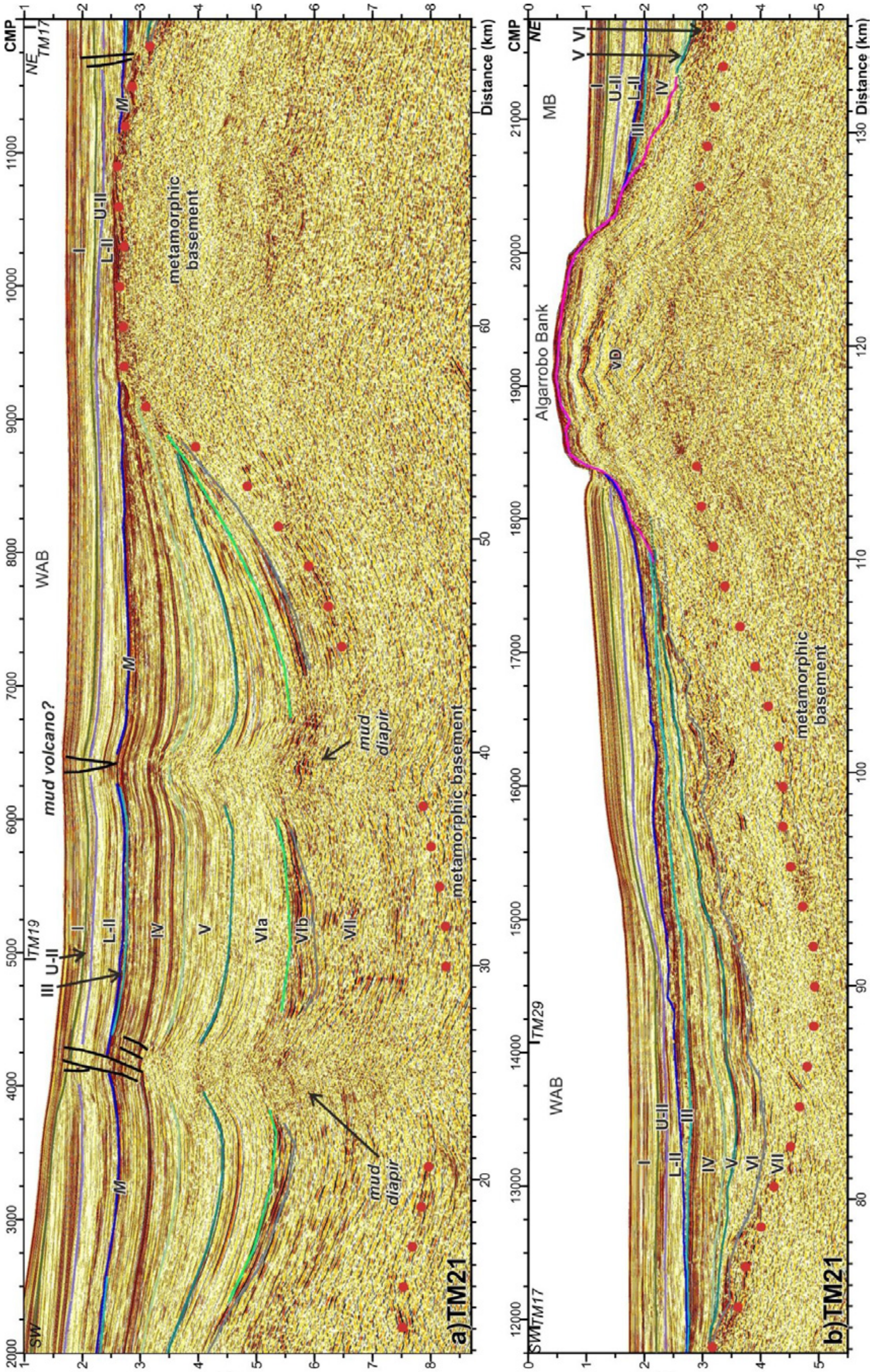
a)TM21
CMP
2000
3000
4000
5000
6000
7000
8000
9000
10000
11000
TWTT (s)
1
2
3
4
5
6
7
8
Distance (km)
20
30
40
50
60
SW
NE
TM17
TM19
WAB
mud volcano?
mud diapir
mud diapir
metamorphic basement
metamorphic basement
I
U-II
L-II
III
IV
V
VIa
VIb
VII
M
b)TM21
CMP
12000
13000
14000
15000
16000
17000
18000
19000
20000
21000
TWTT (s)
0
1
2
3
4
5
Distance (km)
80
90
100
110
120
130
SW
NE
TM17
TM29
WAB
MB
Algarrobo Bank
VD
I
U-II
L-II
III
IV
V
VI
VII
metamorphic basement

◄ ***Figure 6.8:*** *Time migration of profile TM21, running across the WAB in a SW-NE section (see location in Figure 6.2). This profile is divided in a) Southwestern section and b) Northeaster section. The SW side is characterized by a thick unit VII, and the presence of unit VIb. These units are feeding the mud diapirs. The easternmost diapir possibly arrives till the seafloor, forming a mud volcano. The sedimentary sequence shows similar characteristics that in previous profiles, with the Miocene units onlapping above the basement and a unit IV that increases its thickness towards the basin depocenter. The M reflection seems concordant in the SW (CMP 2000-6000), and becomes an unconformity near the basement high (CMP 8000-9000) and at the northern side (CMP 12000-21000). Main structures and seismostratigraphic units are identified. Age of the units is defined in Figure 6.3. Vertical exaggeration is of ~x:2.5 taking into account a suitable velocity for the sediments.*

6.2.3. Alboran Basin stratigraphical evolution

Along this section, we will interpret the characteristics of the seismic units mapped across the Alboran Basin, from the oldest to the most recent, and taking into account the previous description of the similarities and differences among the sub-basins.

- *Early Miocene units: Aquitanian – Early Serravallian*

Only two regions have sedimentary records of the Early Miocene: The WAB extending into the MB, and the HBB with PB.

Unit VII is the oldest identified unit and it is only found at the **WAB** and **MB** (Fig. 6.1). In the areas where it is undisturbed by mud diapirism it is characterized by high amplitude reflections with poor lateral continuity that onlap the basement (Fig. 6.6a CMP 20000-15000, Fig. 6.7b CMP 11000-14000, Fig. 6.9, Fig. 6.11). This unit reaches a maximum thickness of ≤3 s TWTT at the WAB, while its maximum thickness in the MB is ~1 s TWTT. Unit VII is confined by basement highs.

Unit VI onlaps unit VII (Fig. 6.5b CMP 11000-10000, Fig. 6.8a CMP 2000-3000, 7000-9000). Two sub-units are identified: VIb and VIa. Sub-unit VIb is characterized by a chaotic seismic facies (Fig. 6.6a CMP 20000-16000, Fig. 6.7 CMP 12000-17000) alternating with well-layered zones (Fig. 6.8, Fig. 6.10). This unit has a maximum thickness of 0.8 s TWTT. Units VIb and VII, appear to be overpressure being the source of the mud diapirism observed at the WAB (e.g. Fig. 6.5a CMP 14000-12000, Fig. 6.7a-b, CMP 4000-10000) (Comas et al., 1999; Soto et al., 2012). Some diapirs pierce the sediment cover to the seafloor, generating mud volcanism (Fig. 6.8a CMP 6000-7000, Fig. 6.10 CMP 3000-2000). Unit VIa shows parallel continuous reflections, usually with lower reflectivity than underlying units (Figs. 6.7, 6.8) and a maximum thickness ~1 s TWTT both in the WAB and MB (Fig. 6.11).

In **HBB** and **PB**, the oldest sediment is unit L (Early Serravalian – Langhian?). This unit is characterized by scattered reflections with a base that is not clear in seismic images, and transitions to a high-reflectivity basement (Figs. 6.14, 6.15). Above it, unit S (Late Serravallian – Early Tortonian) is characterized by low continuity reflections with changing dips that indicate folding of strata that appears syn-sedimentary (Fig. 6.15d). This unit shows variations in thickness, ranging from 0.3-1 s TWTT (Figs. 6.14, 6.15, 6.16). Units L and S define a gentle synclinorium with its deepest part at the basin depocenter (Fig. 6.14, Fig. 6.15c, 6.16b).

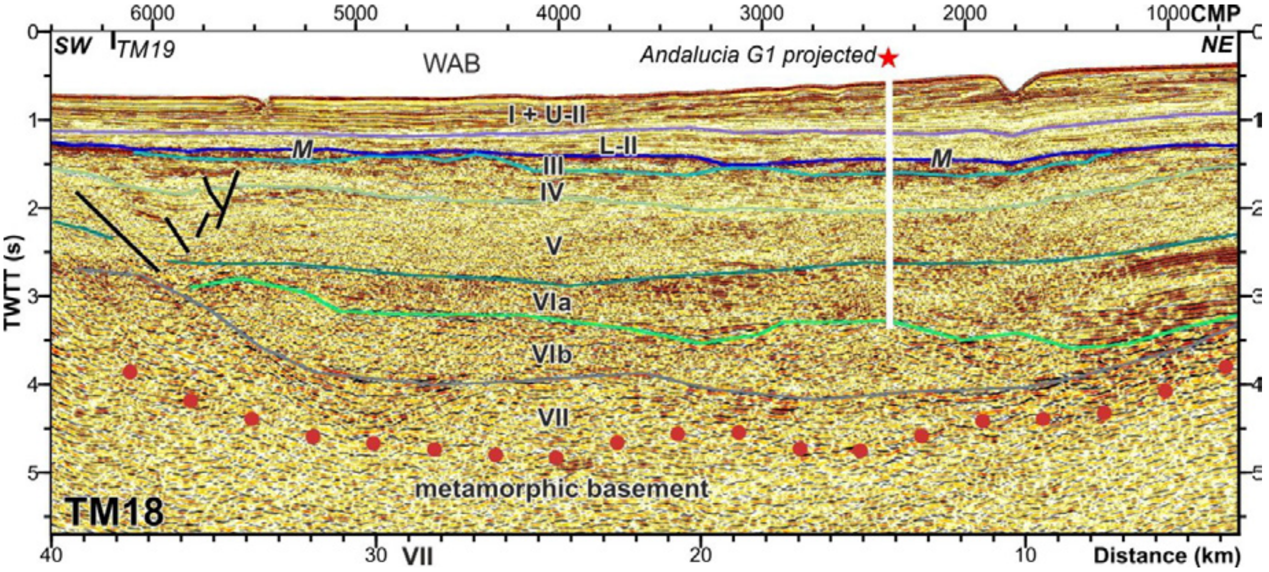

***Figure 6.9* ▲:** *Time migration of profile TM18 (see location in Figure 6.2). This line runs parallel to the northern margin of the WAB. Although due to the steepness of the margin the sedimentary thickness highly increases in N-S direction, this profile is correlated with the Andalucia G-1 well, located north, using the CAB cruise profiles (Fig. 6.2). Main structures and seismostratigraphic units are identified. Age of the units is defined in Figure 6.3. Vertical exaggeration is of ~x:2.5 taking into account a suitable velocity for the sediments.*

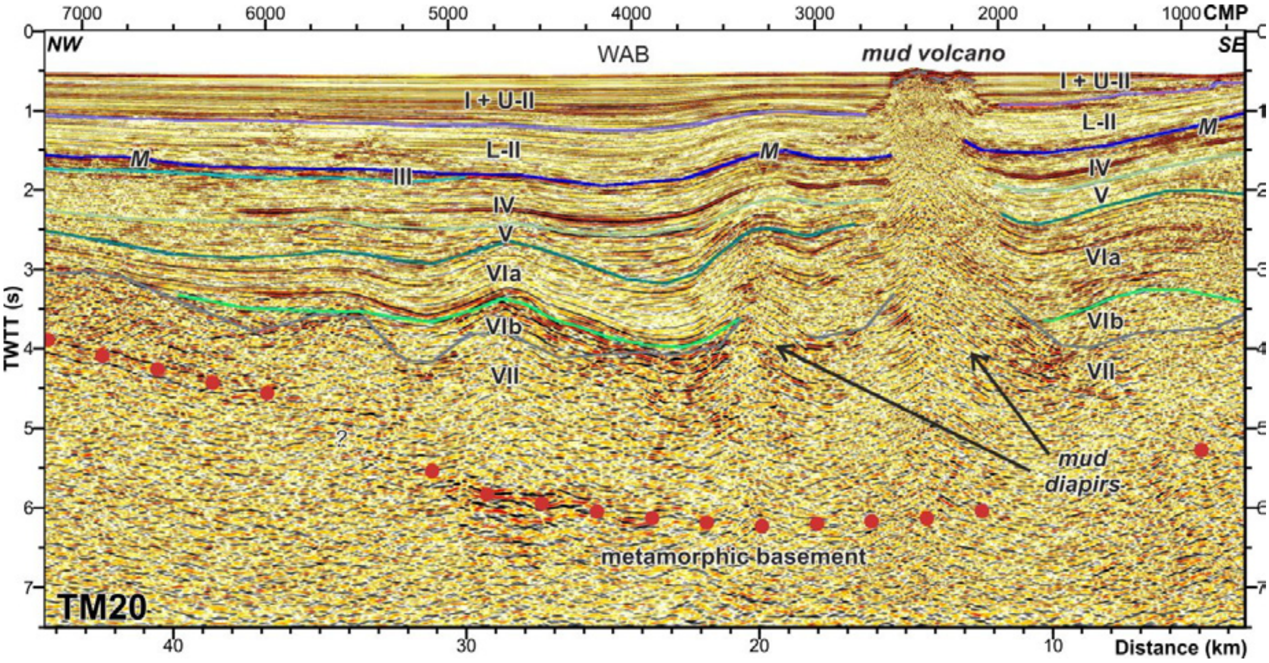

***Figure 6.10* ▲:** *Time migration of profile TM20 (see location in Figure 6.2). This profile runs parallel to the SW margin of the WAB. Above the basement, a thick unit VII is imaged, feeding a mud diapir that clearly arrives till the seafloor and creates a mud volcano. The M reflection is concordant. Main structures and seismostratigraphic units are identified. Age of the units is defined in Figure 6.3. Vertical exaggeration is of ~x:2.5 taking into account a suitable velocity for the sediments.*

- *Late Miocene units: Late Serravallian - Messinian*

During the Tortonian different processes coexisted in the Alboran Basin. While the sedimentation at the WAB and MB, and at the HBB and PB depocenters continued, magmatic activity in the SAB, Djibouti Plateau and EAB began (Fig. 6.3).

In the **WAB** and **MB** depocenters, Tortonian period is represented by two units: unit V (Late-Serravallian – Early Tortonian) and unit IV (Late Tortonian) (Fig. 6.3). Unit V is characterized by parallel reflections (Fig. 6.7b 10000-14000, Fig. 6.8a) <2.7 s TWTT thick in the WAB (Fig. 6.6a) and <1 s TWTT in the MB (Fig. 6.11a). In the WAB, this unit exhibits a wedge-shape increasing its thickness towards the basin depocenter and laps on the oldest sediment unit and basement top (Fig. 6.6a CMP 20000-15000). Unit IV is characterized by parallel well stratified reflections (Figs. 6.7b, 6.11) that laps on unit V (Fig. 6.6a CMP 20000-18000). At the WAB it maximum thickness is 0.9 s TWTT, and at the MB is 1.3 s TWTT.

Unit III (Messinian) in the WAB and MB is represented by discontinuous deposits with a chaotic appearance (Fig. 6.6a, 6.7, 6.11). This unit is bounded at its top by the M reflection, that appears a conformity across the central parts of WAB and MB sub-basin (Fig. 6.6a CMP 19000-17000, Fig. 6.7a CMP 3000-4000, Fig. 6.7b CMP 10000-14000, Fig. 6.8a CMP 2000-8000, Fig. 6.9, Fig. 6.10, Fig. 6.11a CMP 1000-10000) and exhibits an erosive character towards the flanks (Fig. 6.8a CMP 8500-9500), where a toplap of unit IV reflections occurs against the M.

Towards the east of the MB, the sediment units are intercalated with volcanic units of the Carboneras Fault (vC). At the easternmost end of the MB it is found the Chella Bank. We interpret that the structure of this high supports that is a volcanic construction with two aprons on either side of the Bank (Fig. 6.11b CMP 12000-16000). The volcanic building onlaps unit V and is covered by unit IV and younger sediments, so a Tortonian age is proposed for this volcanic structure. Towards the south, a similar situation occurs with the volcanic units of the Djibouti Plateau (vD) (Fig. 6.12). Again, the volcanic unit onlaps sediment unit V, and is covered by unit IV, implying a Tortonian age. Profile TM28 (Fig. 6.13) displays a W-E transect across the Djibouti Plateau, showing how the sediment cover thins to a maximum ≤1 s TWTT and the oldest unit identified is III, and perhaps unit IV, which agrees with a Late Tortonian age for vD units.

In the **HBB** and **PB**, unit T (Late Tortonian) displays a large change compared to older units S and L. It is filling with onlapping geometry lows created by previous folding of units S and L (Figs. 6.14, 6.15c-d). The thickness of this unit is variable, reaching ≤1.3 s TWTT (Fig. 6.15b).

Lapping on unit T, occurs unit III that can be divided in the HBB in sub-unit IIIb (Lower Messinian) with well-layered continuous packages of reflections (Fig. 6.14 CMP 4000-2000, Fig. 6.15c), and sub-unit IIIa (Upper Messinian) with high-amplitude reflections (Fig. 6.14, Fig. 6.15c). Above unit T, occurs a chaotic body (c) exhibiting a boudinage morphology. The body is not continuous along the profiles; it is limited by an irregular M reflection at its top, and a relatively smooth reflection at its base (Fig. 6.14, Fig. 6.15c, 15d). It thickness is <0.4 s TWTT. The M reflection presents an erosive geometry at the HBB (Fig. 6.14, 15b CMP 1000-3000), while seems to be rather concordant at the PB (Fig. 6.16), but channel incision is locally recognized along the M reflection (Fig. 6.14 CMP 5250-6000 and CMP 1250-1750). Unit III thickens toward the HBB depocenters, where it is ~1.4 s TWTT thick, and thins towards the west, where in the HBB is ≤0.7 s TWTT.

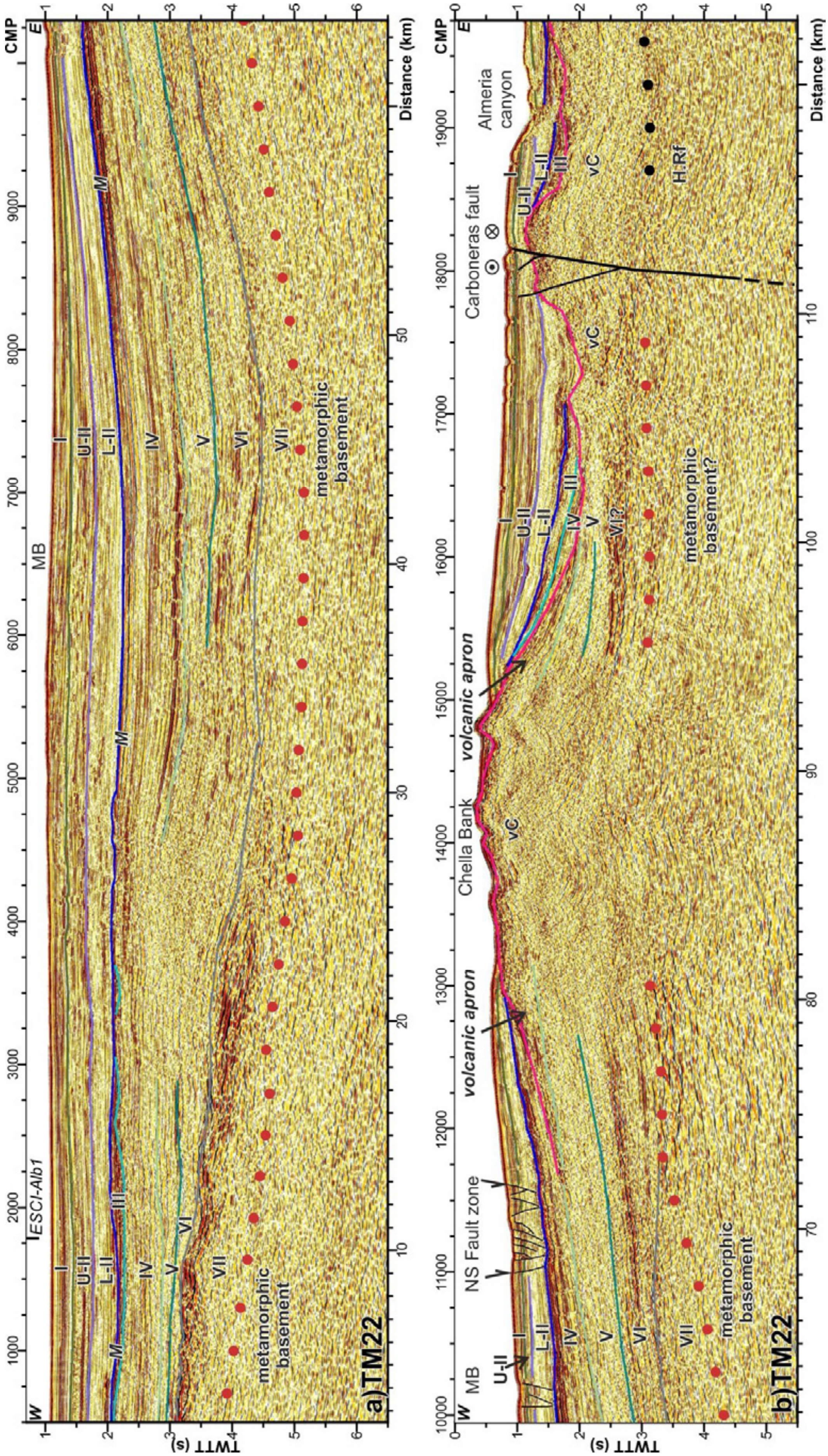
a)TM22
b)TM22
CMP
W
E
TWTT (s)
Distance (km)
ESCI-Alb1
MB
I
U-II
L-II
III
IV
V
VI
VII
M
metamorphic basement
metamorphic basement?
VI?
NS Fault zone
volcanic apron
Chella Bank
vC
Carboneras fault
Almeria canyon
H-Rf
1000
2000
3000
4000
5000
6000
7000
8000
9000
10000
11000
12000
13000
14000
15000
16000
17000
18000
19000
10
20
30
40
50
70
80
90
100
110
0
1
2
3
4
5
6

◄ ***Figure 6.11:*** *Time migration of profile TM22 (see location in Figure 6.2). This profile is divided in a) Western section and b) Eastern section. This profile runs across the southern margin of Iberia, imaging in a W-E section the northern part of the Alboran Basin. Starting from the eastern part, we can see a deep sedimentary basin, the Malaga Basin, with a maximum thickness of almost 5 s in TWTT. The sedimentary units are correlated with the ones in the WAB (Fig.7. 8). This sedimentary sequence is getting thinner towards the east, where is disrupted by the Chella Bank, a volcanic high. Layering is recognized inside this high, which could be related with the volcanic activity. This volcanic building is constructed above unit V, and is postdated by units IV and III. The most relevant tectonic structure in this profile is the Carboneras fault, a left-lateral strike-slip fault, southernmost end of the Eastern Betics Shear Zone. It is an active fault, also affecting the basement of the basin. The erosive structure located to its east side corresponds to the Almeria Canyon. Main structures and seismostratigraphic units are identified. Age of the units is defined in Figure 6.3. Vertical exaggeration is of ~x:2.5 taking into account a suitable velocity for the sediments.*

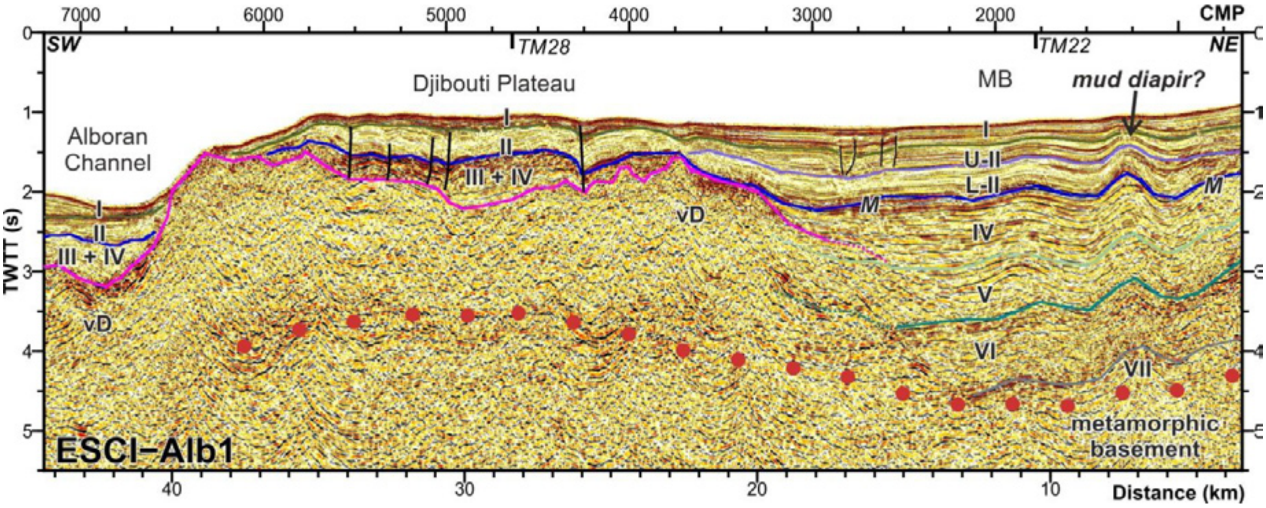

Figure 6.12 **▲:** *Time migration of profile ESCI-Alb1 (see location in Figure 6.2). This profile runs in a NNE-SSW direction along the MB, imaging its connection with the Djibouti Plateau. The northern part of the profile shows the deep sedimentary basin, with similar characteristics to the WAB, and its abrupt contact with the volcanic unit of the Djibouti Plateau (CMP 3500-2000). The Miocene units are onlapping the high, while the Pliocene units get over vD. Main structures and seismostratigraphic units are identified. Age of the units is defined in Figure 6.3. Vertical exaggeration is of ~x:2.5 taking into account a suitable velocity for the sediments.*

In the **SAB,** stratigraphy supports that the first volcanic activity begun at the Late Serravallian – Early Tortonian. Two volcanic units are identified in this area: Unit vA2 with a rough top with highs and lows reliefs associated (e.g. Fig. 6.17c), and a base that is not clearly imaged, and has been associated with a gradual change in reflectivity (dashed black line, Fig. 6.17b, c). Above unit vA2 is unit vA1 (Fig. 6.17b) showing also a volcanic character: internal structure consists of alternating high-amplitude reflections and chaotic zones (Fig. 6.17b CMP 17000-17500) with stratified bodies showing parallel reflections (Fig. 6.17b CMP 16000-14000). Line EVDT1-3a (Fig. 6.17b) images the deep-basin part of unit vA1. Southern this profile, at line TM16, unit vA1 is not present and the sedimentary sequence is located directly above unit vA2.

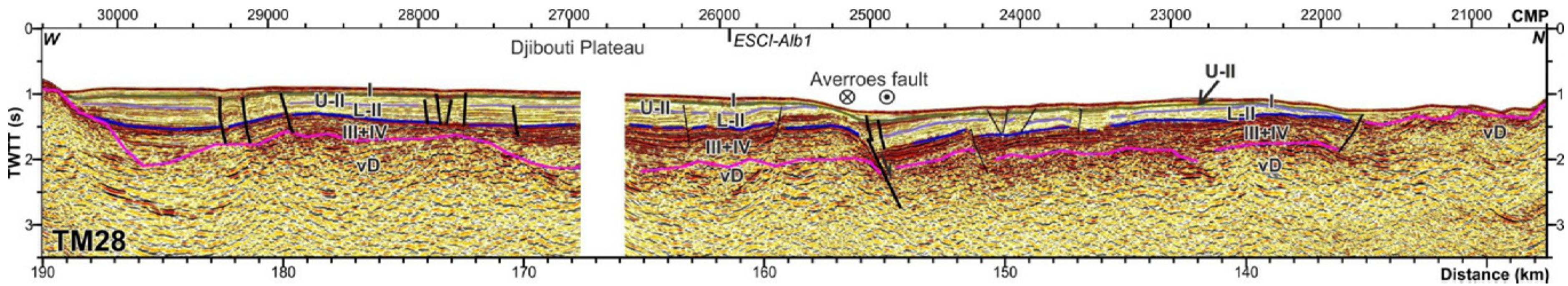

▲ ***Figure 6.13:*** *Time migration of profile TM28 (see location in Figure 6.2). This profile images the Djibouti Plateau. It is noticed the difference in the sedimentary cover between the Djibouti Plateau and the WAB and MB. Here, the sedimentary sequence is less than 1 s TWTT and the record begins with unit III-IV?. Main structures and seismostratigraphic units are identified. Age of the units is defined in Figure 6.3. Vertical exaggeration is of ~x:2.5 taking into account a suitable velocity for the sediments.*

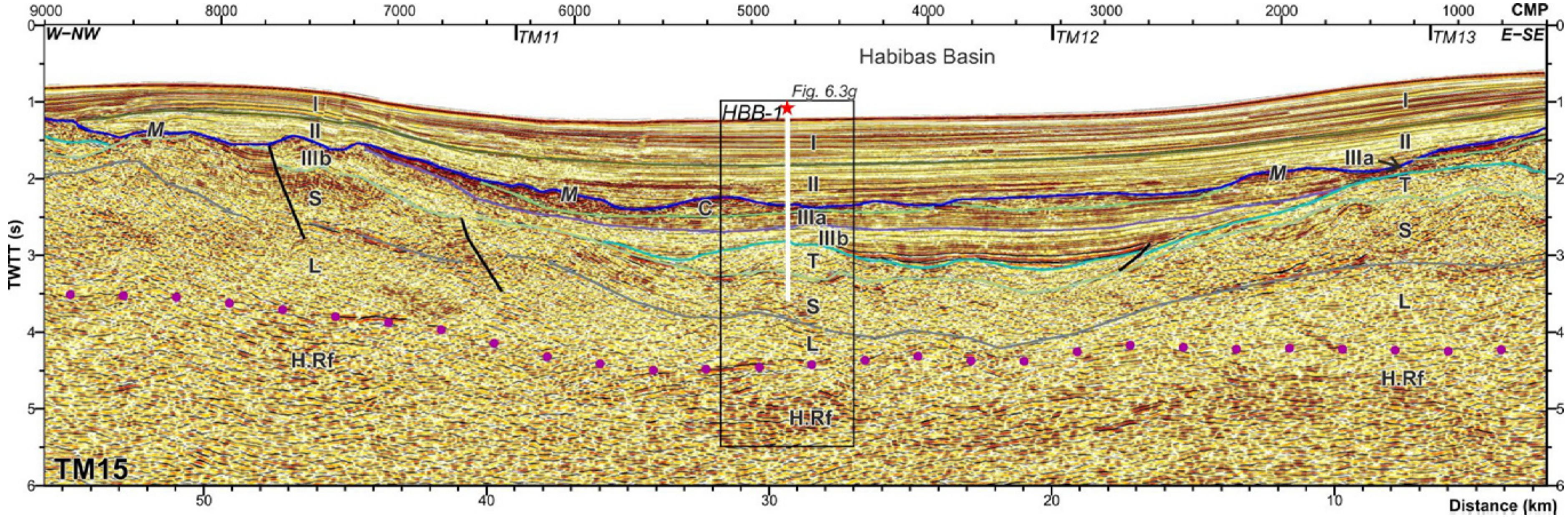

▲ ***Figure 6.14:*** *Time migration of profile TM15 (see location in Figure 6.2). This profile runs across the HBB. The top of the crustal high reflectivity body is imaged. The deeper sedimentary units, S and L, appear folded, with units T and III onlaping them. The Messinian reflection exhibits signs of erosion and channel incision. HBB-1 well site is depicted. Main structures and seismostratigraphic units are identified. Age of the units is defined in Figure 6.3. Vertical exaggeration is of ~x:2.5 taking into account a suitable velocity for the sediments.*

The first non-volcanic sedimentary unit in this area is (upper Tortonian?) Messinian unit III, only identified within volcanic basement lows in segments of the profiles (e.g. Fig. 6.17c CMP 12000-10000, Fig. 6.17c CMP 7000-6000), while in other segments the Messinian erosion cuts into the volcanic basement (Fig. 6.17c CMP ~10000). Unit III is <0.5 s TWTT with chaotic internal reflectivity. The top M reflection is conformable in the deeper parts of the deepest sub-basins (Fig. 6.17c CMP 7000-4000). The thickness of unit III increased from south to north, being a discontinuous unit infilling the basement lows at the SAB (Fig. 6.17, 18) and ~1.2 s TWTT thick near the Alboran Ridge (Fig. 6.3, 6.18c, "Chapter 9: The Alboran Ridge").

Finally, the volcanic basement of **the EAB** was also created about that age. On the basis of dredged rocks dating (e.g. Duggen et al., 2004) and seismic images, three successive volcanic units occur in this area. The oldest unit vY2 located to the east next the Yusuf Ridge, with parallel wavy reflections, high dips and fan shape strata toward the steep flanks (Fig. 6.19a CMP 12000-11000) with a maximum thickness of ~1 s TWTT. Unit vY1 crops out at the Al-Mansour Ridge (Fig. 6.19a CMP 13500-11250). This high exhibits a characteristic triangular shape, with internal wavy reflections defining an apron along each flank. The limit between these two units is not sharp, and they are probably overlapped in time and inter fingered with a lateral change of facies (Fig. 6.19a CMP 11500-9500, Fig. 6.19b CMP 4000-1000). Towards the Algero-Balearic Basin, a third and oldest volcanic vY3 unit forms a roughly E-W ridge in bathymetry (Figs. 6.1, 6.2). Its age is unknown. The base of all volcanic units is a change in the reflectivity rather than a sharp boundary (dashed green line in Figure 6.19).

Above the volcanic basement, the first sedimentary unit identified in the EAB is a <0.3 s TWTT thick unit IV (Fig. 6.19a) with a top-lap geometry against the base of Unit III (Fig. 6.19a CMP 10750-11000). Unit III changes from west to east: In the western part exhibits high-reflectivity reflections with variable dips (Fig. 6.19a CMP 11500-1000) <0.3 s TWTT thick, and bounded at its top by an erosional M unconformity. In the eastern part, unit IV is not identified and unit III greatly increase in thickness to ≤1.3 s TWTT. It can be divided in sub-unit IIIa and IIIb. Sub-unit IIIb exhibits low reflectivity and parallel reflections (Fig. 6.19b, c). Sub-unit IIIa can be subdivided in three (UU, MU, LU, Fig. 6.3) at the eastern deep basin, where evaporites are found (Fig. 6.19c, d). The base of the MU is an inverse polarity continuous reflection (Fig. 6.19c CMP 13000-9250, Fig. 6.19d CMP 3500-5000) that acts as a décollement surface promoting sliding of the overlaying sediments. This gliding causes normal faulting of units I and II, with faults of listric geometry (Fig. 6.19c CMP 10000-9250). The M reflection at top of this sequence is a concordant surface in the eastern sector of the deep basin (Fig. 6.19c, d).

- *Plio-Pleistocene units*

The Plio-Pleistocene units are easily correlated along the entire basin, as they are not confined to the different depocenters and onlap basement highs blanketing the entire basin. Differences between units can be proposed by changes in particular tectonic features in different areas.

Figure 6.15* ►:** *Time migration of profiles TM14* ***(a)*, TM13* ***(b)****, TM12* ***(c)****, and TM11* ***(d)*** *(see location in Figure 6.2), running perpendicular to TM15 (Fig. 6.14). These profiles show the HBB variations from east to west. Main structures and seismostratigraphic units are identified. Age of the units is defined in Figure 6.3. Vertical exaggeration is of ~x:2.5 taking into account a suitable velocity for the sediments*

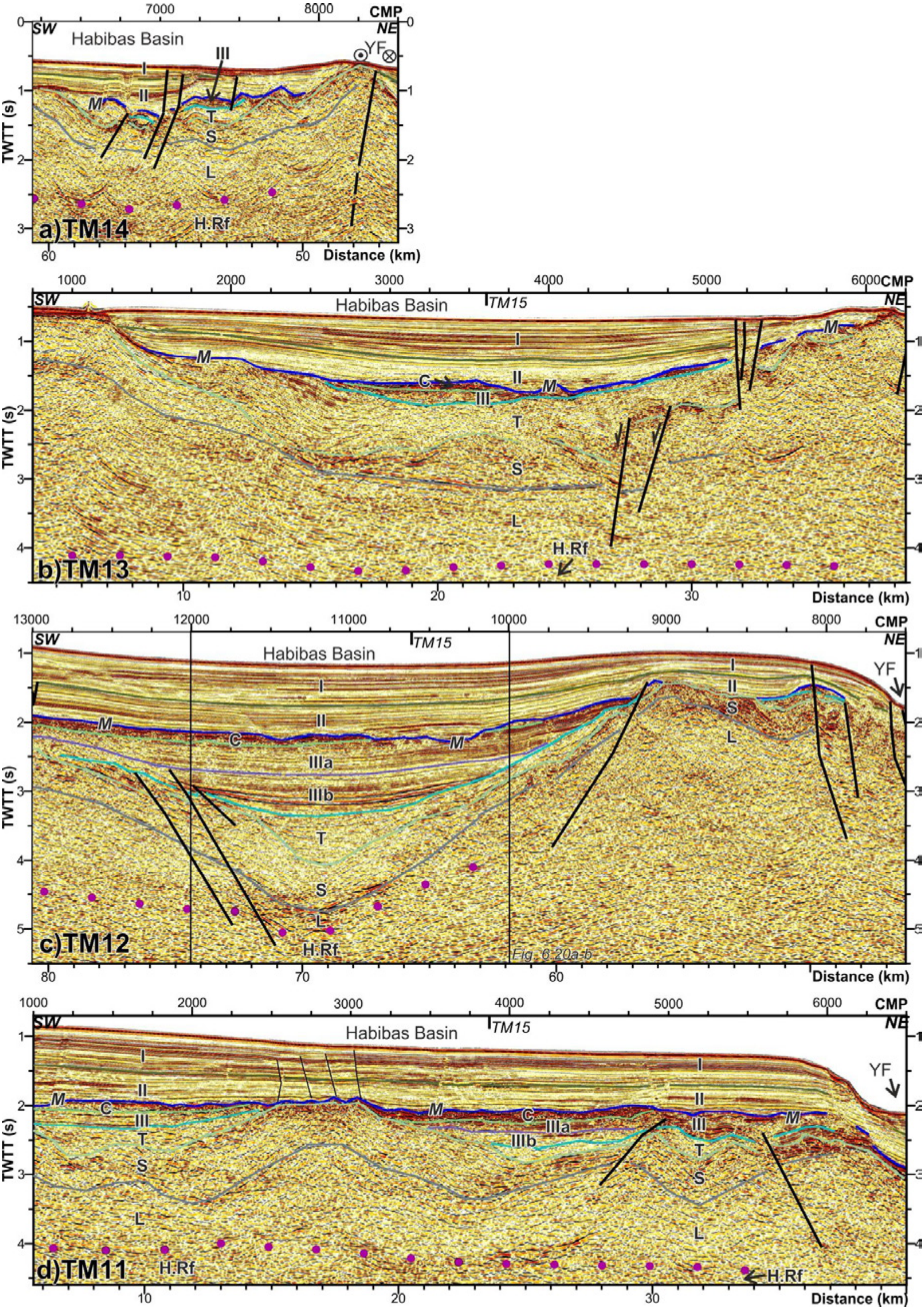
a)TM14
SW
NE
Habibas Basin
CMP
7000
8000
YF
I
II
III
M
T
S
L
H.Rf
TWTT (s)
0
1
2
3
60
50
Distance (km)
b)TM13
Habibas Basin
TM15
1000
2000
3000
4000
5000
6000
M
C
I
II
III
T
S
L
H.Rf
10
20
30
c)TM12
Habibas Basin
TM15
13000
12000
11000
10000
9000
8000
YF
I
II
IIIa
IIIb
M
C
T
S
L
H.Rf
Fig. 6.20a-b
80
70
60
d)TM11
Habibas Basin
TM15
1000
2000
3000
4000
5000
6000
YF
I
II
III
IIIa
IIIb
M
C
T
S
L
H.Rf

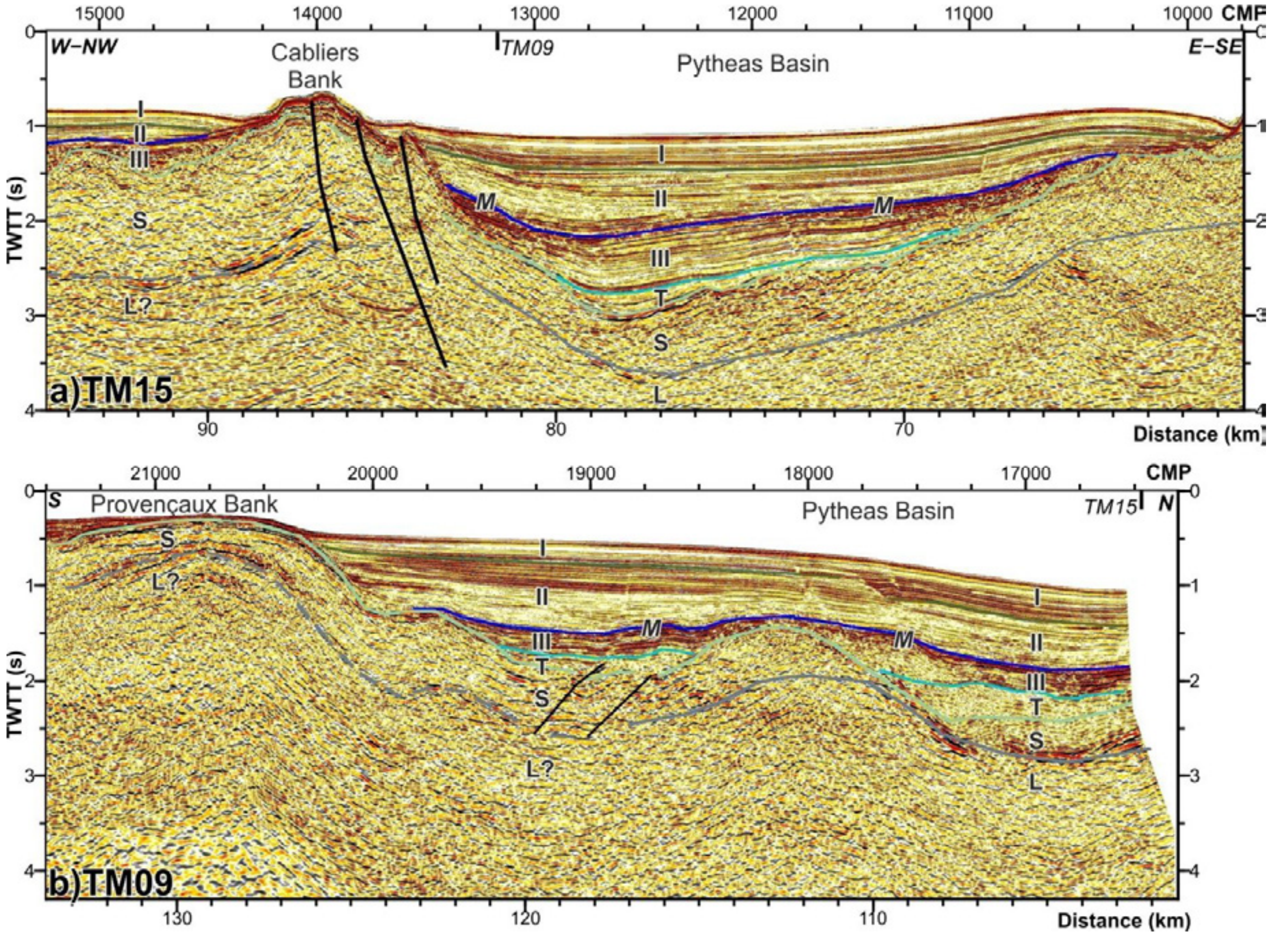

Figure 6.16* ▲*: *Time migration of profiles TM15* ***(a)*** *and TM09* ***(b)*** *in the PB section (Fig. 6.2). This basin presents similar characteristics than the HBB, with the lower units S and L folded and the Late Miocene – Pliocene sequence lapping them. Main structures and seismostratigraphic units are identified. Age of the units is defined in Figure 6.3. Vertical exaggeration is of ~x:2.5 taking into account a suitable velocity for the sediments.*

Unit II (Pliocene – Gelasian) in the **WAB** is subdivided in two: L-II (Lower Pliocene) and U-II, Upper Pliocene (Gelasian, Fig. 6.3). This unit presents well-layered continuous parallel reflections, with a low reflectivity character for unit L-II. In the WAB it is associated with contourites and turbidite deposits (e.g. Estrada et al., 1997; Palomino et al., 2011; Somoza et al., 2012; Juan et al., 2016). These units thin toward the basin flanks, to ≤1.6 s TWTT (Fig. 6.7a CMP 1000-4500). In the **MB**, it presents similar characteristics and is ≤1 s TWTT thick. In the **HBB** and **PB** unit II is ≤0.7 s TWTT thick, with parallel continuous reflections that cannot be subdivided (Figs. 6.14, 6.15), and laps on the M reflection. In the **SAB** it is affected by the Alboran Ridge uplift and as a consequence of the deformation, four internal sub-units are identified (Martínez-García, 2012). Sub-unit IId and IIc. Sub-unit IId, ≤0.35 s TWTT thick, and sub-unit IIc, ≤0.4 s TWTT thick, are characterized by parallel reflections. These units are lapping on Messinian unit III or on volcanic basement. Their thickness is fairly constant, except in the easternmost SAB (Fig. 6.18c) where they thin away from the Alboran Ridge. Sub-unit IIb has a similar seismic expression as unit IIc but its top is defined by an erosional unconformity (e.g. Fig. 6.18b CMP 5000-4000). Sub-unit IIb thickens towards the depocenter, ≤0.5 s TWTT (Fig. 6.8c). Sub-unit IIa laps on the erosional unconformity bounding unit IIb. It is a discontinuous unit (Fig. 6.18b) ≤0.25 s TWTT thick and bounded at its top by another erosional unconformity (Fig. 6.18b CMP 5000-4000, Fig. 6.18c CMP 5250-7000).

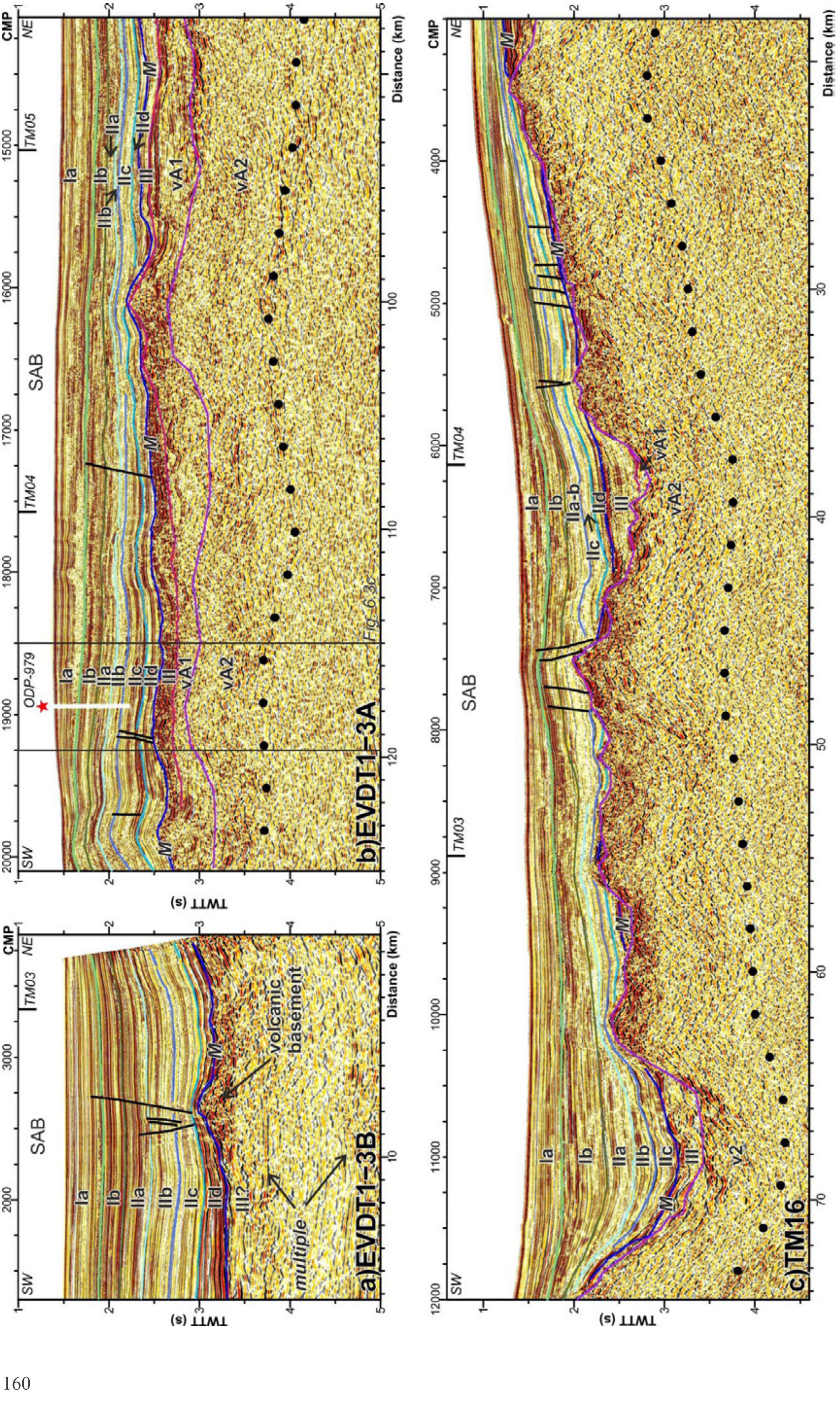
a) EVDT1-3B
b) EVDT1-3A
c) TM16
CMP
SW
NE
TWTT (s)
Distance (km)
SAB
TM03
TM04
TM05
ODP-979
Fig. 6.3c
Ia
Ib
IIa
IIb
IIc
IId
III
III?
IIa-b
M
vA1
vA2
v2
volcanic basement
multiple

◄ ***Figure 6.17:*** *Time migration of profiles EVDT1-3B* ***(a),*** *EVDT1-3A* ***(b)*** *and TM16* ***(c),*** *parallel to the SAB depocenter (Fig. 6.2). Profiles EVDT1-3A and EVDT1-3B were acquired during the EVENT-DEEP cruise (2010) with different seismic acquisition parameters than the TOPOMED –GASSIS cruise (2011). While TM16 and EVDT1-3B profiles has been processed following the processing flow presented at the Data and methods section, processing of profile EVDT1-3A has been different. The main goal was to obtain a clear image of the sedimentary infill in the SAB, in order to allow a neat unit correlation and to characterize the high variability across the SAB. Seismic processing includes trace position based on the shots position, spherical divergence correction, normal-move-out correction based on velocity semblance analysis, stretching mute, amplitude recovery, time migration and a time and spatial variant band-pass filter. Main structures and seismostratigraphic units are identified. Age of the units is defined in Figure 6.3. ODP 979: ODP Leg 161 site 979. Vertical exaggeration is of ~x:2.5 taking into account a suitable velocity for the sediments.*

The two bounding unconformities are also identified in the southern sector of the WAB, and possibly extend to the western sector of the **EAB**. In the eastern EAB, unit II is ≤0.4 s TWTT, with continuous parallel reflections.

Unit I (Calabrian – Upper Pleistocene) exhibits similar characteristics in the **WAB, MB, HBB** and **EAB**, being ≤0.7 s TWTT thick with a well-layered internal structure. In the WAB and the HBB, it gently thickens toward the basin depocenter (Fig. 6.8a, 6.15b). In the **SAB**, it is deformed by the Alboran Ridge tectonics and can be divided in sub-units Ib and Ia. Both units are characterized by parallel continuous reflections, but they are separated by an angular unconformity with sub-unit Ia lapping on this unconformity (Fig 6.18a CMP 7000-8000). The maximum thickness of sub-unit Ib is ≤0.7 s TWTT thick, and sub-unit Ia is ≤0.6 s TWTT thick. The gradual thinning towards the Alboran Ridge of both units II and I indicates a tectonic controlled discussed in the Alboran Ridge chapter (Chapter 9, this volume).

6.3. Discussion

6.3.1. Formation and evolution of the West Alboran and Malaga basins

The first sedimentary deposit is unit VII that occurs at the deepest part of the depocenters. Internal geometry and thickness appear fairly regular, but due to the extensive mud diapirism its depositional geometry is unclear. Unit VII has been interpreted as an olistostromic unit linked to the first deposits of the basin (Comas et al., 1999; Martínez del Olmo and Comas, 2008; Soto et al., 2010; Soto et al., 2012), although Do Couto et al. (2016) hypothesizes it is part of the Malaguide complex of the Alboran Domain. Units VIa and V slightly thicken towards the depocenter (e.g. Fig. 6.8a CMP 2000-9000). This thickening is more pronounced for unit IV that exhibits a fan shape towards the basin centre (e.g. Fig 6.8a CMP 2000-9000). This sequence is is bounded at its top by the M reflection. Sediment infill is 4 s TWTT in the MB (Fig 6.8), thinner than in the WAB, where it is >7 s TWTT in the deepest parts (e.g. Figs. 6.6, 6.7). This difference in basin subsidence may be related to the differences in basement thickness, as discusses in the previous chapter ("Chapter 5: Crustal domains").

The M reflection interpreted as top of Messinian unit III in the most of the MB and deepest sector of WAB appears concordant (Fig. 6.7b CMP 7000-11000, Fig. 6.8a CMP 2000-8000, Fig. 6.10, Fig. 6.11a CMP 5000-9000). It only presents a clear erosive character near the basement highs of basin flanks (Fig. 6.6a CMP 16000-15000, Fig. 6.8a CMP 8500-9500). This supports that parts of the WAB and MB may not have been fully desiccated during the Messinian Salinity Crisis. It is worth noticing the similarity between the Pre-Messinian sequence of the WAB and that of HBB. On the basis of this similar seismic expression of the units, we propose an alternative interpretation of the units found in the WAB, which includes preserved sedimentary deposition in Messinian times under the M reflection and a thicker Tortonian unit

(Fig. 6.20). This interpretation is supported by the roughly similar ages of the Mass Transport Deposits found at the Messinian top. In the HBB, the uppermost Miocene sequence ends with chaotic deposits, discontinuous along the profiles (indicated with a "c" at Figures 6.14, 6.15, 6.20b). Below these chaotic deposits, we interpreted an upper Messinian unit, unit IIIa, characterized by parallel continuous reflections. It is underlaid by lower Messinian unit IIIb with typical parallel reflections that increase in reflectivity toward the unit´s base. This sequence overlies the T unit, with lower reflectivity and Tortonian in age (Figs. 6.14, 6.15, 6.20b).

In the WAB, we interpreted the late Miocene units based on previous studies (Soto et al., 2010, 2012, Do Couto et al., 2016), which describe a thin Messinian unit, unit III, with a chaotic geometry and discontinuous character (Figs. 6.5 – 6.10, 6.20d). This unit is above a Tortonian unit IV characterized by high reflectivity layering. Unit V, Tortonian - Serravallian in age and immediately below unit IV, is characterized by a lower reflectivity in its upper part and presents internal discordances (Figs. 6.5 – 6.10, 6.20d). Due to the similarities in seismic expression of Late Miocene sediment of the HBB and WAB, and the non-erosive character of the M reflection at the centre of the WAB, we propose a revised interpretation for the WAB, in which a thicker Messinian unit III is included (Fig. 6.20e). The current unit III, discontinuous and with a chaotic internal structure, may be the equivalent for the upper Messinian chaotic deposits found at the HBB (and in other regions like the Valencia Through, e.g. Cameselle and Urgeles, 2015). The upper part of unit IV in WAB is correlated with upper Messinian unit IIIa in HBB, with a similar seismic facies of continuous, parallel reflections (Fig. 6.20d-e). The lower part of unit IV and the upper part of unit V in WAB will be the equivalent to unit IIIb in HBB, exhibiting a characteristic increase in layer reflectivity towards its base (Fig. 6.20d-e). Finally, the newly interpreted unit IV in WAB will be the low reflectivity upper part of the previously interpreted unit V (Fig. 6.20d-e). The new unit V will correspond to only the lower part of the previously interpreted unit V (Fig. 6.20e). This new interpretation is in agreement with available drillings information, but might be tested with a revision of the core samples of Andalucia G-1, ODP Leg 161 Site 976 and DSDP Leg 121. Pliocene units cover the entire Alboran basin, presenting relatively similar seismic characteristics along the basin.

These observations imply three distinct phases of subsidence for the WAB and MB depocenter: 1) Pre-Burdigalian, 2) Serravallian-Messinian, and 3) Plio-Quaternary. The first pulse should be previous to the deposition of units VII and VI, because they are infilling the basement lows and show little evidence of syn-sedimentary extension. Assuming that unit's thickness is fundamentally driven by subsidence, the second pulse shows a maximum during the deposition of unit IV (Tortonian), which presents a fan shape towards the WAB centre. However, clearly subsidence was also active during the sedimentation of unit V, which depositional geometry is difficult to infer due to the deformation produced by mud diapirism. Subsidence seems to have changed for post-Messinian because sedimentation is no longer confined to the sub-basins and extends overlaying the entire basement for the Plio-Quaternary units, present along the whole area and with similar characteristics. It is worth noting the lack of extensional structures that could control basin extension and subsidence even though part could be due to masking of faulting by magmatic activity. Thus, we suggest a vertical subsidence model that will be further discussed at section 6.3.5 "Alboran Basin evolution".

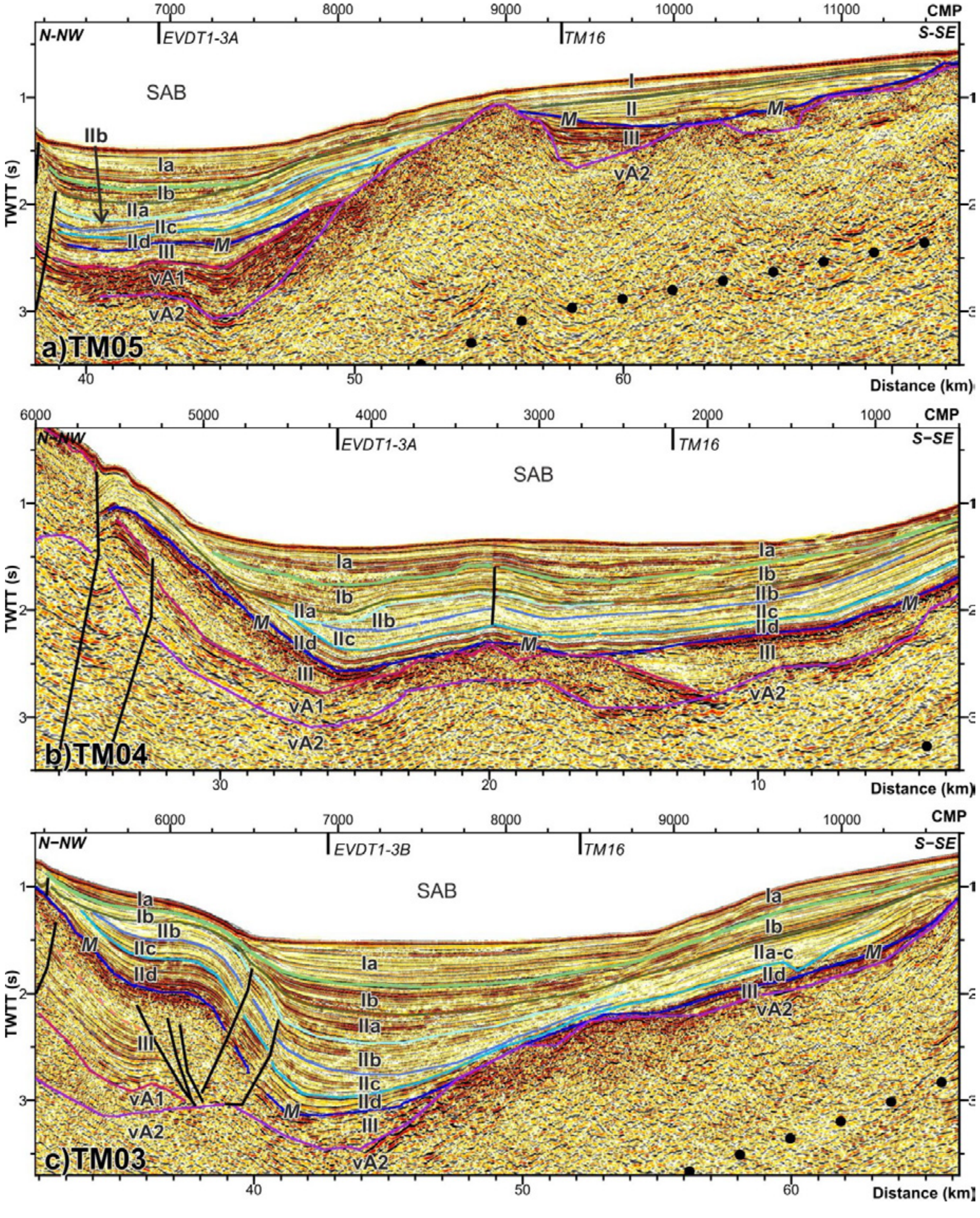

Figure 6.18: *Time migration of profiles TM05* ***(a),*** *TM04* ***(b)*** *and TM03* ***(c),*** *perpendicular to the SAB depocenter (see location in Figure 6.2). These profiles depict the Alboran Ridge uplift in the Pliocene and Quaternary units, which forms wedge shapes towards the high. Main structures and seismostratigraphic units are identified. Age of the units is defined in Figure 6.3. Vertical exaggeration is of ~x:2.5 taking into account a suitable velocity for the sediments.*

6.3.2. Formation and evolution of the Habibas and Pytheas basins

The Habibas Messinian-Quaternary basin contains a sequence of folded sediment units. Unit L (Langhian – Early Serravallian?) deposited over basement displays gently folded strata that are interpreted as synsedimentary deformation. The overlaying unit S, also exhibits folding with steeply-dipping reflections that seem to onlap unit L (Fig. 6.14 CMP 6000-5500). Unit S has a top and base that are roughly parallel and approximately constant thickness. Unit T onlaps unit S, exhibits also evidence of folding, and has a limited lateral extension with thickness variations (Fig. 6.14 CMP 6000-1000, Fig. 6.15c CMP 10000-11000). Folding affecting unit T is comparatively minor. This deformation appears limited to pre-Tortonian units. The sedimentation of the post-Tortonian sequence implies a major change because the layering shows no deformation, with parallel reflections onlapping unit T (Figs. 6.14, 6.15). The post-Tortonian sedimentary sequence thins abruptly towards the basin flanks, creating a roughly square to circular shaped basin - visible in bathymetric maps (Fig. 6.1) - with the depocenter located in the centre.

We propose that the oldest units of the basin were deposited coeval with the Serravallian–Tortonian deformation phase. Folding started during the subsidence phase and deposit of units L and S (Late Langhian? - Serravalian) and continued but gradually attenuated during subsidence and deposit of Tortonian unit T. The end of this localised subsidence and folding pulse agrees with the end of extension proposed by Medaouri et al., (2014) based on industry seismic data from the Algerian margin. We propose that the subsidence and deformation in the PB and HBB is linked to a strike-slip setting as will be discusses later (section 6.3.5).

Deposition of unit III occurred in a different tectonic setting, dominated by gentle subsidence that led to the present-day basin configuration. The basin geometry is peculiar because it appears with a similar concave geometry along perpendicular transects, without clear normal faults bounding sediment accumulation and creating the needed space for sedimentation. We interpret this geometry as a pull-apart basin, originated largely by vertical subsidence in a transtensional setting. As discussed below, this setting is coherent with our basin evolution model (section 6.3.5), as a transform lithospheric fault is required to allow the independent evolution observed in the stratigraphy of the WAB and MB, and the PB and HBB sub-basins.

Figure 6.19* ►*: *Time migration of profiles TM11* ***(a)****, TM12* ***(b)****, TM13* ***(c)****, and TM14* ***(d)*** *(see location in Figure 6.2), running perpendicular to the Yusuf Fault in the EAB (Figs. 6.1, 6.2). These profiles show the EAB structuration from west to east. The volcanic basement is imaged, with volcanic edifices that crop out in the Yusuf Ridge and the Al-Mansour Seamount (Fig. 6.19a). First sedimentary unit identified is unit IV, from Late Tortonian. Towards the Algero Balearic Basin, halokinesis phenomena is imaged (Fig. 6.19c, d). Main structures and seismostratigraphic units are identified. Age of the units is defined in Figure 6.3. ODP 977: ODP Leg 161 site 977. Vertical exaggeration is of ~x:2.5 taking into account a suitable velocity for the sediments.*

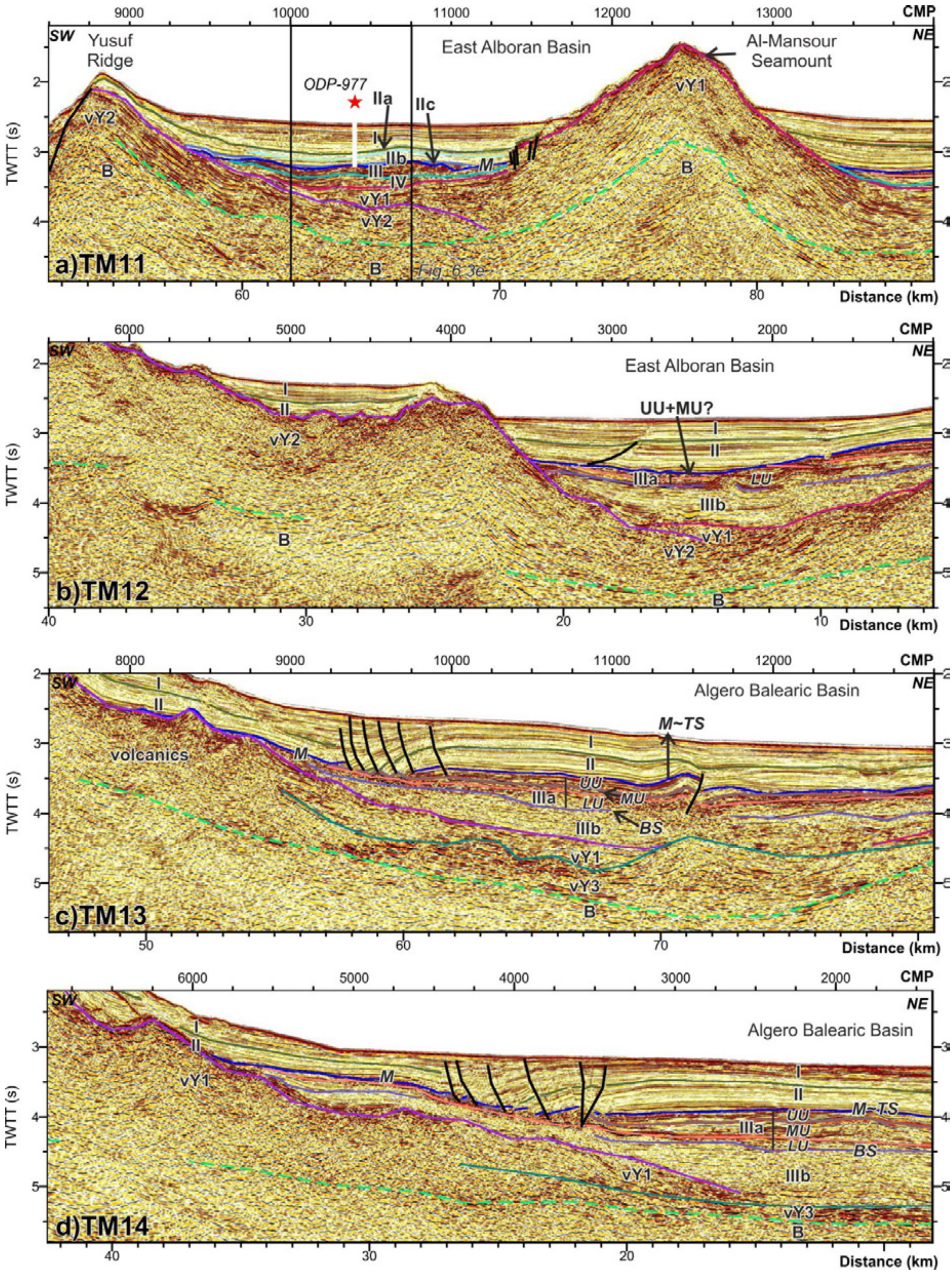
a)TM11
CMP
9000
10000
11000
12000
13000
SW
NE
Yusuf Ridge
East Alboran Basin
Al-Mansour Seamount
ODP-977
IIa
IIc
I
IIb
III
IV
M
vY1
vY2
B
Fig. 6.3e
TWTT (s)
Distance (km)
60
70
80
b)TM12
6000
5000
4000
3000
2000
East Alboran Basin
UU+MU?
I
II
IIIa
LU
IIIb
vY1
vY2
B
40
30
20
10
c)TM13
8000
9000
10000
11000
12000
Algero Balearic Basin
M~TS
I
II
volcanics
M
IIIa
UU
MU
LU
IIIb
BS
vY1
vY3
B
50
60
70
d)TM14
6000
5000
4000
3000
2000
Algero Balearic Basin
I
II
vY1
M
UU
IIIa
MU
LU
M~TS
BS
IIIb
vY3
B
40
30
20

6.3.3. Formation and evolution of the South Alboran Basin

The history of the SAB starts in the Tortonian, when the volcanic basement of this basin was created. First non-volcanic sediments found in this basin are Messinian in age. Its later evolution is strongly related to the tectonic processes causing the Alboran Ridge uplift ("Chapter 9: The Alboran Ridge").

6.3.4. Formation and evolution of the East Alboran Basin

The EAB basement contains at least three volcanic units, identified in seismic images as vY1, vY2 and vY3. Dredged samples provide age of ~8.7 Ma for unit vY1 outcropping at the Al-Mansour High and ~10.7 Ma for unit vY2 sampled at Yusuf Ridge (Duggen et al., 2004; Duggen et al., 2008). Due to their geometrical relationships unit vY3 is the oldest (> 10.7 Ma).

The oldest erosion-related sediment unit deposited in the EAB is Messinian unit III. The thickness of this unit significantly increases from west to east, having maximum values further east in the Algero-Balearic Basin. In the western EAB unit III is ~0.2 s in TWTT (Fig. 6.19a CMP 12000-9000), whereas in the eastern EAB it is ~1.4 s TWTT thick unit divided in IIIa and IIIb, and characterized by the presence of evaporites (Fig. 6.19c CMP 12000-9000), similar to the Algero-Balearic Basin (Fig. 6.19d CMP 1500-5000).

In the EAB, the evaporites layer (MU) is the responsible of halokinesis phenomena, despite its thickness of ~0.1 s in TWTT. Profile TM13 images a gliding structure, in which the sediment layers above the MU slide downslope, and MU base acts as a décollement level. This gliding generates listric faulting at the slide head (Fig. 6.19c CMP 10000-9250). Due to the wedge-shaped geometry of unit I, infilling the accommodation space created by faulting, and the approximately constant thickness of unit II, we infer that halokinetic processes began between the deposition of unit II and I (~1.8 Ma), and continue presently, as faulting affects the seafloor. This is in agreement with the halokinetic processes described in the Palomares Margin, northern EAB ("Chapter 7: The Palomares Margin", this volume).

Unit II also presents changes from west to east: in the west it has four sub-units (Fig. 6.19a CMP 12000-9000) related to the Alboran Ridge deformation (Martinez-Garcia, 2012; "Chapter 9: The Alboran Ridge", this volume), in the east they are not identifiable (Fig. 6.19d CMP 1500-5000). We propose that this change is caused by the partition of deformation affecting the Alboran Basin, as the Eurasian – African plate convergence is accommodated along several structures. The presence of structures acting as crustal boundaries, such as the Alboran Ridge or the Yusuf Fault, allows the strain partitioning at a lithospheric scale and the independent development of each sub-basin.

On the basis of the geometric relation between sediment units and age of volcanic units, we suggest that the Al-Mansour Seamount relief has a volcanic origin, while the Yusuf Ridge relief may have resulted from a combination of volcanic and tectonic processes. The Al-Mansour Seamount shows a triangular shape on cross-section (TM11, Fig. 6.19a CMP 14000-11000) that together with geometry of the volcanic units suggests a volcanic construction ("Chapter 5: Crustal domains"). The top of this high has been dated at 8.7 Ma, so it is older than the deposit of the sedimentary infill, formed by units III-I that onlaps the flanks of the high and show little deformation. We propose that the origin of this relief is a volcanic construction, or that the tectonic processes occurred coeval to volcanism prior to the first deposit of unit III. The Yusuf Ridge is imaged on lines TM11 (Fig. 6.19a CMP 10000-8000) and TM12 (Fig. 6.19b CMP 6500-5000), and distal part of TM13 (Fig. 6.19c CMP ~8000). Units III and II onlap the high flanks. Unit II thins slightly towards the high, while unit I thins abruptly above the high.

We propose that a volcanic construction formed ≤10.7 Ma, but that the thickness variation of unit II reveals tectonic activity and that the geometry of unit I indicated increased syn-sedimentary tectonism. Thus, we interpret that Yusuf Ridge relief is the consequence of Tortonian or older volcanic activity and post Messinian tectonic deformation, associated to the Yusuf Fault system. Tectonic compression of the high started during the Pliocene, while unit II was deposited in the basin, and highly increased in the Pleistocene, when the evident thinning of unit I confirmed the shortening occurrence.

Our data reveals that there is not a generalized compression event affecting the entire EAB, as it occurred in neighbour areas such as Alboran Ridge. Pliocene contractional deformation occurs in the western side that we interpret as related to Alboran Ridge formation. We propose that convergence between Eurasian and African plates in the EAB has been accommodated by the dextral strike-slip at Yusuf Fault system.

The northern boundary of the EAB is depicted by the Carboneras Fault (Fig. 6.1, 6.11 CMP ~18000). This is an active left-lateral strike-slip fault characterized by shallow earthquakes of low to moderate magnitude (Moreno et al., 2016 and references therein). First evidences of activity are dated from Late Miocene (Gràcia et al., 2006, 2012; Moreno et al., 2016).

The EAB is affected by pre-Messinian magmatic processes that led to the formation of two highs, the Yusuf Ridge (≤~10.7 Ma) and the Al-Mansour Seamount (≤~8.7 Ma). We propose a purely volcanic origin for the Al-Mansour Seamount, while the Yusuf Ridge may have a volcanic origin and a later tectonic component in its current structure. Deformation in the EAB is mainly absorbed by the Yusuf and Carboneras fault systems, as suggests the lack of relevant tectonic structures in the area. Active halokinesis processes have been identified, starting at ~1.8 Ma.

6.3.5. Alboran Basin evolution

In this section, we propose a revised model for the formation of the Alboran Basin from the previously discussed observations of the stratigraphy and tectonics of each of the sub-basins. This reconstruction is based on the distribution of sedimentary units, and of large-scale structures related to the subduction system on the basis of previous works (Fig. 6.21). The geodynamics of the subduction system conditioned the basin evolution leading to current configuration. While there are two depocenters formed above the Late Oligocene - pre-Miocene metamorphic basement (WAB & MB and HBB & PB), the SAB, EAB and the NE Alboran Basin developed above the volcanic basement created mainly during Tortonian times. This fact is recorded in the sediment deposits characteristics found and in the tectonic evolution of the depocenters, as the creation of new crust involves the large horizontal displacement of existing basins (Fig. 6.21).

Based on our analysis, we propose that the evolutionary history of the Alboran Basin can be divided into two distinct main stages: 1) the **formation stage**, during Miocene times, in which the Alboran Basin evolves in an extensional setting led by the slab roll-back and slab delamination (Lonegan and White 1989; Wortel and Spakman, 2000; Spakman and Wortel, 2004; Bezada et al., 2013; Chertova et al., 2014a; Faccenna et al., 2014; Van Hinsbergen et al., 2014), and 2) the **deformation stage**, of Plio-Quaternary age, and controlled by the NW-SE convergence between the African and European tectonic plates. Many of the structures involved in this phase have been the focus of dedicated studies that we have integrated in our analysis (e.g. Gràcia et al., 2006; Gràcia et al., 2012; Soto et al., 2012; Martínez-García et al., 2013; Lafosse et al., 2016; Moreno et al., 2016; Perea et al., 2016, Gràcia et al., submitted 2017). Further, the results of the detailed studies of the Yusuf Fault and Alboran Ridge uplifts (Chapter 8 and Chapter 9, this volume) support that a contractive reorganization of the basin starts at post-Messinian times.

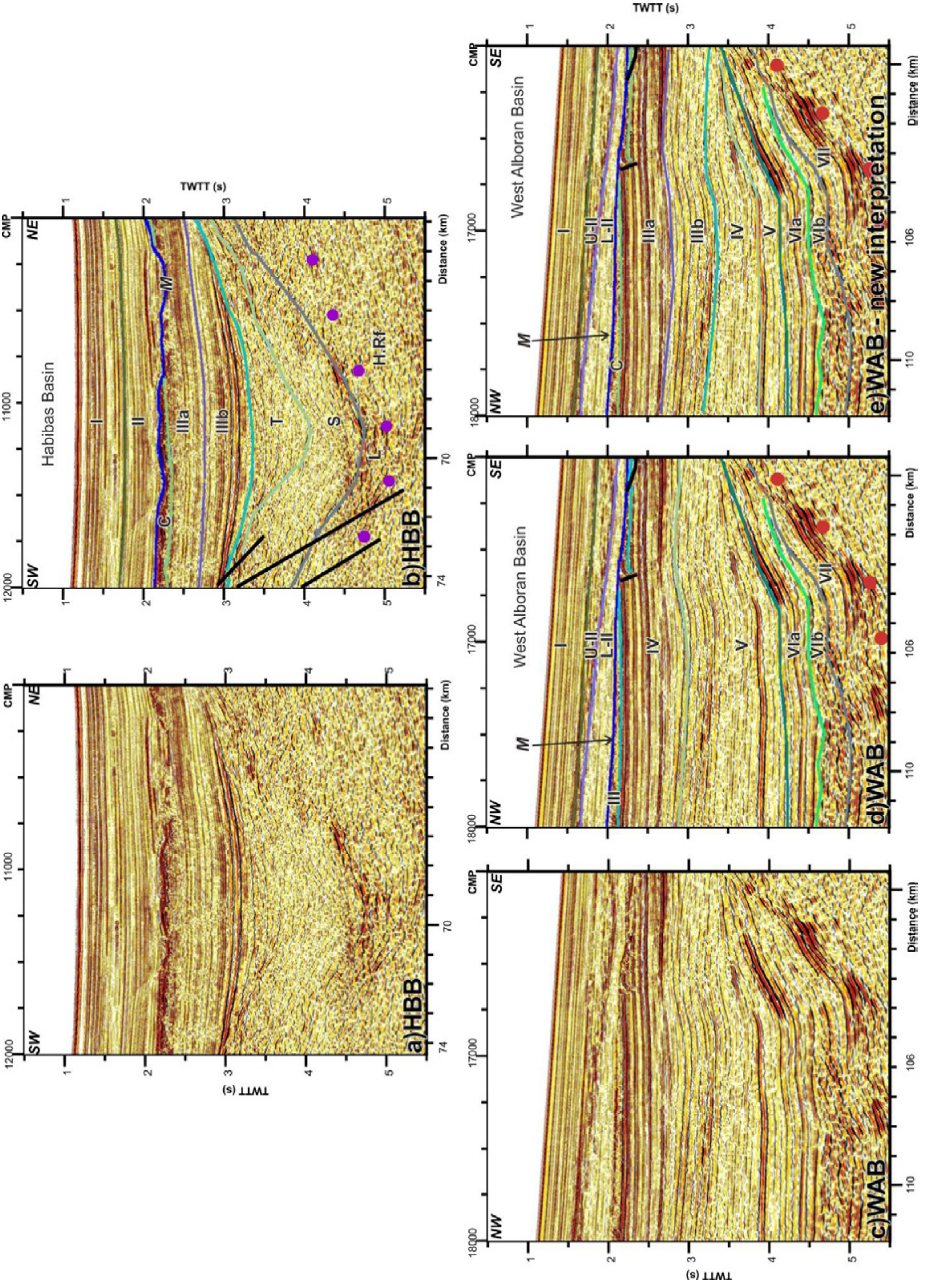
a)HBB
b)HBB
c)WAB
d)WAB
e)WAB - new interpretation
Habibas Basin
West Alboran Basin
TWTT (s)
Distance (km)
CMP
SW
NE
NW
SE
12000
11000
17000
18000
74
70
106
110
1
2
3
4
5
I
II
IIIa
IIIb
T
S
L
H.Rf
M
C
U-II
L-II
III
IV
V
VIa
VIb
VII

◄ ***Figure 6.20:*** *New interpretation proposed for the upper Miocene sediments at the WAB.* ***(a, b)*** *Uninterpreted and interpreted sections of profile TM12 (see location in Figure 6.15c), running across the HBB (Figs. 6.1, 6.2).* ***(c, d)*** *Un-interpreted and interpreted sections of profile TM17 (see location in Figure 6.6a), across the WAB (Fig.7. 1, 7. 2).* ***(e)*** *New interpretation of the sane section as Figures 6.20c and d, in the basis of the similarities in the seismic expression of the upper Miocene sediments of the HBB and the WAB.*

This is coherent with the stratigraphic record, which presents particular characteristics on each depocenter till the Pliocene, when a common sediment record develops for the entire Alboran Basin.

The first sediment record in the Alboran Basin is interpreted possibly as Aquitanian or perhaps Burdigalian, represented by seismic unit VII. This unit was deposited in the WAB and MB (Fig. 6.21a), in restricted basement lows. The position of the WAB and MB during the opening time should be restored towards the east, a distance equivalent to the extension in the back-arc, which is not well constrained (e.g. Faccenna et al., 2004), plus the extension in the magmatic arc. Taking into account the width of the arc, we obtain a minimum value of ~300 km. Roll-back had possibly already started at these times (e.g. Rosenbaum et al., 2002). Following the geodynamic model proposed by Vergés and Fernàndez (2012), we suggest a northwest migration of the slab and a later westward retreat. We associated this change to a westward migration with the Burdigalian – Serravallian boundary, as the width of the WAB and MB is similar at Burdigalian but a widening in a E-W direction of the WAB is observed during the Langhian-Serravallian, while the width of the MB (E-W oriented) remains constant (Fig. 6.21a). The WAB and MB were developed behind the subduction front, above the slab hinge, as its present-day position suggests (e.g. Do Couto et al., 2016). We suggest a vertical subsidence model, dependent on the gravity anomaly generated below these fore-arc basins due to the asthenospheric influx (Ranero et al., 2000, Pownall et al., 2016, Do Couto et al., 2016).

During Langhian – Serravallian, sedimentation at the WAB & MB continues, and the widening in a W-E direction of the WAB suggests a change in the subduction dynamics, now migrating towards the west (Fig. 6.21a-b). First sediment deposits of Langhian – Serravallian age at the HBB & PB indicate that a new depocenter is subsiding (Fig. 6.21b). While no signs of deformation are imaged at the WAB & MB, the pre-Tortonian sequence at the HBB & PB is folded. Deformation of pre-Messinian units in the continental platform of eastern Algeria have been explained as a consequence of the collision of the subduction front with the north African margin (Bouyahiaoui et al., 2015). However, they have a local distribution and may not extend towards the west (Strzerzynski et al., 2010; Badji et al., 2015; Bouyahiaoui et al., 2015). Due to the local character of these units and the lack of evidence of compressional deformation onland in the HAB & PB area, we proposed another hypothesis for these units, relating this deformation with the transform fault that limits the basin (Fig. 6.21b). The exact position of the WAB & MB depocenter at this time is not well known, but inferred considering the approximate amount of extension in the arc and the back-arc, while the HBB & PB have been located taking into account the palaeo-tectonic reconstruction of the North African coastline (Mazzoli and Helman, 1994; Gueguen et al., 1998). The different stratigraphic records and crustal domains ("Chapter 5: Crustal domains") between the WAB & MB and the HBB & PB supports they were separated by a major tectonic structure. This fault should allow the westward displacement of the WAB & MB continental crustal block with respect to the North African continental crust and the HBB & PB developed on it. The origin of the HBB & PB is probably linked to transtensional stresses related to a major strike-slip lithospheric boundary.

In Early Tortonian (Fig. 6.21c), the beginning of the magmatic activity implies the creation of new areas with volcanic basement. This magmatism has as a result the formation of the volcanic arc and back-arc and the creation of new depocenters in the Alboran Basin. Volcanic activity led to the formation of the Djibouti

Plateau, the SAB and EAB basements, and the basement of the Carboneras Fault area, almost completed by the Late Tortonian (Fig. 6.21d).

End of volcanism and beginning of dominant subaerial-erosion-derived sedimentation in these new areas started in Latemost Tortonian – Messinian (Fig. 6.21d, 6.21e). Tortonian units are different among depocenters: They are ≤0.5 s TWTT and have intercalated volcanic layers in the SAB, EAB, NE Alboran and HBB and PB basin, and are much thicker in the WAB & MB related to an important subsidence pulse in this depocenter. In the HBB & PB, a less intense subsidence event continues in the Tortonian, but it is restricted to the narrow depocenters.

While the pre-Tortonian units of this area are intensely folded, the Tortonian unit is less deformed. A latemost-Tortonian to Messinian end of deformation is coherent with a strike-slip setting, as the WAB & MB sub-basin migrated westwards right to the north of the comparatively stable region of the HBB & PB (Fig. 6.21d). The magmatic activity in Alboran basin is related to subduction (Duggen et al., 2004; Duggen et al., 2008) and the westward migration of WAB & MB, is related to the migration of the subduction front (Fig. 6.21a-d). In Latemost Tortonian times (~9 Ma), the volcanic activity in the arc is decreasing (Booth-Rea et al., 2007 and this work) and the associated westward migration has brought WAB & MB west of HBB & PB based on the reconstructed position of the deformation front proposed by Crespo-Blanc et al., (2016), based on block rotations and other tectonic features observed onland.

Messinian sediment deposits fundamentally accumulate is the areas where subsidence remains restricted presenting differences between each of those depocenters. In much of the WAB & MB they are identified as thin discontinuous deposits with a chaotic aspect. In the SAB and the western side of the EAB, the seismic character of this unit is similar to the WAB but deposits are more continuous. In the EAB and HBB & PB, Messinian units thicken to ≤1.5 s TWTT, and two sub-units are identified. In the HBB, a chaotic body occur at the unit top. Finally, in the eastern part of the EAB and in the Algero-Balearic Basin the Messinian consists largely of evaporites. The M reflection marking the top of the Messinian shows different characters on each sub-basin. In the WAB, MB and SAB it is clearly erosive on the basin flanks and near basement highs (e.g. WAB: Fig. 6.8a, MB: Fig. 11, SAB: Fig. 6.18). In the HBB & PB, it exhibits an erosive character also on its deepest parts (HBB: Fig. 6.14, 6.15, PB: Fig. 6.16), while in the EAB it is erosive only in the western sector (Fig. 6.19a), but becomes concordant towards the east (Fig. 6.19c, d), where the basin is deeper. Further east it is the top of the evaporites deposits. In Messinian time the volcanic arc (see “Chapter 5: Crustal domains”) was largely formed.

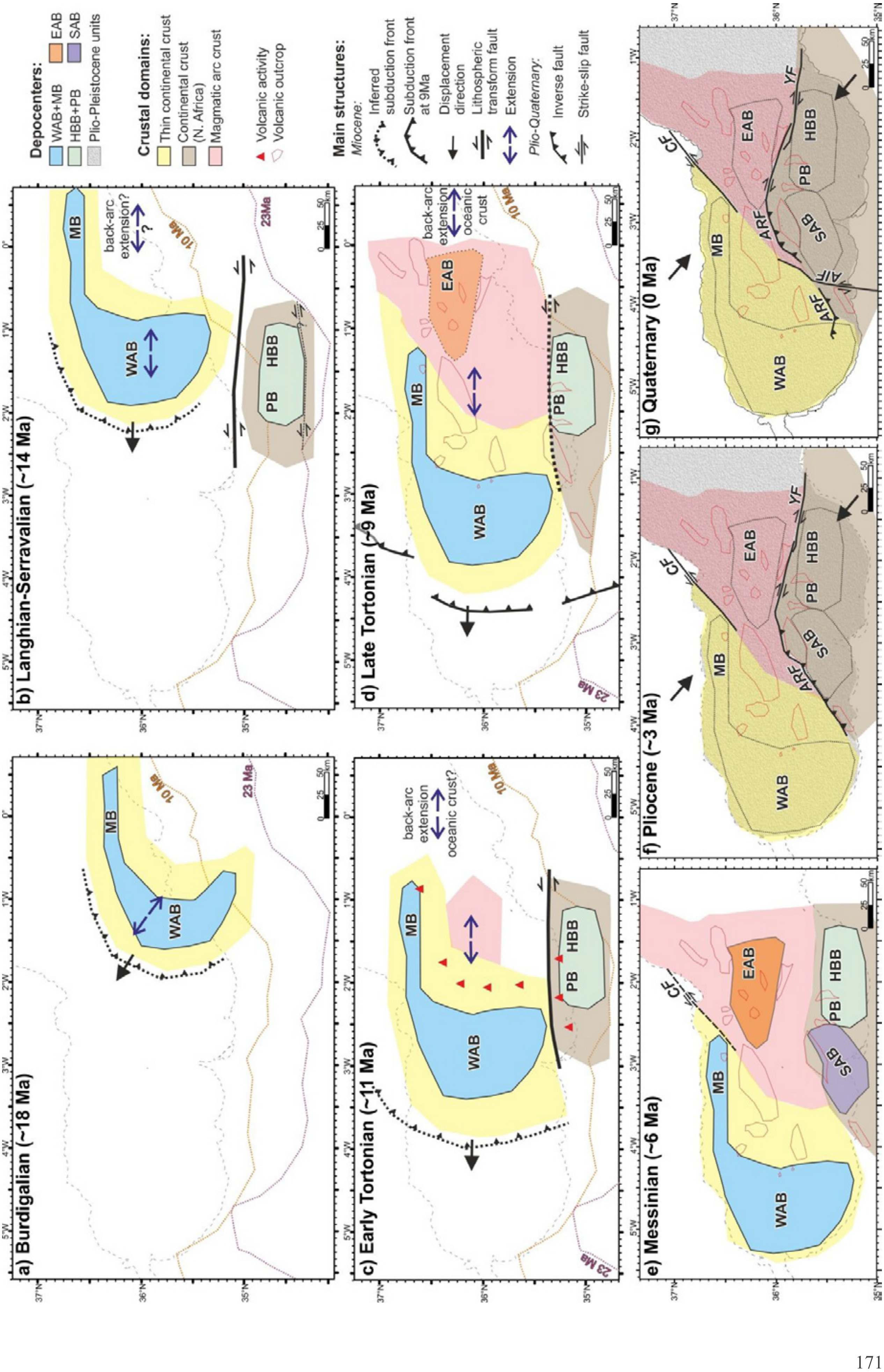
a) Burdigalian (~18 Ma)
b) Langhian-Serravalian (~14 Ma)
c) Early Tortonian (~11 Ma)
d) Late Tortonian (~9 Ma)
e) Messinian (~6 Ma)
f) Pliocene (~3 Ma)
g) Quaternary (0 Ma)
WAB
MB
EAB
HBB
PB
SAB
CF
YF
ARF
AIF
back-arc extension?
back-arc extension oceanic crust?
back-arc extension oceanic crust
10 Ma
23 Ma
37°N
36°N
35°N
5°W
4°W
3°W
2°W
1°W
0°
0
25
50
km
Depocenters:
WAB+MB
HBB+PB
Plio-Pleistocene units
EAB
SAB
Crustal domains:
Thin continental crust
Continental crust (N. Africa)
Magmatic arc crust
Volcanic activity
Volcanic outcrop
Main structures:
Miocene:
Inferred subduction front
Subduction front at 9Ma
Displacement direction
Lithospheric transform fault
Extension
Plio-Quaternary:
Inverse fault
Strike-slip fault

◄ ***Figure 6.21:*** *Reconstruction of the Alboran Basin evolution based on the sedimentary units distribution and deformation. Main depocenters and structures are depicted (see figure legend). The African coastlines at 23 Ma (pink dash line) and at 10 Ma (orange dash line) are depicted as reference (Mazzoli and Helman, 1994; Gueguen et al., 1998). CF: Carboneras Fault, ARF: Alboran Ridge front fault, YF: Yusuf Fault, AIF: Al-Idrissi Fault.* ***(a) Burdigalian****. Only the WAB & MB depocenter was created. The shape of this basin mimics the subduction front.* ***(b) Langhian-Serravallian****. Sedimentation at the WAB & MB depocenters continues, and the basin expands. A new depocenter, the HBB & PB, appears. The extensional directions changes from NW-SE to E-W. A transform fault, interpreted as a STEP fault, is inferred between these two depocenters, in order to allow the westward displacement of the WAB & MB.* ***(c) Early Tortonian****. The WAB & MB depocenter continues travelling towards the west, following the slab roll-back. First volcanic activity (red triangles) take place.* ***(d) Late Tortonian****. The magmatic activity in the area continues, creating a volcanic arc (volcanic outcrops are depicted with red polygons and the areas floored by volcanic basement are depicted with red lines). The extension in the arc and the westward migration of the subduction zone derives in a rapid migration of the WAB & MB. At this time, the position of the subduction front and the WAB are well constrained on the basis of Crespo-Blanc et al. (2016) reconstruction. First sediments in the EAB, intercalated with volcanic layers, are identified.* ***(e) Messinian****. Extensional processes in the basin ceased. The volcanic activity in the basin finished, and main depocenters are already created. Contractive reorganization of the basin begins in some areas, as at the NE margin, where the Carboneras Fault starts its activity.* ***(f) Pliocene****. The general contractive reorganization of the basin occurred. The Yusuf Fault and the Alboran Ridge front fault begins to accommodate this convergence. Activity along these boundaries has a direct consequence the NW displacement of the SAB and the HBB & PB depocenters. Sedimentation is no more controlled by the basement distribution, and a Pliocene unit with similar characteristics over the entire Alboran Basin is observed.* ***(g) Quaternary****. The basin continues its evolution in this compressive setting, till acquired is current configuration. The Carboneras Fault, the Yusuf fault and the Alboran Ridge frontal fault are still active, and the Al-Idrissi fault appears. This fault disrupted the Alboran Ridge frontal fault, and conditioned the evolution of this structure (see "Chapter 9: The Alboran Ridge" for details). Sedimentation continues homogenous along the entire basin.*

The first unit with a distribution not conditioned by local subsidence depocenters and volcanic basement growth is unit II of Pliocene – Early Quaternary in age (Fig. 6.21f). The lateral extension of unit II, across the entire basin with similar character, supports a change in the style of subsidence. The change in subsidence is coeval to changes in the dynamics of the slab at about the Messinian time (e.g. Lonergan and White, 1997; Rosenbaum et al., 2002; Faccenna et al., 2004; Vergés and Fernández, 2012). We hypothesise that slab rollback drastically decreased, perhaps due to the slab tearing in the eastern region. This change, together with the end of the magmatic fluid supply (Duggen et al., 2004; Duggen et al., 2008) can explain the general subsidence of the entire basin. The absence of hot asthenospheric/lithospheric fluids under the crust will derive in a cooling of the magmatic arc lithosphere that will drive a thermal subsidence process towards the isostatic equilibrium (e.g. Chalot-Prat and Girbacea, 2000; Teixell et al., 2009). The temperature anomaly at the base of the lithosphere causes subsidence in a larger area than the originally affected by this anomaly (e.g. White and McKenzie, 1988), and explains the entire basin subsidence. Based on backstripping of marine wells located at the south Iberian margin, Docherty and Banda (1995) performed a subsidence analysis of the North Alboran Basin. Results shown that the subsidence was concentrated in the west part during the Miocene, and that the east part does not subside until the Early Pliocene. Although the deep crustal configuration was not include in Docherty and Banda (1995) analysis, these results are coherent with our proposed model, in which the particular subsidence history of each sub-basin is different for the Miocene, while they presented a common Plio-Quaternary evolution.

Due to the differences in stratigraphy and tectonic structure of the seismic units we propose an individual evolution for groups of sub-basins till the Messinian, and a later common evolution for the whole Alboran Basin. The Plio-Pleistocene units are conditioned by contractional to strike-slip tectonic activity across the basin, and no much by the original basement configuration. A change in the stress configuration took place, and the Alboran Basins entered into a phase of shortening where the main tectonic structures started to develop in the Latemost Messinian or Early Pliocene (Fig. 6.21e-g). These are the Carboneras Fault (Gràcia et al., 2006; Moreno, 2011; Gràcia et al., 2012; Moreno et al., 2016), Al-Idrissi Fault (Martínez-

Garcia et al., 2013; Lafosse et al., 2016; Medina and Cherkaoui, 2017, Gràcia et al., submitted 2017), the Alboran Ridge Fault system (Martínez-García et al., 2013, Chapter 9 this volume) and the Yusuf Fault system (Alvarez-Marrón, 1999; Martínez-García et al., 2011; Martínez-García et al., 2013, Chapter 8 this volume). Two of these tectonic features: the Alboran Ridge and the Yusuf Fault, were main targets of the TOPOMED-GASSIS cruise, and will be analysed in detail in the next chapters. During the Plio-Quaternary, the Alboran Ridge accommodates a NW-SE shortening estimated in ~20-30 km ("Chapter 9: The Alboran Ridge"), while the Yusuf Fault has accommodated ~15 km of displacement in a ESE-WNW direction ("Chapter 8: The Yusuf Fault"). Taking into account these values, we "moved" in the reconstruction the HBB, PB and SAB ~20 km NW of their original position during the Plio-Quaternary (Fig. 6.21e-g). The lack of compressive structures in the sedimentary basins suggests that the main shortening deformation is accommodated along these crustal-scale few structures.

The rational for the revised geodynamic model that led to the formation of the Alboran Basin is going to be further discussed in comparison to previous existing models in "Chapter 10: Implications for geodynamic models" (Part IV: Discussion, this volume).

6.4. In summary

Each of these sub-basins has a particular evolutionary history conditioned by the crustal domain underneath them. The correlation of the different sedimentary units between depocenters allows us to determine their evolutionary history, and to understand the regional evolution of the entire Alboran basin.

The present-day basin distribution is not the same as during the generation of the basins. Extensional processes in the back-arc and magmatic activity created new basement and types of crust, which conditioned the location and evolution of old and new depocenters. The formation of the Alboran Basin initiated in the Burdigalian and extended until the Messinian. Later, during the Pliocene, the basin entered a compressive setting. Compartmentalised subsidence, domain displacement, and later contractional regime allow us to reconstruct the approximate position of the depocenters through time.

The older depocenter is the WAB & MB (Burdigalian), initiated in a position at least 300 km eastward of its current location. Lack of extensional structures in the WAB & MB depocenter, together with its position above the slab hinge suggests a vertical subsidence evolution model for this basin.

The subsequent created depocenter of the HBB & PB (Langhian) display appear folded strata, while no signs of deformation are found in the WAB & MB, strata older or of that age. We propose that the WAB & MB and the HBB & PB depocenters were separated by a major lithosphere-scale strike-slip fault that allowed the westward motion of the WAB & MB and is coherent with a transtensional origin for the HBB & PB depocenter.

During the Tortonian, the formation of the volcanic basement in the central, eastern and northeaster Alboran Basin allows the development of new sediment depocenters, which record starts in the Late Tortonian. Meanwhile, sedimentation in the WAB & MB and HBB & PB depocenters continues.

Until the Messinian time, each depocenter evolves independently. However, a change in the sedimentation style occurred near the Miocene – Pliocene transition. While the Miocene sedimentary units were conditioned by basement characteristics, the Plio-Quaternary sedimentary units are widespread, presenting similar characteristics along the entire basin. This period is characterized by the contractional deformation of the basin. A general subsidence of the basin is observed, with the Plio-Quaternary sedimentary units presenting a common aspect along the entire basin. Deformation is accommodated mainly by re-activation of pre-existing crustal structures, such as the Carboneras Fault, the Yusuf Fault or the Alboran Ridge front fault.

Chapter 7

The Palomares margin

Published in Tectonophysics (2016), 689, 25-39
Gómez de la Peña, L., Gràcia, E., Muñoz, A., Acosta, J., Gómez-Ballesteros, M., R. Ranero, C., and Uchupi, E.
Geomorphology and Neogene tectonic evolution of the Palomares continental margin (Western Mediterranean).
doi: 10.1016/j.tecto.2016.03.009

The Palomares Margin is located SE Spain, and represents the northern connection between the Alboran Basin and the Algero Balearic Basin. Deformation is distributed over a large number of faults onland with terminations offshore, forming what has been defined as the Eastern Betics Shear Zone (EBSZ) among other structures (e.g. Bousquet, 1979; Sanz de Galdeano et al., 1990; Andeweg and Cloetingh, 2001). The EBSZ corresponds to a large, active seismogenic fault-system that from north to south is composed by the Bajo Segura Fault, the Alhama de Murcia Fault, the Palomares Fault and the Carboneras Fault, which continues into the Alboran Sea (Fig. 7.1) (e.g. Gràcia et al., 2006; Moreno et al., 2016). There is limited evidence of relevant seismic activity offshore the southeastern Betics (e.g. Stich et al., 2003; García Mayordomo, 2005; Martín et al., 2015). Instrumental events of low to moderate magnitude (MW < 5.2) have been recorded, and historical earthquakes, such as the 1518 Vera Earthquake of I0=X (Fig. 7.1), indicate slip along large structures. Recently acquired geodetic data also show evidence of ongoing deformation in the area (Echeverria et al., 2013, 2015). Strain rates deduced from geodetic measurements are around 2 mm/yr (e.g. Nocquet, 2012; Echeverria et al., 2013). These low values, combined with the erosive and depositional processes occurring at the Palomares margin, may explain the few evidences of active deformation in the offshore areas, as well as in the narrow continental shelf. New bathymetric maps and multichannel seismic reflection profiles have been collected along the margin to unveil the detailed geomorphology of this area and to reconstruct its recent tectono-sedimentary evolution. The Palomares continental margin is heterogeneous and displays a rough bathymetry due to the presence of prominent ridges and deep canyons, thus marking a difference with adjacent western Mediterranean margins (e.g. Pérez-Hernández et al., 2009, 2014). The deep structure of the Palomares margin has recently been presented and discussed by Giaconia et al. (2015). The aim of this work is to further extend the characterization of the margin, focusing on the shallow structure using new high-resolution data. This approach is essential to characterize the active tectonic and sedimentary processes occurring along the Palomares continental margin. In this work we present full-coverage high-resolution bathymetric data from the continental shelf to the deep basin along the Palomares margin. In addition, we have re-processed multichannel seismic reflection (MCS) profiles TM23 and TM24 presented in Giaconia et al. (2015) to improve the resolution of the shallow structure and added profile TM25 to our study.

The objectives of this chapter are: (i) To characterize in detail the geomorphologic features of the margin, which is now possible on the basis of new high-resolution bathymetric data; (ii) To link the shallow expression of these structures with their origin at depth, through the analysis of the seismic images; and (iii) To explain these structures in their present-day compressive geodynamic framework, linking them with the geodynamic evolution of the margin.

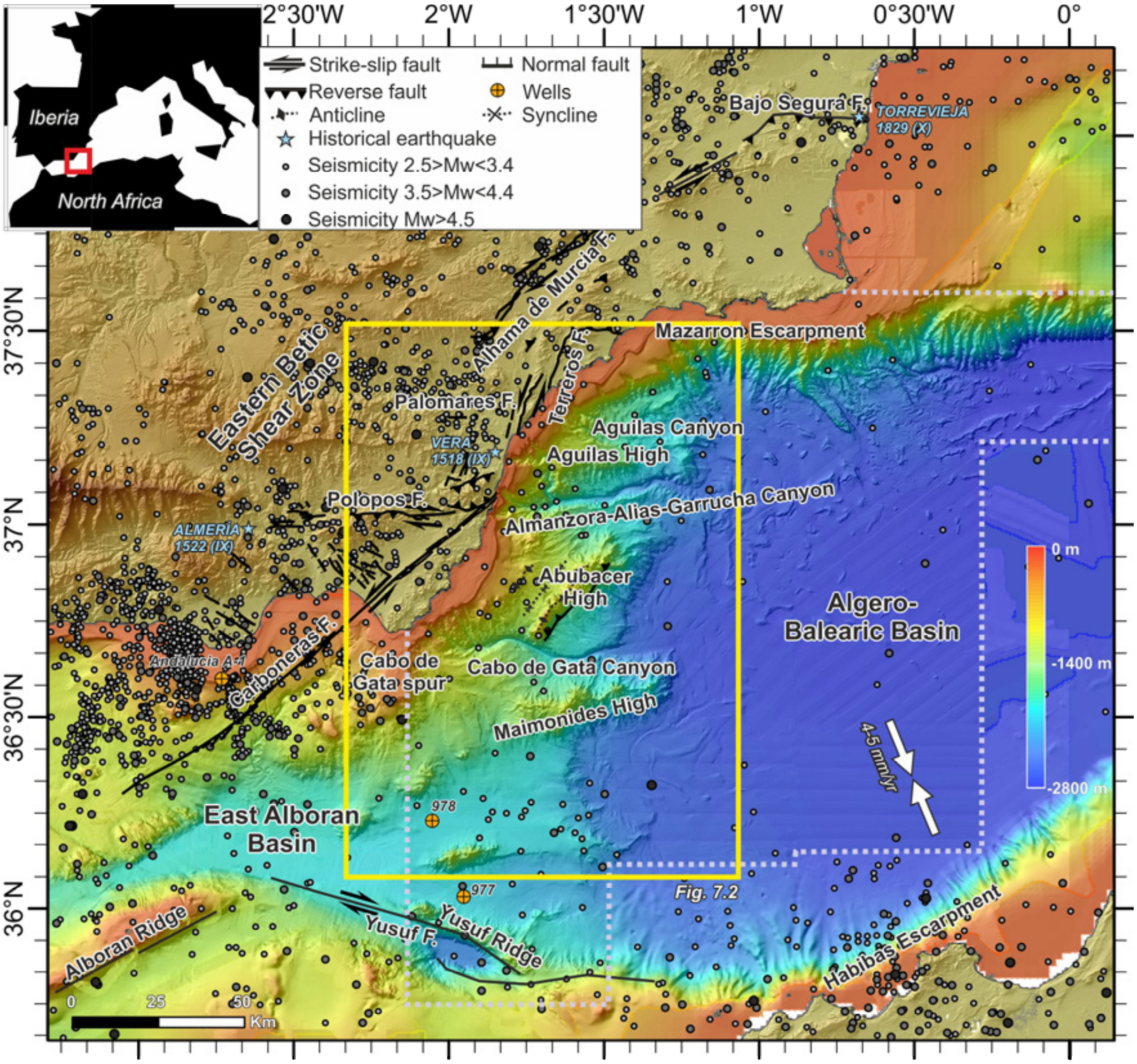

Figure 7.1: *Regional bathymetric map of the Alboran Sea constructed from digital grids released by SRTM-3, IEO bathymetry, GEBCO compilation and data acquired during our own cruises (Ballesteros et al., 2008, Gràcia et al., 2012). Location of the earthquakes occurred in this area since 1916 is shown. Light gray dots correspond to moment magnitudes (Mw) between 2.5 and 3.4, while dark gray dots represents events with magnitude larger than 3.5. The maximum magnitude registered is Mw 5.2 (Instituto Geográfico Nacional catalog, available online at http://www.ign.es/). Historical events occurred in the area are also located. Main tectonic structures, as the faults belonging to the EBSZ (from north to south, Bajo Segura, Alhama de Murcia, Palomares and Carboneras faults) are displayed (Gràcia et al., 2012). Orange-filled dots correspoind to the wells location, including the scientific ODP-161 sites 977 and 988 and the industry well Andalucia-A1. The area bounded by the the dotted purple polygon shows the coverage of the new bathymetry acquired. The yellow rectangle depicts the area presented in Figure 7.2. Inset: Location of the Palomares margin (red rectangle) in SE Iberia.*

7.1. Geological setting of the Palomares Margin

The Palomares continental margin, with a NNE-SSW trend, is located in the southeaster part of the Iberian Peninsula (from 36º30'N to 37º15'N, and from 2º15'W to 1ºW), including the eastern termination of the Betics and the easternmost part of the Alboran Basin. This margin is formed by thinned continental crust affected by volcanism (Booth-Rea et al., 2007). The volcanism is dated between 12 Ma and 6 Ma (Duggen, 2008), and the volcanic rocks sampled belong to tholeiitic, calc-alkaline and shoshonitic series (Comas et al., 1999; Duggen, 2004). The margin is composed by an extremely narrow linear shelf parallel to the coastline, suggested to be controlled by the Palomares Fault (PF) (Comas and Ivanov, 2006), and by a broad slope with a rough bathymetry with deeply incised submarine canyons and prominent volcanic and plutonic ridges (Comas and Ivanov, 2006). Strike-slip and reverse faulting and folding dominate the deformation in this region, with Carboneras Fault and PF as the most important structures onshore (Fig. 7.1). The PF is well defined onshore as a NNE-SSW left-lateral strike-slip fault, (e.g. Silva et al., 1993; Comas et al., 2000; Booth-Rea et al., 2004; García Mayordomo, 2005), but its potential extension offshore is unclear. Several segments form the PF, with a fault deformation zone about 4 km wide, and a lateral displacement of around 15 km. The PF has been active since the Tortonian, and during the Quaternary, only the easternmost segments have been clearly active (e.g. Booth-Rea et al., 2004). The PF reaches the coastline ending in reverse fault splays at the southern and northern sides of the Sierra Cabrera (Giaconia et al., 2012). The presence offshore of other PF segments is not clear, and has been proposed that deformation is transferred to its conjugate dextral Polopos Fault zone and associated reverse structures in Sierra Alhamilla and Sierra Cabrera (Giaconia et al., 2012; 2013) (Fig. 7.1, 7.2).

7.2. Data and methods used to survey the Palomares Margin

This study results from the integration of two different datasets: a) High-resolution bathymetry and b) MCS profiles. The new swath-bathymetry, which covers from the continental shelf, across the slope and to the deep basin of the Palomares margin, was acquired on board of the Spanish R/V "Vizconde de Eza". A Kongsberg EM-300 multibeam echosounder, operating 135 beams at 30 KHz frequency was used. Between years 2001 and 2003, a total of four oceanographic cruises were carried out in the framework of the project "Fishing Charts of the Mediterranean" (CAPERMA) by the Spanish Institute of Oceanography (IEO) and the General Secretariat of Maritime Fisheries (SGPM). Multibeam data have been processed using Neptune software, and interpolated to a 100x100 m side regular grid. Detailed bathymetric and slope maps have been obtained (Figs. 7.1, 7.2, 7.3).

The MCS profiles were acquired during the TOPOMED-GASSIS cruise (October 2011), on board of the Spanish R/V "Sarmiento de Gamboa". The seismic data were acquired using a 5100 meters long active section of a Sentinel SERCEL streamer with 408 active sections (12.5 m channel interval), towed at 10 m depth, and a 50.15 l (3060 ci) air-gun source. The source array was composed of 8 G-GUN IIIa guns deployed at 7.5 m depth, in a single cluster distribution. The airgun shots were fired every 50 m at a pressure of 2000 psi. The total record length was 14 s (Two Way Travel Time, TWTT), with a sample rate of 2 ms.

Three MCS profiles have been used for this study: TM23, TM24 and TM25 (Fig. 7.2). These profiles have been processed using "GLOBE Claritas" software. Lines TM23 and TM24 have been published by Giaconia et al. (2015) with a processing aimed at deep penetration. For this work, the processing flow was designed to obtain the maximum resolution of the shallow subsurface structure, to ensure a high-resolution imaging of the sedimentary cover and top of the basement (< 6 s TWTT). Processing steps include minimum-phase conversion, geometry definition accounting for streamer feathering, spherical divergence correction, predictive deconvolution in Tau-P domain (to eliminate the bubble and short periods multiple reverberations), surface consistent deconvolution, normal-move-out correction based on velocity semblance analysis, stretching mute, amplitude recovery, time migration and a high-pass frequency filter

(1-3 Hz). Finally, we used the IHS Kingdom Advanced software to represent the stratigraphic and structural interpretation of the MCS dataset presented here.

7.3. Results

7.3.1. Seafloor morphology

The margin has three areas differentiated: (i) the continental shelf, (ii) the continental slope and (iii) the Algero-Balearic deep basin (Fig. 7.2).

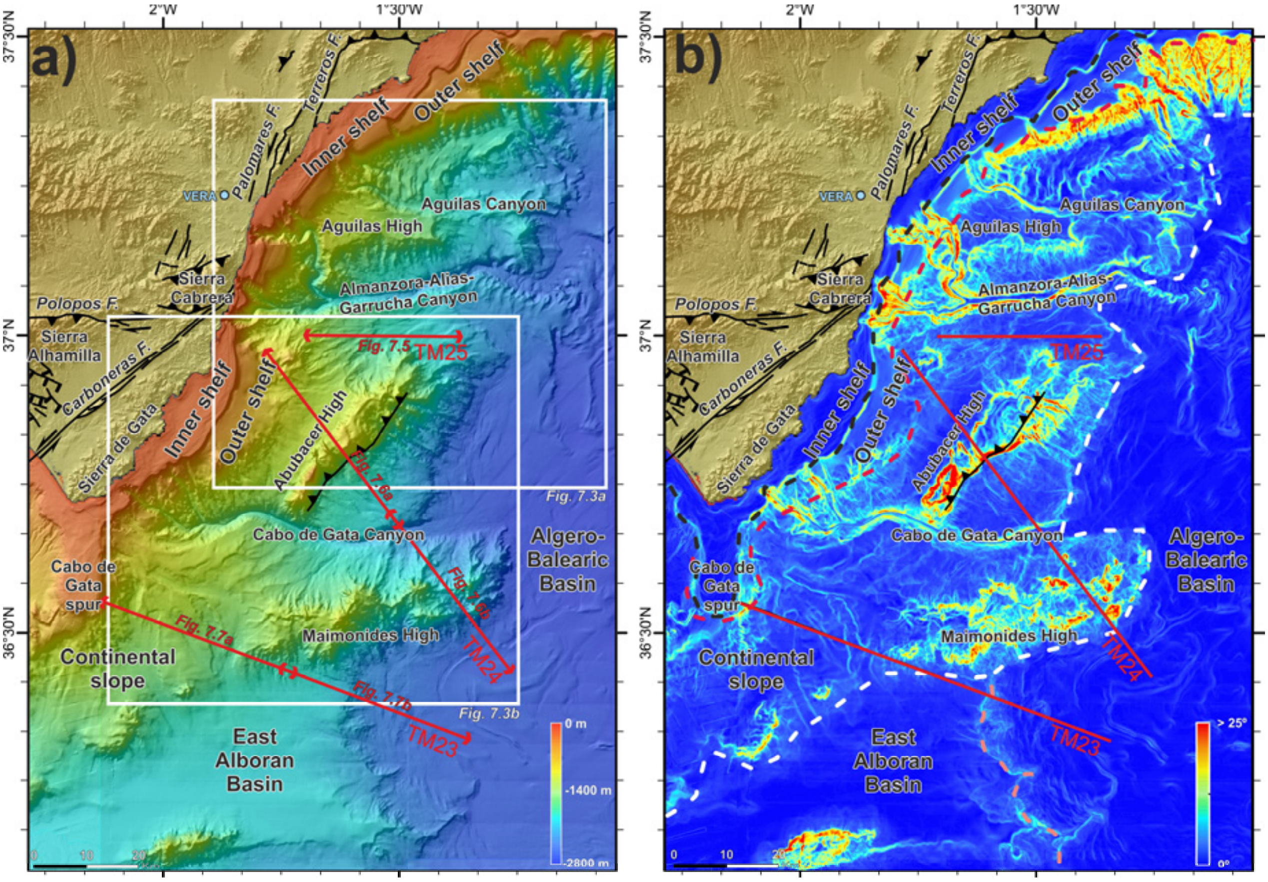

Figure 7.2: ***(a)*** *Colour shaded-relief bathymetric map of the Palomares margin (illumination from the NW) (see Figure 1 for location). Main geomorphological features and structures are depicted. MCS profiles presented in this work (TM23, TM24, and TM25) are located. Location of the close up figures (Figs. 7.3a, 7.3b) is depicted.* ***(b)*** *Slope map of the Palomares margin, same area as Figure 7.2a. The boundaries between the geomorphologic zones are located: black line corresponds to the inner - outer shelf boundary, red line to the outer shelf - continental slope boundary, gray line to the eastern boundary of the Algero-Balearic Basin and pink line, to the continental slope – East Alboran Basin boundary. MCS profiles are depicted.*

The **continental shelf** is divided in two parts, the inner shelf and the outer shelf that are separated by a pronounced escarpment (Acosta et al., 2013) (Fig. 7.2). The inner shelf has an average width of 4 km, extending up to 19 km in the southern part of the study area, at the Cabo de Gata Spur. The slope angle is less than 1º and the maximum depth is close to 80 m. On its outer part, an undulated topography can be recognized (Fig. 7.3). The escarpment separating the inner and outer shelves is located between 80 and 120m depth, and has a dip between 7º and 15º (Fig. 7.2b). This scarp shows an undulating trace north of 37˚20'N. It is slightly concave from 37˚20'N to 37˚N and convex south of 37˚N (Fig. 7.2a), and it is modelled by erosional structures, as gullies or submarine canyon heads. The outer shelf, although locally eroded by canyons and gullies (Fig. 7.2a), is relatively flat with dips ranging from 1º in the north to 2º in the southern part (Fig. 7.2b). Thus, the outer shelf has been extended down to 450 m water depth (Acosta et al., 2013). The base of the outer shelf is defined by an undulated topography easily recognized on the slope map (Fig. 7.2b).

The **continental slope** extends from ~450 to 2500 m depth, and corresponds to the transition zone between the shelf and the basin. The outer shelf reaches 450 m and is unusually deep for a continental shelf structure, but the term is used because of its dip, which is much lower than at the continental slope (Acosta et al., 2013). Along the slope there are three large topographic highs, which are the most characteristic features of this part of the margin. From north to south, they are: the Aguilas High, the Abubacer High and the Maimonides High. These elongated highs are separated by prominent submarine canyons that will be described later (Fig. 7.2). The Aguilas High is 40 km long and 15 km wide and follows an east-west linear trend. Its deepest point is located at 2000 m water depth, and the shallower one is at 850 m water depth (Figs. 7.2a, 7.3a). The dip of the northern side of the Aguilas High varies between 13º and 19º; being slightly steeper than the dip of the southern side, which ranges between 8º and 12º (Fig. 7.2b). The Aguilas High can be divided into two different sections: The western part shows a flat top at a water depth of around 1000 m, with a south flank highly affected by gullies, while the eastern part exhibits a more rugged topography (Fig. 7.3a). The Abubacer High is 40 km long, 12 km wide and trends NE-SW (Figs. 7.2a, 7.3b). The shallower depth is 290 m and its base is located at 1600 m depth. The northern part shows an irregular topography due to the presence of abundant gullies (Fig. 7.3b). The southern part of the Abubacer High is named as Polacra Ridge, characterized by a sharp, narrow crest and steep slopes higher than 35º (Fig. 7.3b). To the east of the Polacra Ridge, a large (22 km wide x 12 km long) sedimentary lobe is observed (Fig. 7.3b). The W-E trending Maimonides High has a maximum length of 62 km, and it is up to 25 km wide (Fig. 7.2a). It highest point is located at 820 m depth, while the base of the high is at 2300 m water depth. The Maimonides High shows a very rough, irregular relief, and the slope dip varies considerably, from 2º to 30º (Fig. 7.2b). These very steep slopes together with strong erosive processes cause a progressive dismantlement of the flanks of Maimonides High (Fig. 7.2a, 3b). Towards the east, the Maimonides High splits into two ridges, the Genoveses Ridges, separated by a narrow and elongated trough (Fig. 7.3b).

Along the Palomares margin, the **Algero-Balearic Basin** has an average depth of 2500 m and a subtle eastward dip of less than 1o (Figs. 7.2a, 7.2b). The basin is characterized by comparatively small-scale morphologies of swells and furrows (Figs. 7.2a, 7.3).

- *Erosional features*

The most prominent erosional features affecting the entire margin are submarine canyons. The canyons run from the continental shelf to the Algero-Balearic Basin. The three main canyons are from north to south: Aguilas Canyon, Almanzora-Alias-Garrucha Canyon and Cabo de Gata Canyon (Fig. 7.2). The W-E Aguilas Canyon is 50 km long running from 100 m to 2400 m depth, with an average gradient of 2º (Figs. 7.2, 7.3a). The canyon´s maximum width, less than 3 km, is reached at the canyon mouth. The Aguilas Canyon runs between the northern flank of the Aguilas High to the south, and a trough terrain with a downward sequence of east-facing steps, to the north (Fig. 7.3).

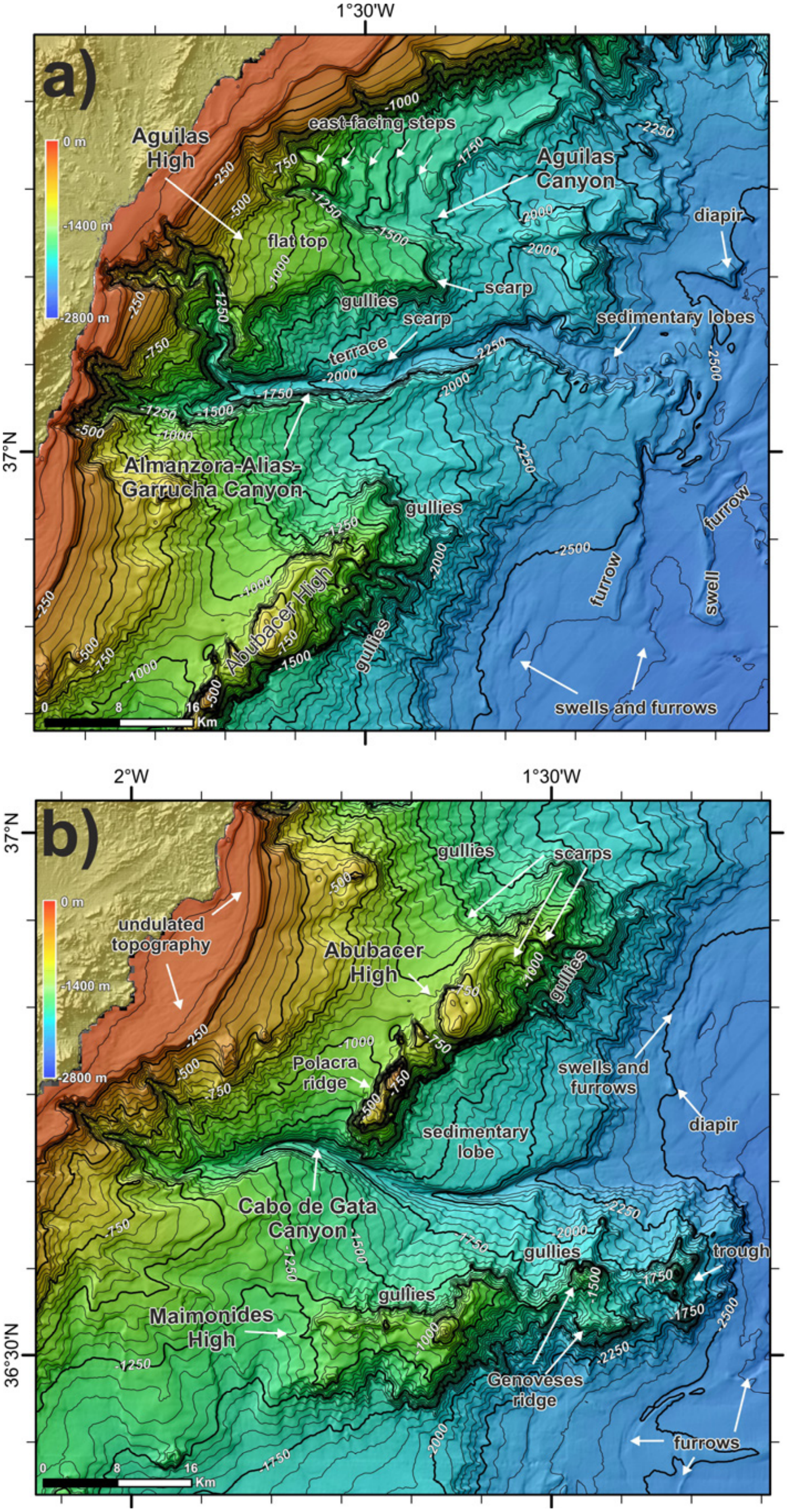

Figure 7.3: *Zooms of the bathymetric map, with contour lines every 50m. Main structures named and described in the text are located. See Figure 7.2a for location.* ***(a)*** *Close up of Aguilas Canyon, Aguilas Canyon and Almanzora-Alias-Garrucha Canyon area.* ***(b)*** *Close up of Abubacer High, Cabo de Gata Canyon and Maimonides High area.*

The Aguilas Canyon is composed of two small canyon heads, both cutting the escarpment between the inner and outer shelf (Fig. 7.3a). The Almanzora-Alias-Garrucha Canyon is a N45 trending, relative linear structure with a very asymmetric cross section. It is 80 km long, running from 50 to 2550 m depth, has an average gradient of 2º, and a width of 0.5 to 3 km (Figs. 7.2, 7.3a). The northern flank of the canyon is characterized, from the shallower to the deepest part, by a gullied escarpment south of the Aguilas High, a 5 km wide terraced scarp and a steep embayed scarp (Fig. 7.3a). The southern wall is narrow, steep and linear, locally disrupted by gullies. The Almanzora-Alias-Garrucha Canyon is composed by two deeply-incised canyon heads that feed a meandering system made of multiple tributary channels. The canyon mouth is characterized by a succession of sedimentary lobes, stepping towards the east (Fig. 7.3a). The W-E trending Cabo de Gata Canyon is located between the Abubacer and Maimonides highs. It is 72 km long, ranging from 80 to 2500 m depth, with an average gradient of 2º, and a width from 500 m at the upper-middle part to 2.5 km at the canyon mouth (Figs. 2, 3b). The Cabo de Gata Canyon is formed by two narrow canyon heads that cut the inner shelf (Fig. 7.3b). The geomorphology of both canyon walls is diverse, probably dominated by the different erosive processes between the Abubacer (northern wall) and Maimonides highs (southern wall). The lower part of the Cabo de Gata Canyon north wall is deeply incised in the sedimentary lobe located to the east of the Polacra Ridge (Fig. 7.3b). The south wall of the Cabo de Gata Canyon is wider, with a low-dip angle, and highly eroded by gullies (Fig. 7.3b).

7.3.2. Seismostratigraphic units

The post-Tortonian stratigraphy of the Eastern Alboran Basin is reasonably well established (e.g.Jurado and Comas, 1992; Comas et al., 1995; Alvarez-Marrón, 1997; Comas et al., 1999; Moreno, 2011; Booth-Rea et al., 2007; Giaconia et al., 2015; Moreno et al., 2016). These studies integrate commercial and scientific wells (ODP Leg 161, Comas et al., 1996), essential to calibrate the Alboran Basin sedimentary infill. A better definition of the Late Miocene series is achieved by the onshore-offshore correlation of the pre-Pliocene sedimentary units (e.g. Martín et al., 2003; Giaconia et al., 2014; Giaconia et al., 2015). We have defined five main seismostratigraphic units on the basis of their seismic expression and correlation with previous works, allowing us to assign an age to the sedimentary units identified in the Palomares continental margin (Fig. 7.1). From top to bottom, the seismostratigraphic units are labeled I to V, and below them we found the basement of the margin (Figs. 7.4-7.7).

A detailed description of these units is carried out at "Chapter 6: Basin evolution". In Figure 7.3 we are presenting the specific seismic units used in this chapter.

- *Basement characteristics*

In the Palomares margin, the basement (B) has been interpreted as thinned continental crust intruded by magmatism that transitions into the oceanic crust of the Algero-Balearic Basin (e.g. Booth-Rea et al., 2007). On the seismic images, the top of the basement corresponds to a high-amplitude reflection marking an irregular surface, with no coherent reflections underneath (Figs. 7.4-7.7).

7.3.3. Tectonic structure and stratigraphy of the Palomares margin

The multichannel seismic profiles presented show the main tectonic features of the Palomares margin. They cross some of the main structures, imaging the topographic highs (TM23 and TM24) and the southern flank of the Almanzora-Alias-Garrucha Canyon (TM25) (Fig. 7.2a). Now, we individually describe, from north to south, each of the seismic sections because they image different structures from three distinct areas.

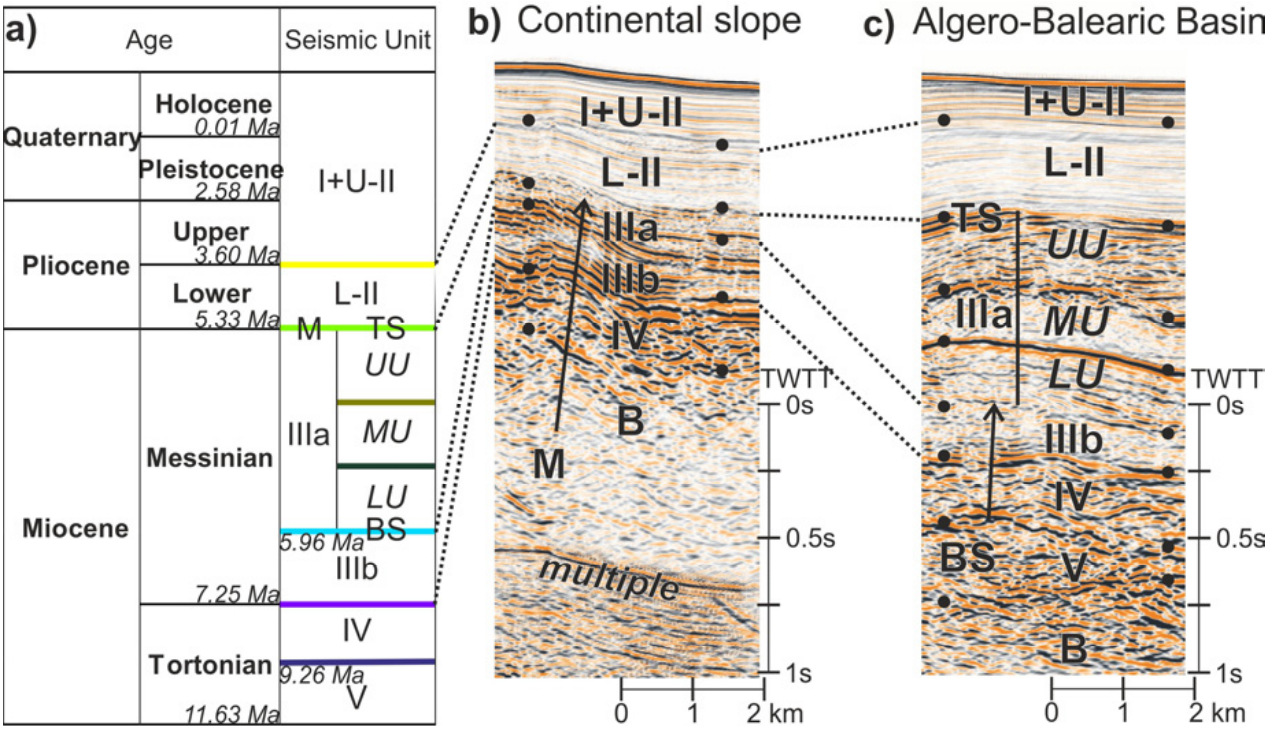

Figure 7.4: ***(a)*** *Ages and seismostratigraphic units identified in the TOPOMED MCS profiles, on both,* ***(b)*** *the continental slope and* ***(c)*** *the Algero-Balearic Basin. Units used are the following: I+U-II: Quaternary + Upper Pliocene, L-II: Lower Pliocene, IIIa: Upper Messinian, IIIb: Lower Messinian, IV: Upper Tortonian, V: Upper Serravalian? + Lower Tortonian, B: top of the basement. The unit IIIa (Upper Messinian) has been subdivided in three units in the Algero Balearic Basin, where evaporites are present. These units have been correlated with the ones proposed by Lofi et al., 2010 (see text for details). The M points out the Messinian unconformity, which is the boundary between unit IIIa and unit L-II. This boundary is correlated with the TS/TES (Top Surface/Top Erosion Surface) in the areas where the salt layers exist. In these areas, the boundary between the unit IIIb and unit IIIa is the BS/BES (Bottom Surface/Bottom Erosion Surface). See Figure 7.7 for location.*

The northern **profile TM25** (Figs. 7.2a, 7.5) runs approximately W-E along the southern flank of the Almanzora-Alias-Garrucha Canyon (Fig. 7.2a), which shows surface incisions associated to a large gully system. The top of the crystalline basement shows an irregular topography, defining some gentle highs and lows mainly filled by the pre-Messinian unconformity sedimentary series (units IIIa, IIIb and IV). The deposition of these units was affected by faults that are now sealed by the Messinian unconformity (M). These deformation processes are evident on unit IIIa that presents reflections conformable with the limit between units IIIb and IIIa, but with a current high-dipping angle. However, some of the reflections ending in a toplap geometry against M can also be due to deep erosion during the Messinian, and not only caused by a tectonic deformation process. Above the M reflection, we find a parallel, well-stratified unit L-II, with its characteristic transparent facies. Above lays unit I+U-II, represented by parallel and continuous reflections. These reflections are disrupted on their uppermost part by the incision of gullies and erosive slide scars, such as the lateral scars of a slope failure (i.e. between 15 and 23 km, Fig. 7.5). In the westernmost part of profile TM25, there is a vertical fault clearly affecting the basement and almost all the sedimentary units. The topmost reflections of unit I+U-II are continuous above the uppermost branch of this fault, so we infer that the fault does not reach the seafloor, or that the offset is too small to be resolved (Fig. 7.5). However, the seafloor seems to be slightly deformed, thus we cannot reject that the fault may be still active.

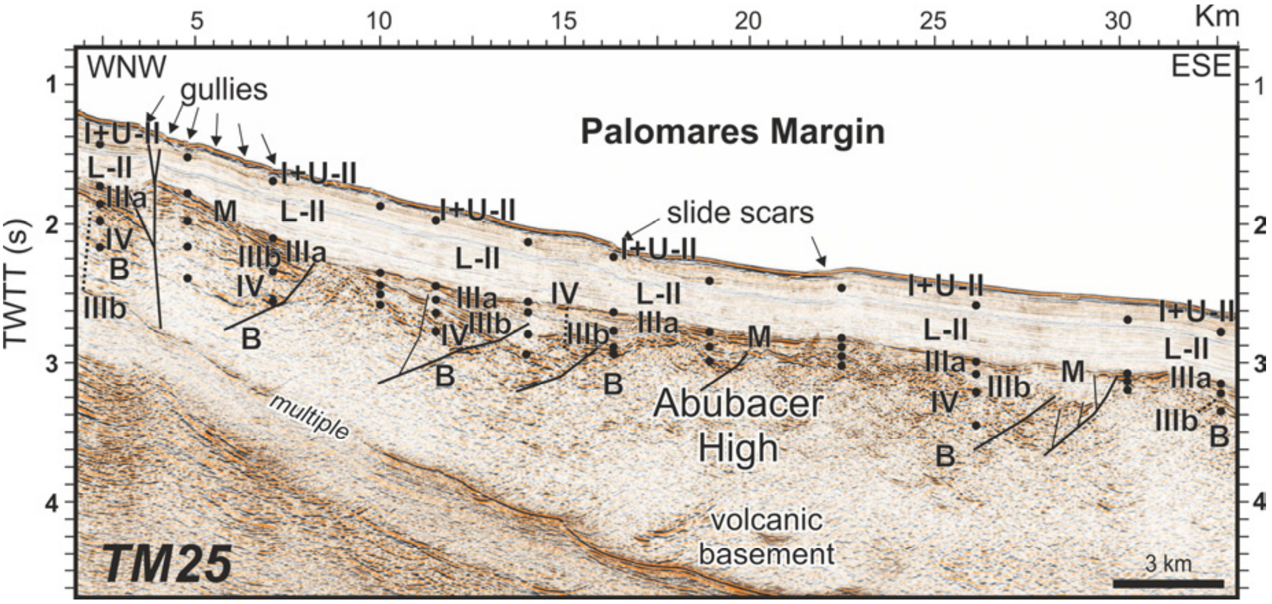

Figure 7.5: Time migration of profile TM25 (see Figure 7.2 for location). Main structures, seismostratigraphic units and seafloor multiple are identified. Age of the units is defined in caption of Figure 7.4. Vertical exaggeration is of x:5, taking into account water velocity.

Profile TM24 (Fig. 7.2a, 7.6) runs in a NW-SE direction from the south flank of the Almanzora-Alias-Garrucha Canyon until the Algero-Balearic Basin, which allows us to image in detail the Abubacer and the Maimonides highs, the sedimentary apron along the southern flank of the Abubacer High and the mouth of the Cabo de Gata Canyon. Along this profile, the basement also exhibits an irregular topography, affected by deeply rooted faults. The roughness of the top of the basement is more evident due to the presence of the two large basement highs: the Abubacer and the Maimonides highs. These highs configure three main sectors of the TM24 profile, in terms of sedimentary characteristics. The northwestern part of the profile (Fig. 7.6a) has a thin sedimentary cover progressively thickening towards the Abubacer High, where the Abubacer Basin is located. On this part of the section, unit IV is only identified in the deepest local basin, located at the northwestern flank of the Abubacer High. Units IIIb and IIIa are not continuous along this part of the profile, they appear folded and faulted. Above them, units L-II and I+U-II show similar characteristics as in the previous profile. The top of unit I+U-II also displays evidence of gullies. At the eastern part of the Abubacer High there is a sedimentary lobe that covers its southern flank. The maximum sedimentary thickness in this part of the profile reaches 1.5 s in TWTT. Unit V is identified at the deepest part of the basin. Units IV, IIIb and IIIa appear less deformed than in the northwest section of the profile and are characterized by parallel and continuous reflections (Fig. 7.6a). The M unconformity is covered by units L-II and I+U-II, and again some erosive gully-type features are identified at the seafloor. The sedimentary lobe is cut by the lowermost part of the Cabo de Gata Canyon (Fig. 7.6b). It corresponds to a deep, asymmetric incision that almost reaches down to the M unconformity. The seismic image clearly displays the asymmetry between the two flanks of the canyon, with a steep northwestern flank and a relatively flat southeaster one. Southeast of Cabo de Gata Canyon (Fig. 7.6b) is the Maimonides High, a basement topographic high with rough topography and chaotic seismic facies that difficult a clear seismic imaging. Some of the roughness seems to be related to cone-shaped and ridge-like structures observed on the bathymetry and also imaged in the seismic data (Figs. 7.2, 7.3b, 7.6b).

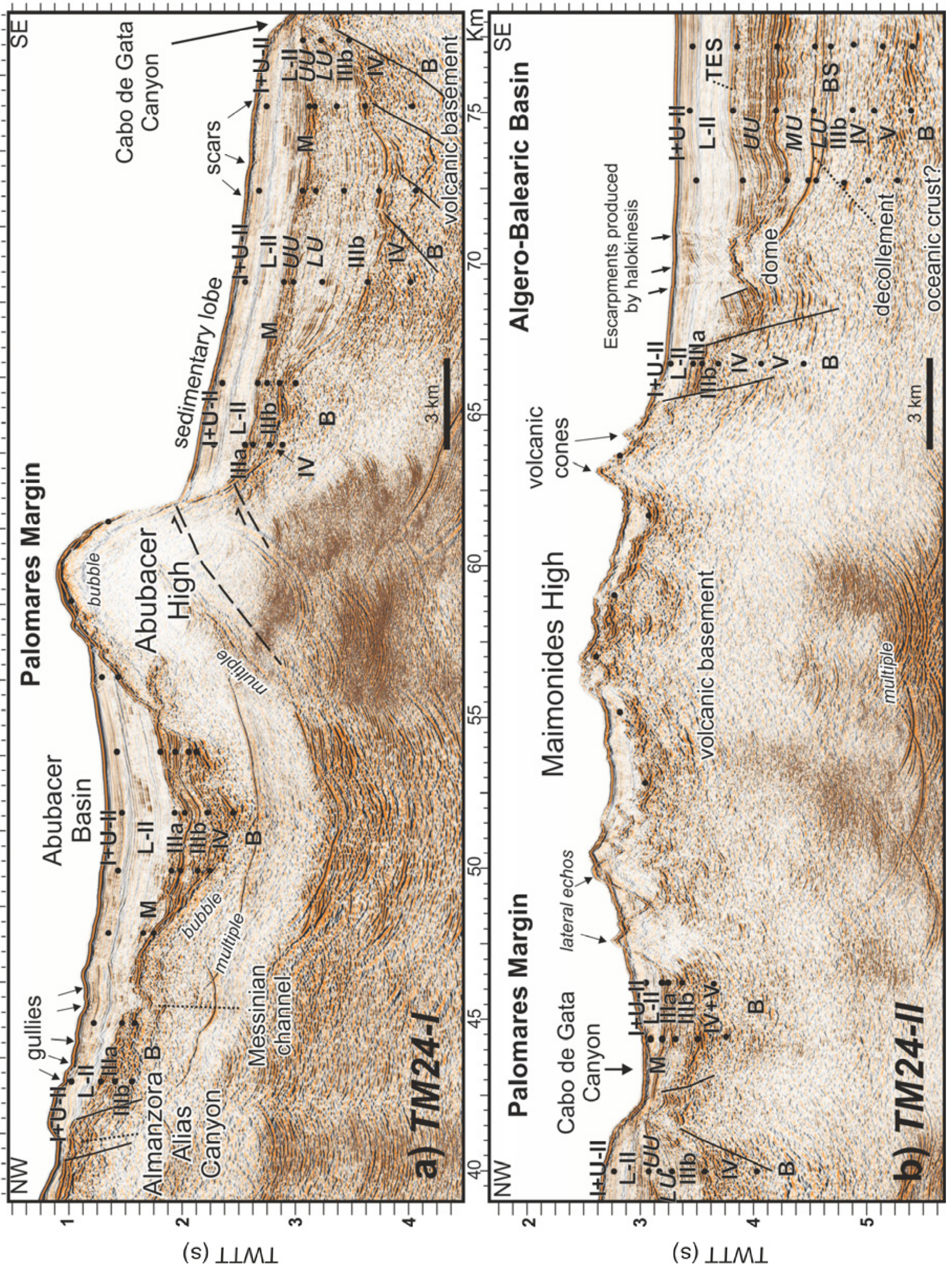
a) TM24-I
NW
SE
Km
TWTT (s)
Palomares Margin
Abubacer Basin
Abubacer High
Almanzora Alias Canyon
Cabo de Gata Canyon
gullies
scars
sedimentary lobe
bubble
multiple
Messinian channel
volcanic basement
3 km
I+U-II
L-II
M
IIIa
IIIb
IV
UU
LU
B
b) TM24-II
Palomares Margin
Maimonides High
Algero-Balearic Basin
Cabo de Gata Canyon
lateral echos
volcanic cones
volcanic basement
Escarpments produced by halokinesis
dome
decollement
oceanic crust?
TES
BS
MU
IV+v
V
multiple

◄ ***Figure 7.6:*** *Time migration of profile TM24 (see Fig. 7.1 for location). Main structures and seismostratigraphic units are identified, as well as the seafloor multiple and the source bubble reverberation. The dashed line corresponds to the inferred fault trace responsible of the Abubabcer High uplift. Age of the units is defined in the caption of Figure 7.3. Vertical exaggeration is of x:5, taking into account water velocity.*

The southern end of the profile images the western part of the Algero-Balearic Basin. In this area, halokinesis stands out. Two sub-vertical normal faults separate the Maimonides High from the deep basin. Within unit IIIa, we recognize characteristic deposits of evaporites (Fig. 7.6b), in which halokinesis processes are active. The flowing of these salt deposits produces faulting in the overlying sediments that affects the seafloor surface, creating long escarpments clearly visible in the bathymetry (Figs. 7.2, 7.7). The migration and deformation of the evaporites is responsible of the formation of furrows and swells observed in the relatively smooth and flat seafloor of the deep Algero-Balearic Basin (Figs. 7.2, 7.3).

Profile TM23 strikes WNW – ESE (Figs. 7.2a, 7.7) and runs from the Cabo de Gata Spur, across the continental slope and south Maimonides High, down to the Algero-Balearic Basin (Fig. 7.2a). The basement shows an irregular topography as in previous profiles. Worth noting is the section of basement located between the Cabo de Gata Spur and the Maimonides High that is affected by numerous faults defining a normal faulting block structuration (Fig. 7.7a). Along this profile, the pre-Messinian sedimentary sequences are relatively thick (almost 0.8 s TWTT) and appear faulted and folded. At the westernmost part of the section, we have identified two high-angle faults with a normal displacement (km 5 – 7.5 in Fig. 7.7a) and a vertical strike-slip fault (km 10 in Fig. 7.5a), affecting the basement and sedimentary cover up to the seafloor, suggesting that they are probably active. Taking into account the present-day stress regime, the strike-slip fault will probably have a left-lateral motion. Between 12 - 15 km and 25 - 30 km, we observed the lateral scarps of two submarine landslides (Fig. 7.2). The southern flank of the Maimonides High appears buried and covered by sediments from units IIIa, II and I. Towards the eastern part of the TM23 profile, the Algero-Balearic Basin is imaged. Similarly to profile TM24 (Fig. 7.6b), we recognize the evaporitic deposits within unit IIIa and halokinesis-related structures (Fig. 7.7b). The easternmost part of the profile shows gliding structures producing deformation of the uppermost sedimentary layers, and causing the rotation and faulting of units I+II and UU above the evaporite layers (MU) (Fig. 7.7b). These faults have listric geometry and are rooted at the base of unit MU, which acts as a décollement (Fig. 7.7b). The faults reach up to the surface, creating a step-like relief that can be observed on the bathymetric map (Figs. 7.2, 7.3b). Just above the décollement there are salt welds that connect remains of the original evaporite layer (Fig. 7.7b).

7.4. Discussion

7.4.1. Nature of the basement

Igneous activity in the Alboran Basin was controlled by the convergence between the European and African Plates, and the collisional – subduction system that was created between them. It has been active from the Middle Miocene, when tholeiitic rocks were emplaced, till Lower Pliocene (e.g. Duggen, 2004, Booth-Rea et al., 2007). The Abubacer and Maimonides highs have been dredged (Fernández-Soler et al., 2000), and the recovery of volcanic and plutonic rocks from the top of the highs confirms its igneous nature (e.g. Duggen et al, 2008). They belong to the Cabo de Gata volcanic province, where volcanic activity occurred between 7.7 and 6.6 Ma. Later, volcanism continued to the north in the Mazarron-Cartagena region, where dated samples indicate an age of 3 Ma (Duggen, 2008). On seismic line TM24

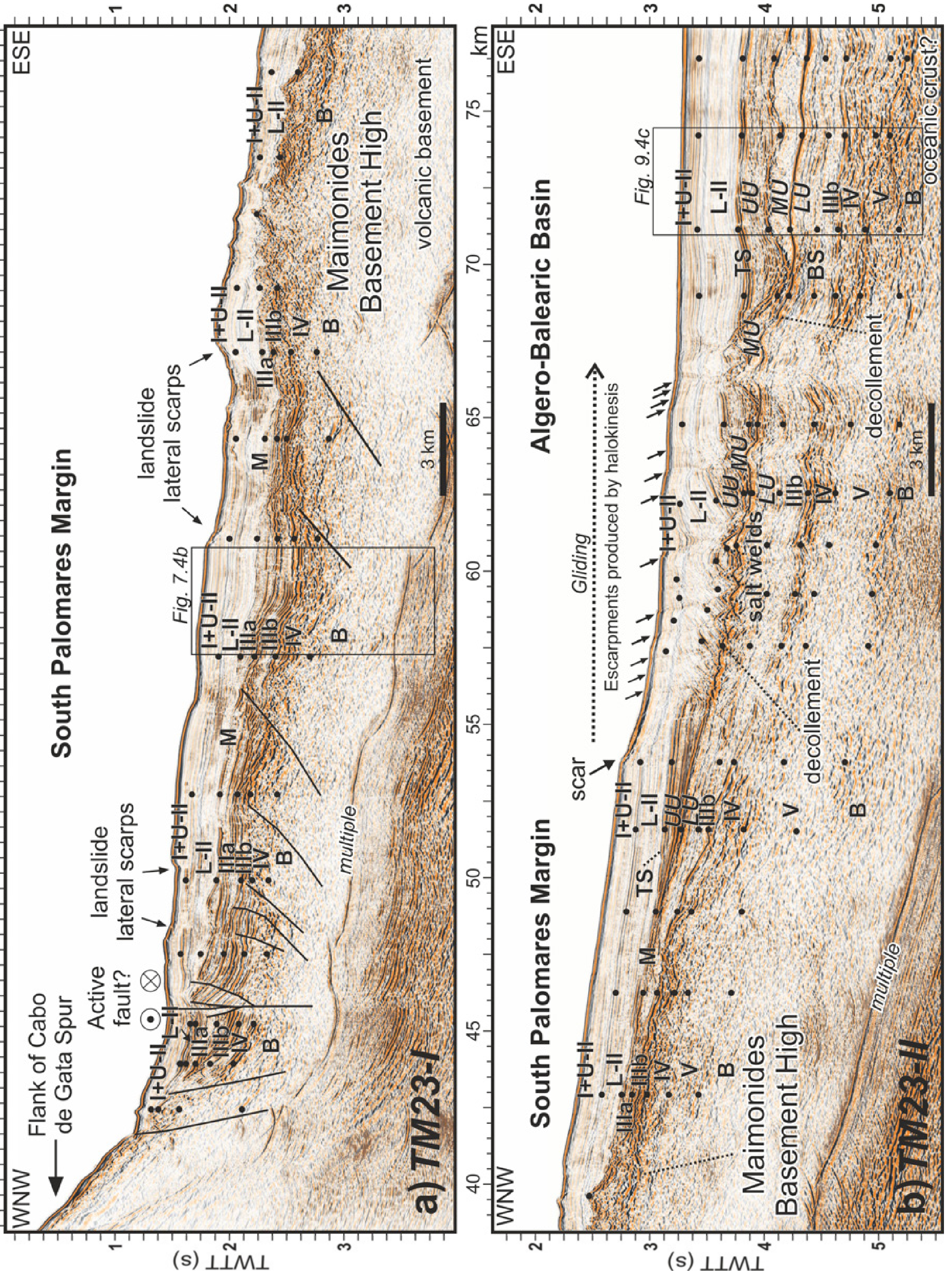
a) TM23-I
WNW
ESE
South Palomares Margin
Flank of Cabo de Gata Spur
Active fault?
landslide lateral scarps
Fig. 7.4b
Maimonides Basement High
volcanic basement
multiple
I+U-II
L-II
IIIa
IIIb
IV
B
M
3 km
TWTT (s)
km
b) TM23-II
WNW
ESE
South Palomares Margin
Algero-Balearic Basin
Maimonides Basement High
scar
Gliding
Escarpments produced by halokinesis
salt welds
decollement
Fig. 9.4c
TS
BS
UU
MU
LU
V
oceanic crust?
multiple
3 km

◄ ***Figure 7.7:*** *Time migration of profile TM23 (see Fig. 7.1 for location). Main structures, seismostratigraphic units and the seafloor multiple are identified. Age of the units is defined in caption of Figure 7.4. Vertical exaggeration is of x:5, taking into account water velocity. Location of seismic units displayed in Figure 7.4 is depicted.*

(Fig. 7.6b) and on the bathymetric maps (Figs. 7.2, 7.3b, 7.8) we recognize volcanic features, such as cones and ridges, along the Abubacer and Maimonides highs.

Although the igneous nature of the Abubacer High is confirmed, the prominent ridge topography is not only generated by volcanic processes but partially generated by thrust and associated anticline, as suggested by Giaconia et al. (2015). The line TM24 across the Abubacer ridge (Fig. 7.6a) does not show any evidence of volcanic aprons that are usually formed by volcanoclastic deposits during the growth of a volcanic edifice. Moreover, the infill of the Abubacer Basin shows syntectonic deformation, and although the faults responsible of the uplift of the Abubacer ridge are not visible, a kinematic analysis supports thrust faulting in the Abubacer High (Giaconia et al., 2015).

The Abubacer High shows evidence of erosion. It is affected by a system of gullies, especially on its northern part, and also by mass-wasting processes. On the other hand, the Maimonides High has a sharp topography, and does not display any evidence of mass transport deposits. These different erosion degrees may suggest that the Maimonides structures are younger, hypothesis also supported by the recovery of fresh glassy vesicular rocks from the top of the Maimonides High (Fernández-Soler et al., 2000).

7.4.2. Tectonic evolution

The driving force of the neotectonic activity in the Alboran Basin, and especially at the Palomares margin, is the convergence between the European and African plates. West of the Palomares margin, however, GPS data indicate other tectonic mechanisms (e.g. Koulali et al., 2011; Galindo-Zaldivar et al., 2015; Pérez-Peña et al., 2015) related to the detaching slab that affect the tectonic activity observed in the central and western Betics (Martínez-Martínez et al., 2006; Galindo-Zaldivar et al., 2015; Mancilla et al., 2015). The NW-SE trending convergence (4.5 – 5.6 mm/yr, e.g. Nocquet, 2012) between these two tectonics plates is accommodated along a series of active faults, such as the Eastern Betic Shear Zone (EBSZ) in SE Iberia and East Alboran Basin (e.g. Bousquet, 1979) (Fig. 7.1). This structure has a clear trace onshore and the PF segment runs along the coastline near Vera (Fig. 7.2). Although there are no proofs of its offshore continuation, some authors affirm that the PF continues at sea (e.g. Comas et al., 1999; Booth-Rea et al., 2004). Other hypothesis defends that the PF ends at the shoreline (e.g. Gràcia et al., 2006; Moreno et al., 2016), and deformation is instead accommodated along the reverse faults segments located at the southwestern termination of the Palomares Fault, at the northern and southern sides of the Cabrera anticline, and also at the E-W dextral-reverse Polopos Fault zone (Fig. 7.1, 7.2) (Giaconia et al., 2012, 2013). The high-resolution bathymetric and slope map of the shelf area as well as the MCS profiles (Fig. 7.2, 7.5, 7.6, 7.7); do not show any evidence of an offshore continuation of the Palomares Fault. The roughly coast-parallel scarps in the area between the inner and the outer shelf are likely of exogenic origin and related to the Pleistocene glacial-induced regressions and transgressions (Acosta et al., 2013; Lobo et al., 2015). Reverse instrumentally-recorded earthquakes have been recorded in the area (Stich et al., 2003, Giaconia et al., 2015), but there is not enough accuracy on the seismicity location to make a relationship between the earthquakes and these small scarps (Fig. 7.1). Thus, we suggest that the PF ends near the shoreline at the westernmost end of Sierra Cabrera, or its slip greatly decreases offshore, not forming characteristic deformational structures that could be observed in the bathymetry or in the MCS profiles (Fig. 7.2, 7.3a).

Most of the faults imaged by the MCS profiles are considered as inactive, as they are either covered by undeformed sediments of units L-II and I+U-II (Fig. 7.5 between 10 – 15 km), or they affect only the basement and oldest sedimentary units (Fig. 7.6a at 30 km, Fig. 7.7a between 13 – 17 km). Only a few faults located in the upper slope appear to deform Plio-Quaternary deposits. The large majority of these faults were generated during the basin opening extension, with normal fault kinematics. Units V and IV appear largely confined to basement relief that was formed by normal faulting. The strata from unit V are rotated and locally form wedge-shaped deposits that onlap the basement. We interpret unit V as syn-rift. Unit IV is also interpreted as a syn-rift unit due to its thickness variation, increasing at the deepest part of fault-controlled local depocenters, and with an onlap configuration against the top of unit V. However, unit IV is considerably more widespread than unit V and filled the fault-controlled depocenters, possibly indicating a late syn-tectonic character. Unit IIIb presents parallel reflections, and its thickness variations are probably related with the Messinian Salinity Crisis erosion. Reflections in unit IIIa are parallel and the unique deformation observed in this unit is related to halokinesis processes and not to tectonic structures, suggesting that the deposition of this unit took place once the rifting phase finished.

The geometry of strata and relative position of the units, support that only a few of the normal faults formed during rifting may have been later reactivated with reverse or oblique slip. We interpret that the faults are reactivations of inherited structures because compressive deformation is especially visible affecting pre-Pliocene sediment, possibly because those sediments were compartmentalized in narrow bodies and fault reactivation strengthens the discontinuous character of the deposits of older units. However, the reason why reactivation has occurred only at a few structures from those formed during rifting, and mainly along structures in the middle and upper continental slope is unclear, and perhaps it is related to a priori favorable orientation.

Along line TM25 only one large structure appears active, cutting from depth into the Pliocene and perhaps Quaternary section in the upper slope (km 2.5 – 4.5 in Fig. 7.5). The deformation is limited and does not seem to cut the seafloor, or it is below the data resolution of our bathymetric and seismic data. However, the seafloor shows some small-scale relief that appears to indicate some recent deformation. The structure is then possibly active but accommodates minor ongoing deformation, or alternatively, the structure corresponds to a growth fault with offset decreasing towards the surface.

Line TM24 images the deformation associated to the relief of the Abubacer Ridge that is a structure with at least part of its relief related to contraction (Giaconia et al., 2015) (Fig. 7.6a). The relief of the igneous basement is related to a landward dipping thrust fault cutting from deep under the structure (Giaconia et al. 2015). The sediment in the small depocenter overlaying the basement (Abubacer Basin in Fig. 7.6a), formed in the hanging wall to the fault, shows that the entire sequence seems gently folded, but that folding has probably attenuated since Early Pliocene. Pre-Messinian Unconformity units appear folded. The thickness of unit IIIb seems to be constant, so we inferred that the deposit of this unit is still previous to the beginning of the thrust. Unit L-II (Early Pliocene) shows evidence of folding, and presents parallel internal reflections and its thickness increases slightly towards the depocenter. Unit I+U-II (Late Pliocene – Quaternary) presents almost a constant thickness, onlapping above unit L-II (km 11 – 22 in Fig. 7.6a). Thus, it is likely that the thrust initiated in Late Messinian or Earliest Pliocene, and during the Pliocene and Quaternary slip rates decreased. It is also unclear how much ongoing deformation may currently occur in the Abubacer High, but instrumentally recorded earthquakes showing reverse mechanisms occur near it (Giaconia et al., 2015).

Line TM23 images also two major structures that seem currently active in the upper slope (km 5 - 8 in Fig. 7.7a). The narrow anticline fold deforming up to unit I+U-II (km 6 in Fig. 7.7a) may have been formed by a steep blind thrust or may alternatively correspond to a positive flower structure of a strike-slip fault, similar to faults onshore in the neighbouring region. The high dip angle of the fault trace and the stratigraphic relations between the oldest units (like the fan shape of unit IIIb, km 6 – 10 in Fig. 7.6a), drive us to think that these faults were normal faults. The compressive deformation associated with the younger units, like the anticline previously described, supports that these faults have been reactivated as compressive structures. Here again, deformation is higher in units II-IV, still fairly clear in unit L-II and subdued in unit I+U-II. The deformation structures support an initiation of the contraction in the Late Messinian – Early Pliocene with the largest slip at the time and a much slower slip in Pleistocene time. This decrease in slip rate is supported by the relatively constant sedimentation rates averaged across the Plio-Quaternary time (calculated sedimentation rates from ODP Site 978 are 154 m/Ma for the Upper Miocene, 120 m/Ma for the Lower Pliocene, 111 m/Ma for the Upper Pliocene and 127 m/Ma for the Pleistocene) (Braga and Comas, 1999). These ages are coherent with the ages and rifting phases described for the opening of the western Mediterranean and its later compressive reorganization, which is proposed to have started at around 8 Ma (late Tortonian) (e.g.Mauffret et al., 2007; Billi et al., 2011; Medauri et al., 2012, 2014; Giaconia et al., 2015).

The seafloor mapping is of sufficient resolution to detect structures ~10 m high in the slope and a few meters high in the shelf so that we interpret that the relief data does not support the presence of significantly deformed structures and thus, current deformation is very limited in the study region. This is also supported by the images of the subsurface structures described above from the three seismic profiles. So, we infer that ongoing deformation due to the Eurasian - African plate convergence has shifted from the older offshore structures and it is currently mainly accommodated by structures onshore and few uppermost slope faults offshore along this margin. Instead, we proposed that the ongoing deformation in the deep basin offshore the Palomares margin should be accommodated at the evaporites layer, due to gravity driven salt-tectonics.

7.4.3. Halokinesis

During Messinian times, the connection between the Atlantic Ocean and Mediterranean Sea through the Straits of Gibraltar was closed, resulting in what has been referred as the "Messinian Salinity Crisis" (MSC), which occurred about 5.96-5.33 Ma ago (e.g. Krijgsman et al., 1999; Duggen et al., 2003; García-Castellanos et al., 2009, 2011; Roveri et al., 2014). The ductile deformation processes affecting evaporite deposits are responsible for the sediment deformation observed in some of the MCS profiles. This thin-skinned deformation is mainly driven by gravity (Sage et al., 2005; Hudec and Jackson, 2007; Lofi et al., 2011). Halokinesis is also the responsible of the swell and furrow topography present across the Algero-Balearic Basin (Figs. 7.2, 7.3 and 7.8). Furthermore, this topography has been imaged in the nearby areas of the Palomares continental margin (Camerlenghi et al., 2009; Acosta et al., 2013). This characteristic deformation of the sediments is due to the displacement of the evaporite layer in the deeper part of the basin, where the salt flow produces salt anticlines and pillows (Camerlenghi et al., 2009). Other typical structures derived from halokinesis have been identified. On profile TM24, we imaged a salt dome. The upward flow of this evaporite accumulation has generated faulting and block rotation in the above sediments that mainly affects units I+U-II and L-II (Fig. 7.6b). We interpret that this is an active process, as evidenced by seafloor deformation (Figs. 7.6b and 7.8). In the eastern section of the TM23 profile (Fig. 7.7b) we observe structures related to gliding processes. Similar situations have been described across the whole Mediterranean Sea (e.g.Sage et al., 2005; Lofi et al., 2011).

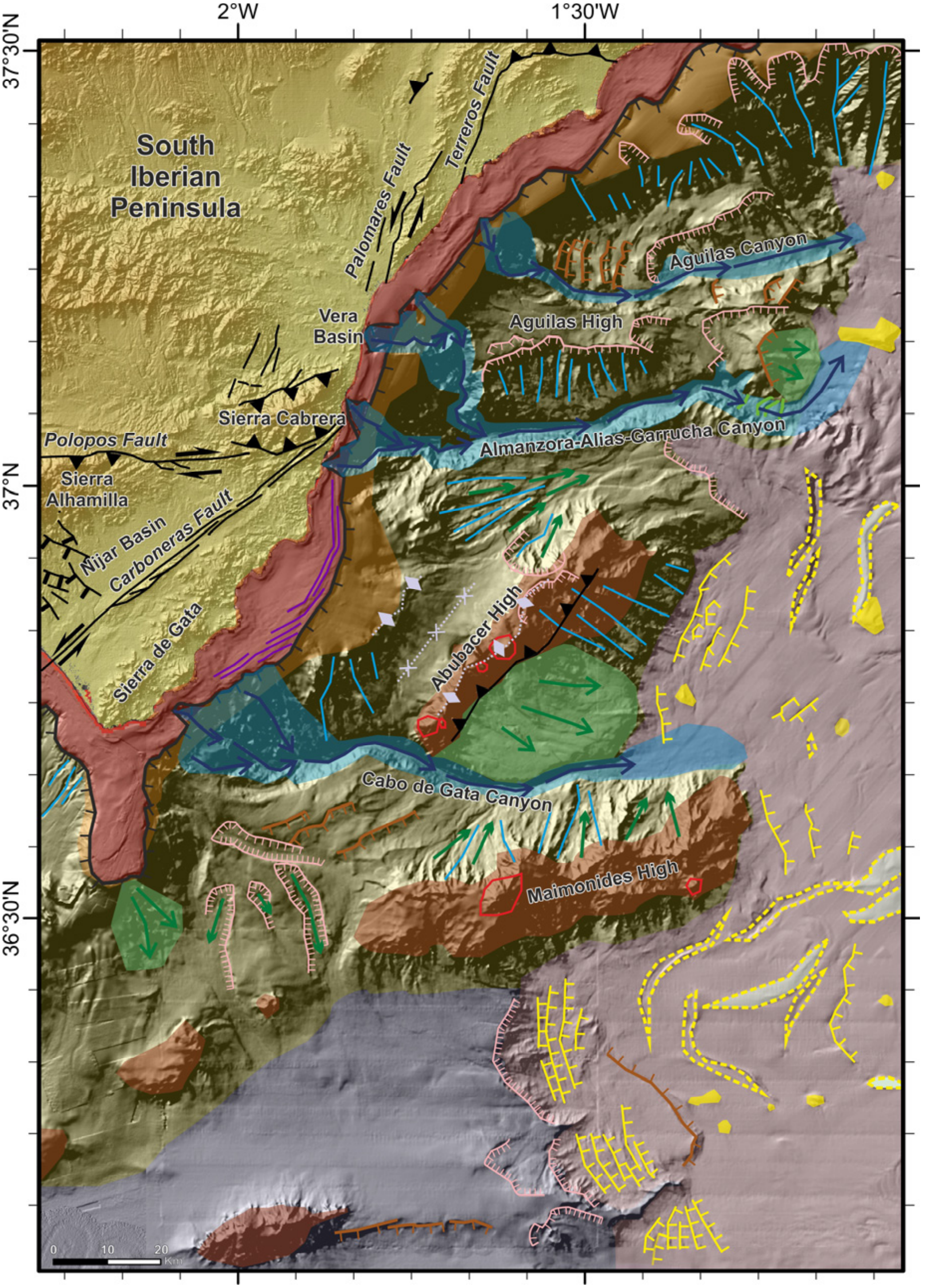
2°W
1°30'W
37°30'N
37°N
36°30'N
South Iberian Peninsula
Terreros Fault
Palomares Fault
Aguilas Canyon
Vera Basin
Aguilas High
Sierra Cabrera
Polopos Fault
Almanzora-Alias-Garrucha Canyon
Sierra Alhamilla
Nijar Basin
Carboneras Fault
Abubacer High
Sierra de Gata
Cabo de Gata Canyon
Maimonides High
0
10
20
Km

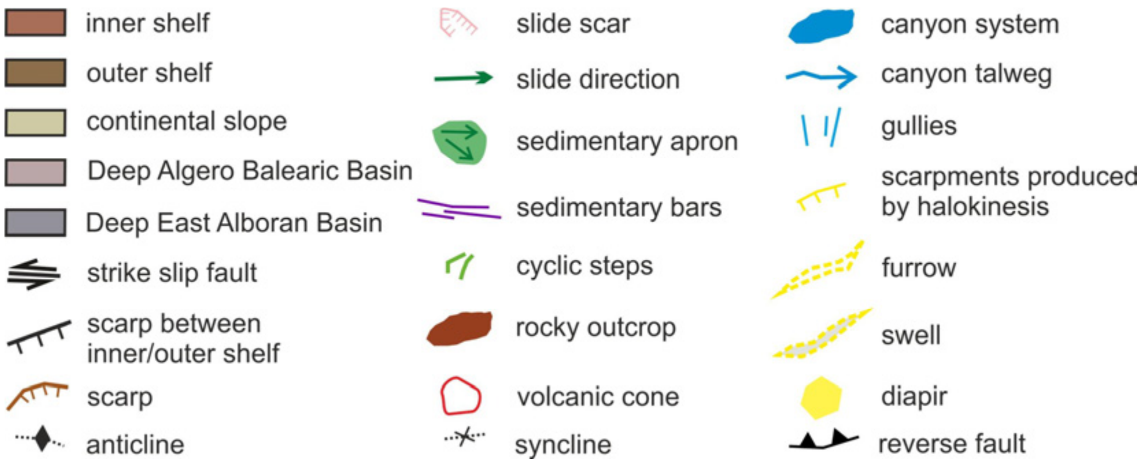

Figure 7.8: *Morphostructural interpretation of the Palomares margin (same area as Figure 7.2, see Figure 7.1 for location). Main features are located. See caption for significance of different symbol categories.*

Sedimentary units L-II and I+U-II have been gravitationally sliding over a thin salt layer, which base acts as a weak décollement surface. This seismic reflection shows strong inverse polarity (Fig. 7.7b), which defines the base of the evaporites. Gliding is probably due to their low coefficient of friction and the flow of evaporites from the shallower part of the continental slope into the deeper basin. The migration of salt has generated normal faulting and block rotation in the uppermost sediments corresponding to units L-II and I+U-II (Fig. 7.7b). The different sedimentary load of the sediment wedge at the continental slope have been proposed as a possible triggering mechanism (Gaullier and Vendeville, 2005; Camerlenghi et al., 2009). We interpret that this process is also active, as faulting is affecting the seafloor. On both profiles, where Subunit MU is identified, unit L-II is composed of parallel reflections without internal deformation, while unit I+U-II is onlapping above L-II where halokinesis phenomena occurred, and its thickness increases toward the deeper part of the basin at the top of unit L-II (Fig. 7.6b, 67-70 km). On the basis of this internal structuration, we propose that the salt movement at the Palomares continental margin began after the deposition of unit L-II, and that unit I+U-II is coetaneous with this activity (Late Pliocene – Quaternary).

7.4.4. Sedimentation and mass wasting processes

In the area, sedimentary fluxes are conditioned by two main processes: a relatively constant hemipelagic sedimentation, and a high-energy sedimentation driven by slope failures and turbidite currents. Regarding the occasional sedimentation related to bottom currents and mass-transport processes, the role of the canyons as sediment pathways feeding sediments from the shelf to the abyssal plains is fundamental. These canyons are highly erosive structures (Fig. 7.2), which location in origin may be related to a fault in depth (Fig. 7.6). In the cases of the Cabo de Gata Canyon (Fig. 7.6b) and the Almanzora-Alias-Garrucha Canyon (Fig. 7.6a), it is clear that they are related to a fault trace at depth (Fig. 7.6b). These faults are most likely inactive, because they are not affecting the Pliocene – Quaternary sedimentary sequence. We suggest that the other canyons of this area may also follow fault traces as weakness areas for preferential erosional pathways, at least at their early stages. Due to the complex topography of the margin, the present pathways are also determined by topographic factors, such as topographic highs. The mass-wasting processes affecting the canyon flanks, the narrow crests between them, and the depositional sedimentary bedforms recognized in some of the canyons, such as the "cyclic steps" (e.g. Cartigny et al., 2011) identified at the mouth of the Almanzora-Alias-Garrucha canyon (Figs. 7.2b, 7.8), are indicative of current activity along these three canyons, which is consistent with recent studies (Perez-Hernandez et al., 2014).

The inner shelf corresponds to an erosional platform covered by a thin layer of Pleistocene sediments. Along this part of the shelf, sedimentary bars with parallel to sub-parallel orientation relative to the shoreline are recognized (Fig. 7.8). Sedimentary bars with similar orientation have been recognized at the northern adjacent area, the Mazarrón margin (Acosta et al., 2013). In this area, bars parallel to the shoreline have been interpreted as relict structures constructed during the Holocene transgression by alongshore currents (Acosta et al., 2013). At the Mazarron margin active sediment bars have been identified. They are related to southwest flowing (the Liguro-Provençal-Catalan or North Current), and have a SW-NE orientation (Acosta et al., 2013). Due to the proximity between the two areas and the similarity between the processes described, we inferred that the sediment bars recognized at the Palomares margin with a parallel-subparallel orientation relative to the shoreline are relict. The relief of the outer-shelf is mainly dominated by erosive processes, such as slope failures, tributary valleys, gullies, and canyon erosion (Fig. 7.8). It is still unclear how fast these erosional processes are and whether they can obliterate relief formed by slow-slip active faulting common in the region. Recent sedimentation at the Southeaster Iberian shelf is poorly known (Lobo et al., 2014). The suspended fine sediments travel with the dominant current (Liguro-Provençal-Catalan or North Current) from North to South. At the southernmost area, the abrupt shelf configuration favors the sediment capture by submarine canyons, and they are exported to deeper parts of the basin (Lobo et al., 2014). Sedimentary processes have been identified at the deeper part of the continental slope and the Algero-Balearic Basin, such as the sedimentary lobe covering the southeaster flank of the Polacra Ridge (Figs. 7.2a, 7.8). A large number of mass transport deposits have been recognized (Fig. 7.8), and possibly different triggering mechanisms should be considered. Seismic activity may be a plausible one, although is scarce along the margin. Sediment loading has also been proposed as a trigger mechanism (Acosta et al., 2013), although our data does not provide evidences to support it.

7.5. In summary

The Palomares margin is characterized by a complex relief mainly generated by the presence of three large highs, and three deeply eroded submarine canyons in between them. We have recognized the following areas: (i) the continental shelf, (ii) the continental slope and (iii) the Algero-Balearic Basin. Active processes and tectonic structures present on each area are different, and determine their specific seafloor morphology.

The shelf may be divided into the inner and outer shelf. These two levels are separated by an escarpment that is probably related to a previous cliff cut during the Pleistocene glacially induced regressions and transgressions (Acosta et al., 2013, Lobo et al., 2014). The continental slope is characterized by the presence of highs and canyons. Three highs are identified: (i) the Aguilas High, (ii) the Abubacer High and (iii) the Maimonides High. They are affected by erosive and mass-wasting processes, although we infer that the Maimonides High is probably younger than the remaining two due to its sharp relief. Three canyons are also mapped: (i) the Aguilas canyon, (ii) the Almanzora-Alias-Garrucha canyon and (iii) the Cabo de Gata canyon. At least the Cabo de Gata and Almanzora-Alias-Garrucha Canyon seem to follow possibly inactive fault traces as preferential erosion direction. The complex topography of this area has probably conditioned the later evolution of canyon pathways. They show evidence of erosional processes, with gully systems on their flanks, slope failures and erosive slide scars, and mass transport deposits. Finally, the geomorphology of the Algero-Balearic Basin at the Palomares margin area is mainly controlled by halokinesis processes related to the Messinian evaporites that formed a series of troughs and swells.

The bathymetry of the Palomares margin and the imaged structures with the MCS profiles reveal that the geomorphology of the area is controlled mainly by erosional and halokinesis processes. Faults identified in the MCS profiles do not seem to affect the seafloor, and deformation apparently decreases from the Messinian till present. We suggest that the ongoing deformation in the area is then accommodated by onshore structures. Offshore, there are only few active faults located at the uppermost slope.

The Palomares margin formed during the Early Tortonian. The rift stage continued in the margin till the Late Tortonian, when compressive deformation started to control the evolution of the area. This change in the dominant tectonic mechanism produced the reactivation, as thrusts and/or strike-slip faults, of the few previously extensional structures, mainly located at the continental slope.

Chapter 8

The Yusuf Fault

The subduction system related to the convergence between the European and African plates led to the formation of the Alboran and the Algero-Balearic basins in the western Mediterranean. The origin of these basins is debated in different evolutionary processes (e.g. Comas et al., 1999; Vergés and Fernández, 2012; Van Hinsbergen et al., 2014). The Algero-Balearic Basin has a fairly smooth seafloor with 2500 < water depth < 3000 m (Abyssal > 3000 m) that is generally assumed to be floored by oceanic crust formed during the Middle to Late Miocene (Rehault et al., 1984; Dewey et al., 1989; Mauffret et al., 2004; Booth-Rea et al., 2007; Mauffret et al., 2007; Billi et al., 2011; Grevemeyer et al., 2011; Leprêtre et al., 2013; Bouyahiaoui et al., 2015). To the west, it the seafloor gradually shoals to <2500 m water depth of the Alboran Basin. Most accepted hypotheses interpreted the Alboran Basin as the result of extensional processes in the inner part of Gibraltar Arc system. While at the western and southern parts of the Alboran Sea metamorphic basement remains (Comas et al., 1992; Medaouri et al, 2012), magmatic activity and extension generated an arc magmatic crust in the middle section, and finally an oceanic crust in the easternmost section joined with the Algero-Balearic Basin basement (Duggen et al., 2004; Booth-Rea et al., 2007).

Offshore North Algeria and Morocco occurs one of the largest tectonic structures of the area, the Yusuf Fault system (Fig. 8.1), so that it appears a key structure to understand the evolution of this part of the Alboran Basin. Previous studies attempting to characterize this area focused in the post-Messinian evolution (Martínez García et al., 2011, Martínez-García, 2012; Martínez-García et al., 2013). This is mainly due to the difficulties of imaging pre-Messinian strata with vintage data, and lack of constrains of pre-Messinian stratigraphy from ODP-Leg 161 in the Eastern Alboran Basin that stopped in Messinian strata (e.g. Jurado and Comas, 1992; Comas et al., 1999; Juan et al., 2015; Martínez-García et al., 2013). Recent works (Medaouri et al., 2012; 2014) describes the general structure of the north Algerian margin, but does not attempt to characterize the fault system.

In this study we use three new datasets of different resolution and penetration to characterize the Yusuf Fault system and surrounding area. With this modern, multi-scale data, we characterize both, deep crustal structure and sediment infill, to investigate the evolution of the architecture of the deposits associated to the Yusuf Fault kinematics. One dataset is a dense high-resolution seismic grid imaging Yusuf Fault system faults, pull-apart basin and surrounding region to map the deformation and displacement associated to Yusuf Fault. Furthermore, we also pre-stack-depth-migrated a long-offset deep-penetration section, showing the real geometry of the structures and allowing to measure and quantify deformation. Here we describe, for the first time, the kinematics of this zone and the role of the Yusuf Fault in the present-day stress regime, which is fundamental to understand the seismogenic potential and associated hazard that this structure implies for the Alboran region.

The objectives of this study are: (i) To describe the Yusuf Fault system at a regional scale; (ii) To estimate map sediment structure in the pull-apart basin, and estimate fault displacement and propose an evolutionary model for the Yusuf Fault; (iii) To understand the role of this structure accommodating the

Eurasian – African plate convergence and integrate it into a kinematic model; and (iv) To evaluate the potential seismic hazard of the Yusuf Fault.

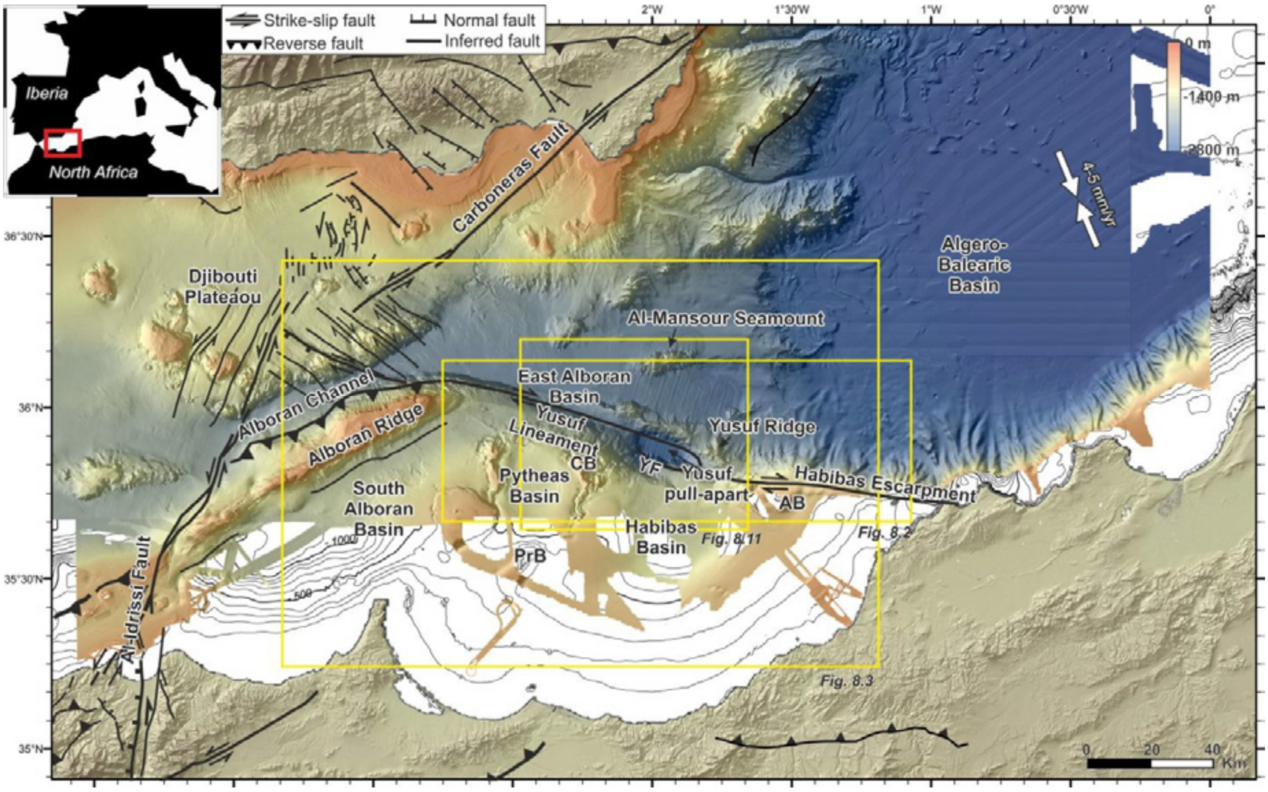

Figure 8.1: *Regional bathymetric map of the Alboran Sea constructed from swath-bathymetric data acquired during the IMPULS-06, EVENT-10, TOPOMED-11, SHAKE-15 and IDRISSI-16 marine cruises (e.g. Gràcia et al., 2006, 2012), the SARAS cruise (PI: d'Acremont & Gorini; d'Acremont et al., 2014; Lafosse et al. 2016; Rodriguez et al. 2017) and a compilation of existing datasets from IEO (Ballesteros et al., 2008) and GEBCO. Land topography is from the SRTM-3 grid. Main tectonic structures are displayed (Gràcia et al., 2006, 2012). The yellow rectangles depict the areas presented in Figures 8.2, 8.3 and 8.13. AB: Alidade Bank, CB: Cabliers Bank, PrB: Provençaux Bank, YF: Yusuf Fault. Inset: Location of the shown area (red rectangle).*

8.1. Geological setting of the Yusuf Fault system

The contact between the two westernmost Mediterranean basins is found offshore Algeria. To the west, it is located the Alboran Basin, while to the east, is the Algero-Balearic Basin (Fig. 8.1). In the Alboran Basin, the deformation controlled by the NW-SE trending convergence (4.5 – 5.6 mm/yr) between the Eurasian and African plates is accommodated by numerous active structures, forming a diffuse plate boundary between the European and African tectonics plates (e.g. Fernández-Ibáñez et al., 2007; Serpelloni et al., 2007; Koulali et al., 2011; Nocquet, 2012) (Fig. 8.1), where shallow events occur over a broad area (Stich, 2003; Stich et al., 2006; Stich et al., 2010; Meghraoui and Pondrelli, 2012; Martín et al., 2015) (Fig. 8.2).

Running along the southeastern Alboran Basin is located the Yusuf Fault (YF), one of the most prominent tectonic structures of the area. This is a ~150 km long dextral strike-slip fault system, composed by two nonparallel segments (West and East YF segments) that overlap where they generate a lozenge-shaped pull-apart basin (Figs. 8.1, 8.2) (Álvarez-Marrón, 1997; Martínez-García et al., 2011).

Figure 8.2: ***(a)*** *Colour shaded-relief bathymetric map of the Yusuf Fault area (see Figure 8.1 for location). The two segments of the Yusuf Fault are depicted.The location of earthquakes that occurred in this area since 1916 are shown (gray dots, Instituto Geográfico Nacional catalog, available online at http://www.ign.es/).* ***(b)*** *Slope map of the Yusuf Fault zone, same area as Figure 8.2a*

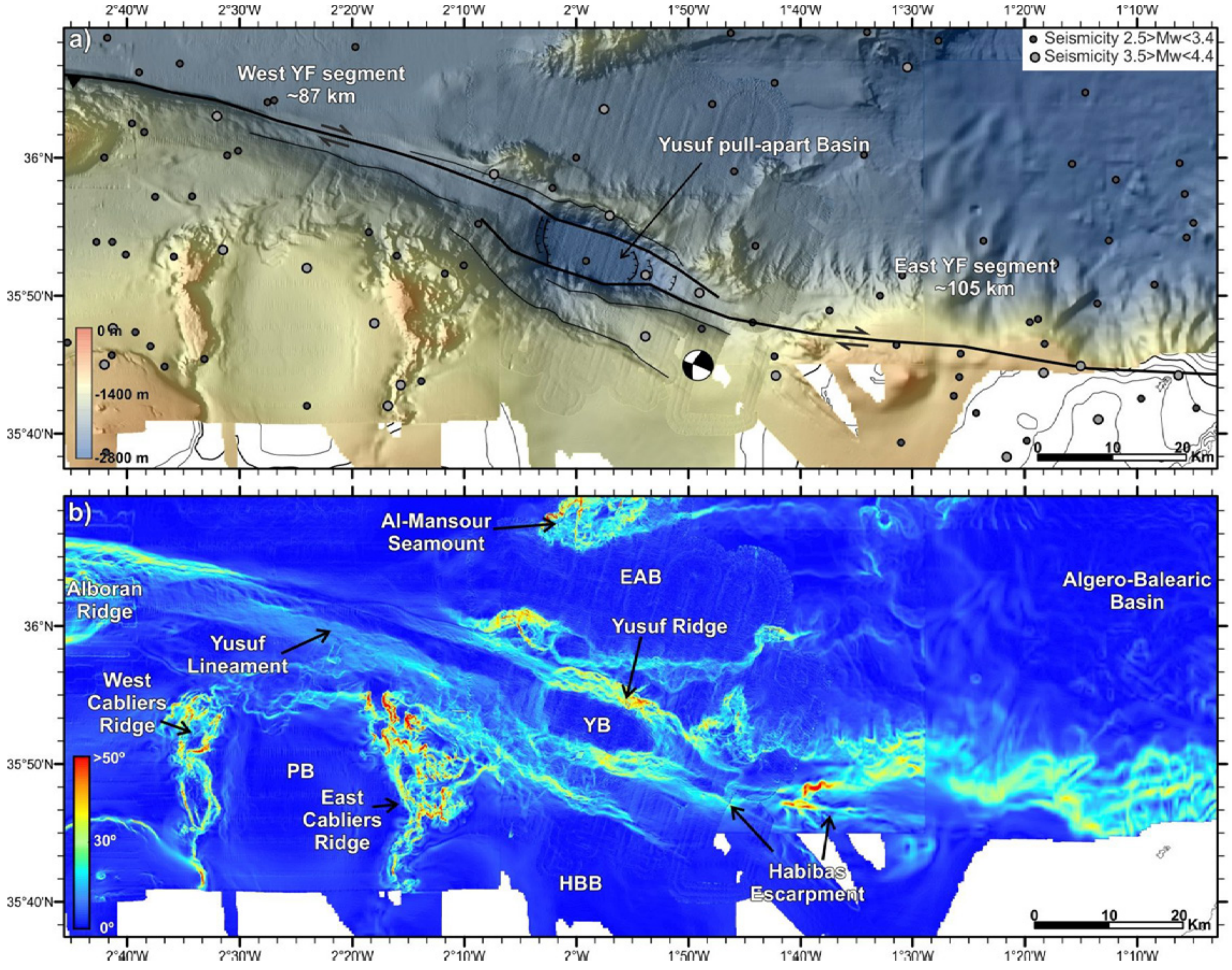

Parallel to the West YF segment is located the Yusuf Ridge (Fig. 8.1), an elongated NW-SE trending high. North of this, is located the East Alboran Basin (EAB), a triangular-shaped deep basin with a flat floor with a maximum depth of ~2000 m. It widens towards the east, where it gradually connects to the Algero-Balearic Basin through a gentle slope. Within of the EAB a prominent volcanic high, the Al-Mansour Seamount is found, with a southwest-northeast elongation. ODP Leg 161 Sites 978 and 977 were drilled at the north and the south of Al-Mansour Seamount (Alvarez-Marrón, 1997) (Fig. 8.1). The East YF segment bound the Habibas and Yusuf escarpments (Figs. 8.1, 8.2). Between these escarpments and the African shore are located the Pytheas (PB) and Habibas basins (HBB), separated by two volcanic highs, the Provençaux and the Cabliers Banks (Fig. 8.1). Within the Habibas basin, in the Algerian margin, is located the HBB-1 well site (Fig. 8.3).

While the basement of the Algero-Balearic Basin is of oceanic nature (Booth-Rea et al., 2007; Grevemeyer et al., 2011; Badji et al., 2013; Leprêtre et al., 2013), the nature of the basement in the Alboran Basin is still debated. Our work indicates that south of YF thin continental crust is locally intruded by arc magmatism, whereas north of YF of the East Alboran Basin it is formed by magmatic arc crust. Alternatively, a well-developed Continent-Ocean-Transition zone (COT) in the East Alboran Basin, east of 1ºW has been interpreted based on industry MCS data (Medaouri et al., 2014).

The processes that led to the formation of the Alboran basin also had magmatic activity associated that formed the Al-Mansour Seamount and the Yusuf Ridge (Figs. 8.1, 8.2). Dredging recovered 10.7 ± 0.3 Ma andesites in the Yusuf Ridge, and 8.9 ± 0.8 Ma basaltic andesites in the Al-Mansour Seamount (Duggen et al., 2008). Medaouri et al. (2012) proposed that the Yusuf Ridge was formed during the Tortonian time due to the collision of the Alboran plate with the Rif and Betic domains ~10 Ma ago. Three post-Messinian contractional pulses have been described in the area: Early Pliocene (5.33 – 1.24 Ma), Late Pliocene (3.28-2.45 Ma) and Early Pleistocene (1.81-0.79 Ma) (Martínez-García et al., 2013).

8.2. Data and methods used to survey the Yusuf Fault area

8.2.1. Seismic profiles used in this chapter

A sparse grid of deep-penetration Multichannel Seismic reflection (MCS) profiles and high-resolution closer spacing grid have been used for this study. Data presented here came from three different surveys: (a) the TOPOMED-GASSIS, (b) the EVENT-DEEP Leg 1, and (c) the EVENT-DEEP Leg 2 (Figure 8.3).

The MCS profiles from the TOPOMED-GASSIS cruise Leg 1 (October 2011) were acquired on board of the Spanish RV "Sarmiento de Gamboa" (Fig. 8.3), using a 5100 meters long active section of a solid state Sentinel SERCEL streamer with 408 active sections (12.5 m channel interval), towed at 10 m depth, and using a 50.15 l (3060 c.i.) air-gun source. The source array was composed of 8 G-GUN II guns deployed at 7.5 m depth, in a single cluster distribution. The air-guns were fired every 30 m (TM01, TM02), 40 m (TM03-TM05) and 50 m (TM06 to TM25) at a pressure of 2000 psi. The total record length was 14 s (Two Way Travel Time, TWTT) with a sample rate of 2 ms.

Lines from EVENT-DEEP Leg 2 were acquired in June 2010on board the RV "Sarmiento de Gamboa" (Fig. 8.3), using a 3400 m long Sentinel SERCEL streamer with 276 channels separated 12.5 meters each and a seismic source formed by an array of ten air-guns, with a total volume of 1880 c.i. shot every 37.5 m. A window of 12 s TWTT with a sample rate of 2 ms was acquired.

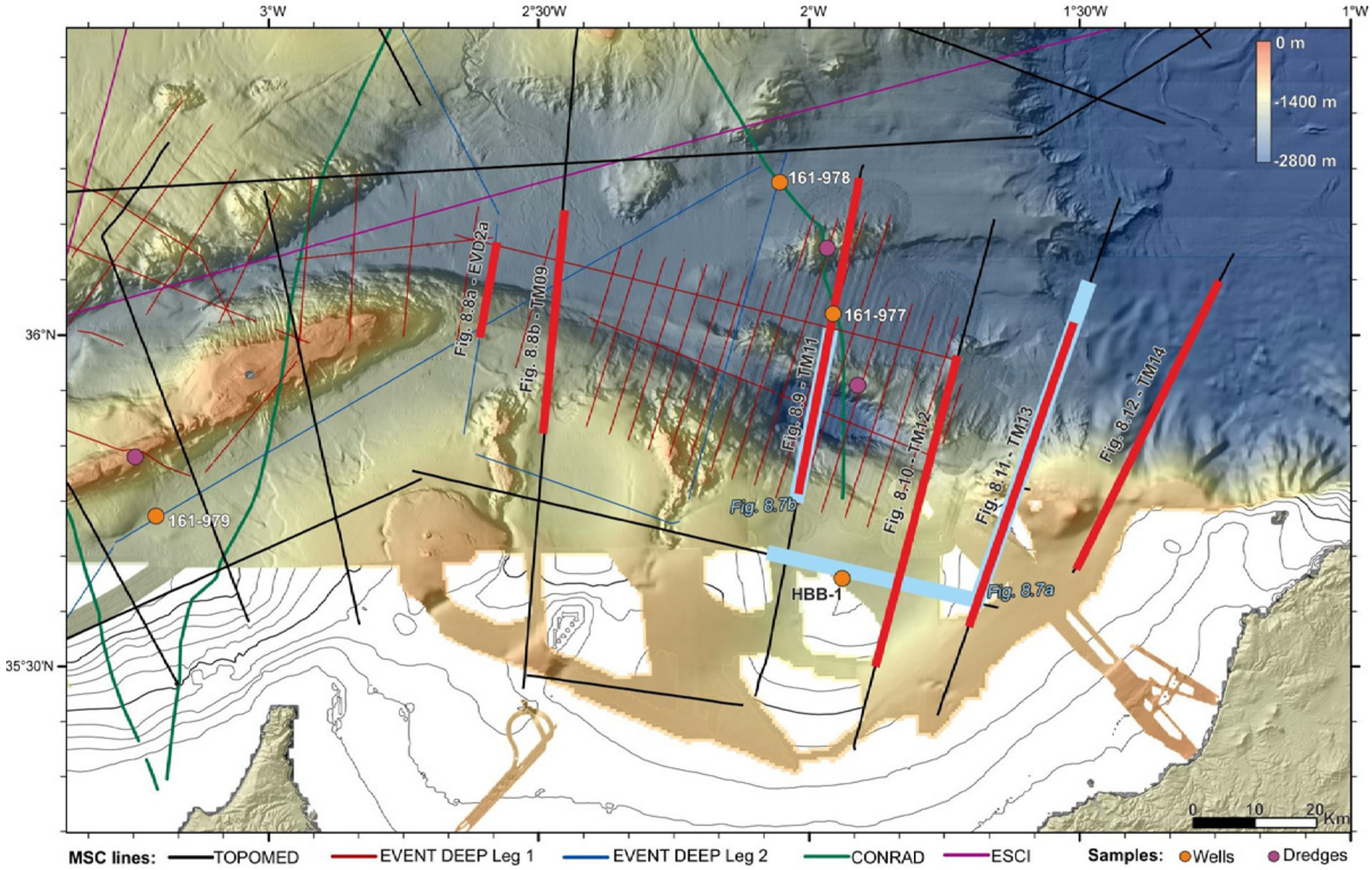

Figure 8.3: *Colour shaded-relief bathymetric map of the Yusuf Fault area. In the areas without multibeam bathymetry, contours are each 100 m. MCS profiles and wells are located. Black lines: Topomed-Gassis profiles, Blue lines: Event-Deep Leg 2 profiles, Red lines: Event-Deep Leg 1 profiles, Pink lines: ESCI profiles, Green lines: Conrad profiles. Orange dots depict the position of wells; pink dots depict the position of dredged samples. Location of the presented MCS profiles are depicted by red and blue lines. See Figure 1 for location.*

High resolution MCS from EVENT-DEEP Leg 1 were acquired during the same 2010 EVENT-DEEP cruise (May 2010) on board the RV "Sarmiento de Gamboa" but in this case, focused on shallow target (Fig. 8.3). To ensure a high-resolution in the MCS profiles a multichannel SEAL seismic streamer with 96 active sections, channel spacing of 6.25 m and towed at 2.5 m water depth was rented in the frame of the project "EVENT-SP2". The source array was composed by 10 air guns with a total volume of 13.1 l, fired every 12.5 / 18.95 m, depending on the location of the lines. A maximum window of 8 s TWTT with a sample rate of 2 ms was acquired.

TOPOMED and EVENT-DEEP Leg 2 profiles have been processed using "GLOBE Claritas" software. The processing flow was designed to obtain a crustal scale image, preserving the resolution in the sedimentary basins but also imaging the deeper parts of the crust and the upper mantle. Processing steps in time domain include minimum-phase conversion, real geometry definition accounting for streamer feathering, spherical divergence correction, predictive deconvolution in Tau-P domain (to eliminate the bubble and short periods multiple reverberations), surface consistent deconvolution, Surface Related multiple elimination (SRME) demultiple, Radon filter demultiple, normal-move-out correction based on velocity semblance analysis, Dip Move Out (DMO) correction, stretching mute, amplitude recovery, time migration and a time and spatial variant band-pass filter. In order to obtain the real geometry of the structures in depth, we have performed a Pre-stack Depth Migration (PSDM) to profile TM11 (Fig. 8.3). This PSDM has been performed using the Echos software.

EVENT-DEEP Leg 1 profiles have been processed using ProMAX and GLOBE Claritas software, with the aim of obtaining a high-resolution image of the sedimentary cover. The main processing steps applied for these profiles include statics correction, trace editing, top mute from 0 time to seabed, bandpass filter, FK filtering for a specific dip noise, true amplitude recovering due to spherical divergence loss energy, Common Depth Point (CDP) sorting, Normal Move Out after picking a velocity model, CDP stack, trace equalization, time migration, and SEGY export format.

Finally, we used the IHS Kingdom Advanced software to interpret the stratigraphy and the main structures of the MCS dataset integrating the multibeam bathymetry map, and we used Generic Mapping Tools (GMT, Wessel and Smith, 1991) to plot seismic images. Seafloor map analysis and display was done with ArcGIS software.

8.2.2. Seismic potential estimation

We apply empirical relationship (Wells and Coppersmith, 1994; Stirling et al., 2008; Wesnousky, 2008) that consider the type of crust, the tectonic setting and the dimensions of the faults to provide a maximum magnitude earthquake value.

Wells and Coppersmith (1994) formulation is based on a worldwide compilation of 421 historical earthquakes with moment magnitude (Mw) > 4.5, in which all events occurred at continental crust. Events taking place at subduction zones are excluded. Comparing the source parameters (slip, rupture length, rupture width, rupture area, maximum and average displacement per event and moment magnitude), results shown that the regressions between magnitude and surface rupture length are well-correlated, having correlation coefficients > 0.85 (Fig. 8.4a). Furthermore, the empirical regressions do not vary significantly as a function of the sense of slip. This is especially important for poor-known areas, in where the slip of the faults is not well characterized. However, as the YF is clearly a strike-slip fault system, we are going to work with the strike-slip proposed equation (Fig. 8.4a, Table 8.1).

Wesnousky (2008) used a worldwide dataset of 37 earthquakes, again limit to continental events. This compilation is formed by 22 strike, 7 normal and 8 reverse slip events. Due to the number of observations, results are more reliable for strike-slip faults. A well correlation between the moment magnitude and the length of the fault trace is observed (Fig. 8.5b). Obtained results for the YF system following the strike-slip Wesnousky relation are shown on Table 8.1.

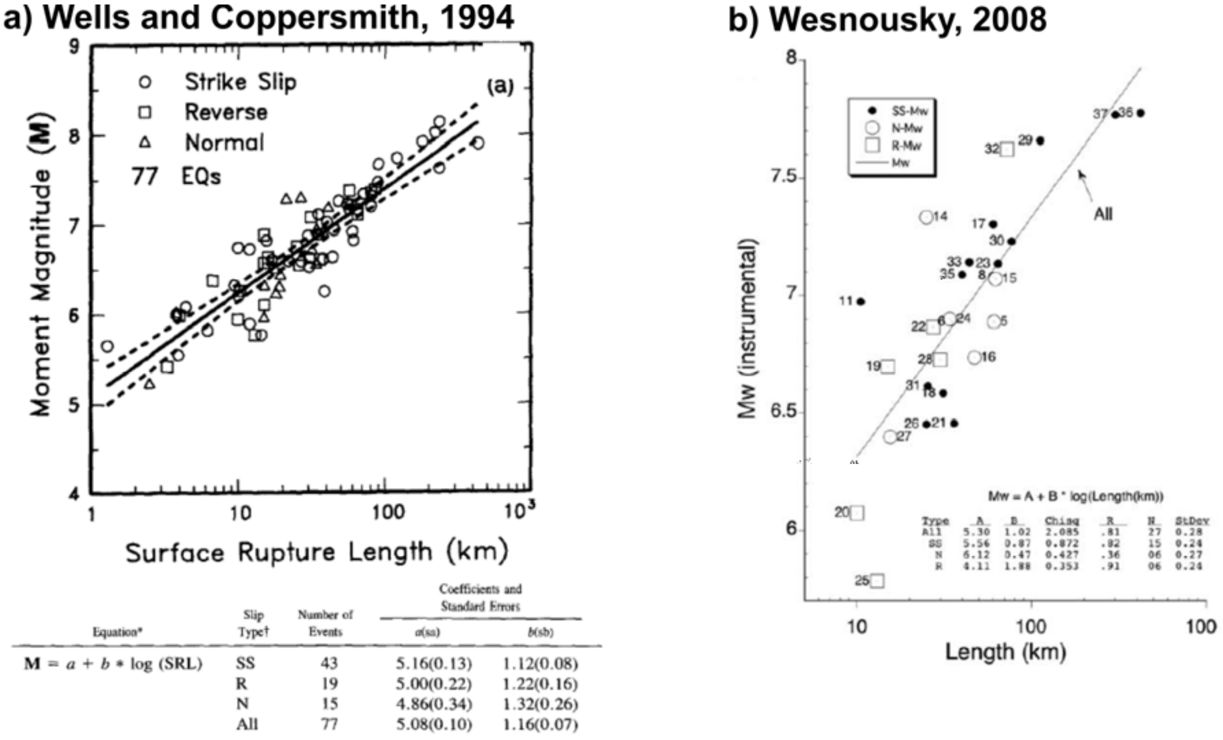

Equation*	Slip Type†	Number of Events	Coefficients and Standard Errors	
			a(sa)	b(sb)
M = *a* + *b* * log (SRL)	SS	43	5.16(0.13)	1.12(0.08)
	R	19	5.00(0.22)	1.22(0.16)
	N	15	4.86(0.34)	1.32(0.26)
	All	77	5.08(0.10)	1.16(0.07)

Mw = A + B * log(Length(km))

Type	A	B	Chisq	R	N	StDev
All	5.30	1.02	2.085	.81	27	0.28
SS	5.56	0.87	0.872	.82	15	0.24
N	6.12	0.47	0.427	.36	06	0.27
R	4.11	1.88	0.353	.91	06	0.24

Figure 8.4: ***(a)*** *Regression of surface rupture length on moment magnitude (Mw) from Wells and Coppersmith (1994), and equation of the regression line for the different slip senses (SS: strike-slip, R: reverse slip, N: normal slip, All: mean for all-slip-type relations). Dash line indicates 95% confidence interval.* ***(b)*** *Regression of fault length on moment magnitude (Mw) from Wesnousky (2008). Equation of the regression line for the different slip senses is depicted (All: mean for all-slip-type relations, SS: strike-slip, R: reverse slip, N: normal slip).*

Stirling et al. (2008) performed a comprehensive fault analysis of the Canterbury region (New Zealand), including onshore and offshore structures. Results are especially relevant for 1) strike-slip faults, including plate boundary ones, and 2) reverse and oblique-slip faults (Table 8.1). In the case of the plate boundary faults, the magnitude is correlated with the rupture area. For strike, reverse and oblique slip non plate boundaries faults, the moment magnitude is correlated with the fault width and length at the surface. As the YF marks the limit between two different crustal domains ("Chapter 5: Crustal domains"), we perform both estimations. However, the area of the fault is not well constrained. We estimated this value taking into account a mean depth of 10 km along the entire fault trace (Table 8.1).

Results are shown on Table 8.1.

Segment	Length (km) ~SRL (km)	Width (Km)	Area (km^2)	Estimated Mw			
				Wells and Coppersmith	Wesnousky	Stirling	Stirling (plate boundary)
West YF	87	3.5	870	7.3	7.3	7.1	7.0
East YF	105	4.5	1050	7.4	7.3	7.3	7.1
W+E YF	150	18	1500	7.6	7.5	7.9	7.3

Wells and Coppersmith (1994): $Mw = 5.16 + 1.12 \log (SRL)$
Wesnousky et al., (2008): $Mw = 5.56 + 0.87 \log L$
Stirling et al., (2008): $Mw = 4.18 + (2/3) \log W + (4/3) \log L$
Stirling et al., (2008) (strike-slip plate boundary): $Mw = 3.09 + 4/3 \log A$

Table 8.1: *Estimated maximum earthquake for the Yusuf Fault system, taking as input parameters the length and width of the segment and following the empirical relationship proposed by Wells and coppersmith (1994), Stirling et al., 2008 and Wesnousky et al., 2008. Mw: Moment magnitude, L: Length, SRL: Surface Rupture Length, W: Width, A: area.*

8.2.3. Slip quantification

In order to quantify the offset along the master faults of the Yusuf Fault system, we use the results from the mathematical modelling perform by Rodgers (1980), based on the elastic dislocation theory. To apply the equations of this theory, an isotropic, homogeneous and linearly half-space are assumed. Obtained results show that the geometry of the pull-apart basin is controlled by the amount of overlap and the separation between the two fault segments (Fig. 8.5), and whether the faults cut the sea-floor or not.

Modelling supported that the basin depocenter depth is equal to ~10%-15% of the total offset accommodated along the fault (Rodgers, 1980). The resulting values range between an maximum depth equal to the 10% of the offset for a separation half of the overlap till and an maximum depth equal to the 15% of the offset for a separation twice the overlap, being the maximum depth always <20 % offset. (Rodgers et al., 1980). The maximum depth is measured along a line joining the ends of the two master faults (Fig. 8.5).

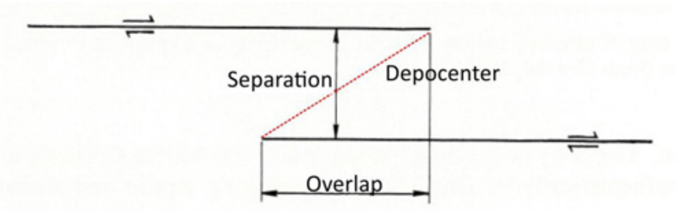

Figure 8.5: *Scheme of an en echelon right-lateral fault. Separation and overlap parameters are defined, as well as the estimated position of the pull-apart basin depocenter (modified from Rodgers, 1980).*

The maximum depocenter depth measure on the PSDM section is 2.5 km. Thus, the theoretical offset of the Yusuf Fault following the Rodgers (1980) estimation should be comprised between 16.6 and 25 km.

8.3. Results

8.3.1. Seismic stratigraphy

The seismic units have been described in the Basin evolution chapter (Chapter 6, this volume). In Figure 8.6 we present a compilation of the seismostratigraphic units defined in this area, which have been used in this chapter. Here we summarise the most relevant aspects.

The post-Messinian stratigraphy of the East Alboran Basin is reasonably well established and calibrated with commercial and ODP wells (e.g. Martínez-García, 2012; Martínez-García et al., 2013; Juan et al., 2015). The HBB-1 well in the Habibas Basin (Algerian Margin) sampled the entire sedimentary sequence (Medaouri et al., 2014) drilling Langhian strata overlaying metamorphic basement. We used HBB-1 calibration and mapped the stratigraphy of the Habibas Basin and Algerian Margin with. In addition, we used ODP-Leg 161 Site 977, drilled in the deep EAB (Comas et al., 1999), for post Tortonian calibration too. Additionally, the two highs at the EAB volcanic sequences outcropping at Al-Mansour Seamount and Yusuf Ridge provide a minimum age for the oldest sediment (e.g. Hoernle et al., 1995; Duggen et al., 2004, Duggen et al., 2005, Duggen et al., 2008).

We mapped the oldest stratigraphic sequence in the region and integrated previous studies (e.g. Martínez-García et al., 2011; Medaouri et al., 2012; Martínez-García et al., 2013; Medaouri et al., 2014; Giaconia et al., 2015; Gómez de la Peña et al., 2016) . Post-Messinian units show similar characteristics on both sides of the Yusuf Fault system, while pre-Messinian sequences on other side differ. We defined four sediment units in the East Alboran Basin (I-IV), and six sediment units in the HBB (I-III, T, S and L) (Fig. 8.6). In addition, three volcanic units have been described flooring the EAB and the westernmost Algero-Balearic Basin (vY1-3) (Fig. 8.6). In the westernmost end of the Yusuf Fault, the volcanic units are correlated with the Alboran Ridge volcanic units. The youngest Alboran Ridge (vA) volcanic units is dated on ~8.6 Ma (e.g. Duggen et al., 2004; Duggen et al., 2008).

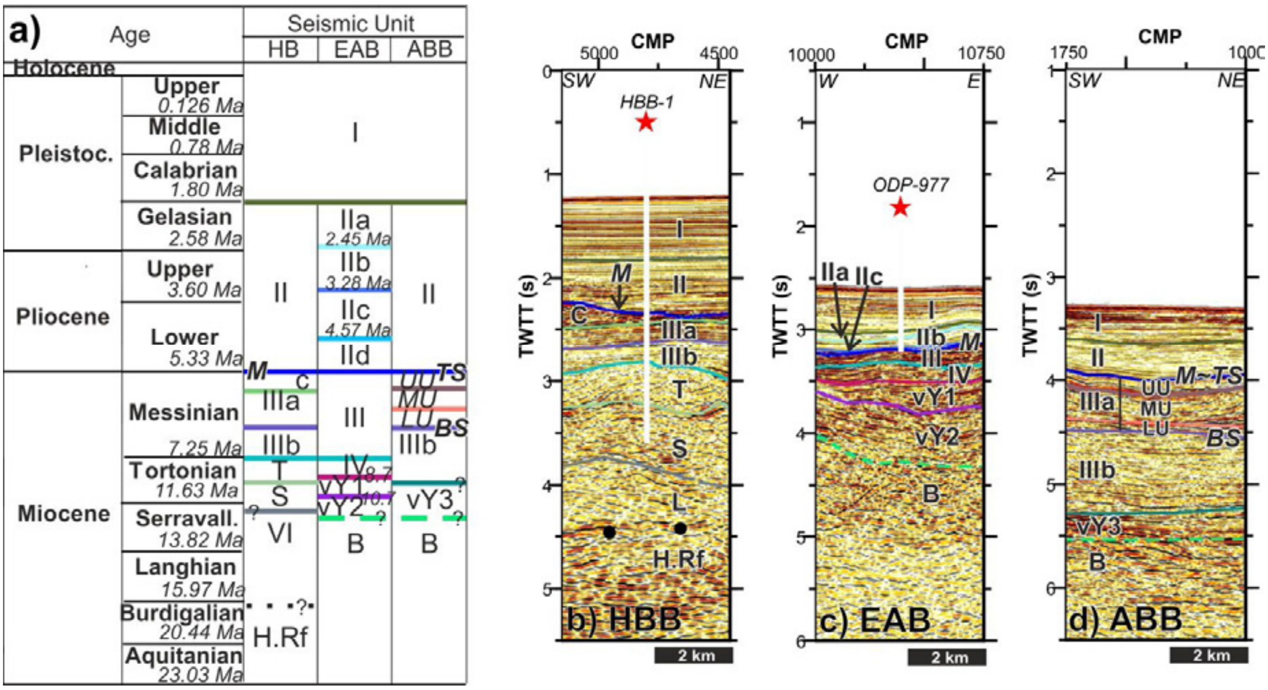

Figure 8.6: ***(a)*** *Ages and seismostratigraphic units identified in the MCS profiles in the Habibas Basin* ***(HB, Fig. 8.6b)****, the East Alboran Basin* ***(EAB, Fig. 8.6c)****, and in the Algero-Balearic Basin* ***(ABB, Fig. 8.6d)****. H. Rf: High Reflectivity unit, B: Basement. See text for details.*

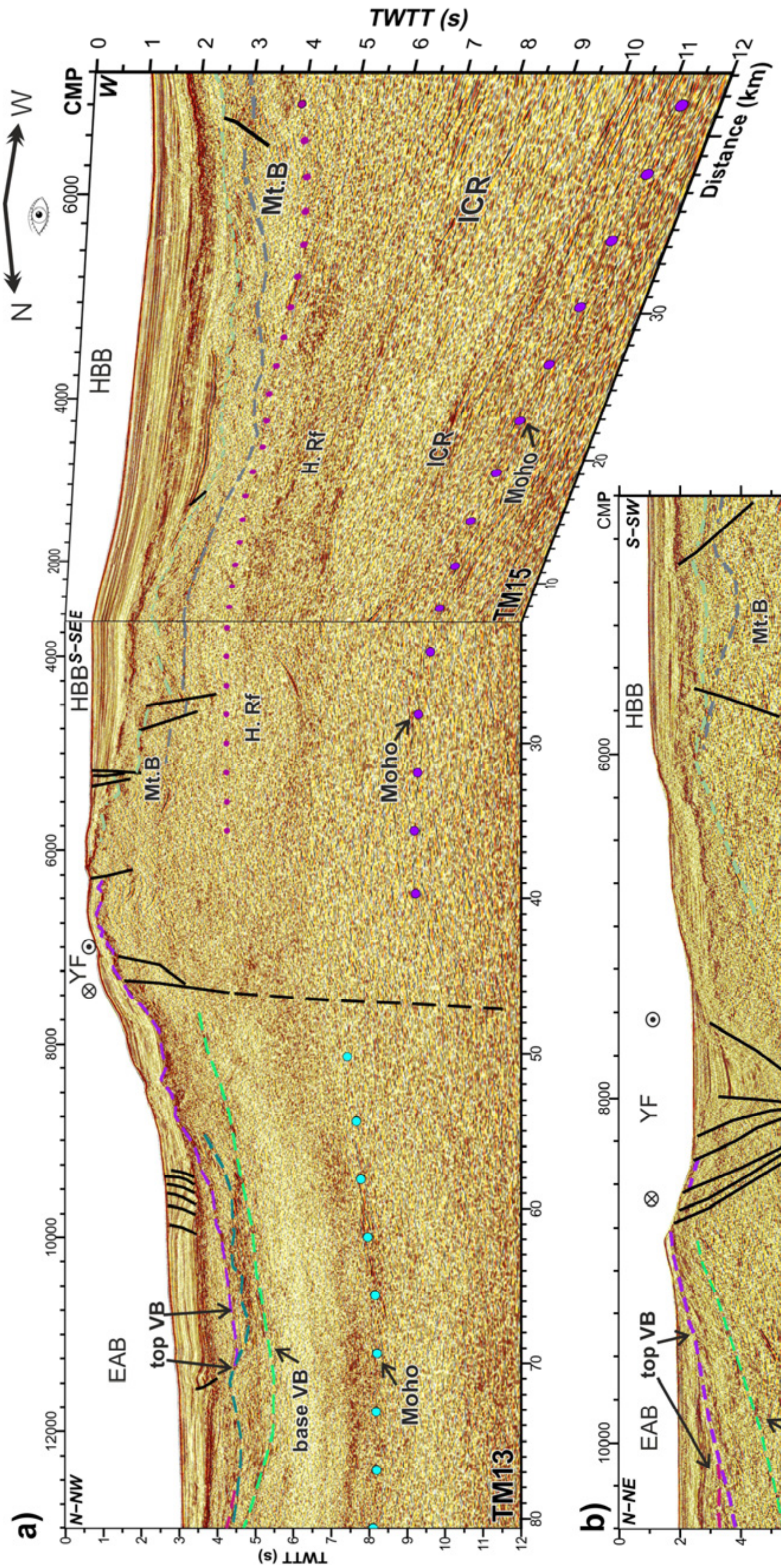

Figure 8.7: *Crustal scale structure of the Yusuf Fault area.* ***(a)*** *Perspective view of profiles TM13 (across the Yusuf Fault) and TM15 (running parallel to the Yusuf Fault). Different basement configuration and Moho depths are observed on both sides of the fault.* ***(b)*** *Pre-Stack Depth Migration of profile TM03. Pink dots: top of high reflective, blue dots: magmatic crust Moho, purple dots: continental crust Moho.*

- *Basement characteristics*

Basement on either side of the Yusuf Fault system shows distinct a character. South of the Yusuf Fault system, the oldest sedimentary unit recognized in the African continental margin is unit L (Fig. 8.6). The base of this unit cannot be clearly identified, and grades into a high-reflectivity basement (Fig. 8.7). In profile TM15, Moho under the shelf edge is clearly imaged below 10 s TWTT, gently dipping towards the continent reaching 11 s TWTT (Fig. 8.7a). Line TM11 pre-stack depth migrated section, shows the Moho south of the Yusuf Fault between 12-13 km (Fig. 8.7b), with a basement ~10 km thick. North of the Yusuf Fault, the basin is floored by volcanic units of the EAB. The base of these units is defined by a gradual change in reflectivity and not by a well-defined reflection. The basement underneath them exhibits an overall low-reflectivity character that contrasts with the Habibas Basin crust (Fig. 8.7). In the north Yusuf Fault area, the Moho is ~8 s TWTT deep, and the basement is ~5 s TWTT thick (Fig. 8.7a). The pre-stack depth migrated profile TM11 shows a 10 km deep Moho below the EAB, with an ~8 km thick basement (Fig. 8.7b).

8.3.2. Structure and kinematics of the Yusuf Fault

The Yusuf Fault is a ~150 km long , WNW-ESE trending dextral, high dipping (90º± 30º) strike-slip fault system, the largest active tectonic structure of the Alboran Sea (e.g. Martínez-García et al., 2011; Gràcia et al., 2014). The fault is composed by two main segments: the West and East YF (Fig. 8.2). These segments meet at a central step-over, the Yusuf pull-apart basin, bounded to the north by the Yusuf Ridge and to the south by the Habibas Escarpment (Figs. 8.1, 8.2). The West YF segment is ~87 km long, trends N100º running from the foot of slope of the Alboran Ridge to the Yusuf Basin. The East YF segment is ~105 km long, trends N95º running from the Yusuf Basin and Habibas Escarpment to its eastern end near the Algerian coast (Fig. 8.2). The Yusuf Fault is a lithospheric boundary between two different crustal domains: the continental crust in the Moroccan and Algerian Margin to south and the magmatic arc crust in the Eastern Alboran Sea (Fig. 8.7).

Profiles TM09 and EVD-2A, image the transition of the West YF towards the Alboran Ridge. Here, YF is a transpressive structure (Fig. 8.8a CMP 10500-12000) and frontally bounded by a high-dip thrust with geometry very similar to the Alboran Ridge bounding faults (Fig. 8.8b CMP 15000-3000). In the Yusuf Basin the two YF fault segments interact. Active steep faults define a transtensional area generating a ~10-km-wide and ~40-km-long pull-apart basin, imaged in profiles TM11 and TM12 (Fig. 8.9a, 8.9b CMP 9000-7000; Fig. 8.10 CMP 7000-8000). The East YF segment is imaged on profiles TM13 and TM14 as steeply-dipping structures, with associated compressional folding (Fig. 8.12 CMP 7000-8000, Fig. 8.11 CMP 8000-6000). East of the Alidade Bank, the East YF segment appears as a very steep, E-W trending rectilinear escarpment that extends into the Algerian shelf (Fig. 8.1). During the TOPOMED-GASSIS cruise in 2011 permit to survey in the Algerian EEZ, stop at 12 miles zone territorial waters, and could not survey the easternmost sector of the YF.

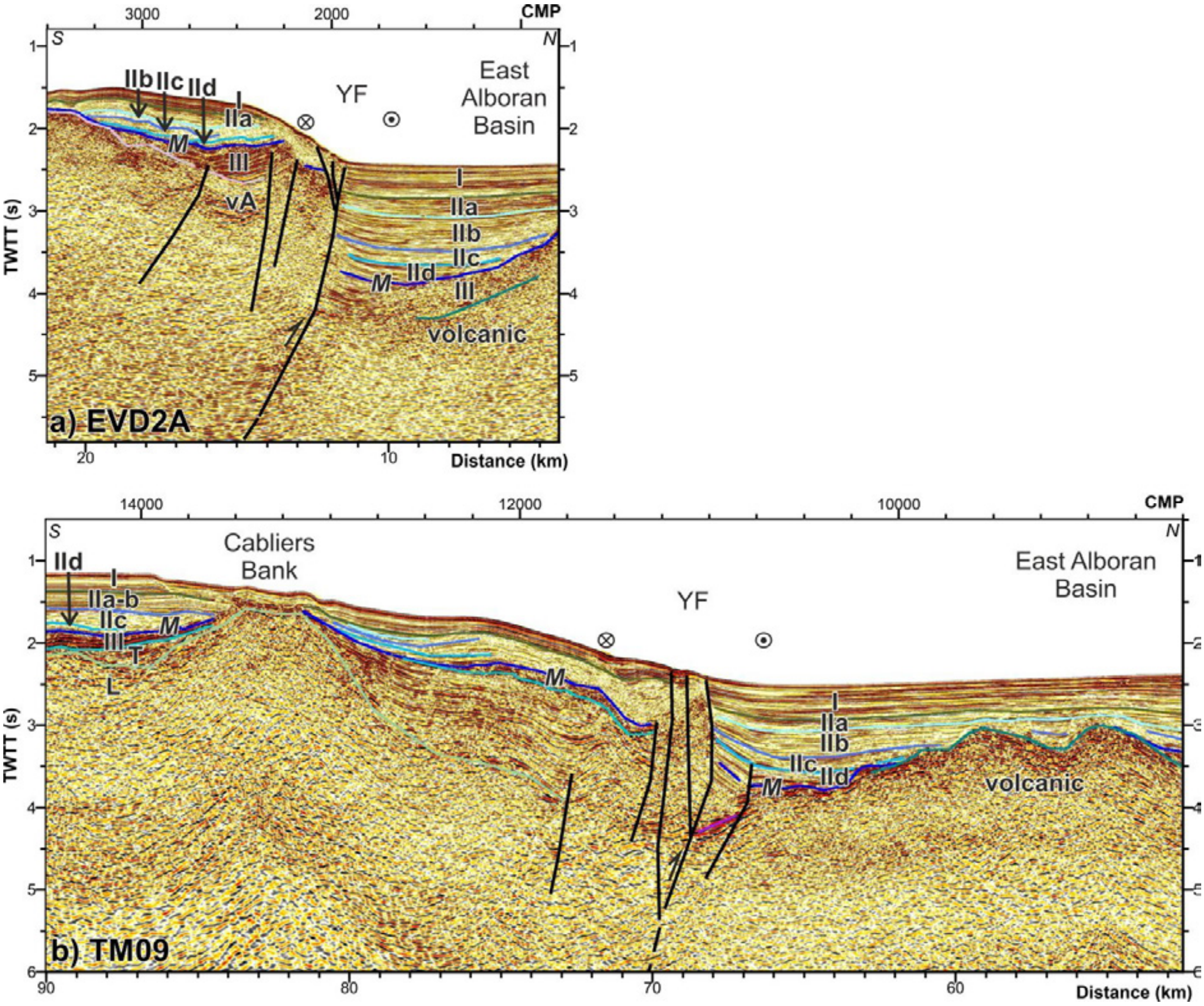

Figure 8.8: ***(a)*** *Time migration of profile EVD2a (see Figure 8.3 for location). Main structures and seismostratigraphic units are identified. Age of the units is defined in Figure 8.6. Vertical exaggeration is of ~x:2.* ***(b)*** *Time migration of profile TM09 (see Figure 8.3 for location). Main structures and seismostratigraphic units are identified. Age of the units is defined in Figure 8.6. Vertical exaggeration is of ~x:2.*

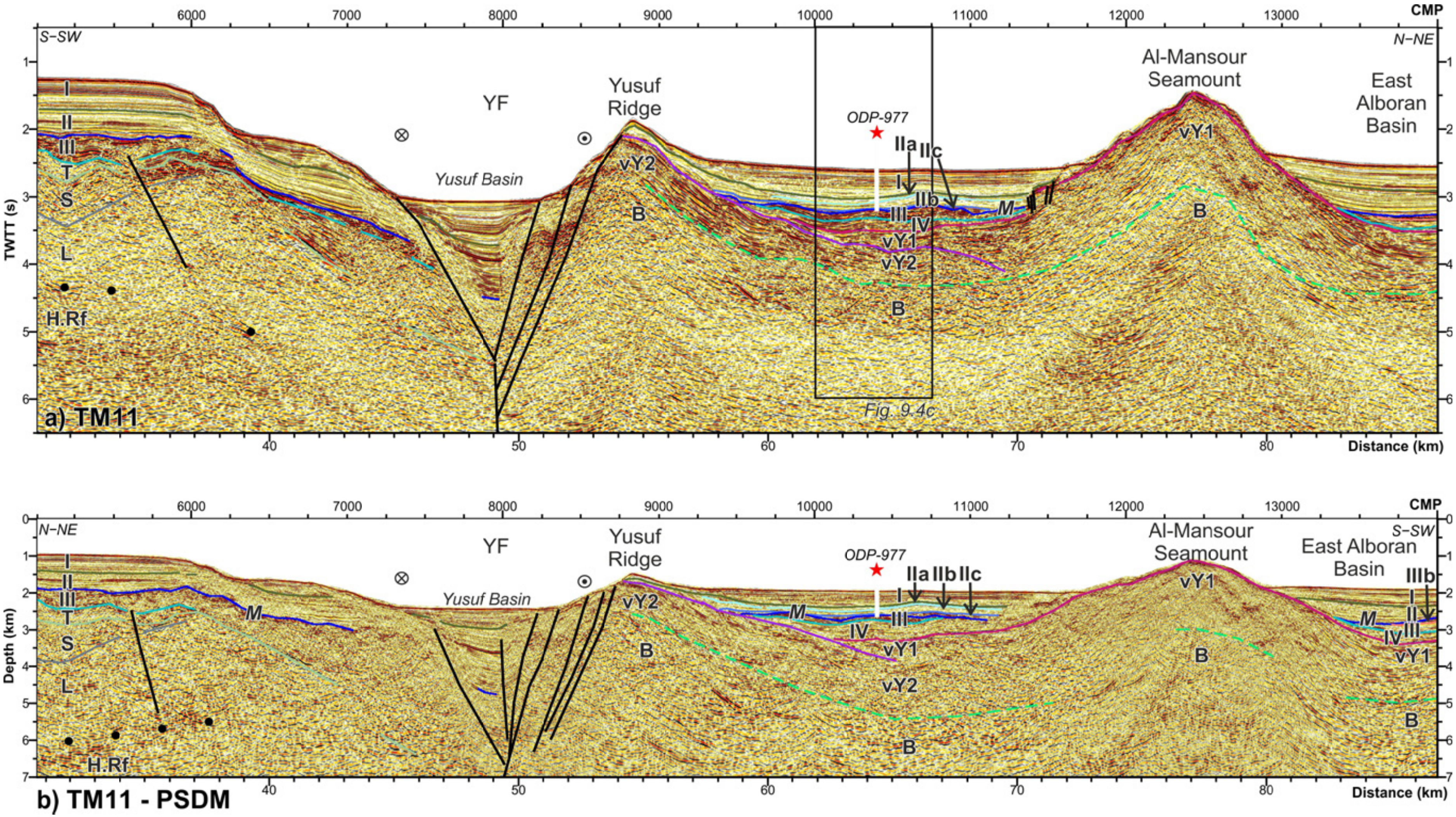

Figure 8.9: ***(a)*** *Time migration of profile TM11 (see Figure 8.3 for location). Main structures and seismostratigraphic units are identified. Age of the units is defined in Figure 8.6. Vertical exaggeration is of ~x:2.* ***(b)*** *Depth migration of profile TM11 (see Figure 8.3 for location). Main structures and seismostratigraphic units are identified. Age of the units is defined in Figure 8.6. Vertical exaggeration is of x:1.6.*

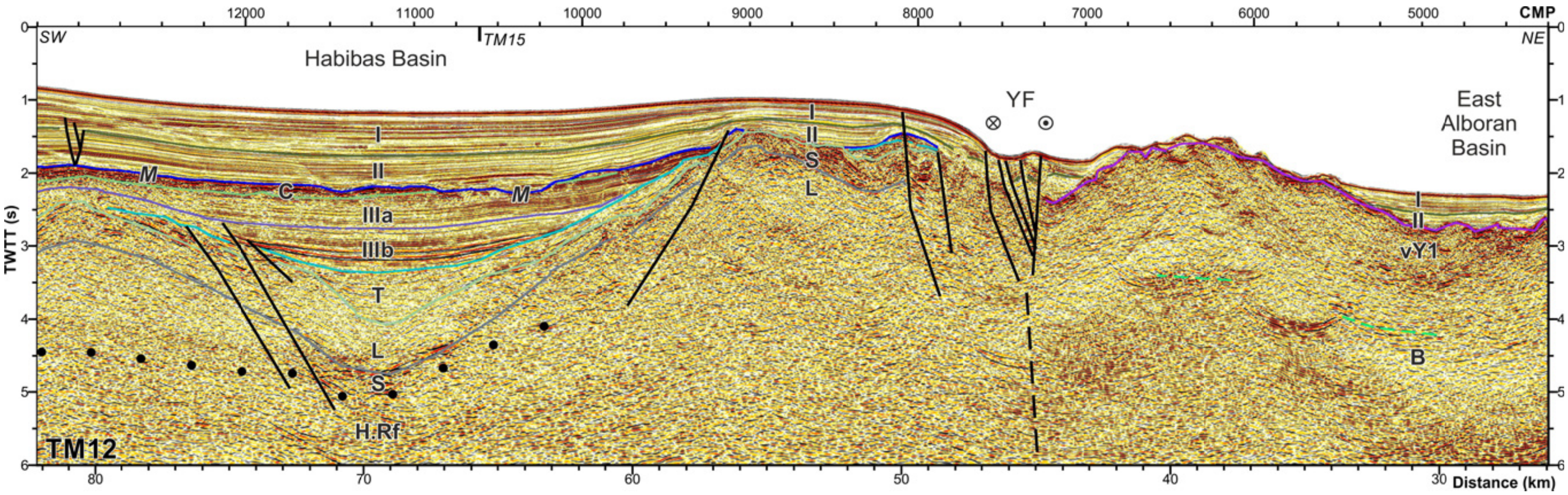

Figure 8.10: *Time migration of profile TM12 (see Figure 8.3 for location). Main structures and seismostratigraphic units are identified. Age of the units is defined in Figure 8.6. Vertical exaggeration is of ~x:2.*

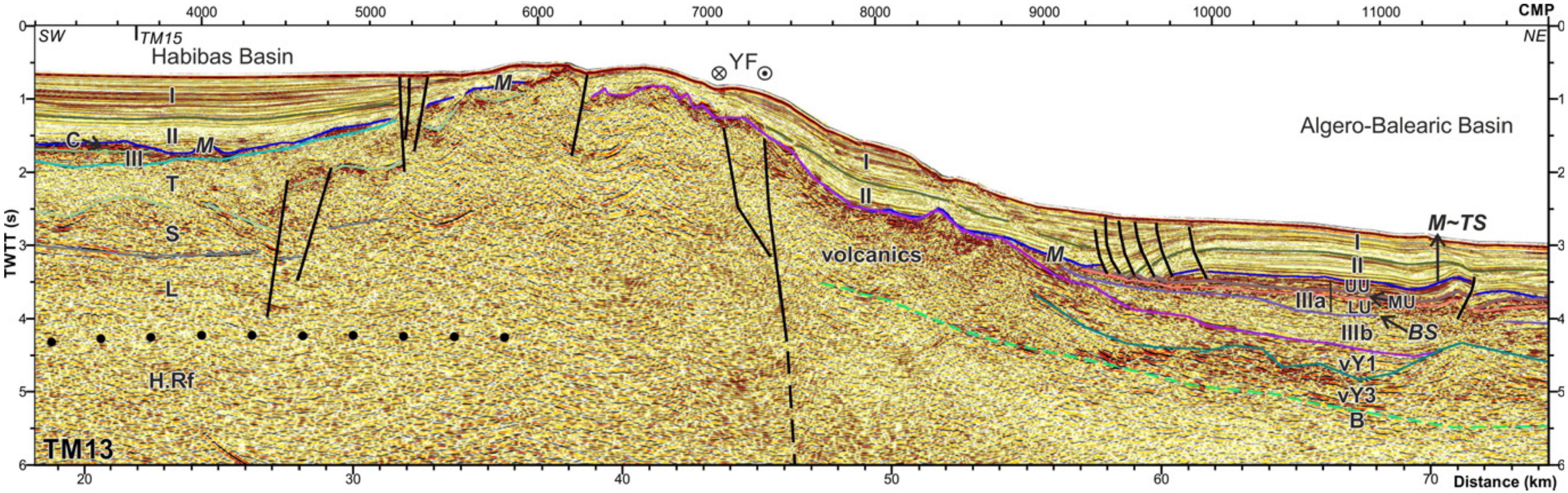

Figure 8.11: *Time migration of profile TM13 (see Figure 8.3 for location). Main structures and seismostratigraphic units are identified. Age of the units is defined in Figure 8.6. Vertical exaggeration is of ~x:2.*

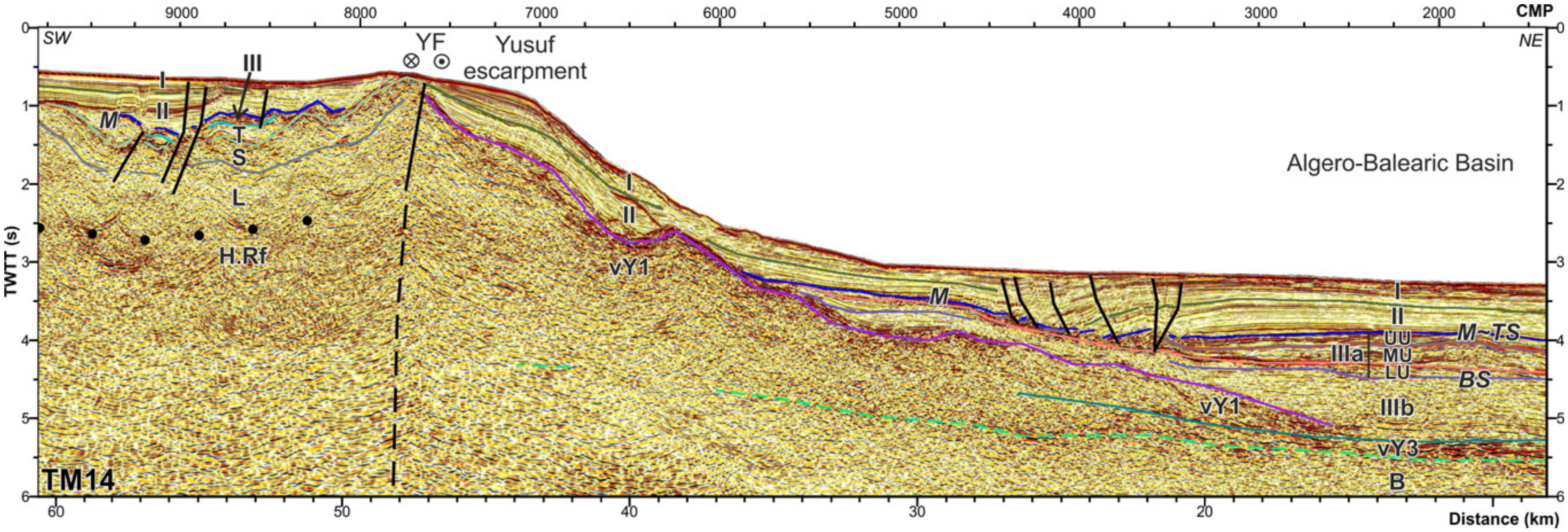

Figure 8.12: *Time migration of profile TM14 (see Figure 8.3 for location). Main structures and seismostratigraphic units are identified. Age of the units is defined in Figure 8.6. Vertical exaggeration is of ~x:2.*

8.3.3. The Yusuf pull-apart basin

- *Detailed seismic stratigraphy*

The sedimentary infill of the Yusuf Basin has been imaged with the high-resolution EVENT-DEEP Leg 1 dataset (Figs. 8.3, 8.13). The resolution of these profiles allows to establish a detailed stratigraphy of the deposits associated to the right-lateral motion of the Yusuf Fault, being fundamental to determine the extension-related slip of this structure. We have identified 8 sedimentary units, labelled as S1 to S8 on the profiles, and the basement top, labelled as B. Due to the steeps flanks of the Yusuf Basin, correlation between the units identified in the pull-apart and the units interpreted in the East Alboran Basin is not always possible. We used two horizons: q1 dated in 0.79 Ma (Fig. 8.13b) (ODP Leg 161 Sites 977 and 978, Martínez-García, 2012), and the Messinian unconformity M dated as 5.33 Ma (ODP Leg 161 Site 977, Martínez-García, 2012). These two horizons have been correlated with the ODP Leg 161 Site 977 trough EVENT-DEEP Leg 1 and Leg 2 profiles (Fig. 8.1). The horizons are identified in the western part of strike-parallel profile EVD-132 (Fig. 8.13a), although are not identified in the deeper part of the Yusuf Basin. The same two horizons were mapped in the East Alboran Basin (Fig. 8.13b).

The precise age of every unit mapped in the Yusuf pull-apart basin are is unknown, but we established a chronology on the basis of their relations with the q1 and M horizons. Units S7 and S8 are clearly Pre-Pliocene. Units S5 and S6 are older than the q1 reflector, while the upper part of unit S4 is cut by this surface. Units S3, S2 and S1 are younger than q1 (Fig. 8.13). This stratigraphic framework is only present in the YF system area and thus relevant for its study, but it is not recognised for the entire basin because it is clear dominated by YF-related tectonic processes. Thus, much of this detailed stratigraphy was not discussed in the stratigraphy chapter (“Chapter 6: Basin evolution”).

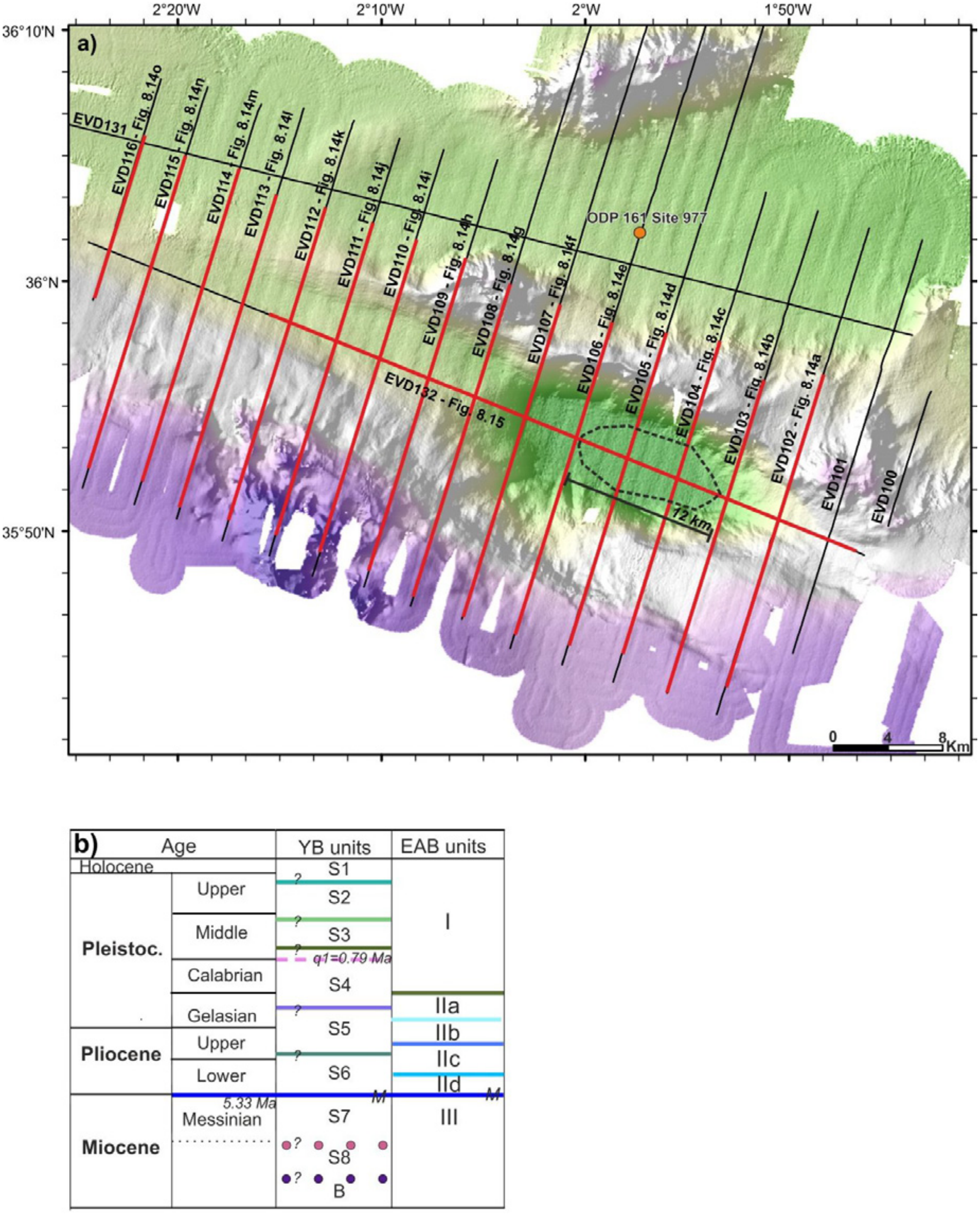

Figure 8.13: ***(a)*** *Bathymetry of the Yusuf Basin (see Figure 1 for location). Location of figures 8.14 and 8.15 are depicted. The area where the Messinian unit is not identified is depicted by a doted circle.* ***(b)*** *Ages and seismostratigraphic units identified in the high-resolution MCS profiles in the Yusuf pull-apart Basin (from S1 to S8), and its correlation with the East Alboran Basin (EAB) units. M: Messinian unconformity, B: Basement.*

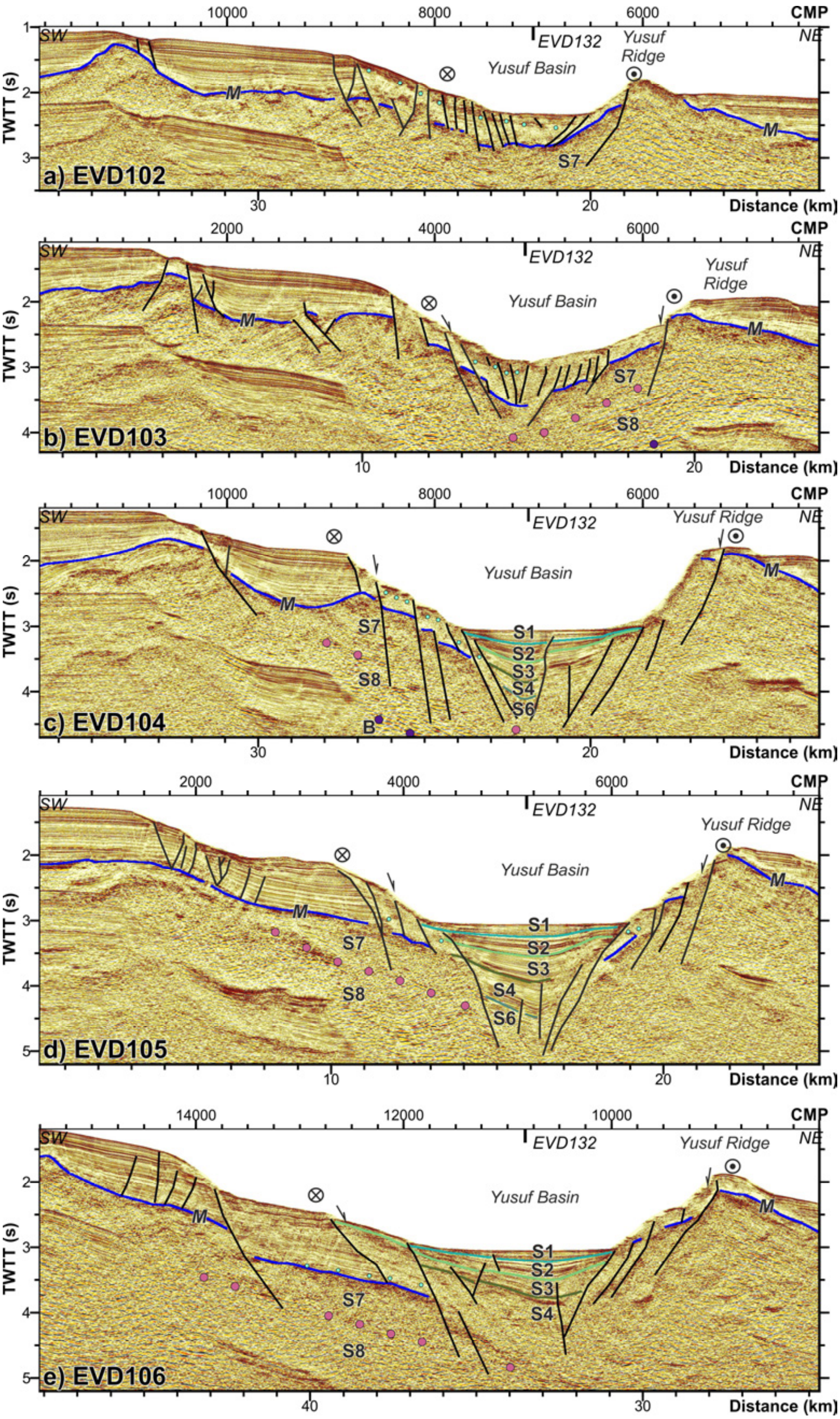
a) EVD102
SW
NE
CMP
10000
8000
6000
EVD132
Yusuf Ridge
Yusuf Basin
M
S7
TWTT (s)
1
2
3
30
20
Distance (km)
b) EVD103
2000
4000
6000
S8
10
c) EVD104
S1
S2
S3
S4
S6
B
d) EVD105
e) EVD106
14000
12000
40
5

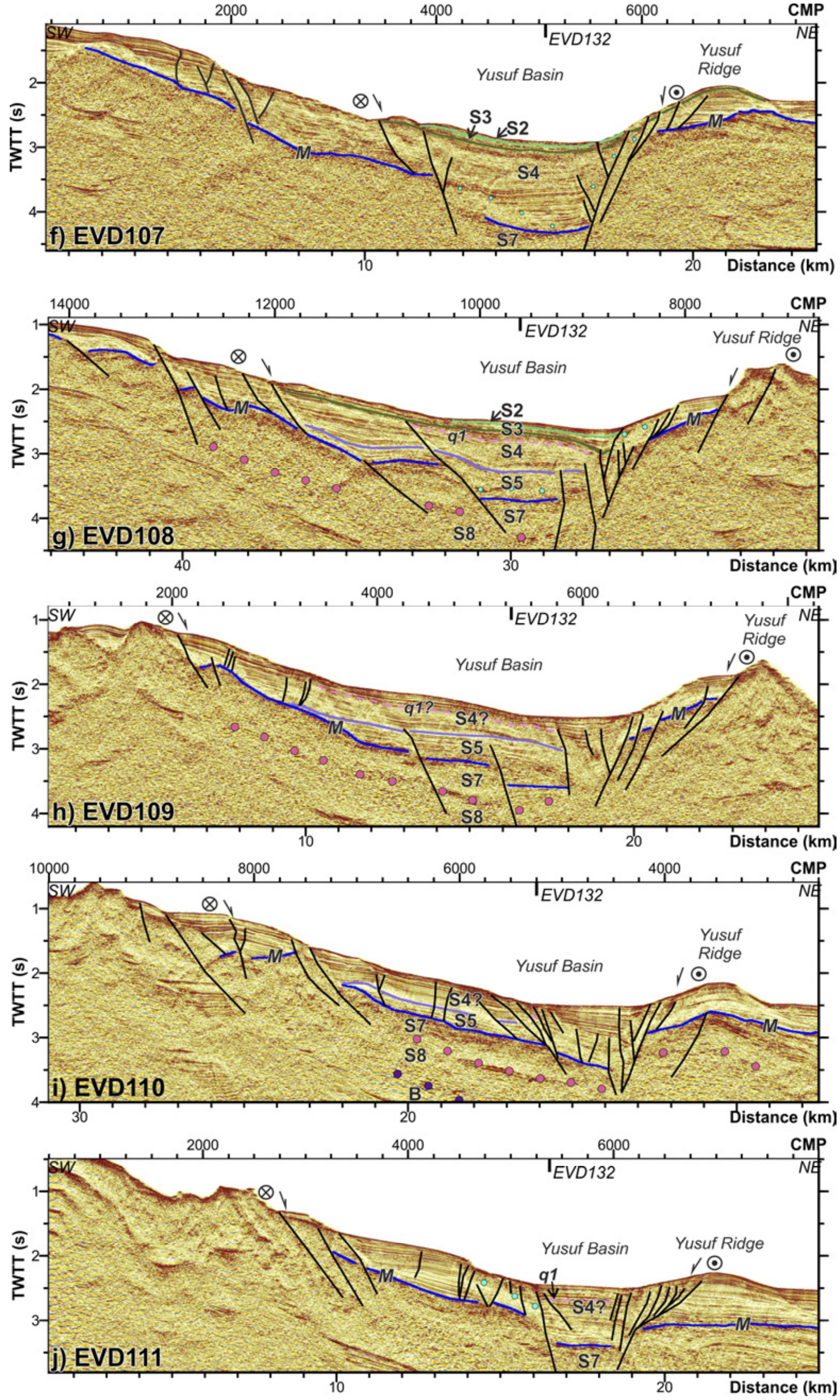
CMP
2000
4000
6000
SW
NE
EVD132
Yusuf Basin
Yusuf Ridge
TWTT (s)
S3
S2
S4
S7
M
f) EVD107
10
20
Distance (km)
14000
12000
10000
8000
S3
q1
S5
S8
g) EVD108
40
30
q1?
S4?
h) EVD109
10000
B
i) EVD110
30
q1
j) EVD111

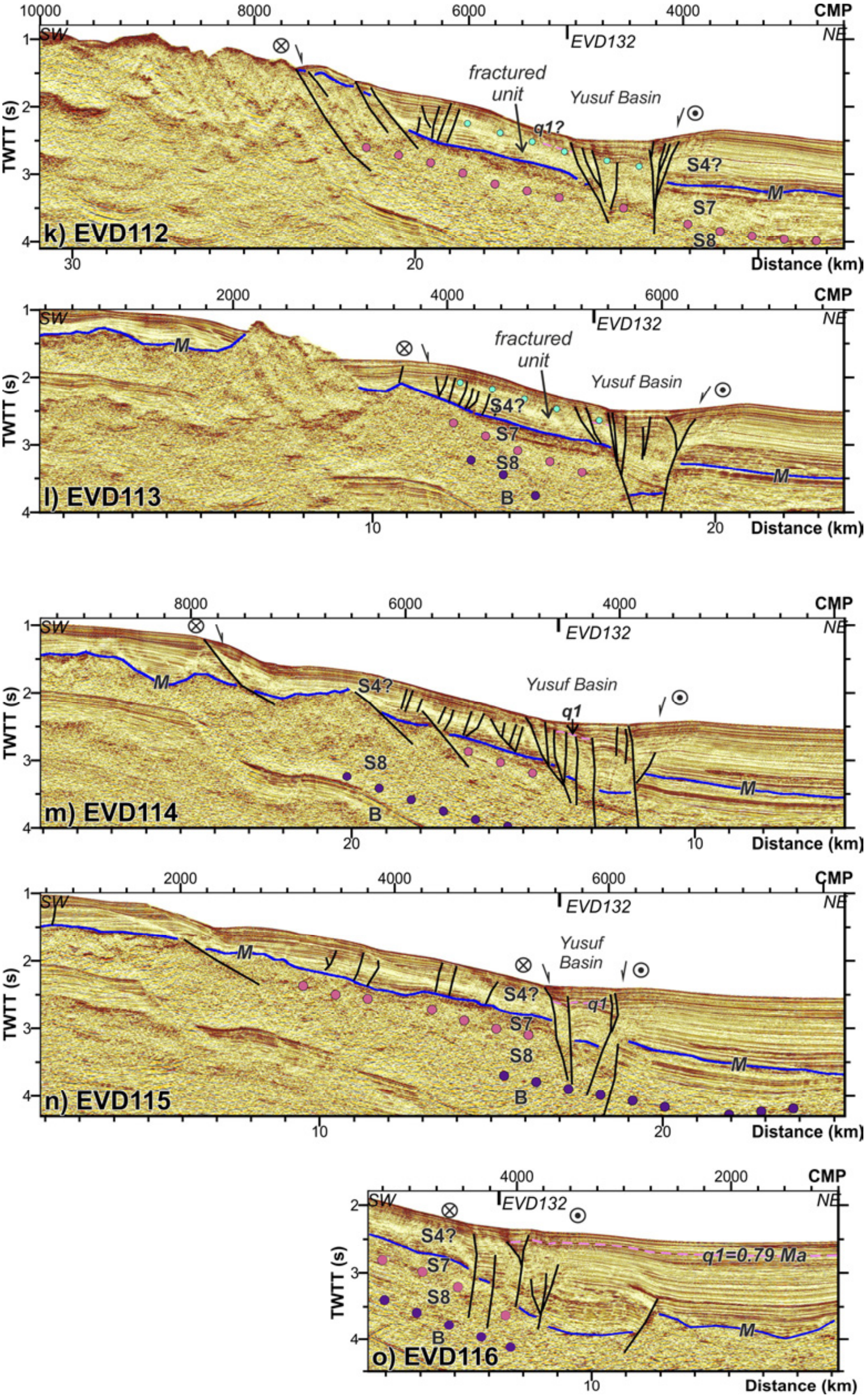
k) EVD112
SW
NE
CMP
10000
8000
6000
4000
EVD132
TWTT (s)
fractured unit
q1?
Yusuf Basin
S4?
S7
S8
M
Distance (km)
30
20
l) EVD113
2000
4000
6000
S4?
S7
S8
B
M
10
20
m) EVD114
q1
S4?
S8
B
n) EVD115
q1
o) EVD116
q1=0.79 Ma

Figure 8.14 (previous pages): *Interpreted time migration of profiles* ***(a)*** *EVD102,* ***(b)*** *EVD103,* ***(c)*** *EVD104,* ***(d)*** *EVD105,* ***(e)*** *EVD106,* ***(f)*** *EVD107,* ***(g)*** *EVD108,* ***(h)*** *EVD109,* ***(i)*** *EVD110,* ***(j)*** *EVD111,* ***(k)*** *EVD112,* ***(l)*** *EVD113,* ***(m)*** *EVD114,* ***(n)*** *EVD115 and* ***(o)*** *EVD116 (see Figure 8.13a for location). Main structures and seismostratigraphic units are identified. Age of the units is defined in Figure 8.13b. Vertical exaggeration is of ~x:2.5.*

- *Basin configuration*

Profiles perpendicular to the YF image the pull-apart basin bounded to the north and by a series of secondary steep strike-slip faults (Fig. 8.14), located on both flanks of the Yusuf Basin. The seismic grid shows the along-axis variability of the basin (Figs. 8.14, 8.15). The sediment below the M unconformity exhibit a pre-kinematic character, being affected by extensional processes and faulting, while the sediments post-M unconformity show syn-kinematic characteristics, presenting thickness variations related to the basin extension, such as thickening towards the basin depocenter as discussed below. The eastern side of the Yusuf Basin is inadequately surveyed (due to permit restrictions), but the entire western side of the Yusuf Basin has been covered with the seismic grid (Fig. 8.13, 8.14e-o). The basin forms an elongated depression filled with <2 s TWTT of post-Messinian sediments. The sedimentary infill of the basin is made of strongly faulted units that display little internal stratification (e.g. fracture unit at Figure 8.14k EVD-112 CMP 6000-4000 and Figure 8.14l EVD-113 CMP 4000-6000) whereas the most recent infill exhibits little faulting. On the NE side (Fig. 8.14a, 8.14b) the basin basement is steep and with a thin sedimentary cover of <~0.5 s TWTT disrupted by faults, that thickens abruptly towards the basin depocenter, where the post-Messinian infill is >2 s TWTT thick. Units S6 to S1 thicken toward the basin depocenter forming a synclinal. In the deepest part of the basin, the M unconformity, clearly visible on the flanks, has not been identified. The most recent units are confined to the centre of the the Yusuf Basin, being identified only in the depocenter and nearby area (Fig. 8.14c-g): Unit S1 is confined under the region of smooth seafloor, marking roughly the post-Messinian basin extension, but units S2 and S3 also thin abruptly towards the basin edges.

Profile EVD-132 runs approximately parallel to the East YF trend, crossing the basin depocenter roughly parallel to the direction of extension of the pull apart (Fig. 8.15a, b). The SE flank of the basin is bounded by a normal fault (Fig. 8.15b, CMP ~4000), and in the NW side is cut at least by three large normal faults, labelled F1, F2 and F3 (Fig. 8.15b F1 at CMP 6500-5500, F3 at CMP 12000-1000). The movement on the major faults has created a roll-over structure, and has associated abundant smaller-scale deformation of the infill (Fig. 8.15a CMP 12000-8000) creating complex deformation patterns with opposite dipping faults (Fig. 8.15a CMP 12000-8000). This profile images how units S7 and S8 (pre-M unconformity), are disrupted by the normal faults that have controlled the basin subsidence, reflecting the pre-tectonic character of these units. The image shows the thinning of these units towards the basin depocenter, where S7 is absent (Fig. 8.15b CMP 8000-3500). Sediment units S3-S1 are confined to the deep basin area.

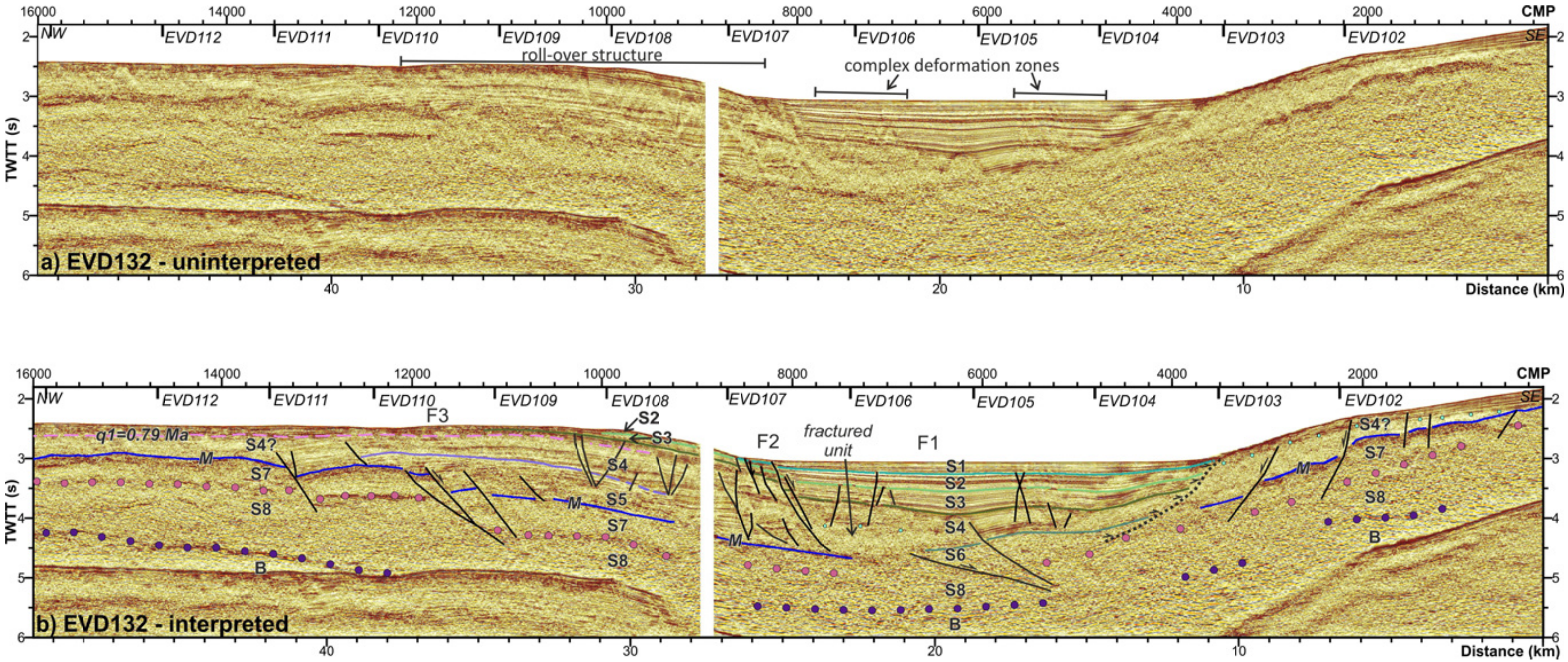

Figure 8.15: *Interpreted time migration profile EVD132, running along the Yusuf Basin depocenter (see Figure 8.13a for location). Main structures and seismostratigraphic units are identified. Age of the units is defined in Figure 8.13b. Vertical exaggeration is of ~x: 2.5.*

8.4. Discussion

8.4.1. Nature of the basement

North of the Yusuf Fault, the East Alboran Basin is floored by volcanic units (Duggen et al., 2004; 2008; "Chapter 5: Crustal domains"). South of the Yusuf Fault, a different type of crust is imaged. All units filling the Habibas Basin are sedimentary strata characterized by relatively continuous reflections (Fig. 8.12 CMP 6000-2000), drilled in the HBB-1 well, where a metamorphic continental basement was found (Medaouri et al., 2014). Below the last sedimentary unit, a high reflectivity body characterises the upper part of the basement, with the top located between 4-5 s TWTT, and the high reflectivity extending to 6-7 s TWTT, i.e. into the upper-middle crust.

In addition to a different basement, the Habibas Basin displays thicker crust. North of the Yusuf Fault the crust is <8 km (Fig. 8.7b), while south of the fault, the minimal crustal thickness is ~10 km, thickening to ~18-20 km under the shelf. These differences indicate that the Yusuf Fault acts as a crustal boundary. North of the Yusuf Fault occurs thinner crust formed at the volcanic arc. South of the fault, occurs continental metamorphic basement with a highly reflective thicker crust of the North African continental margin.

8.4.2. Activity of the Yusuf Fault

The different types of basements found on either side of the Yusuf Fault system support that this fault is a crustal boundary. Although it is difficult to image the deep structure of narrow basins using MCS profiles, mainly because of the presence of lateral echoes that may mask the real signal (Bécel et al., 2009; Bécel et al., 2010), the combination of high-penetration with high-resolution profiles allows us to define the bottom of the pull-apart basin, to image in detail the sedimentary infill and also to image the deep structure on either side of the fault system.

The eastern segment of the Yusuf Fault appears to end at the Yusuf Basin, while the western segment extends westwards (Fig 8.2). This segment forms a transpression zone; creating positive flower structures (Fig. 8.8a CMP 10500-12000, Fig. 8.8b CMP ~2000) and increasing it dip towards the west. Due to the evolution of the fault into a compressive structure, as also reflected in the bathymetric map of the area, we hypothesize that the western YF segment connects with the northern end of the Alboran Ridge, which has been interpreted as a compressional boundary (Fig. 8.1, Martínez-García et al., 2011; Martínez-García, 2012). This behavior has been described in other large strike-slip faults, similar to the evolution of the North Anatolian Fault (Sea of Marmara), where this fault controlled the opening of the Cinarcik and Marmara pull-apart basins and, due to its orientation with respect to the plate movement, it evolved into a restraining bend area (e.g. Gokaşan et al., 2003).

- *The opening of the Yusuf pull-apart basin*

The existence of a releasing bend between the two segments of the Yusuf Fault led to the formation of the Yusuf pull-apart basin. We base our analysis in previous pull-apart basin models (e.g. Rodgers, 1980; Christie-Blick and Biddle, 1985; Lemiszki and Brown, 1988; Sylvester, 1988; Basile and Brun, 1999; Wu et al., 2009), and studies from similar basins establishing a chronological tectonic evolution (e.g. Robertson and Woodcock, 1980; Zachariasen and Sieh, 1995; Okay et al., 2000; Gokaşan et al., 2003; Carton et al., 2007; Laigle et al., 2008; Bluck, 2009; Bécel et al., 2010; Rodriguez et al., 2011; May et al., 2015).

Pull-apart basins are formed at releasing bends or steps along strike-slip fault systems. Common characteristics include elongated geometry, depocenter migration, high sedimentation rate and rapid subsidence (e.g. Noda, 2013). Pull-apart basins developed between two parallel or sub-parallel strike-slip fault segments, that are the principal displacement zones (e.g. Basile and Brun, 1999; Wu et al., 2009). The longitudinal ends of the basin are delineated by an extensional or oblique-extensional fault system (e.g. Basile and Brun, 1999; Wu et al., 2009). Different pull-apart geometries are observed comparinbg transtensional with pure strike-slip strucutres. Transtensional pull-apart basins are wider, and usually develop two depocenters separated by a structural high. The sidewall faults of the pure strike-slip pull-apart basins are one continuous fault, whereas in the transtensional pull-apart basins are a system of en-echelon oblique-extensional faults (e.g. Wu et al., 2009). The evolution of the pull-apart basins occurs in successive stages. At the earliest stage, the basin presents a S or Z shape, shape, regarding to the left- or right-lateral motion of the fault, and the faults limiting the basin are not well-defined. At middle stages, a well-defined rhomb-shaped pull-apart basin is identified, clearly demarcated by oblique and extensional faults (e.g. Zhang et al., 1989; Basile and Brun, 1999). The final stages of the pull-apart are characterized by the development of strike-slip faults along the basin that intersect the main strike-slip faults with an angle <25º (e.g. Zhang et al., 1989).

The main fault controlling the opening of the Yusuf pull-apart changed through time. We identified three main faults, F1, F2 and F3 in Figure 8.15. Currently only F2 reaches the seafloor, being a sub-vertical fault system. F1 is a normal fault that presents a low dip and is sealed by units S5 and S4 (lower Pleistocene). We interpret that at its formation F1 was steeper, and has been rotated during extension forming the pull-apart. F3 fault, the westernmost of the large faults, presents similar structural characteristics and is also sealed by S5. We propose that F1 and F3 initiated with the opening of the pull-apart, and that later deformation focused on F1, forming the depocenter till deposit of Unit S5. Further rotation of these structures made them mechanically unsuitable and forced extensional deformation to create F2. F2 is the active fault currently controlling the deformation in the Yusuf basin. The well-defined lateral faults together with the lack of oblique-cutting faults across the basin supports the focusing of the activity on the structure and indicate a relative early stage of basin evolution (e.g. Peizhen Zhang et al., 1989; Basile and Brun, 1999).

Sedimentation in the pull-apart basin and surrounding areas allows establishing the chronological history of the Yusuf Fault activity. We identified units S8 and S7 as pre-kinematic units, because their geometry indicates that their sedimentation was not conditioned by the fault, and they are cut and displaced by the Yusuf Fault (Fig. 8.14g CMP ~11000, Fig. 8.15 CMP ~12000). These units exhibit thinning towards the basin depocenter that indicates extension during pull-apart opening. Due to this extension, unit S7 is almost absent under the basin depocenter (Fig. 8.14c-e, Fig. 8.15 CMP 7000-3000). The first unit identified as a syn-tectonic corresponds to S6. This unit appears restricted to the basin depocenter, filling the accommodation space created by F1 (Fig. 8.15 CMP ~6000). The subsequent syn-tectonic unit is S5 with a distribution that appears related to F3 activity. Lapping on S5 is unit S4 that appears syntectonic to F3 too. Units S3, S2 and S1 seem to be controlled by the F2 fault activity, being mainly confined to the present-day basin. We proposed that S3, S2 and S1 units are younger than the q1 reflector, dated in 0.79 Ma. As these recent units show a syn-kinematic character, exhibiting a thickening towards the basin depocenter, and the faults of the F2 fault-zone reach up to the seafloor, we propose that the Yusuf Fault is an active fault and that extension in the pull-apart is presently ongoing and give a minimum estimate of the age and displacement on the Yusuf Fault system.

- *Seismic activity and seismogenic potential*

Although the Yusuf Fault is a large active structure, there are few historical and instrumental earthquakes in its vicinity (Fig. 8.2). Only relatively low-magnitude events have been recorded along most of its length, although the poor re-location precision for the area makes difficult to assign any event to a particular segment of the Yusuf Fault. The largest event is the 1973 Mw 5.0 pure dextral strike-slip earthquake (Meghraoui and Pondrelli, 2012) that may have ruptured the SW shorter branch of the fault or the East segment (Fig. 8.2).

We have estimated the maximum potential magnitude earthquake for the Yusuf Fault segments independently, and for the Yusuf Fault as a single structure using the empirical relationships proposed by Wells and Coppersmith (1994), Wesnousky et al. (2008) and Stirling et al., (2008) (Table 8.1). Small variations are obtained for the different method, probably associated with assumptions of the model. Wells and Coppersmith (1994) and Wesnousky (2008) are suitable for any sense of slip, although they are based on continental crust faults. Stirling et al. (2008) compilation has a local character, but continental and oceanic crust faults are included. Stirling et al. (2008) is especially relevant for strike, reverse and oblique slip faults, and can be applied for plate boundary strike slip faults. Given the Yusuf Fault system characteristics, possibly Stirling et al. (2008) formulations are the most suitable, although all give similar values (Table 8.1). Using Stirling et al. (2008) formulation, the maximum earthquake is Mw~7.1 – 7.3 for the fault segments and a Mw ~7.9 if the rupture propagates along the entire fault system length. This values are slightly minor is we consider the plate boundary scenario, although it can be due to the error in the estimated area value.

- *Quantification of slip*

The amount of slip accumulated along the Yusuf Fault system is key to understand the evolution of the Eastern Alboran Basin. In order to measure it, we mapped pre-kinematic sediment units, in particular S7 that is the older pre-kinematic unit. Extensional processes affecting this unit caused thinning towards the basin depocenter. This thinning led to full break up and the absence of S7 underneath the nowadays basin depocenter. The longitude of the area without unit S7 measured parallel to the Yusuf Fault is 12 km. Since focal mechanism suggest a pure dextral strike-slip system (Morel and Meghraoui, 1996; Meghraoui and Pondrelli, 2012) the amount of minimum accumulated slip is also 12 km (Fig. 8.13a). We proposed that this value is the minimum extension because it does not take into account the slip of faults that has thinned S7 from its original thickness, which is difficult to constrain. Based on previous studies, the large faults individually accommodate 40%-75% of the total extension, while smaller faults accommodate the remaining 25%-60% (Marret and Allmendinger, 1992). Thus, the total extension along the YF system may be ~16-30 km. This hypothesis is coherent with the numerical models estimations proposing that the basin depocenter depth is equal to ~10%-15% of the total offset accommodated along the fault (Rodgers, 1980). The PSDM section reveals a basin depocenter depth of 2.5 km (Fig. 8.9b). Although the PSDM is not running exactly along the depocenter of the pull-apart basin, this depth is a minimum reference to perform the offset estimation. Following the relationship proposed by Rodgers (1980), the theoretical offset of the Yusuf Fault should be comprised between 16.6 and 25 km. Taking into account an average convergence rate for the Iberian and African plates of 4.5 ± 1 mm/yr from the Messinian (5.33 Ma) (e.g. McClusky et al., 2003), the total convergence should be 24 ± 5 km. Although the total convergence could potentially be also accommodated by other compressive and strike-slip features in the EAB, the minimum slip estimate for Yusuf Fault system support that this structure has accommodated most of the plate convergence in this area.

8.7. In summary

Our data documents that Yusuf Fault system is a crustal-scale structure, separating two different types of crusts with different thickness and basement characteristics. North of the Yusuf Fault a volcanic-arc type basement makes up a low reflective crust of ~8 km covered by several volcanoclastic units and volcanic constructions. South of the Yusuf Fault system basement is metamorphic continental rocks with a high intra-basement reflectivity and a crustal thickness of ~10 km at the shelf edge and ~18 km towards the shore.

Yusuf Fault system is an active fault, with an estimated maximum earthquake magnitude of Mw=7.1-7.3 for each fault segment, and Mw=7.9 for the entire system. Thus, it should be take into account in earthquake risk maps and seismic hazards prevention plants of the coastal areas.

The deformation pattern supports an initiation of the Yusuf Fault activity in Post-Messinian times, being Early Pliocene the first syn-kinematic unit. Both, the fault and the extension at the pull-apart basin are active nowadays. The total slip of the fault since the beginning of the activity at the Early Pliocene is estimated between 16 and 30 km. This lateral movement may have accommodated most of the Iberian – African plate convergence since the Miocene – Pliocene boundary (5.33 Ma), which is estimated to be ~24 ± 5 km. Minor potentially remaining stress related to convergence is consistent with the lack of other major offset structures in the area and may have been accommodated by small scale features. Towards the west, the Yusuf Fault connects with the northern Alboran Ridge transpressive fault that may have also accommodated a similar amount of slip as discussed in "Chapter 9: The Alboran Ridge".

Chapter 9

The Alboran Ridge

The Alboran Basin exhibits a complex physiography resulting from compressional deformation over imposed on the extensional structures created during earlier basin formation. This basin is located at the boundary between the Eurasian and African tectonics plates, that here corresponds to a wide deformation zone associated to the NW-SE trending convergence (4.5-5.6 mm/yr) between these two plates (e.g. Serpelloni et al., 2007; Koulali et al., 2011; Nocquet, 2012). Deformation is distributed over a large number of faults; a number of them may represent a seismic and even tsunami hazard for the neighbouring Iberian and North African shores (e.g. De Larouzière et al., 1988; Gràcia et al., 2006; Álvarez-Gómez et al., 2011).

Along the North African margin occur the most prominent tectonic structures of the area: The Alboran Ridge (AR) and Yusuf Fault systems (see Chapter 8). The AR is possibly a major crustal scale boundary because it is more than 100 km long and active at present (e.g. Martínez Garcia et al., 2013). Although it appears a key structure its characterization, origin and evolution are still inadequate. Recent studies describe the tectonic evolution and sedimentary record of the area (e.g. Martínez-García et al., 2011, 2013). However, the quantification of deformation accommodated by the structure has not been attempted. This has occurred because previous seismic studies did not image the internal structure of the AR, or the deep structure of the AR and South Alboran Basin. Better imaging is required to understand the role of the AR in accommodating Eurasian-African convergence, as well as to estimate the seismic hazard associated to this structure. The dataset presented here sheds light into the pre-Messinian sediment structures, that has traditionally no been studied in detail, which permits to further analyse kinematic indicators. Moreover, the analysis of pre-stack-depth-migrated section provides the real geometry of the structures, key to quantify the deformation accommodated in the area.

The objectives of this chapter are: (i) To define the basement and deep sedimentary infill of the AR region to determine age of fault activity; (ii) To characterize the AR structure itself, and its relation to three other highs nearby, the Francesc Pagés, Tofiño, and Xauen Banks; (iii) To characterize and estimate quantitatively the deformation, estimating shortening values along the structure; and (iv) To integrate all these results in a geodynamic evolutionary model.

9.1. Geological setting of the Alboran Ridge

From a physiographic point of view, the Alboran Basin is composed of different sub-basins, separated mainly by seafloor relief (Fig. 9.1). The most prominent seafloor relief of the entire basin is the SW-NE Alboran Ridge (AR) forming a SW-NE trending high, 105 km long and 25 km wide, which reaches up to the sea surface forming the Alboran Island (15 m a.s.l.). Towards the west, the ridge relief proper stops at a sharp SSW-NNE oriented depression formed by the Al-Idrissi Fault. However, a broader relief with similar orientation of the AR extends forming the Tofiño and Xauen Banks. Towards the east, the plateau around the Aboran Island stops abruptly and it is replaced by a more subdued topography associated to the Yusuf right-lateral strike-slip fault (Fig. 9.1). The AR is bounded by the Alboran Channel to the north and by the South Alboran Basin (SAB) to the south. The Alboran Channel is a narrow trough >70 km long and 1600-1850 m deep that extends from the West Alboran Basin to the East Alboran Basin. To the north, the Alboran Channel is bounded by the Djibouti Plateau (Fig. 9.1). The SAB, a NW-SE depression roughly delineated by the 1000 m isobath (Martínez-García et al., 2011) and up to ~1100 m deep. ODP Leg 161 Site 979 was drilled in this basin (e.g. Comas et al., 1999). The Francesc Pagès and Tofiño Banks expose volcanic rocks, while at the Xauen Bank only sediment has been dredged. All these highs are related to contractional deformation (e.g. Bourgois et al., 1992; Chalouan et al., 1997; Ammar et al., 2007; Mauffret et al., 2007; D'Acremont et al., 2012; Lafosse et al., 2016). The highs are discontinuous from the AR, being separated by a strike-slip fault trace (Ammar et al., 2007; Mauffret et al., 2007).

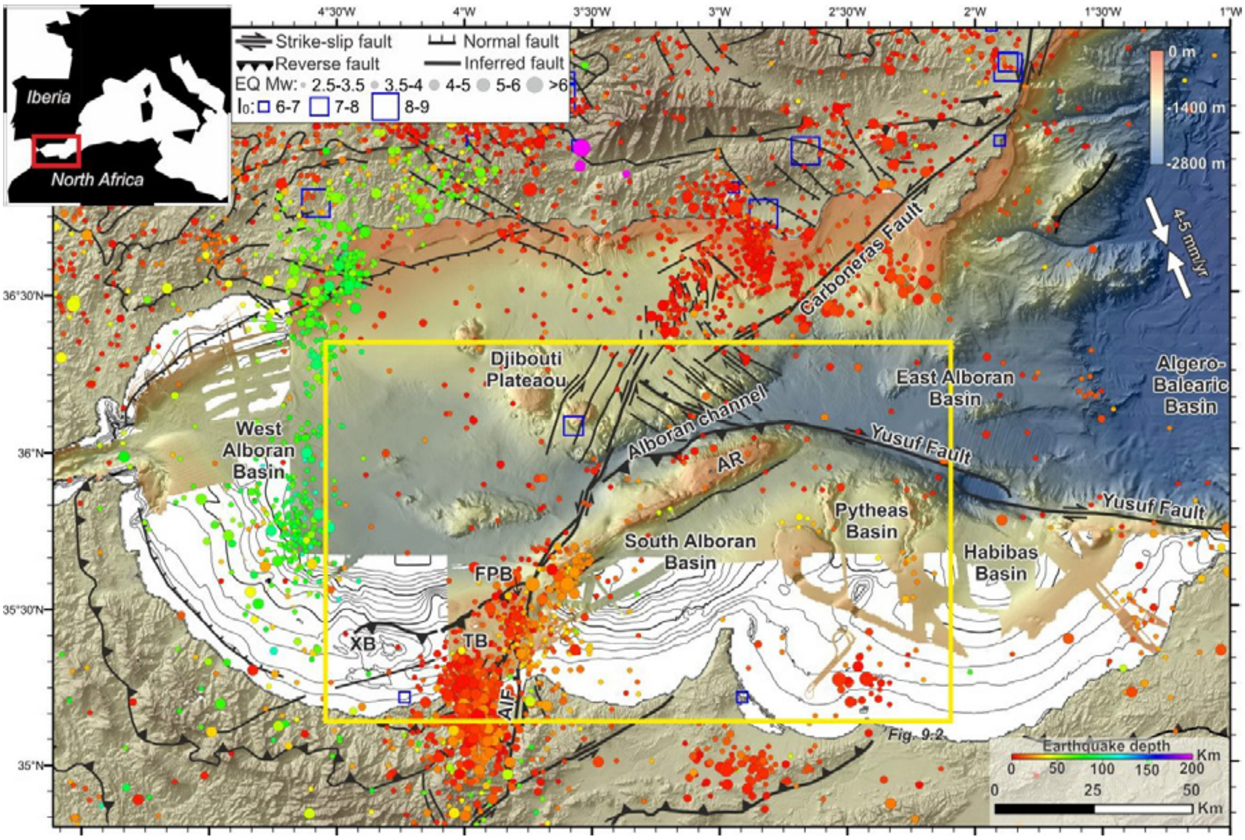

Figure 9.1: Regional bathymetric map of the Alboran Sea constructed from swath-bathymetric data acquired during the IMPULS-06, EVENT-10, TOPOMED-11, SHAKE-15 and IDRISSI-16 marine cruises (e.g. Gràcia et al., 2006, 2012) the SARAS cruise (PI: d'Acremont & Gorini; d'Acremont et al., 2014; Lafosse et al. 2016; Rodriguez et al. 2017) and a compilation of existing datasets from IEO (Ballesteros et al., 2008) and GEBCO. Land topography is from the SRTM-3 grid. In the areas without multibeam bathymetry, contours each 100 m are shown. Main tectonic structures are displayed (Gràcia et al., 2006; 2012), as well as historical (1400-1960, blue squares) and instrumental seismicity (1980-2015, coloured circles) (from IGN: http://www.ign.es/web/ign/portal/sis-catalogo-terremotos). The yellow rectangle depicts the area presented in Figure 9.2. Inset: Location of the shown area (red rectangle). AIF: Al-Idrissi Fault, AR: Alboran Ridge, FPB: Francesc Pagès Bank, TB: Tofiño Bank, XB: Xauen Bank.

Although the Pre-Messinian history of the area remains inadequately studied, the post-Messinian evolution has been recently studied (Martínez-García et al., 2011, 2012, 2013). Three contractive phases have been identified for the Pliocene evolution of the South and East Alboran Basins: Early Pliocene (5.33 – 1.24 Ma), Late Pliocene (3.28-2.45 Ma) and Early Pleistocene (1.81-1.19 Ma) (Martínez-García et al., 2013). The most relevant of these pulses is the Late Pliocene, when the Alboran Ridge and other compressional structures uplifted (Martínez-García et al., 2013).

ODP sites in the area stopped at the top of the Messinian, but commercial HBB-1 well offshore of the Algerian margin went deeper into lower Miocene and basement (Fig. 9.2). The continental basement of the SAB is supposed to be similar to the metamorphic basement dredged at the HBB-1 well (Fig. 9.2), intruded by magmatism (e.g. Medaouri et al., 2012, 2014). The continental crust is intruded by magmatism south of Yusuf Fault, and it is magmatic arc crust north of it (Booth-Rea et al., 2007). This magmatism, consequence of extension and slab subduction, is different inside the Alboran Basin and onshore surrounding areas, related to changes in thickness and composition of the lithosphere (Hoernle et al., 1999; Duggen et al., 2008; Lustrino et al., 2011). Volcanic rocks dredged in the Alboran Basin included Middle to Late Miocene tholeiitic to calc-alkaline rocks, whereas magmatic activity in the continental margin comprises Late Miocene to Pleistocene shoshonitic rocks and basanites/alkali basalts (Duggen et al., 2005; Duggen et al., 2008). Along the AR and the Alboran Island, andesites and rhyolites 9.26 - 9.37 Ma old have been sampled (Fig. 9.2) (Aparicio et al., 1991; Hoernle et al., 1999; Duggen et al., 2004; Gill et al., 2004; Duggen et al., 2008).

9.2. Data and methods used to survey the Alboran Ridge area

9.2.1. Seismic data acquisition and processing

A grid of Multichannel Seismic reflection (MCS) profiles used for this study was collected in two different surveys: (a) the TOPOMED-GASSIS and (b) the EVENT-DEEP Leg 2 cruises (identified as TM and EVD in Figure 9.2, respectively).

MCS profiles TM01-05, TM16, TM17 and TM19, from the TOPOMED-GASSIS cruise (October 2011) (Fig. 9.2), were acquired on board the RV “Sarmiento de Gamboa”. A Sentinel SERCEL streamer with 408 active sections (12.5 m channel interval, 5100 meters total length) and a source array composed of 8 G-GUN II guns fired at 50.15 l (3060 ci) were used. The air-guns were fired every 30 m (TM01, TM02), 40 m (TM03-TM05) and 50 m (TM16) at a pressure of 2000 psi. The total record length was 14 s (Two Way Travel Time, TWTT) with a sample rate of 2 ms.

MCS profiles EVDT1-3A and EVDT1-3B were acquired during the 2010 EVENT-DEEP Leg 2 survey (May-June 2010, PI: E. Gràcia) (Fig. 9.2) on board the RV “Sarmiento de Gamboa”. The Sentinel SERCEL streamer had 276 channels, separated 12.5 m each, with a total lengh of 3400 m. The seismic source was two sub-arrays of ten air-guns, shot at 1880 c.i. every 37.5 m. A window of 12 s TWTT with a sample rate of 2 ms was acquired.

All TOPOMED profiles and profile EVDT1-3A presented in this chapter have been processed similarly using “GLOBE Claritas” software. The processing flow was designed to obtain a crustal-scale image, preserving resolution in the sedimentary basins, but also imaging deep parts of the crust and the uppermost mantle. Processing steps in time domain (see “Chapter 3: Multichannel seismic reflection data” for details) include minimum-phase conversion, real geometry definition accounting for streamer feathering, spherical divergence correction, predictive deconvolution in Tau-P domain (to eliminate the bubble and short periods multiple reverberations), surface consistent deconvolution, Surface Related Multiple Elimination (SRME) demultiple, Radon filter demultiple, normal-move-out correction based on velocity semblance analysis, Dip Move Out (DMO) correction, stretching mute, amplitude recovery, stack, time migration and a time and spatial variant band-pass filter. To study the real geometry of the structures, we performed a Pre-stack Depth Migration (PSDM) of profile TM03 (Fig. 9.2) using “*Echos GeoDepth*” software.

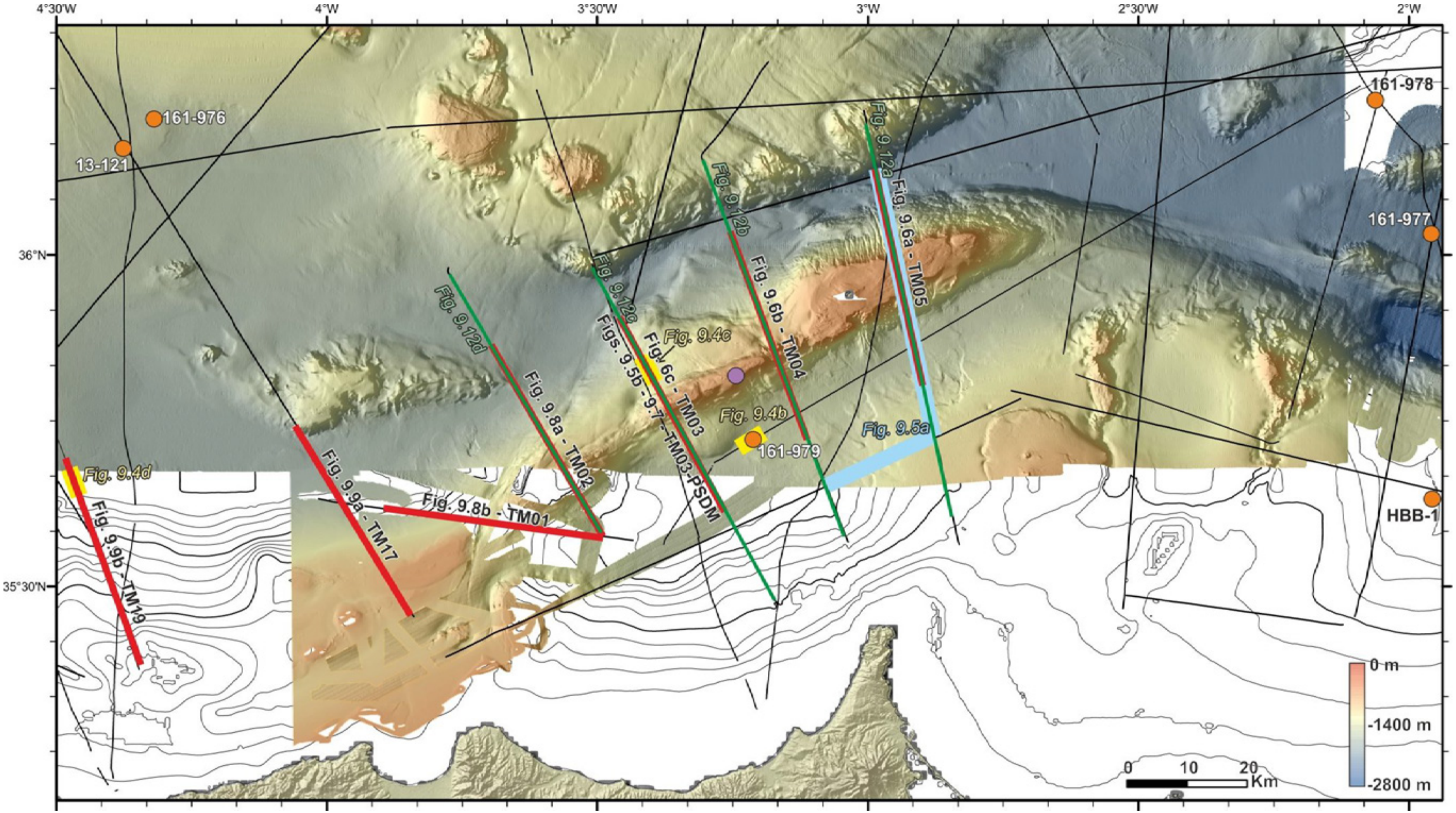

Figure 9.2: *Colour shaded-relief bathymetric map of the Alboran Ridge area. In the areas without multibeam bathymetry, contours each 100 m are shown. MCS profiles and wells are located. Orange dots depict the position of wells, and pink dots depict the position of the dredged sample. Location of the figures (red, blue and green lines) is displayed. See Figure 9.1 for location. TM: TOPOMED-GASSIS cruise MCS profiles. EVD: EVENT-DEEP Leg2 cruise MCS profiles.*

Profile EVDT1-3B has been obtained through another processing flow, with the objective of high-resolution imaging of the sedimentary infill in the SAB, to perform the sediment unit correlation. This processing includes the real geometry, spherical divergence correction, normal-move-out correction based on velocity semblance analysis, stretching mute, amplitude recovery, time migration, and a time and spatial variant band-pass filter.

We used the IHS Kingdom Advanced software to map the stratigraphic and structural interpretation of the MCS dataset presented here, and Generic Mapping Tools (GMT, Wessel and Smith, 1991) to plot the figures. Map analysis and displays have been performed with ArcGIS software.

9.2.2. Shortening estimation

We performed time-depth conversion of mapped sediment horizons to estimate shortening recorded in the area. We carried out this task using the IHS Kingdom Advanced software. The conversion is based on an interval velocity model, in which each layer is defined by a horizon and the horizon immediately below it, being the seafloor the first horizon used. The velocity model is a smoothed version of the pre-stack-depth-migration macro-velocity field of TM03. To estimate shortening, we measured the length of the horizon in the target section against the length of the section. Estimations are minimum shortening values because the erosion of some horizons and error induced by the time-depth conversion, which reduces the dip of the layers especially in the steeply-dipping areas (i.e. flanks of the fold, Figure 9.3).

Interval velocities used for the conversion have been tested on the pre-stack depth migration of TM03. We picked horizons in both, two-way travel time and depth along TM03, and compared the results. The comparison between the horizons picked in the depth section (considered as real geometry) and horizons resulting from the time-depth conversion indicates that the conversion provides good results for the sedimentary sequence, although depth conversion of steeply-dipping segments (e.g. flanks of the Alboran Ridge fold) is less accurate (Fig. 9.3a). Depth conversion of the horizon of the volcanic basement is less satisfactory due to the complexity of the velocity model in these areas. Those horizons have been used as depth reference, but not included in the shortening estimation. Comparison between the PSDM picked horizons and time-depth converted horizons reveals that the time-depth converted horizons generally has lower dip than the real ones. This implies that shortening measured along the time-depth converted horizon provides a minimum estimate. In the case of the TM03 section, shortening of the Messinian horizon measured with the PSDM section is 1.3 km, while along the time-depth converted horizon is 1.1 km.

For the sediment horizons, we have estimated uncertainty in measurements based on the variability of the result using a range of velocities (Figs. 9.3b, c). Assuming a 50 m/s error in the velocity assigned to the interval, shortening estimates vary with a maximum of 0.03 km. Assuming the improbable velocity error in our model of 200 m/s results relatively small change of 0.089 km (Figs. 9.3b and c). The robustness of the shortening estimation resides in that differences in velocity affect depth position of reflections (i.e. with 50 m/s alteration, the reflection is displaced 0.5 km in vertical, but with 200 m/s change in the original velocity the reflection is displaced almost 3 km), but the lineal morphology of the reflections remains rather similar (Fig. 9.3b). Depth variations of the position of the reflections are more evident on deeper and steeper reflections (Fig. 9.3b). Taking into account several velocity models due to the uncertainty associated to our velocity model, and the differences in the depth of the reflections, we assume an average uncertainty value of ≤0.05 km for the estimated shortening values in mapped horizons (Fig. 9.3c).

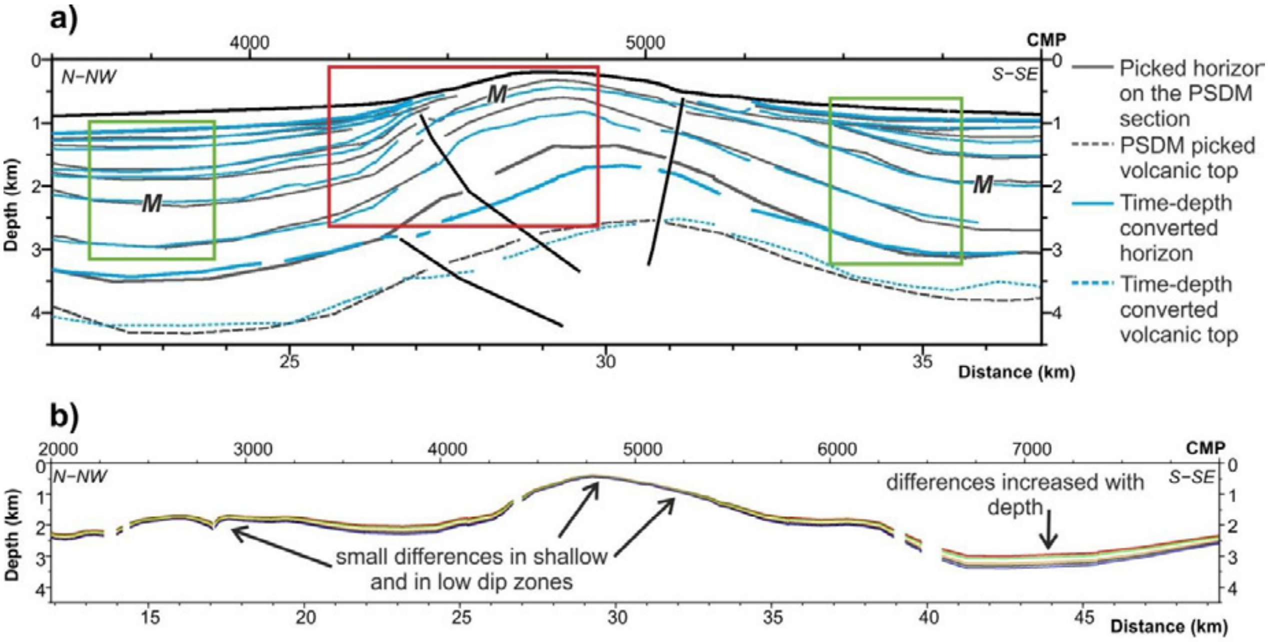

c)

Horizon	Tested velocity (m/s)	Estimated shortening (km)	Error (real v. shortening-test v. shortening)
Blue	2800	1.089	0.010
Black - real conversion velocity	**2700**	**1.079**	**0.000**
Orange	2600	1.139	0.030
Green	2400	1.158	0.089
Red	2300	1.168	0.079
		Mean	0.047

Figure 9.3: *Error estimation for the time-depth horizon conversion.* ***(a)*** *Error estimation based on the comparison between the horizons picked along the PSDM section and the time-depth converted horizon from the same section in time. Having the image in time and depth allows us to assign a confidence value to our results. Grey lines represent the horizons picked along the PSDM section, considered as the real ones. Blue lines are the corresponding time-depth converted horizons. When the dip of the reflections is near to zero, the time-depth conversion obtains a more accurate result (green rectangles). In the cases when the reflections show a high dip angle, the adjustment is poorer (red rectangle). It is observed that when the fit is not well achieved, the length of the time-depth converted horizons is less than the length of the real one. This method works only for the sedimentary series. In the case of the volcanic basement top (dash lines), the adjustment is not well accomplished due to the increment in the complexity of the velocity structure. M: Messinian unconformity.* ***(b)*** *Error estimation based on the influence of the velocity model used. We presented the Messinian horizon converted for different velocities, in order to estimate the error in the shortening measured associated to the velocity variation. We tested different velocity models, and we define as real ones the model that best fits the PSDM picked horizons with the time-depth converted horizon along section TM03. In this way, the real velocity of the Messinian horizon has been calculated in 2700 m/s (black line), and velocities of 2800 m/s (blue), 2600 m/s (orange), 2400 m/s (green) and 2300 m/s (red) have been tested. Results are described on Figure 9.3c.* ***(c)*** *Table showing the associated shortening values to the different velocity values tested. The “Error” column corresponds to the shortening estimated for the horizon converted with the most suitable velocity (“real” velocity) minus the estimated shortening value for the different tested velocities. Velocity variations mainly produce a change in the horizon depth, but it conserves its shape. This fact give as a result that the shortening value, our target, is almost constant (± 50 m) in spite of the velocity variation.*

9.3. Results

9.3.1. Seismostratigraphic units

The post-Messinian stratigraphy of the Alboran Ridge area is reasonably well established (e.g. Martínez-García, 2012, Martínez-García et al., 2013). To complete the stratigraphic sequence of the ODP Leg 166 Site 979 located in the South Alboran Basin, we have correlated the sedimentary units defined at HBB-1 well (Fig. 9.2, Medaouri et al., 2012, 2014) and at the West Alboran Basin (e.g. Comas et al., 1999; Soto et al., 2010, 2012; Do Couto et al., 2016) with our data. We defined three main sedimentary units (I-III), three volcanic units (vA1, vA2 and vD) (Fig. 9.4) and a deep high-reflectivity unit. These units are described in detail in "Chapter 6: Basin evolution".

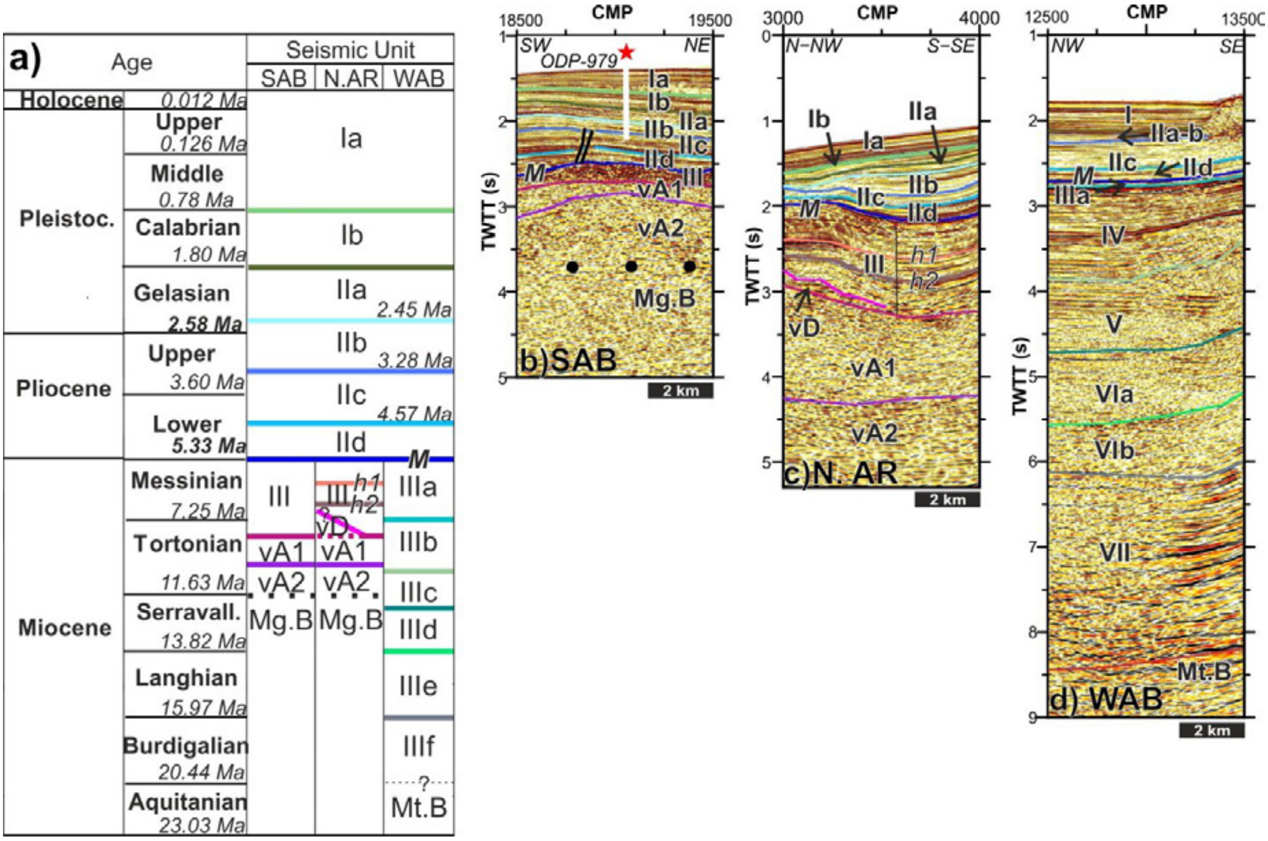

Figure 9.4: ***(a)*** *Ages and seismostratigraphic units identified in the MCS profiles, at the South Alboran Basin (SAB,* ***b****), the North Alboran Ridge sediments (N.AR,* ***c****) and in the West Alboran Basin (WAB,* ***d****). Mg.B: Magmatic Basement, Mt. B: Metamorphic Basement, ODP-979: ODP Leg 161 Site 979. See Figures 9.2, 9.4b, 9.7c and 9.10b for location.*

- *Basement characteristics*

Several units interpreted as volcanic products overlay a highly reflective basement (Figs. 9.5, 9.6, 9.7, 9.8), characterized by strong reflections with low lateral continuity and relative low frequency. Correlation with HBB-1 well supports that these volcanic units are emplaced over the North African metamorphic basement.

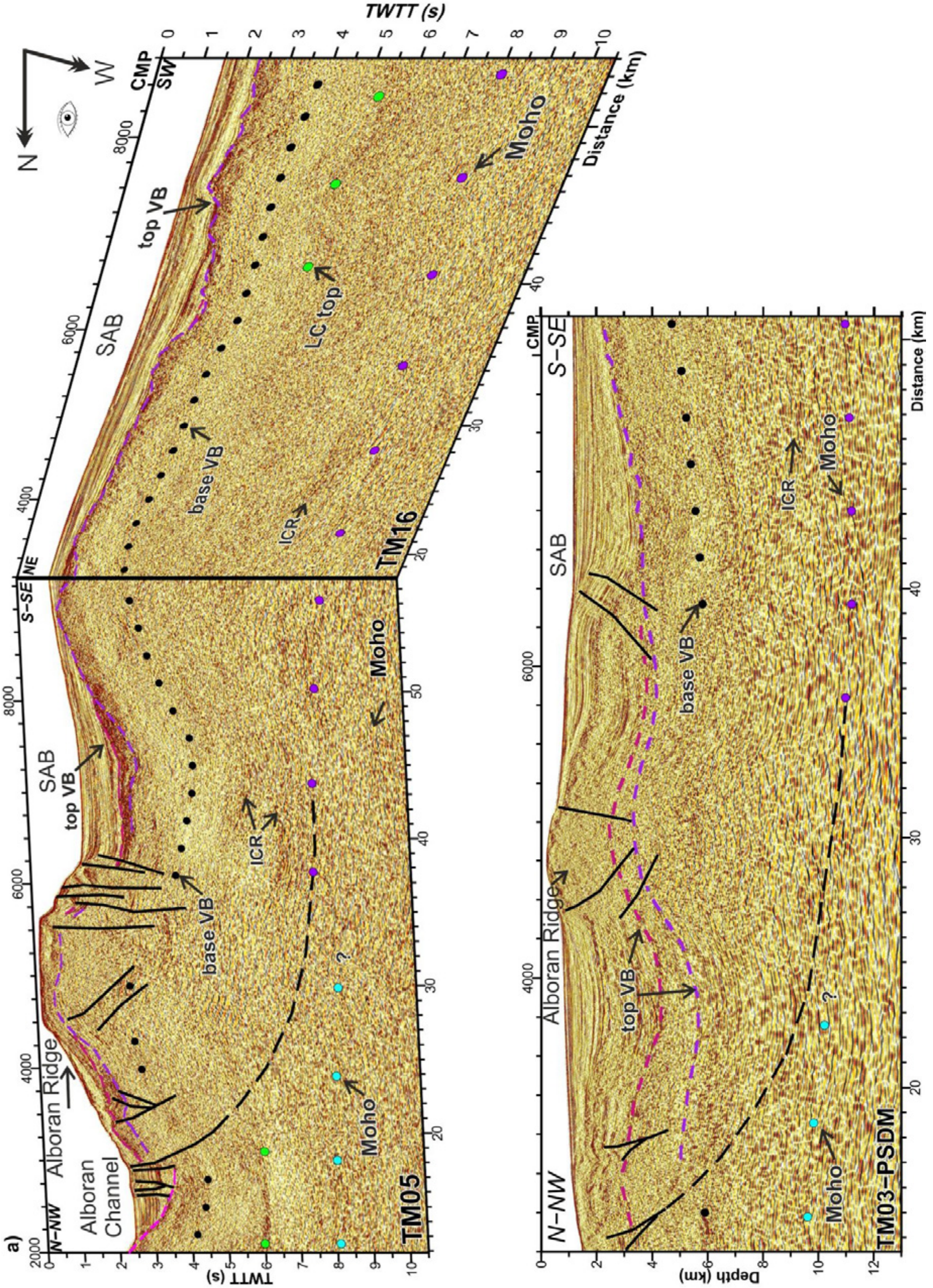
a)
N
W
TWTT (s)
CMP
SW
NE
S–SE
N–NW
SAB
top VB
base VB
LC top
ICR
Moho
TM16
TM05
Alboran Ridge
Alboran Channel
?
Distance (km)
TM03–PSDM
Depth (km)

◄ ***Figure 9.5:*** *Crustal scale structure of the Alboran Ridge (AR) area.* ***(a)*** *Perspective view of profiles TM05 and TM16, running perpendicular and parallel to the AR.* ***(b)*** *Pre-Stack Depth Migration of profile TM03. Black dots: base of the volcanic basement, blue dots: magmatic crust Moho, purple dots: continental crust Moho. See location in Figure 9.2. ICR: Intra Crustal Reflection, LC: lower crust, SAB: South Alboran Basin, VB: volcanic basement.*

The profiles show the Moho discontinuity indicating a basement thickness difference between the north and southern sides of the AR (Fig. 9.5). In the southern flank occurs at ~8 s TWTT, with a basement thickness of ~5.0–5.5 s TWTT (Fig. 9.5a). On the northern flank, the Moho is located around the same TWTT, but basement thickness is ~4.5-5 s TWTT (Fig. 9.5a). The Pre-Stack Depth Migration of TM03 (Fig. 9.2, 9.5b), displays the Moho under the AR. In the southern flank Moho is ~11 km depth, and basement thickness >~7 km. Under the north flank the Moho is slightly shallower, at ~10 km, and basement thickness is ~6 km (Fig. 9.5b).

9.3.2. The Alboran Ridge

From a structural point of view, the AR presents variability from West to East (Fig. 9.2). The AR in its eastern segment is a volcanic high that forms the Alboran Island, while in the southwest segment is a narrower, convex sedimentary ridge.

On the easternmost side, profile TM05 (Fig. 9.6a) images the flat top of the high. Here, vA2 volcanic unit appears at the core of the high, while unit vA1 seems to be absent at the top of it. Above them, we found sediments from unit III, which appear folded and faulted, and units II and I fill the lows at the top of unit III. On this profile, the ridge is bounded by a thrust on its front (northern side, Fig. 9.6a CMP ~3000) and several sub-vertical faults on its back southern flank, which form possibly a transpressive structure (Fig. 9.6a, CMP 5500-6500). These faults affect the lower sedimentary units and enter into the basement. A possible strike-slip fault zone on the southern flank is active and cuts the seafloor. Towards the west, profile TM04 (Fig. 9.6b) shows how the volcanic basement, formed by units vA1 and vA2, crops out on the top of the high. Here, it exhibits a narrow ridge topography, instead of a flat top (Fig. 9.6b CMP ~6000). Deformation at the thrust front is more widely distributed, and we identify at least three reverse faults cutting the strata (Fig. 9.6b CMP 8250, 7500 and 6500). The southern flank is bounded by two steep faults (Fig. 9.6b, CMP 5250, 5750). Here, faults also deform the basement, and on the southern flank cut into the seafloor. On profile TM03 (Fig. 9.6c), the structure of the high has changed, and the AR is a narrow anticline cored by folded strata. This fold is formed by volcanic units (vA1, vA2), folded in the core of the fold. The sedimentary sequence above them is composed of units III to I. While unit III has an approximately constant thickness along the fold, units II and I show a clear thinning above the high. Three fault zones are identified. The front of the high is bounded by two blind thrusts, involving the basement (Fig. 9.6c CMP ~6750). At the back of the high, there are two back-thrusts, faulting units III and II and rooting into the top of the volcanic units (Fig. 9.6c CMP 6250-7000).

The PSDM of TM03 shows that on the western flank of the AR, the narrow fold (Fig. 9.7 CMP 4000-6000) evolves into gentler anticline structure (Fig. 9.8a, profile TM02 CMP 4000-1000), becoming a wider smooth fold on its western end (Fig. 9.8b, profile TM01 CMP 3000-7000). At the western end, the fold remains composed of sediment and volcanic strata. Thinning of unit I and gentle thinning of unit II can be recognized at the high (Fig. 9.8b CMP 5500-7000), but the thickness of unit III appears constant. On profile TM02 the frontal thrust of the high is also identified (Fig. 9.8a CMP 2750), and the back thrust of the high resembles a transpressive structure formed by sub-vertical faults that generate a positive flower structure (Fig. 9.8a CMP 1500-2250). The westernmost profile TM01 shows AR as a gentle fold bounded by a low-dip blind thrust (inactive?), rooted below the volcanic basement (Fig. 9.8b CMP 5500-6000). A second apparently inactive thrust is identified on the southern side of the AR, which affects up to unit IIb (Fig. 9.8b CMP ~7000).

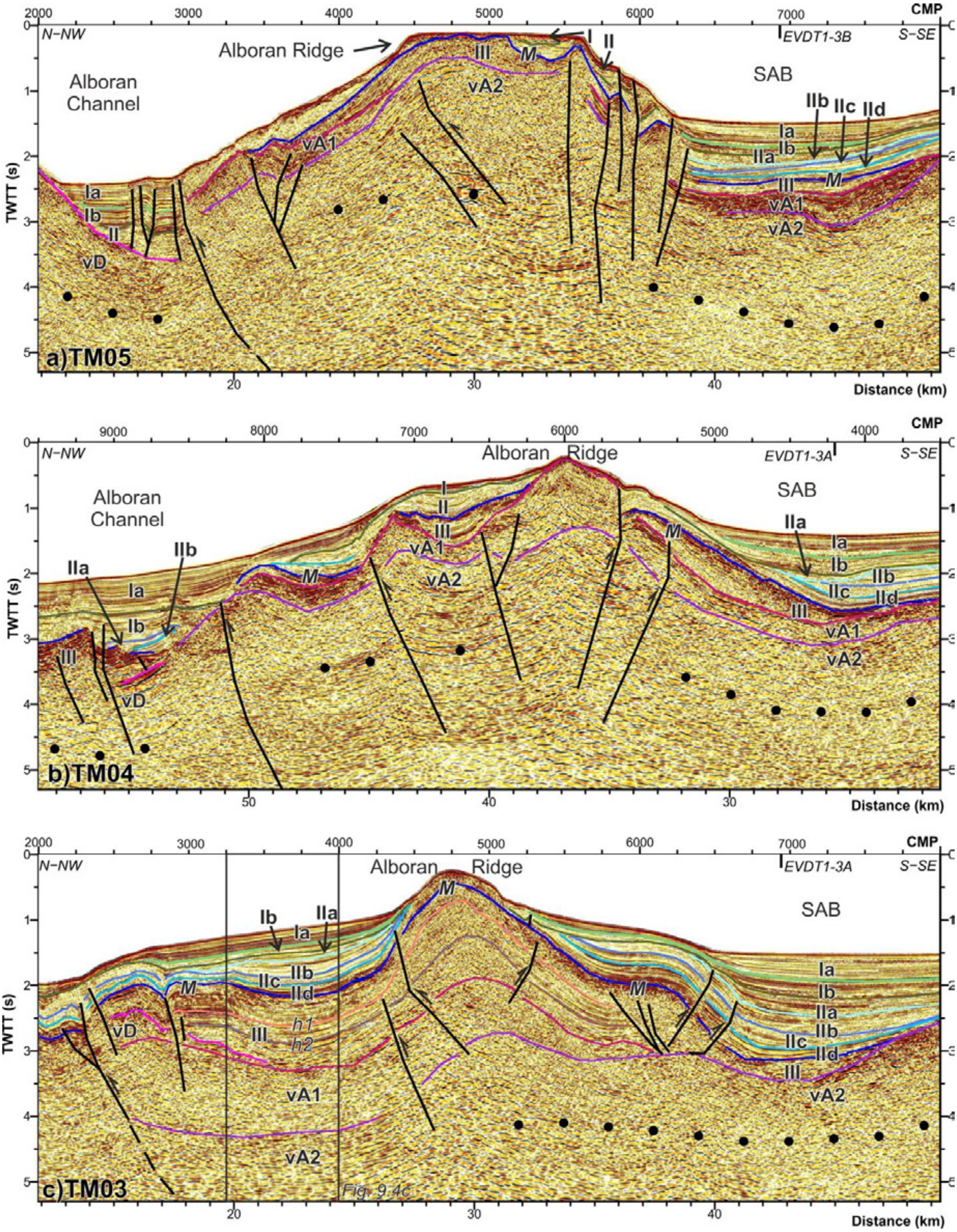

__Figure 9.6:__ Time migration of profiles __(a)__ TM05, __(b)__ TM04 and __(c)__ TM03 (see location in Figure 9.2). Main structures and seismostratigraphic units are identified. Units are defined in Figure 9.4. Vertical exaggeration is of ~x:1.8. SAB: South Alboran Basin.

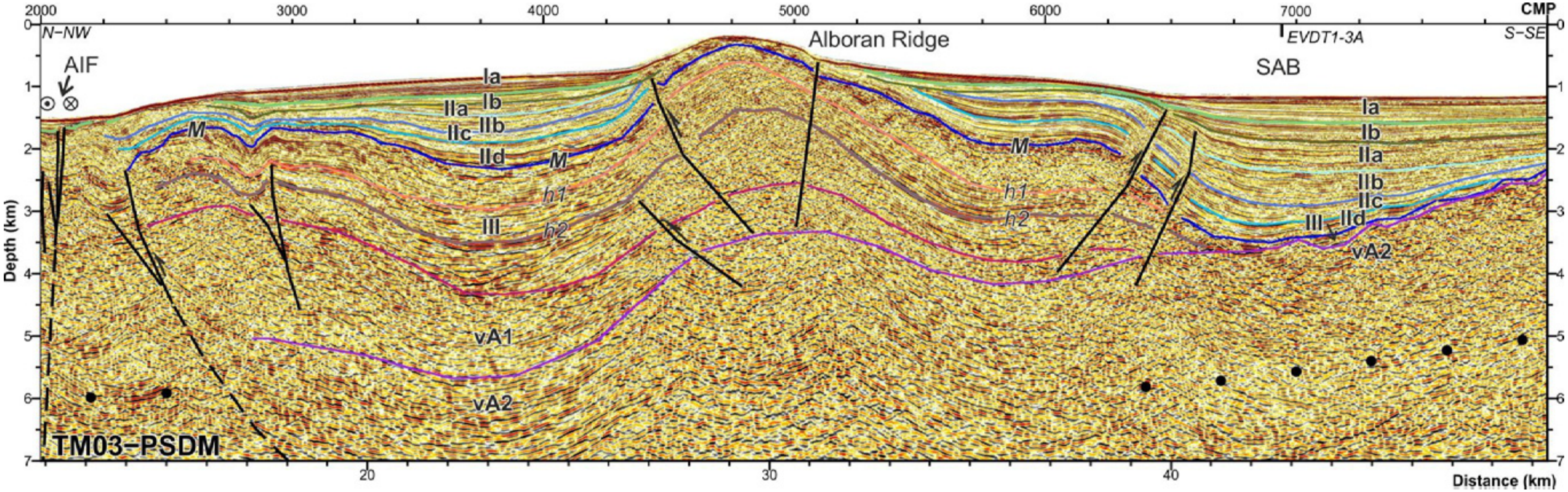

Figure 9.7: *Depth migration of profile TM03 (see location in Figure 9.2). Main structures and seismostratigraphic units are identified. Units are defined in Figure 9.4. Vertical exaggeration is of ~x:1.5. AIF: Al-Idrissi Fault, SAB: South Alboran Basin.*

The southwestern part of the AR is cut by the Al-Idrissi fault (Fig. 9.1), imaged on profiles TM02 and TM01 (Fig. 9.8a CMP 4000-4500, Fig. 9.8b CMP 4500-5250). The Al-Idrissi fault is a sub-vertical left-lateral strike-slip fault that in this area shows positive flower structures (Fig. 9.8a, b). This fault is roots in the basement, and deformation is affecting the most recent sediments cutting to the seafloor (Fig. 9.8a CMP 3250-4000, Fig. 9.8b CMP 4250-5000). The basins formed at the top of the flower structure seem to be filled by unit I sediments (Fig. 9.8b CMP 4500-5000). The depositional geometry of units II and III appears unrelated to the Al-Idrissi fault.

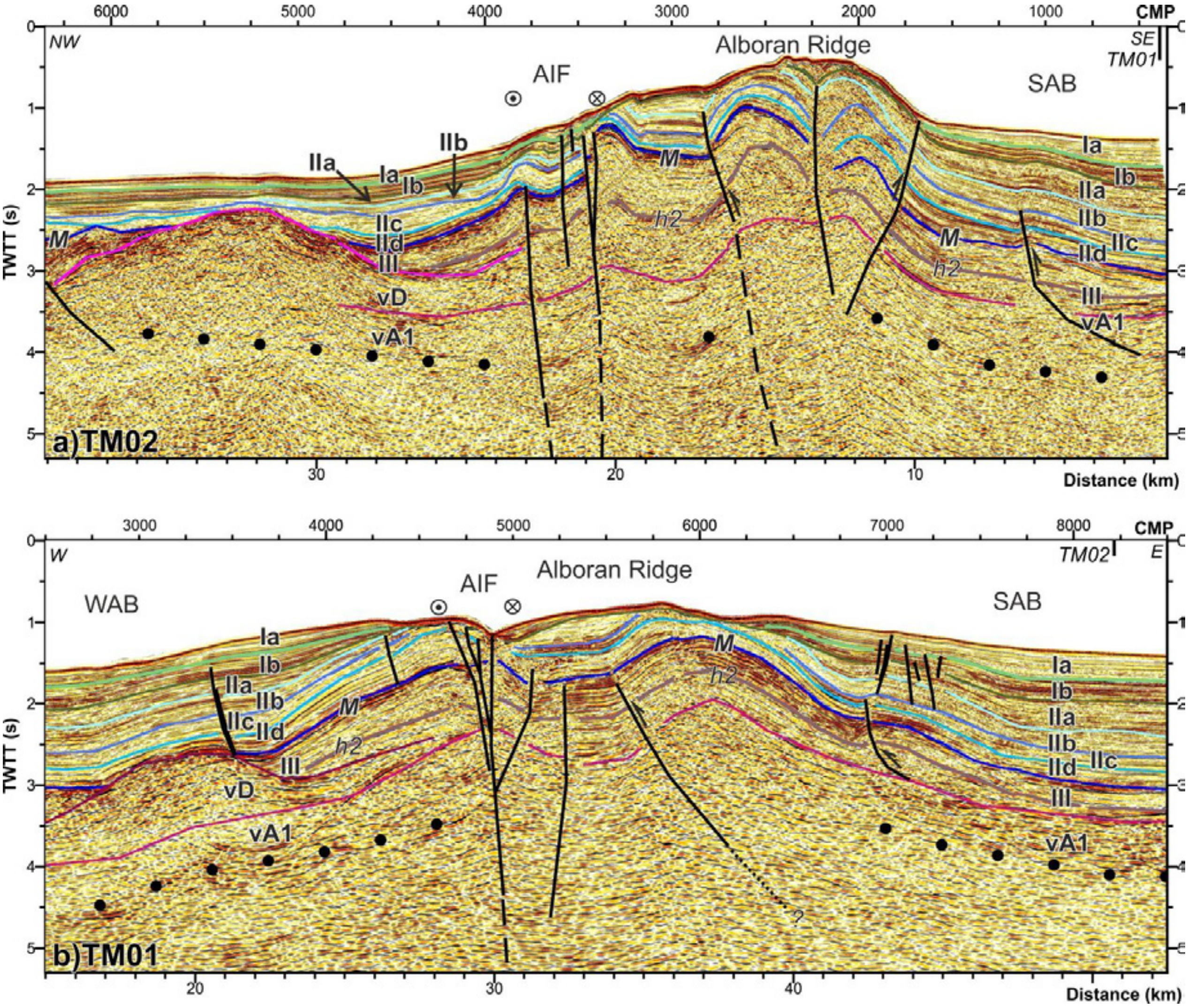

*Figure 9.8: Time migration of profiles **(a)** TM02 and **(b)** TM01 (see location in Figure 9.2). Main structures and seismostratigraphic units are identified. Units are defined in Figure 9.4. Vertical exaggeration is of ~x:1.8. AIF: Al-Idrissi Fault, SAB: South Alboran Basin, WAB: West Alboran Basin.*

The sediment architecture surrounding the AR shows that unit Ia thinning towards the AR high (e.g. Fig. 9.6c CMP 4000-6000), and it is onlapping unit Ib (e.g. Fig. 9.6b CMP 5500- 4500). In a similar way, Ib thinning towards the AR high (Fig. 9.6c CMP 5000-7000, Fig. 9.8b CMP 2000 - 1500) and onlaps unit II, and in some parts its base appears erosional and truncating the top of unit II (Fig. 9.6c CMP 5000-6000). Below unit I, there is unit IIa that is not continuous along the profiles, and has an erosive base (Fig. 9.6b CMP 5000-4000). Internal reflections end in a downlap geometry against the top of unit IIb (Fig. 9.6a CMP 7250-6500, Fig. 9.6b CMP 5000-4000, Fig. 9.6c CMP 7000). Unit IIb slightly increases its thickness away from the AR high, until it reaches the basin margin (Fig. 9.6c CMP 5000-8000). The lower part of unit II (units IIc and IId) shows parallel reflections and minor thickness variations. Thinning towards the AR is strongest for unit IIc (Fig. 9.6c CMP 3500-4500). Under the M unconformity, unit III, defined by two internal reflections (Fig. 9.6c CMP 3000-6000) or just one (Fig. 9.8a CMP 3500-1000, Fig. 9.8b CMP 4000-7000) extends across the AR, delineating the folding. The thickness of unit III and its internal layers are approximately constant.

Underneath the sediment sequence, the volcanoclastic units fill basement top relief. Figure 9.6b images the volcanic basement outcrops on the eastern part of the AR top (CMP 6000). These volcanic layers are characterized by chaotic zones that alternate with stratified bodies. Although lateral continuity of the internal structure of the volcanoclastic units is limited, folding is apparent in all seismic cross sections (Fig. 9.6a CMP 3000-4000, Fig. 9.6c CMP 4000-6000, Fig. 9.8b CMP 5000-6500).

9.3.3. Francesc Pagès, Tofiño and Xauen Banks

Francesc Pagès, Tofiño (Fig. 9.2, Fig. 9.9a profile TM17) and Xauen (Fig. 9.2, Fig. 9.9b profile TM19) banks appear the SW extension of the AR, but the Al-Idrissi fault system abruptly dissects the continuity of the structure. The Francesc Pagès and Tofiño Banks are anticlinal structures floored by volcanic basement, with a deformation style similar to the AR. Unit vA2 is the oldest, and is covered by sediment from units III-I (Fig. 9.9a, b). Units IId and IIc are filling just the deeper part of the basin, while the shallower units (i.e. units IIb, IIa and I) are more widespread and show a thickness decrease toward the Tofiño high.

The Xauen Bank, located to the west, shows a contrasting structure, made of a folded thick sediment package (Fig. 9.9b). Its north-westernmost part is made of sediment of the West Alboran Basin, which depocenter contains >7 s TWTT of Miocene to Pliocene sediment (Fig. 10b CMP 15500 – 14000), and a metamorphic basement (e.g. Comas et al., 1992). No volcanic units are identified on TM19 (Fig 9.9b). The Xauen Bank is structured as a series of synclines and anticlines related to deep faulting (Fig. 10b CMP 14000 – 18000). While folds affect the whole sedimentary sequence, faults stop at the top of unit III at the resolution of our images. Under the Xauen Bank, deformation involves basement blocks. Faults exhibit a sub-vertical attitude, with reverse faults (Fig. 10b CMP 14000, 15000) and normal offsets (Fig. 10b CMP 17000-18000). The shallowest Xauen Bank area shows a flat top with a prograding Quaternary sediment sequence (unit I and probably upper part of unit II, Fig. 10b CMP 17500-18250).

9.4. Discussion

9.4.1. Nature of the basement

The basement of most of the area is covered by volcanic units vA1, vA2 and vD, identified by their characteristic seismic facies with well stratified zones alternating with chaotic areas, their limited spatial extension, typical wedge-shape geometry (e.g. Fig. 9.6a CMP 3000-4500) and abrupt lateral changes of seismic facies (Fig. 9.6c CMP 2500-4000). Their nature is confirmed by volcanic rocks dredged along the Alboran Ridge (see Figure 9.2 for location). Unit vA1 is dated as ~9.3 Ma (Duggen et al., 2004, 2008), and consequently, unit vA2 minimum age is Early Tortonian. Late Miocene sediment units fill the relief of this volcanoclastic deposits. Unit III gently on laps the volcanic highs without lateral thickness variations (Fig. 9.6a CMP 3000). Locally, units II and I lap directly on the volcanic units (e.g. Fig. 9.6b CMP 7000-6000).

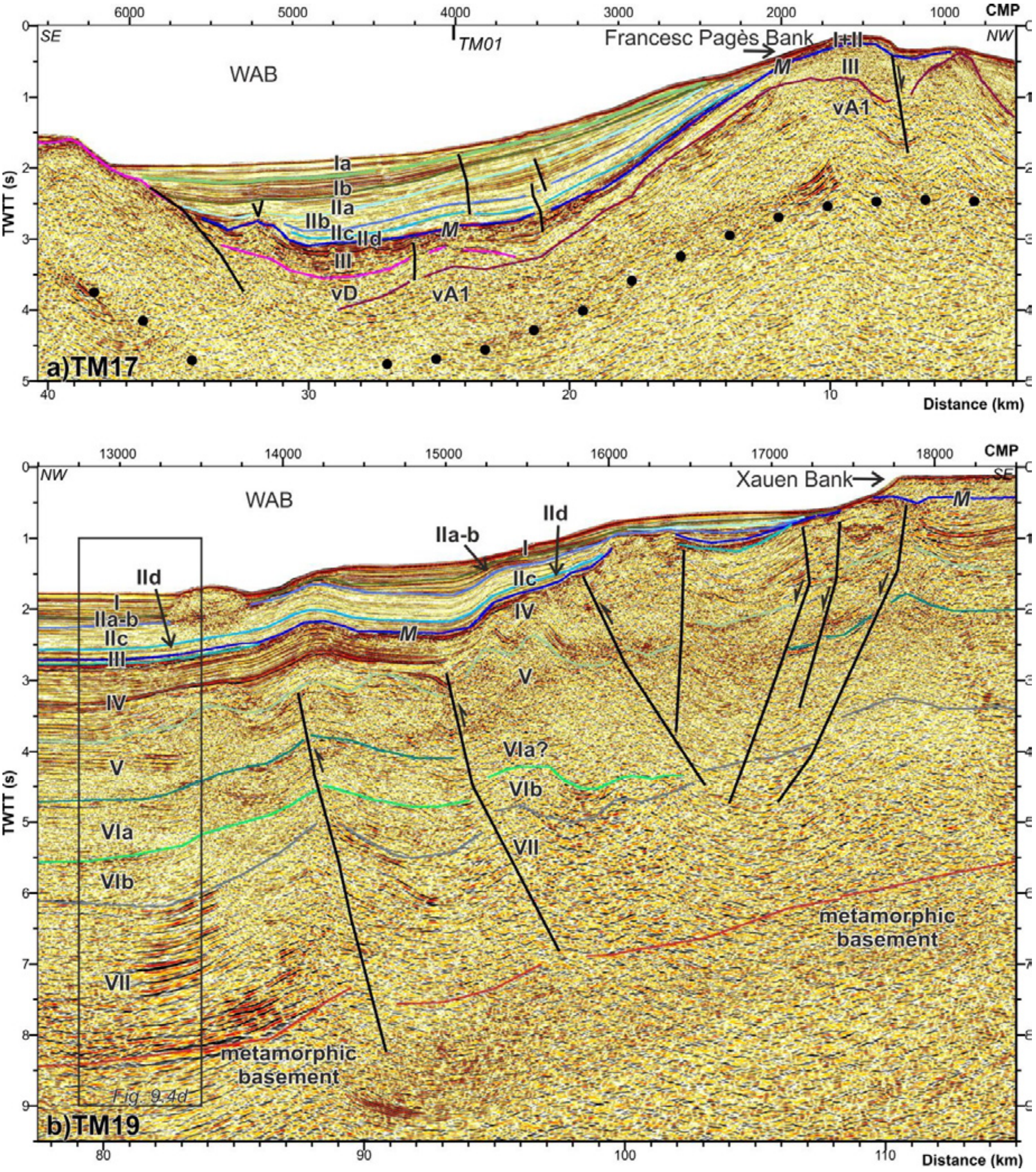

Figure 9.9: *Time migration of profiles* ***(a)*** *TM17 and* ***(b)*** *TM19 (see location in Figure 9.2). Main structures and seismostratigraphic units are identified. Units are defined in Figure 9.4. Vertical exaggeration is of ~x:1.8. WAB: West Alboran Basin.*

Below these volcanic units, the upper section of the basement displays high-reflectivity (Figs. 9.5, 9.6, 9.7, 9.8, 9.9a). This high-reflectivity zone does not have a well-defined base, but deeper into the crust gives way to a more transparent basement (e.g. Fig. 9.6, black dots layer). This high-reflectivity basement has an internal structure formed by discontinuous reflections, which follows the long wavelength folding of the region (Fig. 9.6a, CMP 6000-8000, Fig. 9.6b CMP 5500-7000). This unit disappears towards the West

Alboran Basin, where the sedimentary basin is inferred to be underlaid by metamorphic basement (Fig. 9.9b) (Comas et al., 1992; 1999; Chalouan et al., 1997). We interpret the high-reflectivity zone resulting from crustal modification at the southern edge of the region affected by arc-related magmatism.

We interpret the AR fault system to have formed at the transition between two crustal domains. To the north is the magmatic-arc crust and to the south is the continental crust drilled at HBB-1 site. The AR fault system may have formed in the magmatically intruded transition between the two domains and currently forms a crustal-sale boundary (Fig. 9.5, see "Chapter 5: Crustal domains").

9.4.2. Contractional phases

It is proposed that extension in the Alboran Basin occurred till the Tortonian, when a change in the stress regimen took place leading to a contractive reorganization of the basin (e.g. Comas et al., 1999; Wortel and Spakman, 2000; Rosenbaum et al., 2002). However, it has also been proposed that this change does not occur with the same intensity and at the same time for the entire Alboran basin. At the latemost Tortonian, extension episodes still occurred in the South Iberian margin (Krautworst and Brachert, 2003; Booth-Rea et al., 2004; Giaconia et al., 2014). In the AR area, we identify three contractional pulses. These pulses produced well developed structures at the eastern flank of the structure, and deformation decreases towards the west, where folding is more open and changes in the geometry of the sedimentary units are gentle.

In contrast to previous works, we interpret the Messinian unit III, as a pre-tectonic to the contraction phase. The M reflection marking the top of unit III is an erosional unconformity across much of the basin and generally is well-defined. There are no clear variations in sediment packages thickness or contractional deformation structures previous or during the deposition of this unit. Within unit III, we mapped two reflections to evaluate internal changes in thickness or geometry (h1 and h2 at Figures 9.6c, 9.7 and 9.8a, b). Reflections h1 and h2 define layers that do not exhibit important thickness variations, and display internal parallel reflections and concordant contacts. Thus, we interpret unit III deposition previous to the first contraction pulse. While unit III has constant thickness in the core of the main fold, unit II thins towards the shallowest part of the AR, supporting syn-tectonic deposition.

Three intra-Pliocene discontinuities provide an accurate chronology of the deformation also studied by Martinez-Garcia et al, (2013). The oldest Pliocene units IId and IIc deposited between 5.33 and 3.28 Ma lap on the M unconformity. These units show small variations in their thickness, especially clear in the gentle wedge-shape geometry of unit IIc (Fig. 9.6a CMP 6250-8000). We interpret that the first compressive pulse occurred in the Early Pliocene, during deposit of units IIc and IId. The younger unit IIb exhibits clear thinning towards the AR (Fig. 9.6c CMP 5000-8000), and may represent a second deformation pulse during the Middle Pliocene age (3.28–2.45 Ma). Unit IIa has a more local distribution filling lows, and where present laps on unit IIb. Unit I has an erosive base that partially truncates units IIa and IIb, reaching units IIc and IId in some areas (Fig. 9.6c CMP 6000-5000). Unit I is divided in unit Ib that laps on the erosive base and thins towards the high, with wedge-shape geometry. Unit Ia, shows similar discordant character and thinning towards the AR. The discontinuity between units Ia and Ib have been related to a change in the convergence direction (Martínez-García et al., 2013). In agreement with Martínez-García et al. (2013), we interpret that there was a tectonic quiescence period between the Middle Pliocene contraction and the sedimentation of the Quaternary units Ib and Ia, when the erosion of unit II occurred. The present-day configuration of unit I implies a third tectonic pulse during the Early Quaternary: Unit Ia has a clear wedge-shape, thins towards the AR, and faulting affects the shallowest units and seafloor (Fig. 9.6b CMP 6000-5500, Fig. 9.6c CMP 5750-6250), supporting that the AR uplift is still active.

The Al-Idrissi fault system is imaged in Figure 9.8 as a sub-vertical strike-slip fault forming flower structures. The Al-Idrissi fault cuts the seafloor and recent seismicity support that it is an active structure. Unit II changes in thickness around this fault, but it is unclear how much is related to the AR uplift and to Al-Idrissi fault deformation. The shallowest sediment forms wedge geometries (Fig. 9.8a CMP 4250-4500, Fig. 9.8b CMP 4500-5250), supporting that the activity of the Al-Idrissi fault system started in the Quaternary (~1.8 Ma, base of unit Ia) and continues at the present-day. This fault plays a major role in strain partitioning, as it bounds the deformation affecting west of the AR structure along the Francesc Pagès, Tofiño and Xauen banks.

9.4.3. Connection between the Alboran Ridge and the Francesc Pagès, Tofiño and Xauen Banks

Francesc Pagès and Tofiño Banks follow the same structural trend of the AR, with folding exhibiting the same characteristics of the southwestern sector of the AR. In the Xauen Bank (Fig. 9.9b), there are indications of pre-Messinian deformation disrupting Middle and Lower Miocene units -which might be related to the abundant mud diapirism in the West Alboran Basin. The post-Messinian evolution is however coherent with the deformation observed to the east, along the Francesc Pagès and Tofiño Banks and at the AR. On either sides of the Al-Idrissi fault (east side, profile TM01, Fig. 9.8b and west side profile TM17, Fig. 9.9a), the structure of the ridge displays similar folding, involving the sedimentary sequence and volcanic basement in a gentle anticlinal fold.

We interpret that the AR, Francesc Pagès, Tofiño and Xauen Banks may have been originally formed along the same structure or during the same phases of contraction, however, their lateral continuity is fully disrupted by strike-slips of the Al-Idrissi fault system. It is an important structure, with a high lateral continuity and displaces both, the sedimentary infill of the basin but also the basement, and constrains the deformation to the AR area. Deformation along the AR-Francesc Pagès-Tofiño-Xauen ridge started in Early Pliocene times, and continues active along the AR area as indicated by structure and seismic activity, while it is greatly diminished along Francesc Pagès and Tofiño Banks and may have stopped or waning along the Xauen Bank.

9.4.4. Slip estimation

Two methods were used to estimate total slip along an assumed basal detachment: (i) the fault-bend folding model and (ii) the excess-area graphical technique. The measurements for the calculation had been done on a 1:1 scale plot of the Pre-Stack Depth Migration of profile TM03 (see Figure 2 for location). Due to the acquisition geometry with a 5100 m streamer length, and a target depth shallower than 4 km for all mapped horizons, we consider that the velocity model obtained during PSDM is very accurate, so that the depth section provides an accurate geometry.

Figure 9.10* ►:** *Total slip estimation.* ***(a) *Bend folding model (Lavé and Avouac, 2000; Bernard et al., 2007), assuming only one fault. Our data depicts an uplift of 2 km and a detachment angle ~5º, giving at total slip ~23 km.* ***(b)*** *Bend folding model (Lavé and Avouac, 2000; Bernard et al., 2007), assuming strain partitioning between two faults. Fault 1 has an associated uplift of 1km, and a detachment angle ~5º, giving at total slip ~11.5 km, and Fault 2 has an associated uplift of 2km, and a detachment angle ~5º, giving at total slip ~23 km. The total slip will be the sum of both, being close to 35 km. Location of Figure 9.10c is depicted.* ***(c*** *and* ***d)*** *Excess-area method (Epard and Groshong, 1993) (see location of the zoomed section in Figure 9.10b). On the PSDM section we have measured the exceed area (S) of 6 deformed horizons and its respectively high (h) taking as reference a 5 km depth level. The exceed area (S) is measured as the remaining area from the deeper point of the horizon (h) to the horizon itself. The high (h) is measured from the reference level to the deeper point of the horizon, and it represented the horizon position before the deformation. Plotting these values in an S-h graph* ***(d)****, the result is a cloud of points that can be adjusted to a straight line. The slope value of this line is equal to the slip, and for S=0, the depth of the detachment is obtained. The results are a total slip value 16.2 ± 3.3 km and a detachment depth of 5.3 ± 1.2 km depth.*

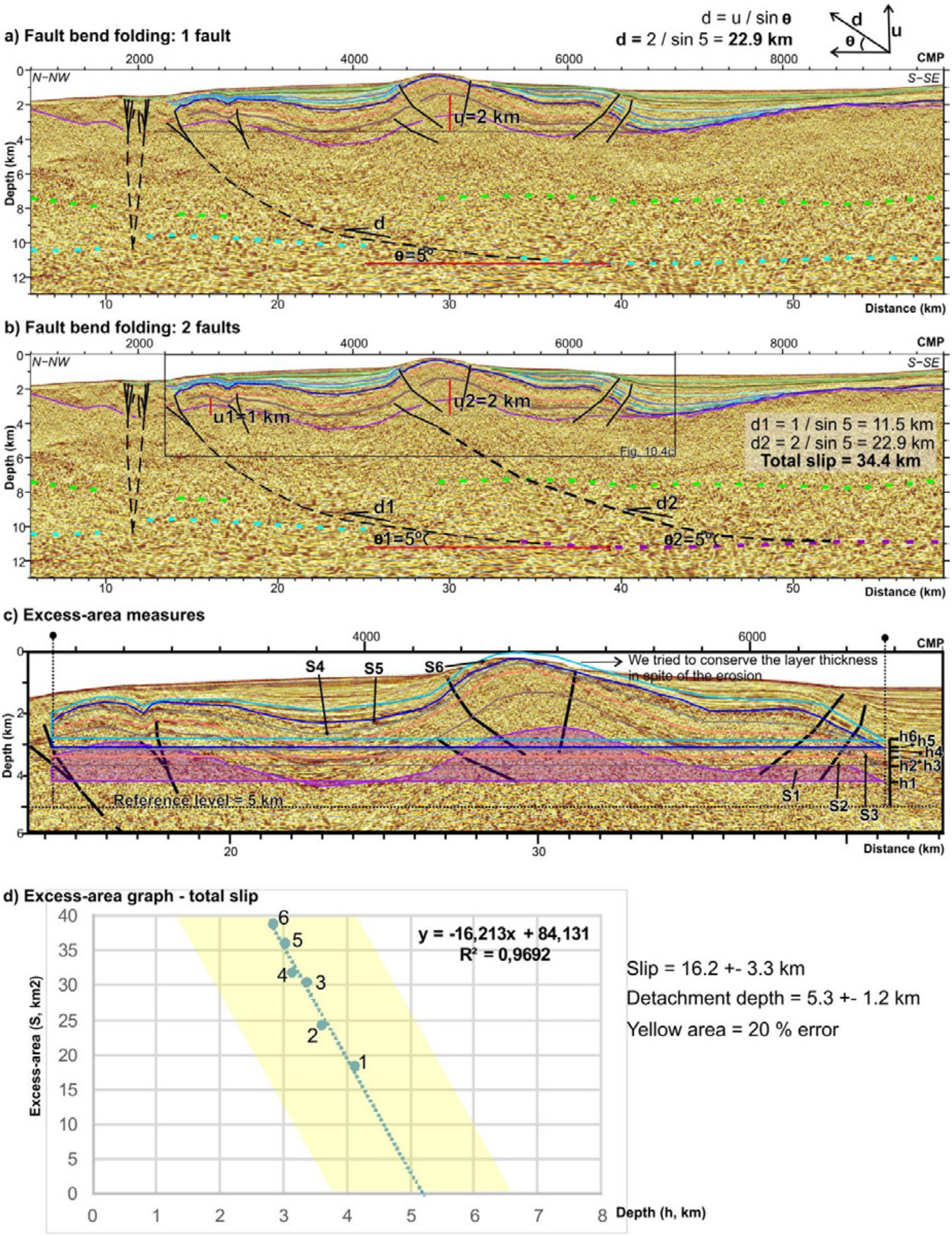
a) Fault bend folding: 1 fault
d = u / sin θ
d = 2 / sin 5 = 22.9 km
d
u
θ
CMP
2000
4000
6000
8000
N-NW
S-SE
u=2 km
d
θ=5°
Depth (km)
0
2
4
6
8
10
12
10
20
30
40
50
Distance (km)
b) Fault bend folding: 2 faults
u1=1 km
u2=2 km
d1 = 1 / sin 5 = 11.5 km
d2 = 2 / sin 5 = 22.9 km
Total slip = 34.4 km
Fig. 10.4c
d1
d2
θ1=5°
θ2=5°
c) Excess-area measures
S4
S5
S6
We tried to conserve the layer thickness in spite of the erosion
h6
h5
h4
h3
h2
h1
S1
S2
S3
Reference level = 5 km
d) Excess-area graph - total slip
y = -16,213x + 84,131
R² = 0,9692
Excess-area (S, km2)
Depth (h, km)
1
2
3
4
5
6
Slip = 16.2 +- 3.3 km
Detachment depth = 5.3 +- 1.2 km
Yellow area = 20 % error

The first method, the bend folding model (Lavé and Avouac, 2000; Bernard et al., 2007) proposes that the total uplifted area (u) is related with the slip along the detachment (d) and the detachment angle (θ), following the relation d= u/sin θ (Fig. 9.10a). In the case of one frontal fault linking at depth with the detachment (Fig. 9.10a), we infer a maximum uplift equal to 2 km, and a detachment angle of 5º, yielding an estimated total slip of 22.9 km. However, we cannot discard the existence of a second major fault under the ridge (Fig. 9.10b). In this case, there will be strain partitioning between both and the total slip will be the sum of the resulting slip of each fault. We obtained a slip of 11.5 km for the frontal fault and 22.9 km of slip for the second fault, or a total slip of 34.4 km.

Since the estimations are dependent on the interpretation fault geometry, we used the excess-area graphical method to have a second independent estimation. The excess-area graphical technique (Epard and Groshong, 1993) uses the excess-area to determine the depth to detachment and the slip along it, and it is independent on the interpreted detachment geometry and depth. The excess area of a fold is the area of material uplifted by deformation (Epard and Groshong, 1993). The excess-area graph is created by plotting the excess areas of different stratigraphic levels (S, Fig. 9.10c, d) versus the depth of these levels to a constant reference horizon (h, Fig. 9.10c, d). The result is a straight line for detachment folds (Fig. 9.10d), in which the slope is the displacement on the detachment and the value of excess area equal to zero is the detachment depth. One of the conditions to use the method is that the horizon relief must be consequence of the slip that we are measuring. For syn-tectonic deposits and sedimentary layers presenting an stratigraphic relief, it is necessary to restore the original geometry in order to perform accurate measures (Gonzalez-Mieres and Suppe, 2006; Dae et al., 2007). We performed several tests with different reference levels and different reflections, in order to estimate a mean slip value for the entire detachment surface. We have used 6 reflections, labelled from 1 to 6, in order to have enough data to confidently fit a line: basement top (1), four pre-tectonic reflections (2-5), and one early sin-tectonic reflection (6) (Fig. 9.10c). We acknowledge that there is an error in our measurements induced by: (i) non-parallel stratification of all sedimentary layers, (ii) unknown geometry prior to the shortening, and (iii) possible erosion of the surfaces. Although we do not restore the original geometry layer, we performed measurements following layers with constant thickness. However, taking into account all those uncertainties, we estimate an error in our calculations between 15% - 20% (yellow area in Figure 9.10d). A compilation of detachment depths obtained with different methods have been published by Bulnes and Poblet (1999). In the case of the excess-area method, the average error between the estimated detachment depth and the real detachment depth is >45 %. Our results depicted a detachment depth of 5.3 ± 1.2 km, and a total slip of 16.2 ± 3.3 km, being the model´s coefficient of determination R^2=0.9692 (Fig. 9.10d). Due to the prominent relief associated with this detachment, we feel more confident about the deepest values obtained for the detachment (~6.5 km). In the case of the excess-area technique, the obtained value corresponds to the total slip of the area, independently of this slip is accommodated by one fault or several faults (Epard and Groshong, 1993).

9.4.5. Partitioning of the deformation

One of the most prominent characteristics of the AR-Francesc Pagès-Tofiño-Xauen structural trend is the variability on the style of deformation and the folding characteristics in such a geographically restricted area (Fig 9.1). We proposed that these differences results from an inherited structure, which was composed of different basement blocks previous to the compressional deformation. The AR-Francesc Pagès-Tofiño-Xauen High is the result of the convergence and collision of three different types of crust: (i) continental crust modified by magmatism that forms the north African margin, (ii) magmatic arc crust found in the northern part of the AR (central Alboran) and on its eastern side, and (iii) thin continental crust of the West

Alboran Basin ("Chapter 5: Crustal domains"). We propose that the thin sediment sequence at the upper part of the ridge in the northeaster sector (profiles TM05, TM04, Fig. 9.6a, b) is inherited from the presence of an igneous basement block previous to the folding process, with reduced sediment deposition, while the sediment fold at the southwestern sector of the AR results from deformation of a sedimentary basin.

The seismic images support that deformation is not uniform along the AR-Francesc Pagès-Tofiño-Xauen trend, which is confirmed by the estimated shortening values (Fig. 9.11, Table 9.1). The estimated shortening is not uniformly distributed along the AR (Table 9.1), showing a general decrease from NE to SW. The eastern part (Fig. 9.6a,b, profiles TM05 and TM04) has accommodated the largest shortening values. The calculated shortening values for the M unconformity ranges from 2.1 km in the NE sector (profile TM05, 5.6% shortening), to 1.4 km in the SW sector (profile TM02, 3.7% shortening) (Table 9.1). This trend is observed for all the horizons. Shortening estimations support that the main compressional pulse is the Mid-Pliocene (Table 9.1), in agreement with previous studies (Martínez García, 2012, Martínez-García et al., 2013).

The Alboran Ridge is separated from Francesc Pagès, Tofiño and Xauen Banks by the Al-Idrissi Fault. Eastern of the Al-Idrissi Fault, at profile TM02, the estimated shortening at the M horizon is 1.4 km (3.7%), while western of the fault, at profile TM17, the shortening is ~0.5 km (~1.6%) (Table 9.1, Fig. 9.11). Although the deformation values decrease from east to west, the difference shortening observed at both sides of the Al-Idrissi Fault is too high to be explained by this trend. This difference is especially noticeable for Quaternary units (units Ia and Ib) that present almost no shortening at TM17 (Tofiño Bank) and ~100 m at TM19 (Xauen Bank) (Table 9.1, Fig. 9.11). This data is coherent with the Quaternary age inferred from the analysis Al-Idrissi Fault activity on seismic images. We conclude that the Al-Idrissi Fault is a barrier for the transfer of the stress deforming the AR further towards the western sector of the Francesc Pagès, Tofiño and Xauen Banks. In agreement, shortening values estimated at Francesc Pagès, Tofiño and Xauen Bank are smaller than for the AR.

Taking into account an average 4.5 ± 1 mm/yr convergence between the Iberian and African plates (McClusky et al., 2003), total convergence since the Earliest Pliocene estimated as the initiation of shortening from deformation of the Messinian top (5.3 Ma) is of 24 ± 5 km. This value is much larger that estimated shortening for any of the structures along the ridge, with a maximum estimated shortening value of ~2.1 km in the eastern AR sector (Table 9.1). Furthermore, extension in the Yusuf Fault, which is connected to the AR on its western part, has been estimated between ~16 and ~30 km ("Chapter 8: The Yusuf Fault"). Maximum calculated shortening values along the AR structure are ~2 km, so this deformation is not enough to accommodate the convergence. However, we have estimated that the deformation associated to shortening corresponds to a considerable larger amount of slip at depth, and we propose that the main part of the convergence is being accommodated in a deep level forming a major decollement (Fig. 9.12, 9.13). We propose a decollement rooted at lower crustal or Moho depths, along which the North African crust overthrusts the magmatic arc crust of the northern AR (Fig. 9.12, 9.13).

Our hypothesis is supported by the estimated total slip along the detachment. The fault-bend-folding approximation (Lavé and Avouac, 2000; Bernard et al., 2007), yields a minimum estimated slip of ~23 km (Fig. 9.10a, b), and the excess area method (Epard and Groshong, 1993) yields a slip value of 16.2 ± 3.3 km and a detachment depth 5.3 ± 1.3 km (Fig. 9.10c, d). Therefore, the AR has accommodated a large amount of the slip due to convergence since the Messinian and along with the Yusuf fault are the most important structures absorbing that deformation.

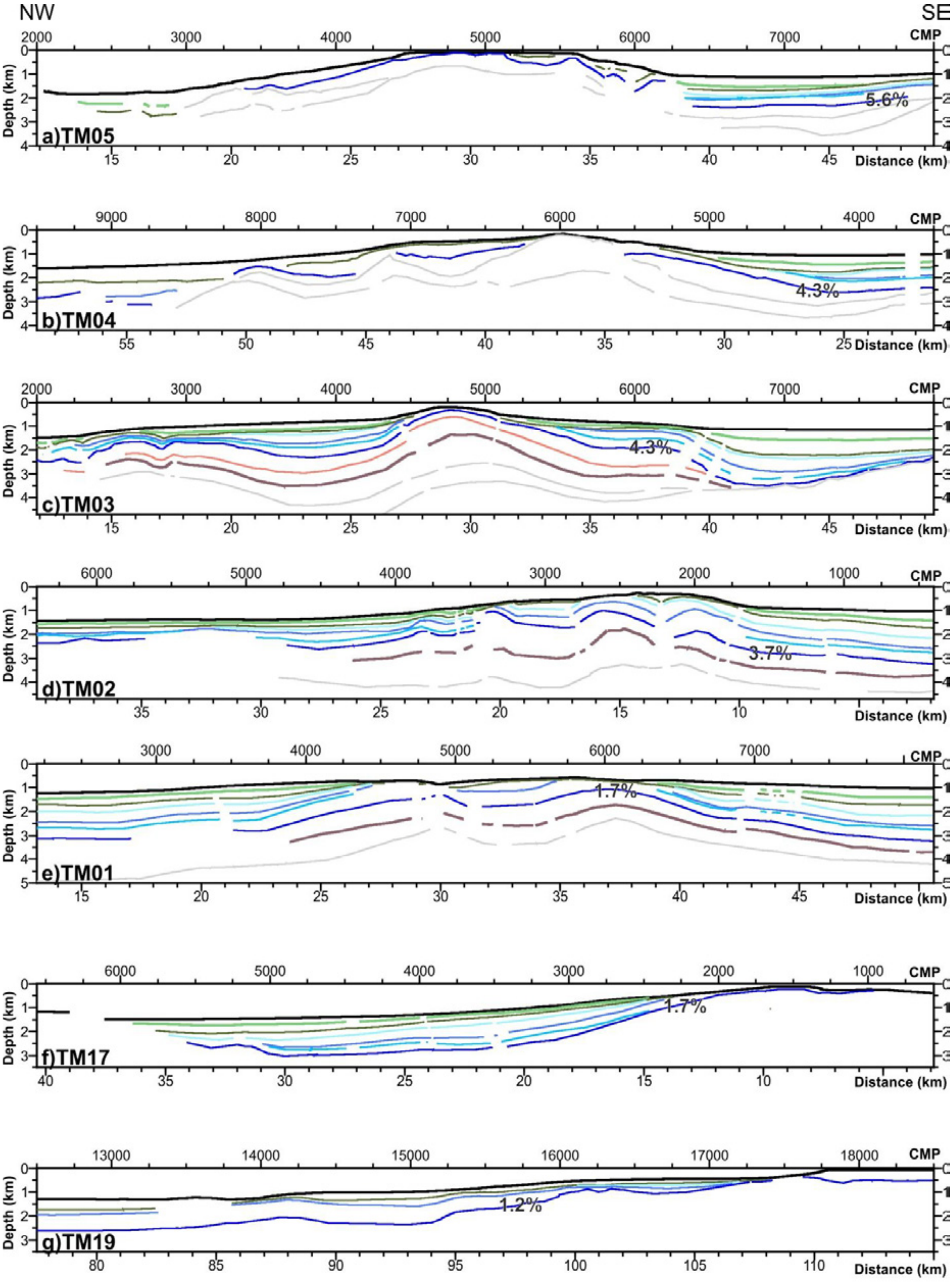
NW
SE
a)TM05
5.6%
b)TM04
4.3%
c)TM03
4.3%
d)TM02
3.7%
e)TM01
1.7%
f)TM17
1.7%
g)TM19
1.2%
CMP
Depth (km)
Distance (km)

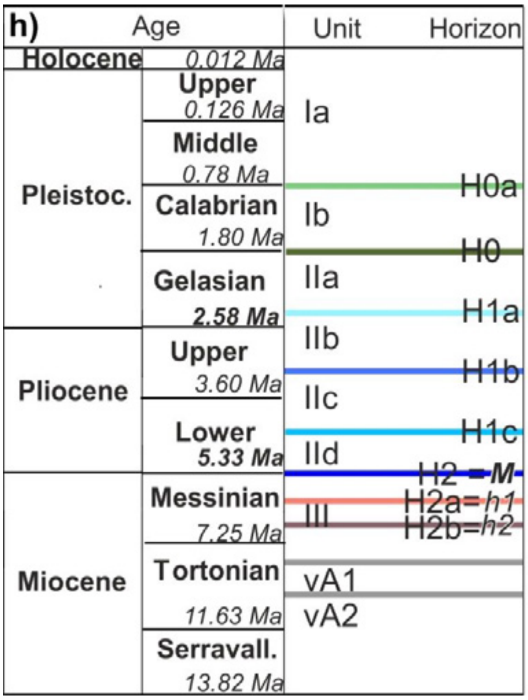

Figure 9.11: *Time-depth converted horizons plot at 1:1 scale.* ***(a)*** *TM05,* ***(b)*** *TM04,* ***(c)*** *TM03,* ***(d)*** *TM02,* ***(e)*** *TM01,* ***(f)*** *TM17 and* ***(g)*** *TM19.* ***(h)*** *Legend. This conversion allows us to perform the shortening calculations. The % of shortening measured for the Messinian unconformity is displayed for each profile. Displayed horizons are plotted with the same colours as the interpreted seismic sections (see Figure 9.4, legend in Figure 9.11h). Grey horizons correspond to the volcanic units. Seafloor is displayed in black.*

		Profile													
		TM05		**TM04**		**TM03**		**TM02**		**TM01**		**TM17**		**TM19**	
		km	***%***	***km***	***%***	***km***	***%***	***km***	***%***	***km***	***%***	***km***	***%***	***km***	***%***
Horizon	**H0a**					0,46	1,22	0,31	0,83	0,06	0,17	*0,04*	*0,12*		
	H0	1,31	3,50	0,65	1,72	0,75	2,00	0,38	1,00	0,13	0,33	*-0,02*	*-0,06*	0,13	0,33
	H1a							0,79	2,11	0,27	0,72	*0,35*	*1,59*		
	H1b					1,13	3,00	0,79	2,11	0,71	1,89	*0,02*	*0,12*	*0,10*	*0,36*
	H1c					1,38	3,66	0,98	2,61	0,77	2,05	*0,02*	*0,12*		
	H2	2,10	**5,60**	1,60	**4,27**	1,63	**4,33**	1,40	**3,72**	0,63	**1,66**	*0,52*	***1,67***	0,46	**1,22**
	H2a					*1,00*	*3,44*								
	H2b					*1,19*	*4,08*	*0,83*	*3,42*	*0,85*	*3,20*				

Table 9.1 **▲***: Shortening values in km and % measured for each horizon in each seismic section (see horizon's legend in Figure 9.11g).*

Figure 9.12 (next pages)*: Crustal scale sections of profile* ***(a)*** *TM05,* ***(b)*** *TM04,* ***(c)*** *TM03 and* ***(d)*** *TM02. Shortening values are displayed, as well as the depth detachment level. AIF: Al-Idrissi Fault, ICR: Intra Crustal Reflections, LC: Lower Crust, SAB: South Alboran Basin.*

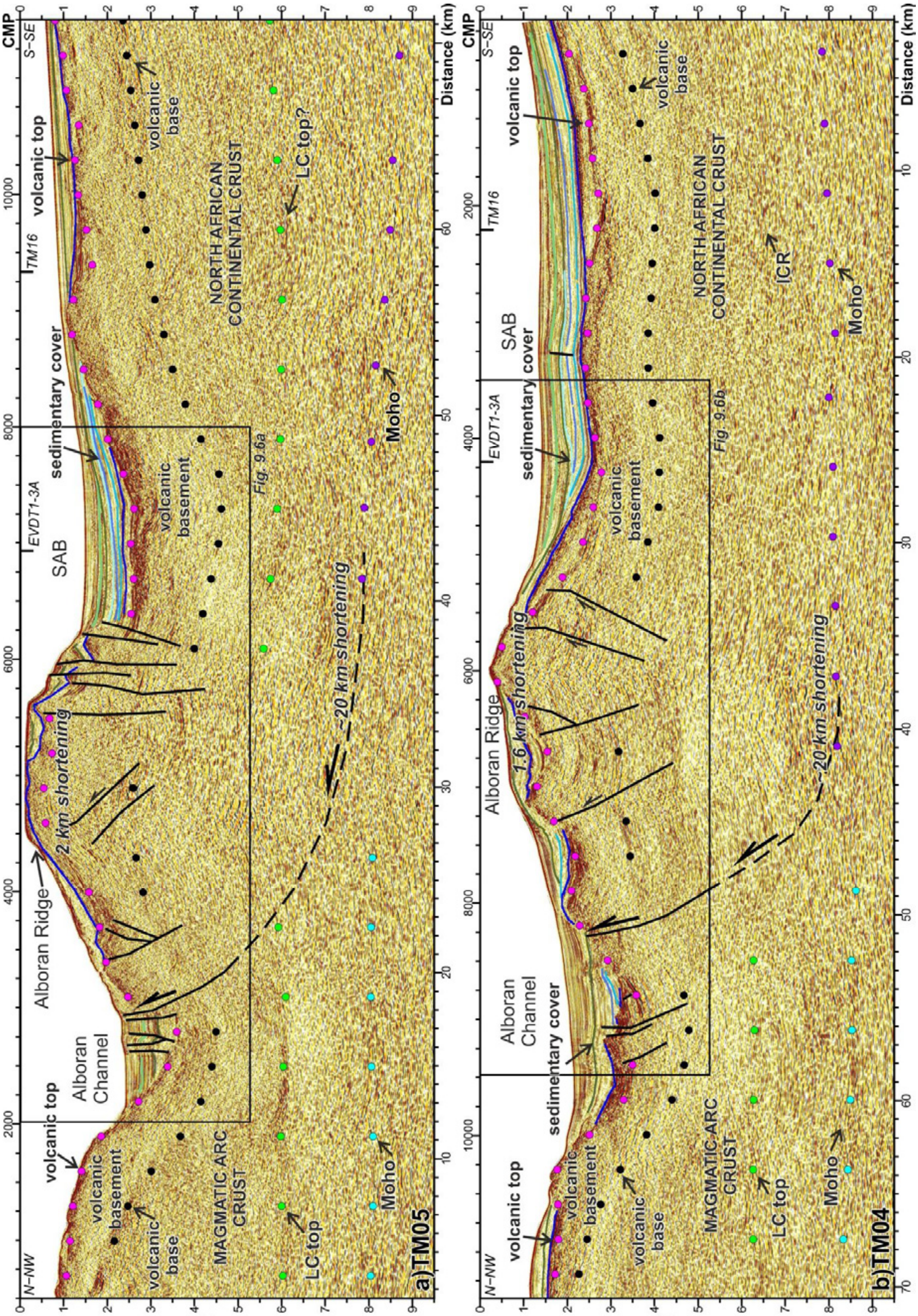
a)TM05
N–NW
S–SE
CMP
TWTT (s)
Distance (km)
I TM16
I EVDT1-3A
volcanic top
volcanic base
volcanic basement
sedimentary cover
SAB
Alboran Ridge
Alboran Channel
MAGMATIC ARC CRUST
NORTH AFRICAN CONTINENTAL CRUST
LC top
LC top?
Moho
2 km shortening
~20 km shortening
Fig. 9.6a
b)TM04
ICR
1.6 km shortening
Fig. 9.6b

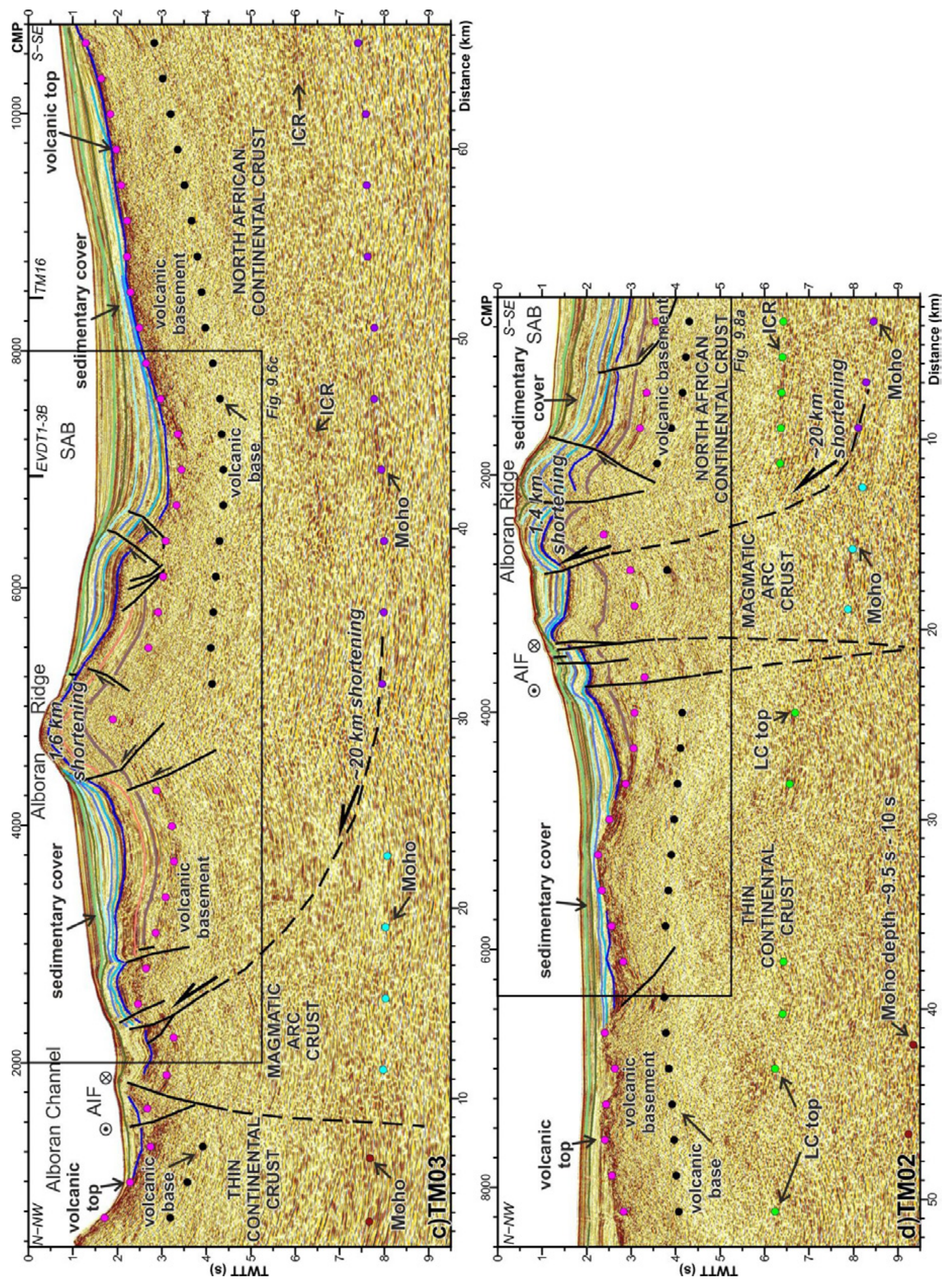
c) TM03
N-NW
S-SE
CMP
TWTT (s)
Distance (km)
Alboran Channel
AIF
volcanic top
volcanic base
THIN CONTINENTAL CRUST
Moho
sedimentary cover
volcanic basement
MAGMATIC ARC CRUST
Alboran Ridge
1.6 km shortening
~20 km shortening
SAB
EVDT1-3B
TM16
Fig. 9.6c
volcanic base
ICR
NORTH AFRICAN CONTINENTAL CRUST
d) TM02
LC top
Moho depth ~9.5 s - 10 s
1.4 km shortening
Fig. 9.8a
cover

This decollement is the main fault in this area, causing the associated uplift of ~2 km and shortening of the shallow layers of ~2 km of the Alboran Ridge, We have also used the empirical relationship of Wesnousky (2008) to obtain the maximum magnitude earthquake in reverse slip continental crust faults (Mw=4.11+1.88logL, being L=fault length in km). The Alboran Ridge front fault has a total length ~100 km, which provides a maximum magnitude Mw=7.9 associated earthquake, which associated to its current activity represents an important seismogenic and tsunamigenic hazard for the region.

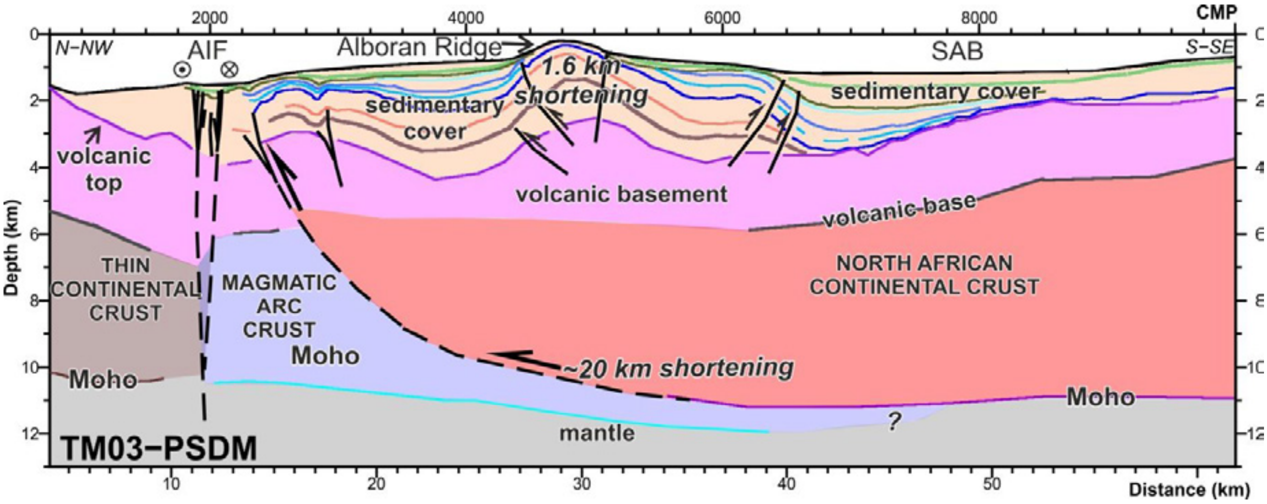

Figure 9.13: *Cartoon of the AR area. This figure shows the inferred relationship between the different types of crust identified and the Alboran Ridge frontal thrust, the main tectonic structure accommodating the shortening. AIF: Al-Idrissi Fault., SAB: South Alboran Basin.*

9.5. In summary

The Alboran Ridge, Francesc Pagès Bank, Tofiño Bank and Xauen Bank are elements of the same structural trend, disrupted by the strike-slip faults of the Al-Idrissi Fault system. Lateral variability in the deformational structure is mainly explained by the complexity of the inherited structure of local sediment basins and igneous highs, and by differences in deformation rates, increasing from SW to NE.

Along the AR, both, geomorphology and deep structure changed from west to east. While in the western side the high shows a gentle convex geometry that becomes stronger to the middle section, related to a sedimentary anticline, in the eastern region the Alboran Ridge presents a flat top with an erosional surface. In this eastern section, the volcanic floor outcrops at the top of the high.

The AR current structure is the result of the Iberian-African plate convergence, and marks the limit between two different types of crust: a continental crust, extended and intruded by magmatism in the south and a magmatic arc crust in the north. These crustal types are the result of subduction process. The basement of the Miocene sedimentary basin is mainly formed by volcanic units (dated as Late Serravallian – Tortonian), except in the westernmost section, where metamorphic basement has been described.

Three contractional pulses are identified: 1) Lower Pliocene (3.28 – 5.33 Ma), 2) Middle Pliocene (2.45 – 3.28 Ma) and 3) Quaternary (from 1.8 Ma till present). Folding and faulting involve the basement and the recent most sediments, so we propose that it is still an active structure.

Estimated shortening values measured on strata in different locations along the AR, Francesc Pagès, Tofiño and Xauen highs are too low to accommodate the Iberian and African tectonic plate convergence since the Messinian times, when the first shortening pulse is identified. However, total uplift calls for the existence of large-scale deep faulting. We propose a deep decollement level accommodating this convergence that will allow the displacement of the North African crust over the magmatic arc crust of the Alboran Basin. This hypothesis is supported by the relationship between tectonic uplift and slip on a deep decollement that supports a total slip ~ 20 km in a 5-7 km deep decollement.

Differences in the deformation between the Alboran Ridge and Francesc Pagès, Tofiño and Xauen Banks result from strain partitioning related to left-lateral strike-slip faulting. The most important of these strike slip faults is the Al-Idrissi fault system, which from the Quaternary constrains most of the changes in deformation between Francesc Pagès Bank and the Alboran Ridge.

Part IV

DISCUSSION

"To be, or not to be,
that is the question"

William Shakespeare
(Hamlet, act III, scene I)

Chapter 10

Implications for geodynamic models

As outlined on the Geological setting chapter (Chapter 2, this volume), different geodynamics models have been proposed to explain the origin of the Alboran Basin. These geodynamics models can be summarized on the basis of three main processes:

i. Convective removal: This model proposes a lithospheric thickening caused by the Iberian – African plate convergence. This thickening results in the formation of a gravitationally unstable root. Due to its instability, this root is removed by convective currents and replaced by asthenospheric material, which leads extensional processes in the basin (Dewey, 1988; Platt and Vissers, 1989) (Fig. 10.1a).

ii. Mantle delamination: This model suggests an initial lithospheric thickening similar to the convective removal, although it proposes a different removal mechanism. The gravitational instability of the complex led to the detachment of the root (García-Dueñas et al., 1992; Seber et al., 1996; Calvert et al., 2000; Platt et al., 2006) (Fig. 10.1b).

iii. Subduction models: These models can be divided in two groups: slab roll-back (Fig. 10.1c) and slab break-off (Fig. 10.1d). All these models propose that extension in a back-arc setting is related to variations in the geometry of the subduction system including the slab, and/or changes in the velocity of convergence. Slab roll-back hypothesis (Royden, 1993; Lonergan and White, 1997) suggests a westward rotation of the subducting slab as driving mechanism of the extension (Fig. 10.1c). On the other hand, slab break-off proposes that the detachment of the slab leads to upper-plate extensional processes, as the cold slab is replaced by hot asthenospheric material (Blanco and Spakman, 1993) (Fig. 10.1d). There are also models that call for both processes, slab roll-back and slab break-off (e.g. Zeck, 1999).

Due to the ambiguity intrinsic to the interpretation of land geological data and poor resolution of the first mantle tomographic models, it was unclear which model was the most suitable. The progress on both, geological and geophysical observations, shed light into the geodynamic evolution of the Alboran Basin. The convective removal and mantle delamination models are based on the removal of an orogenic root as triggering mechanism of the extension. Growing evidence with geological and geophysical data supports an E-W direction of the extension (e.g., García-Dueñas et al., 1992; Mauffret et al., 2004; Leprêtre et al., 2013; Bouyahiaoui et al., 2015) and of the deformation (i.e. unit displacement with respect to the foreland (Platt et al., 2013; Gonzalez-Castillo et al., 2015) and at a crustal scale (Garate et al., 2015), and not a radial extension as some models predict (Dewey, 1988; Seber et al., 1996; Platt and Vissers, 1989; Calvert et al., 2000). Moreover, geochemical data from magmatic rocks on and offshore cannot be explained only by continental delamination. The geochemistry of the most volcanic rocks can be better explained as a consequence of subduction-related melts (Duggen et al., 2004; Duggen et al., 2005; Duggen et al., 2008). The integration of Travel Time Tomography (TTT) models of the mantle caused a qualitative leap in the understanding of the Western Mediterranean geodynamics. These results support a model combining both, slab roll-back and lithospheric tearing, as the drivers of extensional mechanisms (Fig. 10.2) (Wortel and

Spakman, 2000; Spakman and Wortel, 2004; Bezada et al., 2013; Faccenna et al., 2014; Van Hinsbergen et al., 2014a; Chertova et al., 2014b). All these models propose the subduction of the Tethys oceanic lithosphere and some segments of continental lithosphere, however, the amount and nature of lithosphere subducted is still under debate (e.g., Duggen et al., 2008; Platt et al., 2013; Faccenna et al., 2014; Levander et al., 2014).

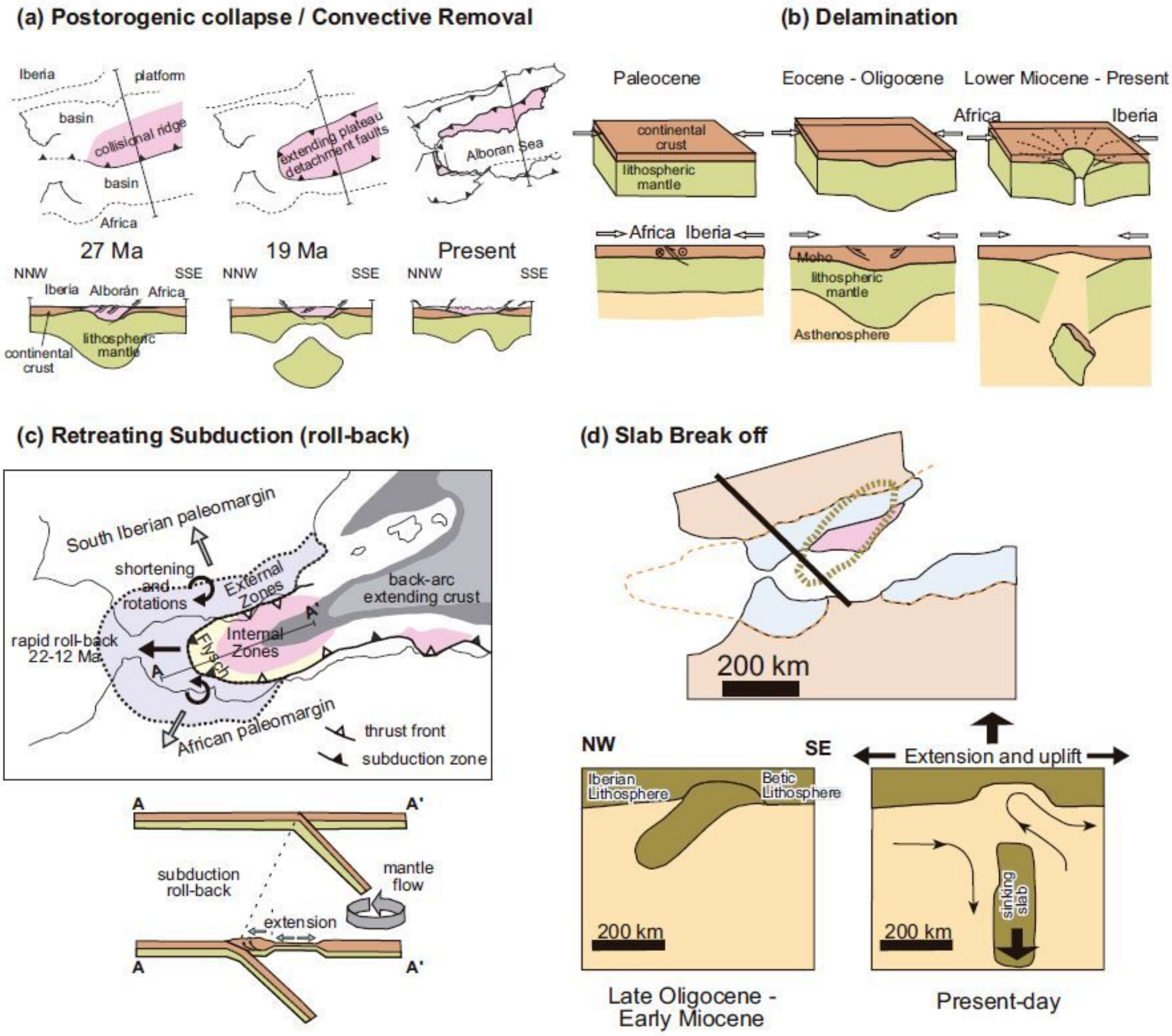

Figure 10.1* ▲:** *Conceptual models of the different geodynamic models proposed to explain the extension in the Alboran Basin.* ***(a) *Convective removal: the root is removed due to its gravity instability.* ***(b)*** *Delamination: the root is detached from the lower part of the crust.* ***(c)*** *Slab roll-back: the subduction zone retreats.* ***(d)*** *Slab break-off: the slab is detached (From Martínez-García, 2012).*

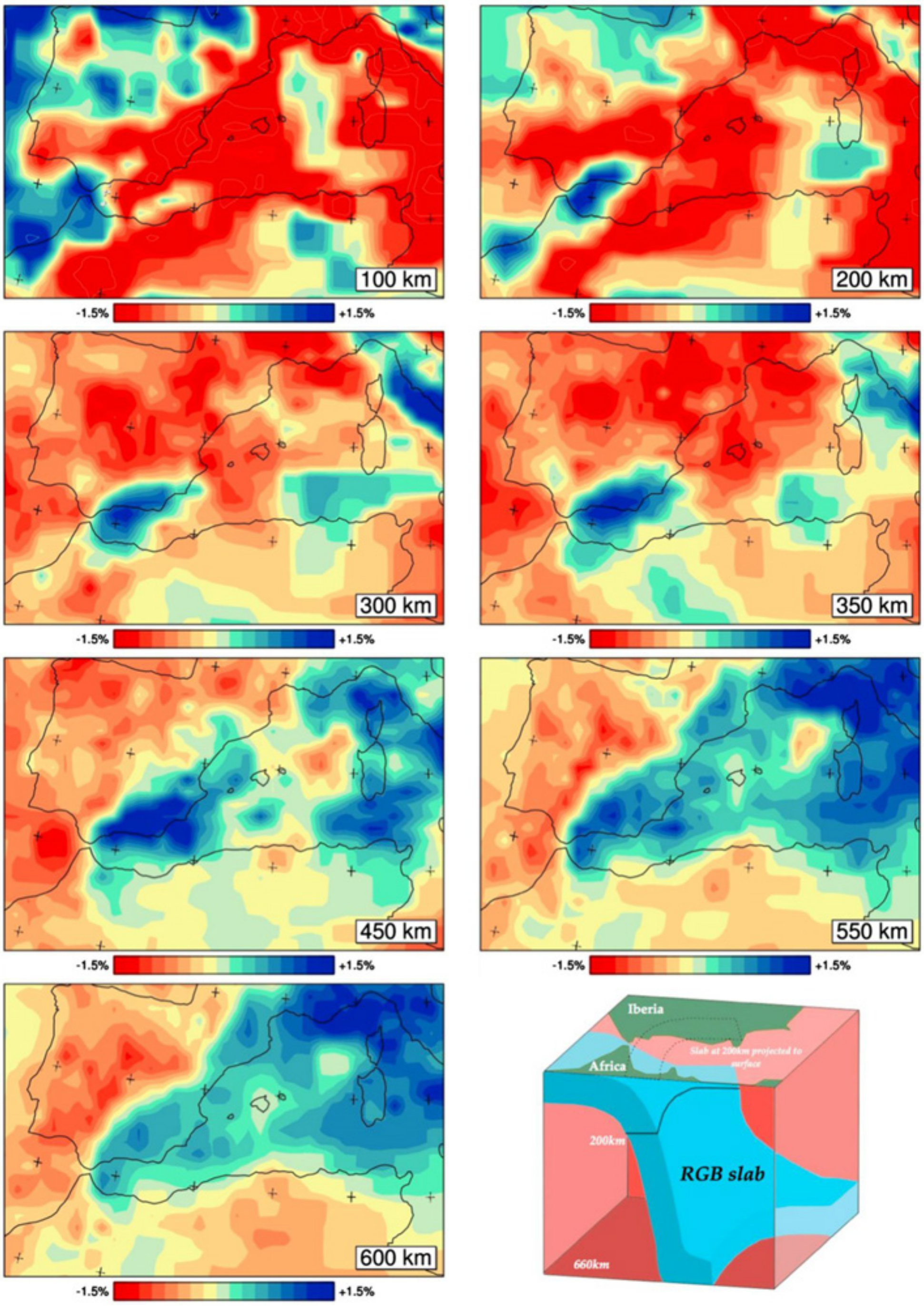

***Figure 10.2* ▲:** *Mantle structure of the western Mediterranean region. Colours are indicative of the P-wave seismic velocity anomalies. The blue anomaly in south Spain and north Morocco corresponds to the Rif-Gibraltar-Betic (RGB) slab. We can observe how this anomaly is present through all figures from 100 km until 600 km below the Straits of Gibraltar, while it appears 200-300 km below the Eastern Betics where is interpreted as the slab is detached under this area. A cartoon with the interpretation of the RGB slab is presented at the lowest right (Chertova et al., 2014b).*

More recently Full Waveform Tomography has confirmed and refined the images of slabs in the mantle (Fichtner and Villaseñor, 2015). These higher resolution tomographic models images a discontinuous slab, detached under the Betics, and two possible deeper slabs below north Algeria. The Alboran slab runs from south of the Straits of Gibraltar till the eastern Betics, being detached under the western Betics (near Malaga), where it is found at ~200 km depth (Fig. 10.3). Below north Morocco, there is no positive velocity anomaly indicating a slab. Below north Algeria, two velocity anomalies are found at ~200-600 km depth, which indicate the presence of two slab segments. This methodology improves the model resolution and has taken advantage of large and focused projects such as TOPO-IBERIA that provided a regularly spaced seismological grid across the Iberian Peninsula and North Morocco, PICASSO and RIFSIS that increased the coverage in North Africa, and NEAREST in the Gulf of Cadiz region (Geissler et al., 2010;; Monna et al., 2013; Sallarès et al., 2013; Bonnin et al., 2014; Gil et al., 2014; Díaz et al., 2015; Mancilla and Diaz, 2015; Monna et al., 2015; Quintana et al., 2015; Villaseñor et al., 2015; Díaz et al., 2016a).

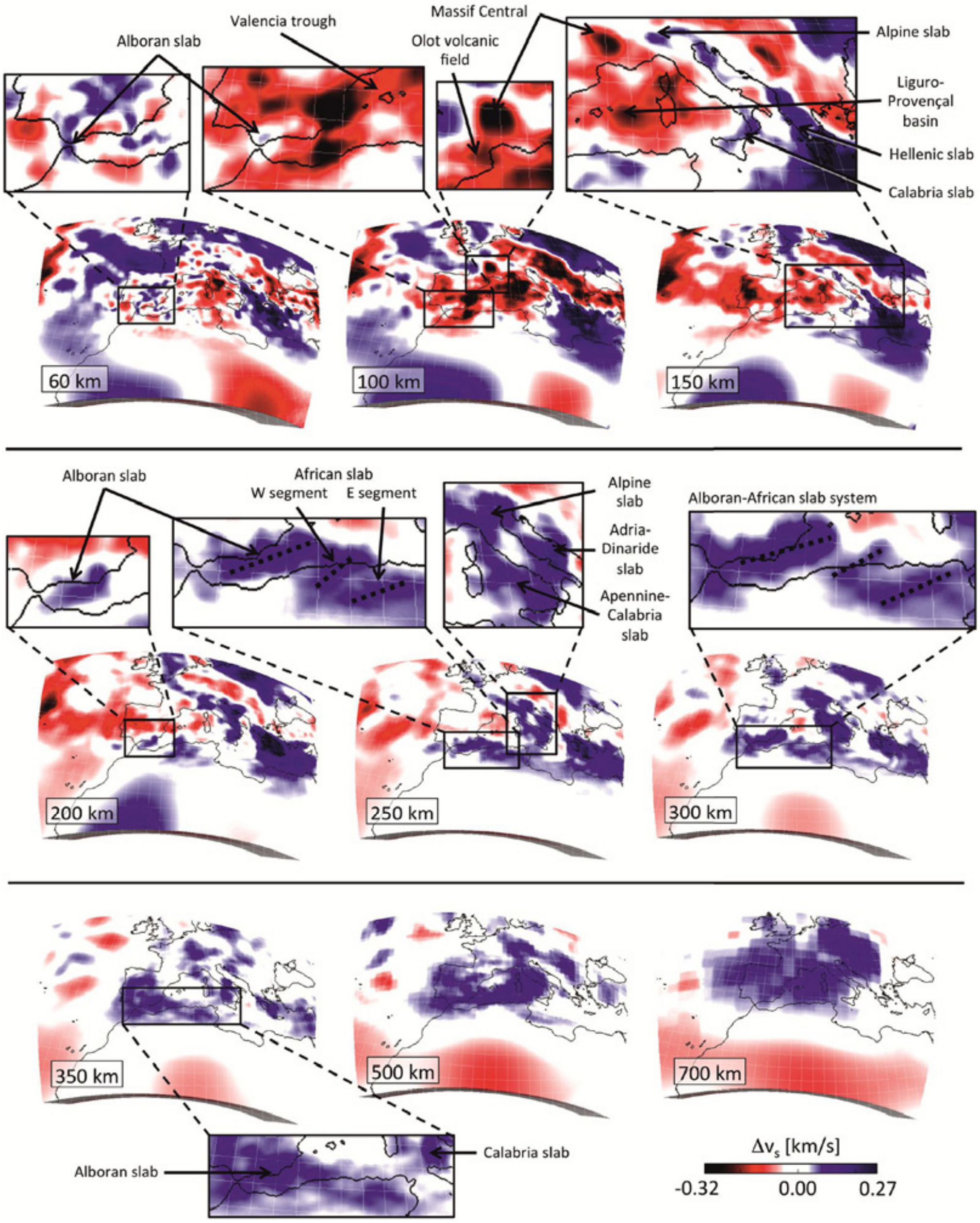

Figure 10.3: *Full-waveform tomographic model of the western Mediterranean (Fichtner and Villaseñor, 2015). Resolution of the model allows the imaging of the slab from 60 km depth till around 500 km depth. Detail of the upper images shows how the Alboran slab remains under the Straits of Gibraltar, but it is detached under the Betics on its shallowest part (till ~200 km). Looking at the deeper sections, up to three slabs can be identified along the North African margin (between 250 km – 300 km, and marked with dashed lines) (from Fichtner and Villaseñor, 2015).*

Based on the tomographic results and our results of the Alboran Basin, we will review and discuss existing subduction models. In a first step, it appears now that models that invoke convective removal or mantle delamination as unique triggering mechanisms of the extension can be discarded. Despite the considerable advances in the understanding of the mantle structure, the driving mechanisms are debated, and there is not consensus on the evolution of the subduction zone. Differences between the models often rely on the geometry of the subduction front, the initiation of the subduction, and the timing of subduction-related events.

In this chapter, we review the geodynamic models proposed for the Alboran Basin, comparing them with the most recent tomographic observations and the new results obtained in this thesis. The main objectives of this chapter are: (i) To describe geodynamic models proposed to explain the formation and evolution of the Alboran Basin, (ii) To contrast these models with our results, (iii) To discuss which models can successfully explain the data, and, (iv) based in our results and in this discussion, to propose some refinement of the geodynamic evolutionary history of the Alboran Basin.

10.1. Observations to be fit

Although some of the models have been applied to the entire western Mediterranean, we focus the review on their ability to explain the different observations performed in the Alboran Basin. A good geodynamic model should explain the deep structure of the basin, together with the characteristics of the sedimentary infill, and the evolutionary history of the basin from the opening till the most recent deformation. We propose the following topics, including published results and new results obtained from this thesis, as the main aspects to consider for a successful geodynamic model:

- *Slab dimensions and geometry*

Travel Time Tomography (TTT) models of the western Mediterranean lithosphere have improved their resolution and accuracy particularly in the last ~5 years. The development of the TOPOIBERIA, PICASSO and RISFIS projects promoted a step forward in the understanding of the Gibraltar Arc deep structure (eg., Monna et al., 2013; Bonnin et al., 2014; Gil et al., 2014; Bonatto et al., 2015; Díaz et al., 2015; Mancilla and Diaz, 2015; Monna et al., 2015; Quintana et al., 2015; Villaseñor et al., 2015; Díaz et al., 2016a). The IberArray stations from the TOPOIBERIA project provided a regular grid of stations that completed the irregular coverage of permanent stations along the entire Iberian Peninsula, and especially in north of Africa, where seismological data are scarcer (e.g., Villaseñor et al., 2015; Díaz et al., 2016a). The North African margin information was completed with the RIFSIS stations deployment (e.g., Ayarza et al., 2014; Gil et al., 2014; Villaseñor et al., 2015). In addition, during the PICASSO project transects along South Iberia and North Morocco were acquired (Ayarza et al., 2010; Alpert et al., 2013; Díaz et al., 2015; Díaz et al., 2016a; Díaz et al., 2016b). The inclusion of the data acquired during these projects provided a better resolution for the TTT models of the Gibraltar Arc area. These data shows a slab below the Betics - Straits of Gibraltar - Rif zone (Fig 10.4), detached in the shallower part towards the eastern Betics. High velocity anomalies related to the presence of a slab are found in western Morocco and under the Straights of Gibraltar (Fig. 10.4). The deep part of this slab, below 410 km depth, is planar, whereas on its shallower part presents a steep arcuate shape (Monna et al., 2013; Monna et al., 2015) (Fig. 10.4). This shape variation has been related to a change in the subduction dynamics with time. While the deep, planar shape will reflect the slab roll-back dominance, the curvature of the upper part will be the result of the African – Iberian tectonic plate convergence as the dominant mechanism (Monna et al., 2013).

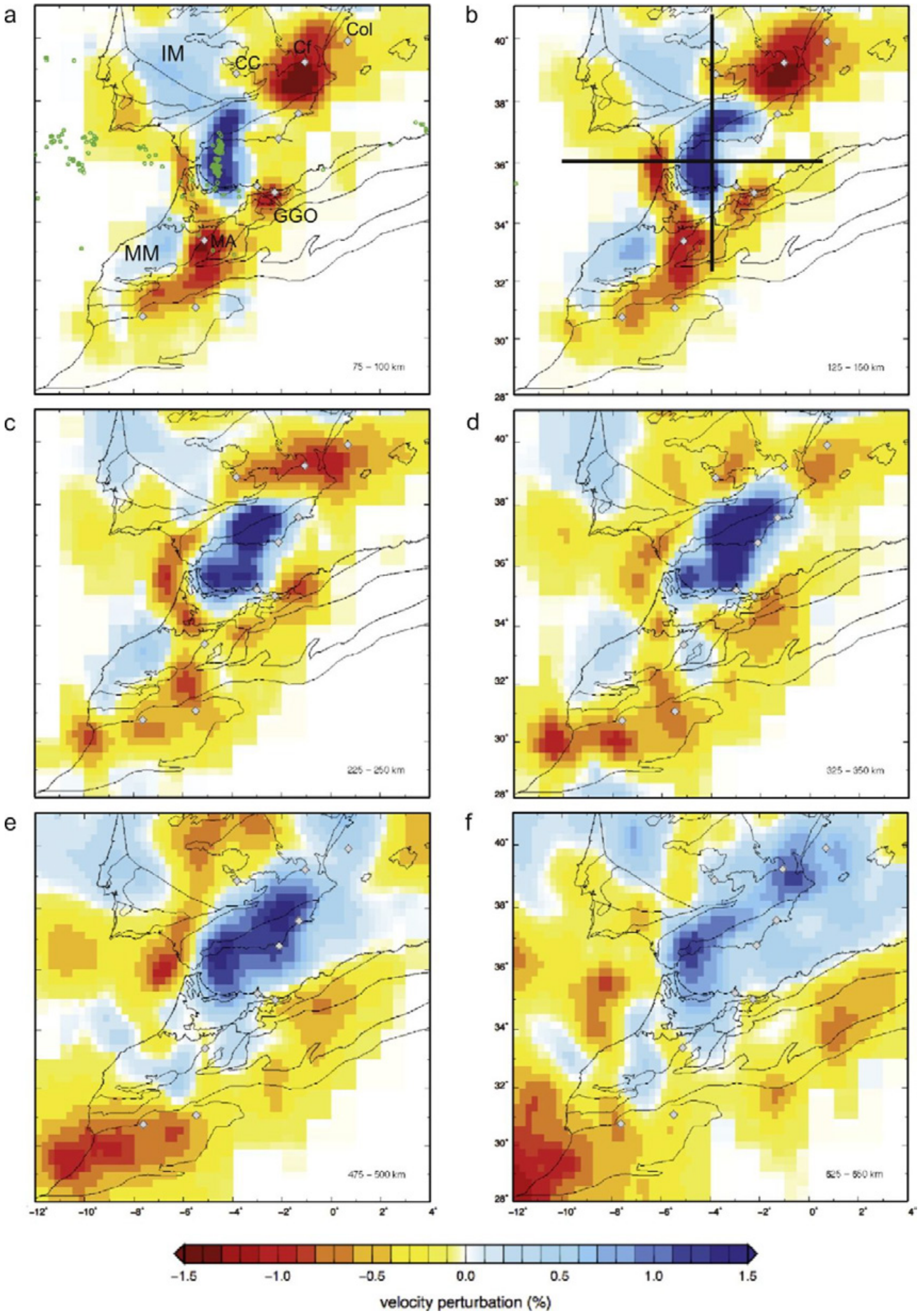

***Figure 10.4* ▲:** *Horizontal slices of P-waves velocity for the Gibraltar Arc system area (from Villaseñor et al., 2015). The arcuate shape of the slab, following the orogenic front, and the slab detachment in the Eastern Betics is observed.*

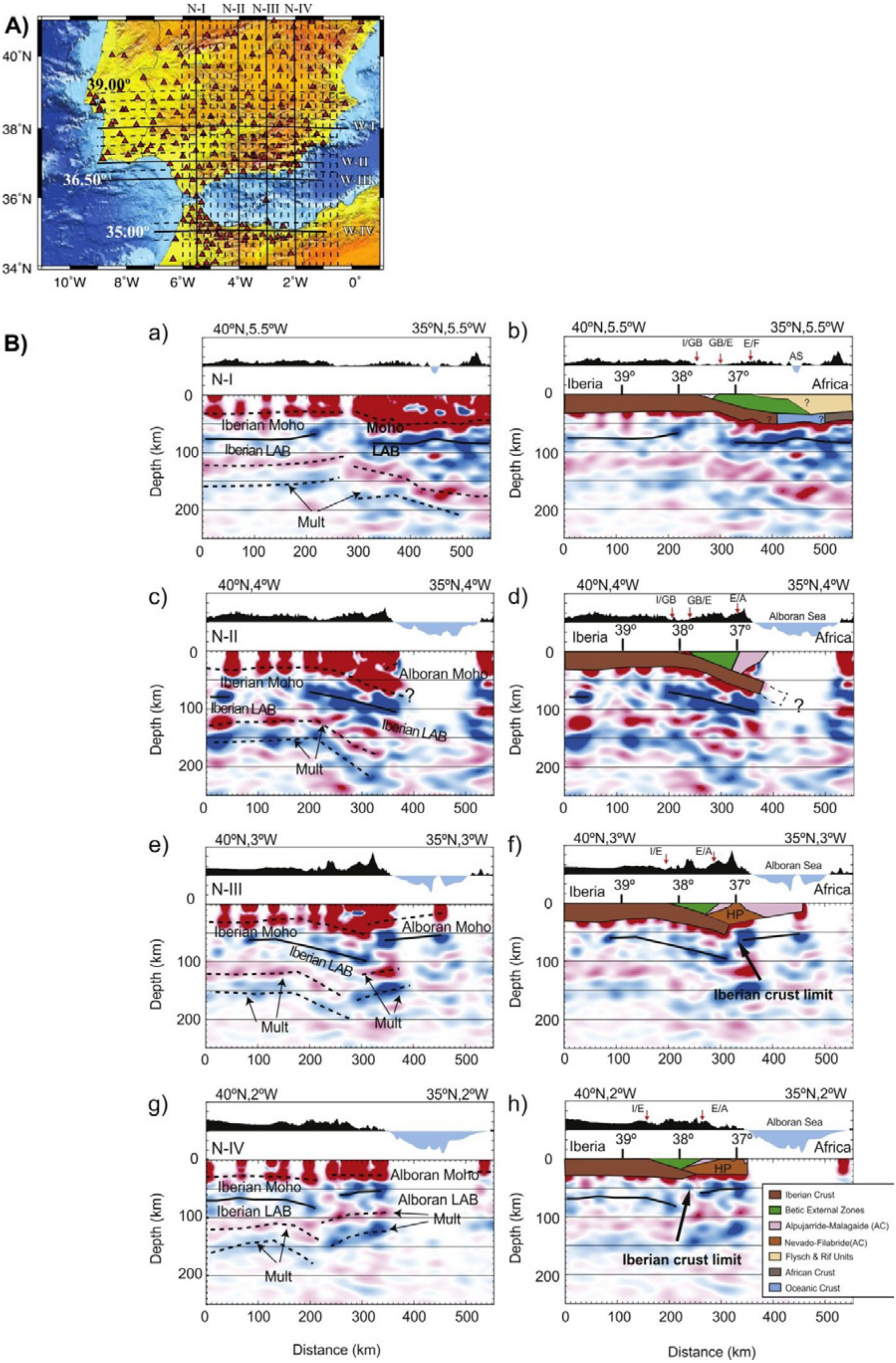
A)
N-I
N-II
N-III
N-IV
40°N
38°N
36°N
34°N
10°W
8°W
6°W
4°W
2°W
0°
39.00°
36.50°
35.00°
W-I
W-II
W-III
W-IV
B)
a)
40ºN,5.5ºW
35ºN,5.5ºW
N-I
Iberian Moho
Iberian LAB
Moho
LAB
Mult
b)
I/GB
GB/E
E/F
AS
Iberia
39º
38º
37º
Africa
c)
40ºN,4ºW
35ºN,4ºW
N-II
Iberian Moho
Iberian LAB
Alboran Moho
Iberian LAB
Mult
d)
I/GB
GB/E
E/A
Alboran Sea
e)
40ºN,3ºW
35ºN,3ºW
N-III
Iberian Moho
Iberian LAB
Alboran Moho
Mult
f)
I/E
E/A
HP
Iberian crust limit
g)
40ºN,2ºW
35ºN,2ºW
N-IV
Alboran Moho
Iberian Moho
Alboran LAB
Iberian LAB
Mult
h)
Iberian crust limit
Iberian Crust
Betic External Zones
Alpujarride-Malagaide (AC)
Nevado-Filabride(AC)
Flysch & Rif Units
African Crust
Oceanic Crust
Depth (km)
Distance (km)
0
100
200
300
400
500

C)

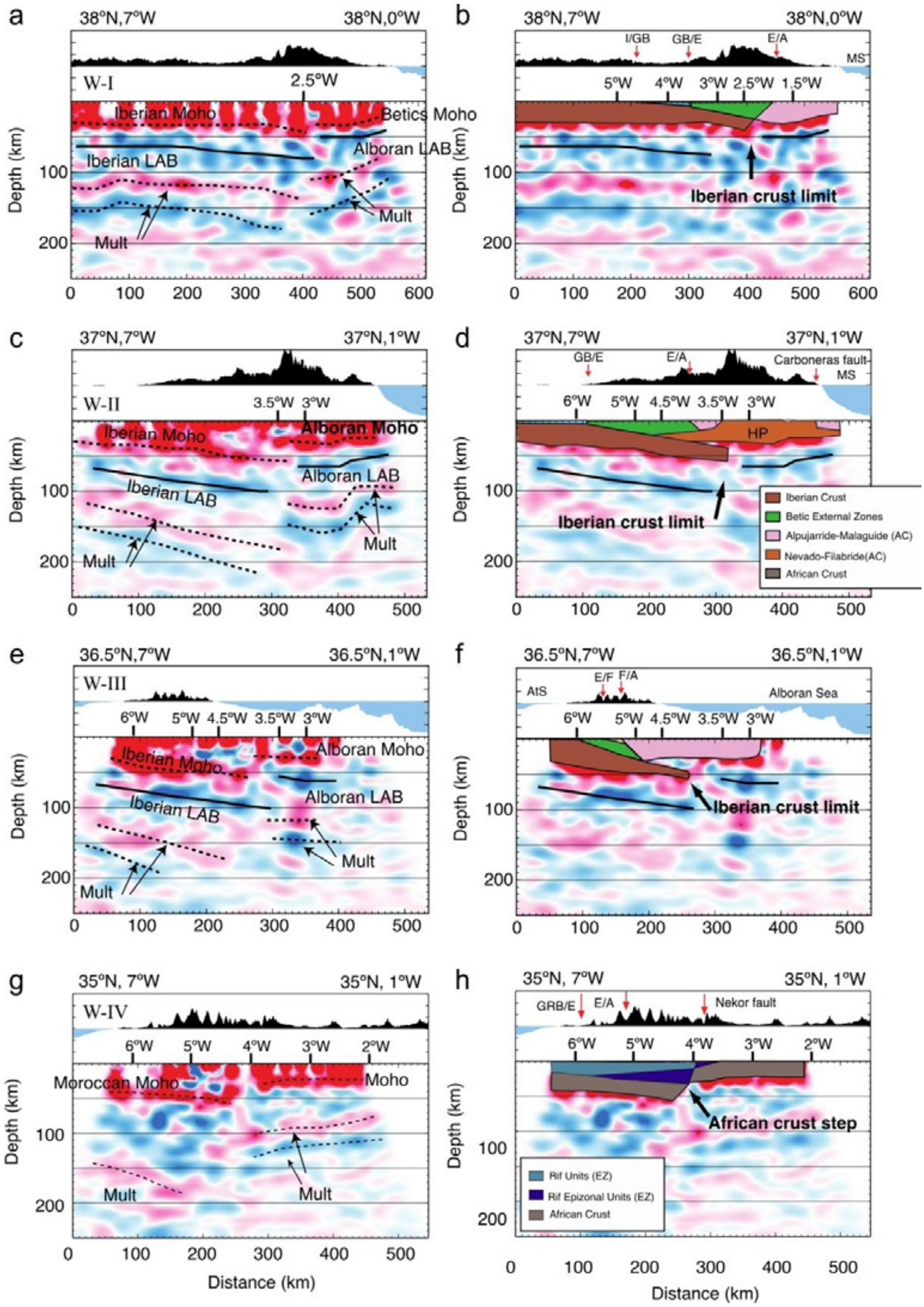

◄▲ ***Figure 10.5:*** *Lithospheric structure of the Gibraltar Arc system area obtained by receiver function analysis (Mancilla et al., 2015).* ***(A)*** *Location of the cross sections.* ***(B)*** *N-S oriented cross sections.* ***(C)*** *W-E oriented cross-sections. HP: High pressure, LAB: Lithosphere - Asthenosphere boundary. The Iberian lithosphere subducting below the Alboran Basin is observed (B, C).*

Additionally, Mancilla et al. (2015) constrained the deep geometry of the slab under the Betics and Rif areas with receiver functions data (Fig. 10.5). The images have been interpreted to show how the Iberian lithosphere dives below the African plate, and how the Alboran Domain (Alpujarride and Malaguide units) is thrusting above them (Fig. 10.5). The images of the Iberian lithosphere underneath Africa have important implications for the geodynamical formation models, as we will discuss later.

- *Magmatic activity*

Geochemical analysis of dredged rocks and drill hole core samples of the volcanic rocks of the Alboran Basin (Carminati et al., 1998; Hoernle et al., 1999; Maury et al., 2000; Duggen et al., 2004; Duggen et al., 2005; Duggen et al., 2008; Lustrino et al., 2011; Carminati et al., 2012), provide clues that help to constrain the geodynamic evolution of the basin. These rocks can be divided into two groups: a first group, with a tholeiitic and calk-alkaline affinity, sampled in the central part and near the margins of the Alboran Basin (High-Si in Figure 10.6a), and a second group exhibiting an alkaline affinity and located mainly onland (Low-Si in Figure 10.6a). The Si-enriched rocks is related to subduction-related fluids and partial melting of the subcontinental lithosphere, while the Si-depleted volcanism is related to the upwelling of the asthenospheric mantle that replaced the delaminated lithosphere (Fig. 10.6b) (Duggen et al., 2004; Duggen et al., 2005; Duggen et al., 2008).

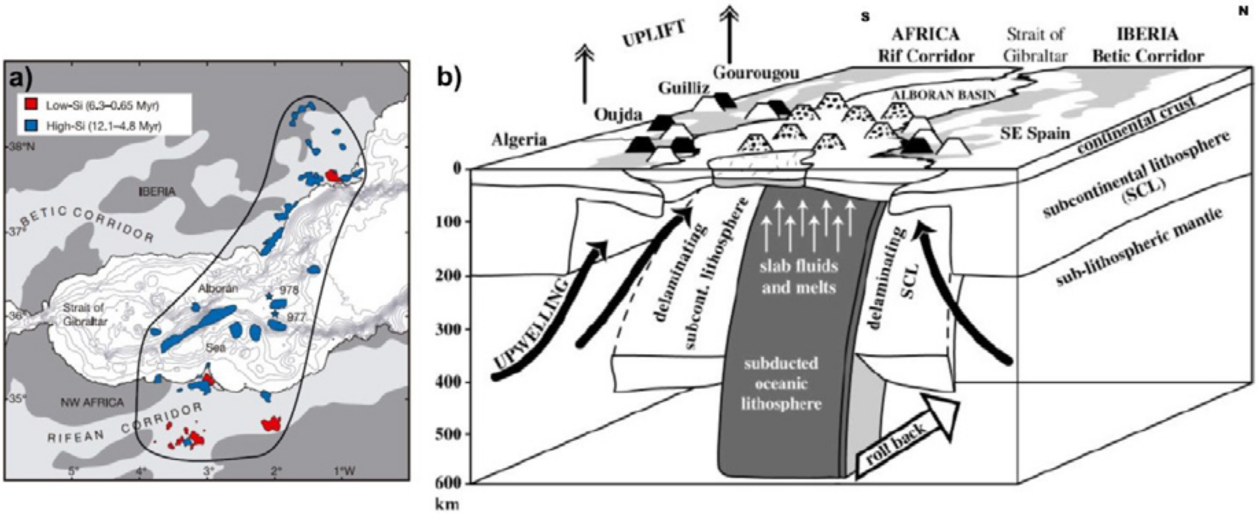

Figure 10.6: (a) *Volcanic affinities distribution along the Alboran Basin. In red are depicted the low-Si samples, and in blue the high-Si ones (from Duggen et al., 2003).* ***(b)*** *Three dimensional geodynamic model of the Alboran Basin. The model explains the origin of the tholeiitic and calk-alkaline volcanism in relation with the subduction melts, and the intraplate volcanism in the basin margin as a consequence of upwelling of asthenospheric fluids due to continental delamination (from Duggen et al., 2005).*

- *Crustal domains*

As described along "Chapter 5: Crustal domains", there are different crustal types flooring the Alboran Basin. There is thin continental crust possibly of the Alboran Domain under the WAB and MB basins, and the PB and HBB basins, at the southern part, developed above continental crust of North Africa. Magmatic arc crust is found under the EAB (Fig. 10.7a) (see "Chapter 5: Crustal domains"). While the magmatic arc crust is the result of the extension in the basin, the two continental crusts existed prior to this process. Any plausible geodynamic model should explain how these different crustal domains coexist in the basin and the particular evolution of each.

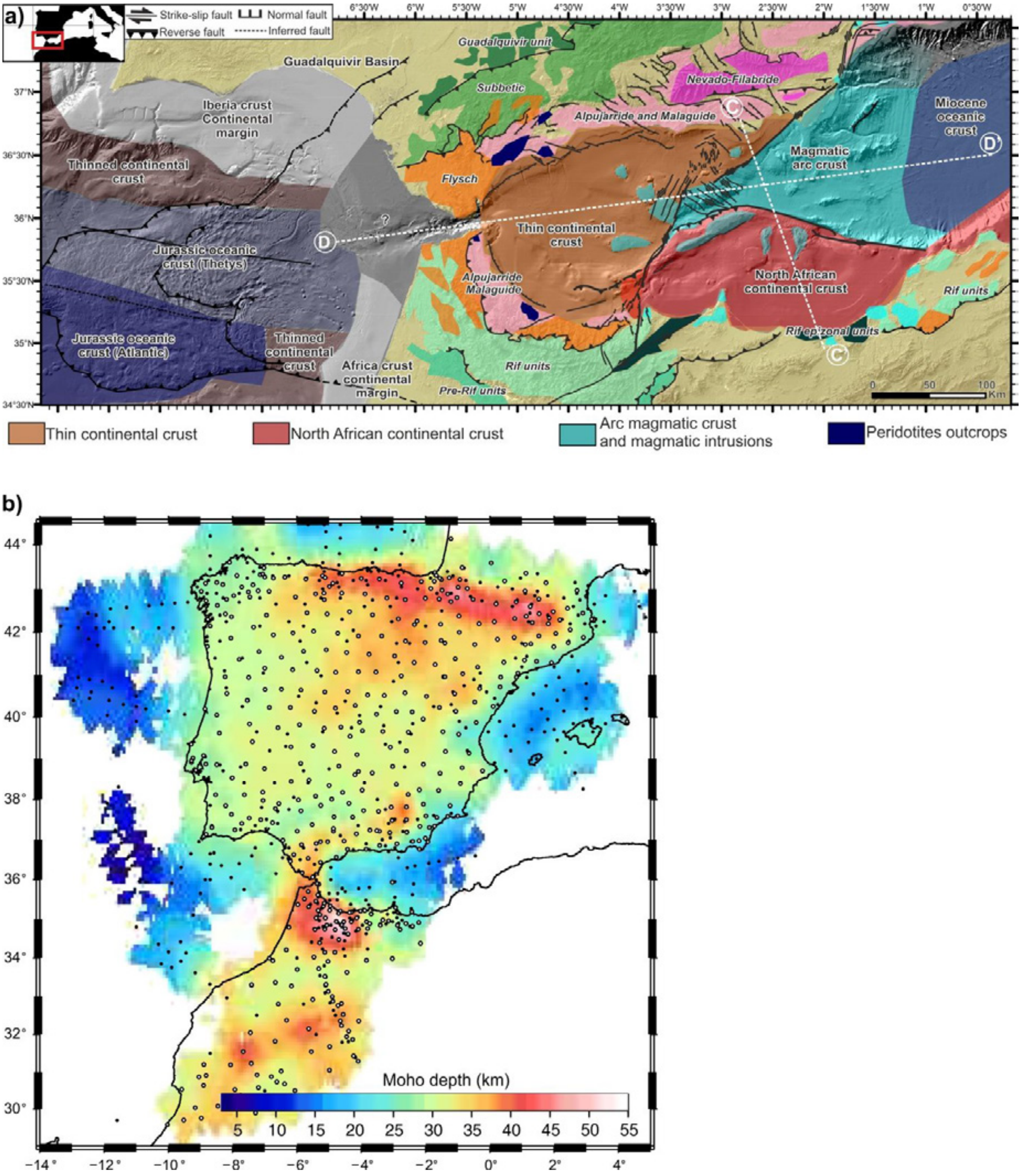

Figure 10.7: ***(a)*** *Different crustal domains identified in the Alboran Basin (Chapter 6: Crustal domains, this volume). The dashed white lines depicted the position of the present-day lithospheric cross-section shown in Figures 10.19c and d.* ***(b)*** *Moho depth map, obtained from deep seismic sounding and receiver functions data (from Díaz et al., 2016a).*

Although the Moho depth map obtained from earthquake data with onshore recordings is not enough to image in detail the Moho variations of the Alboran Basin, it provides a good estimation of the Moho depth in the surrounding emerged areas (Mancilla and Diaz, 2015; Díaz et al., 2016a). The Moho depth is highly heterogeneous in the Gibraltar Arc system, ranging from ~10 km on the eastern side (Algero-Balearic

Basin) to ~55 km below NW Morocco, at the Rif belt (Fig. 10.7b) (Díaz et al., 2016a). This is one of the most remarkable features related to the Moho depth in the North Africa margin. While the Moho depth below the Rif belt (NW Morocco) is located between 40-55 km depth, in NE Morocco and NW Algeria it occurs between 25-35 km (Fig. 10.7b) (Mancilla and Diaz, 2015; Díaz et al., 2016a). The boundary between these two areas is defined by the Al-Idrissi fault system and the onshore continuation. This difference in crustal thickness is related to the Rif orogenic belt formation, caused by the collision of the Alboran domain with the NW Morocco margin. A similar collision event is not recorded in the NE Moroccan margin or NW Algeria (Fig. 10.7b), where the Moho is shallower and crustal thickening is not observed. This observation must be explained by valid geodynamic models.

- *Basin evolution*

The offshore dataset data also have been completed since the 90s, improving the Alboran basin characterization. The main results presented in this thesis came from the TOPOMED-GASSIS (October 2011) and the EVENT-DEEP (May 2010) cruises. The TOPOMED dataset were especially acquired with the aim to link the shallow sedimentary structure with lithospheric observations.

On the basis of the seismostratigraphic analyses performed, there are different aspects to take into account in order to explain the sedimentary infill of the Alboran Basin (Fig. 10.8):

- The two oldest depocenters, the West Alboran and Malaga basins (WAB & MB) and the Pytheas and Habibas basins (HBB & PB), developed above different crustal domains and evolved differently. While it has been interpreted that the WAB & MB migrated westward at least 300 km, the HBB & PB evolved possibly almost in the same position above the African continental margin until the Plio-Quaternary, when the area may have been displaced ~20 km to the NW by the Yusuf Fault System.

- The arcuate shape of the WAB & MB depocenter should be explained from its origin, as the oldest sediment distribution presented this shape, and there are not evidences of more recent deformation.

- The migration of the WAB & MB is inferred to relate to the westward slab roll-back. However, since the Messinian times, when magmatism in the arc and extensional processes in the back-arc where practically finished, the WAB & MB may have been at its current position.

Figure 10.8* ►*: Basin evolution model ("Chapter 6: Basin Evolution", this volume). The cross sections presented in Figure 10.19 are depicted (red white lines).

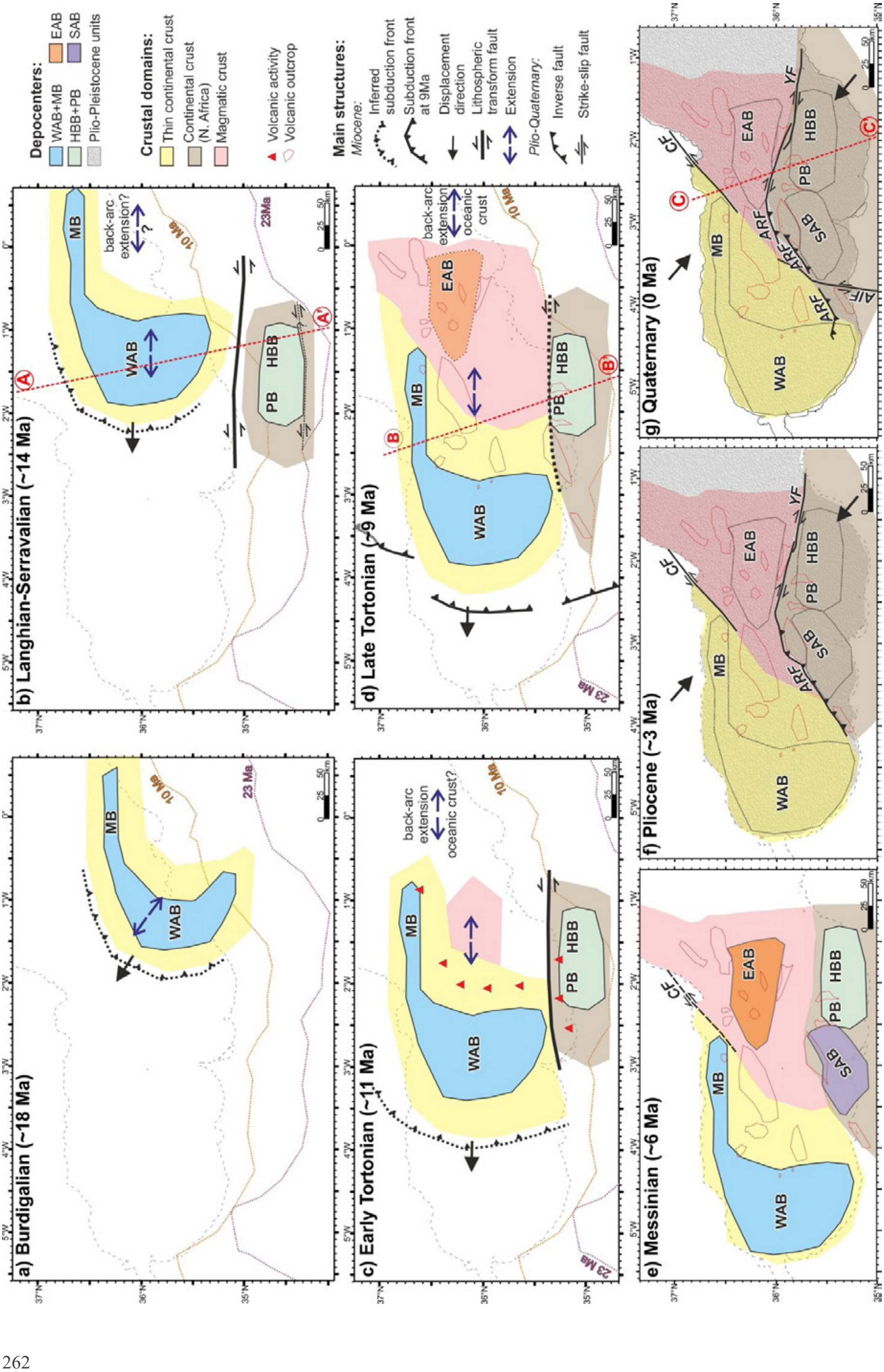
a) Burdigalian (~18 Ma)
b) Langhian-Serravalian (~14 Ma)
c) Early Tortonian (~11 Ma)
d) Late Tortonian (~9 Ma)
e) Messinian (~6 Ma)
f) Pliocene (~3 Ma)
g) Quaternary (0 Ma)
WAB
MB
EAB
SAB
PB
HBB
10 Ma
23 Ma
back-arc extension?
back-arc extension oceanic crust?
back-arc extension oceanic crust
A
A'
B
B'
C
C'
CF
YF
ARF
AIF
37°N
36°N
35°N
5°W
4°W
3°W
2°W
1°W
0°
0 25 50 km
Depocenters:
WAB+MB
EAB
HBB+PB
SAB
Plio-Pleistocene units
Crustal domains:
Thin continental crust
Continental crust (N. Africa)
Magmatic crust
Volcanic activity
Volcanic outcrop
Main structures:
Miocene:
Inferred subduction front
Subduction front at 9Ma
Displacement direction
Lithospheric transform fault
Extension
Plio-Quaternary:
Inverse fault
Strike-slip fault

- *Timing of the extension and the Pliocene contractive reorganization*

The initiation of the extension that led the formation of the Alboran Basin is not well constrained. However, the first evidences of extension recorded in the basin are from Early Miocene (e.g. Comas et al. 1999, Do Couto et al. 2016). Additionally, there is some indication of extension during the latemost Oligocene (e.g. Garrido et al., 2011). Consequently, in this review we assume a Late Oligocene – Early Miocene age as the most probable date for the extension initiation.

The end of the extensional phase occurred during the Late Tortonian, but may not be exactly coetaneous along the entire system (e.g., Krautworst and Brachert, 2003; Booth-Rea et al., 2004; Giaconia et al., 2014). The post-Messinian evolution of the basin is characterized by the activation of crustal faults that accommodate the African and Iberian plate convergence (e.g, Gràcia et al., 2006, 2012; Martínez-García et al., 2011, 2013; Medaouri et al., 2014; Moreno et al., 2016, Chapters 7, 8 and 9 this volume). Some of these structures, such as the Carboneras and the Palomares faults, begin their activity in Latemost Miocene times or early Pliocene (Gràcia et al., 2006; Moreno et al., 2016, "Chapter 8: The Palomares margin"). The contractive reorganization of the basin mainly occurred during the Plio-Quaternary, when the N Alboran Ridge Front, Yusuf and Al-Idrissi faults appeared (Gràcia et al., 2006; Martínez-García et al., 2011; Martínez-García et al., 2013; Medaouri et al., 2014; Moreno et al., 2016; "Chapter 9: The Yusuf Fault" and "Chapter 10: The Alboran Ridge").

10.2. Proposed geodynamic models: compilation and discussion

We classify the subduction models in three main groups following the classification proposed by Chertova et al. (2014a): (10.2.1) An initial north-directed subduction zone located south of the Balearic Islands and later westward-directed slab roll-back, evolving as a continuous subduction front (Fig. 10.9a), (10.2.2) An initial northern subduction zone located south of the Balearic Islands and later westward roll-back but including a lithospheric tearing that compartmentalized the slab (Fig. 10.9b), and (10.2.3) an initial southern subduction zone located in the north African margin and later westward slab roll-back (Fig. 10.9c). Although each model presents some particular characteristics, the subduction system and basin opening evolution are similar for each group, allowing a joined discussion. Most published models are developed for the entire western Mediterranean basins; but we focus in the Alboran Basin area. The discussed models are referred with the name of the first author of each paper.

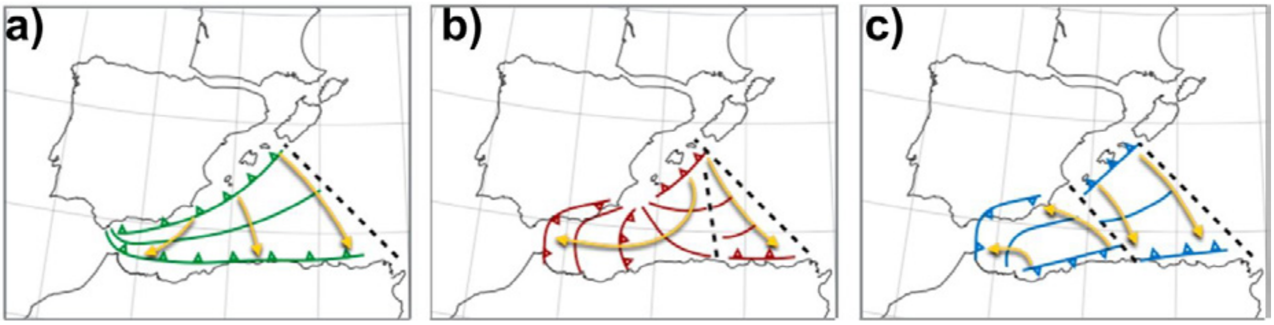

Figure 10.9: *Illustration of the three different subduction scenarios for the opening of the Alboran Sea.* ***(a)*** *Long initial trench along the entire Gibraltar-Balearic margin (e.g., Rosenbaum et al., 2002; Faccenna et al., 2004; Jolivet et al., 2009; Do Couto et al., 2016).* ***(b)*** *Initial subduction zone near the Balearic Islands, north-dipping discontinuous slab (e.g., Spakman and Wortel, 2004; van Hinsbergen et al., 2014).* ***(c)*** *S-SE dipping initial subduction zone under North Africa (e.g., Gelabert et al., 2002; Vergés and Fernández, 2012) (modified from Chertova et al., 2014).*

10.2.1. North-dipping continuous slab

In this group we have included all the models that started from an initial north-dipping subduction zone at the southern margin of the Balearic Islands that evolve as a continuous subduction zone (Fig. 10.9a). We have included four models: (a) the “Jolivet” model (Jolivet et al., 1999; Jolivet and Faccenna, 2000; Jolivet et al., 2009), (b) the “Rosenbaum” model (Rosenbaum et al., 2002), (c) the “Faccenna” model (Faccenna et al., 2004, Faccenna et al., 2014) and (d) the “Do Couto” model (Do Couto et al., 2016).

a) *The “Jolivet” model*

This model starts from a long south-Balearic subduction zone that in Oligocene times (30 Ma) went from north Algeria to north Italia (Fig. 10.10). This subduction evolves migrating southward and westward. At 23 Ma, the Alboran segment had already its arcuated shape. From the Aquitanian time, the westward migration continues, giving as a result a wider arcuate front (Fig. 10.10). Extension in the Alboran Basin starts at some point between 30 and 23 Ma (Late Oligocene), in an W-E direction (Jolivet and Faccenna, 2000), and although the end of the extension is not discussed, at age ~5 Ma the deformation front position is located roughly on its current position (Fig. 10.9).

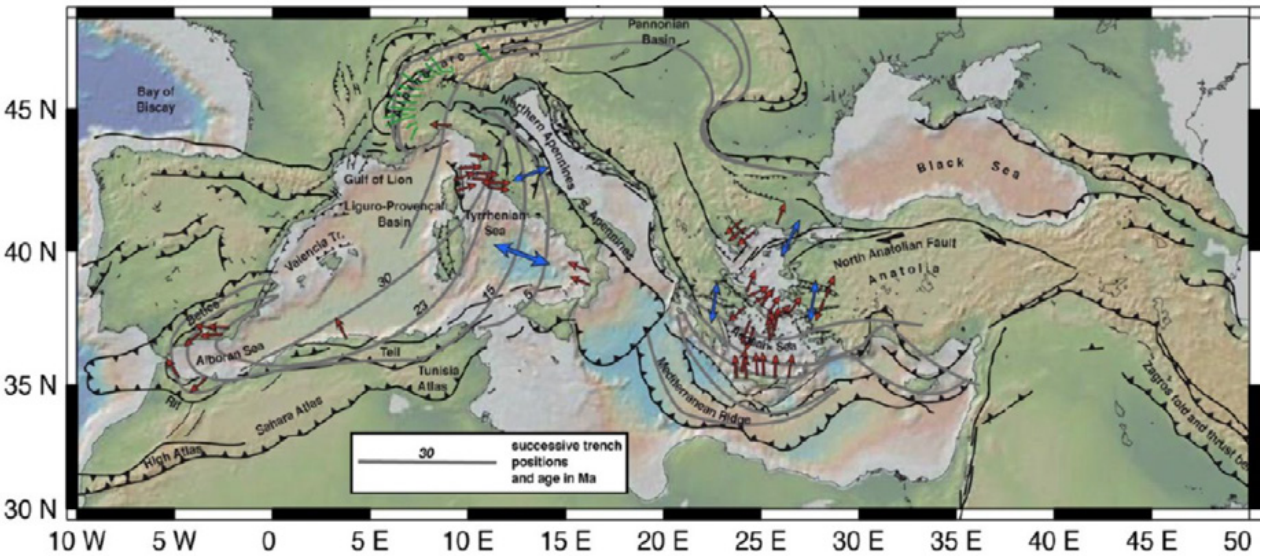

__Figure 10.10:__ The “Jolivet” model (from Jolivet et al., 2009). Grey lines represent the successive positions of the subduction front, red arrows are indicative of the deformation direction at the inner zones (metamorphic complexes), and blue arrows depicted the direction of extension in the back-arc domains.

b) *The “Rosenbaum” model*

The initial subduction zone of this model starts in the southern Balearic margin (Fig. 10.11), but extends northern and is longer that the “Jolivet” initial subduction front (Fig. 10.10). The subduction has a north direction, and the trench progressively migrates to the south. In the Late Oligocene westward slab roll-back begins, proposing as a result an ~E-W extension in the Alboran Basin in the Late Burdigalian times. This extension is accompanied of magmatic activity, and both continued during the Middle Miocene (Fig. 10.11). In the Tortonian, the subduction front reaches its current position, and extension ceases (Fig. 10.11), although volcanism is still active (Fig. 10.10). In the Messinian, both, the extension and the volcanic activity have finished (Fig. 10.11).

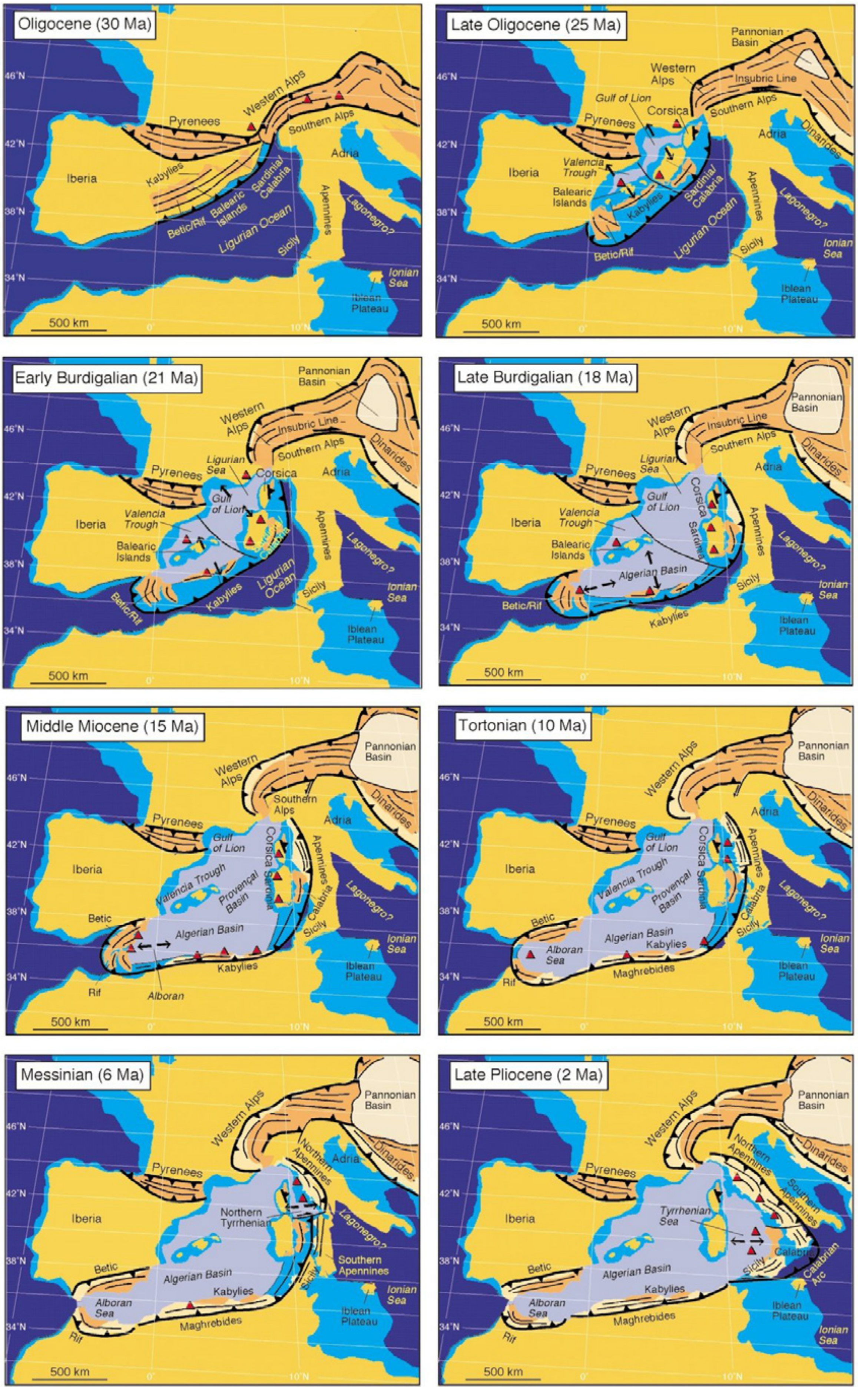
Oligocene (30 Ma)
Late Oligocene (25 Ma)
Early Burdigalian (21 Ma)
Late Burdigalian (18 Ma)
Middle Miocene (15 Ma)
Tortonian (10 Ma)
Messinian (6 Ma)
Late Pliocene (2 Ma)
Iberia
Pyrenees
Western Alps
Southern Alps
Insubric Line
Pannonian Basin
Dinarides
Adria
Apennines
Northern Apennines
Southern Apennines
Lagonegro?
Ionian Sea
Iblean Plateau
Sicily
Calabria
Calabrian Arc
Corsica
Sardinia
Sardinia/Calabria
Kabylies
Balearic Islands
Betic/Rif
Betic
Rif
Ligurian Ocean
Ligurian Sea
Gulf of Lion
Valencia Trough
Provençal Basin
Algerian Basin
Alboran
Alboran Sea
Maghrebides
Northern Tyrrhenian
Tyrrhenian Sea
46°N
42°N
38°N
34°N
0°
10°N
500 km

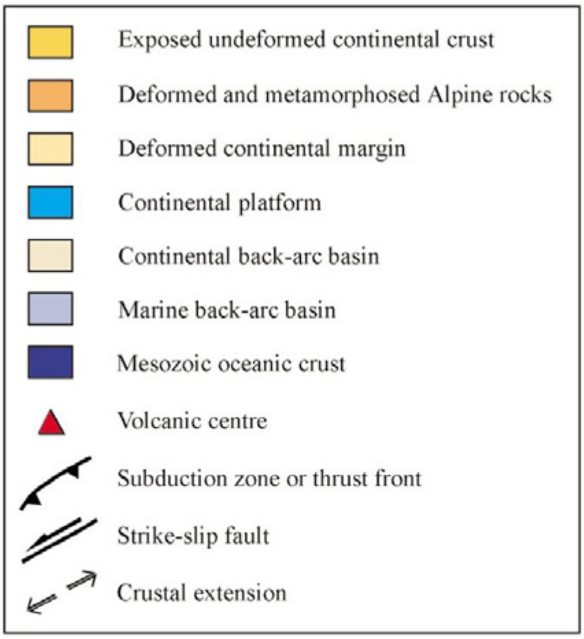

Figure 10.11: *The "Rosenbaum" model (Rosenbaum et al., 2002). Reconstruction of the western Mediterranean evolution since the Oligocene. See map legend for details.*

c) *The "Faccenna" model*

This model starts from a similar subduction zone as "Jolivet" (Fig. 10.9), with a northward subduction direction that progressively migrates towards the south (Fig. 10.12). Although it does not include lithosphere-tearing faults, this is not a purely continuous slab model: it requires a broken slab in order to produce slab rollback. A wider subduction zone is broken into two slab tongues, resulting in the Gibraltar Arc towards the west and the Calabrian Arc towards the east. Slab rupture is explained as a consequence of mantle dynamics (Faccenna et al., 2004). At 15 Ma (Late-Middle Miocene, Fig. 10.12b), westward slab roll-back had already caused the opening of the Alboran Basin in a W-E direction. During the opening, subduction related volcanism occurred (Fig. 10.12). Subduction stops at 5 Ma, when anorogenic volcanism starts (Fig. 10.12c) in relation with the opening of slab windows (Faccenna et al., 2004; 2014).

d) *The "Do Couto" model*

This model is focused on the West Alboran Basin geographical area (Fig. 10.13). An initial N-S extension is proposed, due to a north-directed subduction and a southward motion of the subduction front. The West Alboran Basin starts subsiding in the Late Oligocene (Fig. 10.13). In the Burdigalian (Early Miocene), the direction of extension changed to E-W as slab rollback changes to a westward direction. The westward slab-roll back and E-W extension continued till Serravallian time. Extension and volcanism stopped in Tortonian time (Do Couto et al., 2016). From Tortonian time, the Alboran Basin is proposed to be a sag basin evolving in a NW-SE compressional setting (Do Couto et al., 2016).

The size of the WAB increased with time from the Late Oligocene till the Tortonian, but acquired its arcuate shape during Serravallian – Tortonian times (Fig. 10.13) (Do Couto et al., 2016).

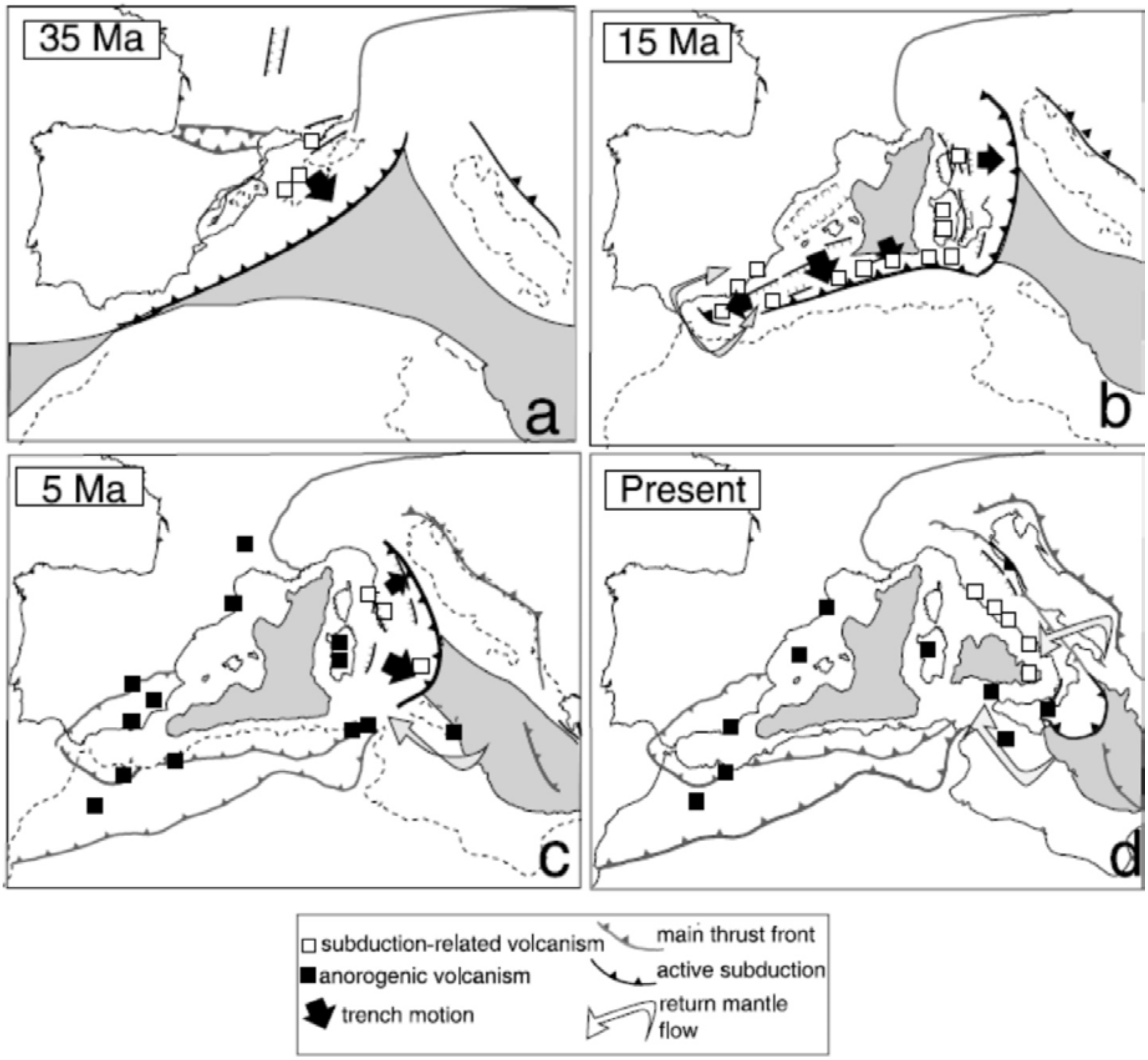

Figure 10.12* ▲*: *The "Faccenna" model (Faccenna et al., 2004). Reconstruction of the western Mediterranean evolution in four stages since the Early Oligocene. See map legend for details.*

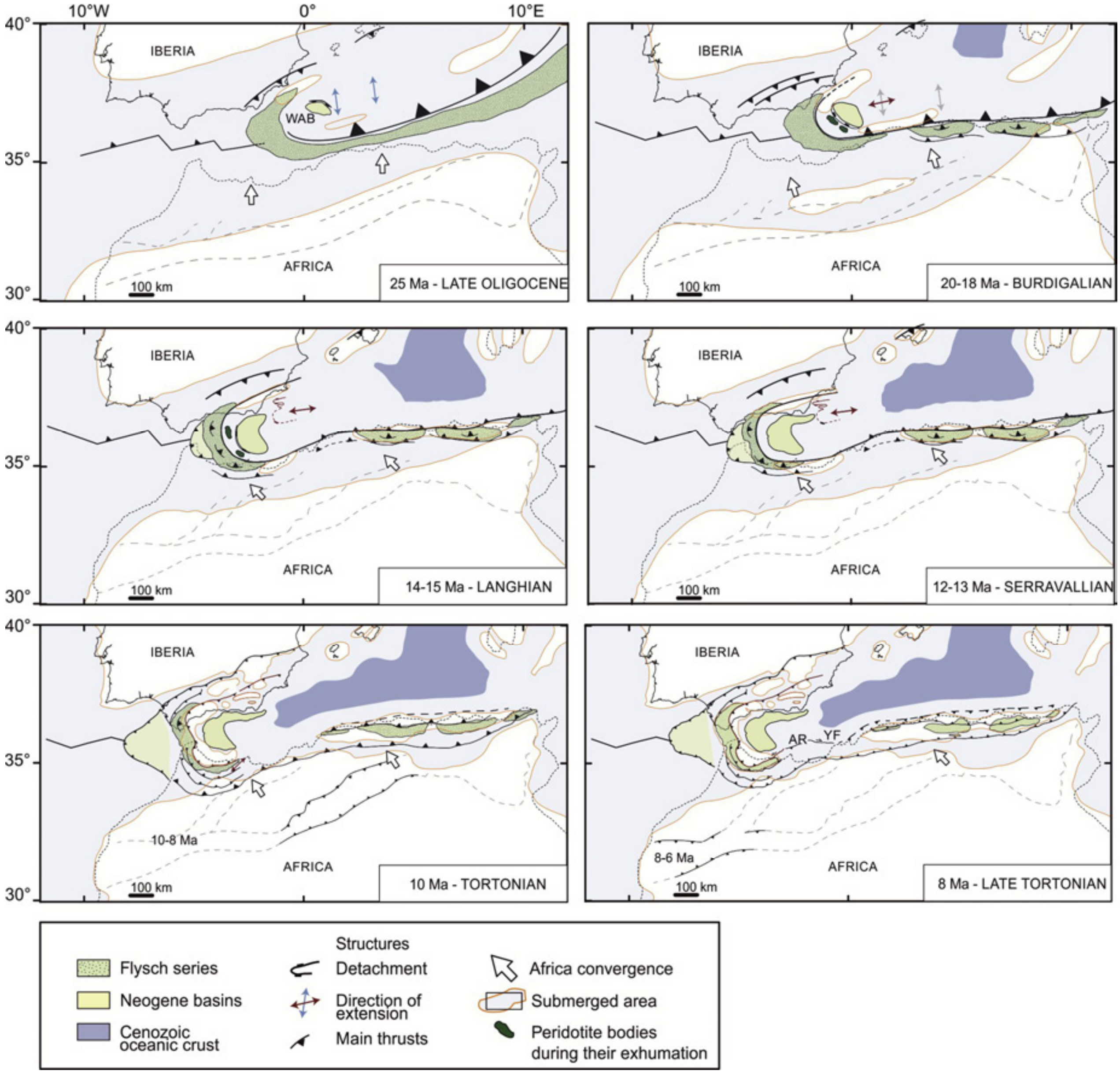

Figure 10.13* ▲*: *The “Do Couto” model (Do Couto et al., 2016). Paleogeographic maps of the Alboran Basin area from the Early Oligocene to the Late Tortonian, focused on the evolution of the West Alboran Basin (WAB, yellow area). The main tectonic structures are depicted. Green areas: Alboran domain, AR: Alboran Ridge, YF: Yusuf Fault.*

- Testing the models

These models are broadly coherent with magma geochemistry, and timing of extension and contractive reorganization, but they cannot explain some of the recent observations of the lithospheric structure, the basin evolution and distribution of crustal domains.

The calk-alkaline volcanic activity can be explained due to the presence of a slab under the Alboran Basin, but only the “Faccenna” model tries to explain the later alkaline volcanism, with slab tears under the zones where alkaline volcanism occurred (black squares at Figure 10.12) that allow the influx of asthernospheric fluids (Faccenna et al., 2004).

Regarding timing, all models are coherent with a Late Miocene end of the extension, and therefore intrinsically do not disagree with an Early Pliocene contractive reorganization. The "Faccenna" model stops the subduction at 5 Ma (Late Messinian), when the subduction front is represented as inactive. The "Do Couto" model placed the Alboran Basin in a compressional setting from the Tortonian, while the "Jolivet" and "Rosenbaum" models lock the westward migration of the subduction front at 5 and 6 Ma respectively (Fig. 10.10, 10.11).

The main drawback of these models is related to the deep structure under the basin. A north-dipping continuous slab is inconsistent with recent observations showing: (i) subduction of Iberia below Africa, (ii) the segmented slab imaged with TTT and FWI, and (iii) maps of Moho depth, as the models propose a continuous collision front along North Africa margin and the mapped Moho support crustal thickening only under the Rif belt area (Fig. 10.7b). The juxtaposition of different crustal domains as well as the independent evolution of the different Alboran sub-basins remains unexplained by these models, as lithospheric structures are needed in order to explain these observations. Additionally, the "Do Couto" model proposed that the arcuate shape of the WAB & MB was acquired through time, while stratigraphic observations (Fig. 10.8, "Chapter 6: Basin evolution") confirmed that the first sedimentary units of the basin (Early Miocene) already had this shape.

10.2.2. North-dipping slab, lithosphere tearing

In this section we include models that started from an initial subduction towards the north, south of the Balearic margin, and migrated to the south and then west. They include lithospheric slab tears, which allow the independent evolution of different segments of slabs. The two models to consider in section are: (e) the "Spakman" model (Spakman and Wortel, 2004), and (f) the "van Hinsbergen" model (van Hinsbergen et al., 2014).

e) The "Spakman" model

This is the first geodynamic model based on mantle tomography results. It corresponds to the culmination of previous works (Carminati et al., 1998; Wortel and Spakman, 2000), in which the importance of lithospheric rupture areas as lithosphere tearing of slab detachment was pointed out (Fig. 10.14). In this model, the initial subduction front is ~500 km long and is located south of the Balearic margin (Fig. 10.14a-c). The slab migrates in a south-west trend and finally west direction, giving as a result the opening of the Alboran Basin (Fig. 10.14a). The age of the opening is not well constrained, but the later 3D reconstruction performed by Chertova et al., (2014b) suggested that occurred ~25 Ma ago (Latemost Oligocene) (Fig. 10.14d). The active subduction front is bounded by lithospheric faults long the slab lateral edges (lithosphere tearing along North Africa margin and Balearic Islands, Fig. 10.14a, Fig. 10.14c) that allow the horizontal displacement of the different crustal domains and are able to explain the anorogenic magmatism in the basin margins as they allow the influx of asthenospheric fluids.

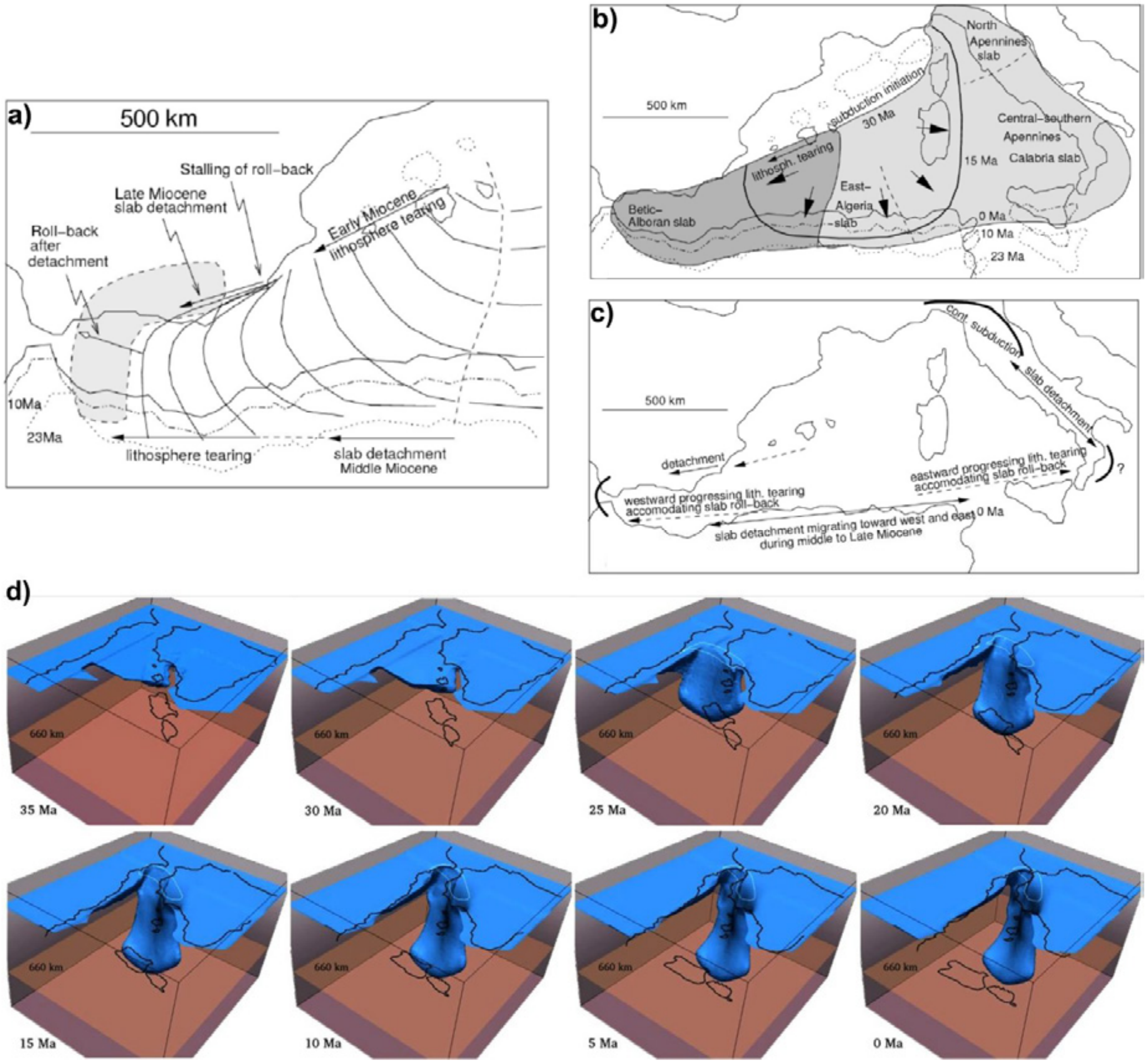

Figure 10.14: *The "Spakman" model (Spakman and Wortel, 2004).* ***(a)*** *Kinematic reconstruction of the slab roll-back in the Gibraltar Arc system area. The curved lines represented the successive positions of the subduction front, and the circle area is the current position of the slab at 200 km depth projected to the surface. Dot lines represent the position of the Africa margin at different times (Spakman and Wortel, 2004).* ***(b)*** *Reconstruction of the original surface of the subducted oceanic lithosphere in the basis of the tomography model (Spakman and Wortel, 2004).* ***(c)*** *Scheme of the slab detachment and lithosphere tearing occurred during the development of the subduction front (Spakman and Wortel, 2004).* ***(d)*** *3D modelling of the slab evolution for this model from the Early Oligocene to the present-day (Chertova et al., 2014b).*

f) The "van Hinsbergen" model

This model tries to explain the distribution of the internal zones of the Betics, Rif and Tell mountain belts (i.e. the allochtonous terrains represented by blue areas in Figure 10.15). The resulting model, the "van Hinsbergen" model (Fig. 10.15), is similar to the "Spakman" model. The "van Hinsbergen" model proposes a well-defined transform fault separating the west and the east sections of the slab since the Early Miocene (Fig. 10.15). The southward and later westward motion of the western section of the original slab derives in the formation of the Alboran Basin that begins its formation at ~ 21 Ma (Lower Miocene) in a position located south of the Balearic Islands. At these times, the subduction front presents an arcuate shape in which the southern and western flanks are subduction zones, while the northern is limited by a transform fault that allows the horizontal south-westward motion of the slab (Fig. 10.15). At 16 Ma (Langhian) the southern section collides with the North Algerian margin, giving as a result the Kabylides and Tell orogenic belts. A second transform lithospheric fault appears south of the subduction front at Langhian time, limiting the active subduction to the westernmost section (Fig. 10.15). This transform fault allows the emplacement of the alochtonous terrains in the Betics and Rif orogenic belts (Fig. 10.15).

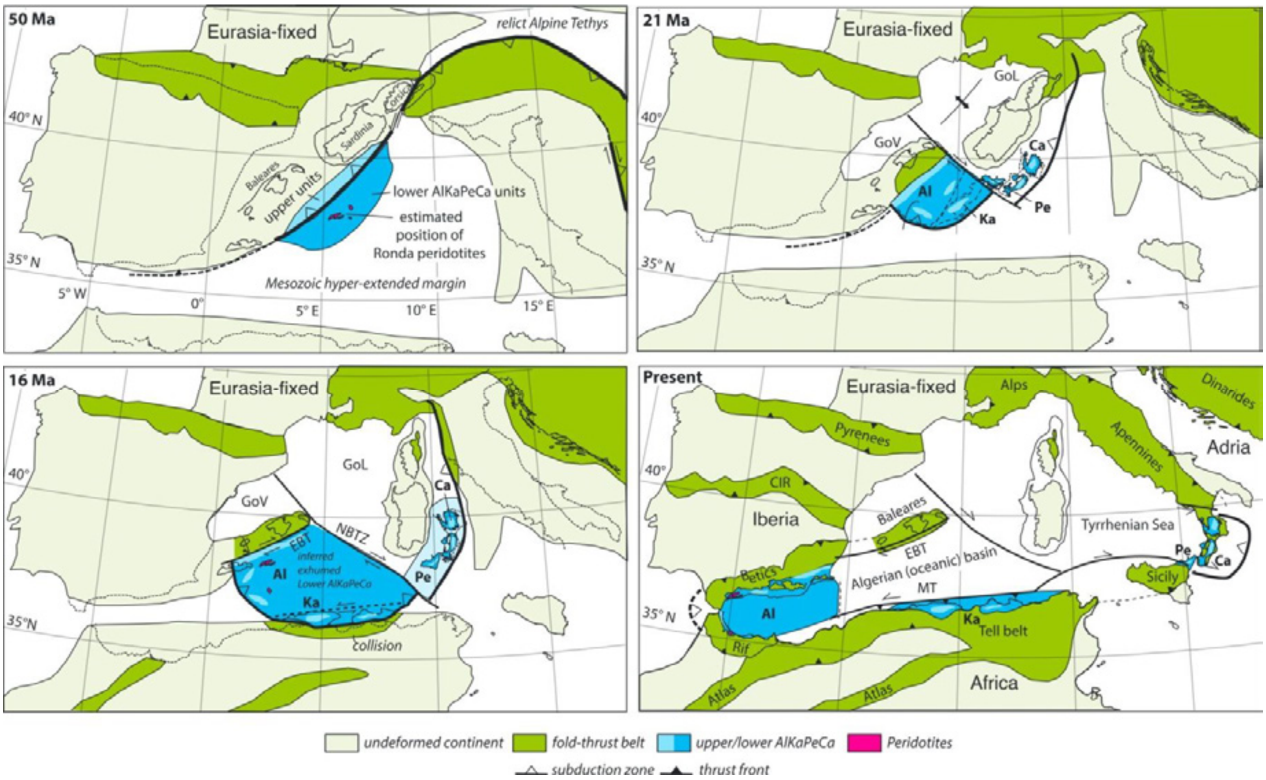

Figure 10.15: *The "van Hinsbergen" model (van Hinsbergen et al., 2014). Reconstruction of the western Mediterranean from the AlKaPeCa distribution (blue areas), since 50 Ma (Early Eocene). Al: Alboran, Ca: Calabria, CIR: Central Iberian Ranges, EBD: Emile Baudot Transform, GoL: Gulf of Lions, GoV: Gulf of Valencia, Ka: Kabylies, NAT: North African Transform, NBTZ: North Balearic Transform Zone, Pe: Peloritani Mountains.*

- Testing the models

Although these models fail explaining the Iberia under Africa subduction, successfully explain the segmented slab observations, general crustal structure and volcanism. A direct consequence of introducing lithospheric faults is that the discontinuous slab image with tomographic methods can be explained, together with the different evolution of the crustal domains under the Alboran Basin. A discontinuous subduction front may also explain Moho depth distribution along North Africa margin, although it is difficult to understand how the northeaster Morocco and northwester Algeria margins remained undeformed in the proposed compressional setting (neither by inverse and/or strike-slips faults). The subduction-related volcanism is explained by the presence of the slab. Additionally, the lithospheric tearing generated spaces that are infill by asthenospheric material, which may explain late-stage volcanism taking place in the basin margins.

There are observations of the basin evolution that remain unclear: Assuming that the fore-arc basin mimics the shape of the subduction front, the WAB & MB shape is not coherent with the subduction front proposed by these models (Fig. 10.14a, Fig. 10.15 at 16 Ma), as this geometry will result in a fore-arc basin with a south E-W-trending branch, and not a north E-W-oriented branch as the present-day position of the MB supports. Furthermore, the reconstruction of the "Spakman" model for Tortonian times proposes a slab located very close to its present-day location, which does not account for the westward displacement of the WAB & MB during the Tortonian with the formation of the magmatic arc and reconstructions - based on land data- of previous subduction fronts (Crespo-Blanc et al., 2016).

These models discuss the opening stage of the basin but do not evaluate constraints of the end of extension which are well constrained by our data.

10.2.3. South-dipping slab, lithosphere tearing

This group is the most different one, which include the models that disagree with a southward migration of the slab (Fig. 10.16). In these models, the slab is originally segmented in different sections that evolve independently. It allows a southward and eastward retreat of the Calabrian and North-Africa slabs, while the Gibraltar arc slab subducted southward with a front that retreats towards the north (Fig. 10.16b). Below we explain (g) the "Gelabert" (Gelabert et al., 2002) and (h) the "Vergés" models (Vergés and Fernàndez, 2012).

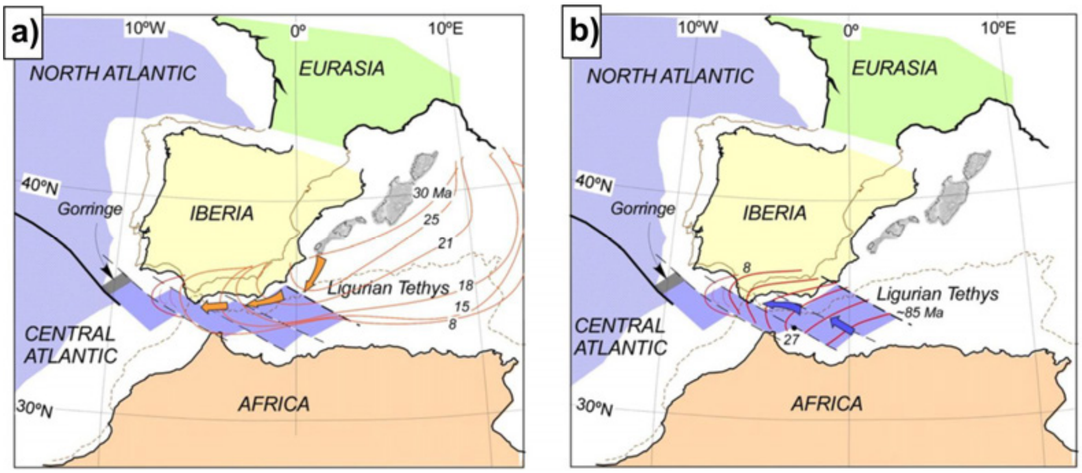

Figure 10.16* ▲:** *Cartoon showing the geometry of the subduction zone in the Alboran Basin area.* ***(a) *Generic sketch for the models based on a northward dipping slab retreating to the south and towards Iberia (north-dipping slab models, Jolivet et al., 2000; Rosenbaum et al., 2002; Faccenna et al., 2004; Spakman and Wortel, 2004; van Hinsbergen et al., 2014; Do Couto et al., 2016).* ***(b)*** *Model based on a northward subduction retreating to the west (Gelabert et al., 2002; Vergés and Fernàndez, 2012). From Vergés and Fernàndez (2012).*

Figure 10.17* ►:** *The "Gelabert" model (Gelabert et al., 2002).* ***(a) *Paleotectonic reconstruction of the western Mediterranean, since the Early Oligoce till present-day (Gelabert et al., 2002).* ***(b)*** *Cartoons illustrating the paleotectonic reconstruction showed in Figure 10.17a. Three independent slabs since 35-30 Ma are identified. The westernmost one, the Alboran slab, subducts towards the north, being Iberia the lower plate of the subduction system.*

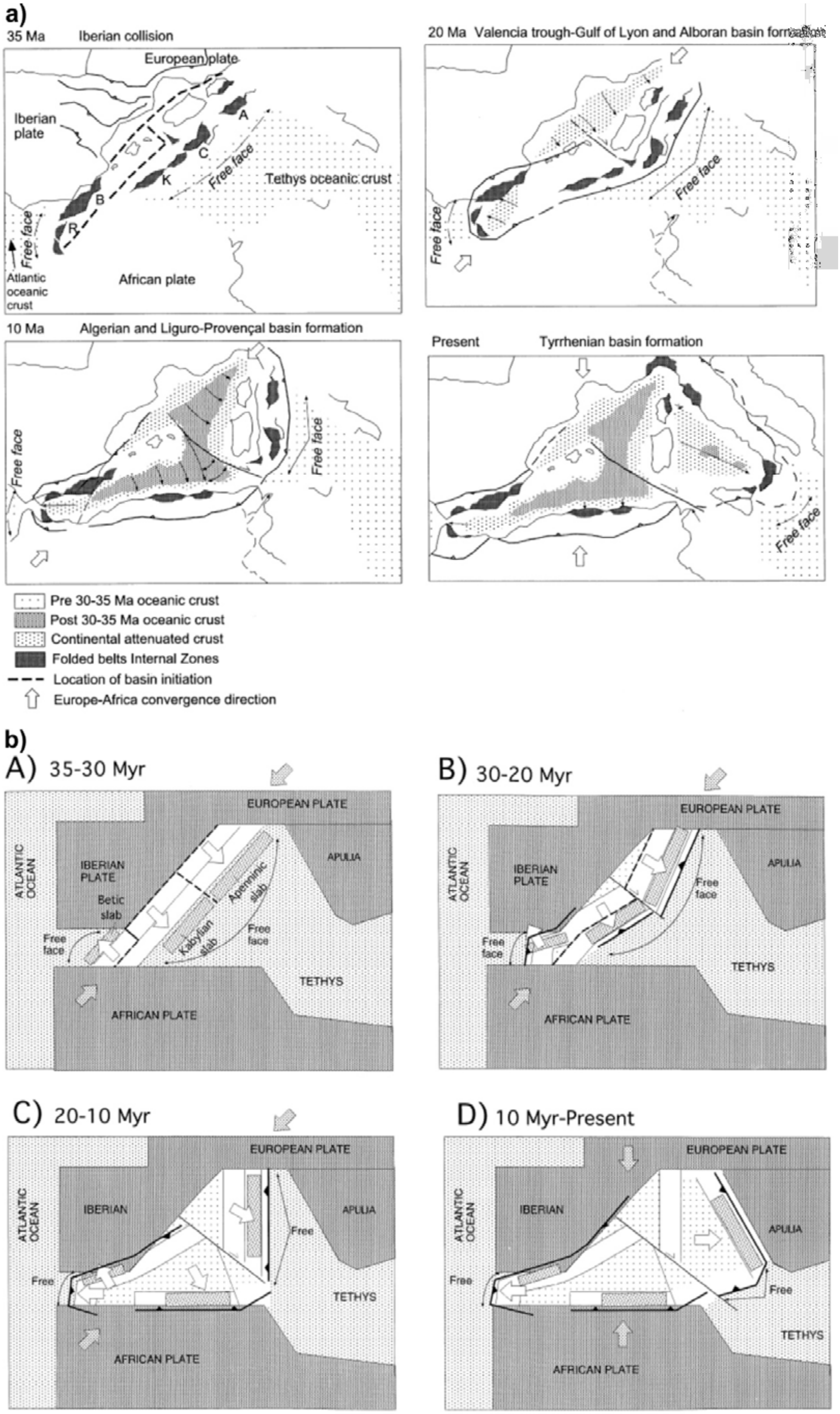
a)
35 Ma Iberian collision
European plate
Iberian plate
A
C
K
B
R
Free face
Free face
Tethys oceanic crust
Atlantic oceanic crust
African plate
20 Ma Valencia trough-Gulf of Lyon and Alboran basin form
Free face
Free face
10 Ma Algerian and Liguro-Provençal basin formation
Free face
Free face
Present Tyrrhenian basin formation
Free face
Pre 30-35 Ma oceanic crust
Post 30-35 Ma oceanic crust
Continental attenuated crust
Folded belts Internal Zones
Location of basin initiation
Europe-Africa convergence direction
b)
A) 35-30 Myr
EUROPEAN PLATE
ATLANTIC OCEAN
IBERIAN PLATE
APULIA
Betic slab
Kabylian slab
Apenninic slab
Free face
Free face
TETHYS
AFRICAN PLATE
B) 30-20 Myr
EUROPEAN PLATE
ATLANTIC OCEAN
IBERIAN PLATE
APULIA
Free face
Free face
TETHYS
AFRICAN PLATE
C) 20-10 Myr
EUROPEAN PLATE
ATLANTIC OCEAN
IBERIAN
APULIA
Free
Free
TETHYS
AFRICAN PLATE
D) 10 Myr-Present
EUROPEAN PLATE
ATLANTIC OCEAN
IBERIAN
APULIA
Free
Free
TETHYS
AFRICAN PLATE

g) *The "Gelabert" model*

This model proposed an evolution in three stages (Fig. 10.17). The first stage (Cretaceous – Oligocene) is characterized by the Tethys subduction. A second stage (Oligocene) comprised the collision of the continental margins with blocks of the internal zones. Finally, the third stage (from Late Oligocene) is characterized by the opening of the basins. In this model, the slab is segmented in three parts, each of them with an independent evolution. The Alboran slab is south directed, and retreats toward the northwest (Fig. 10.17a, b). The roll-back is produced towards the free faces of the subduction front (Fig. 10.17b), which leads a westward roll-back in the Alboran Basin. The limits between the segments of the slabs are clearly identified as transform-type boundaries (Fig. 10.17), but these structures are inferred conceptually and not based on related observation.

h) The "Vergés" model

The "Vergés" model (Fig. 10.18) is based on large-scale plate reconstruction, distribution of the internal units, kinematics of the internal/external zones boundaries and timing of compression along the Betic-Rif orogenic belts (Vergés and Fernàndez, 2012). This model starts from a SE-dipping subduction migrating towards the north that later evolves in an E-dipping subduction retreating westward (Fig. 10.8a, b). The model starts in the Cretaceous, with an early subduction initiation stage of the Tethys oceanic crust below the North African margin. This processes led to the subduction of the Iberian margin below Africa in the Middle Eocene (~47 Ma). In the Late Oligocene – Early Miocene (~30 Ma), peridotites are exhumed, and the direction of extension changes from N-S to W-E. This gives as a result the opening of the Alboran Basin (from ~27 Ma, Early Miocene). The extension continues through the Miocene, and the slab is detached below the Betics. At ~5 Ma, extension stopped and the basins evolved in a compressional setting (Fig. 10.18). Calk-alkaline volcanism is used to support active subduction. Alkaline volcanism is not discussed in this model. Mantle delamination or lithosphere detachment along the basin margins are integrated but their significance not discussed (Vergés and Fernàndez, 2012).

- <u>Testing the models</u>

The most important advantage of these models over the previous ones is the south-dipping slab, as this is in agreement with recent seismic data of lithospheric structure (Mancilla et al., 2015). Although the behaviour of the subduction zone is similar in both models, the "Vergés" model is further developed, including the presence of lithospheric faults, while in the "Gelabert" model the role of lithospheric fracture zones is not considered and contains many aspects that remain unclear.

A south-dipping segmented slab is coherent with (i) recent geophysical models of lithosphere structure, (ii) the crustal-domains distribution and (iii) the Moho mapped depths, as there is not a subduction front colliding with most of the North Africa margin.

Magma geochemistry and basin evolution can be largely integrated although they are not discussed in detail, as it is not discussed the role of mantle delamination and changes in geometry of the subduction front, respectively.

The end of the extension is only mentioned in the "Vergés" model, and it is coherent with the results of this thesis, as the contractional reorganization of the basins is proposed to start at ~5 Ma (Early Pliocene) (Fig. 10.18). However, in the "Vergés" model the initiation subduction in the Alboranb region is proposed at ~85 Ma (Late Cretaceous) which is not supported by local structure.

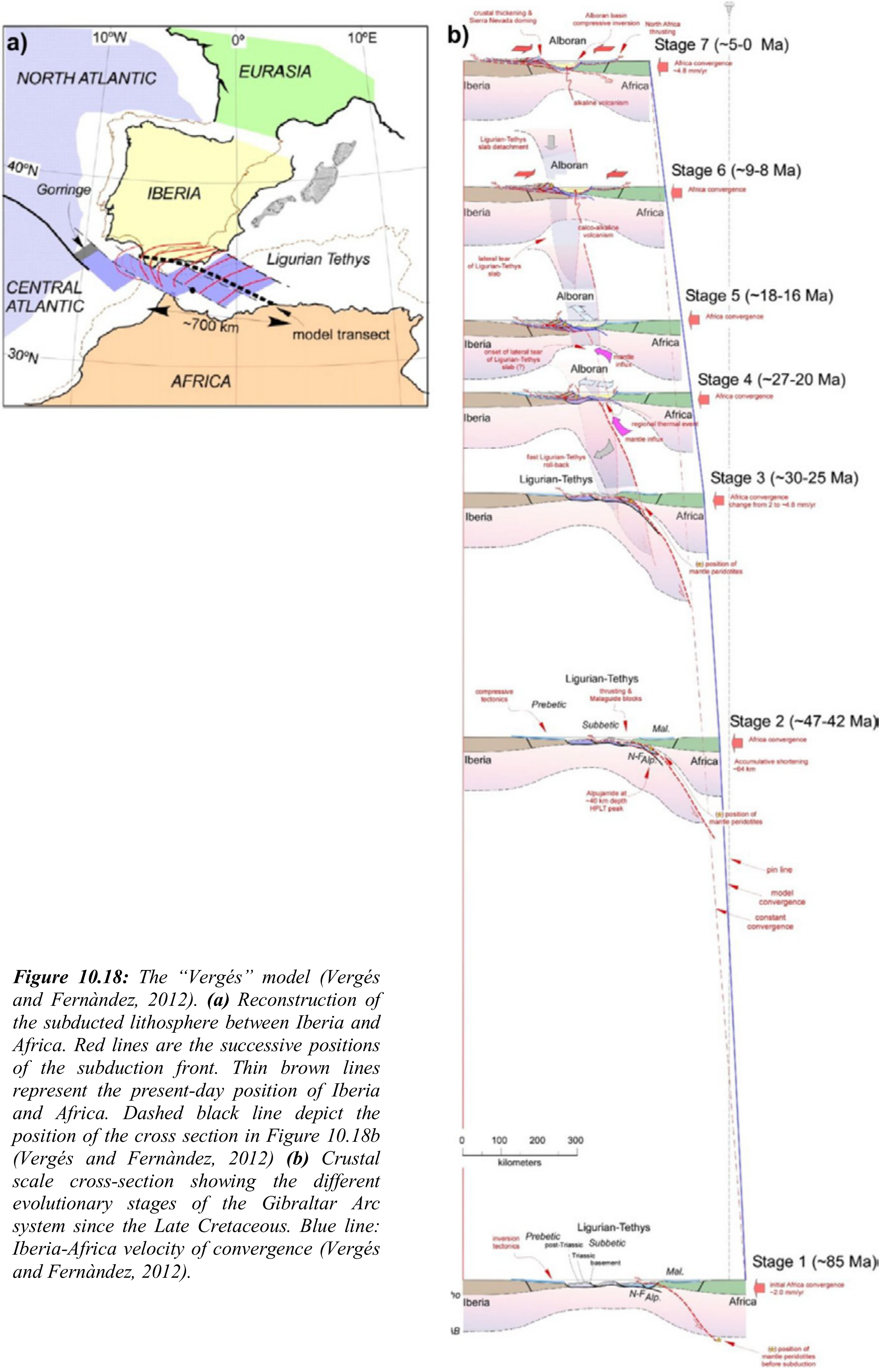

Figure 10.18: *The "Vergés" model (Vergés and Fernàndez, 2012).* ***(a)*** *Reconstruction of the subducted lithosphere between Iberia and Africa. Red lines are the successive positions of the subduction front. Thin brown lines represent the present-day position of Iberia and Africa. Dashed black line depict the position of the cross section in Figure 10.18b (Vergés and Fernàndez, 2012)* ***(b)*** *Crustal scale cross-section showing the different evolutionary stages of the Gibraltar Arc system since the Late Cretaceous. Blue line: Iberia-Africa velocity of convergence (Vergés and Fernàndez, 2012).*

10.2.4. Concluding remarks

In this chapter we have compared 8 evolutionary models that try to explain the origin of the Alboran Basin (Table 10.1). Comparing these models with the mantle structure observations, geochemical affinity and distribution of the volcanism, crust characteristics, timing of basin formation from stratigraphy and deformation processes, we have tested which of these models agrees/explains observations including our new results presented in this thesis.

There are three main groups of models, considering the main characteristics of the subduction zone (Chertova et al., 2014a): (10.2.1) north-dipping continuous subduction, (10.2.2) north-dipping segmented subduction, and (10.2.3) south-dipping subduction. A first result of this comparison is the recognition that there is not a single model that can perfectly explain all the previous observations (Table 10.1).

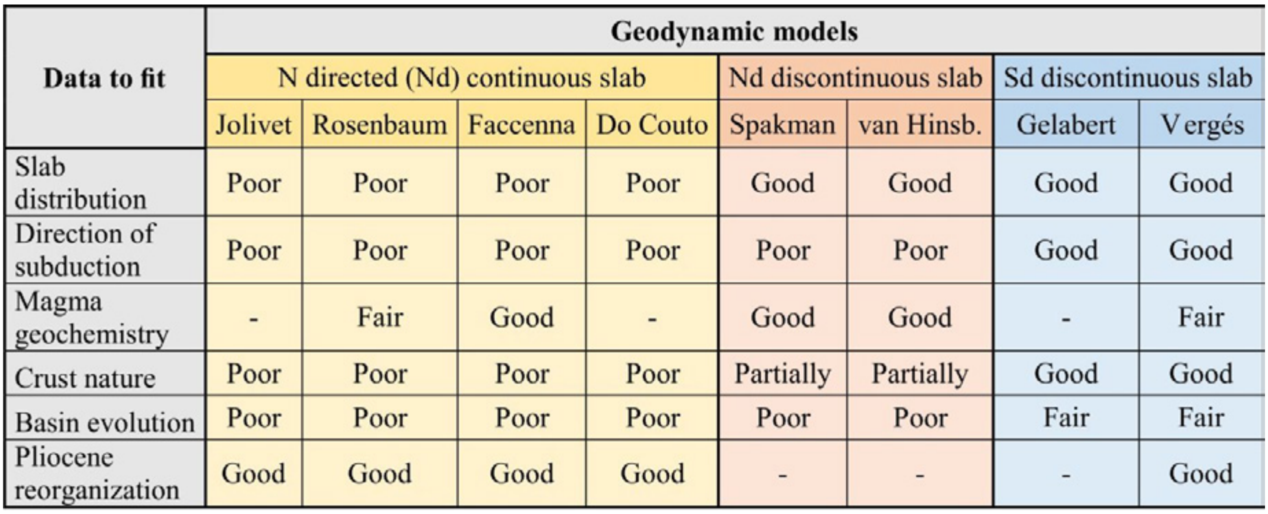

Data to fit	**Geodynamic models**							
	N directed (Nd) continuous slab				Nd discontinuous slab		Sd discontinuous slab	
	Jolivet	Rosenbaum	Faccenna	Do Couto	Spakman	van Hinsb.	Gelabert	Vergés
Slab distribution	Poor	Poor	Poor	Poor	Good	Good	Good	Good
Direction of subduction	Poor	Poor	Poor	Poor	Poor	Poor	Good	Good
Magma geochemistry	-	Fair	Good	-	Good	Good	-	Fair
Crust nature	Poor	Poor	Poor	Poor	Partially	Partially	Good	Good
Basin evolution	Poor	Poor	Poor	Poor	Poor	Poor	Fair	Fair
Pliocene reorganization	Good	Good	Good	Good	-	-	-	Good

Table 10.1: *Comparison between the different models and the data to fit. Nd: North directed, Sd: South directed.*

Kinematic models have been evolving since the year 2000, at the same time that the geophysical observations have been improving and geological data become more extensive. The increment in available data and better resolution decreased the degrees of freedom of geodynamical mechanisms to explain the observations, as the local processes that led to the basin formation and deformation were better constrained.

The south directed slab formed by a continuous subduction front model (section 10.2.1) should be understood inside of this framework: Most of these models do not take into account the deep geological information, either of the crust characteristics or the slab distribution. Although the "Faccenna" model is based on a tomography model, the resolution of this model does not allow observing discontinuities in the slab front below the Gibraltar Arc system. These models usually consider mainly onland data and ignore the marine basin evolution (i.e. the "Jolivet", the "Rosenbaum" and the "Faccenna" models), or only integrate local observations (as in the "Do Couto" model for WAB). As a result, this group of models might explain the alochtonous metamorphic terrains distributed onland, but do not specifically explain crustal domains, observed slab segments and Alboran-wide basin evolution. The volcanic activity is commonly not integrated, and the "Faccenna" model specifically uses that information for the reconstruction (Table 10.1).

With the improvement of the mantle tomography results, new ideas were introduced to explain the geodynamic situation of the Gibraltar Arc system. The presence of a segmented slab needed to be integrated. The integration of slab-bounding faults, as the Subduction-Transform Edge Propagator (STEP) faults, that allows the independent evolution of different segments of the subduction front was a major outcome of these new mantle images. The STEP faults (Govers and Wortel, 2005) are nucleated at the subduction front lateral edges as a consequence of slab tearing and allow the migration of the subduction front. Another important concept in the description of the Gibraltar Arc system subduction is the recycling of continental margin lithosphere (Levander et al., 2014). This hypothesis suggests that the subducted oceanic lithosphere can sweep part of the adjacent continental lithosphere, being the triggering mechanism for continental delamination (Levander et al., 2014). The existence of a segmented slabs, STEP faults, lithosphere tearing and continental mantle delamination are current basic concepts of any geodynamical model to explain the western Mediterranean geodynamic evolution (e.g. Wortel and Spakman, 2000; Spakman and Wortel, 2004; Govers and Wortel, 2005; Levander et al., 2014).

The models that segmented the south-dipping slab appeared (section 10.2.2). The concept of a compartmentalized slab is introduced not only in the tomographic-based models (i.e. the “Spakman” model), but also in the onland geological observation models (i.e. the “van Hinsbergen” model). Although these models fit better the observed data than the south-dipping continuous slab group (Table 10.1), there are some open questions and unexplained features. The main observable not included in these models is the image of a south directing slab (Mancilla et al., 2015). Another feature that remains unclear is the crustal thickening limited just to NW Morocco. With this subduction geometry, it is difficult to explain how a section undeformed in the Miocene of the North-African margin could exist between the Rif and Kabylides. Further, these models do not take into account the marine geology and, as consequence, evolutionary aspects of the Alboran Basin are not integrated in any detail (Table 10.1).

The third group of models proposed a segmented slab that in the Alboran Basin area dips towards the south (section 10.2.3). The first model that introduces this concept is the “Gelabert” model, in 2002. However, it is sketchy, including the magma geochemistry and timing of the end of the extension, which are not mentioned. The “Vergés” model further develops this geodynamic scenario, including more recent geological data and timing constraints. However, although most observations might be explained with this model, some points need to be refined. The initiation of the subduction zone in the Cretaceous-Middle Eocene is not supported by geological evidences. Volcanic affinity is partially explained, but it is not a resulting of the model: The model does not exclude a lithospheric detachment below the Betics or Rif, which may explain the alkaline volcanism, but this scenario is not discussed in largely 2D model. Finally, as in previous models, available marine data are not integrated in detail, so the basin evolution is only partially explained. A subduction system dipping south might have associated a fore-arc basin like the WAB & MB, but the proposed subduction front should be slightly modified. A front that evolves with and arcuate geometry since the Early Miocene is needed to explain the West Alboran and Malaga fore-arc basin shape, instead of a longitudinal front that acquired its curvature later in time (Fig. 10.18a).

On the basis of these results, we conclude that a geodynamic model suitable to explain the origin and evolution of the Alboran Basin should be a subduction model in which a south dipping slab retreats first to the north and later to the west, with an initial geometry of the subduction front able to explain the arcuate shape of the WAB & MB at Burdigalian times, and with lithospheric faults bounding the active subduction front allowing its displacement and putting in contact the different crustal domains coexisting under the Alboran Basin.

10.3. Lithospheric structure

On the basis of (i) the new results presented in this thesis on the crustal domains and the evolution of sedimentary basins, and (ii) the new insights on the shallow mantle and slab distribution mainly provided by the TOPOIBERIA, RIFSIS and PICASSO projects (e.g., Monna et al., 2013; Bonnin et al., 2014; Gil et al., 2014; Bonatto et al., 2015; Díaz et al., 2015; Mancilla and Diaz, 2015; Monna et al., 2015; Quintana et al., 2015; Villaseñor et al., 2015; Díaz et al., 2016a), we are thus able to describe the lithospheric structure across the Alboran Basin and its margins (Fig. 10.19, see Figures 10.7a and 10.8 for location). We restored the lithospheric structure through time, focusing on three evolutionary stages: Langhian-Serravallian (~14 Ma), Late Tortonian (~9 Ma) and present-day.

Approximately 14 Ma ago (Fig. 10.19a, see Figure 10.8b for location), at Langhian times, the Alboran Basin was in an early stage of development. The first sedimentary depocenter, composed by the West Alboran and Malaga sub-basins (WAB & MB), had been generated (Fig. 10.8b) above thin continental crust. Subsidence was linked to thin continental crust in the fore-arc region of the subduction system. Towards the subduction front, this crust gets thicker due to the collision between the thin continental crust of the upper plate, under the WAB and MB, with the Iberian crust that is the lower plate of the system (Fig. 10.19a). Towards the south, a new depocenter was being generated: the Habibas and Pytheas sub-basins (HBB & PB). These basins are developed on the North African continental margin. We propose that the HBB & PB basins were formed in a transtensional setting because: (i) They occur where two different crustal domains appear juxtaposed, (ii) the different evolution of the depocenters, (iii) the westward migration of the WAB & MB and (iv) the lows-and-highs structuration of the older sedimentary units of the HBB & PB depocenters (Fig. 10.19a) (see chapters 5 and 6, Crustal domains and Basin evolution, respectively). The upper plate crust and the North African continental crust should be in contact through a lithospheric fault that allows the westward motion of the upper plate. This lithospheric boundary should be a wide deformation fault zone. We propose that related to it, a large scale strike-slip system affected the North African margin giving as a result transtensional areas where the HBB & PB developed (Fig. 10.19a).

In Tortonian times the basin evolution was conditioned by magmatic activity (Fig. 10.19b, see Figure 10.8d for location) consequence of the subduction process. We inferred a depth ~100 – 120 km of the top of the Iberian slab below the arc magmatic area, as it is the common depth where calk-alkaline subduction related fluids are formed and it is coherent with the current position of the slab (Fig. 10.19b) (e.g., Tatsumi et al., 1983; Pearce and Peate, 1995; Kushiro, 2007). The WAB & MB continued its westward migration, accelerated by the creation of new magmatic crust in the arc region (Fig. 10.8, 10.19b). This crust is also separated of the North African continental crust by a lithospheric fault (Fig. 10.8, 10.19b). How the slab and this lithospheric boundary interacted still is unclear. On the North Africa margin, the HBB & PB were subsiding. Due to the location of the subduction front, close to its present-day position, and the final age of the volcanism, in the Latemost Tortonian to Messinian, we inferred that the lithospheric fault was losing its role, and becoming inactive, as the westward migration of the WAB & MB was almost complete. This is coherent with the HBB & PB record, as the deformation in the sedimentary units affected only the pre-Messinian sequence, and clearly decreased between the Langhian-Serravallian and the Tortonian units (Fig. 10.9b, "Chapter 7: Basin evolution"). Thus, we propose that the strike-slip regime in the North Africa margin was almost inactive at Latemost Tortonian times (Fig. 10.19b).

The nowadays lithospheric structure and slab distribution is currently well constraint by mantle tomographic studies (Bonatto et al., 2015; Fichtner and Villaseñor, 2015; Mancilla and Diaz, 2015; El Moudnib et al., 2015; Villaseñor et al., 2015) and receiver function analysis (Smith et al., 2006; Pasyanos and Nyblade, 2007; Ayarza et al., 2014; Mancilla et al., 2015) (Fig. 10.19c, d, see Figure 10.7a for location). The slab is detached below much of the South Iberian margin (Fig. 10.2, 10.3, 10.4, 10.9c), where it is found ~120 km depth. The South Iberian margin is formed by continental crust, resulting from a series of thrust sequences (e.g., Alonso-Chaves et al., 2004; Balanyá et al., 2007; Chalouan and Michard, 2004; Sanz De Galdeano, 1990; Vergés and Fernàndez, 2012). This upper plate crust should floor the WAB and Malaga basins (Fig. 10.9b). The situation is similar in a W-E section (Fig. 10.19d), but the crust under the WAB & MB thickens towards the Straits of Gibraltar (SoG in Figure 10.19d), were the crust is ~40-50 km thick (e.g., Mancilla and Diaz, 2015) (Fig. 10.19d). The lithospheric thickness below the West Alboran and Malaga basins is ~75 km (Mancilla et al., 2015). The southern Alboran margin contains continental crust of the North African margin affected by magmatism (Fig. 10.19c). Lithospheric thickness in this area is >100 km onland (e.g., Torne et al., 2000; Pasyanos and Nyblade, 2007), and we assume a thinning towards the north due to the extensional process that affected the crust (Habibas and Pytheas basins, volcanic intrusions). The crustal thickness of the North African margin is related to the Rif mountain range. While below the Rif, the crust reaches 50 km in thickness, in NE Morocco and NW Algeria it is <30 km thick (e.g., Mancilla and Diaz, 2015) (Fig. 10.4, 10.19d). This crustal distribution must be consequence of the subduction system. The subduction front has an arcuate shape that can be followed through the South Iberian margin (Betic ranges), the Straits of Gibraltar and in NW Morocco (Rif range). No evidences of compressive deformation are found NE Morocco and NW Algeria, where <30 km thick continental crust occurs (e.g., Mancilla and Diaz, 2015).

Between the WAB & MB thin continental crust and the North Africa continental crust domains, the magmatic arc crust is found. Northwards and southwards, it is limited by structural contacts. Towards the north, the magmatic arc crust is in contact with the thin continental crust of the Malaga Basin through the Carboneras Fault (Fig. 10.19c), and towards the south, it is contact with the North African continental crust by the Yusuf Fault (Fig. 10.19c, 10.8g) and the Alboran Ridge Front fault (Fig. 10.8g). These faults system are thus lithospheric scale, juxtaposing two types of crustal domains with different lithospheric thickness. While the lithospheric thickness below the magmatic arc is close to 50 km (Mancilla et al., 2015), it is around 70 km below the WAB and deeper than 70 km in the African margin (Mancilla et al., 2015) (Fig. 10.19c). The distribution of crustal domains is previous to these faults, which become active with current kinematics during the Pliocene, when the convergence between the African and Iberian plates started to define the evolution of the basin. As a consequence, we propose that these faults were nucleated in inherited weak zones, coincident with lithospheric transitions between domains (Fig. 10.19b and c).

Finally, towards the east, magmatic arc crust smoothly transitions to oceanic crust of the Algero-Balearic Basin, where the lithospheric thickness is ~30 km and the crust is < 8 km thick (Fig. 10.19d) (Mancilla et al., 2015; Mancilla and Diaz, 2015).

Figure 10.19 (next pages): *Lithospheric structure of the Alboran Basin.* ***(a)*** *N-S cross section at Langhian-Serravallian (see Figure 10.8b for location).* ***(b)*** *NNW-SSE cross section at Late Tortonian (see Figure 10.8c for location).* ***(c)*** *NNE-SSE cross-section at the present-day (see Figures 10.7a and 10.8f for location).* ***(d)*** *W-E cross-section at the present-day (see Figure 10.7a for location). Present-day lithospheric thickness, slab distribution and Moho depths values are mainly from Torné et al., 2000; Pasyanos and Nyblade, 2007; Díaz et al., 2015; Mancilla et al., 2015, Mancilla and Díaz, 2015, Villaseñor et al., 2015; Díaz et al., 2016a and Díaz et al., 2016b.*

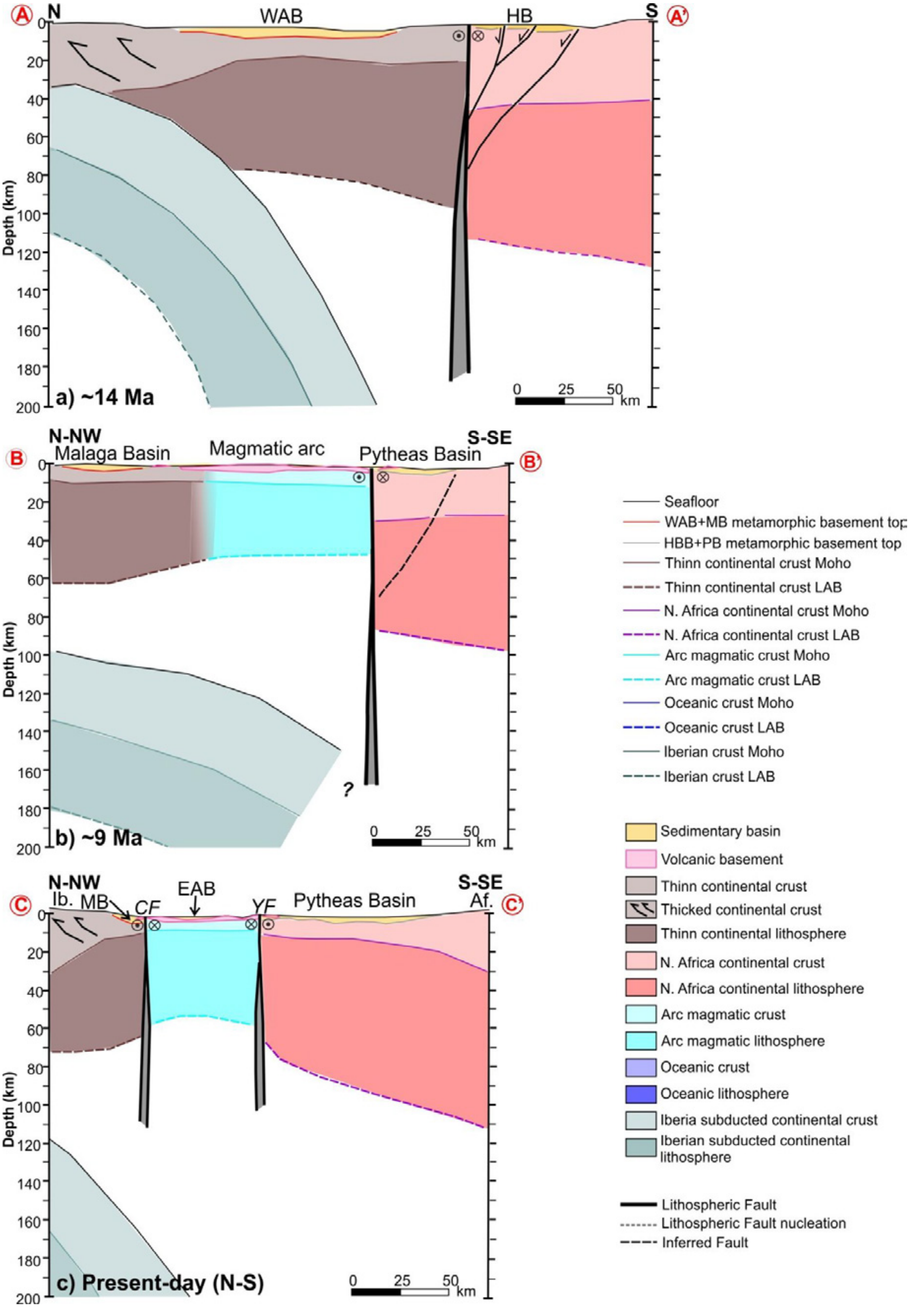
A
N
WAB
HB
S
A'
Depth (km)
0
20
40
60
80
100
120
140
160
180
200
a) ~14 Ma
0 25 50 km
N-NW
Malaga Basin
Magmatic arc
Pytheas Basin
S-SE
B
B'
?
b) ~9 Ma
0 25 50 km
N-NW
Ib.
MB
CF
EAB
YF
Pytheas Basin
S-SE
Af.
C
C'
c) Present-day (N-S)
0 25 50 km
Seafloor
WAB+MB metamorphic basement top
HBB+PB metamorphic basement top
Thinn continental crust Moho
Thinn continental crust LAB
N. Africa continental crust Moho
N. Africa continental crust LAB
Arc magmatic crust Moho
Arc magmatic crust LAB
Oceanic crust Moho
Oceanic crust LAB
Iberian crust Moho
Iberian crust LAB
Sedimentary basin
Volcanic basement
Thinn continental crust
Thicked continental crust
Thinn continental lithosphere
N. Africa continental crust
N. Africa continental lithosphere
Arc magmatic crust
Arc magmatic lithosphere
Oceanic crust
Oceanic lithosphere
Iberia subducted continental crust
Iberian subducted continental lithosphere
Lithospheric Fault
Lithospheric Fault nucleation
Inferred Fault

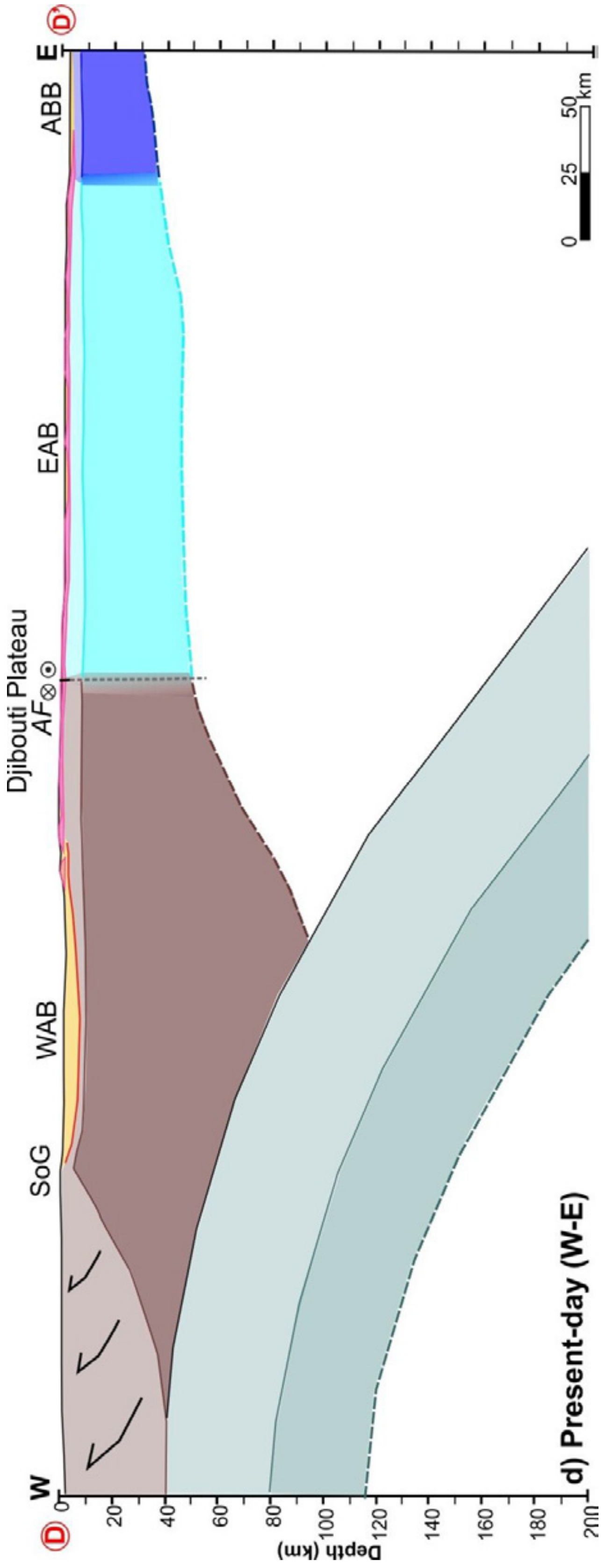
D
W
SoG
WAB
Djibouti Plateau
AF⊗⊙
EAB
ABB
E
D'
d) Present-day (W-E)
Depth (km)
0
20
40
60
80
100
120
140
160
180
200
0
25
50
km

All observations support that the Miocene evolution of the Alboran Basin was controlled by slab roll-back and the dynamics of the subduction system, while the Plio-Quaternary history is influenced by the lithospheric inherited structure in a contractional setting. During the Miocene, slab roll-back and lithosphere tearing lead the extensional processes in the inner part of the Gibraltar Arc System that led to the Alboran Basin formation. In the Messinian, the stress setting changed from this extensional regime to a compressional framework. The end of the extension might not be exactly coetaneous across the entire basin, but it occurred during the Messinian (7.2 – 5.3 Ma) (e.g., Booth-Rea et al., 2004; Giaconia et al., 2014; Krautworst and Brachert, 2003), when occur the first active structures in this new tectonic frame (e.g. the Carboneras Fault, Fig. 10.8e). The Plio-Quaternary contractive reorganization of the basin is not affecting indiscriminately the whole area. Instead, it is concentrated on few tectonic structures, such as the Carboneras Fault, the Al-Idrissi Fault system, the Alboran Ridge Fault and the Yusuf Fault systems (Fig. 10.8g). The location of these faults seems to be conditioned by the lithospheric structure created during the basin opening, as they occur in transitions between main crustal domains.

10.4. In summary

The new seismological projects providing a data grid with regular distribution and surveying both, the South Iberian and the North African margins, represented a qualitative leap in the understanding of the deep structure of the Gibraltar Arc system. New insights confirm the slab distribution below the Gibraltar Arc system and the detachment points, and reveal that the Iberian lithosphere is the one subducting. These results, together with the crustal domains distribution and the basin evolution model presented in this thesis, help to constrain the geodynamic evolution of the area.

Different subduction models have been proposed to explain the Alboran Basin formation. These models can be divided in three main groups: a) a continuous north-dipping slab, b) a discontinuous north-dipping slab, and c) a discontinuous south-dipping slab. In the basis of the most recent results, the most suitable group of models is the discontinuous south-dipping slab. However, none of the discussed geodynamic models can completely explain all recent observations.

Our observations support a 3D model with a south-dipping slab, with a subduction front that retreats northward, and later westward, giving as a result the West Alboran and Malaga fore-arc basins and the magmatic arc. The geometry of the subduction front in Burdigalian times should be coherent with the arcuate shape of the West Alboran and Malaga basins depocenter. Lithospheric faults are needed between the West Alboran and Malaga basins continental crust and the North African continental crust in order to explain their different evolution. The westward migration of the subduction front possibly stopped in the Messinian (7.2 – 5.3 Ma), when the extensional processes ended and contractive deformation took over inside the basin.

The lithospheric structure is now well known, and should be integrated in the evolutionary model of the area. Different lithospheric domains are coexisting in the Alboran Basin. While the Miocene evolution is conditioned by the slab roll-back, the Plio-Quaternary development is determined contraction and reactivation of the inherited lithospheric structuration created during the opening stage.

In the current contractive tectonic setting, initiated in the Pliocene (<5.3 Ma), strain is mainly accommodated in few prominent tectonic structures, such as the Carboneras Fault, the Al-Idrissi Fault, the Alboran Ridge Front fault and the Yusuf Fault. These faults nucleated at the transitions between the different lithospheric domains, as these areas represent the weakest rheological zones of the basin.

Part V

CONCLUSIONS

AND

FORWARD LOOK

"Y luego, sosegada, le contaré, para dormirla,
aventuras de olas, de galeones, de arcabuces, de rumbos marinos,
de lugares vividos y soñados: de lo que fue
y que no fue y que pudo ser mi vida.
Abre tus ojos verdes, Marta, que quiero oír el mar."

Lope, la noche. Marta.
José Hierro (De Agenda, 1991)

Chapter 11

Conclusions

This thesis provides new insights in the formation and deformation of the Alboran Basin. The results shown in this thesis shed light on the geodynamic processes that governed the opening of the Alboran Basin during the Miocene and its later evolution into a compressive setting during the Plio-Quaternary. The most relevant findings of this research are summarized below.

12.1. Final conclusions

1) The Alboran Basin is floored by three different crustal domains: thin continental crust, magmatic arc crust, and North African continental crust. These domains conditioned the later evolution of the depocenters of sub-basins and the location of the present-day active tectonic structures.

2) We presented the first comprehensive seismostratigraphic analysis of the entire Alboran Basin. Based on wells and dredge data, we have performed the correlation of units among the different sub-basins and correlated our proposed stratigraphy with all available previous studies.

3) From the Early Miocene till the Late Miocene, the Alboran Basin was affected by extensional processes fundamentally controlled by the slab dynamics. Extension ceased during the Late Miocene, and since the Pliocene and during the Quaternary the Alboran Basin has been deformed due to the Iberia – Africa tectonic plates convergence. This new stress framework produced the contractive reorganization of the basin, focused on a few first-order structures that act as lithospheric boundaries.

4) Present-day tectonic activity is not widespread along the basin. Instead, it is focused on few active structures, as the Alboran Ridge, Yusuf, and Al-Idrissi fault systems and to a lesser degree the Carboneras fault system. The estimated slip values for the Alboran Ridge and Yusuf fault systems support that the main part of the plate convergence since the Early Pliocene have been accommodated at these two structures.

12.2. Specific conclusions

- *Deep structure*

We have characterized the deep structure of the basin. The TOPOMED-GASSIS multichannel seismic profiles have allowed for the first time a comprehensive study of the crustal configuration of the Alboran Basin with enough resolution to identify different crustal domains and the relationships between them. We have been able to define three different crustal domains coexisting at the Alboran Basin:

(i) Thin continental domain: Composed of metamorphic rocks, it is found below the West Alboran Basin and Malaga Basin. The basement presents thickness variations, being <2 s TWTT under the West Alboran Basin and ~5.5 s TWTT under the Malaga Basin. We propose that they are part of the same crust affected by different degrees of extension. The presence of peridotite outcrops onland together with a high-velocity anomaly following the arcuate shape of the Betic and Rif orogens under the basin and connecting these outcrops (El Moudnib et al., 2015), supports that along this velocity anomaly the crust under the basin is extremely thin, or may even be floored by exhumed mantle.

(ii) Magmatic arc domain: In the central part of the Alboran Basin the crust is made of magmatic intrusions and volcanic constructions. The basins located in this area have a volcanic basement (Late Serravallian? – Tortonian) of ~5 s TWTT thick (~15 km). In the deepest parts, layered reflections are seen, which are interpreted as magmatic layering. All the observations support that this domain was formed during the subduction process and represents the volcanic arc of the system.

(iii) North African continental domain: Offshore Algeria, the crust is defined by a metamorphic basement of >7 s TWTT thick (~19-22 km). Towards the west, below the South Alboran Basin, basement thickness slightly decreases to ~5 s TWTT thick (~14-16 km) and locally volcanic intrusions increase, until forming a basin floored continental crust heavily modified by volcanic activity. We associated this domain with the continental crust of the Africa plate.

The boundaries between these domains can be a smooth transition or a well-defined tectonic boundary.

We interpreted that these domains are the result of the extension. During the subduction process, the crustal characteristics were gradually modified to produce the present-day configuration. The Alboran Basin is mainly formed by a) a fore-arc basin, represented by the West Alboran Basin and the Malaga Basin, b) a magmatic arc, represented by the central and northeaster part of the basin, and c) the North African continental margin basins. The Alboran Basin is not a back-arc basin to the Gibraltar structural arc, since the back-arc basin of the system corresponds to the easternmost Alboran Basin and mainly the Algero Balearic Basin, were extension led to the formation of oceanic crust.

- *Basin evolution*

The different crustal domains found below the basins conditioned the later evolution of the different depocenters of sub-basins. The correlation of the seismostratigraphic units between the depocenters allows us to determine their evolution, at an individual scale and at the scale of the entire basin.

The basin distribution has changed within time. Extensional processes in the back-arc and magmatic activity conditioned the location and evolution of the depocenters. The extensional formation of the Alboran Basin took place between the Burdigalian and the Messinian. Later, during the Pliocene, the basin evolved to a compressive stress regime. Both, the extensional displacement and the later compressional structures provide information to reconstruct the approximate position of the depocenters through time.

The first depocenter found is the West Alboran and Malaga basins, Burdigalian in age. The lack of deformation let us to suggest a vertical subsidence evolutionary model for this depocenter, which we inserted that has migrated at least 300 km to the west above the slab hinge.

The second depocenter identified is formed above the North Africa margin. The Habibas and Pytheas basins were created by strike-slip local tectonics, and were separated of the West Alboran and Malaga basins by a lithospheric strike-slip boundary. This depocenter has remained almost in the same position with respect to the African margin till the Pliocene.

At Late Serravallian – Tortonian, the magmatic activity that led to the magmatic arc formation conditioned the basin evolution. New depocenters were created above the new volcanic basement.

At the Messinian, all the Alboran Basin depocenters were already formed (i.e. the West Alboran, Malaga, Habibas, Pytheas, East Alboran and South Alboran basins). In this period, sedimentation is still conditioned by the basement distribution and presents different characteristics for each depocenter.

The Pliocene is characterized by a change in the stress setting. Extensional processes ended, and the Alboran Basin evolves in a compressive tectonic framework. Main tectonic structures, as the Carboneras Fault, the Yusuf Fault, the Alboran Ridge Front fault and the Al-Idrissi Fault appeared at the boundaries between crustal domains, being still active at the present-day. Plio-Quaternary units are similar for the entire basin, pointing out a general subsidence for the entire basin.

- *Palomares margin*

The Palomares margin includes the northeaster connection between the Alboran Basin and the Algero-Balearic Basin. It presents a complex bathymetry characterized by the presence of highs and deeply eroded submarine canyons between them. It can be divided in (i) the continental shelf, (ii) the continental slope and (iii) the Algero-Balearic Basin. Active processes and tectonic structures present on each area are different, and determine their specific seafloor morphology.

A detailed analysis of the bathymetry together with the MCS profiles support that the geomorphology of this area is mainly driven by erosional and halokinesis processes, while active faults are not clearly identified outside of the uppermost continental slope. The tectonic activity of the structures located off-shore seems to decrease since the Messinian. Due to this observations, we suggest that the nowadays deformation is accommodated by onshore structures.

The sedimentary record of the margin points out an Early Tortonian formation age in relation to the magmatic arc. Extensional processes are identified till the Late Tortonian. Since the Latemost Tortonian, the margins evolved to a compressive regime that produces the reactivation as thrusts and/or strike-slip faults of the previous extensional structures, especially those located in the continental slope.

- *The Yusuf Fault*

The Yusuf Fault is a crustal boundary that puts in touch two different crustal domains: the magmatic arc crust, located north of it, and the North African continental crust, south of the fault. It is a right-lateral strike-slip fault that connects toward the west with the northern Alboran Ridge transpressive fault; and towards the east ends at the Algerian coast.

The observed deformation and the detailed analyses of the Yusuf pull-apart basin sediments allow us to propose a post-Messinian activity for this fault. The first syn-kinematic unit is from the Early Pliocene, and the fault is currently active.

The total slip along the Yusuf Fault has been estimated between 16 and 30 km, which within the uncertainty is enough to accommodate the main part of the Iberian – African convergence since the Messinian time (~24 km).

- *The Alboran Ridge system*

This ridge is part of a heterogeneous structure formed by the Alboran Ridge, the Francesc Pagès, Tofiño and Xauen banks. This variability is understood as result of the combination between the inherited structure, sedimentary basins and igneous highs, and the deformation rates, increasing from west to east. The difference between these highs is the result of strain partitioning by left-lateral strike-slip faults, being the most important is the Al-Idrissi Fault system.

The Alboran Ridge relief is a Plio-Quaternary structure. Three compressional pulses are identified: 1) Early Pliocene (3.28 – 5.33 Ma), 2) Middle Pliocene (2.45 – 3.28 Ma) and 3) Quaternary (from 1.8 Ma till present). Folding and faulting involved the basement and the most recent sediments, so it is still an active structure. Shortening values measured along the Alboran Ridge are not high enough to accommodate the Iberian and African plate convergence since ~5.3 Ma (Messinian top). We propose that this convergence has been accommodated at a deep detachment level. Estimations of the slip needed to created the uplift with a deep detachment provide a total slip of ~20 km. We interpreted that the detachment may be at the Moho level, as it corresponds to the tectonic boundary between the magmatic arc crust, to the north, and the North African margin continental crust, south of it. The accumulated slip implies that has taken most deformation produced by convergence in this region.

- *Geodynamic evolution*

Through the integration of the most recent data, including the results presented in this volume, we have evaluated existing geodynamic models and to enumerate the characteristics that should have a suitable geodynamic model.

recent geophysical results do not support models that propose subduction to the north of the African plate. Only two models (Gelabert et al., 2002; Vergés and Fernàndez, 2012) consider subduction of the Iberia plate towards the south, although these models have not integrated a wealth of recent data.

We conclude that a geodynamic model that explains the origin and evolution of the Alboran Basin integrate subduction a south dipping Iberian slab, that first retreats to the north and later to the west, with an initial geometry of the subduction front able to explain the arcuate geometry of the WAB&MB since Burdigalian times, and with lithospheric faults bounding the active subduction front, so that allow its westward motion juxtaposing different crustal domains during the basin development.

These observations, together with the lithospheric structures, allow us to differentiate two main evolutionary stages:

(i) The opening stage (Miocene), in which the Alboran Basin evolved as an extensional setting, consequence of the westward migration of the subduction front and slab roll-back, and
(ii) The deformational stage (Plio-Quaternary), in which the contractive reorganization of the basin occurred. Slab driven geodynamic processes lose importance and the driving force for the basin evolution is the lithospheric structure in a convergence setting. The boundaries between different lithospheric domains correspond to inherited weak zones that conditioned the location of the main faults accommodating the Iberian and African plates convergence (i.e. Carboneras Fault, Al-Idrissi Fault, CAlboran Ridge Front fault and Yusuf Fault systems).

Chapter 12

Forward look

In this Thesis work, we study the crustal structure, the Miocene formation and the Plio-Quaternary deformation of the Alboran Basin. Previous studies regarding these topics at crustal-scale are scarce and local-scale observations are not always coherent with the results at a basin scale. Focusing on the most important open questions, we propose the following issues to be developed in the future as open and important research questions:

12.1. Lithospheric structure: Crust and upper mantle seismic imaging

Within this work, we performed a crustal domain analysis on the basis of multichannel seismic (MCS) profiles and vintage data available. We have showed the importance of the deep structure to understand basin evolution. Although the MCS give us a relatively high-resolution information along the profile, key where different crustal domains coexist in a small area, the MCS profiles alone cannot totally constraint the nature of the crust. They provide information on the approximate thickness and reflectivity structure, which can be complemented using supplementary information from wells and dredges to better characterize the crust. However, with the objective of unequivocally define the Alboran Basin crustal domains and their boundaries, and as this is a key issue to understand the basin evolution and current configuration, we need to obtain an accurate crustal-scale seismic velocity models. Thus, a seismic refraction study is required in the Alboran Basin in order to accurately define and characterize the different crustal domains.

We proposed the modelling of 1 existing unpublished Wide Angle Seismic (WAS) profile, and the acquisition of 3 new WAS profiles (Fig. 12.1). The existing data is profiles P-01 from the WESTMED project (2006). The resulting velocity model of P-01 has not been obtained yet, and it will shed light in the transition between the magmatic arc crust and the continental crust of the Malaga Basin and North-African margin (profile WAS-1 in Figure 12.1), and in the eastern Alboran Basin configuration and its transition towards the Algero Balearic Basin (profile P-02 in Figure 12.1). A new profile WAS-3 would be the continuation towards the west of existing profile P-02 (Vp model unpublished but available in collaboration with Geomar), imaging the transition between the magmatic arc crust and the thin continental crust below the West Alboran Basin (Fig. 12.1). We propose to acquire this profile almost coincident to TM29 and TM28 MCS profile. The westernmost part of this profile may help to confirm if the western section of the West Alboran Basin is floored by exhumed mantle. To complete this grid, we propose the acquisition of profile WAS-4 (Fig. 12.1), coincident with the TM21 MCS profile, to better constraint the transition between the two continental crusts of the West Alboran and Malaga basins. Finally, the acquisition of profile WAS-5 (Fig. 12.1), coincident with profile TM03 on its southern part, would help us to image the transition between the Malaga Basin continental crust and the arc magmatic crust and, a key point, as it corresponds to the boundary between the magmatic arc crust and the north African continental crust across the Alboran Ridge.

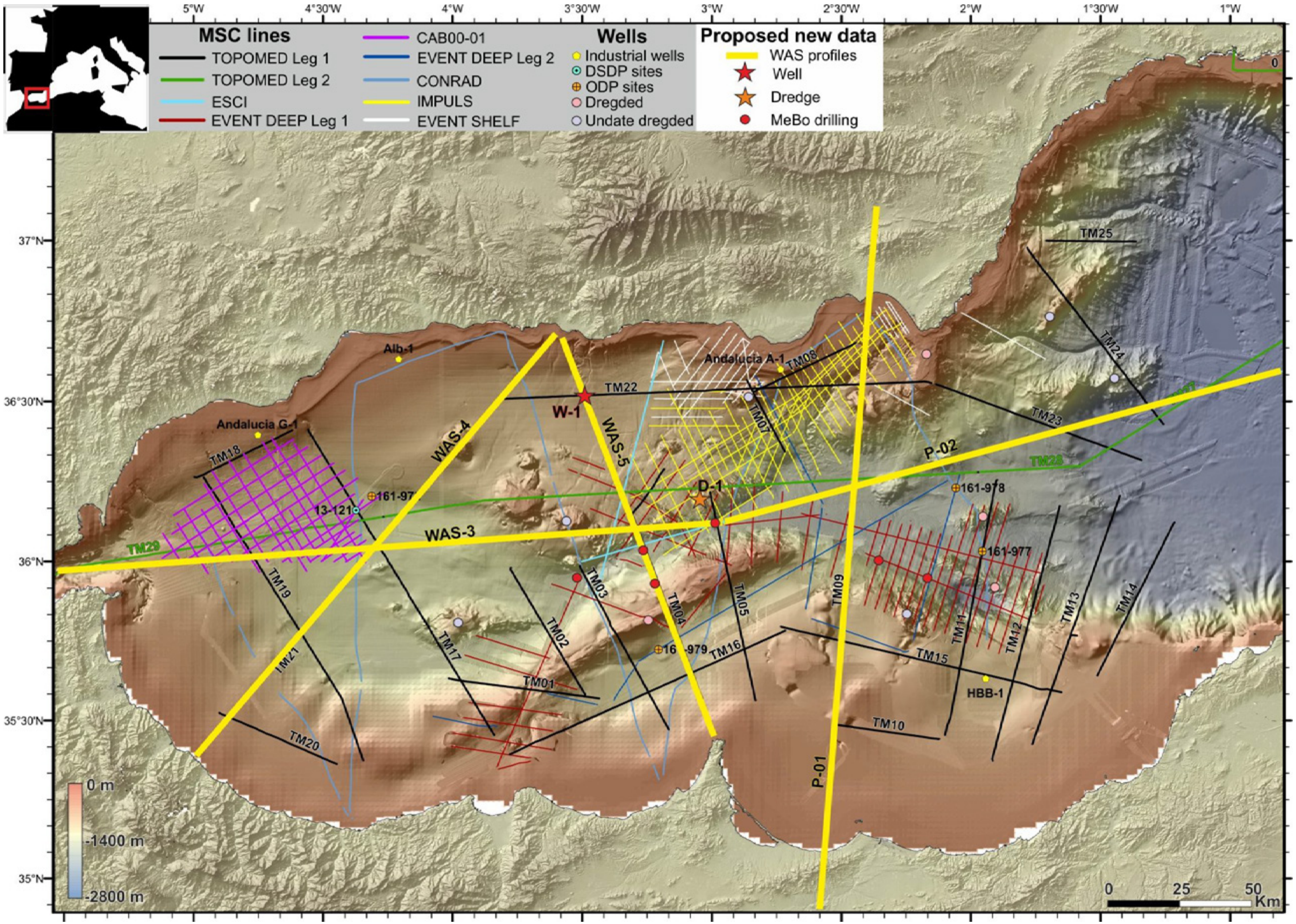
MSC lines
TOPOMED Leg 1
TOPOMED Leg 2
ESCI
EVENT DEEP Leg 1
CAB00-01
EVENT DEEP Leg 2
CONRAD
IMPULS
EVENT SHELF
Wells
Industrial wells
DSDP sites
ODP sites
Dregded
Undate dregded
Proposed new data
WAS profiles
Well
Dredge
MeBo drilling
5°W
4°30'W
4°W
3°30'W
3°W
2°30'W
2°W
1°30'W
1°W
37°N
36°30'N
36°N
35°30'N
35°N
0 m
-1400 m
-2800 m
0
25
50
Km
WAS-3
WAS-4
WAS-5
P-01
P-02
W-1
D-1
Alb-1
Andalucia G-1
Andalucia A-1
HBB-1
161-97
13-121
161-978
161-977
16 -979
TM01
TM02
TM03
TM04
TM05
TM07
TM08
TM09
TM10
TM11
TM12
TM13
TM14
TM15
TM16
TM17
TM18
TM19
TM20
TM21
TM22
TM23
TM24
TM25
TM28
TM29

◄ ***Figure 12.1:*** *Regional bathymetric map of the Alboran Sea constructed from multibeam data acquired during our cruises in the Alboran Sea (Gràcia et al., 2006, 2012), completed with IEO bathymetry (Ballesteros et al., 2008) and released SRTM-3 and GEBCO digital data. Inset: Location of the shown area (red rectangle). Seismic datasets used in this thesis are depicted (see map legend for references) and the ones acquired during the TOPOMED-GASSIS (TM) are labelled. Existing wells and dredged sites are located. The proposed new surveys are depicted: Yellow lines: WAS profiles, red star: new well, orange star: new dredged.*

12.2. Well sites and seafloor sampling data

Rock samples in the area are scarce and not always accessible. Sampling is distributed along the entire basin, an almost all the sub-basins have a drill site to constrain the sedimentary units and inn some cases the nature of the basement. To complete available data we propose a new drill site in the Malaga Basin (W-1 in Figure 12.1), as this is the depocenter with an entire sedimentary sequence since the Burdigalian and with the shallower basement top. This well may also confirm its correlation to the West Alboran Basin, done based only in the MCS images. This well would be located at the intersection between MCS profile TM22 and the proposed WAS-5 profile, as it is the point with the shallower basement and a complete sedimentary sequence. Thus, the results would constrain the seismostratigraphic units defined in the MCS profile and also will help the crustal characterization through the WAS profile.

We also propose to perform additionally sampling in the western Djibouti Plateau area (D-1 in Figure 12.1), where there are not samples, although its volcanic nature seems to be clear from seismic images. Instead of dredges, we propose to use ROVs (Remotely Operated Vehicles), in order to collect a high-quality rock samples using the robotic arm of the ROV. Collected samples would be stored in a basket with a reference number, as well as precise information of their location (i.e. latitude, longitude, depth). With the exception of the CyanAlboran cruise on board the RV Le Suroit (1994) using the submersible Cyana (IFREMER, France) in which direct basement samples were collected, most of the dredges previously acquired have been collected by using sampling devices towed behind the vessel, in which the positioning is approximate and collected samples are mixed in the towed dredge.

However, during the development of this study, the main problem we found related to sediment samples was the difficulty to correlate the information between different wells. Examples are the ODP Leg 161 Sites 978 and 977, easily connected through EVENT-DEEP leg 1 MCS profiles (Fig. 12.2). ODP wells in the area are from 1995. The definition of the main chronostratigraphic series has changed since them, especially for the Quaternary boundary, which has changed from 1.8 Ma (currently the Calabrian stage base, and till 2012 the Neogene – Quaternary boundary) to 2.58 Ma (currently the Gelasian stage base and the Neogene – Quaternary boundary). This can derive in inconsistencies in the age assigned to the different units, especially for the recent most sediment, which have direct consequences in the characterization of the recent most fault activity, and for the seismic and tsunamic hazard estimations. Furthermore, in the case of the HBB-1 well (Medaouri et al., 2014), the proposed time stage and the age in Ma assigned are not coherent (Fig. 12.3).

All this inconsistencies diminish the confidence level in the age assigned to the sedimentary units, and should be resolved in order to obtain an accurate analysis of the sedimentary record of the Alboran Basin, especially for the Plio-Quaternary units that showed the largest variations (Fig. 12.2).

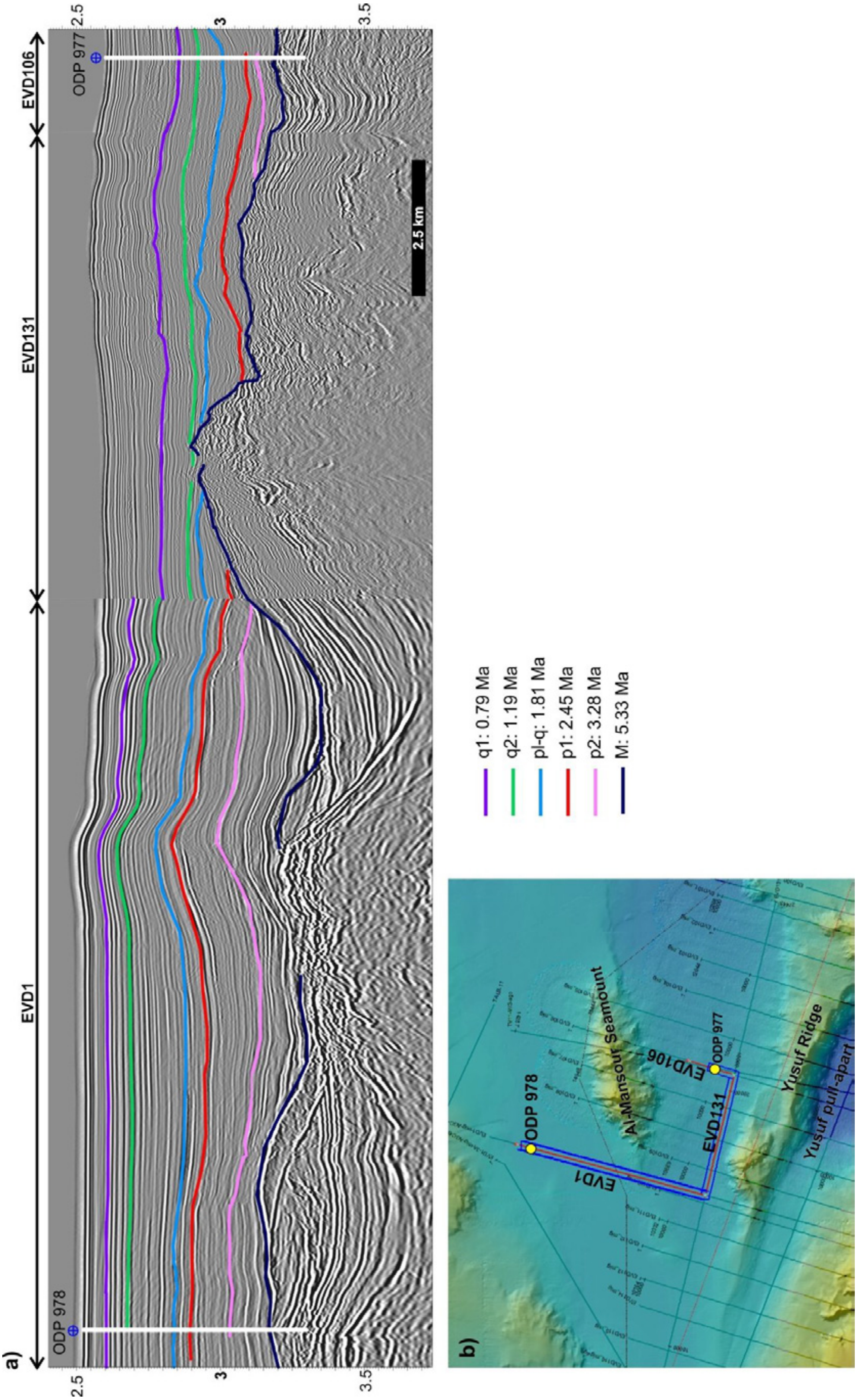

Figure 12.2: ***(a)*** *Seismic section along profiles EVD1, EVD131 and EVD106 showing the inconsistency between the seismostratigraphic units defined at well ODP 978 and ODP 977.* ***(b)*** *Location of the seismic section and the wells.* ***(c)*** *Seismostratigraphic units used (from Martinez-Garcia et al., 2013).*

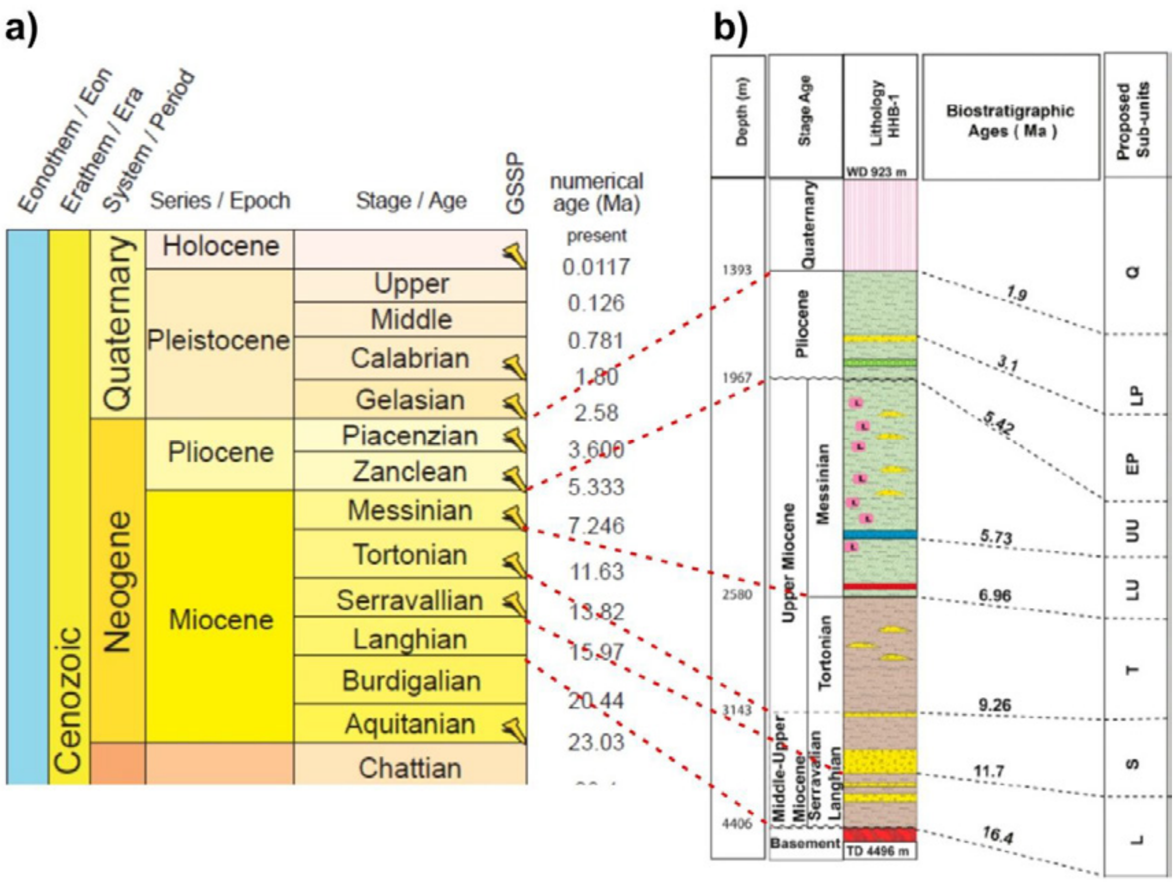

Figure 12.3: ***(a)*** *Chronostratigraphic chart (International Commission on Stratigraphy version 2015), zoomed on the Neogene and Quaternary systems.* ***(b)*** *Stratigraphy of the HBB-1, from Medaouri et al., 2014. The ages defined in the chronostratigraphic chart for the stage limits and the same ages assigned to the stage boundaries at the HBB-1 are not coincident. This supposed an uncertainty in the seismostratigraphy units ages.*

In order to solve the recent most sediment dating, we propose to perform a MeBo drilling survey. This system is able to recover cores till 100 m length from soft and hard sediments <2000 m water depth, and can be operate from a standard research vessel (Freudenthal and Wefer, 2013). We select two areas: The Alboran Channel and the northwester segment of the Yusuf pull-apart basin (due to the water-depth limitation) (Fig. 12.1). In both sections, the sediment age is unconstrained, and it is important for the basin evolution history and the recent tectonic activity linked to the Alboran Ridge Fault and the Yusuf Fault systems.

12.3. Active tectonic structures and their associated seismic and tsunami hazard

Finally, we propose to carry out further the seismic hazard analysis, taking into account the characterization performed in this thesis of two of the main structures in the area, the Yusuf Fault and the Alboran Ridge front thrust. It is imperative to update the seismic hazard prevention plans of the Alboran Sea coastal areas, as they are not considering the offshore structures in their actual importance. Although several geodetic studies reveal the movement across this basin (Koulali et al., 2011; Nocquet, 2012; Echeverria et al., 2013; Echeverria et al., 2015), the low seismicity derived of the slowness of the structures has not highlighted the seismic and tsunamigenic potential of these faults. Due to the recent earthquakes recorded in the region, with magnitude high enough to affect to the near settlement and causing considerable damage, this concept may be changing. Moreover, in spite of the low slip rate of these faults, its seismic potential resides in their large dimensions. Most of them acts as crustal scale boundaries, well oriented in the nowadays stress regime and active. Having into account the considerable depth extend of these faults joined to its horizontal longitude, the maximum earthquake that could be generated in one of this faults has a potential magnitude Mw = 7 – 7.5 (following the empirical relationship proposed by Wesnousky et al., 2008). Their tsunamigenic potential resides in its capacity of modify the sea-floor surface topography, by the own vertical slip of the fault but also triggering mass transport deposits.

Although as far we know a seismic characterization of the Yusuf Fault and the Alboran Ridge have not been performed yet, there are similar studies in the area, as for the Carboneras Fault (e.g., Gràcia et al., 2006; Moreno et al., 2016), the Averroes Fault (Perea et al., 2016) and the Adra Fault (Gràcia et al., 2012). All of them show that the Alboran Basin is an active region, and that events located there may be a seismic and even a tsunamigenic hazard for the region (e.g., Álvarez-Gómez et al., 2011). For that reason, we find important to complete the seismic and tsunami characterisation of the Yusuf Fault and the Alboran Ridge Fault systems. These data will contribute to improve the seismic hazard assessments studies and the earthquake action plan in the coastal areas.

References

Acosta, J., Fontán, A., Muñoz, A., Muñoz-Martín, A., Rivera, J., and Uchupi, E., 2013, The morpho-tectonic setting of the Southeast margin of Iberia and the adjacent oceanic Algero-Balearic Basin: Marine and Petroleum Geology, v. 45, p. 17–41, doi: 10.1016/j.marpetgeo.2013.04.005.

Allaby, M., 2008, Oxford dictionary of Earth Science: Oxford University Press.

Allen, P.A., and Allen, J.R., 2005, Basin Analysis: Principles and Applications: Blackwell Publishing.

Alonso, B., and Maldonado, A., 1992, Plio-Quaternary Margin Growth Patterns in a Complex Tectonic Setting : Northeastern Alboran Sea: Geo-Marine Letters, v. 12, p. 137–143.

Alonso-Chaves, F.M., Andreo, B., Arias, C., Azañón, J.M., and Balanyá, J., 2004, Cordillera Bética y Baleares, in Vera, J.A. ed., Geología de España, IGME, p. 347–464.

Alpert, L.A., Miller, M.S., Becker, T.W., and Allam, A.A., 2013, Structure beneath the Alboran from geodynamic flow models and seismic anisotropy: Journal of Geophysical Research: Solid Earth, v. 118, no. 8, p. 4265–4277, doi: 10.1002/jgrb.50309.

Álvarez-Gómez, J.A., Aniel-Quiroga, Í., González, M., Olabarrieta, M., and Carreño, E., 2011, Scenarios for earthquake-generated tsunamis on a complex tectonic area of diffuse deformation and low velocity: The Alboran Sea, Western Mediterranean: Marine Geology, v. 284, no. 1–4, p. 55–73, doi: 10.1016/j.margeo.2011.03.008.

Alvarez-Marrón, J., 1999, Pliocene to Holocene structure of the Eastern Alboran sea (Western Mediterranean): Proceedings of the Ocean Drilling Program, Scientific Results, Vol. 161, v. 161, p. 345–355.

Amar, N., Khattach, D., Azdimousa, A., Chourak, M., Jabaloy, A., Manar, A., and Amar, M., 2015, Structure and peridotite of Gibraltar arc southern bloc: gravimetric and aeromagnetic evidences: Arabian Journal of Geosciences, v. 8, no. 11, p. 9801–9813, doi: 10.1007/s12517-015-1879-3.

Ammar, A., Mauffret, A., Gorini, C., and Jabour, H., 2007, The tectonic structure of the Alboran margin of Morocco: Revista de la Sociedad Geológica de España, v. 20, p. 247–272.

Andeweg, B., and Cloetingh, S., 2001, Evidence for an active sinistral shear zone in the western Alboran region: Terra, v. 13, p. 44–50.

Aparicio, A., Mitjavila, J.M., Araña, V., and Villa, I.M., 1991, La edad del volcanismo de las islas Columbrete Grande y Alborán (Mediterráneo occidental): Boletín Geológico Minero, v. 102, no. 4, p. 562–570.

Ayarza, P., Carbonell, R., Teixell, A., Palomeras, I., Marti, D., Kchikach, A., Harnafi, M., Levander, A., Gallart, J., Arboleya, M.L., Alcalde, J., Fernandez, M., Charroud, M., and Amrhar, M., 2014, Crustal thickness and velocity structure across theMoroccan Atlas fromlong offset wide-angle reflection seismic data: The SIMA experiment: Geochemistry, Geophysics, Geosystems, v. 15, p. 1698–1717, doi: 10.1002/2013GC005164.Received.

Ayarza, P., Palomeras, I., Carbonell, R., Afonso, J.C., and Simancas, F., 2010, A wide-angle upper mantle reflector in SW Iberia: Some constraints on its nature: Physics of the Earth and Planetary Interiors, v. 181, no. 3–4, p. 88–102, doi: 10.1016/j.pepi.2010.05.004.

Azañón, J.M., Crespo-Blanc, A., and García-Dueñas, V., 1997, Continental collision, crustal thinning and nappe forming during the pre-Miocene evolution of the Alpujarride Complex (Alboran Domain: Journal of Structural Geology, v. 19, no. 8, p. 1055–1071.

Badji, R., Charvis, P., Bracene, R., Galve, a., Badsi, M., Ribodetti, a., Benaissa, Z., Klingelhoefer, F., Medaouri, M., and Beslier, M.-O., 2015, Geophysical evidence for a transform margin offshore Western Algeria: a witness of a subduction-transform edge propagator? Geophysical Journal International, v. 200, p. 1027–1043, doi: 10.1093/gji/ggu454.

Balanyá, J.C., Crespo-Blanc, A., Díaz Azpiroz, M., Expósito, I., and Luján, M., 2007, Structural trend line pattern and strain partitioning around the Gibraltar Arc accretionary wedge: Insights as to the mode of orogenic arc building: Tectonics, v. 26, no. 2, doi: 10.1029/2005TC001932.

Ballesteros, M., Rivera, J., Muñoz, A., Muñoz-Martín, A., Acosta, J., Carbó , A., Uchupi, E., 2008, Alboran Basin, southern Spain – Part II: Neogene tectonic implications for the orogenic float model. Mar. Petr. Geol, 25, 75–101.

Barcos, L., Balanyá, J.C., Díaz-Azpiroz, M., Expósito, I., and Jiménez-Bonilla, A., 2015, Kinematics of the Torcal Shear Zone: Transpressional tectonics in a salient-recess transition at the northern Gibraltar Arc: Tectonophysics, v. 663, p. 62–77, doi: 10.1016/j.tecto.2015.05.002.

Bartolome, R., Gracia, E., Stich, D., Martinez-Loriente, S., Klaeschen, D., de Lis Mancilla, F., Lo Iacono, C., Danobeitia, J.J., and Zitellini, N., 2012, Evidence for active strike-slip faulting along the Eurasia-Africa convergence zone: Implications for seismic hazard in the southwest Iberian margin: Geology, v. 40, no. 6, p. 495–498, doi: 10.1130/G33107.1.

Basile, C., and Brun, J.P., 1999, Transtensional faulting patterns ranging from pull-apart basins to transform continental margins: An experimental investigation: Journal of Structural Geology, v. 21, no. 1, p. 23–37, doi: 10.1016/S0191-8141(98)00094-7.

Bécel, A., Laigle, M., de Voogd, B., Hirn, A., Taymaz, T., Galvé, A., Shimamura, H., Murai, Y., Lépine, J.C., Sapin, M., and Özalaybey, S., 2009, Moho, crustal architecture and deep deformation under the North Marmara Trough, from the SEISMARMARA Leg 1 offshore-onshore reflection-refraction survey: Tectonophysics, v. 467, no. 1–4, p. 1–21, doi: 10.1016/j.tecto.2008.10.022.

Bendel, V., Fouquetl, Y., Auzende, J.-M., Lagabrielle, Y., Grimaud, D., and Urabe, T., 1993, The white lady hydrothermal field north Fiji Back-arc basin, southwest pacific: Geology, v. 88, p. 2237–2249.

Bernard, S., Avouac, J., and Simoes, M., 2007, Kinematics of fault-related folding derived from a sandbox experiment: v. 112, no. 1, p. 1–24, doi: 9.929/2005JB004149.

Berndt, T., Ruiz-Martínez, V.C., and Chalouan, A., 2014, New constraints on the evolution of the Gibraltar Arc from palaeomagnetic data of the Ceuta and Beni Bousera peridotites (Rif, northern Africa): Journal of Geodynamics, v. 84, p. 19–39, doi: 10.1016/j.jog.2014.09.014.

Bezada, M.J., Humphreys, E.D., Toomey, D.R., Harnafi, M., Dávila, J.M., and Gallart, J., 2013, Evidence for slab rollback in westernmost Mediterranean from improved upper mantle imaging: Earth and Planetary Science Letters, v. 368, p. 51–60, doi: 10.1016/j.epsl.2013.02.024.

Billi, A., Faccenna, C., Bellier, O., Minelli, L., Neri, G., Piromallo, C., Presti, D., Scrocca, D., and Serpelloni, E., 2011, Recent tectonic reorganization of the Nubia-Eurasia convergent boundary heading for the closure of the western Mediterranean: Bulletin de la Societe Geologique de France, v. 182, no. 4, p. 279–303, doi: 10.2113/gssgfbull.182.4.279.

Blanco, M.J., and Spakman, W., 1993, The P-wave velocity structure of the mantle below the Iberian Peninsula: evidence for subducted lithosphere below southern Spain: Tectonophysics, v. 221, no. 1, p. 13–34, doi: 10.1016/0040-1951(93)90025-F.

Bonatto, L., Schimmel, M., Gallart, J., and Morales, J., 2015, The upper-mantle transition zone beneath the Ibero-Maghrebian region as seen by teleseismic Pds phases: Tectonophysics, v. 663, p. 212–224, doi: 10.1016/j.tecto.2015.02.002.

Bonnin, M., Nolet, G., Villaseñor, A., Gallart, J., and Thomas, C., 2014, Multiple-frequency tomography of the upper mantle beneath the African/Iberian collision zone: Geophysical Journal International, v. 198, no. 3, p. 1458–1473, doi: 10.1093/gji/ggu214.

Booth-Rea, G., Azañón, J.M., and García-Dueñas, V., 2004, Extensional tectonics in the northeastern Bethics (SE Spain): Case study of extension in a multilayered upper crust with contrasting rheologies: Journal of Structural Geology, v. 26, no. 11, p. 2039–2058, doi: 10.1016/j.jsg.2004.04.005.

Booth-Rea, G., Azañón, J.M., Martínez-Martínez, J.M., Vidal, O., García-Dueñas, V., 2005. Contrasting structural and P-T evolution of tectonic units in the southeastern Betics: Key for understanding the exhumation of the Alboran Domain HP/LT crustal rocks (western Mediterranean). Tectonics 24, 1–23. doi:10.1029/2004TC001640.

Booth-Rea, G., Ranero, C.R., Martínez-Martínez, J.M., and Grevemeyer, I., 2007, Crustal types and Tertiary tectonic evolution of the Alborán sea, western Mediterranean: Geochemistry, Geophysics, Geosystems, v. 8, no. 10, doi: 10.1029/2007GC001639.

Booth-Rea, G., Martínez-Martínez, J.M., and Giaconia, F., 2015, Continental subduction, intracrustal shortening, and coeval upper-crustal extension: P-T evolution of subducted south Iberian paleomargin metapelites (Betics, SE Spain): Tectonophysics, v. 663, p. 122–139, doi: 10.1016/j.tecto.2015.08.036.

Bourgois, J., Mauffret, A., Ammar, A., and Demnati, A., 1992, Multichannel Seismic data imaging of inversion tectonics of the Alboran Ridge (Western Mediterranean Sea): Geo-Marine Letters, v. 12, p. 117–122.

Bousquet, J.C., 1979. Quaternary strike-slip faults in southeastern spain. Tectonophysics 52, 277–286. doi:10.1016/0040-1951(79)90232-4.

Bouyahiaoui, B., Sage, F., Abtout, A., Klingelhoefer, F., Yelles-Chaouche, K., Schnürle, P., Marok, A., Déverchère, J., Arab, M., Galve, A., and Collot, J.Y., 2015, Crustal structure of the eastern Algerian continental margin and adjacent deep basin: Implications for late Cenozoic geodynamic evolution of the western Mediterranean: Geophysical Journal International, v. 201, no. 3, p. 1912–1938, doi: 10.1093/gji/ggv102.

Braga, J.C., Comas, M.C., 1999. Environmental significance of an uppermost Pliocene carbonate debris flow at Site 978. In Zahn, R., Comas, M.C., and Klaus, A. (Eds.), Proc. ODP, Sci. Results, 161: College Station, TX (Ocean Drilling Program), 77–81. doi:10.2973/odp.proc.sr.161.209.1999.

Brooymans, R., Mojesky, T., and Pham, L., 2003, A Review of Current Marine Demultiple Techniques with Examples from the East Coast of Canada: v. 1, no. c, p. 1–7.

Buforn, E., Bezzeghoud, M., Udías, A., Pro, C., 2004. Seismic Sources on the Iberia-African Plate Boundary and their Tectonic Implications. Pure Appl. Geophys. 161, 623–646. doi:10.1007/s00024-003-2466-1.

Bulnes, M., and Poblet, J., 1999, Estimating the detachment depth in cross sections involving detachment folds: Geological Magazine, v. 136, no. 2, p. 395–412, doi: 9.917/S0016756899002794.

Calvert, A., Sandvol, E., Seber, D., Barazangi, M., Roecker, S., Mourabit, T., Vidal, F., Algualcil, G., and Jabour, N., 2000, Geodynamic evolution of the lithosphere and upper mantle beneath the Alboran region of the western Mediterranean: Constraints from travel time tomography: Journ, v. 105, no. B5, p. 10871–10898.

Calvert, A.J., 2011, The seismic structure of Island Arc crust, in Brown, D. and Ryan, P.D. eds., Arc-Continent Collision, Springer-Verlat Berlin Heidelberg, p. 493.

Camerlenghi, A., Accettella, D., Costa, S., Lastras, G., Acosta, J., Canals, M., and Wardell, N., 2009, Morphogenesis of the SW Balearic continental slope and adjacent abyssal plain, Western Mediterranean Sea: International Journal of Earth Sciences, v. 98, no. 4, p. 735–750, doi: 10.1007/s00531-008-0354-8.

Cameselle, A.L., and Urgeles, R., 2017, Large-scale margin collapse during Messinian early sea-level drawdown: The SW Valencia trough, NW Mediterranean: Basin Research, v. 29, p. 576–595, doi: 10.1111/bre.12170.

Campos, J., Maldonado, A., and Campillo, a. C., 1992, Post-Messinian evolutional patterns of the central Alboran Sea: Geo-Marine Letters, v. 12, no. 2–3, p. 173–178, doi: 10.1007/BF02084929.

Carminati, E., Wortel, M.J.R., Spakman, W., and Sabadini, R., 1998, The role of slab detachment processes in the opening of the western-central Mediterranean basins: Some geological and geophysical evidence: Earth and Planetary Science Letters, v. 160, no. 3–4, p. 651–665, doi: 10.1016/S0012-821X(98)00118-6.

Carminati, E., Lustrino, M., and Doglioni, C., 2012, Geodynamic evolution of the central and western Mediterranean: Tectonics vs. igneous petrology constraints: Tectonophysics, v. 579, p. 173–192, doi: 10.1016/j.tecto.2012.01.026.

Cartigny, M.J.B., Postma, G., Van Den Berg, J.H., Mastbergen, D.R., 2011. A comparative study of sediment waves and cyclic steps based on geometries, internal structures and numerical modeling. Mar. Geol. 280, 40–56. doi:10.1016/j.margeo.2010.11.006.

Chalot-Prat, F., and Girbacea, R., 2000, Partial delamination of continental mantle lithosphere, uplift-related crust-mantle decoupling, volcanism and basin formation: A new model for the Pliocene-Quaternary evolution of the Southern East-Carpathians, Romania: Tectonophysics, v. 327, no. 1–2, p. 83–107, doi: 10.1016/S0040-1951(00)00155-4.

Chalouan, A., Saji, R., Michard, A., and Bally, A.W., 1997, Neogene tectonic evolution of the southwestern Alboran basin as inferred from seismic data off morocco: AAPG Bulletin, v. 81, 7, p. 1161–1184.

Chalouan, A., and Michard, A., 2004, The Alpine Rif Belt (Morocco): A Case of Mountain Building in a Subduction-Subduction-Transform Fault Triple Junction: Pure and Applied Geophysics, 161, doi: 10.1007/s00024-003-2460-7.

Chalouan, A., Michard, A., El Kadiri, K., Negro, F., Frizon de Lamotte, D., Soto, J.I., and Saddiqi, O., 2009, The Rif Belt, in Continental Evolution: The Geology of Morocco. Lecture Notes in Earth Sciences, Springer-Verlat Berlin Heidelberg.

Chertova, M. V., Spakman, W., Geenen, T., van den Berg, A.P., and van Hinsbergen, D.J.J., 2014a, Underpinning tectonic reconstruction of the western Mediterranean region with dynamic slab evolution from 3-D numerical modeling: Journal of Geophysical Research, v. 119, p. 1–26, doi: 10.1002/2013JB010500.Received.

Chertova, M. V., Spakman, W., van den Berg, A.P., and van Hinsbergen, D.J.J., 2014b, Absolute plate motions and regional subduction evolution: Geochemistry, Geophysics, Geosystems, p. 1–13, doi: 10.1002/2014GC005494.

Christensen, N.I., Mooney, W.D., and Christensen, N.I., Mooney, W.D., 1995, Seismic velocity structure and composition of the continental crust: A global view: Journal of Geophysical Research: Solid Earth (1978–2012), v. 100, no. B6, p. 9761–9788, doi: 10.1029/95JB00259.

CIESM, 2008. The Messinian Salinity Crisis from mega-deposits to microbiology - A consensus report. No. 33. CIESM Workshop Monographs, Monaco, 168 pp.

Clauzon, G., Suc, J., Gautier, F., Berger, A., and Loutre, M., 1996, Alternate interpretation of the Messinian salinity crisis : Controversy resolved ? Alternate interpretation of the Messinian salinity crisis : Controversy resolved ? The Geological Society of America, v. 846, no. August 2015, p. 363–366, doi: 10.1130/0091-7613(1996)024<0363.

Comas, M.C., García-Dueñas, V., and Jurado, M.J., 1992, Neogene Tectonic Evolution of the Alboran Sea from MCS Data: , p. 157–164.

Comas, M.C., Dañobeitia, J.J., Álvarez-Marrón, J., and Soto, J.I., 1995, Crustal reflections and structure in the Alborán basin: preliminary results of the ESCI-Alborán survey: Rev. Soc. Geol. España, v. 8 (4), p. 529–542.

Comas, M.C., Zahn, R., and Klaus, A., et al., 1996. Proc. ODP, Init. Repts., 161: College Station, TX (Ocean Drilling Program). doi:10.2973/odp.proc.ir.161.1996

Comas, M.C., Platt, J.P., Soto, J.I., and Watts, A.B., 1999, 44. The origin and tectonic history of the Alboran Basin: Insights from leg 161 results: Proceedings of the Ocean Drilling Program, Scientific Results, v. 161, p. 555–580.

Comas, M.C., and Soto, J.I., 1999, Brittle deformation in the metamorphic basement at Site 976: implications for middle Miocene extensional tectonics in the Western Alboran Basin: Proceedings of the Ocean Drilling Program, 161 Scientific Results, v. 161, p. 331–344, doi: 10.2973/odp.proc.sr.161.225.1999.

Comas, M., Talukder, A., Woodside, J., Volkonskaya, A., 2000. V. 3. South Balearic Basin: The Palomares and Mazarrón margin. V.3.1. Seismic data. Multidisciplinary Study of Geological Processes on the North East Atlantic and Western Mediterranean Margin ICO Technical Series No. 56, UNESCO 2000, 91-95.

Comas, M., Ivanov, M., 2006. II.4. The Palomares and Cartagena margins. Interdisciplinary Geoscience Studies of the Gulf of Cadiz and the Western Mediterranean Basins. IOC Technical Series No. 70, UNESCO, 2006, 55-56.

Cox, A., and Hart, R.B., 1986, Plate Tectonics: How it works: Wiley-Blackwell.

Crespo-Blanc, A., and Frizon de Lamotte, D.F., 2006, Structural evolution of the external zones derived from the Flysch trough and the South Iberian and Maghrebian paleomargins around the Gibraltar arc: A comparative study: Bulletin de la Societe Geologique de France, v. 177, no. 5, p. 267–282, doi: 10.2113/gssgfbull.177.5.267.

Crespo-Blanc, A., Comas, M., and Balanyá, J.C., 2016, Clues for a Tortonian reconstruction of the Gibraltar Arc: Structural pattern, deformation diachronism and block rotations: Tectonophysics, v. 683, p. 308–324, doi: 10.1016/j.tecto.2016.05.045.

d'Acremont, E., Gutscher, M.A., Rabaute, A., Mercier de Lépinay, B., Lafosse, M., Poort, J., Ammar, A., Tahayt, A., Le Roy, P., Smit, J., Do Couto, D., Cancouët, R., Prunier, C., Ercilla, G., et al., 2014, High-resolution imagery of active faulting offshore Al Hoceima, Northern Morocco: Tectonophysics, v. 632, p. 160–166, doi: 10.1016/j.tecto.2014.06.008.

Dae, M., Avouac, J., Charreau, J., and Shan, T., 2007, Modeling the shortening history of a fault tip fold using structural and geomorphic records of deformation: v. 112, p. 1–19, doi: 9.929/2006JB004460.

Dash, R., Spence, G., Hyndman, R., Grion, S., Wang, Y., and Ronen, S., 2009, Wide-area imaging from OBS multiples: Geophysics, v. 74, no. 6, p. Q41–Q47, doi: 10.1190/1.3223623.

De Larouzière, F.D., Bolze, J., Bordet, P., Hernandez, J., Montenat, C., and Ott d'Estevou, P., 1988, The Betic segment of the lithospheric Trans-Alboran shear zone during the Late Miocene: Tectonophysics, v. 152, no. 1–2, p. 41–52, doi: 9.916/0040-1951(88)90028-5.

DeMets, C., Gordon, R.G., and Argus, D.F., 2010, Geologically current plate motions: Geophysical Journal International, v. 181, no. 1, p. 1–80, doi: 10.1111/j.1365-246X.2009.04491.x.

Dewey, J.F., 1988, Extensional collapse of orogens: Tectonics, v. 7, no. 6, p. 1123–1139, doi: 10.1029/TC007i006p01123.

Dewey, J.F., Helman, M.L., Knott, S.D., Turco, E., and Hutton, D.H.W., 1989, Kinematics of the western Mediterranean: Geological Society, London, Special Publications, v. 45, no. 1, p. 265–283, doi: 10.1144/GSL.SP.1989.045.01.15.

Díaz, J., Gallart, J., Morais, I., Silveira, G., Pedreira, D., Pulgar, J.A., Dias, N.A., Ruiz, M., and González-Cortina, J.M., 2015, From the Bay of Biscay to the High Atlas: Completing the anisotropic characterization of the upper mantle beneath the westernmost Mediterranean region: Tectonophysics, v. 663, p. 192–202, doi: 10.1016/j.tecto.2015.03.007.

Díaz, J., Gallart, J., and Carbonell, R., 2016a, Moho topography beneath the Iberian-Western Mediterranean region mapped from controlled-source and natural seismicity surveys: Tectonophysics, v. 692, p. 74–85, doi: 10.1016/j.tecto.2016.08.023.

Díaz, J., Gil, A., Carbonell, R., Gallart, J., and Harnafi, M., 2016b, Constraining the crustal root geometry beneath Northern Morocco: Tectonophysics, v. 689, p. 14–24, doi: 10.1016/j.tecto.2015.12.009.

Dickinson, W.., 1995, Forearc basins, in Busby, J.. and Ingersoll, R.V. eds., Tectonics of sedimentary basins, Blackwell Science, Oxford UK, p. 221–261.

Dietz, R.S., 1961, Continent and Ocean Basin Evolution by Spreading of the Sea Floor: Nature, v. 190, p. 372–373, doi: 10.1038/190854a0.

Do Couto, D., Gorini, C., Jolivet, L., Lebret, N., Augier, R., Gumiaux, C., d'Acremont, E., Ammar, A., Jabour, H., and Auxietre, J.-L., 2016, Tectonic and stratigraphic evolution of the Western Alboran Sea Basin in the last 25Myrs: Tectonophysics, v. 18, p. 14715, doi: 10.1016/j.tecto.2016.03.020.

Docherty, C., and Banda, E., 1995, Evidence for the eastward migration of the Alboran Sea based on regional subsidence analysis: A case for basin formation by delamination of the subcrustal lithosphere?: Tectonics, v. 14, no. 4, p. 804–818.

Duggen, S., Hoernle, K., van den Bogaard, P., Rüpke, L., and Morgan, J.P., 2003, Deep roots of the Messinian salinity crisis.: Nature, v. 422, no. 6932, p. 602–606, doi: 10.1038/nature01553.

Duggen, S., Hoernle, K., van den Bogaard, P., and Harris, C., 2004, Magmatic evolution of the Alboran region: The role of subduction in forming the western Mediterranean and causing the Messinian Salinity Crisis: Earth and Planetary Science Letters, v. 218, no. 1–2, p. 91–108, doi: 10.1016/S0012-821X(03)00632-0.

Duggen, S., Hoernle, K., van den Bogaard, P., and Garbe-Schönberg, D., 2005, Post-collisional transition from subduction-to intraplate-type magmatism in the westernmost Mediterranean: Evidence for continental-edge delamination of subcontinental lithosphere: Journal of Petrology, v. 46, no. 6, p. 1155–1201, doi: 10.1093/petrology/egi013.

Duggen, S., Hoernle, K., Klügel, A., Geldmacher, J., Thirlwall, M., Hauff, F., Lowry, D., and Oates, N., 2008, Geochemical zonation of the Miocene Alborán Basin volcanism (westernmost Mediterranean): geodynamic implications: Contributions to Mineralogy and Petrology, v. 156, no. 5, p. 577–593, doi: 10.1007/s00410-008-0302-4.

Echeverria, A., Khazaradze, G., Asensio, E., Gárate, J., Dávila, J.M., Suriñach, E., 2013. Crustal deformation in eastern Betics from CuaTeNeo GPS network. Tectonophysics 608, 600–612. doi:10.1016/j.tecto.2013.08.020.

Echeverria, A., Khazaradze, G., Asensio, E., and Masana, E., 2015, Geodetic evidence for continuing tectonic activity of the Carboneras fault (SE Spain): Tectonophysics, v. 663, p. 302–309, doi: 10.1016/j.tecto.2015.08.009.

El Bakkali, S., Gourgaud, A., Bourdier, J.L., Bellon, H., and Gundogdu, N., 1998, Post-collision neogene volcanism of the Eastern Rif (Morocco): Magmatic evolution through time: Lithos, v. 45, no. 1–4, p. 523–543, doi: 10.1016/S0024-4937(98)00048-6.

El Moudnib, L., Villaseñor, A., Harnafi, M., Gallart, J., Pazos, A., Serrano, I., Córdoba, D., Pulgar, J.A., Ibarra, P., Himmi, M.M., and Chourak, M., 2015, Crustal structure of the Betic-Rif system, western Mediterranean, from local earthquake tomography: Tectonophysics, v. 643, p. 94–105, doi: 10.1016/j.tecto.2014.12.015.

Epard, J., and Groshong, J., 1993, Excess area and depth to detachment: The American Association of Petroleum Geologists Bulletin, v. 77, no. 8, p. 1291–1302.

Estrada, F., Ercilla, G., and Alonso, B., 1997, Pliocene-Quaternary tectonic-sedimentary evolution of the NE Alboran Sea (SW Mediterranean Sea): Tectonophysics, v. 282, p. 423–442.

Estrada, F., Ercilla, G., Gorini, C., Alonso, B., Vázquez, J.T., García-Castellanos, D., Juan, C., Maldonado, A., Ammar, A., and Elabbassi, M., 2011, Impact of pulsed Atlantic water inflow into the Alboran Basin at the time of the Zanclean flooding: Geo-Marine Letters, v. 31, no. 5–6, p. 361–376, doi: 10.1007/s00367-011-0249-8.

Faccenna, C., Piromallo, C., Crespo-Blanc, A., Jolivet, L., and Rossetti, F., 2004, Lateral slab deformation and the origin of the western Mediterranean arcs: Tectonics, v. 23, no. 1, doi: 10.1029/2002TC001488.

Faccenna, C., Becker, T.W., Auer, L., Billi, A., Boschi, L., Brun, J.P., Capitanio, F.A., Funiciello, F., Horvàth, F., Jolivet, L., Piromallo, C., Royden, L., Rossetti, F., and Serpelloni, E., 2014, Mantle dynamics in the Mediterranean: Reviews of Geophysics, v. 52, p. 283–332, doi: 10.1002/2013RG000444.Received.

Fernández Soler, J., Martínez-Ruiz, F., Akhmanov, G., Akhmetzhanov. A., Stadnitskaya, A., Kozlova, E., Sautkin, A., Mazurenko, L., Ovsyannikov. D, Belenkaya I, Suslova, E., Goncharov., D., 2000. V. 3. South Balearic Basin: The Palomares and Mazarrón margin. V.3.3. Bottom Sampling results. Multidisciplinary Study of Geological Processes on the North East Atlantic and Western Mediterranean Margin ICO Technical Series No. 56, UNESCO 2000, 98-99.

Fernández-Ibáñez, F., Soto, J.I., Zoback, M.D., and Morales, J., 2007, Present-day stress field in the Gibraltar Arc (western Mediterranean): Journal of Geophysical Research, v. 112, no. B8, p. B08404, doi: 10.1029/2006JB004683.

Fichtner, A., and Villaseñor, A., 2015, Crust and upper mantle of the western Mediterranean - Constraints from full-waveform inversion: Earth and Planetary Science Letters, v. 428, p. 52–62, doi: 10.1016/j.epsl.2015.07.038.

Fowler, C.M.R., 2005, The Solid Earth: An introduction to global geophysics: Eos, Transactions American Geophysical Union, v. 72, no. 40, p. 427–427, doi: 10.1029/90EO00309.

Frizon de Lamotte, D., Raulin, C., Mouchot, N., Wrobel-Daveau, J.-C., Blanpied, C., and Ringenbach, J.-C., 2011, The southernmost margin of the Tethys realm during the Mesozoic and Cenozoic: Initial geometry and timing of the inversion processes: Tectonics, v. 30, no. 3, doi: 10.1029/2010TC002691.

Fuller, C.W., Willett, S.D., and Brandon, M.T., 2006, Formation of forearc basins and their influence on subduction zone earthquakes: Geology, v. 34, no. 2, p. 65–68, doi: 10.1130/G21828.1.

Galindo-Zaldivar, J., Gil, A.J., Sanz de Galdeano, C., Lacy, M.C., García-Armenteros, J.A., Ruano, P., Ruiz, A.M., Martínez-Martos, M., and Alfaro, P., 2015, Active shallow extension in central and eastern Betic Cordillera from CGPS data: Tectonophysics, v. 663, p. 290–301, doi: 10.1016/j.tecto.2015.08.035.

Garate, J., Martin-Davila, J., Khazaradze, G., Echeverria, A., Asensio, E., Gil, A.J., de Lacy, M.C., Armenteros, J.A., Ruiz, A.M., Gallastegui, J., Alvarez-Lobato, F., Ayala, C., Rodríguez-Caderot, G., Galindo-Zaldívar, J., et al., 2015, Topo-Iberia project: CGPS crustal velocity field in the Iberian Peninsula and Morocco: GPS Solutions, v. 19, no. 2, p. 287–295, doi: 10.1007/s10291-014-0387-3.

García Mayordomo, J., 2005. Caracterización y análisis de la peligrosidad sísmica en el sureste de España. Doctoral Thesis, Universidad Complutense de Madrid. 372 pages.

Garcia-Castellanos, D., Estrada, F., Jiménez-Munt, I., Gorini, C., Fernàndez, M., Vergés, J., and De Vicente, R., 2009, Catastrophic flood of the Mediterranean after the Messinian salinity crisis.: Nature, v. 462, no. 7274, p. 778–781, doi: 10.1038/nature08555.

Garcia-Castellanos, D., and Villaseñor, A., 2011, Messinian salinity crisis regulated by competing tectonics and erosion at the Gibraltar arc: Nature, v. 480, no. 7377, p. 359–363, doi: 10.1038/nature10651.

García-Dueñas, V., Balanyá, J.C., and Martínez-Martínez, J.M., 1992, Miocene extensional detachments in the outcropping basement of the northern Alboran Basin (Betics) and their tectonic implications: Geo-Marine Letters, v. 12, no. 2, p. 88–95, doi: 10.1007/BF02084917.

Garrido, C.J., Gueydan, F., Booth-Rea, G., Precigout, J., Hidas, K., Padrón-Navarta, J.A., and Marchesi, C., 2011, Garnet lherzolite and garnet-spinel mylonite in the Ronda peridotite: Vestiges of Oligocene backarc mantle lithospheric extension in the western Mediterranean: Geology, v. 39, no. 10, p. 927–930, doi: 10.1130/G31760.1.

Gaullier, V., Vendeville, B.C., 2005. Salt tectonics driven by sediment progradation: Part II - Radial spreading of sedimentary lobes prograding above salt. AAPG Bulletin 89, 1081-1089.

Gelabert, B., Sàbat, F., and Rodríguez-Perea, A., 2002, A new proposal for the late Cenozoic geodynamic evolution of the western Mediterranean: Terra Nova, v. 14, no. i, p. 93–100.

Giaconia, F., Booth-Rea, G., Martínez-Martínez, J.M., Azañón, J.M., Pérez-Peña, J. V., 2012. Geomorphic analysis of the Sierra Cabrera, an active pop-up in the constrictional domain of conjugate strike-slip faults: The Palomares and Polopos fault zones (eastern Betics, SE Spain). Tectonophysics 580, 27–42. doi:10.1016/j.tecto.2012.08.028.

Giaconia, F., Booth-Rea, G., Martínez-Martínez, J.M., Azañón, J.M., Pérez-Romero, J., Villegas, I., 2013. Mountain front migration and drainage captures related to fault segment linkage and growth: The Polopos transpressive fault zone (southeastern Betics, SE Spain). J. Struct. Geol. 46, 76–91. doi:10.1016/j.jsg.2012.10.005.

Giaconia, F., Booth-Rea, G., Martínez-Martínez, J.M., Azañõn, J.M., Storti, F., and Artoni, A., 2014, Heterogeneous extension and the role of transfer faults in the development of the southeastern Betic basins (SE Spain): Tectonics, v. 33, no. 12, p. 2467–2489, doi: 10.1002/2014TC003681.

Giaconia, F., Booth-Rea, G., Ranero, C.R., Gràcia, E., Bartolome, R., Calahorrano, A., Lo Iacono, C., Vendrell, M.G., Cameselle, A.L., Costa, S., Gómez de la Peña, L., Martínez-Loriente, S., Perea, H., and Viñas, M., 2015, Compressional tectonic inversion of the Algero-Balearic basin: Latemost Miocene to present oblique convergence at the Palomares margin (Western Mediterranean): Tectonics, v. 34, no. 7, p. 1516–1543, doi: 10.1002/2015TC003861.

Gil, A., Gallart, J., Diaz, J., Carbonell, R., Torne, M., Levander, A., and Harnafi, M., 2014, Crustal structure beneath the Rif Cordillera, North Morocco, from the RIFSIS wide-angle reflection seismic experiment: Geochemistry, Geophysics, Geosystems, v. 15, no. 12, p. 4712–4733, doi: 10.1002/2014GC005485.

Gill, J.B., 1981, Orogenic andesites and plate tectonics: Springer-Verlag, New York.

Gill, R.C.O., Aparicio, A., El Azzouzi, M., Hernandez, J., Thirlwall, M.F., Bourgois, J., and Marriner, G.F., 2004, Depleted arc volcanism in the Alboran Sea and shoshonitic volcanism in Morocco: Geochemical and isotopic constraints on Neogene tectonic processes: Lithos, v. 78, no. 4, p. 363–388, doi: 10.1016/j.lithos.2004.07.002.

Gokaşan, E., Ustaömer, T., Gazioğlu, C., Yucel, Z.Y., Öztürk, K., Tur, H., Ecevitoğlu, B., and Tok, B., 2003, Morpho-tectonic evolution of the Marmara Sea inferred from multi-beam bathymetric and seismic data: Geo-Marine Letters, v. 23, no. 1, p. 19–33, doi: 10.1007/s00367-003-0120-7.

Gómez de la Peña, L., Gràcia, E., Muñoz, A., Acosta, J., Gómez-Ballesteros, M., R. Ranero, C., and Uchupi, E., 2016, Geomorphology and Neogene tectonic evolution of the Palomares continental margin (Western Mediterranean): Tectonophysics, v. 689, p. 25–39, doi: 10.1016/j.tecto.2016.03.009.

Gonzalez-Castillo, L., Galindo-Zaldivar, J., de Lacy, M.C., Borque, M.J., Martinez-Moreno, F.J., García-Armenteros, J.A., and Gil, A.J., 2015, Active rollback in the Gibraltar Arc: Evidences from CGPS data in the western Betic Cordillera: Tectonophysics, v. 663, p. 310–321, doi: 10.1016/j.tecto.2015.03.010.

Gonzalez-Mieres, R., and Suppe, J., 2006, Relief and shortening in detachment folds: v. 28, p. 1785–1807, doi: 9.916/j.jsg.2006.07.001.

Govers, R., and Wortel, M.J.R., 2005, Lithosphere tearing at STEP faults: Response to edges of subduction zones: Earth and Planetary Science Letters, v. 236, no. 1–2, p. 505–523, doi: 10.1016/j.epsl.2005.03.022.

Gràcia, E., Ondréas, H., and Bendel, V., 1994, Multi-scale morphologic variability of the North Fiji Basin ridge (Southwest Pacific): Marine Geology, v. 116, no. 1–2, p. 133–151, doi: 10.1016/0025-3227(94)90173-2.

Gràcia, E., Dañobeitia, J.J., Vergés, J., and Parsifal Team, 2003a, Mapping active faults offshore Portugal (38ºN-36ºN): Implications for seismic hazard assessment along the southwest Iberian Margin: Geology, 31, 83-86.

Gràcia, E., Dañobeitia, J., Vergés, J., and Bartolome, R., 2003b, Crustal Architecture & Tectonic Evolution of the Gulf of Cadiz (SW Iberian Margin) at the Convergence of the Eurasian & African Plates: Tectonics, v. 22, no. 4, p. 1–18, doi: 10.1029/2001TC901045.

Gràcia, E., Pallàs, R., Soto, J.I., Comas, M., Moreno, X., Masana, E., Santanach, P., Diez, S., García, M., and Dañobeitia, J., 2006, Active faulting offshore SE Spain (Alboran Sea): Implications for earthquake hazard assessment in the Southern Iberian Margin: Earth and Planetary Science Letters, v. 241, no. 3–4, p. 734–749, doi: 10.1016/j.epsl.2005.11.009.

Gràcia, E., Vizcaino, A., Escutia, C., Asioli, A., Rodés, Á., Pallàs, R., Garcia-Orellana, J., Lebreiro, S., and Goldfinger, C., 2010, Holocene earthquake record offshore Portugal (SW Iberia): testing turbidite paleoseismology in a slow-convergence margin: Quaternary Science Reviews, v. 29, no. 9–10, p. 1156–1172, doi: 10.1016/j.quascirev.2010.01.010.

Gràcia, E., Bartolome, R., Lo Iacono, C., Moreno, X., Stich, D., Martínez-Diaz, J.J., Bozzano, G., Martínez-Loriente, S., Perea, H., Diez, S., Masana, E., Dañobeitia, J.J., Tello, O., Sanz, J.L., et al., 2012, Acoustic and seismic imaging of the Adra Fault (NE Alboran Sea): in search of the source of the 1910 Adra earthquake: Natural Hazards and Earth System Science, v. 12, no. 11, p. 3255–3267, doi: 10.5194/nhess-12-3255-2012.

Gràcia, E., Bartolome, R., Perea, H., Moreno, X., Gómez de la Peña, L., Ranero, C.R., Lo Iacono, C., Martínez-Loriente, S., Diez, S., Masana, E. and Dañobeitia, J. ,2014, Seismic hazard of active faults in the Alborán sea inferred from submarine paleosismology. In: Una aproximación multidisciplinar al estudio de las fallas activas, los terremotos y el riesgo sísmico, 101-104. IGME.

Gràcia, E., Grevemeyer, I., Perea, H, Bartolomé, R., Martínez-Lorinete, S., Villaseñor, A., Ranero, C., Gómez de la Peña., L., Diez, S., d'Acremont, E., Rabaute, A., submission 2017, Earthquake crisis alerts of significant hazard along an overlooked submarine fault system: Nat. Geo.

Grevemeyer, I., Ranero, C.R., Leuchters, W., Pesquer, D., Booth-Rea, G., and Gallart, J., 2011, Seismic constraints on the nature of crust in the Algerian-Balearic Basin - implications for lithospheric construction at back-arc spreading centres: AGU Fall Meeting Abstracts,.

Grion, S., Exley, R., Manin, M., Miao, X.G., Pica, A., Wang, Y., Granger, P.Y., and Ronen, S., 2007, Mirror imaging of OBS data: First Break, v. 25, no. 11, p. 37–4.2, doi: 10.3997/1365-2397.2007028.

Gueguen, E., Doglioni, C., and Fernandez, M., 1998, On the post-25 Ma geodynamic evolution of the western Mediterranean: Tectonophysics, v. 298, no. 1–3, p. 259–269, doi: 10.1016/S0040-1951(98)00189-9.

Gutscher, M.A., Malod, J., Rehault, J.P., Contrucci, I., Klingelhoefer, F., Mendes-Victor, L., and Spakman, W., 2002, Evidence for active subduction beneath Gibraltar: Geology, v. 30, no. 12, p. 1071–1074, doi: 10.1130/0091-7613(2002)030<1071:EFASBG>2.0.CO;2.

Gutscher, M.A., Dominguez, S., Westbrook, G.K., Le Roy, P., Rosas, F., Duarte, J.C., Terrinha, P., Miranda, J.M., Graindorge, D., Gailler, A., Sallares, V., and Bartolome, R., 2012, The Gibraltar subduction: A decade of new geophysical data: Tectonophysics, v. 574–575, p. 72–91, doi: 10.1016/j.tecto.2012.08.038.

Guzman Vendrell, M., 2015, Understanding the proceses that controlled rifting of the Tyrrhenian Basin. Doctoral Thesis, Universitat de Barcelona, 299 p.

Hamblin, W.K., 1992, Earth's dynamic systems: Mcmillan publishing company.

Hamilton, W., 1979, Tectonics of the Indonesian Region: Geological Society of Malaysia, Bulletin, v. 6, no. July, p. 3–10.

Haskey, P., and Ashdown, J., 1991, Transform techniques applied to the attenuation of long period multiples: Exploration geophysics, v 22 , p. 165–168.

Heezen, B.C., 1960, The Rift in the Ocean Floor: Scientific American, v. 203, no. 4, p. 98–110, doi: 10.1038/scientificamerican1060-98.

Hergert, T., and Heidbach, O., 2010, Slip-rate variability and distributed deformation in the Marmara Sea fault system: Nature Geoscience, v. 3, no. 2, p. 132–135, doi: 10.1038/ngeo739.

Hess, H.H., 1962, History of Ocean Basins: Pretrologic studies: A volume to honor A.F. Buddington, v. November, p. 599–620.

Heuret, A., and Lallemand, S., 2005, Plate motions, slab dynamics and back-arc deformation: Physics of the Earth and Planetary Interiors, v. 149, no. 1–2, p. 31–51, doi: 10.1016/j.pepi.2004.08.022.

Hoernle, K., van den Bogaard, P., Duggen, S., Mocek, B., and Garbe-Schönberg, D., 1999, Evidence for Miocene subduction beneath the Alboran Sea: 40Ar/39Ar dating and geochemistry of volcanic rocks from Holes 977A and 978A: Proceedings of the ocean drilling program, v. 161, p. 357–373, doi: 10.2973/odp.proc.sr.161.264.1999.

Hoernle, K., Zhang, Y.-S., and Graham, D., 1995, Seismic and geochemical evidence for large-scale mantle upwelling beneath the eastern Atlantic and western and central Europe: Nature, v. 374, no. 6517, p. 34–39, doi: 10.1038/374034a0.

Hsü, K. J., Cita, M. B., Ryan, W.B.F., 1973. The Origin of the Mediterranean Evaporites. In Ryan, W.B.F, Hsu, K. J., et al., Init. Repts. DSDP, 13, Pt. 2: Washington (U.S. Govt. Printing Office), 1203-1231.

Hsü, K.J., Montadert, L., Bernoulli, D., Cita, M.B., Erickson, A., Garrison, R.E., Kidd, R.B., Melieres, F., Müller, C., and Wright, R., 1977, History of the Mediterranean salinity crisis: Nature, v. 267, no. 2, p. 399–403.

Hudec, M.R., Jackson, M.P, 2007. Terra infirma: Understanding salt tectonics. Earth-Science Rev. 82, 1–28. doi:10.1016/j.earscirev.2007.01.001.

Iribarren, L., Vergés, J., Camurri, F., Fullea, J., and Fernàndez, M., 2007, The structure of the Atlantic-Mediterranean transition zone from the Alboran Sea to the Horseshoe Abyssal Plain (Iberia-Africa plate boundary): Marine Geology, v. 243, no. 1–4, p. 97–119, doi: 10.1016/j.margeo.2007.05.011.

Isacks, B., Oliver, J., and Sykes, L.R., 1968, Seismology and the new global tectonics: Journal of Geophysical Research, v. 73, no. 18, p. 5855–5899, doi: 10.1029/JB073i018p05855.

Ishibashi, J., and Urabe, T., 1995, Hydrothermal activity related to arc-backar magamtis in the western Pacific, in Taylor, B. ed., Back-Arc Basins: Tectonics and Magmatism, Plenum Press, p. 451–495.

Jolivet, L., and Faccenna, C., 2000, Mediterranean extension and the Africa-Eurasia collision: Tectonics, v. 19, no. 6, p. 1095–1106.

Jolivet, L., Faccenna, C., and Piromallo, C., 2009, From mantle to crust: Stretching the Mediterranean: Earth and Planetary Science Letters, v. 285, no. 1–2, p. 198–209, doi: 10.1016/j.epsl.2009.06.017.

Jolivet, L., Frizon de Lamotte, D., Mascle, A., and Seranne, M., 1999, The Mediterranean Basins: Tertiary Extension within the Alpine Orogen - an introduction: Geological Society, London, Special Publications, v. 156, no. 1, p. 1–14, doi: 10.1144/GSL.SP.1999.156.01.02.

Juan, C., Ercilla, G., Javier Hernández-Molina, F., Estrada, F., Alonso, B., Casas, D., García, M., Farran, M., Llave, E., Palomino, D., Vázquez, J.T., Medialdea, T., Gorini, C., D'Acremont, E., et al., 2016, Seismic evidence of current-controlled sedimentation in the Alboran Sea during the Pliocene and Quaternary: Palaeoceanographic implications: Marine Geology, doi: 10.1016/j.margeo.2016.01.006.

Jurado, M.J., and Comas, M.C., 1992, Well log interpretation and seismic character of the Cenozoic sequence in the norhtern Alboran Sea: Geo-Marine Letters, v. 12, p. 129–136.

Kay, S.M., and Kay, R.W., 1985, Role of crystal cumulates and the oceanic crust in the formation of the lower crust of the Aleutian arc.: Geology, v. 13, no. 7, p. 461–464, doi: 10.1130/0091-7613(1985)13<461:ROCCAT>2.0.CO;2.

Kearey, P., Klepeis, K.A., and Vine, F.J., 2009, Global tectonics (Wiley-Blackwell, Ed.).

Kelley, S.P., and Platt, J., 1999, Ar-Ar dating of biotite and muscovite from Alboran basement samples, site 976: Proceedings of the Ocean Drilling Program. Scientific results, v. 161, p. 301–305, doi: 10.2973/odp.proc.sr.161.215.1999.

Koulali, A., Ouazar, D., Tahayt, A., King, R.W., Vernant, P., Reilinger, R.E., McClusky, S., Mourabit, T., Davila, J.M., and Amraoui, N., 2011, New GPS constraints on active deformation along the Africa-Iberia plate boundary: Earth and Planetary Science Letters, v. 308, no. 1–2, p. 211–217, doi: 10.1016/j.epsl.2011.05.048.

Krautworst, U.M.R., and Brachert, T.C., 2003, Sedimentary facies during early stages of flooding in an extensional basin: The Brèche Rouge de Carboneras (Late Miocene, Almería/SE Spain): International Journal of Earth Sciences, v. 92, no. 4, p. 610–623, doi: 10.1007/s00531-003-0337-8.

Krijgsman, W., Hilgen, F.J., Raffi, I., Sierro, F.J., and Wilson, D.S., 1999, Chronology, causes and progression of the Messinian salinity crisis: Nature, v. 400, no. 6745, p. 652–655, doi: 10.1038/23231.

Kushiro, B.I., 2007, Origin of magmas in subduction zones : Proc. Jpn. Acad. Ser. B. v. 83, no. 1, p. 1–15.

Lafosse, M., d'Acremont, E., Rabaute, A., Mercier de Lépinay, B., Tahayt, A., Ammar, A., and Gorini, C., 2016, Evidence of quaternary transtensional tectonics in the Nekor basin (NE Morocco): Basin Research, p. 1–20, doi: 10.1111/bre.12185.

Lavé, J., and Avouac, J.P., 2000, Active folding of fluvial terraces across the Siwaliks Hills , Himalayas of central Nepal: Journal of Geophysical Research. v. 105, p. 5735–5770.

Le Pichon, X., 1968, Sea-floor spreading and continental drift: Journal of Geophysical Research, v. 73, no. 12, p. 3661–3697, doi: 10.1029/JB073i012p03661.

Lemiszki, P.J., and Brown, L.D., 1988, Variable Crustal Structure of Strike-Slip-Fault Zones as Observed on Deep Seismic-Reflection Profiles: Geological Society of America Bulletin, v. 100, no. 5, p. 665–676, doi: 10.1130/0016-7606(1988)100<0665:VCSOSS>2.3.CO;2.

Leprêtre, A., Klingelhoefer, F., Graindorge, D., Schnurle, P., Beslier, M.O., Yelles, K., Déverchère, J., and Bracene, R., 2013, Multiphased tectonic evolution of the Central Algerian margin from combined wide-angle and reflection seismic data off Tipaza, Algeria: Journal of Geophysical Research: Solid Earth, v. 118, no. 8, p. 3899–3916, doi: 10.1002/jgrb.50318.

Lester, R., and McIntosh, K., 2012, Multiple attenuation in crustal-scale imaging: examples from the TAIGER marine reflection data set: Marine Geophysical Research, doi: 10.1007/s11001-012-9149-1.

Levander, A, Bezada, M.J., Niu, F., Humphreys, E.D., Palomeras, I., Thurner, S.M., Masy, J., Schmitz, M., Gallart, J., Carbonell, R., and Miller, M.S., 2014, Subduction-driven recycling of continental margin lithosphere: Nature, v. 515, no. 7526, p. 253–256, doi: 10.1038/nature13878.

Liner, C.L., 1999, Tutorial Concepts of normal and dip moveout: Geophysics. v. 64, no. 5, p. 1637–1647.

Lo Iocano, C., Mateo, M.A., Gràcia, E., Guasch, L., Carbonell, R., Serrano, L., Serrano, O., and Dañobeitia, J., 2008, Very high-resolution seismo-acoustic imaging of seagrass meadows (Mediterranean Sea): Implications for carbon sink estimates: Geophysical Research Letters, v. 35, no. 18, p. 1–5, doi: 10.1029/2008GL034773.

Lobo F.J., Ercilla, G., Fernández-Salas, L.M., Gámez, D., 2014. Chapter 11: The Iberian Mediterranean shelves, in: Chiocci, F. L., Chivas, A.R. (Ed.), Continental Shleves of the World: Their Evolution During the Last Glacio-Eustatic Cycle. The Geological Society of London, Memoirs, 41, pp. 147–170.

Lofi, J., Déverchère, J., Gorini, C., Gaullier, V., Giller, H., Guennoc, P., Loncke, L., Maillard, A., Sage, F., and Thinon, I., 2011, Atlas of the Messinian Salinity Crisis markers in the Mediterranean and Black Seas.: Seas Mémoires de la Société géologique de Frace 179. World Geological Map Commission.

Mauffret, A., Ammar, A., Gorini, C., Jabour, H., 2007. The Alboran Sea (Western Mediterranean) revisited with a view from the Moroccan Margin. Terra Nov. 19, 195–203. doi:10.1111/j.1365-3121.2007.00734.x.

Lonergan, L., 1993, Timing and kinematics of deformation in the Malaguide complex, internal zone of the Betic Coridllera, Southeast Spain. Tectonics, v. 12, no. 2, p. 460–476.

Lonergan, L., and White, N., 1997, Origin of the Betic-Rif mountain belt: Tectonics, v. 16, no. 3, p. 504–522.

Lowrie, W., 2007, Fundamentals of geophysics: Cambridge University Press, 393 p.

Lustrino, M., Duggen, S., and Rosenberg, C.L., 2011, The Central-Western Mediterranean: Anomalous igneous activity in an anomalous collisional tectonic setting: Earth-Science Reviews, v. 104, no. 1–3, p. 1–40, doi: 10.1016/j.earscirev.2010.08.002.

Maldonado, A., Somoza, L., and Pallarés, L., 1999, The Betic orogen and the Iberian-African boundary in the Gulf of Cadiz: Geological evolution (central North Atlantic): Marine Geology, v. 155, no. 1–2, p. 9–43, doi: 10.1016/S0025-3227(98)00139-X.

Mancilla, F. de L., and Diaz, J., 2015, High resolution Moho topography map beneath Iberia and Northern Morocco from receiver function analysis: Tectonophysics, v. 663, p. 203–211, doi: 10.1016/j.tecto.2015.06.017.

Mancilla, F. de L., Booth-Rea, G., Stich, D., Pérez-Peña, J.V., Morales, J., Azañón, J.M., Martin, R., and Giaconia, F., 2015, Slab rupture and delamination under the Betics and Rif constrained from receiver functions: Tectonophysics, v. 663, p. 225–237, doi: 10.1016/j.tecto.2015.06.028.

Maraj, S., 2011, Applications of the tau-p Inversion Method: Theoretical seismology.

Marchesi, C., Garrido, C.J., Bosch, D., Bodinier, J.L., Hidas, K., Padrón-Navarta, J.A., and Gervilla, F., 2012, A Late Oligocene Suprasubduction Setting in the Westernmost Mediterranean Revealed by Intrusive Pyroxenite Dikes in the Ronda Peridotite (Southern Spain): The Journal of Geology, v. 120, no. 2, p. 237–247, doi: 10.1086/663875.

Marrett, R., and Allmendinger, R.W., 1992, Amount of extension on "small' faults: an example from the Viking graben: Geology, v. 20, no. 1, p. 47–50, doi: 10.1130/0091-7613(1992)020<0047:AOEOSF>2.3.CO.

Martín, J.M., Braga, J.C., Betzler, C., 2003. Late Neogene - Recent uplift of the Cabo de Gata volcanic province, Almería, SE Spain. Geomorphology 50, 27–42. doi:10.1016/S0169-555X(02)00206-4.

Martín, R., Stich, D., Morales, J., and Mancilla, F., 2015, Moment tensor solutions for the Iberian-Maghreb region during the IberArray deployment (2009-2013): Tectonophysics, v. 663, p. 261–274, doi: 10.1016/j.tecto.2015.08.012.

Martínez del Olmo, W., and Comas, C., 2008, Arquitectura sísmica, olistostromas y fallas extensionales en el norte de la cuenca oeste del mar de Alborán: Revista de la Sociedad Geológica de España, v. 21, p. 151–167.

Martinez, F., Okino, K., Ohara, Y., Reysenbach, A.-L., and Goffredi, S., 2007, Back-Arc Basins: Oceanography, v. 20, no. 1, p. 116–127, doi: 10.5670/oceanog.2007.85.

Martínez-García, P., Soto, J.I., and Comas, M., 2011, Recent structures in the Alboran Ridge and Yusuf fault zones based on swath bathymetry and sub-bottom profiling: Evidence of active tectonics: Geo-Marine Letters, v. 31, no. 1, p. 19–36, doi: 10.1007/s00367-010-0212-0.

Martínez-García, P., 2012, Recent tectonic evolution of the Alboran Ridge and Yusuf regions: Doctoral Thesis, Universidad de Granada, 276 p.

Martínez-García, P., Comas, M., Soto, J.I., Lonergan, L., and Watts, A. B., 2013, Strike-slip tectonics and basin inversion in the Western Mediterranean: the Post-Messinian evolution of the Alboran Sea: Basin Research, v. 25, no. 4, p. 361–387, doi: 10.1111/bre.12005.

Martínez-Loriente, S., Gràcia, E., Bartolome, R., Sallarès, V., Connors, C., Perea, H., Lo Iacono, C., Klaeschen, D., Terrinha, P., Dañobeitia, J.J., and Zitellini, N., 2013, Active deformation in old oceanic lithosphere and significance for earthquake hazard: Seismic imaging of the Coral Patch Ridge area and neighboring abyssal plains (SW Iberian Margin): Geochemistry, Geophysics, Geosystems, v. 14, no. 7, p. 2206–2231, doi: 10.1002/ggge.20173.

Martinez-Loriente, S., Bartolome, R., Perea, H., Klaeschen, D., Zitellini, N., Wynn, R.B., and Masson, D.G., 2016, Morphostructure, tectono-sedimentary evolution and seismic potential of the Horseshoe Fault, SW Iberian Margin: , no. 5, p. 1–19, doi: 10.1111/bre.12225.

Martínez-Martínez, J.M., Soto, J.I., and Balanyá, J.C., 2002, Orthogonal folding of extensional detachments: Structure and origin of the Sierra Nevada elongated dome (Betics, SE Spain): Tectonics, v. 21, no. 3, doi: 10.1029/2001TC001283.

Martínez-Martínez, J.M., Booth-Rea, G., Azañón, J.M., Torcal, F., 2006. Active transfer fault zone linking a segmented extensional system (Betics, southern Spain): Insight into heterogeneous extension driven by edge delamination. Tectonophysics 422, 159–173. doi:10.1016/j.tecto.2006.06.001.

Mauffret, A., Ammar, A., Gorini, C., and Jabour, H., 2007, The Alboran Sea (Western Mediterranean) revisited with a view from the Moroccan Margin: Terra Nova, v. 19, no. 3, p. 195–203, doi: 10.1111/j.1365-3121.2007.00734.x.

Mauffret, a., Frizon de Lamotte, D., Lallemant, S., Gorini, C., and Maillard, A., 2004, E-W opening of the Algerian Basin (Western Mediterranean): Terra Nova, v. 16, no. 5, p. 257–264, doi: 10.1111/j.1365-3121.2004.00559.x.

Mauffret, A., 2007, The Northwestern (Maghreb) boundary of the Nubia (Africa) Plate: Tectonophysics, v. 429, no. 1–2, p. 21–44, doi: 10.1016/j.tecto.2006.09.007.

Maury, R., Fourcade, S., Coulon, C., El Azzouzi, M., Bellon, H., Coutelle, A., Ouabadi, A., Semroud, B., Megartsi, M., Cotten, J., Belanteur, O., Louni-Hacini, A., Piqué, A., Capdevila, R., et al., 2000, Post-collisional Neogene magmatism of the Mediterranean Maghreb margin: A consequence of slab breakoff: Comptes Rendus de l'Academie de Sciences - Serie IIa: Sciences de la Terre et des Planetes, v. 331, no. 3, p. 159–173, doi: 10.1016/S1251-8050(00)01406-3.

Mazzoli, S., and Helman, M., 1994, Neogene patterns of relative plate motion for Africa-Europe: some implications for recent central Mediterranean tectonics: Geologische Rundschau, v. 83, no. 2, p. 464–468, doi: 10.1007/BF00210558.

McCaffrey, R., 2009, The Tectonic Framework of the Sumatran Subduction Zone: Annual Review of Earth and Planetary Sciences, v. 37, no. 1, p. 345–366, doi: 10.1146/annurev.earth.031208.100212.

McClusky, S., Reilinger, R., Mahmoud, S., Ben Sari, D., and Tealeb, A., 2003, GPS contraints on Africa and Arabi plate motions: Geophys.J.Int., v. 155, p. 126–138.

Medaouri, M., Bracene, R., Deverchere, J., Graindorge, D., Ouabadi, A., and Yelles-Chaouche, A.K., 2012, Structural styles and neogene petroleum system around the Yusuf-Habibas ridge (Alboran basin, Mediterranean sea): The Leading Edge, v. Special se, p. 776–785.

Medaouri, M., Déverchère, J., Graindorge, D., Bracene, R., Badji, R., Ouabadi, A., Yelles-Chaouche, K., and Bendiab, F., 2014, The transition from Alboran to Algerian basins (Western Mediterranean Sea): Chronostratigraphy, deep crustal structure and tectonic evolution at the rear of a narrow slab rollback system: Journal of Geodynamics, v. 77, p. 186–205, doi: 10.1016/j.jog.2014.01.003.

Medina, F., and Cherkaoui, T.-E., 2017, The South-Western Alboran Earthquake Sequence of January-March 2016 and Its Associated Coulomb Stress Changes: Open Journal of Earthquake Research, v. 6, no. 1, p. 35–54, doi: 10.4236/ojer.2016.61002.

Meghraoui, M., and Pondrelli, S., 2012, Active faulting and transpression tectonics along the plate boundary in North Africa: Annals of Geophysics, v. 55, no. 5, p. 955–967, doi: 10.4401/ag-4970.

Michard, A., de Lamotte, D.F., Saddiqi, O., and Chalouan, A., 2008, Continental Evolution: The Geology of Morocco:

Milia, A., and Torrente, M.M., 2015, Tectono-stratigraphic signature of a rapid multistage subsiding rift basin in the Tyrrhenian-Apennine hinge zone (Italy): A possible interaction of upper plate with subducting slab: Journal of Geodynamics, v. 86, p. 42–60, doi: 10.1016/j.jog.2015.02.005.

Monk, D. J. (1993), Wave-Equation Multiple Suppression using constrained gross equalization. Geophysical prospecting 41, 725-736.

Monna, S., Argnani, A., Cimini, G.B., Frugoni, F., and Montuori, C., 2015, Constraints on the geodynamic evolution of the Africa-Iberia plate margin across the Gibraltar Strait from seismic tomography: Geoscience Frontiers, v. 6, no. 1, p. 39–48, doi: 10.1016/j.gsf.2014.02.003.

Monna, S., Cimini, G.B., Montuori, C., Matias, L., Geissler, W.H., and Favali, P., 2013, New insights from seismic tomography on the complex geodynamic evolution of two adjacent domains: Gulf of Cadiz and Alboran Sea: Journal of Geophysical Research: Solid Earth, v. 118, no. 4, p. 1587–1601, doi: 10.1029/2012JB009607.

Morel, J.L., and Meghraoui, M., 1996, Goringe-Alboran-Tell tectonic zone: A transpression system along the Africa-Eurasia plate boundary: Geology, v. 24, no. 8, p. 755–758, doi: 10.1130/0091-7613(1996)024<0755:GATTZA>2.3.CO;2.

Moreno, X., 2011: Neotectonic and Paleoseismic onshore-offshore integrated study of the Carboneras Fault (Eastern Betics, SE Iberia). Doctoral Thesis. Universitat de Barcelona, 283 pages.

Moreno, X., Gràcia, E., Bartolome, R., Martínez-Loriente, S., Perea, H., Gómez de la Peña, L., Iacono, C. Lo, Piñero, E., Pallà s, R., Masana, E., and Dañobeitia, J.J., 2016, Seismostratigraphy and tectonic architecture of the Carboneras Fault offshore based on multiscale seismic imaging: Implications for the Neogene evolution of the NE Alboran Sea: Tectonophysics, v. 689, p. 115–132, doi: 10.1016/j.tecto.2016.02.018.

Morgan, W.J., 1968, Rises, trenches, great faults, and crustal blocks: Journal of Geophysical Research, v. 73, no. 6, p. 1959–1982.

Nocquet, J. M., 2012. Present-day kinematics of the Mediterranean: A comprehensive overview of GPS results. Tectonophysics 579, 220–242. doi:10.1016/j.tecto.2012.03.037.

Noda, A., 2013, Strike-Slip Basin – Its Configuration and Sedimentary Facies: Mechanism of Sedimentary Basin Formation - Multidisciplinary Approach on Active Plate Margins, doi: 10.5772/56593.

Noda, A., 2016, Forearc basins: Types, geometries, and relationships to subduction zone dynamics: Geological Society of America Bulletin, v. 128, no. 5/6, p. B31345.1, doi: 10.1130/B31345.1.

Palano, M., González, P.J., and Fernández, J., 2015, The Diffuse Plate boundary of Nubia and Iberia in the Western Mediterranean: Crustal deformation evidence for viscous coupling and fragmented lithosphere: Earth and Planetary Science Letters, v. 430, p. 439–447, doi: 10.1016/j.epsl.2015.08.040.

Palomeras, I., Thurner, S., Levander, A., Liu, K., Villasenor, A., Carbonell, R., and Harnafi, M., 2014, Finite-frequency Rayleigh wave tomography of the western Mediterranean: Mapping its lithospheric structure: Geochemistry, Geophysics, Geosystems, v. 15, no. 1, p. 140–160, doi: 10.1002/2013GC004861.

Palomino, D., Vázquez, J.T., Ercilla, G., Alonso, B., López-González, N., and Díaz-del-Río, V., 2011, Interaction between seabed morphology and water masses around the seamounts on the Motril Marginal Plateau (Alboran Sea, Western Mediterranean): Geo-Marine Letters, v. 31, no. 5–6, p. 465–479, doi: 10.1007/s00367-011-0246-y.

Pasyanos, M.E., and Nyblade, A.A., 2007, A top to bottom lithospheric study of Africa and Arabia: Tectonophysics, v. 444, no. 1–4, p. 27–44, doi: 10.1016/j.tecto.2007.07.008.

Pearce, J.., and Peate, D.W., 1995, Tectonic implications of the composition of volcanic arc magmas: Annu. Rev. Earth Planet. Sci., v. 23, p. 251–85.

Peizhen Zhang, Burchfiel, B.C., Shefa Chen, and Qidong Deng, 1989, Extinction of pull-apart basins: Geology, v. 17, no. 9, p. 814–817, doi: 10.1130/0091-7613(1989)017<0814:EOPAB>2.3.CO;2.

Perea, H., Gràcia, E., Bartolome, R., Martínez-Loriente, S., Gómez de la Peña, L., Lo Iacono, C., Díez, S., Tello, O., Gómez-Ballesteros, M., de Mol, B., and Dañobeitia, J., 2016, Active deformation and seismogenic characterization of secondary faults in the Alboran Sea constrained by high-resolution bathymetry and seismic data., in AGU Fall Meeting, San Francisco.

Pérez-Belzuz, F., Alonso, B., and Ercilla, G., 1997, History of mud diapirism and trigger mechanisms in the Western Alboran Sea: Tectonophysics, v. 282, no. 1–4, p. 399–422, doi: 10.1016/S0040-1951(97)00226-6.

Pérez-Hernández, S., Comas, M.C., Escutia, C., Martínez-García, P., 2009: The Águilas Submarine Slides (Palomares Margin, Western Mediterranean). Geogaceta 47, 93-96.

Pérez-Hernández, S., Comas, M.C., Escutia, C., 2014. Morphology of turbidite systems within an active continental margin (the Palomares Margin, western Mediterranean). Geomorphology 219, 10–26. doi:10.1016/j.geomorph.2014.04.014.

Pérez-Peña, J.V., Azañón, J.M., Azor, A., Booth-Rea, G., Galve, J.P., Roldán, F.J., Mancilla, F., Giaconia, F., Morales, J., and Al-Awabdeh, M., 2015, Quaternary landscape evolution driven by slab-pull mechanisms in the Granada Basin (Central Betics): Tectonophysics, v. 663, p. 5–18, doi: 10.1016/j.tecto.2015.07.035.

Platt, J.., Kelley, S.P., Carter, A., and Orozco, M., 2005, Timing of tectonic events in the Alpujárride Complex, Betic Cordillera, southern Spain: Journal of Geological Society, London, v. 162, p. 451–462.

Platt, J.P., Allerton, S., Kirker, A., Mandeville, C., Mayfield, A., Platzman, E.S., and Rimi, A., 2003, The ultimate arc: Differential displacement, oroclinal bending, and vertical axis rotation in the External Betic-Rif arc: Tectonics, v. 22, no. 3, doi: 10.1029/2001TC001321.

Platt, J.P., Anczkiewicz, R., Soto, J.I., Kelley, S.P., and Thirlwall, M., 2006, Early Miocene continental subduction and rapid exhumation in the western Mediterranean: Geology, v. 34, no. 11, p. 981–984, doi: 10.1130/G22801A.1.

Platt, J.P., and Vissers, R.L.M., 1989, Extensional collapse of thikened continental lithosphere: A working hipothesis for the Alboran Sea and Gibraltar Arc: Geology, v. 17, p. 540–543.

Platt, J.P., Behr, W.M., Johanesen, K., and Williams, J.R., 2013, The Betic-Rif Arc and Its Orogenic Hinterland: A Review: Annual Review of Earth and Planetary Sciences, v. 41, no. 1, p. 313–357, doi: 10.1146/annurev-earth-050212-123951.

Platt, J.P., Soto, J.I., Comas, M.C., and Party, L. 161 S.S., 1996, Decompression and high-temperature - low-pressure metamorphism in the exhumed floor of an extensional basin, Alboran Sea, western Mediterranean.: Geology, v. 24, p. 450–477.

Pownall, J.M., Hall, R., and Lister, G.S., 2016, Rolling open Earth's deepest forearc basin: Geology, v. 44, no. 11, p. 947–950, doi: 10.1130/G38051.1.

Prada, M, 2014, The structure and formation of the Tyrrhenian basin in the Western Mediterranean back-arc setting. Doctoral Thesis, Barcelona University, 294 p.

Quintana, L., Pulgar, J.A., and Alonso, J.L., 2015, Displacement transfer from borders to interior of a plate: A crustal transect of Iberia: Tectonophysics, v. 663, p. 378–398, doi: 10.1016/j.tecto.2015.08.046.

Ranero, C.R., Von Huene, R., Flueh, E., Duarte, M., Baca, D., and McIntosh, K., 2000, A cross section of the convergent Pacific margin of Nicaragua: Tectonics, v. 19, no. 2, p. 335–357, doi: 10.1029/1999TC900045.

Rehault, J.-P., Boillot, G., and Mauffret, A., 1984, The Western Mediterranean Basin geological evolution: Marine Geology, v. 55, no. 3–4, p. 447–477, doi: 10.1016/0025-3227(84)90081-1.

Rodriguez, M., Fournier, M., Chamot-Rooke, N., Huchon, P., Bourget, J., Sorbier, M., Zaragosi, S., and Rabaute, A., 2011, Neotectonics of the Owen Fracture Zone (NW Indian Ocean): Structural evolution of an oceanic strike-slip plate boundary: Geochemistry, Geophysics, Geosystems, v. 12, no. 12, p. 1–24, doi: 10.1029/2011GC003731.

Rodriguez, M., Maleuvre, C., Jollivet-Castelot, M., D'acremont, E., Rabaute, A., Lafosse, M., Ercilla, G., Vázquez, J.T., Alonso, B., Ammar, A., and Gorini, C., 2017, Tsunamigenic submarine landslides along the Xauen–Tof no banks in the Alboran Sea (Western Mediterranean Sea): Geophysical Journal International, , no. January, doi: 10.1093/gji/ggx028.

Rodríguez-Fernández, J., Comas, M.C., Soria, J., Martín-Pérez, J.A., and Soto, J.I., 1999, 5. The sedimentary record of the alboran basin: an attempt at sedimentary sequence correlation and subsidence analysis: Proceedings of the Ocean Drilling Program, Scientific Results, v. 161, p. 69–76.

Rohling, E.J., Schiebel, R., and Siddall, M., 2008, Controls on Messinian Lower Evaporite cycles in the Mediterranean: Earth and Planetary Science Letters, v. 275, no. 1–2, p. 165–171, doi: 10.1016/j.epsl.2008.08.022.

Ronen, S., Comeaux, L., and Mioa, X., 2005, Imaging Downgoing waves from Ocean Bottom Stations: 75th Annual International Meeting, SEG, Expanded Abstracts.

Rosenbaum, G., Lister, G.S., and Duboz, C., 2002, Reconstruction of the tectonic evolution of the western Mediterranean since the Oligocene: Journal of the Virtual Explorer, v. 8, p. 107–126.

Rouchy, J.M., and Caruso, A., 2006, The Messinian salinity crisis in the Mediterranean basin: A reassessment of the data and an integrated scenario: Sedimentary Geology, v. 188–189, p. 35–67, doi: 10.1016/j.sedgeo.2006.02.005.

Roveri, M., Flecker, R., Krijgsman, W., Lofi, J., Lugli, S., Manzi, V., Sierro, F.J., Bertini, A., Camerlenghi, A., De Lange, G., Govers, R., Hilgen, F.J., Hübscher, C., Th Meijer, P., et al., 2014, The Messinian Salinity Crisis: Past and future of a great challenge for marine sciences: Marine Geology, v. 352, p. 25–58, doi: 10.1016/j.margeo.2014.02.002.

Royden, L.H., 1993, Evolution of retreating subduction boundaries formed during continental collision: Tectonics, v. 12, no. 3, p. 629–638, doi: 10.1029/92TC02641.

Rutter, E.H., Faulkner, D.R., and Burgess, R., 2012, Structure and geological history of the Carboneras Fault Zone, SE Spain: Part of a stretching transform fault system: Journal of Structural Geology, v. 45, p. 68–86, doi: 10.1016/j.jsg.2012.08.009.

Sage, F., Gronefeld, G. Von, Déverchère, J., Gaullier, V., Maillard, A., and Gorini, C., 2005, Seismic evidence for Messinian detrital deposits at the western Sardinia margin, northwestern

Mediterranean: Marine and Petroleum Geology, v. 22, p. 757–773, doi: 10.1016/j.marpetgeo.2005.03.007.

Sallarés, V., Gailler, A., Gutscher, M.-A., Graindorge, D., Bartolome, R., Gracia, E., Díaz, J., Doñabeitia, J., Zitellini, N., 2011, Seismic evidence for the presence of Jurassic oceanic crust in the central Gulf of Cadiz (SW Iberian margin): Earth Planet. Sci. Lett. 311, 112–123.

Sanz De Galdeano, C., 1990, Geologic evolution of the Betic Cordilleras in the Western Mediterranean, Miocene to the present: Tectonophysics, v. 172, no. 1–2, p. 107–119, doi: 10.1016/0040-1951(90)90062-D.

Schettino, A., and Turco, E., 2011, Tectonic history of the western Tethys since the Late Triassic: Geological Society of America Bulletin, v. 123, no. 1–2, p. 89–105, doi: 10.1130/B30064.1.

Schettino, A., and Turco, E., 2006, Plate kinematics of the Western Mediterranean region during the Oligocene and Early Miocene: Geophysical Journal International, v. 166, no. 3, p. 1398–1423, doi: 10.1111/j.1365-246X.2006.02997.x.

Scholz, C.H., and Campos, J., 1995, On the mechanism of seismic decoupling and back arc spreading at subduction zones: Journal of Geophysical Research: Solid Earth, v. 100, no. B11, p. 22103–22115, doi: 10.1029/95JB01869.

Seber, D., Barazangi, M., Ibenbrahim, A., and Demnati, A., 1996, Geophysical evidence for lithospheric delamination beneath the Alboran Sea and Rif-Betic mountains: Nature, v. 379, no. 6568, p. 785–790.

Serpelloni, E., Vannucci, G., Pondrelli, S., Argnani, A., Casula, G., Anzidei, M., Baldi, P., and Gasperini, P., 2007, Kinematics of the Western Africa-Eurasia plate boundary from focal mechanisms and GPS data: Geophysical Journal International, v. 169, no. 3, p. 1180–1200, doi: 10.1111/j.1365-246X.2007.03367.x.

Silva, P.G., Goy, J.L., Somoza, L., 1993. Landscape response to strike-slip faulting linked to collisional settings : Quaternary tectonics and basin formation in the Eastern Betics , southeastern Spain 224, 289–303.

Smith, D.K., Cann, J.R., and Escartín, J., 2006, Widespread active detachment faulting and core complex formation near 13 degrees N on the Mid-Atlantic Ridge.: Nature, v. 442, no. 7101, p. 440–3, doi: 10.1038/nature04950.

Smith, P.J., 1973, Topics in geophysics: The Open University Press.

Somoza, L., Medialdea, T., León, R., Ercilla, G., Vázquez, J.T., Farran, M., Hernández-Molina, J., González, J., Juan, C., and Fernández-Puga, M.C., 2012, Structure of mud volcano systems and pockmarks in the region of the Ceuta Contourite Depositional System (Western Alboran Sea): Marine Geology, v. 332–334, p. 4–26, doi: 10.1016/j.margeo.2012.06.002.

Soto, J.I., and Platt, J.P., 1999, Petrological and Structural Evolution of High-Grade Metamorphic Rocks from the Floor of the Alboran Sea Basin , Western Mediterranean: v. 40, no. 1, p. 21–60.

Soto, J.I., Fernández-Ibáñez, F., and Talukder, A.R., 2012, Recent shale tectonics and basin evolution of the NW Alboran Sea: The Leading Edge, p. 768–775.

Soto, J.I., Fernández-Ibáñez, F., Talukder, A.R., and Martínez-García, P., 2010, Miocene Shale Tectonics in the Northern Alboran Sea (Western Mediterranean): AAPG Memories, v. 93, p. 119–144, doi: 10.1306/13231312M933422.

Spakman, W., and Wortel, R., 2004, A tomographic view on Western Mediterranean Geodynamics: The TRANSMED Atlas, The Mediterranean Region from Crust to Mantle, p. 31–52, doi: 10.1007/978-3-642-18919-7_2.

Stein, S., and Wyssession, M., 2003, An introduction to seismology, earthquakes, and earth structure:

Stern, R.J., 2002, Subduction zones: Reviews of Geophysics, v. 40, no. 4, p. 37, doi: 10.1029/2001RG000108.

Stich, D., Ammon, C.J., Morales, J., 2003. Moment tensor solutions for small and moderate earthquakes in the Ibero-Maghreb region. Journal of Geophysical Research, 108, NO. B3, 2148, doi:10.1029/2002JB002057.

Stich, D., Serpelloni, E., de Lis Mancilla, F., and Morales, J., 2006, Kinematics of the Iberia-Maghreb plate contact from seismic moment tensors and GPS observations: Tectonophysics, v. 426, no. 3–4, p. 295–317, doi: 10.1016/j.tecto.2006.08.004.

Stich, D., Martín, R., and Morales, J., 2010, Moment tensor inversion for Iberia-Maghreb earthquakes 2005-2008: Tectonophysics, v. 483, no. 3–4, p. 390–398, doi: 10.1016/j.tecto.2009.12.006.

Stirling, M., M. Gerstenberger, N. Litchfield, G. Mcverry, W. Smith, J. Pettinga, and P. Barnes, 2008, Seismic hazard of the Canterbury region, New Zeland: New earthquake source model and methodology, Bull. New Zel. Soc. Earthq. Eng., 41(2), 51–67.

Strzerzynski, P., Déverchère, J., Cattaneo, A., Domzig, A., Yelles, K., De Lépinay, B.M., Babonneau, N., and Boudiaf, A., 2010, Tectonic inheritance and Pliocene-Pleistocene inversion of the Algerian margin around Algiers: Insights from multibeam and seismic reflection data (Tectonics 29 (TC3099)): Tectonics, v. 29, no. 3, doi: 10.1029/2010TC002716.

Sylvester, A.G., 1988, Strike-slip faults: Geological Society of America Bulletin, , no. November, p. 1–38, doi: 10.1130/0016-7606(1988)100<1666.

Talukder, A. R., Comas, M.C., and Soto, J.I., 2003, Pliocene to Recent mud diapirism and related mud volcanoes in the Alboran Sea (Western Mediterranean): Geological Society, London, Special Publications, v. 216, no. 1, p. 443–459, doi: 10.1144/GSL.SP.2003.216.01.29.

Tandon, K., Lorenzo, J.M., and de La Linde Rubio, J., 1998, Timing of rifting in the Alboran Sea basin: correlation of borehole (ODP Leg 161 and Andalucia A-1) to seismic reflection data: implications for basin formation: Marine Geology, v. 144, p. 275–294.

Tatsumi, Y., Sakuyama, M., Fukuyama, H., and Kushiro, I., 1983, Generation of arc basalt magmas and thermal structure of the mantle wedge in subduction zones: Journal of Geophysical Research, v. 88, no. B7, p. 5815, doi: 10.1029/JB088iB07p05815.

Taylor, B., 1995, Backarc Basins: Tectonics and magmatism (B. Taylor, Ed.): Plenum.

Teixell, A., Bertotti, G., de Lamotte, D.F., and Charroud, M., 2009, The geology of vertical movements of the lithosphere: An overview: Tectonophysics, v. 475, no. 1, p. 1–8, doi: 10.1016/j.tecto.2009.08.018.

Thurner, S., Palomeras, I., Levander, A., Carbonell, R., and Lee, C.T., 2014, Ongoing lithospheric removal in the western Mediterranean: Evidence from Ps receiver functions and thermobarometry of Neogene basalts (PICASSO project): Geochemistry, Geophysics, Geosystems, v. 15, no. 4, p. 1113–1127, doi: 10.1002/2013GC005124.

Torne, M., Fernàndez, M., Comas, M.C., and Soto, J.I., 2000, Lithospheric Structure Beneath the Alboran Basin: Results from 3D Gravity Modeling and Tectonic Relevance: Journal of Geophysical Research, v. 105, no. B2, p. 3209, doi: 10.1029/1999JB900281.

Torres-Roldan, R.L., Poli, G., and Peccerillo, A., 1986, An early Miocene arc-tholeitic magmatic dyke event from the Alboran sea: Evidence for precollision subduction and back-arc crustal extension in the westernmost Mediterranean: Geologische Rundschau, v. 75, p. 219–234.

Tortella, D., Torne, M., and Pérez ‐ Estáun, A., 1997, Geodynamic Evolution of the Eastern Segment of the Azores-Gibraltar Zone: The Gorringe Bank and the Gulf of Cadiz Region: Marine Geophysical Researches, v. 19, no. 3, p. 211–230, doi: 10.1023/A:1004258510797.

Underwood, M.B., Moore, G.F., Taira, A., Klaus, A., Wilson, M.E.J., Fergusson, C.L., Hirano, S., and Steurer, J., 2003, Sedimentary and Tectonic Evolution of a Trench-Slope Basin in the Nankai Subduction Zone of Southwest Japan: Journal of Sedimentary Research, v. 73, no. 4, p. 589–602, doi: 10.1306/092002730589.

Van Hinsbergen, D.J.J., Vissers, R.L.M., and Spakman, W., 2014, Origin and consequences of western Mediterranean subduction, rollback, and slab segmentation: Tectonics, v. 33, no. 4, p. 393–419, doi: 10.1002/2013TC003349.

Van Rensbergen, P., Morley, C.K., Ang, D.W., Hoan, T.Q., and Lam, N.T., 1999, Structural evolution of shale diapirs from reactive rise to mud volcanism : 3D seismic data from the Baram delta , off shore Brunei Darussalam: Journal of the Geological Society, London, v. 156, p. 633–650.

Vergés, J., and Fernández, M., 2012, Tethys-Atlantic interaction along the Iberia-Africa plate boundary: The Betic-Rif orogenic system: Tectonophysics, v. 579, p. 144–172, doi: 10.1016/j.tecto.2012.08.032.

Villaseñor, A., Chevrot, S., Harnafi, M., Gallart, J., Pazos, A., Serrano, I., Córdoba, D., Pulgar, J.A., and Ibarra, P., 2015, Subduction and volcanism in the Iberia-North Africa collision zone from tomographic images of the upper mantle: Tectonophysics, v. 663, p. 238–249, doi: 10.1016/j.tecto.2015.08.042.

Vine, F.J., and Matthews, D.H., 1963, Magnetic Anomalies over Oceanic Ridges: Nature, v. 201, no. 4897, p. 947–949, doi: 10.1038/201591a0.

Vissers, R.L.M., Platt, P., and van der Wal, D., 1995, Late orogenic extension of the Betic Cordillera and the Alboran Domain: A lithosphecir view: Tectonics, v. 14, no. 4, p. 786–803, doi: 10.1029/95TC00086.

von Huene, R., and Scholl, D.W., 1991, Observations at convergent margins concerning sediment subduction, subduction erosion, and the growth of continental crust: Reviews of Geophysics, v. 29, no. 3, p. 279, doi: 10.1029/91RG00969.

Wang, Y, 2003, Multiple subtraction using an expanded multichannel matching filter, Geophysics, 68 (1), 346-356.

Watts, A.B., Platt, J.P., and Buhl, P., 1993, Tectonic evolution of the Alboran Sea basin: Basin Research, v. 5, p. 153–177.

Wegener, A., 1915, The origin of continents and oceans: Courier Corporation.

Wells, D.L., and Coppersmith, K.J., 1994, New empirical relationships among magnitude, rupture length, rupture area and surface displacement: Bull.Seismol.Soc.A., v. 84, p. 974–1002.

Wesnousky, S. G. (2008), Displacement and Geometrical Characteristics of Earthquake Surface Ruptures: Issues and Implications for Seismic-Hazard Analysis and the Process of Earthquake Rupture, Bull. Seismol. Soc. Am., 98(4), 1609–1632, doi:10.1785/0120070111.

Wessel, P., and Smith, W.H.F., 1991, Free software helps map and display data: Eos, Transactions American Geophysical Union, v. 72, no. 41, p. 441–446, doi: 10.1029/90EO00319.

White, N., and McKenzie, D., 1988, Formation of the steer's head'' geometry of sedimentary basins by differential stretching of the crust and mantle: Geology, v. 16, no. 3, p. 250–253, doi: 10.1130/0091-7613(1988)016<0250:FOTSSH>2.3.CO;2.

White, R.S., McKenzie, D., and O'Nions, R.K., 1992, Oceanic crustal thickness from seismic measurements and rare earth element inversions: Journal of Geophysical Research, v. 97, no. B13, p. 19683–19715, doi: 10.1029/92JB01749.

White, S.M., Crisp, J.A., and Spera, F.J., 2006, Long-term volumetric eruption rates and magma budgets: Geochemistry, Geophysics, Geosystems, v. 7, no. 3, doi: 10.1029/2005GC001002.

Whitsmarsh, R.B., Bull, J.M., Rothwell, R.G., and Thomson, J., 1996, The evolution and structure of ocean basins, in Summerhayes, C.. and Thorpe, S.A. eds., Oceanography: An illustrated guide, Manson Publishing Ltd, p. 113–135.

Wilson, J.T., 1963, Hypothesis of Earth's Behaviour: Nature, v. 198, no. 4884, p. 925–929, doi: 10.1038/198925a0.

Wilson, J.T., 1965, A new class of faults and their bearing on continental drift.: Nature, v. 207, no. 4995, p. 343–347, doi: 10.1038/207343a0.

Wortel, M.J., and Spakman, W., 2000, Subduction and slab detachment in the Mediterranean-Carpathian region.: Science (New York, N.Y.), v. 290, no. 5498, p. 1910–1917, doi: 10.1126/science.290.5498.1910.

Wu, J.E., McClay, K., Whitehouse, P., and Dooley, T., 2009, 4D analogue modelling of transtensional pull-apart basins: Marine and Petroleum Geology, v. 26, no. 8, p. 1608–1623, doi: 10.1016/j.marpetgeo.2008.06.007.

Yilmaz, O., 1987, Seismic data analysis: Processing, Inversion and Interpretation of seismic data. Society of Exploration Geophysicists, 2027 p.

Zachariasen, J., and Sieh, K., 2009, The transfer of slip between two en echelon strike-slip faults: A case study from the 199.2 Landers earthquake, southern California: Security, v. 299, no. 5613, p. 1719–1722, doi: 10.1063/1.2978249.

Zeck, H.P., 1999, Alpine plate kinematics in the western Mediterranean: a westward-directed subduction regime followed by slab roll-back and slab detachment: Geological Society, London, Special Publications, v. 156, no. 1, p. 109–120, doi: 10.1144/GSL.SP.1999.156.01.07.

Zitellini, N., Gràcia, E., Matias, L., Terrinha, P., Abreu, M.A., De Alteriis, G., Henriet, J.P., Dañobeitia, J.J., Masson, D.G., Mulder, T., Ramella, R., Somoza, L., Diez, S., 2009, The Quest for the Africa-Eurasia plate boundary west of the Strait of Gibraltar. Earth Planet Sci. Lett., 280, 13-50.

ANNEXES

List of acronyms

a.s.l.: avobe sea level

ABB: Algero-Balearic Basin

AGC: Amplitude Gain Control

AIF: Al-Idrissi Fault system

AR: Alboran Ridge

CDP: Common Depth Point

CF: Carboneras Fault

CMP: Common Mid Point

CRP: Common Reflection Point

DMO: Dip Move Out

DSDP: Deep Sea Drilling Project

EAB: East Alboran Basin

EEZ: Exclusive Economic Zone

EVD: EVENTDEEP profiles

H. Rf.: Hihg reflectivity

HBB: Habibas Basin

ICR: Intra Crustal Reflection

MB: Malaga Basin

MCS: Multichannel Seismic

Mg. B: magmatic basement

Mt. B: Metamorphic basement

NMO: Normal Move Out

OBH: Ocean Bottom Hydrophone

OBS: Ocean Bottom Seismometer

ODP: Ocean Drilling Programme

PB: Pytheas Basin

PF: Palomares Fault

PSDM: Pre-Stack Depth Migration

RV: Research Vessel

SAB: South Alboran Basin

SC deconvolution: Surface Consistent deconvolution

SRME: Surface-Related Multiple Elimination

TM: TOPOMED profiles

TTT: Travel Time Tomography

TWTT: Two Way Travel Time

VB: volcanic basement

WAB: West Alboran Basin

WAS: Wide Angle Seismic

YF: Yusuf Fault system

Scientific output related with this thesis

<u>**Publications**</u>

- ***ISI publications***

Gómez de la Peña, L., Gràcia, E., Muñoz, A., Acosta, J., Gómez-Ballesteros, M., Ranero, C.R, Uchupi, E. (2016): Geomorphology and Neogene tectonic evolution of the Palomares continental margin (Western Mediterranean). *Tectonophysics*, doi: 10.1016/j.tecto.2016.03.009.

Moreno, X., Gràcia, E., Bartolome, R., Martínez-Loriente, S., Perea, H., **Gómez de la Peña, L.**, Lo Iacono, C., Piñero, E., Pallàs, R., Masana, E., Dañobeitia, J.J. (2016): Seismostratigraphy and tectonic architecture of the Carboneras Fault offshore based on multiscale seismic imaging: Implications for the Neogene evolution of the NE Alboran Sea. *Tectonophysics*,doi:10.1016/j.tecto.2016.02.018.

Gràcia, E., Grevemeyer, I., Perea, H, Bartolomé, R., Martínez-Lorinete, S., Villaseñor, A., Ranero, C., **Gómez de la Peña., L.**, Diez, S., d'Acremont, E., Rabaute, A., submission 2017, Earthquake crisis alerts of significant hazard along an overlooked submarine fault system: Nat. Geo.

- ***Non-ISI publications***

Gómez de la Peña, L., Ranero, C.R., Gràcia, E., Bartolome, R. and TopoMed cruise party (2014): Técnicas avanzadas de procesado de datos de sísmica de reflexión multicanal aplicadas a mejorar la visualización de fallas activas del Mar de Alborán. In: Una aproximación multidisciplinar al estudio de las fallas activas, los terremotos y el riesgo sísmico, 229-232. IGME.

Gràcia, E., Bartolome, R., Perea, H., Moreno, X., **Gómez de la Peña, L.**, Ranero, C.R., Lo Iacono, C., Martínez-Loriente, S., Diez, S., Masana, E. and Dañobeitia, J. (2014): Seismic hazard of active faults in the Alborán sea inferred from submarine paleosismology. In: Una aproximación multidisciplinar al estudio de las fallas activas, los terremotos y el riesgo sísmico, 101-104. IGME.

Perea, H., Gràcia, E., Bartolomé, R., **Gómez de la Peña, L.**, Martínez-Loriente, S., Moreno, X., de Mol, B., Tello, O., Ballesteros, M. and EVENT-DEEP cruise party (2014): Evidence of quaternary active faults across the Djibouti High and the Adra Ridge (Alborán Sea). In: Una aproximación multidisciplinar al estudio de las fallas activas, los terremotos y el riesgo sísmico, 97-100. IGME.

<u>**Conference and workshop contributions**</u>

Eulàlia Gràcia, Hector Perea, Rafael Bartolome, Claudio Lo Iacono, Sergio Costa, Susana Diez, Xavier Placaud, Chris Smith, Pablo Rodríguez, Héctor Sánchez, Olivier Quedec, Juanjo Dañobeitia and **SHAKE cruise team (among them Laura Gómez de la Peña)**: First AUV and ROV investigation of seismogenic faults in the Alboran Sea (Western Mediterranean). Martech 2016: Marine Technology Workshop.

Hector Perea, Eulàlia Gràcia, Rafael Bartolomé, Sara Martínez-Loriente, **Laura Gómez de la Peña**, Claudio Lo Iacono, Susana Díez, Olvido Tello, Maria Gómez-Ballesteros, Ben de Mol and Juanjo Dañobeitia: Active deformation and seismogenic characterization of secondary faults in the Alboran Sea constrained by high-resolution bathymetry and seismic data. 2016 AGU Fall Meeting.

C.R. Ranero, E. Gràcia, **L. Gómez de la Peña**, A. Calahorrano, X. García, I. Grevemeyer*:* Miocene formation and Plio-Pleistocene deformation of Gibraltar Arc System. RCMNS Interim Colloquium 2015

L. Gómez de la Peña, C.R. Ranero, E. Gràcia, R. Bartolome and TopoMed cruise party*:* New deep multichannel seismic reflection images from the Alboran Basin: The TOPOMED-GASSIS dataset. EGU General Assembly 2015

L. Gómez de la Peña, C.R. Ranero, E. Gràcia, R. Bartolome and TopoMed cruise party*:* New deep multichannel seismic reflection images from the Alboran Basin (Western Mediterranean): The TOPOMED-GASSIS dataset. Congres de doctorants IPGP, 2015.

L. Gómez de la Peña, C.R. Ranero, E. Gràcia, R. Bartolome and TopoMed cruise party: New deep multichannel seismic reflection images from the Alboran Basin: The TOPOMED-GASSIS dataset.16th SEISMIX International Symposium, 2014.

E. Gràcia, R. Bartolome, H. Perea, **L. Gómez de la Peña**, C.R. Ranero, C. Lo Iacono, S. Martínez-Loriente, X. Moreno, and J. Dañobeitia*:* Seismogenic potential of active faults in the Alborán sea revealed by multiscale seismic imaging. 16th SEISMIX International Symposium, 2014.

C.R. Ranero, E. Gràcia, A. Calahorrano, **L. Gómez de la Peña**, I. Grevemeyer, X. García*:* The Miocene formation and the Pliocene deformation of the Gibraltar Arc System. 16th SEISMIX International Symposium, 2014.

L. Gómez de la Peña, C.R. Ranero, E. Gràcia, R. Bartolome and TopoMed cruise party*:* Técnicas avanzadas de procesado de datos de sísmica de reflexión multicanal aplicadas a mejorar la visualización de fallas activas del Mar de Alborán. Iberfault 2014.

H. Perea, E. Gràcia, R. Bartolomé, **L. Gómez de la Peña**, S. Martínez-Loriente, X. Moreno, B. de Mol, Tello, O., Ballesteros, M. and EVENT-DEEP cruise party*:* Evidence of quaternary active faults across the Djibouti High and the Adra Ridge (Alborán Sea). Iberfault 2014.

E. Gràcia, R. Bartolome, H. Perea, X. Moreno, **L. Gómez de la Peña**, C.R. Ranero, C. Lo Iacono, S. Martínez-Loriente, S. Diez, E. Masana and J. Dañobeitia*:* Seismic hazard of active faults in the Alborán sea inferred from submarine paleosismology. Iberfault 2014.

E. Gràcia, C.R. Ranero, H. Perea, R. Bartolome, C. Lo Iacono, X. Moreno, S. Martínez-Loriente, **L. Gómez de la Peña**, E. Masana, A.K. Yelles*:* Multiscale seismic characterization of active faults in the South-Western Mediterranean and Alboran Basin: Implications for earthquake and tsunami. International Symposium “Commemoration of the Boumerdes earthquake of 21 May 2003”, 2013.

H. Perea, E. Gràcia, R. Bartolomé, C.R. Ranero, C. Lo Iacono, S. Martínez-Loriente, X. Moreno, **L. Gómez de la Peña**, and EVENT-DEEP and TOPOMED-GASSIS teams*:* Multi-scale seismic imaging and evidences of Quaternary activity of the Yussuf fault system (Alboran Sea). International Symposium “Commemoration of the Boumerdes earthquake of 21 May 2003”, 2013.